



HAL
open science

Micromechanical models of network materials presenting internal length scales: applications to trabecular bone under stable and evolutive conditions

Ibrahim Goda

► To cite this version:

Ibrahim Goda. Micromechanical models of network materials presenting internal length scales: applications to trabecular bone under stable and evolutive conditions. Other [cond-mat.other]. Université de Lorraine, 2015. English. NNT : 2015LORR0055 . tel-01751647

HAL Id: tel-01751647

<https://hal.univ-lorraine.fr/tel-01751647v1>

Submitted on 29 Mar 2018

HAL is a multi-disciplinary open access archive for the deposit and dissemination of scientific research documents, whether they are published or not. The documents may come from teaching and research institutions in France or abroad, or from public or private research centers.

L'archive ouverte pluridisciplinaire **HAL**, est destinée au dépôt et à la diffusion de documents scientifiques de niveau recherche, publiés ou non, émanant des établissements d'enseignement et de recherche français ou étrangers, des laboratoires publics ou privés.



AVERTISSEMENT

Ce document est le fruit d'un long travail approuvé par le jury de soutenance et mis à disposition de l'ensemble de la communauté universitaire élargie.

Il est soumis à la propriété intellectuelle de l'auteur. Ceci implique une obligation de citation et de référencement lors de l'utilisation de ce document.

D'autre part, toute contrefaçon, plagiat, reproduction illicite encourt une poursuite pénale.

Contact : ddoc-theses-contact@univ-lorraine.fr

LIENS

Code de la Propriété Intellectuelle. articles L 122. 4

Code de la Propriété Intellectuelle. articles L 335.2- L 335.10

http://www.cfcopies.com/V2/leg/leg_droi.php

<http://www.culture.gouv.fr/culture/infos-pratiques/droits/protection.htm>

**Micromechanical models of network materials presenting
internal length scales: applications to trabecular bone
under stable and evolutive conditions**

THÈSE

Pour l'obtention du

Doctorat de l'Université de Lorraine
Spécialité : Mécanique et Énergétique

Présentée par
Ibrahim GODA

Thèse soutenue publiquement le 28 Mai 2015 à Nancy devant le jury composé de :

Thibault LEMAIRE	Pr MSME, Université Paris Est	Rapporteur
Larbi SIAD	Pr BIOS, Université de Reims	Rapporteur
Paul LIPINSKI	Pr LaBPS, ENIM, METZ	Examineur
Halima-Assia KERDJOUDJ	Dr BIOS, Université de Reims	Examineur
Jean-François GANGHOFFER	Pr LEMTA, Université de Lorraine	Directeur de thèse
Rachid RAHOUADJ	Pr LEMTA, Université de Lorraine	Co-directeur de thèse
Gérard MAURICE	Pr LEMTA, Université de Lorraine	Invité

ACKNOWLEDGEMENTS

In the name of **Allah**, the Most Gracious, the Most Merciful. All praise is due to Allah; we praise Him, seek His help, and ask for His forgiveness. I am thankful to Allah, who supplied me with the courage, the guidance, and desire to complete this thesis.

I would like to take this opportunity to express my appreciation to all who have influenced, stimulated, expedited, and warmly supported me to complete this work.

First and foremost, I would like to express my sincere appreciation and gratitude to my advisor, Prof. Jean-François GANGHOFFER, for his guidance, assistance, encouragement, patience, and hearty support at all phases of my doctoral program. Under his guidance I successfully overcame many difficulties and learned a lot. It has been an honor and a privilege to work with him, and it is an opportunity for which I owe him a tremendous debt of gratitude.

I am extremely thankful to my co-advisor, Prof. Rachid RAHOUADJ, for his guidance, advice, constant encouragement and valuable instructions and suggestions that helped me in accomplishing this work successfully.

I would also like to acknowledge the assistance rendered by Prof. Gérard MAURICE for his technical recommendations and scientific support to accomplish some parts in this thesis. His advice and expertise in software Freefem was vital for achievement the bone remodeling part of this work.

Many thanks to my thesis committee members Prof. Thibault LEMAIRE, Prof. Larbi SIAD, Prof. Paul LIPINSKI, and Dr. Halima-Assia KERDJOU DJ for their involvement and the time they spared to review this thesis and for their comments to improve this thesis. My appreciation also goes to the reviewers of my thesis, Prof. Thibault LEMAIRE and Prof. Larbi SIAD for taking the time to review the thesis. I am deeply honored and I thank them sincerely.

Special and profound thanks go to my wonderful parents for their kind care, sincere prayers and moral support. Many thanks go to my brothers and sister for their endless confidence, encouragement, and motivation. I would like to pay my warmest tribute to my wife and kids whose love and strong emotional support make my life pleasant even in the hardest times.

Last but not least, I extend my thanks and appreciation to my friends, colleagues and everyone who helped me to get this work done.

Again, I thank all those who have helped me directly or indirectly in the successful completion of my thesis. Anyone missed in this acknowledgement are also thanked.

CONTENTS

ABBREVIATIONS	IX
NOMENCLATURE	XI
LIST OF FIGURES	XV
LIST OF TABLES	XXIII
RÉSUMÉ EN FRANÇAIS.....	1
CHAPTER 1: INTRODUCTION.....	5
1.1 Cellular lattice structures	5
1.2 Motivation of the research.....	7
1.3 Scope and outline.....	10
CHAPTER 2: DISCRETE HOMOGENIZATION TECHNIQUE TOWARDS MICROPOLAR CONTINUA.....	15
2.1 Homogenization of 3D lattices and construction of a micropolar effective continuum ...	15
2.2 Asymptotic homogenization of discrete media to micropolar continuum considering axial, shear, flexural and torsional deformations.....	18
2.3 Identification of the homogenized 3D micropolar continuum.....	26
2.4 Conclusions.....	30
CHAPTER 3: COMPUTATION OF THE EFFECTIVE MECHANICAL PROPERTIES OF TEXTILES.....	31
3.1 Introduction.....	31
3.2 Review of unit-cell models for woven fabrics.....	32
3.3 Discrete homogenization of textile monlayers	36
3.4 Effective mechanical properties of woven fabrics.....	38
3.4.1 Unit cell of plain weave fabric	39
3.4.2 Unit cell of twill fabric	42
3.4.3 Flexural rigidity on the basis of a micropolar effect	43
3.4.4 Nonlinearities due to crimping.....	45
3.5 Comparison of homogenized moduli with finite element results	48
3.5.1 Strain energy-based method.....	49
3.6 Sensitivity analysis on meso-level.....	55
3.6.1 Effect of yarns transverse shear	56
3.6.2 Effect of friction between yarns on the FE simulated response.....	57

3.6.3	Effect of contact beam rigidities	57
3.7	Measurements of the tensile moduli of plain weave fabric	59
3.8	Conclusions.....	61
CHAPTER 4: MICROPOLAR CONSTITUTIVE MODELS OF TRABECULAR BONE.....		63
4.1	Introduction.....	63
4.2	Review of trabecular bone models.....	64
4.3	Construction of two-dimensional anisotropic Cosserat bone models.....	67
4.3.1	Effective micropolar properties of bone.....	70
4.3.2	Numerical determination of the effective rigidities	76
4.3.3	Application to bone fracture.....	84
4.3.3.1	Four node Cosserat finite element	84
4.3.3.2	Simulation results	86
4.4	Effective mechanical properties of vertebral trabecular bone	92
4.4.1	Results and discussion.....	97
4.4.1.1	Relevance of the choice of a micropolar effective continuum.....	101
4.4.1.2	Finite element validation.....	104
4.4.1.3	Discussion and limitations	108
4.5	Conclusions.....	113
CHAPTER 5: IDENTIFICATION OF COUPLE-STRESS MODULI OF VERTEBRAL TRABECULAR BONE: FINITE ELEMENT STUDY		115
5.1	Introduction.....	115
5.2	Basic equations of couple stress elasticity.....	117
5.3	Effective couple stress continuum model of vertebral trabecular bone.....	118
5.4	Effective couple stress moduli of a two phase material consisting of bone tissue and marrow	138
5.4.1	Material and geometrical models	139
5.4.2	Results of couple stress moduli with and without marrow	140
5.5	Conclusions.....	145
CHAPTER 6: SIZE DEPENDENT STATIC AND DYNAMIC BEHAVIOR OF TRABECULAR BONE		147
6.1	Introduction.....	147
6.2	Age-related change of vertebral bone architecture.....	148
6.3	Size dependent static and dynamic bending behaviors.....	150
6.3.1	Governing equations of the motion of micropolar beams in bending.....	150
6.3.2	Size-dependent static bending behavior.....	153
6.3.3	Size-dependent free flexural vibration behavior	154

6.3.4	Numerical results	155
6.4	Size dependent static and dynamic torsional behaviors.....	159
6.4.1	Governing equations of motion of a twisted micro-structured beam.....	159
6.4.2	Size-dependent static torsional behavior.....	163
6.4.3	Size-dependant free torsional vibration behavior.....	165
6.4.4	Numerical results	166
6.5	Conclusions.....	169

**CHAPTER 7: PLASTIC COLLAPSE AND BRITTLE FRACTURE SURFACE
MODELS OF TRABECULAR BONE.....171**

7.1	Introduction.....	171
7.2	Homogenization scheme for plastic yield and brittle fracture	173
7.2.1	3D elementary unit cell for trabecular bone.....	173
7.2.2	Determination of the plastic yield and fracture surfaces in stress space	175
7.2.2.1	Microscopic stresses versus the macroscopic deformation tensor	176
7.2.2.2	Plastic collapse and yield surface.....	177
7.2.2.3	Brittle failure and fracture surfaces.....	178
7.3	Numerical results	181
7.3.1	Plastic yield surface calculations under multiaxial loading	182
7.3.2	Brittle fracture surface under triaxial stress state	187
7.4	2D trabecular lattice.....	188
7.4.1	Plastic collapse validation by the finite element approach.....	189
7.4.2	Plastic yield surface based on micropolar theory	193
7.4.3	Size dependent plastic yield criterion based on micropolar theory	197
7.5	Conclusions.....	203

**CHAPTER 8: COMBINED INTERNAL AND EXTERNAL REMODELING AT
MESOSCOPIC, MICROSCOPIC AND MACROSCOPIC SCALES
.....205**

8.1	Introduction.....	205
8.2	Volumetric and surface growth model.....	207
8.2.1	Bulk growth model.....	208
8.2.1.1	Local dissipation and growth laws involving Eshelby stress	208
8.2.1.2	Evolution of bulk density.....	212
8.2.2	Surface growth model	214
8.3	A coupled bone internal and external remodeling approach	218
8.3.1	Strong formulation	218
8.3.2	Variational formulation.....	223
8.4	Applications to hard tissues like bone	225

8.4.1	Micromechanical simulations of the density and morphological changes of the trabecular structure.....	225
8.4.2	Macroscopic viewpoint	234
8.4.2.1	Homogenization scheme for trabecular bone.....	234
8.4.2.2	Simulation of joined internal and external remodeling.....	236
8.5	Conclusions.....	238
CHAPTER 9:	INTEGRATED REMODELING TO FATIGUE DAMAGE MODEL OF BONE	241
9.1	Introduction.....	241
9.2	Balance laws and constitutive equations of density growth	243
9.3	Elastic damage bone remodeling process	246
9.4	Simulation of internal bone remodelling with damage.....	249
9.5	Conclusions.....	253
CHAPTER 10:	CONCLUSIONS AND PERSPECTIVES.....	255
APPENDICES	261
REFERENCES	267

ABBREVIATIONS

BV/TV	Bone volume fraction (bone volume over total volume)
DH	Discrete homogenization
FE	Finite element
PW	Plain weave
PET	Polyethylene Terephthalate
RUC	Representative unit cell
RVE	Representative volume element
ρ^*/ρ_s	Relative density
2D	Two dimensional space
3D	Three dimensional space

NOMENCLATURE

A	Cross-sectional area of the member
B_R	Set of beams within the reference unit cell
CR	Crimp content
$[C^0]$	Equivalent undamaged stiffness matrix
C^D	Equivalent elastic-damage stiffness tensor
$[D]$	Elastic Cosserat constitutive matrix
D_e	Fatigue damage variable
E_{sf}, E_{sp}	Elastic moduli of weft and warp yarns, respectively
E_x^*, E_y^*, E_z^*	Effective homogenized moduli in x, y, and z, respectively
E_s	Young's modulus of the member material
$E_{tor-x,y,z}^*$	Homogenized torsional elastic moduli in directions x, y, and z
$\varepsilon = l / L$	Small scale parameter
ϵ	Deformation tensor
$\epsilon_{ij} \Big _H$	Hydrostatic strain tensor
f_b	Flexural natural frequency in cycles per second
$[F_p]$	Vector of nodal forces and moments at the extremities in local coordinate system
$F^E = -F^O = F^b$	Resultant forces at nodes of a beam b
F_g	Irreversible growth tensor
F_a	Accommodation tensor or the reversible elastic part of the deformation gradient
g	Jacobian of the transformation from dx to $d\lambda$
\mathbf{g}_a	Acceleration due to gravity
gr	The gain in stiffness due to the micropolar effect
G_s	Shear modulus of the member material
G_{xy}^*	In-plane effective shear modulus
G_{xz}^*, G_{yz}^*	Out-of-plane effective shear moduli
I_y, I_z	Second moments of area of the member cross-section
J	Jacobian of the total deformation gradient
J_a, J_g	Determinants of the accommodation and growth tensors, respectively
J_s	Torsional modulus
KE	Kinetic energy
k_l, k_t, k_r	Extension, bending, torsion rigidities of the beam segments of the yarn
k_{ys}, k_{zs}	Transverse shear correction factors
$[K^S]$	Homogenized stiffness matrix of textile corresponding to stress
$[K^\mu]$	Homogenized stiffness matrix of textile corresponding to couple stress
K_{55}^μ, K_{66}^μ	Micropolar bending constants of textiles
\mathbf{K}_r	Curvature tensor
L	Length of the member
l_b	Characteristic length in bending

l_t	Characteristic length in torsion
\mathbf{m}	Couple stress tensor
$m_t(x, t)$	Distributed torque-per-unit length about x-axis
m_{xx}, m_{yy}, m_{zz}	Torsion couple-stresses
M^n	Moment at node n
M_{\max}^*	Maximum bending moment happens at the clamped end
M_Y^*	Effective initial yielding moment of the micro-structured beam
M_P^*	Homogenized plastic moment of the micro-structured beam
M_{σ}^*	Component of the bending moment due to the classical stress
M_m^*	Component of the bending moment due to couple stress
N/N_f	Proportion of fatigue life
N_R	Set of nodes within the reference unit cell
O, E	The origin and end node of a beam respectively
$q(x, t)$	Distributed lateral forces
$[Q_e]$	Matrix relating the force vector on the unit cell to the homogenized strain
$\mathbf{R}(\lambda^1, \lambda^2, \lambda^3)$	Continuum node position
\mathbf{S}^i	Stress vectors
S_E^b	Elastic section modulus
$[S^{eff}]$	Effective compliance matrix
$[\mathbf{T}]$	Local-to-global transformation matrix
$\mathbf{u}=(u_x, u_y, u_z)$	Displacement vector in 3D
U	Strain energy density of a continuum
U_{cell}	Strain energy over the unit cell
$[\mathbf{U}_p]$	Vector of nodal displacements and rotations at the extremities in local coordinate
$[\mathbf{U}_S]$	Vector of nodal displacements and rotations at the extremities in reference coordinate
U_D	Distortional strain energy
$U_D _Y$	Distortion energy density associated with yielding
U_H	Dilatational part of the strain energy
μ^i	Couple stress vectors
\mathbf{v}	Test (vector) function
$v(x, t)$	Static deflection of the microstructured beam incorporating the size effect
v^n	Virtual translational velocity field of node n
V_u	Volume of the periodic unit cell
v_{xy}^*, v_{yx}^*	In-plane effective Poisson's ratios
v_{xz}^*, v_{yz}^*	Out-of-plane effective Poisson's ratios
\bar{v}	Static bending deflection evaluated by the classical theory
W^{ex}	The external work done on the body
w^n	Virtual rotational velocity field of node n
ω_b	Circular bending natural frequency incorporating the size effect
$\bar{\omega}_b$	Circular bending natural frequency without considering the size effect
ω_T	Torsional natural frequency of the micro-structured beam considering size effect

$\bar{\omega}_f$	Torsional natural frequency of the micro-structured beam from classical theory
χ	Microcurvature tensor or spatial gradients of the microrotation
y_{\max}	Maximum distance on the beam section from the neutral axis
$Z_{\lambda b}$	Plastic section modulus at the plastic hinge section of the trabeculae
$\delta^i (\delta^1, \delta^2, \delta^3)$	Shift factor for nodes belonging to a neighboring cell
λ^i	Curvilinear coordinates associated with the unit vectors
$\phi = (\phi_x, \phi_y, \phi_z)$	Microrotation vector in 3D
$\phi(x, t)$	Torsion angle of the micro-structured beam based on non-classical theory
$\bar{\phi}(x, t)$	Torsion angle derived on the basis of the classical theory
Φ_y, Φ_z	Non-dimensional factors vanishing when transverse shear can be neglected
θ	Inclination angle of hexagonal unit cell
θ_f	Crimp angle of the weft yarn
θ_p	Crimp angle of the warp yarn
ρ^*	Equivalent density of the lattice
ρ_s	Density of the bulk material
\mathcal{K}, μ^*	Micropolar moduli
σ	Stress tensor
σ_a^b	Extensional stress acting on the trabeculae
$\sigma_{ij} _H$	Hydrostatic stress tensor
σ_{fs}	Modulus of rupture of trabecular struts
σ_{ys}	Initial yield strength of the individual trabecular struts (bulk material)
$\sigma_{ij} _D$	Deviatoric stress tensor
σ_{eq}	Equivalent stress
σ_Y^*	Effective homogenized initial yield strength of the beam
δ_{ij}	Kronecker symbol
γ, β	Micropolar bending constants
α_f, β_f	Material fatigue parameters of bone
$\Gamma^g(x, t)$	Rate of mass increase per unit mass
$\Sigma(\mathbf{u})$	Actual volumetric Eshelby stress tensor
Σ_0	Threshold value for the volumetric Eshelby stress stimulus

LIST OF FIGURES

Figure 1.1: Examples of natural and artificial media with discrete structures.	7
Figure 2.1: 3D beam element with six degrees of freedom at each node in local coordinates.....	15
Figure 3.1: Multiscale modelling of woven fabrics.....	32
Figure 3.2: Periodic reinforcement and Representative Unit Cell (RUC): (a) Macrostructure of twill fabric and its periodic macro-unit cell (b) Macrostructure of plain weave fabric and its periodic macro-unit cell.	36
Figure 3.3: A 3D lattice model of 2D plain weave.....	39
Figure 3.4: Geometrical model of an elementary cell of twill.....	42
Figure 3.5: Geometrical parameters of a micropolar beam subjected to a pure bending moment.	44
Figure 3.6: Evolution versus crimp interchanges of effective elastic properties of plain weave and twill fabrics. (a), (b) tensile moduli E_x^*, E_y^* and (c) Poisson's ratio ν_{xy}^*	47
Figure 3.7: Displacement (left) and stress (right) distributions over. (a) plain weave and (b) twill tows due to uniaxial extension in x-direction.....	51
Figure 3.8: Displacement (left) and stress (right) distributions over. (a) plain weave and (b) twill tows due to uniaxial extension in y-direction.....	51
Figure 3.9: Displacement (left) and stress distributions (right) over (a) plain weave and (b) twill tows due to biaxial extension.	52
Figure 3.10: Displacement and stress distributions over (a) plain weave and (b) twill tows due to shearing.....	53
Figure 3.11: Stress distributions over balanced plain weave tows.	55
Figure 3.12: Effect of yarn transverse shear deformations on the effective homogenized mechanical properties of plain weave and twill fabrics. (a), (b) Young's moduli E_x^* and E_y^* respectively, (c) Shear modulus G_{xy}^* , and (d) Poisson's ratio ν_{xy}^*	56
Figure 3.13: Experimental tensile tests of plain weave samples along the weft direction. (Jeguirim and Fontaine, 2008).	60
Figure 3.14: Experimental tensile tests of plain weave samples along the warp direction. (Jeguirim and Fontaine, 2008).	60
Figure 4.1: Multiscale aspects of bone structure.	64
Figure 4.2: Longitudinal section of the femur illustrating cancellous and cortical bone types (Cowin and Doty, 2007).	64
Figure 4.3: Kinematic and static parameters of a beam element.....	69

Figure 4.4: General anisotropic unit cell for two dimensional honeycomb models. The geometrical descriptors are the cell angle (θ), the vertical cell length (h), the inclined cell length (l), and the wall thickness (t).	70
Figure 4.5: Representative unit cell of the investigated lattices: (a) hexagonal lattice, (b) re-entrant lattice ($\theta < 0$).	71
Figure 4.6: Comparison between the homogenized elastic and shear moduli with and without considering shear effects and Gibson model for the hexagonal lattice. $\eta=1/2$, $\alpha=4$.	72
Figure 4.7: Comparison between the homogenized Poisson's ratios ν_{xy}^* and ν_{yx}^* with the values obtained by Gibson for the hexagonal lattice. $\eta=1/2$, $\alpha=4$.	73
Figure 4.8: (a) Comparison between the homogenized shear modulus G_{xy}^* / E_s (with and without shear effects) with the values obtained by Gibson for the hexagonal lattice. $\eta=1/2$, $\alpha=1/2$. (b) Relative difference (in percent) between the effective modulus G_{xy}^* obtained by homogenization and Gibson model.	74
Figure 4.9: (a) and (b) Evolution of the relative tensile moduli versus the geometrical parameter α . (c) Relative shear modulus. (d) Relative difference between the homogenized shear modulus and Gibson model. $\eta=1/2$, $\theta=30$.	75
Figure 4.10: (a) and (b) Equivalent Poisson's ratios versus the geometrical parameter α . (c) Relative difference between homogenized Poisson's ratio ν_{yx}^* and Gibson model. $\eta=1/2$, $\theta=30$.	76
Figure 4.11: (a) Geometrical model of an elementary cell of trabecular bone. (b) Hexagonal honeycomb model representing the trabecular bone lattice.	78
Figure 4.12: Finite element simulation of the hexagonal lattice under tension in x. U1 variable deformation along the x-axis.	79
Figure 4.13: Finite element simulation of the hexagonal lattice under tension in y. U2 variable deformation along the y-axis.	80
Figure 4.14: Iso-displacement of the hexagonal lattice under shear test.	81
Figure 4.15: Von Mises stress distribution of the hexagonal lattice under shear test.	81
Figure 4.16: Hexagonal honeycomb beam model representing the trabecular bone lattice submitted to pure bending moment.	82
Figure 4.17: Iso-displacements along x-axis under the bending moment.	83
Figure 4.18: Four node linear quadrangle Cosserat FE. (a) Arbitrary four-node quadrilateral FE with three degree of freedom (u, v, ϕ). (b) Reference element.	84
Figure 4.19: Applied loading and boundary conditions of the 2D bone specimen with bone fracture. Zoom of the material specimen on two hexagonal unit cells.	87
Figure 4.20: Spatial stress distribution obtained by extrapolation of stresses from the integration points to the nodal points. (a), (c), and (e) correspond to Cosserat finite element results	

and (b), (d), and (f) correspond to the classical four node finite element. Coarse mesh (128 elements).	88
Figure 4.21: Spatial stress distribution obtained by extrapolation of the stresses from integration points to the nodal points. (a), (c), and (e) correspond to Cosserat finite element results and (b), (d), and (f) correspond to the classical four node finite element. Medium mesh (489 elements).	89
Figure 4.22: Spatial stress distribution obtained by extrapolation of stresses from the integration points to nodal points. (a), (c), and (e) correspond to Cosserat finite element results and (b), (d), and (f) correspond to the classical four node finite element. Fine mesh (1188 elements).....	90
Figure 4.23: Displacement distribution. (a), (c) correspond to Cosserat finite element results and (b), (d) correspond to the classical four node finite element (CPS4 from Abaqus). Fine mesh (1188 elements).	91
Figure 4.24: General anisotropic unit cell for 3D hexagonal models. The geometric parameters include the cell angle θ , the in-plane strut lengths (L, h), and the vertical length L_v .	93
Figure 4.25: Reference unit cell of vertebral trabecular bone and its periodicity vectors $Y_1, Y_2,$ and Y_3	93
Figure 4.26: Effective elastic moduli $E_x^*, E_y^*,$ and E_z^* of vertebral trabecular bone versus the geometrical parameter θ	98
Figure 4.27: Effective in-plane Poisson's ratios of vertebral trabecular bone versus θ (a) ν_{xy}^* and (b) ν_{yx}^*	99
Figure 4.28: Effective shear moduli $G_{xy}^*, G_{yz}^*,$ and G_{xz}^* of vertebral trabecular bone versus angle θ . .	99
Figure 4.29: Effective elastic moduli $E_x^*, E_y^*,$ and E_z^* of vertebral trabecular bone versus the relative density ρ^* / ρ_s and impact of transverse shear.	100
Figure 4.30: Effective shear moduli $G_{xy}^*, G_{yz}^*,$ and G_{xz}^* of vertebral trabecular bone versus the relative density ρ^* / ρ_s and impact of transverse shear.	101
Figure 4.31: Effective Poisson's ratios ν_{xy}^* and ν_{yx}^* of vertebral trabecular bone versus the relative density ρ^* / ρ_s and impact of transverse shear.	101
Figure 4.32: (a), (b), (c) Ratio of the characteristic micropolar lengths in bending and torsion to the unit cell size of vertebral trabecular bone and (d) Micropolar coupling number versus the angle $\theta \in [10^\circ - 80^\circ]$	102

Figure 4.33: Non dimensional micropolar anisotropic linear media material constants of vertebral trabecular bone: μ^*/G^* and κ/G^* variations and its corresponding coupling number N versus the geometrical parameter $\theta \in [10^\circ - 80^\circ]$	103
Figure 4.34: Geometry of a repeatable vertebral trabecular structural unit cell with periodic boundary conditions.....	105
Figure 4.35: Contour plot of von Mises effective stress after uniaxial tensile ((a) and (b)) and shear (c) loading.	108
Figure 4.36: Geometric dimensions of rod-like trabecula: Right: base thickness (d_{max}) and minimum thickness at the centre (d_{min}). Left: Equivalent uniform strut with diameter $d = (d_{max} + d_{min})/2$	109
Figure 4.37: Normalized homogenized effective Young's moduli of vertebral trabecular bone and experimental values from literature plotted against relative density.	111
Figure 4.38: Normalized homogenized effective shear moduli of trabecular bone and experimental values from literature plotted against relative density.	112
Figure 4.39: In-plane Poisson's ratios of vertebral trabecular bone plotted against relative density... ..	112
Figure 5.1: Four different 3D periodic model representation of vertebral trabecular bone with (a) a single unit cell denoted 1, (b) $2 \times 2 \times 2$ unit cells, (c) $4 \times 4 \times 4$ unit cells, and (d) $6 \times 6 \times 6$ unit cells. Note that both vertical and horizontal trabeculae are idealized as a circular beam with diameter D_v and D_h , respectively.	120
Figure 5.2: Displacements and Von Mises stress distributions due to uniaxial tensile test in x-direction ($\epsilon_{xx} = 1$).	124
Figure 5.3: Displacements and Von Mises stress distributions due to uniaxial tensile test in z-direction ($\epsilon_{zz} = 1$).	124
Figure 5.4: Displacements and Von Mises stress distributions due to biaxial tensile test	125
Figure 5.5: Displacements and Von Mises stress distributions due to biaxial tensile test	126
Figure 5.6: Displacements and Von Mises stress distributions due to shear test in xy ($\epsilon_{xy} = 1$).	127
Figure 5.7: Displacements and Von Mises stress distributions due to shear test in xz ($\epsilon_{xz} = 1$).....	128
Figure 5.8: Displacements and Von Mises stress distributions due to torsional rotation about x-axis ($\chi_{xx} = 1$).....	131
Figure 5.9: Displacements and Von Mises stress distributions due to torsional rotation about z-axis ($\chi_{zz} = 1$).....	132
Figure 5.10: Displacements and Von Mises stress distributions due to biaxial torsional rotation in xy ($\chi_{xx} = \chi_{yy} = 1$).....	133
Figure 5.11: Displacements and Von Mises stress distributions due to uniform curvature $\chi_{xy} = 1$..	133

Figure 5.12: Displacements and Von Mises stress distributions due to uniform curvature $\chi_{yz} = 1$.	134
Figure 5.13: Displacements and Von Mises stress distributions due to uniaxial tensile test in x within $4 \times 4 \times 4$ unit cells.....	136
Figure 5.14: Displacements and Von Mises stress distributions due to shear test in xz within $4 \times 4 \times 4$ unit cells.....	136
Figure 5.15: Displacements and Von Mises stress distributions due to torsional rotation $\chi_{zz} = 1$ within $4 \times 4 \times 4$ unit cells.....	137
Figure 5.16: Displacements and Von Mises stress distributions due to uniform curvature $\chi_{yz} = 1$ within $4 \times 4 \times 4$ unit cells.....	137
Figure 5.17: Displacement and Von Mises stress distributions due to torsional rotation $\chi_{xx} = 1$ within $6 \times 6 \times 6$ unit cells.....	137
Figure 5.18: Displacement and Von Mises stress distributions due to bending curvature $\chi_{xy} = 1$ within $6 \times 6 \times 6$ unit cells.....	138
Figure 5.19: Displacement and Von Mises stress distributions due to bending curvature $\chi_{yz} = 1$ within $6 \times 6 \times 6$ unit cells.....	138
Figure 5.20: Representation of trabecular bone composed of bony trabecular struts and marrow-filled cavities. (a) bone tissue and (b) marrow.....	140
Figure 5.21: Displacements and Von Mises stress due to uniaxial extension ($\epsilon_{xx} = 1$) considering bony trabecular struts and marrow-filled cavities.....	141
Figure 5.22: Displacements and Von Mises stress due to uniaxial extension ($\epsilon_{zz} = 1$) considering bony trabecular struts and marrow-filled cavities.....	142
Figure 5.23: Displacements and Von Mises stress distributions due to biaxial extension.....	142
Figure 5.24: Displacements and Von Mises stress distributions due to biaxial extension.....	142
Figure 5.25: Displacements and Von Mises stress due to shear test in xy ($\epsilon_{xy} = 1$) considering bony trabecular struts and marrow-filled cavities.....	142
Figure 5.26: Displacements and Von Mises stress due to shear test in xz ($\epsilon_{xz} = 1$) considering bony trabecular struts and marrow-filled cavities.....	143
Figure 5.27: Displacements and Von Mises stress due to torsional rotation ($\chi_{xx} = 1$) considering bony trabecular struts and marrow-filled cavities.....	143
Figure 5.28: Displacements and Von Mises stress due to torsional rotation ($\chi_{zz} = 1$) considering bony trabecular struts and marrow-filled cavities.....	143
Figure 5.29: Displacements and Von Mises stress due to biaxial torsional rotation ($\chi_{xx} = \chi_{yy} = 1$) considering bony trabecular struts and marrow-filled cavities.....	144

Figure 5.30: Displacements and Von Mises stress due to bending curvature ($\chi_{xy} = 1$) considering bony trabecular struts and marrow-filled cavities.....	144
Figure 5.31: Displacement and Von Mises stress due to bending curvature ($\chi_{xz} = 1$) considering bony trabecular struts and marrow-filled cavities.....	144
Figure 5.32: Displacement and Von Mises stress due to bending curvature ($\chi_{yz} = 1$) considering bony trabecular struts and marrow-filled cavities.....	145
Figure 6.1: Representative model of vertebral trabecular bone and its parameters. (a) Reference unit cell and its periodicity vectors $Y_1, Y_2,$ and $Y_3,$ (b) 3D hexagonal unit cell with thick vertical trabeculae and thinner horizontal ones rendering of human vertebral bone, (c) 2D hexagonal lattice.	149
Figure 6.2: Evolution with age of the effective normalized density of trabecular bone.	150
Figure 6.3: Configuration of the micropolar micro-structured beam of the vertebral trabeculae.	151
Figure 6.4: Schematic diagram of a micro-structured cantilever beam with rectangular cross section exposed to a moment at its free end.....	153
Figure 6.5: Variation of the maximum deflection of the micro-structured cantilever beam with age. 156	
Figure 6.6: Variation of the first two flexural natural frequencies of the micro-structured cantilever beam with age.	156
Figure 6.7: Deflection and rotation of the micro-structured cantilever beam.	157
Figure 6.8: Normalized static deflection of a micro-structured-cantilever versus the ratio of the cantilever thickness to the material length scale parameter of trabecular bone.....	158
Figure 6.9: Size effect on the flexural natural frequencies with respect to various sizes for micro-structured cantilevered beam.	158
Figure 6.10: Schematic of the micro-structured beam: Geometry, loading, and coordinate system. .	160
Figure 6.11: Variation with age of the maximum static torsion angle of the micro-structured cantilever beam.....	167
Figure 6.12: Variation with age of the first torsional natural frequencies of the micro-structured cantilever beam.....	167
Figure 6.13: (a) Effect of specimen size on the maximum torsion angle, (b) The normalized maximum torsion angle versus beam diameter. Age is 40 years.....	168
Figure 6.14: (a) Effect of specimen size on the torsional natural frequency, (b) The first normalized torsional natural frequency versus beam diameter. Age is 40 years.....	169
Figure 7.1: Plastic yield surfaces in the stress spaces of (a) $\sigma_x - \sigma_y,$ (b) $\sigma_x - \sigma_z,$ (c) $\sigma_y - \sigma_z,$ (d) $\sigma_{xy} - \sigma_{xz},$ (e) $\sigma_{xy} - \sigma_{yz},$ and (f) $\sigma_{xz} - \sigma_{yz},$ all the stresses are normalized with respect to the yield strength of the bulk material. Age is 40 years with relative density $\rho^*/\rho_s = 0.12.$	184
Figure 7.2: The relationship between yield strength and bone age (or bone relative density) for: (a) uniaxial stress -x, (b) uniaxial stress -y, (c) uniaxial stress -z, (d) in-plane shear x-y, (e) out-of-plane shear x-z, and (f) out-of-plane shear y-z.	186

Figure 7.3: Brittle fracture surfaces in the stress spaces of (a) $\sigma_x - \sigma_y$, (b) $\sigma_x - \sigma_z$, and (c) $\sigma_y - \sigma_z$ for a person aged 85 years with bone relative density $\rho^*/\rho_s = 0.05$. The tension–tension quadrant is colored.....	188
Figure 7.4: Plastic yield stress determined by FE model from the stress-strain curve during tension in x-direction for the trabecular bone lattice. (b) Von Mises stress and (c) Equivalent plastic strain.....	191
Figure 7.5: Plastic yield stress determined by FE model from the stress-strain curve during tension in y-direction for trabecular bone lattice. (b) Von Mises stress and (c) Equivalent plastic strain.....	192
Figure 7.6: Shear yield stress determined by FE model from the shear stress-strain curve during shearing test for trabecular bone lattice. (b) Von Mises stress and (c) Equivalent plastic strain.....	192
Figure 7.7: Biaxial plastic yield stress determined by FE model from biaxial tension test for trabecular bone lattice. (b) Plastic yield surface (c) Von Mises stress and (d) Equivalent plastic strain.....	193
Figure 7.8: Rectangular components of stress and couple stress.....	195
Figure 7.9: Plastic yield surfaces of the trabecular lattice under combined shear and couple stress state (σ_{xy} , m_{xz} , and m_{yz}).....	197
Figure 7.10: Schematic diagram of a micro-structured cantilever beam with rectangular cross section exposed to a concentrated force at its free end.....	201
Figure 7.11: Effect of bone specimen size on the plastic yield moment of the beam. $l_b = 0.12$ mm.....	202
Figure 8.1: External remodeling of a bone. + (resp. –) zones indicate bone apposition (resp. resorption). From Weiss (1988).....	208
Figure 8.2: Schematic representation of the multiplicative decomposition of deformation gradient into its elastic and growth parts.....	209
Figure 8.3: Combined internal and external trabecular bone adaptation under compressive load at the top edge: (a) Initial geometry with uniform density of 1500 kg/m^3 submitted to compressive load; (b) Strain distribution; (c) Bone density distribution; and (d) Initial and new grown geometry meshes. The adaptations lasted 50 time steps.....	229
Figure 8.4: Combined internal and external trabecular bone adaptation under shear load at the top edge: (a) Initial geometry with uniform density of 1500 kg/m^3 submitted to shear load; (b) Strain distribution; (c) Bone density distribution; and (d) Meshes of the new grown geometry. The adaptations lasted 50 timesteps.....	229
Figure 8.5: Combined internal and external trabecular bone adaptation under compressive and shear loads at the top edge: (a) Initial geometry with uniform density of 1500 kg/m^3 submitted to combined compressive and shear loads; (b) Strain distribution; (c) Bone	

density distribution; and (d) Meshes of the new grown geometry. The adaptations lasted 50 timesteps.....	230
Figure 8.6: Combined internal and external trabecular bone adaptation under compressive and shear loads at the right edge: (a) Original bone geometry with uniform density of 1500 kg/m ³ submitted to combined compressive and shear loads; (b) Strain distribution; (c) Bone density distribution; and (d) Plot of the mesh of the newly grown bone geometry. Bone adaptations are shown after 20 growth-timesteps.....	232
Figure 8.7: External trabecular bone adaptation under compressive: (a) Original configuration submitted to compressive stress; (b) Strain distribution; (c) Overlay plots of the original bone and grown bone. The adaptations lasted 60 growth-timesteps.	233
Figure 8.8: External trabecular bone adaptation under shear stress: (a) Original configuration submitted to shear stress; (b) Strain distribution; (c) Overlay plots of the original bone and grown bone meshes. The adaptations lasted 60 growth-timesteps.....	234
Figure 8.9: Trabecular bone and microstructure homogenization towards an effective continuum. ..	235
Figure 8.10: Simulations of internal and external bone growth at the macroscopic level. (a) Loading conditions and original structure with uniform distribution at the beginning of simulation: initial density= 800 kg/m ³ , (b) Bone density distribution after 140 growth-timesteps, (c) Overlay plots of the original bone and grown bone meshes after 140 growth-timesteps.....	237
Figure 9.1: Evolution of damage variable (D_e) versus the normalized number of cycles (the ratio of the number of cycles N to the number of cycles to failure N_f).....	247
Figure 9.2: 3D plot of strain energy density coupled with damage, function	
$W = \frac{1}{2}(1 - D_e) \sigma \epsilon = \frac{1}{2}(1 - D_e) E^* \epsilon^2$	248
Figure 9.3: Bone density distribution of 2D model of the proximal femur. (a) Loading conditions and uniform distribution at the beginning of simulation: initial density= 300 kg/m ³ , (b) Bone response to simulated physiological loading after 50 days with $D_e=0.25$, (c) After 100 days with $D_e =0.25$, (d) After 100 days with $D_e =0$	252

LIST OF TABLES

Table 3.1: Plain weave fabric configuration parameters.	40
Table 3.2: Elastic properties of weft and warp yarns.	40
Table 3.3: Twill fabric configuration parameter	42
Table 3.4: Effective bending stiffness of a homogeneous beam made of a microstructure of plain weave and twill fabrics. gr is the gain in stiffness due to the micropolar effect.....	45
Table 3.5: Effective mechanical properties and crimp amounts of plain weave and twill at different crimp angles.....	46
Table 3.6: Geometrical parameters of plain weave and twill fabrics.	49
Table 3.7: Effective elastic constants of unbalanced plain weave and twill fabrics from discrete homogenization and finite element simulations.	54
Table 3.8: Effective elastic constants of balanced plain weave fabrics from homogenization and finite element simulations.	54
Table 3.9: Effect of extensional, flexural, and torsion rigidities of the contact beam on the fabric effective moduli.	58
Table 3.10: Characteristics of the plain weave tested samples.....	59
Table 4.1: Connectivity array for the hexagonal lattice	71
Table 4.2: The couple-stress elastic constants and characteristics lengths of trabecular bone unit cell.	83
Table 4.3: Comparison of peak stress values for the two models (Cauchy and micropolar).	91
Table 4.4: Connectivity array for the 3D hexagonal lattice.	93
Table 4.5: Normalized elastic constants predicted by homogenization and FE simulations.....	107
Table 4.6: Relationships between the relative Young's and shear moduli as well as Poisson's ratios versus relative density for two types of trabecular geometry.	109
Table 5.1: Micro-structural parameters for vertebral bone based on morphology–age relationships by Mosekilde (1988), age is measured in years.....	119
Table 5.2: Calculated effective couple-stress stiffness tensors of trabecular bone with sample 1, $2 \times 2 \times 2$, $4 \times 4 \times 4$, and $6 \times 6 \times 6$	135
Table 5.3: Effective couple-stress moduli of trabecular bone of sample size $2 \times 2 \times 2$ with and without bone marrow.	141
Table 6.1: Micro-structural parameters for vertebral bone based on morphology–age relationships by Mosekilde (1988), age is measured in years.....	149
Table 7.1: Summary of plastic collapse criteria for 3D vertebral trabecular bone (aged 40 years) unit cell.	185

RÉSUMÉ EN FRANÇAIS

Cette thèse aborde le développement de méthodes d'homogénéisation de la microstructure de l'os trabéculaire, qui est décrite comme un réseau répétitif de poutres quasi périodique, auquel on substitue in milieu continu effectif doté de propriétés mécaniques effectives. Nous avons ainsi abordé successivement les situations statique et dynamique, dans le contexte d'un comportement élastique en petites déformations. Les modèles homogénéisés développés sont ensuite utilisés comme une approche micromécanique pour construire les surfaces de charge de la rupture fragile et du comportement ductile plastique de réseaux de poutres dominées par un comportement flexionnel, en s'appuyant sur des topologies idéalisées de la microstructure trabéculaire.

Dans une deuxième partie de la thèse, des modèles de remodelage osseux sont construits afin de simuler le remodelage externe et interne à différentes échelles.

Nous abordons deux problématiques principales : en premier lieu l'automatisation de la méthode d'homogénéisation discrète afin de traiter les milieux micropolaires, et sa généralisation qui s'appuie sur des modèles de poutres de Timoshenko, plutôt que des poutres de Bernoulli. En second lieu, le développement de modèles théoriques et numériques pour simuler le remodelage externe et interne de l'os trabéculaire dans des situations 2D, dans le cadre de la thermodynamique des processus irréversibles, afin de montrer l'influence de stimuli mécaniques externes sur l'évolution de forme de l'os. Le remodelage interne est simulé pour des géométries 2D dans le contexte de l'élasticité anisotrope endommageable, qui montre l'influence des stimuli mécaniques externe et interne sur les évolutions de la densité osseuse effective.

Dans une première étape, nous dégageons les principales étapes de la méthode d'homogénéisation discrète développée afin de construire un milieu continu effectif de type micropolaire, prenant en compte a priori la nature non centrosymétrique du milieu. Un modèle effectif micropolaire tridimensionnel est construit par homogénéisation; il incorpore des modes de déformation axiaux, en cisaillement, en flexion et en torsion, qui se produisent à l'échelle des travées. Les propriétés mécaniques classiques et micropolaires sont identifiées à partir des équations constitutives qui émergent de la démarche d'homogénéisation d'un milieu continu effectif micropolaire anisotrope.

Une première application de la méthode est faite à des structures tissées d'armure monocouche dont on identifie un motif élémentaire qui répétitif. Les réseaux de fils chaîne et trame entrelacés au sein de la structure sont décrits comme des poutres ondulées connectées par des poutres de contact transversales; elles sont dotées de rigidité en traction et en flexion, en considérant également un mode de cisaillement transverse dans le cadre du modèle de poutres de Timoshenko. Le tissé est décrit comme un milieu effectif anisotrope doté de deux directions matérielles privilégiées dans le plan moyen de la structure. Les propriétés mécaniques membranaire et flexionnelle d'armure toile et sergé sont ainsi calculées en

fonction de leurs caractéristiques microstructurales, incluant des modules de flexion et des longueurs caractéristiques associées.

La pierre angulaire de la thèse qui suit cette première application de la méthode d'homogénéisation développée est la construction de modèles de Cosserat de l'os trabéculaire dans des situations 2D et 3D, afin d'analyser l'impact de la microstructure trabéculaire sur les propriétés macroscopiques effectives de l'os. Les parois des travées osseuses sont modélisées par des poutres de Timoshenko, et une géométrie idéalisée de forme hexagonale est adoptée. Des expressions analytiques des propriétés effectives sont obtenues en fonction des paramètres géométriques et mécaniques, prenant en compte les effets de déformations axiale, de flexion, et du cisaillement transverse ; la torsion est prise en compte spécifiquement pour les géométries 3D. Les modules classiques et micropolaire ainsi que les longueurs en flexion et torsion sont identifiées en fonction des constantes élastiques classiques et non classiques. Des calculs par éléments finis à l'échelle de l'architecture trabéculaire permettent de valider les propriétés obtenues par l'homogénéisation. Un très bon accord est obtenu pour les modules effectifs classiques et non classiques. Un élément fini plan de type milieu de Cosserat a été développé et implémenté dans ABAQUS afin de simuler la distribution des contraintes au voisinage du front d'une fissure, et de montrer l'effet régularisant d'un modèle enrichi de type Cosserat.

Les propriétés effectives de l'os vertébral modélisé dans sa géométrie comme un empilement de feuillet hexagonaux ont été calculées par des analyses EF qui s'appuient sur la méthode de l'énergie équivalente. Des conditions limites de type mixte (déplacement et tractions imposées de façon complémentaire sur les faces des échantillons simulés) et non homogène en déplacement permettent de déterminer toutes les propriétés classiques et non classiques qui reflètent les différentes composantes des tenseurs de rigidité obtenues par l'homogénéisation. Nous avons étendu cette analyse en prenant en compte la présence de moelle osseuse dans les interstices de la microstructure trabéculaire. Il est montré par la comparaison des modules effectifs obtenus sous différents chargements (uniaxial, biaxial, cisaillement, flexion et torsion) que les propriétés effectives sont relativement peu affectées par la présence de moelle osseuse.

Les propriétés dynamiques en flexion et torsion d'échantillons d'os vertébral ont ensuite été calculées par la théorie de Cosserat afin de prendre en compte les effets d'échelle interne. Les équations du mouvement en flexion et en torsion ont été écrites à partir du principe de Hamilton. Les résultats obtenus pour le cas de la flexion statique montrent que la déflexion et la rotation prédite par le modèle micropolaire sont plus faibles que celles prédites par les modèles classiques ; les différences sont très importantes lorsque l'épaisseur de la poutre est petite. Des tendances similaires sont obtenues pour le problème de vibration libre, où l'on montre que la fréquence naturelle prédite par le modèle micropolaire est plus importante que celle qui résulte d'un modèle classique, la différence devenant significative uniquement pour des poutres à section mince.

Des modèles 3D de l'écoulement plastique et de la rupture fragile de l'os trabéculaire ont ensuite été développés sur la base des mêmes approches micromécaniques; la prise en compte des moments de flexion permet d'étendre l'homogénéisation vers le milieu micropolaire qui

constitue un enrichissement de la cinématique en incorporant une variable de microrotation en sus du déplacement. Nous avons ainsi construit les surfaces de charge plastique en chaque point du continuum effectif, ce dernier supportant des couples de contrainte en plus des contraintes de Cauchy. Un critère d'écoulement plastique incorporant un effet de taille a ainsi été construit, sur la base de la théorie de Cosserat réduite; lorsque la taille caractéristique de la microstructure est comparable à la longueur interne de la microstructure, on observe un écart important entre le critère d'écoulement plastique classique et celui formulé dans le cadre de la théorie enrichie de type micropolaire.

Dans la dernière partie de la thèse, nous avons abordé le remodelage interne et externe, par le développement d'une plate forme numérique de simulation des processus d'adaptation externe conjointement à l'adaptation locale au chargement mécanique appliqué, ce aux échelles trabéculaire et macroscopique. Une loi de comportement élastique anisotrope linéaire est obtenue par homogénéisation discrète, les paramètres effectifs continus tels que les rigidités évoluant avec la morphologie lorsque le remodelage se produit au sein de l'os. Le remodelage interne est essentiellement décrit par une évolution de la densité interne de l'os en fonction de la trace d'un tenseur d'Eshelby ; afin de décrire le remodelage externe, une relation entre la vitesse de remodelage en surface et une force motrice pour la croissance est formulée, cette dernière étant identifiée à la divergence de surface d'un tenseur d'Eshelby. L'implémentation numérique des modèles de remodelage développé est très générale, et peut inclure différentes lois de comportement et stimuli mécaniques.

Dans un dernier chapitre, le remodelage interne anisotrope de l'os trabéculaire a été développé, de façon couplée à la théorie de l'endommagement continu, qui a été adaptée au cas de l'os trabéculaire. Nous avons sur cette base simulé les évolutions de la densité osseuse apparent du fémur proximal, en considérant une loi de comportement élastique endommageable pour une géométrie 2D du fémur, avec un stimulus mécanique identifié à la densité d'énergie élastique, force motrice des évolutions de densité interne. Une loi de comportement effective linéaire anisotrope de l'os trabéculaire a été obtenue par homogénéisation à l'échelle continue mésoscopique. Les modules effectifs sont exprimés selon des fonctions puissance de la densité interne effective (qui elle-même évolue avec la morphologie interne au sein de la cellule répétitive de l'os trabéculaire). Les simulations prennent ainsi en compte les variations de l'état d'anisotropie résultant des changements de morphologie au cours du remodelage

En termes de perspectives, les modèles micromécaniques développés dans ce travail pour les tissages sont particulièrement prometteurs en raison de la difficulté de mesurer les propriétés effectives de ces milieux compte tenu de leur faible épaisseur. Les méthodes d'homogénéisation spécifiques développées pour des milieux architecturés sont très efficaces et offrent une adaptabilité importante à la topologie du milieu considéré. Pour les tissages, la méthode pourra être améliorée afin d'incorporer une description quantitative fine du contact variable entre fils ainsi que le glissement relative entre fils. Le comportement en grandes transformations qui a été développé dans le cadre d'une autre thèse au LEMTA pourra également être incorporé dans les analyses du comportement effectif de structures souples

tissées, pour lesquelles les effets de flexion sont responsables des non linéarités géométriques observées.

Les modèles d'homogénéisation développés pour la description du comportement de l'os trabéculaire constituent un moyen d'expérimentation virtuelle intéressant pour analyser son comportement et sa réponse mécanique dans des situations stables et évolutives, en fonction de la topologie considérée à l'échelle trabéculaire. Nous pourrions ainsi dans des travaux futurs aborder des géométries de type tétrakaïdècaédrale ou celles acquises sur des échantillons d'os 3D par microtomographie. Du fait que l'os est un milieu biphasé constitué d'un squelette solide et de moelle au comportement viscoélastique, il conviendra d'étendre les lois de comportement développées au cas de la viscoélasticité. De façon générale, les modèles homogénéisés obtenus à l'échelle mésoscopique pourront ensuite nourrir des calculs de structure à une échelle macroscopique qui est celle de la structure.

La prise en compte des effets de gradient de déformation au sein du volume représentatif constitue une piste de développements futurs prometteurs. Cet enrichissement du milieu continu classique par des gradients d'ordre supérieur des variables cinématiques permettrait de rendre compte des fortes concentrations de contraintes et de déformation observées pour les structures comportant un nombre important de degrés de liberté interne, pour lesquelles le déplacement de ces mêmes nœuds n'est pas affine.

Les méthodes d'homogénéisation spécifiques aux milieux architecturés qui ont été développées pourront être étendues pour aborder le comportement dynamique et acoustique de ces milieux, et en particulier analyser les effets de microstructure et leur impact sur les propriétés à l'échelle d'un continuum effectif doté d'un comportement enrichi (milieu de Cosserat ou du second gradient). La construction des surfaces de charge de l'os trabéculaire pourra être étendue à la prise en compte de l'écroutissage dans des situations de chargement multiaxial.

L'approche micro-méso de calcul des propriétés effectives de structures poreuses ou de milieux fibreux enchevêtrés pourra donner lieu à des calculs de structure dans lesquels la loi de comportement en chaque point de Gauss résulte d'une étape d'homogénéisation de la microstructure sous-jacente, avec un retour possible de l'échelle macro vers l'échelle méso dès lors que des non linéarités seront présentes et demanderont une actualisation de la loi de comportement au cours de l'histoire de la réponse de la structure.

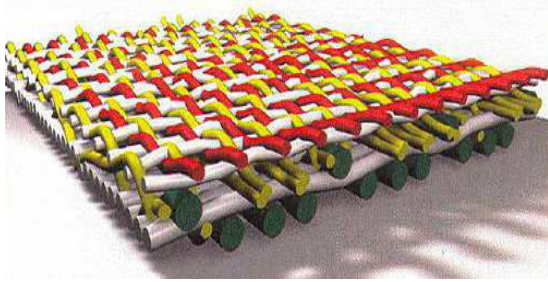
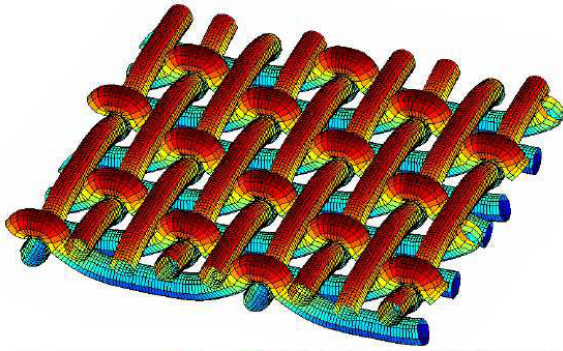
Enfin, les simulations du remodelage interne et externe en présence d'endommagement de la microstructure osseuse permettront de constituer une plateforme numérique qui fournira aux praticiens et aux cliniciens une aide au choix de procédures médicales et de biomatériaux les plus appropriées, ce sur la base de données réelles qui alimenteront les simulations. Cet aspect est particulièrement important dans le contexte de l'ingénierie tissulaire, lors de la réalisation d'insertions ligamentaires au sein de l'os ou lors de l'insertion d'implants osseux.

CHAPTER 1: INTRODUCTION

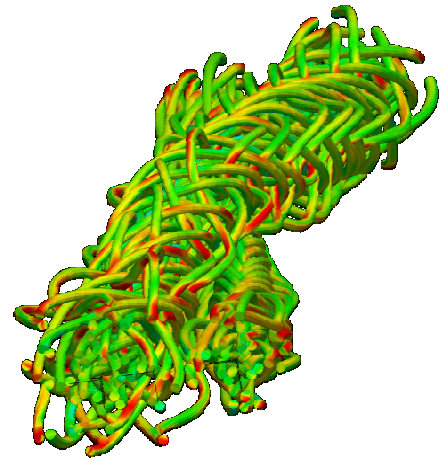
1.1 Cellular lattice structures

Nowadays, cellular solids and network materials such as foams, lattice truss materials and grid materials are widely used in a variety of commercial and military applications such as automotive industry, aerospace, or marine engineering, due to their many advantages, including high mechanical properties and strength, energy absorption capacities, thermal and acoustic insulation properties, lightweight structural components.

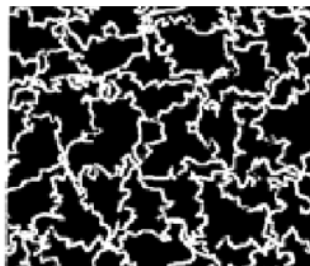
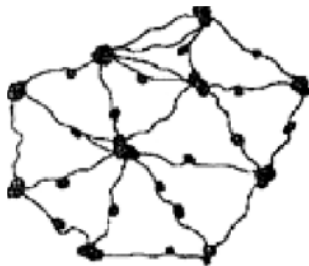
Cellular lattice structures endowed with a specific mechanical behavior due to the presence of an inherent microstructure are encountered in many applications such as lightweight industrial components, trabecular bone and bone scaffolds. Such structures are a complex of cells made of an interconnected network of edges. They are usually categorized as 2-D and 3-D cellular solids, and coined honeycombs and foams respectively. Many man-made and biological structures present a discrete topology, such as fibrous materials (textiles, collagen fiber networks, biological membranes), with a more or less complex organization of the fibrous microstructure (see [Figure 1.1 a-c](#)); the membrane of biological cells shown in [Figure 1.1c](#) is viewed as assembly of filaments which are linked together as part of a network. Since those structures consist of many repetitive elements, a need arose to develop simplified mechanical models for the prediction of their deformation behavior. Later on, architected materials such as metallic or polymeric foams (see [Figure 1.1e](#) and [f](#)) were also developed in diverse fields of engineering and chosen for their high deformability and ability to resist to impact. Biomaterials constitute a wide class of structures which have either a cellular or hierarchical microstructure ([Figure 1.1d](#)). Carbon nanotubes constitute another example – but at a much smaller scale – of a repetitive quasi-periodical lattice structure ([Figure 1.1g](#)).



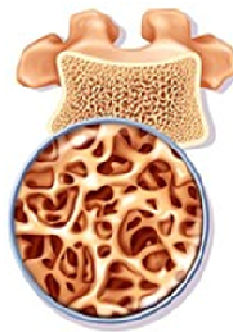
(a) Woven structures: monolayer and multilayers



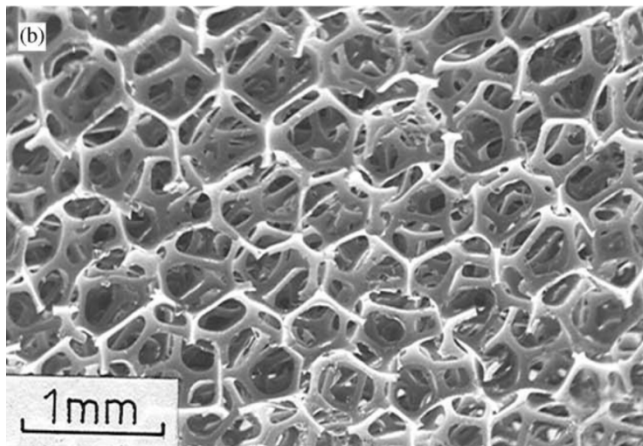
(b) Scaffold for tissue engineering



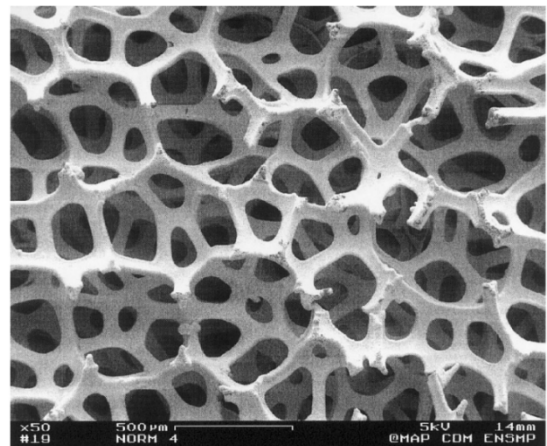
(c) Erythrocyte membrane cytoskeleton ([Assidi et al., 2011](#))



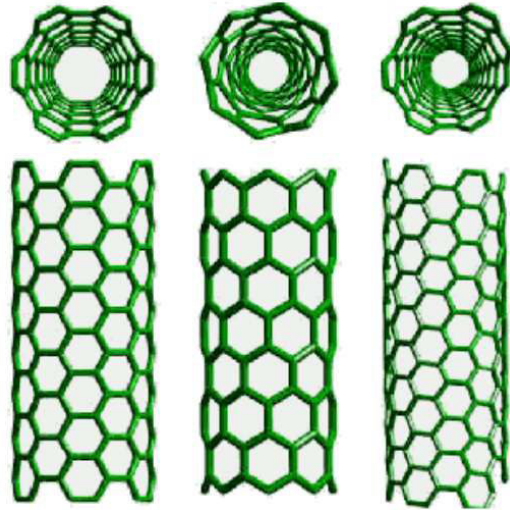
(d) Trabecular bone



(e) Open-cell polyurethane foam ([Gibson, 2005](#))



(f) Open-cell nickel foam ([Badiche et al., 2000](#))



(g) Armchair, zigzag, and chiral nanotubes

Figure 1.1: Examples of natural and artificial media with discrete structures.

Among their notable mechanical properties, the cellular lattice structures are of more importance, since the microstructure of the lattice can be adjusted so that desired mechanical properties can be achieved at the mesoscopic or macroscopic level. In view of exploiting the full potential of cellular solids, their constitutive mechanical response has to be entirely understood and modeled. Recently, researchers worldwide have widely used additive manufacturing methods to fabricate lattice structures. Although these fabrication methods are capable of producing such lattice structures with controllable porosity and pore sizes and with high repeatability, they are costly and time consuming even for fabricating small sizes parts. Accordingly, developing numerical prediction models having the capability to predict the mechanical properties of lattice structures can reduce the required experimental measurements in addition to the manufacturing cost.

1.2 Motivation of the research

As exemplified in previous section, a wide range of materials and structures at different scales is endowed with a discrete architecture, and may be described as large repetitive lattices made of bars or beams. Those lattices are endowed with a specific mechanical behavior because of the presence of an inherent microstructure. The prediction of the effective mechanical behavior of such lattices (in the sense of being endowed with a quasi periodic network) in relation to the geometrical and mechanical parameters at the micro level, is an especially significant issue. The setting up of such predictive models allows to fully understanding the microstructural origin of the mechanical behavior, and the lattice architecture required to achieve optimized properties at the structural level. The suitable size materials, the lattice topology and mechanical properties can be chosen relying on a quantitative understanding of the macroscopic impact of the microstructural parameters.

The mechanics of discrete structure is clearly related to the network architecture and to the elasticity of the building entities of the network. The development of predictive micromechanical models aiming at understanding the impact of the network architecture and mechanical properties on the macro scale is significant, as the experimental determination of the mechanical properties of such structure is delicate, and the overall anisotropy has to be accounted for. Hence, micromechanical approaches are needed in order to bridge the scales and to provide a constitutive law at a continuum scale, whereby the equivalent continuum properties can be related to both the geometrical and mechanical microstructural parameters of the network. Finally, since the computational cost of performing numerical simulations over entire lattices made of a huge number of repetitive entities may be prohibitive despite powerful computers, there is a need to replace these lattices by effective continua at an intermediate scale of description (coined here and in the sequel the mesoscopic scale) so that a compromise between numerical efficiency and accuracy can be obtained.

An essential category of such lattice materials consists of lattices such as textile and trabecular bone having a discrete kinematics and topology, showing size effects at the macroscopic scale of description. Such size effects have been proven to be important when sample dimensions are comparable with the size of the cell (Lakes, 1986). In other words, the effective mechanical properties show size-dependence if the dimension of a specimen or a structure is in a close order to the unit cell size. This behavior called “size effects” (Onck et al., 2001; Tekoglu and Onck, 2008) designates the effect of the macroscopic sample size, relative to the unit cell size, on the mechanical behaviour. However, these effects are not easily accessible from a direct analysis at the macroscopic structure scale. Consequently, the motivation of such micromechanical inspired constitutive models is to increase understanding the behavior of those structures in different loading situations. In addition, the use of continuum models with an enriched kinematics such as Cosserat (i.e. micropolar) continua which incorporates a microrotation in addition to the displacement as kinematic descriptors shall be justified according to length scale considerations.

The main motivation advocated in the current work is to present a general methodology for the determination of the effective behavior of architected materials endowed with a discrete structure at the microscopic scale. It relies on the discrete homogenization method to derive the effective mechanical properties from the topology of the material and the properties of the micro constituents. This method is presently applied to textile monolayers and trabecular bones, wherein their initially discrete architectures are represented at the mesoscopic continuum level by an anisotropic micropolar effective continuum. In particular, such micromechanical methods will be employed to remedy the difficulty to measure the effective mechanical properties at the intermediate (the so-called mesoscopic level) scale. It is thus the main objective of this thesis to circumvent the experimental difficulty in accessing effective classical and non-classical properties of such architected materials by the means of predictive models.

Aiming at investigating microstructure-related scale effects on bone macroscopic properties, we construct micropolar models of vertebral trabecular bone based on micromechanical approaches. The bending and torsion of 3D vertebral trabecular bone beam specimens have been formulated based on the Cosserat theory, a non-classical theory capable of capturing the size-effects. As a second motivation of this work, the static and dynamic bending and torsion behaviors of vertebral trabecular bone in the form of beam structures are studied, in terms of the deflection, torsion and eigenfrequencies of deformations.

One key issue in bone biomechanics is the influence of the microarchitecture trabecular ductility on the overall strength of trabecular bone. With aging and disease, the individual trabeculae become more brittle, so the question arises as to how does this influence the strength of the apparent trabecular bone? In the current work, we study the structural behavior of trabecular bone failure by investigating two extremes behaviors, known as fully ductile and fully brittle. For both trabecular level behaviors, we investigate the failed tissue amount and reactive strength evaluated at the trabecular bone scale at yield or ultimate point, respectively for a ductile or brittle tissue level material behavior. The third motivation aspect of this work is therefore to develop 3D models for describing the multiaxial yield and failure behavior of trabecular bone based on micromechanical approaches. The discrete homogenization technique is developed as a convenient micromechanical approach to construct the plastic yield surfaces of 2D and 3D bending-dominated periodic lattices of articulated beams considered as prototype topologies for cancellous bones. The effective strength of trabecular bone is evaluated in the two situations of fully brittle (fracture with no tissue ductility) and fully ductile failure (yield with no tissue fracture) of the trabecular tissue. An adaptation and extension of the discrete homogenization method towards a micropolar effective medium are subsequently introduced to construct the plastic yield surfaces for which the material point supports couple stresses in addition to Cauchy-type stresses. As a consequence, the plastic yield surfaces of trabecular bone are determined under the external applied couple stresses. A size-dependent non-classical plastic yield criterion is lastly developed relying on the reduced Cosserat theory to capture the size-dependency of the trabecular bone structures.

Growth and remodeling phenomena in biological tissues generally affect both changes in density (or rather mass) and changes in volume. Bone tissues are able to adapt their local density and load bearing capacities as well as their size and shape to mechanical stimuli. Such growth processes result in densification and formation of new material of bone in regions of high mechanically load levels as well as resorption and material removing in regions of low loading levels. As a fourth motivation aspect of this work, we develop models for the internal and external bone remodeling in the framework of the thermodynamics of irreversible processes. A numerical framework has been developed to simulate the process of external bone adaptation jointly with local adaptation with respect to applied mechanical loading at both the cellular level and the macroscopic level. The underlying mechanical framework is configurational mechanics, with Eshelby stress at the origin of the stimuli for both internal and external remodeling. The implementation of the numerical framework is quite general and can accommodate readily different material models and diverse mechanical stimuli.

The resistance of bones to damage by self-repair mechanisms and adaptation to the environmental conditions are the most important bone characteristics. Such adaptive changes are regulated by adaptive physiological process called bone remodeling. A better understanding of such process requires applying the elastic damage theory under the hypothesis of small strain to the bone structure and investigating its mechanical response. From the standpoint of biomechanics, there a significant need to make an attempt to put some of the theoretical framework in which a hypothetical statement can be made regarding the damage consequence on the process of adaptation of bone. To attain this goal, we use the framework of continuum thermodynamics to introduce and model the presence of damage. Thus, the last motivation aspect advocated to this work is to introduce a strategy for modeling the interaction of damage with the remodeling process in bones. We set up a model which combines an anisotropic internal remodeling rule with fatigue damage, based on continuum damage theory. Internal growth of bone is expressed in algorithmic format from a variational formulation of the strong form of the field equations, leading to a numerical implementation for 2D situations.

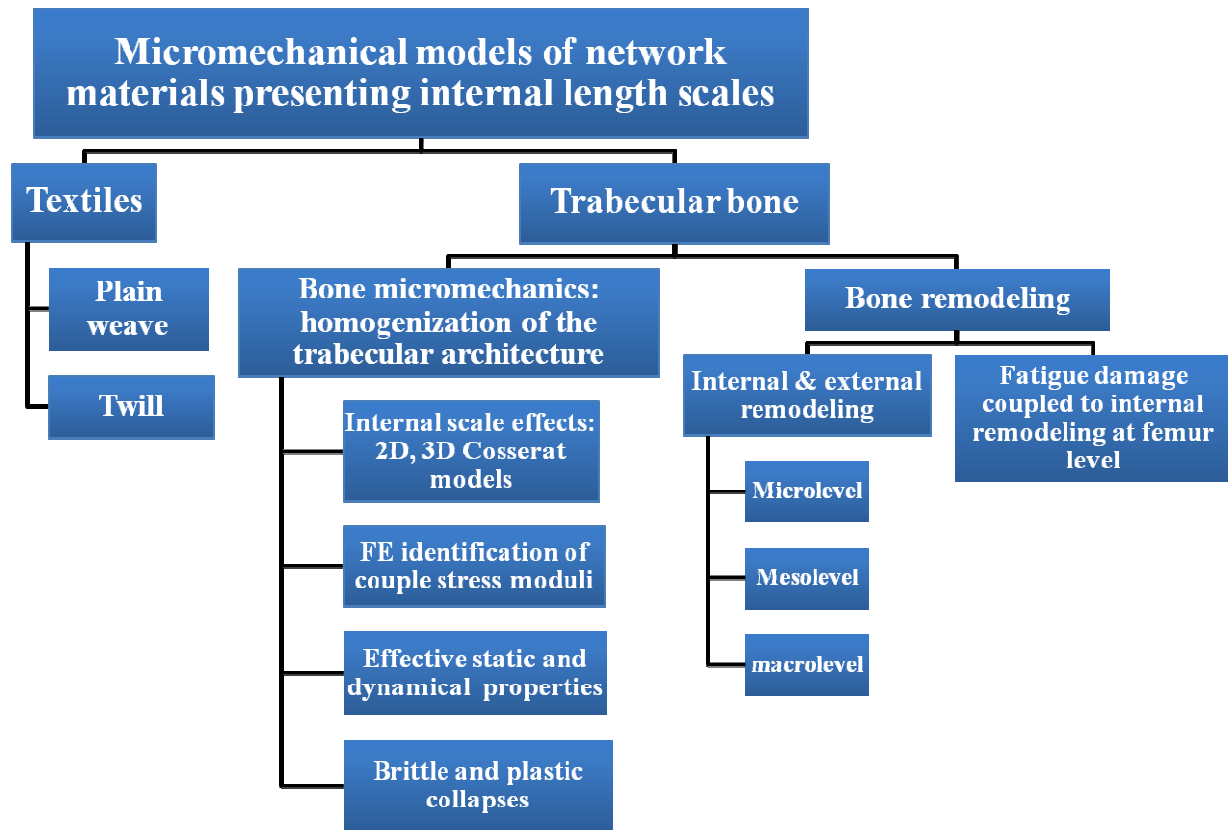
1.3 Scope and outline

The thesis is organized into two parts that develop various aspects of the main topic of the work, namely micromechanics of network materials like textiles and bones. The first part of the dissertation deals with the setting up micromechanical models for the prediction of the bone mechanical properties in relation to its architecture at the trabecular level. Since such microstructured materials very often exhibit internal length scale, requiring generalized continua for their description at an intermediate scale at which a continuum representation makes sense. The main goal of this thesis is thus to construct such generalized continua from initially discrete materials with a truss like topology. Textiles and trabecular bone structures fall within this class. Such structures exhibit size effects that the classical Cauchy continuum cannot properly address; we accordingly shall consider the following issues:

- We develop specific homogenization method prone to substitute an initially discrete network material by an equivalent continuum endowed with anisotropic effective mechanical properties; this homogenization technique is coined the discrete asymptotic homogenization;
- We construct micropolar continuum models describing the effective mechanical behavior of woven fabric monolayers from the homogenization of an identified repetitive pattern of the textile within a representative unit cell.
- We construct Cosserat models of trabecular bone in 2D and 3D situations, relying on micromechanical approaches in order to investigate microstructure-related scale effects on the macroscopic properties of bone.
- Anisotropic micropolar equivalent continuum models are built to capture the size dependent static and dynamic effective behavior of vertebral trabecular bone, in terms of the deflection, torsion and eigenfrequencies of deformations.

- We compute from finite element approaches the effective couple-stress continuum properties of vertebral trabecular bone, based on the equivalent strain energy approach. We model vertebral bone either as a cellular solid or as a two-phase material consisting of bone tissue (stiff phase) forming a trabecular network, and surrounding soft tissue referring to the bone marrow present in the pores.
- We develop an adequate three-dimensional model for describing the multiaxial plastic yielding and brittle fracture behavior of trabecular bone based on micromechanical approaches.
- Extension and adaptation towards a micropolar effective medium leads to construct the plastic collapse surfaces for which the material point supports couple stresses in addition to Cauchy-type stresses. We finally construct a size-dependent non-classical plastic yield criterion relying on micromechanical model in order to capture the plastic collapse size-dependency of trabecular bone structures.

The second part of the dissertation is devoted to bone remodeling, with a classification as either internal or external remodeling. Bone's capability to adapt its internal architecture and external shape to the surrounding environment has been a good subject of research in the last two decades. The common motivate factors for the computational bone remodeling is to understand and quantitatively describe the functional adaptation of bone and then to simulate and predict bone adaptation. For this purpose the second part of the dissertation deals with the simulation of bone remodeling in the framework of the thermodynamics of irreversible processes. We simulate the remodeling of bones relying on a surface growth model, leading to an overall shape change of the macroscopic domain. Since mechanical properties of the bone material evolve with their density, internal remodeling is accounted for in the model. Additionally, an integrated remodeling-to-fracture model is developed to simulate the bone remodelling process considering the anisotropy of trabecular bone. A schematic diagram synthesizing the different aspects of the topic of the thesis is given below



For a comprehensive view of the thesis content, the work will be presented to allow the reader to follow the evolution of our understanding of the problems raised and the adopted methodologies and solutions. The dissertation content is organized as follows.

[Chapter 2](#) of the dissertation is devoted to explore and elaborate the discrete homogenization techniques towards micropolar continua. The general principle of the micropolar asymptotic method is exposed leading to either a Cauchy or a micropolar effective continuum according to the maximum chosen order of asymptotic development of kinematic variables. The main steps of the employed discrete homogenization toward anisotropic micropolar continuum are also outlined. From a kinematic point of view, the articulated beams of the lattice are endowed with axial, transverse shear, flexural, and torsional deformations.

In [Chapter 3](#), micropolar continuum models describing the effective mechanical behavior of woven fabric monolayers are constructed from the homogenization of an identified repetitive pattern of the textile within a representative unit cell. The fabrics are modelled as a network of undulated and interwoven beams representing the yarns. The interwoven yarns within the textile are represented as a network of trusses connected by nodes at their crossover points. Interactions between yarns at the crossover points are captured by beam segments connecting the nodes. Their effective mechanical properties are validated by FE simulations performed over a representative unit cell.

In [Chapter 4](#), we derive the effective mechanical properties of cancellous bone considered as a cellular solid modeled as two-dimensional lattices of articulated beams. The cell walls of the bone microstructure are modeled as Timoshenko thick beams. The asymptotic homogenization is involved to get closed form expressions of the equivalent properties versus

the geometrical and mechanical microparameters, accounting for the effects of bending, axial, and transverse shear deformations. Simulations of a bone sample including a crack are next performed, using the previously obtained homogenized anisotropic micropolar model, highlighting the regularizing effect of the micropolar continuum in comparison to a classical continuum model. At the end of this chapter, 3D anisotropic micropolar continuum models of vertebral trabecular bone are developed in accounting for the influence of microstructure-related scale effects on the macroscopic effective properties; the justification of the micropolar effects and the validation of the method in terms of the accuracy of the predicted effective properties are also analyzed.

In [Chapter 5](#), we develop using finite element approaches, a homogeneous, orthotropic couple-stress continuum model as a substitute of the 3D periodic heterogeneous cellular solid model of vertebral trabecular bone. The effective properties are derived based on the response of the representative volume element under prescribed boundary conditions. Mixed boundary conditions comprising both traction and displacement boundary conditions are applied on the structure boundaries. Vertebral trabecular bone is modeled either as a cellular solid or as a two-phase material consisting of bone tissue (stiff phase) forming a trabecular network, and surrounding soft tissue referring to the bone marrow present in the pores. The effects of scale and boundary conditions on the predicted couple stress moduli of these networks are investigated by varying the size of the bone specimens over which the boundary conditions are applied.

[Chapter 6](#) expounds the characteristic features of the non-classical theory by developing 3D micropolar continuum models for the static and dynamic behaviors of vertebral trabecular bone. A 3D geometric model of a regular hexagonal structure is considered as an idealized representation of vertebral bone, highlighting the structurally relevant, age-controlled parameters in the model which are related to bone volume fraction. For this purpose, microstructure-dependent beam models for vertebral bone are developed for the purpose of evaluating the bending and torsional behaviors in both the static and dynamic regimes. The models contain material length scale parameter and are able to capture size effects. The governing differential equations of bending and torsion are derived employing Hamilton's principle (variational approach) and explicit analytical solutions are derived for the static and vibrational behaviors.

[Chapter 7](#) addresses the issues related to the determination of plastic yield surfaces and brittle failures of vertebral trabecular bone from asymptotic homogenization based on relationships between the morphology and multi-axial failure properties of bone. The plastic yield surface under multi-axial loading is constructed together with the brittle fracture surface in stress space under tri-axial loading conditions. As a second step, an extension and adaptation towards a micropolar effective medium leads to construct the plastic yield surfaces for which the material point supports couple stresses in addition to Cauchy-type stresses. As a consequence, the plastic yield surfaces of trabecular bone would be determined under the external applied couple stresses. Finally, a non-classical size-dependent plastic yield criterion is developed relying on the non-classical continuum theory in order to capture the size dependency observed in the bone structures.

In [Chapter 8](#), models for the surface growth of solid bodies are developed in the framework of the thermodynamics of irreversible processes. The growing surface is endowed by a specific mechanical behavior elaborated from a surface potential, depending upon an elastic surface strain and the normal to the growing surface. Mechanical equilibrium is written in terms of a surface Eshelby stress and involves the surface curvature tensor, while the surface velocity is related to the driving force for growth. The developed formalism is applied to simulate bone external remodeling for 2D geometries, showing the influence of external mechanical stimuli on the evolution of the external shape of bone.

In [Chapter 9](#), an anisotropic internal bone remodeling model is developed based on continuum damage mechanics theory and fatigue damage adapted to trabecular bone. Trabecular bone is modeled as a cellular structure in 2D with the cell walls described as a solid isotropic material. The objective of this chapter is then to simulate the internal remodeling within a two-dimensional model of the proximal femur, by considering an elastic-damage constitutive behavior and strain energy density as the mechanical stimulus driving density evolutions. Relying on the discrete homogenization, an anisotropic linear elasticity constitutive law for trabecular bone is derived at the continuum mesoscopic level, involving an anisotropic stiffness tensor. The computed stiffness coefficients are determined as explicit power functions of the effective internal density (itself a function of the morphological parameters of the selected unit cell), and they evolve with morphology as remodeling occurs, so that anisotropy changes with ongoing remodeling.

Finally, [Chapter 10](#) concludes the thesis by summarizing the achievements and limitations of the work, and ideas for future work are proposed.

CHAPTER 2: DISCRETE HOMOGENIZATION TECHNIQUE TOWARDS MICROPOLAR CONTINUA

In this chapter, a three-dimensional micropolar effective continuum model is constructed using asymptotic homogenization of 3D discrete media considering axial, shear, flexural and torsional deformations of the cell struts. The discrete homogenization method consists in assuming asymptotic series expansions of both the node displacements, tension, moments and external forces versus a small parameter labeled ϵ , defined as the ratio of a characteristic length of the basic cell to a characteristic length of the lattice structure. Those expansions are then inserted into the equilibrium equation, conveniently expressed in weak form. The balance equation of the nodes, forces-displacement relations and the moment-rotation relations of the beams are developed by inserting those series expansions and by using Taylor's expansion of finite differences. The discrete sums are finally converted in the limit of a continuous density of beams into Riemann integrals, thereby highlighting continuous stress and strain measures. The calculations are done for a quite general truss and closed form expressions of the effective (homogenized) properties are obtained from the effective compliance or rigidity matrix. The method has given rise to implementation into dedicated software.

2.1 Homogenization of 3D lattices and construction of a micropolar effective continuum

The microbeams building the fabric are considered as rigidly connected at joints (or nodes), each of which having six degrees of freedom (or displacements)-three translational and three rotational ones. The 12 possible displacements of the two joints of a member may be described relative to the (global) reference axes x , y and z , as shown in Figure 2.1. In a local coordinate system, the vector of nodal displacements of the beam element (Figure 2.1) is built as

$$[\mathbf{U}_p] = [u_{x1_p} \ u_{y1_p} \ u_{z1_p} \ \phi_{x1_p} \ \phi_{y1_p} \ \phi_{z1_p} \ u_{x2_p} \ u_{y2_p} \ u_{z2_p} \ \phi_{x2_p} \ \phi_{y2_p} \ \phi_{z2_p}]^T \quad (2.1)$$

Here and in the sequel, vectors and tensors are represented by boldface symbols.

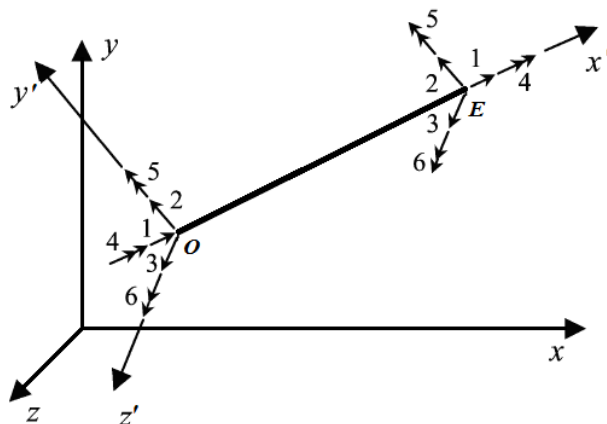


Figure 2.1: 3D beam element with six degrees of freedom at each node in local coordinates.

The forces at the extremities of a given beam undergoing simultaneous axial, transverse shearing, flexural and torsional deformations are related to the corresponding displacements in terms of the reference coordinates $\{x, y, \text{ and } z\}$ by the following equation

$$[\mathbf{F}_p] = [\mathbf{K}_p][\mathbf{T}][\mathbf{U}_s] \quad (2.2)$$

with \mathbf{K}_p the Timoshenko stiffness matrix of the beam and \mathbf{T} the local-to-global transformation matrix, which will be next explicitly written.

The vectors of nodal displacements and loads in (2.2) are successively written as

$$[\mathbf{U}_s] = [u_{xO_s} \ u_{yO_s} \ u_{zO_s} \ \phi_{xO_s} \ \phi_{yO_s} \ \phi_{zO_s} \ u_{xE_s} \ u_{yE_s} \ u_{zE_s} \ \phi_{xE_s} \ \phi_{yE_s} \ \phi_{zE_s}]^T$$

$$[\mathbf{F}_p] = [F_{xO_p} \ F_{yO_p} \ F_{zO_p} \ M_{xO_p} \ M_{yO_p} \ M_{zO_p} \ F_{xE_p} \ F_{yE_p} \ F_{zE_p} \ M_{xE_p} \ M_{yE_p} \ M_{zE_p}]^T \quad (2.3)$$

Consequently, the force vector in (2.2) can be rewritten as

$$\begin{bmatrix} F_{xO_p} \\ F_{yO_p} \\ F_{zO_p} \\ M_{xO_p} \\ M_{yO_p} \\ M_{zO_p} \\ F_{xE_p} \\ F_{yE_p} \\ F_{zE_p} \\ M_{xE_p} \\ M_{yE_p} \\ M_{zE_p} \end{bmatrix} = \begin{bmatrix} \frac{AE_s}{L} & 0 & 0 & 0 & 0 & 0 & -\frac{AE_s}{L} & 0 & 0 & 0 & 0 & 0 \\ 0 & \frac{12E_s I_z}{L^2(1+\Phi_y)} & 0 & 0 & 0 & \frac{6E_s I_z}{L(1+\Phi_y)} & 0 & -\frac{12E_s I_z}{L^2(1+\Phi_y)} & 0 & 0 & 0 & \frac{6E_s I_z}{L(1+\Phi_y)} \\ 0 & 0 & \frac{12E_s I_y}{L^2(1+\Phi_z)} & 0 & -\frac{6E_s I_y}{L(1+\Phi_z)} & 0 & 0 & 0 & -\frac{12E_s I_y}{L^2(1+\Phi_z)} & 0 & -\frac{6E_s I_y}{L(1+\Phi_z)} & 0 \\ 0 & 0 & 0 & \frac{G_s J_s}{L} & 0 & 0 & 0 & 0 & 0 & -\frac{G_s J_s}{L} & 0 & 0 \\ 0 & 0 & -\frac{6E_s I_z}{L^2(1+\Phi_y)} & 0 & \frac{(4+\Phi_z)E_s I_z}{L(1+\Phi_z)} & 0 & 0 & 0 & \frac{6E_s I_z}{L^2(1+\Phi_y)} & 0 & \frac{(2-\Phi_y)E_s I_z}{L(1+\Phi_y)} & 0 \\ 0 & \frac{6E_s I_z}{L^2(1+\Phi_y)} & 0 & 0 & 0 & \frac{(4+\Phi_z)E_s I_z}{L(1+\Phi_z)} & 0 & -\frac{6E_s I_z}{L^2(1+\Phi_y)} & 0 & 0 & 0 & \frac{(2-\Phi_y)E_s I_z}{L(1+\Phi_y)} \\ -\frac{AE_s}{L} & 0 & 0 & 0 & 0 & 0 & \frac{AE_s}{L} & 0 & 0 & 0 & 0 & 0 \\ 0 & -\frac{12E_s I_z}{L^2(1+\Phi_y)} & 0 & 0 & 0 & -\frac{6E_s I_z}{L(1+\Phi_y)} & 0 & \frac{12E_s I_z}{L^2(1+\Phi_y)} & 0 & 0 & 0 & -\frac{6E_s I_z}{L(1+\Phi_y)} \\ 0 & 0 & -\frac{12E_s I_y}{L^2(1+\Phi_z)} & 0 & \frac{6E_s I_y}{L(1+\Phi_z)} & 0 & 0 & 0 & \frac{12E_s I_y}{L^2(1+\Phi_z)} & 0 & \frac{6E_s I_y}{L(1+\Phi_z)} & 0 \\ 0 & 0 & 0 & \frac{G_s J_s}{L} & 0 & 0 & 0 & 0 & 0 & \frac{G_s J_s}{L} & 0 & 0 \\ 0 & 0 & -\frac{6E_s I_z}{L^2(1+\Phi_y)} & 0 & \frac{(2-\Phi_y)E_s I_z}{L(1+\Phi_y)} & 0 & 0 & 0 & \frac{6E_s I_z}{L^2(1+\Phi_y)} & 0 & \frac{(4+\Phi_z)E_s I_z}{L(1+\Phi_z)} & 0 \\ 0 & \frac{6E_s I_z}{L^2(1+\Phi_y)} & 0 & 0 & 0 & \frac{(2-\Phi_y)E_s I_z}{L(1+\Phi_y)} & 0 & -\frac{6E_s I_z}{L^2(1+\Phi_y)} & 0 & 0 & 0 & \frac{(4+\Phi_z)E_s I_z}{L(1+\Phi_z)} \end{bmatrix} \begin{bmatrix} u_{xO_s} \\ u_{yO_s} \\ u_{zO_s} \\ \phi_{xO_s} \\ \phi_{yO_s} \\ \phi_{zO_s} \\ u_{xE_s} \\ u_{yE_s} \\ u_{zE_s} \\ \phi_{xE_s} \\ \phi_{yE_s} \\ \phi_{zE_s} \end{bmatrix} \quad (2.4)$$

with the non-dimensional factors $\Phi_y = 12E_s I_z / G_s A k_{ys} L^2$ and $\Phi_z = 12E_s I_y / G_s A k_{zs} L^2$, vanishing when transverse shear can be neglected (hence a Bernoulli beam model is recovered).

The coefficients E_s , G_s are respectively the Young's modulus and shear modulus of the member material; A , L are respectively, the cross-sectional area and length of the member, I_y and I_z are the second moments of area of the member cross-section; k_{ys} and k_{zs} are the transverse shear correction factors, and J_s is the torsional modulus, which is identical to the polar moment of inertia of the circular cross-sectional area.

\mathbf{T} is the local-to-global transformation matrix, which consists of the four identical 3 x 3 rotation matrices

$$\mathbf{T} = \begin{bmatrix} \underline{t}_{3 \times 3} & 0 & 0 & 0 \\ 0 & \underline{t}_{3 \times 3} & 0 & 0 \\ 0 & 0 & \underline{t}_{3 \times 3} & 0 \\ 0 & 0 & 0 & \underline{t}_{3 \times 3} \end{bmatrix} \quad (2.5)$$

where \mathbf{t} is a 3 x 3 three-dimensional rotation matrix and 0 a 3 x 3 zero matrix. The direction cosines \mathbf{t} can be rewritten as

$$\mathbf{t} = \begin{bmatrix} C_{xx'} & C_{yx'} & C_{zx'} \\ C_{xy'} & C_{yy'} & C_{zy'} \\ C_{xz'} & C_{yz'} & C_{zz'} \end{bmatrix} \quad (2.6)$$

It is convenient to write the set of previous relations using a local basis attached to the frame member, consisting of the unit vector in the member direction $e_x = [C_{xx'} \ C_{yx'} \ C_{zx'}]^T$, the unit vector normal to the member in y' direction $e_y = [C_{xy'} \ C_{yy'} \ C_{zy'}]^T$, and the unit vector normal to the member in z' direction $e_z = [C_{xz'} \ C_{yz'} \ C_{zz'}]^T$. Where $C_{xx'} = \cos \theta_x$, $C_{yx'} = \cos \theta_y$, and $C_{zx'} = \cos \theta_z$ are the direction cosines of x' , describing the transformation between the local and global coordinate system in 3D. Similarly, the components of e_y and e_z are the direction cosines of y' and z' , respectively.

The displacement and rotation vectors at the nodes in the structural coordinate system u_o , u_E , ϕ_o , and ϕ_E are written respectively as:

$$u_o = \begin{bmatrix} u_{xO_s} \\ u_{yO_s} \\ u_{zO_s} \end{bmatrix}, \quad u_E = \begin{bmatrix} u_{xE_s} \\ u_{yE_s} \\ u_{zE_s} \end{bmatrix}, \quad \phi_o = \begin{bmatrix} \phi_{xO_s} \\ \phi_{yO_s} \\ \phi_{zO_s} \end{bmatrix}, \quad \text{and} \quad \phi_E = \begin{bmatrix} \phi_{xE_s} \\ \phi_{yE_s} \\ \phi_{zE_s} \end{bmatrix} \quad (2.7)$$

Since each beam is in self-equilibrium, we choose to define the efforts at node E (efforts at node O are opposite), which is considered in this work as the end node. Using the local coordinate systems for each member element, the normal (tension) force receives the expression

$$F_{xE_p} = \frac{AE_s}{L} (e_x \cdot (u_E - u_o)) \quad (2.8)$$

The transverse force F_{yE_p} is given by

$$F_{yE_p} = \frac{12E_s I_z}{L^3(1+\Phi_y)} \left(e_y \cdot (u_E - u_o) - \frac{L}{2} (e_z \cdot (\phi_o + \phi_E)) \right) \quad (2.9)$$

Similarly, the transverse force F_{zE_p} is given by

$$F_{zE_p} = \frac{12E_s I_y}{L^3(1+\Phi_z)} \left(e_z \cdot (u_E - u_o) + \frac{L}{2} (e_y \cdot (\phi_o + \phi_E)) \right) \quad (2.10)$$

The moments express at both extremities of the member express as follows: for the moments about the x' -axis (twist in y' - z' plane), the load-displacement relationship is very similar to axial loading, viz

$$M_{xO_p} = \frac{G_s J_s}{L} (e_x \cdot (\phi_O - \phi_E)) ; M_{xE_p} = \frac{G_s J_s}{L} (e_x \cdot (\phi_E - \phi_O)) \quad (2.11)$$

The bending moments about the y' -axis write

$$\begin{aligned} M_{yO_p} &= \frac{6E_s I_y}{L^2(1+\Phi_z)} (e_z \cdot (u_E - u_O)) + \frac{E_s I_y}{L(1+\Phi_z)} (e_y \cdot ((4+\Phi_z)\phi_O + (2-\Phi_z)\phi_E)) \\ M_{yE_p} &= \frac{6E_s I_y}{L^2(1+\Phi_z)} (e_z \cdot (u_E - u_O)) + \frac{E_s I_y}{L(1+\Phi_z)} (e_y \cdot ((2-\Phi_z)\phi_O + (4+\Phi_z)\phi_E)) \end{aligned} \quad (2.12)$$

The bending moments about the z' -axis express as

$$\begin{aligned} M_{zO_p} &= \frac{6E_s I_z}{L^2(1+\Phi_y)} (-e_y \cdot (u_E - u_O)) + \frac{E_s I_z}{L(1+\Phi_y)} (e_z \cdot ((4+\Phi_y)\phi_O + (2-\Phi_y)\phi_E)) \\ M_{zE_p} &= \frac{6E_s I_z}{L^2(1+\Phi_y)} (-e_y \cdot (u_E - u_O)) + \frac{E_s I_z}{L(1+\Phi_y)} (e_z \cdot ((2-\Phi_y)\phi_O + (4+\Phi_y)\phi_E)) \end{aligned} \quad (2.13)$$

The previous expressions of the resultant and moments are next involved in the homogenization of the initially discrete lattice towards an equivalent micropolar continuum.

2.2 Asymptotic homogenization of discrete media to micropolar continuum considering axial, shear, flexural and torsional deformations

The homogenisation method enables to define an equivalent macroscopic continuous description from the knowledge of the microstructural behaviour; it has a large field of applications that concern amongst other fields mechanics of materials, geotechnics and structural mechanics. The method is generally based on a continuum mechanics description at the microscale. The homogenization of elastic periodic discrete materials has been investigated by Sab (1996), Pradel and Sab (1998), and Pradel (1998). Asymptotic expansion methods and other related homogenization techniques were used to show that the overall elastic properties of the lattice can be derived by solving a discrete unit cell problem involving a finite number of degrees of freedom. In this contribution, the discrete asymptotic homogenization method proposed by Tollenare and Caillerie (1998), Caillerie et al. (2006), and Dos Reis and Ganghoffer (2012) is exploited for the construction of micropolar continua from elastic lattices endowed with translational and rotational degrees of freedom. As it will be shown, the method allows the treatment of elementary cells, including internal nodes; it is based on the asymptotic development of the kinematic and static variables under consideration, at an arbitrary order a priori. The method relies on a description of the connectivity of the studied structures and on the mechanical equilibrium written at each node.

The lattice under consideration is made of beams and is completely defined by the positions of the nodes and their connectivity: we denote by N_R and B_R respectively, the set of nodes and beams within the reference unit cell. The lattice is immersed in the 3D space and is supposed to be quasi periodical; hence, the cells are numbered by the triplet of integers $v^i = (v^1, v^2, v^3)$. The nodes of the whole lattice can then be parameterized by the quadruplet

$\tilde{n} = (n, v^1, v^2, v^3) \in N_R \times \mathbb{Z}^3$. Similarly, the lattice beams are described by the quadruplet $\tilde{b} = (b, v^1, v^2, v^3) \in B_R \times \mathbb{Z}^3$. Within the reference cell, one can select the origin node of a beam $O(\tilde{b})$ so that it belongs to the reference cell. This origin node can be represented by the quadruplet (n, v^1, v^2, v^3) . Nevertheless, the end node $E(\tilde{b})$ does not necessarily belong to the reference cell, but it is necessarily included in an adjacent cell numbered by $(v^1 + \delta^1, v^2 + \delta^2, v^3 + \delta^3)$. The triplet $(\delta^1, \delta^2, \delta^3) \in \mathbb{Z}^3$, and the end node either belongs to the reference cell or to a cell next to it: this means that in the general case the shift parameter are integers $\delta^i \in \{-1, 0, 1\}$.

The discrete homogenization techniques requires a development of all variables as Taylor series vs. the small parameter ε (the ratio of elementary cell's length to macroscopic lattice's length), namely the beam length L^{eb} , the beam width t^{eb} , the beam thickness e^{eb} , and the two kinematic variables, here the displacement $u^{\varepsilon n} = (u_x, u_y, u_z)$ and the rotation at the lattices nodes $\phi^{\varepsilon n} = (\phi_x, \phi_y, \phi_z)$.

The beam length L^{eb} can be expressed as the following asymptotic expansion $L^{eb} = \varepsilon L^b$ restricting here to a small strain analysis and a similar expansion holds for the width and thickness of the beam, variables t^{eb} and e^{eb} respectively.

For simplicity reasons, a square section of the beam ($t = e$) is considered, leading to a section of area $A = t^2$. Hence, the quadratic moment of the beam is evaluated as $I_y^{\varepsilon b} = I_z^{\varepsilon b} = (t^{eb})^4 / 12$ and the torsional constant is evaluated as $J^{\varepsilon b} \approx (t^{eb})^4 / 7$.

The coefficients Φ_y^ε and Φ_z^ε respectively receive the following expansions

$$\begin{aligned} \Phi_y^\varepsilon &= \frac{12E_s I_z^{\varepsilon b}}{G_s A^{\varepsilon b} k_{ys} (L^{\varepsilon b})^2} = \frac{E_s (t^b)^4}{G_s k_{ys} (t^b)^2 (L^b)^2} = \frac{E_s (t^b)^2}{G_s k_{ys} (L^b)^2} \\ \Phi_z^\varepsilon &= \frac{12E_s I_y^{\varepsilon b}}{G_s A^{\varepsilon b} k_{zs} (L^{\varepsilon b})^2} = \frac{E_s (t^b)^4}{G_s k_{zs} (t^b)^2 (L^b)^2} = \frac{E_s (t^b)^2}{G_s k_{zs} (L^b)^2} \end{aligned} \quad (2.14)$$

It is observed that Φ_y^ε and Φ_z^ε have a similar expansion since a square section is considered (the same shear correction is obtained, viz $k_{ys} = k_{zs} = k_s$).

The asymptotic expansion of the nodal displacement u^ε is written up to the second order as

$$u^\varepsilon(\lambda^\varepsilon) = u_0(\lambda^\varepsilon) + \varepsilon u_1(\lambda^\varepsilon) + \varepsilon^2 u_2(\lambda^\varepsilon) \quad (2.15)$$

For each beam, one denotes O the origin node and E the extremity node. with λ the curvilinear coordinate of the points within the lattice.

The displacement difference $\Delta U^{b\epsilon}$ between the extremity and origin node of each beam is expressed by a Taylor series development, according to

$$\begin{aligned} \Delta U^{b\epsilon} = u^\epsilon(E(b)) - u^\epsilon(O(b)) &= \epsilon \underbrace{\left(u_1^{E_{R(b)}}(\lambda^\epsilon) - u_1^{O_{R(b)}}(\lambda^\epsilon) + \frac{\partial u_0(\lambda^\epsilon)}{\partial \lambda^i} \delta^{ib} \right)}_{\Delta U_1^b} + \epsilon^2 \underbrace{\left(u_2^{E_{R(b)}}(\lambda^\epsilon) - u_2^{O_{R(b)}}(\lambda^\epsilon) \right)}_{\Delta U_2^b} \\ &= \epsilon \Delta U_1^b + \epsilon^2 \Delta U_2^b \end{aligned} \quad (2.16)$$

with δ^{ib} the shift factor (equal to ± 1) for nodes belonging to a neighbouring cell, and nil for nodes located inside the considered cell. The index R indicates a node belonging to the reference unit cell.

The asymptotic expansion of the nodal microrotation $\phi^{n\epsilon}$ is limited to the first order in ϵ ; it is defined successively at the origin and extremity of each beam as

$$\phi^{O(b)\epsilon} = \phi_0^{O_{R(b)}} + \epsilon \phi_1^{O_{R(b)}}; \quad \phi^{E(b)\epsilon} = \phi_0^{E_{R(b)}} + \epsilon \left(\frac{\partial \phi_0}{\partial \lambda^i} \delta^{ib} + \phi_1^{E_{R(b)}} \right) \quad (2.17)$$

wherein we have parameterized any point within the surface element representative of the lattice by curvilinear coordinates λ^i ; this allows treating lattice with curved material lines following the beams in their reference state.

The asymptotic expansions of the normal, transverse efforts, and moments at the beam extremities in the framework of 3D Timoshenko beams versus the kinematic nodal variables are next written; the normal force writes after straightforward calculations as

$$F_x^{\epsilon b} = \frac{A^{\epsilon b} E_s}{L^{\epsilon b}} \left(\mathbf{e}_x \cdot (\epsilon \Delta U_1^b + \epsilon^2 \Delta U_2^b) \right) \quad (2.18)$$

with the first and second order relative displacements given in equation (2.16).

The transverse force in y'-direction and z'-direction express successively as

$$F_y^{\epsilon b} = \frac{12 E_s I_z^{\epsilon b}}{(L^{\epsilon b})^3 (1 + \Phi_y^\epsilon)} \left(\mathbf{e}_y \cdot (\epsilon \Delta U_1^b + \epsilon^2 \Delta U_2^b) - \frac{L^{\epsilon b}}{2} \left(\mathbf{e}_z \cdot \left(\phi_0^{O_{R(b)}} + \phi_0^{E_{R(b)}} + \epsilon \left(\phi_1^{O_{R(b)}} + \phi_1^{E_{R(b)}} + \frac{\partial \phi_0}{\partial \lambda^i} \delta^{ib} \right) \right) \right) \right) \quad (2.19)$$

$$F_z^{\epsilon b} = \frac{12 E_s I_y^{\epsilon b}}{(L^{\epsilon b})^3 (1 + \Phi_z^\epsilon)} \left(\mathbf{e}_z \cdot (\epsilon \Delta U_1^b + \epsilon^2 \Delta U_2^b) + \frac{L^{\epsilon b}}{2} \left(\mathbf{e}_y \cdot \left(\phi_0^{O_{R(b)}} + \phi_0^{E_{R(b)}} + \epsilon \left(\phi_1^{O_{R(b)}} + \phi_1^{E_{R(b)}} + \frac{\partial \phi_0}{\partial \lambda^i} \delta^{ib} \right) \right) \right) \right) \quad (2.20)$$

Similarly, the asymptotic expansions of the moments are obtained after straightforward calculations as follows:

The torsional moments express as

$$M_x^{O(b)\epsilon} = \frac{G_s J_s^{\epsilon b}}{L^{\epsilon b}} \epsilon \left(\mathbf{e}_x \cdot \left(\phi_1^{O_{R(b)}} - \left(\frac{\partial \phi_0}{\partial \lambda^i} \delta^{ib} + \phi_1^{E_{R(b)}} \right) \right) \right); \quad M_x^{E(b)\epsilon} = \frac{G_s J_s^{\epsilon b}}{L^{\epsilon b}} \epsilon \left(\mathbf{e}_x \cdot \left(\phi_1^{E_{R(b)}} - \phi_1^{O_{R(b)}} + \frac{\partial \phi_0}{\partial \lambda^i} \delta^{ib} \right) \right) \quad (2.21)$$

The bending moments about the y'-axis receive the following expressions

$$\begin{aligned} M_y^{O(b)\epsilon} &= \frac{6 E_s I_y^{\epsilon b}}{(L^{\epsilon b})^2 (1 + \Phi_y^\epsilon)} \left(\mathbf{e}_z \cdot (\epsilon \Delta U_1^b + \epsilon^2 \Delta U_2^b) \right) \\ &+ \frac{E_s I_y^{\epsilon b}}{L^{\epsilon b} (1 + \Phi_y^\epsilon)} \left(\mathbf{e}_y \cdot \left((4 + \Phi_z^\epsilon) \phi_0^{O_{R(b)}} + (2 - \Phi_z^\epsilon) \phi_0^{E_{R(b)}} + \epsilon \left((4 + \Phi_z^\epsilon) \phi_1^{O_{R(b)}} + (2 - \Phi_z^\epsilon) \phi_1^{E_{R(b)}} + (2 - \Phi_z^\epsilon) \frac{\partial \phi_0}{\partial \lambda^i} \delta^{ib} \right) \right) \right) \end{aligned} \quad (2.22)$$

$$M_y^{E(b)\varepsilon} = \frac{6E_s I_y^{\varepsilon b}}{(L^{\varepsilon b})^2 (1 + \Phi_z^\varepsilon)} \left(\mathbf{e}_z \cdot (\varepsilon \Delta U_1^b + \varepsilon^2 \Delta U_2^b) \right) \\ + \frac{E_s I_y^{\varepsilon b}}{L^{\varepsilon b} (1 + \Phi_z^\varepsilon)} \left(\mathbf{e}_z \cdot \left((2 - \Phi_z^\varepsilon) \phi_0^{O_{R(b)}} + (4 + \Phi_z^\varepsilon) \phi_0^{E_{R(b)}} + \varepsilon \left((2 - \Phi_z^\varepsilon) \phi_1^{O_{R(b)}} + (4 + \Phi_z^\varepsilon) \phi_1^{E_{R(b)}} + (4 + \Phi_z^\varepsilon) \frac{\partial \phi_0}{\partial \lambda^i} \delta^{ib} \right) \right) \right)$$

Similarly, the bending moments about the z'-axis write

$$M_z^{O(b)\varepsilon} = \frac{6E_s I_z^{\varepsilon b}}{(L^{\varepsilon b})^2 (1 + \Phi_y^\varepsilon)} \left(-\mathbf{e}_y \cdot (\varepsilon \Delta U_1^b + \varepsilon^2 \Delta U_2^b) \right) \\ + \frac{E_s I_z^{\varepsilon b}}{L^{\varepsilon b} (1 + \Phi_y^\varepsilon)} \left(\mathbf{e}_y \cdot \left((4 + \Phi_y^\varepsilon) \phi_0^{O_{R(b)}} + (2 - \Phi_y^\varepsilon) \phi_0^{E_{R(b)}} + \varepsilon \left((4 + \Phi_y^\varepsilon) \phi_1^{O_{R(b)}} + (2 - \Phi_y^\varepsilon) \phi_1^{E_{R(b)}} + (2 - \Phi_y^\varepsilon) \frac{\partial \phi_0}{\partial \lambda^i} \delta^{ib} \right) \right) \right) \\ M_z^{E(b)\varepsilon} = \frac{6E_s I_z^{\varepsilon b}}{(L^{\varepsilon b})^2 (1 + \Phi_y^\varepsilon)} \left(-\mathbf{e}_y \cdot (\varepsilon \Delta U_1^b + \varepsilon^2 \Delta U_2^b) \right) \\ + \frac{E_s I_z^{\varepsilon b}}{L^{\varepsilon b} (1 + \Phi_y^\varepsilon)} \left(\mathbf{e}_y \cdot \left((2 - \Phi_y^\varepsilon) \phi_0^{O_{R(b)}} + (4 + \Phi_y^\varepsilon) \phi_0^{E_{R(b)}} + \varepsilon \left((2 - \Phi_y^\varepsilon) \phi_1^{O_{R(b)}} + (4 + \Phi_y^\varepsilon) \phi_1^{E_{R(b)}} + (4 + \Phi_y^\varepsilon) \frac{\partial \phi_0}{\partial \lambda^i} \delta^{ib} \right) \right) \right) \quad (2.23)$$

The self-equilibrium of forces for the whole lattice writes in virtual power form and after insertion of the asymptotic development of the variables as

$$\sum_{v' \in \mathbb{Z}^3} \sum_{b \in B_R} \mathbf{F}^{\varepsilon b} \cdot (\mathbf{v}^\varepsilon(O(b)) - \mathbf{v}^\varepsilon(E(b))) = 0 \quad (2.24)$$

with $\mathbf{v}(\cdot)$ a virtual velocity field chosen to vanish on the edges. For any virtual velocity field \mathbf{v}^ε , supposed to be regular enough, a Taylor series's development at the first order leads to

$$\mathbf{v}^\varepsilon(O(b)) - \mathbf{v}^\varepsilon(E(b)) \approx \varepsilon \frac{\partial \mathbf{v}(\lambda^\varepsilon)}{\partial \lambda^i} \delta^{ib} \quad (2.25)$$

The vector of efforts $\mathbf{F}^{\varepsilon b}$ decomposes into a normal and two transverse contributions as

$$\mathbf{F}^{\varepsilon b} = F_x^{\varepsilon b} \mathbf{e}_x + F_y^{\varepsilon b} \mathbf{e}_y + F_z^{\varepsilon b} \mathbf{e}_z \quad (2.26)$$

Substituting and ordering previous expressions of the forces according to the successive powers of ε , the vector of efforts $\mathbf{F}^{\varepsilon b}$ becomes

$$\begin{aligned}
\mathbf{F}^{\varepsilon b} = \varepsilon^2 & \left(\begin{aligned} & \left(\frac{(t^b)^2 E_s}{L^b} (\mathbf{e}_x \cdot \Delta \mathbf{U}_1^b) \mathbf{e}_x + \frac{E_s (t^b)^4}{(L^b)^3 \left(1 + \frac{E_s (t^b)^2}{G_s k_s (L^b)^2} \right)} \left(\mathbf{e}_y \cdot \Delta \mathbf{U}_1^b - \frac{L^b}{2} (\mathbf{e}_z \cdot (\phi_0^{O_{R(b)}} + \phi_0^{E_{R(b)}})) \right) \right) \mathbf{e}_y \\ & + \frac{E_s (t^b)^4}{(L^b)^3 \left(1 + \frac{E_s (t^b)^2}{G_s k_s (L^b)^2} \right)} \left(\mathbf{e}_z \cdot \Delta \mathbf{U}_1^b + \frac{L^b}{2} (\mathbf{e}_y \cdot (\phi_0^{O_{R(b)}} + \phi_0^{E_{R(b)}})) \right) \right) \mathbf{e}_z \end{aligned} \right) \\
& + \varepsilon^3 \left(\begin{aligned} & \left(\frac{(t^b)^2 E_s}{L^b} (\mathbf{e}_x \cdot \Delta \mathbf{U}_2^b) \mathbf{e}_x + \frac{E_s (t^b)^4}{(L^b)^3 \left(1 + \frac{E_s (t^b)^2}{G_s k_s (L^b)^2} \right)} \left(\mathbf{e}_y \cdot \Delta \mathbf{U}_2^b - \frac{L^b}{2} \left(\mathbf{e}_z \cdot \left(\phi_1^{O_{R(b)}} + \phi_1^{E_{R(b)}} + \frac{\partial \phi_0}{\partial \lambda^i} \delta^{ib} \right) \right) \right) \right) \mathbf{e}_y \\ & + \frac{E_s (t^b)^4}{(L^b)^3 \left(1 + \frac{E_s (t^b)^2}{G_s k_s (L^b)^2} \right)} \left(\mathbf{e}_z \cdot \Delta \mathbf{U}_2^b + \frac{L^b}{2} \left(\mathbf{e}_y \cdot \left(\phi_1^{O_{R(b)}} + \phi_1^{E_{R(b)}} + \frac{\partial \phi_0}{\partial \lambda^i} \delta^{ib} \right) \right) \right) \right) \mathbf{e}_z \end{aligned} \right) \end{aligned} \quad (2.27)$$

Inserting the equations (2.25) and (2.27) into the equilibrium equation (2.24) and ordering the developed equation according to the successive powers of ε delivers the following double sum

$$\begin{aligned}
& \left(\begin{aligned} & \left(\frac{(t^b)^2 E_s}{L^b} (\mathbf{e}_x \cdot \Delta \mathbf{U}_1^b) \mathbf{e}_x + \frac{E_s (t^b)^4}{(L^b)^3 \left(1 + \frac{E_s (t^b)^2}{G_s k_s (L^b)^2} \right)} \left(\mathbf{e}_y \cdot \Delta \mathbf{U}_1^b - \frac{L^b}{2} (\mathbf{e}_z \cdot (\phi_0^{O_{R(b)}} + \phi_0^{E_{R(b)}})) \right) \right) \mathbf{e}_y \\ & + \frac{E_s (t^b)^4}{(L^b)^3 \left(1 + \frac{E_s (t^b)^2}{G_s k_s (L^b)^2} \right)} \left(\mathbf{e}_z \cdot \Delta \mathbf{U}_1^b + \frac{L^b}{2} (\mathbf{e}_y \cdot (\phi_0^{O_{R(b)}} + \phi_0^{E_{R(b)}})) \right) \right) \mathbf{e}_z \end{aligned} \right) \cdot \frac{\partial \mathbf{v}(\lambda^\varepsilon)}{\partial \lambda^i} \delta^{ib} \\
& + \left(\begin{aligned} & \left(\frac{(t^b)^2 E_s}{L^b} (\mathbf{e}_x \cdot \Delta \mathbf{U}_2^b) \mathbf{e}_x + \frac{E_s (t^b)^4}{(L^b)^3 \left(1 + \frac{E_s (t^b)^2}{G_s k_s (L^b)^2} \right)} \left(\mathbf{e}_y \cdot \Delta \mathbf{U}_2^b - \frac{L^b}{2} \mathbf{e}_z \cdot \left(\phi_1^{O_{R(b)}} + \phi_1^{E_{R(b)}} + \frac{\partial \phi_0}{\partial \lambda^i} \delta^{ib} \right) \right) \right) \mathbf{e}_y \\ & + \frac{E_s (t^b)^4}{(L^b)^3 \left(1 + \frac{E_s (t^b)^2}{G_s k_s (L^b)^2} \right)} \left(\mathbf{e}_z \cdot \Delta \mathbf{U}_2^b + \frac{L^b}{2} \mathbf{e}_y \cdot \left(\phi_1^{O_{R(b)}} + \phi_1^{E_{R(b)}} + \frac{\partial \phi_0}{\partial \lambda^i} \delta^{ib} \right) \right) \right) \mathbf{e}_z \end{aligned} \right) \cdot \frac{\partial \mathbf{v}(\lambda^\varepsilon)}{\partial \lambda^i} \delta^{ib} \\
& \left. \vphantom{\left(\begin{aligned} & \left(\frac{(t^b)^2 E_s}{L^b} (\mathbf{e}_x \cdot \Delta \mathbf{U}_1^b) \mathbf{e}_x + \frac{E_s (t^b)^4}{(L^b)^3 \left(1 + \frac{E_s (t^b)^2}{G_s k_s (L^b)^2} \right)} \left(\mathbf{e}_y \cdot \Delta \mathbf{U}_1^b - \frac{L^b}{2} (\mathbf{e}_z \cdot (\phi_0^{O_{R(b)}} + \phi_0^{E_{R(b)}})) \right) \right) \mathbf{e}_y \right.} \right) \right) \vphantom{\left(\frac{(t^b)^2 E_s}{L^b} (\mathbf{e}_x \cdot \Delta \mathbf{U}_1^b) \mathbf{e}_x + \frac{E_s (t^b)^4}{(L^b)^3 \left(1 + \frac{E_s (t^b)^2}{G_s k_s (L^b)^2} \right)} \left(\mathbf{e}_y \cdot \Delta \mathbf{U}_1^b - \frac{L^b}{2} (\mathbf{e}_z \cdot (\phi_0^{O_{R(b)}} + \phi_0^{E_{R(b)}})) \right) \right) \mathbf{e}_y} \right)} \right) = 0 \quad (2.28)
\end{aligned}$$

Previous equation gives in the limit a continuous integral, basing on the following result: for any regular enough function g , the quantity $\varepsilon^3 \sum_{v^j \in \mathbb{Z}^3} g(\varepsilon v^j)$ can be interpreted as the Riemann integral $\int_{\Omega} g(\lambda) d\lambda$ in 3D when $\varepsilon \rightarrow 0$. The previous discrete equilibrium equation becomes after homogenization the following continuous self-equilibrium in virtual power form

$$\int_{\Omega} \mathbf{S}^i \cdot \frac{\partial \mathbf{v}}{\partial \lambda^i} d\lambda = 0 \quad (2.29)$$

with the stress vector decomposing as $\mathbf{S}^i = \mathbf{S}_1^i + \varepsilon \mathbf{S}_2^i$, introducing therein the first and second order stress vectors $\mathbf{S}_1^i, \mathbf{S}_2^i$, expressed as following sums over all beams of the reference unit cell

$$\begin{aligned} \mathbf{S}_1^i = \sum_{b \in B_R} & \left(\frac{(l^b)^2 E_s}{L^b} (\mathbf{e}_x \cdot \Delta \mathbf{U}_1^b) \mathbf{e}_x + \frac{E_s (l^b)^4}{(L^b)^3 \left(1 + \frac{E_s (l^b)^2}{G_s k_s (L^b)^2} \right)} \left(\mathbf{e}_y \cdot \Delta \mathbf{U}_1^b - \frac{L^b}{2} (\mathbf{e}_z \cdot (\phi_0^{O_{R(b)}} + \phi_0^{E_{R(b)}})) \right) \right) \mathbf{e}_y \\ & + \left(\frac{E_s (l^b)^4}{(L^b)^3 \left(1 + \frac{E_s (l^b)^2}{G_s k_s (L^b)^2} \right)} \left(\mathbf{e}_z \cdot \Delta \mathbf{U}_1^b + \frac{L^b}{2} (\mathbf{e}_y \cdot (\phi_0^{O_{R(b)}} + \phi_0^{E_{R(b)}})) \right) \right) \mathbf{e}_z \end{aligned} \Bigg) \delta^{ib} \quad (2.30)$$

$$\mathbf{S}_2^i = \sum_{b \in B_R} \left(\frac{(l^b)^2 E_s}{L^b} (\mathbf{e}_x \cdot \Delta \mathbf{U}_2^b) \mathbf{e}_x + \frac{E_s (l^b)^4}{(L^b)^3 \left(1 + \frac{E_s (l^b)^2}{G_s k_s (L^b)^2} \right)} \left(\mathbf{e}_y \cdot \Delta \mathbf{U}_2^b - \frac{L^b}{2} \left(\phi_1^{O_{R(b)}} + \phi_1^{E_{R(b)}} + \frac{\partial \phi_0}{\partial \lambda^i} \delta^{ib} \right) \right) \right) \mathbf{e}_y$$

$$+ \left(\frac{E_s (l^b)^4}{(L^b)^3 \left(1 + \frac{E_s (l^b)^2}{G_s k_s (L^b)^2} \right)} \left(\mathbf{e}_z \cdot \Delta \mathbf{U}_2^b + \frac{L^b}{2} \left(\mathbf{e}_y \cdot \left(\phi_1^{O_{R(b)}} + \phi_1^{E_{R(b)}} + \frac{\partial \phi_0}{\partial \lambda^i} \delta^{ib} \right) \right) \right) \right) \mathbf{e}_z \Bigg) \delta^{ib}$$

The moment equilibrium can be written in two different ways: first, the moment equilibrium for the lattice nodes is obtained by analogy to the finite element method applied to beams and in asymptotic form as

$$\sum_{v' \in \mathbb{Z}^3} \sum_{b \in B_R} (\mathbf{M}^{O(b)\varepsilon} \cdot \mathbf{w}^\varepsilon (O(b)) + \mathbf{M}^{E(b)\varepsilon} \cdot \mathbf{w}^\varepsilon (E(b))) = 0 \quad (2.31)$$

This form shall prove useful for the resolution of the unknowns, but for the homogenization stage, one shall instead consider another approach involving the local equilibrium of each individual beam, a balance law that holds true when summed up for all beams; this equilibrium is written at the center of each beam in asymptotic form as

$$\sum_{v' \in \mathbb{Z}^3} \sum_{b \in B_R} (\mathbf{M}^{O(b)\varepsilon} \cdot \mathbf{w}^\varepsilon (O(b)) + \mathbf{M}^{E(b)\varepsilon} \cdot \mathbf{w}^\varepsilon (E(b)) + \varepsilon L^b (\mathbf{e}_x \wedge \mathbf{F}^{\varepsilon b}) \cdot \mathbf{w}^\varepsilon (C(b))) = 0 \quad (2.32)$$

denoting therein \mathbf{e}_x the unit director vector for the beam, $\mathbf{M}^{O(b)}$ and $\mathbf{M}^{E(b)}$ the moments at the origin and extremity nodes of each beam respectively, and $\mathbf{w}(\cdot)$ the virtual rotation velocity, which is similarly expanded taking into account the central node of the beam $C(b)$ as

$$\mathbf{w}^{O(b)\varepsilon} = \mathbf{w}_0(\lambda) \quad (2.33)$$

$$\mathbf{w}^{E(b)\varepsilon}(\lambda + \varepsilon \delta^i) \approx \mathbf{w}_0(\lambda) + \varepsilon \frac{\partial \mathbf{w}_0(\lambda)}{\partial \lambda^i} \delta^{ib}$$

$$\mathbf{w}^{C(b)\varepsilon} = \frac{1}{2} (\mathbf{w}^{E(b)\varepsilon} + \mathbf{w}^{O(b)\varepsilon})$$

The moments at the extremities $\mathbf{M}^{O(b)}$ and $\mathbf{M}^{E(b)}$ can next be expressed as

$$\begin{aligned} \mathbf{M}^{O(b)\varepsilon} &= (M_x^{O(b)\varepsilon} \mathbf{e}_x + M_y^{O(b)\varepsilon} \mathbf{e}_y + M_z^{O(b)\varepsilon} \mathbf{e}_z) \\ &= \frac{G_s J_s^{eb}}{L^{eb}} \varepsilon \left(e_x \cdot \left(\phi_1^{O_{R(b)}} - \left(\frac{\partial \phi_0}{\partial \lambda^i} \delta^{ib} + \phi_1^{E_{R(b)}} \right) \right) \right) \mathbf{e}_x \\ &\quad + \left(\frac{6E_s I_y^{eb}}{(L^{eb})^2 (1 + \Phi_z^\varepsilon)} (e_z \cdot (\varepsilon \Delta U_1^b + \varepsilon^2 \Delta U_2^b)) \right. \\ &\quad \left. + \frac{E_s I_y^{eb}}{L^{eb} (1 + \Phi_z^\varepsilon)} \left(e_y \cdot \left((4 + \Phi_z^\varepsilon) \phi_0^{O_{R(b)}} + (2 - \Phi_z^\varepsilon) \phi_0^{E_{R(b)}} + \varepsilon \left((4 + \Phi_z^\varepsilon) \phi_1^{O_{R(b)}} + (2 - \Phi_z^\varepsilon) \phi_1^{E_{R(b)}} + (2 - \Phi_z^\varepsilon) \frac{\partial \phi_0}{\partial \lambda^i} \delta^{ib} \right) \right) \right) \right) \mathbf{e}_y \\ &\quad + \left(\frac{6E_s I_z^{eb}}{(L^{eb})^2 (1 + \Phi_y^\varepsilon)} (-e_y \cdot (\varepsilon \Delta U_1^b + \varepsilon^2 \Delta U_2^b)) \right. \\ &\quad \left. + \frac{E_s I_z^{eb}}{L^{eb} (1 + \Phi_y^\varepsilon)} \left(e_z \cdot \left((4 + \Phi_y^\varepsilon) \phi_0^{O_{R(b)}} + (2 - \Phi_y^\varepsilon) \phi_0^{E_{R(b)}} + \varepsilon \left((4 + \Phi_y^\varepsilon) \phi_1^{O_{R(b)}} + (2 - \Phi_y^\varepsilon) \phi_1^{E_{R(b)}} + (2 - \Phi_y^\varepsilon) \frac{\partial \phi_0}{\partial \lambda^i} \delta^{ib} \right) \right) \right) \right) \mathbf{e}_z \end{aligned} \quad (2.34)$$

$$\begin{aligned} \mathbf{M}^{E(b)\varepsilon} &= (M_x^{E(b)\varepsilon} \mathbf{e}_x + M_y^{E(b)\varepsilon} \mathbf{e}_y + M_z^{E(b)\varepsilon} \mathbf{e}_z) \\ &= \frac{G_s J_s^{eb}}{L^{eb}} \varepsilon \left(e_x \cdot \left(\phi_1^{E_{R(b)}} - \phi_1^{O_{R(b)}} + \frac{\partial \phi_0}{\partial \lambda^i} \delta^{ib} \right) \right) \mathbf{e}_x \\ &\quad + \left(\frac{6E_s I_y^{eb}}{(L^{eb})^2 (1 + \Phi_z^\varepsilon)} (e_z \cdot (\varepsilon \Delta U_1^b + \varepsilon^2 \Delta U_2^b)) \right. \\ &\quad \left. + \frac{E_s I_y^{eb}}{L^{eb} (1 + \Phi_z^\varepsilon)} \left(e_y \cdot \left((2 - \Phi_z^\varepsilon) \phi_0^{O_{R(b)}} + (4 + \Phi_z^\varepsilon) \phi_0^{E_{R(b)}} + \varepsilon \left((2 - \Phi_z^\varepsilon) \phi_1^{O_{R(b)}} + (4 + \Phi_z^\varepsilon) \phi_1^{E_{R(b)}} + (4 + \Phi_z^\varepsilon) \frac{\partial \phi_0}{\partial \lambda^i} \delta^{ib} \right) \right) \right) \right) \mathbf{e}_y \\ &\quad + \left(\frac{6E_s I_z^{eb}}{(L^{eb})^2 (1 + \Phi_y^\varepsilon)} (-e_y \cdot (\varepsilon \Delta U_1^b + \varepsilon^2 \Delta U_2^b)) \right. \\ &\quad \left. + \frac{E_s I_z^{eb}}{L^{eb} (1 + \Phi_y^\varepsilon)} \left(e_z \cdot \left((2 - \Phi_y^\varepsilon) \phi_0^{O_{R(b)}} + (4 + \Phi_y^\varepsilon) \phi_0^{E_{R(b)}} + \varepsilon \left((2 - \Phi_y^\varepsilon) \phi_1^{O_{R(b)}} + (4 + \Phi_y^\varepsilon) \phi_1^{E_{R(b)}} + (4 + \Phi_y^\varepsilon) \frac{\partial \phi_0}{\partial \lambda^i} \delta^{ib} \right) \right) \right) \right) \mathbf{e}_z \end{aligned}$$

Previous equation can be rewritten after some developments and ordering according to the successive powers of ε under the form

$$\begin{aligned} \mathbf{M}^{O(b)\varepsilon} &= \varepsilon^3 (M_{1y}^{O(b)} \mathbf{e}_y + M_{1z}^{O(b)} \mathbf{e}_z) + \varepsilon^4 (M_{2x}^{O(b)} \mathbf{e}_x + M_{2y}^{O(b)} \mathbf{e}_y + M_{2z}^{O(b)} \mathbf{e}_z) \\ \mathbf{M}^{E(b)\varepsilon} &= \varepsilon^3 (M_{1y}^{E(b)} \mathbf{e}_y + M_{1z}^{E(b)} \mathbf{e}_z) + \varepsilon^4 (M_{2x}^{E(b)} \mathbf{e}_x + M_{2y}^{E(b)} \mathbf{e}_y + M_{2z}^{E(b)} \mathbf{e}_z) \end{aligned} \quad (2.35)$$

with the successive components therein expressing as

$$\begin{aligned} M_{1y}^{O(b)} &= \frac{E_s (t^b)^4}{2(L^b)^2 \left(1 + \frac{E_s (t^b)^2}{G_s k_s (L^b)^2} \right)} (e_z \cdot \Delta U_1^b) + \frac{E_s (t^b)^4}{12L^b \left(1 + \frac{E_s (t^b)^2}{G_s k_s (L^b)^2} \right)} \left(e_y \cdot \left(\left(4 + \frac{E_s (t^b)^2}{G_s k_s (L^b)^2} \right) \phi_0^{O_{R(b)}} + \left(2 - \frac{E_s (t^b)^2}{G_s k_s (L^b)^2} \right) \phi_0^{E_{R(b)}} \right) \right) \\ M_{1z}^{O(b)} &= \frac{E_s (t^b)^4}{2(L^b)^2 \left(1 + \frac{E_s (t^b)^2}{G_s k_s (L^b)^2} \right)} (-e_y \cdot \Delta U_1^b) + \frac{E_s (t^b)^4}{12L^b \left(1 + \frac{E_s (t^b)^2}{G_s k_s (L^b)^2} \right)} \left(e_z \cdot \left(\left(4 + \frac{E_s (t^b)^2}{G_s k_s (L^b)^2} \right) \phi_0^{O_{R(b)}} + \left(2 - \frac{E_s (t^b)^2}{G_s k_s (L^b)^2} \right) \phi_0^{E_{R(b)}} \right) \right) \\ M_{2x}^{O(b)} &= \frac{G_s (t^b)^4}{7L^b} \left(e_x \cdot \left(\phi_1^{O_{R(b)}} - \left(\frac{\partial \phi_0}{\partial \lambda^i} \delta^{ib} + \phi_1^{E_{R(b)}} \right) \right) \right) \end{aligned}$$

$$\begin{aligned}
M_{2y}^{O(b)} &= \frac{E_s(t^b)^4}{2(L^b)^2 \left(1 + \frac{E_s(t^b)^2}{G_s k_s (L^b)^2}\right)} (e_z \cdot \Delta U_2^b) + \frac{E_s(t^b)^4}{12L^b \left(1 + \frac{E_s(t^b)^2}{G_s k_s (L^b)^2}\right)} \left(e_y \cdot \left(\left(4 + \frac{E_s(t^b)^2}{G_s k_s (L^b)^2}\right) \phi_1^{O_{R(b)}} + \left(2 - \frac{E_s(t^b)^2}{G_s k_s (L^b)^2}\right) \phi_1^{E_{R(b)}} + \left(2 - \frac{E_s(t^b)^2}{G_s k_s (L^b)^2}\right) \frac{\partial \phi_0}{\partial \lambda^i} \delta^{ib} \right) \right) \\
M_{2z}^{O(b)} &= \frac{E_s(t^b)^4}{2(L^b)^2 (1 + \Phi_y^e)} (-e_y \cdot \Delta U_2^b) + \frac{E_s(t^b)^4}{12L^b (1 + \Phi_y^e)} \left(e_z \cdot \left(\left(4 + \frac{E_s(t^b)^2}{G_s k_s (L^b)^2}\right) \phi_1^{O_{R(b)}} + \left(2 - \frac{E_s(t^b)^2}{G_s k_s (L^b)^2}\right) \phi_1^{E_{R(b)}} + \left(2 - \frac{E_s(t^b)^2}{G_s k_s (L^b)^2}\right) \frac{\partial \phi_0}{\partial \lambda^i} \delta^{ib} \right) \right) \\
M_{1y}^{E(b)} &= \frac{E_s(t^b)^4}{2(L^b)^2 \left(1 + \frac{E_s(t^b)^2}{G_s k_s (L^b)^2}\right)} (e_z \cdot \Delta U_1^b) + \frac{E_s(t^b)^4}{12L^b \left(1 + \frac{E_s(t^b)^2}{G_s k_s (L^b)^2}\right)} \left(e_y \cdot \left(\left(2 - \frac{E_s(t^b)^2}{G_s k_s (L^b)^2}\right) \phi_0^{O_{R(b)}} + \left(4 + \frac{E_s(t^b)^2}{G_s k_s (L^b)^2}\right) \phi_0^{E_{R(b)}} \right) \right) \\
M_{1z}^{E(b)} &= \frac{E_s(t^b)^4}{2(L^b)^2 \left(1 + \frac{E_s(t^b)^2}{G_s k_s (L^b)^2}\right)} (-e_y \cdot \Delta U_1^b) + \frac{E_s(t^b)^4}{12L^b \left(1 + \frac{E_s(t^b)^2}{G_s k_s (L^b)^2}\right)} \left(e_z \cdot \left(\left(2 - \frac{E_s(t^b)^2}{G_s k_s (L^b)^2}\right) \phi_0^{O_{R(b)}} + \left(4 + \frac{E_s(t^b)^2}{G_s k_s (L^b)^2}\right) \phi_0^{E_{R(b)}} \right) \right) \\
M_{2x}^{E(b)} &= \frac{G_s(t^b)^4}{7L^b} \left(e_x \cdot \left(\phi_1^{E_{R(b)}} - \phi_1^{O_{R(b)}} + \frac{\partial \phi_0}{\partial \lambda^i} \delta^{ib} \right) \right) \\
M_{2y}^{E(b)} &= \frac{E_s(t^b)^4}{2(L^b)^2 \left(1 + \frac{E_s(t^b)^2}{G_s k_s (L^b)^2}\right)} (e_z \cdot \Delta U_2^b) + \frac{E_s(t^b)^4}{12L^b \left(1 + \frac{E_s(t^b)^2}{G_s k_s (L^b)^2}\right)} \left(e_y \cdot \left(\left(2 - \frac{E_s(t^b)^2}{G_s k_s (L^b)^2}\right) \phi_1^{O_{R(b)}} + \left(4 + \frac{E_s(t^b)^2}{G_s k_s (L^b)^2}\right) \phi_1^{E_{R(b)}} + \left(4 + \frac{E_s(t^b)^2}{G_s k_s (L^b)^2}\right) \frac{\partial \phi_0}{\partial \lambda^i} \delta^{ib} \right) \right) \\
M_{2z}^{E(b)} &= \frac{E_s(t^b)^4}{2(L^b)^2 \left(1 + \frac{E_s(t^b)^2}{G_s k_s (L^b)^2}\right)} (-e_y \cdot \Delta U_2^b) + \frac{E_s(t^b)^4}{12L^b \left(1 + \frac{E_s(t^b)^2}{G_s k_s (L^b)^2}\right)} \left(e_z \cdot \left(\left(2 - \frac{E_s(t^b)^2}{G_s k_s (L^b)^2}\right) \phi_1^{O_{R(b)}} + \left(4 + \frac{E_s(t^b)^2}{G_s k_s (L^b)^2}\right) \phi_1^{E_{R(b)}} + \left(4 + \frac{E_s(t^b)^2}{G_s k_s (L^b)^2}\right) \frac{\partial \phi_0}{\partial \lambda^i} \delta^{ib} \right) \right)
\end{aligned}$$

Proceeding similarly as for the equilibrium of efforts, the equations (2.27), (2.33), and (2.35) are inserted into the equilibrium of moments expressed into virtual power form, equation (2.32). One finally obtains after some lengthy algebra the following equation

$$\sum_{v' \in \mathbb{Z}^3} \sum_{b \in B_R} \left(\begin{aligned} & \varepsilon^4 \left(\frac{E_s(t^b)^4}{12L^b} \left((e_y \cdot (\phi_0^{E_{R(b)}} - \phi_0^{O_{R(b)}})) e_y + (e_z \cdot (\phi_0^{E_{R(b)}} - \phi_0^{O_{R(b)}})) e_z \right) \right) + \\ & \varepsilon^5 \left(\frac{G_s(t^b)^4}{7L^b} \left(e_x \cdot \left(\phi_1^{E_{R(b)}} - \phi_1^{O_{R(b)}} + \frac{\partial \phi_0}{\partial \lambda^i} \delta^{ib} \right) e_x \right) \right. \\ & \left. + \frac{E_s(t^b)^4}{12L^b} \left((e_y \cdot (\phi_1^{E_{R(b)}} - \phi_1^{O_{R(b)}} + \frac{\partial \phi_0}{\partial \lambda^i} \delta^{ib})) e_y + (e_z \cdot (\phi_1^{E_{R(b)}} - \phi_1^{O_{R(b)}} + \frac{\partial \phi_0}{\partial \lambda^i} \delta^{ib})) e_z \right) \right) \end{aligned} \right) \delta^{ib} \cdot \frac{\partial \mathbf{w}_0(\lambda)}{\partial \lambda^i} = 0 \quad (2.36)$$

Similarly as for the equilibrium of efforts, the moment equilibrium (2.36) is homogenized. After some developments and simplifications and passing to the limit $\varepsilon \rightarrow 0$ in the discrete sum, the moment equilibrium equation after homogenization takes the following form

$$\int_{\Omega} \mu^i \cdot \frac{\partial \mathbf{w}(\lambda)}{\partial \lambda^i} d\lambda = 0 \quad (2.37)$$

The homogenization of the discrete moment equilibrium leads to the identification of the couple stress vectors incorporating the first and second order contributions $\boldsymbol{\mu}^i = \varepsilon \boldsymbol{\mu}_1^i + \varepsilon^2 \boldsymbol{\mu}_2^i$, with

$$\begin{aligned}
\boldsymbol{\mu}_1^i &= \sum_{b \in B_R} \left(\frac{E_s (t^b)^4}{12L^b} \left((\mathbf{e}_y \cdot (\phi_0^{E_{R(b)}} - \phi_0^{O_{R(b)}})) \mathbf{e}_y + (\mathbf{e}_z \cdot (\phi_0^{E_{R(b)}} - \phi_0^{O_{R(b)}})) \mathbf{e}_z \right) \right) \delta^{ib} \\
&= \sum_{b \in B_R} \left(\frac{1}{2} (M_{1y}^{E(b)} - M_{1y}^{O(b)}) \mathbf{e}_y + \frac{1}{2} (M_{1z}^{E(b)} - M_{1z}^{O(b)}) \mathbf{e}_z \right) \delta^{ib} \\
\boldsymbol{\mu}_2^i &= \sum_{b \in B_R} \left(\left(\frac{G_s (t^b)^4}{7L^b} \left(\mathbf{e}_x \cdot \left(\phi_1^{E_{R(b)}} - \phi_1^{O_{R(b)}} + \frac{\partial \phi_0}{\partial \lambda^i} \delta^{ib} \right) \right) \mathbf{e}_x \right) \right. \\
&\quad \left. + \frac{E_s (t^b)^4}{12L^b} \left((\mathbf{e}_y \cdot (\phi_1^{E_{R(b)}} - \phi_1^{O_{R(b)}} + \frac{\partial \phi_0}{\partial \lambda^i} \delta^{ib})) \mathbf{e}_y + (\mathbf{e}_z \cdot (\phi_1^{E_{R(b)}} - \phi_1^{O_{R(b)}} + \frac{\partial \phi_0}{\partial \lambda^i} \delta^{ib})) \mathbf{e}_z \right) \right) \delta^{ib} \\
&= \sum_{b \in B_R} \left(M_{2x}^{E(b)} \mathbf{e}_x + \frac{1}{2} (M_{2y}^{E(b)} - M_{2y}^{O(b)}) \mathbf{e}_y + \frac{1}{2} (M_{2z}^{E(b)} - M_{2z}^{O(b)}) \mathbf{e}_z \right) \delta^{ib}
\end{aligned} \tag{2.38}$$

One next formulates the effective anisotropic micropolar behavior by identifying the homogenized formulation with the constitutive equations of a continuous (anisotropic) micropolar continuum, the formulation of which is recalled in the next section.

2.3 Identification of the homogenized 3D micropolar continuum

The constitutive equations of a micropolar linear anisotropic elastic solid write

$$\boldsymbol{\sigma}_{ij} = E_{ijkl} \boldsymbol{\epsilon}_{kl} + B_{ijkl} \boldsymbol{\chi}_{kl}, \quad m_{ij} = B_{klij} \boldsymbol{\epsilon}_{kl} + K_{ijkl} \boldsymbol{\chi}_{kl} \quad (i, j, k, l = x, y, z) \tag{2.39}$$

where E_{ijkl} , B_{ijkl} and K_{ijkl} are the micropolar fourth rank stiffness tensors respectively; the stiffness tensor with components E_{ijkl} relates stresses to strains, while the curvature tensor with components K_{ijkl} relates couple stresses to microrotations. For periodical uniform structures endowed with centro-symmetry, the stiffness coefficients are invariant under a coordinate inversion, hence the pseudo-tensor B_{ijkl} vanishes. This tensor is responsible of the coupling between stresses and microcurvatures and between couple stresses and strains. Moreover, it must be noticed that E_{ijkl} and K_{ijkl} enjoy the major symmetries

$E_{ijkl} = E_{klij}$ and $K_{ijkl} = K_{klij}$, traducing the fact that both tensors are associated with a potential energy. The constitutive equations of the effective micropolar continua can then be written as follows

$$\boldsymbol{\sigma}_{ij} = E_{ijkl} \boldsymbol{\epsilon}_{kl}, \quad m_{ij} = K_{ijkl} \boldsymbol{\chi}_{kl} \tag{2.40}$$

In the case of orthotropic solids, the elasticity tensor is defined by at most 15 independent coefficients. For isotropic solids, each elasticity tensor is defined by three independent elastic constants; in this last case, the elasticity coefficients can be expressed in any Cartesian reference frame as

$$\begin{aligned}
E_{ijkl} &= \lambda \delta_{ij} \delta_{kl} + \mu^* \delta_{il} \delta_{jk} + (\mu^* + \kappa) \delta_{ik} \delta_{jl}, \\
K_{ijkl} &= \alpha \delta_{ij} \delta_{kl} + \beta \delta_{il} \delta_{jk} + \gamma \delta_{ik} \delta_{jl}
\end{aligned} \tag{2.41}$$

where δ_{ij} is the Kronecker symbol, and $\lambda, \mu^*, \kappa, \alpha, \beta$ and γ are six micropolar elastic constants, satisfying the relation $\mu = \mu^* + \kappa/2$. In those expressions, λ and μ are the classical Lamé constants with dimensions of force/length², κ, α, β and γ are new micropolar constants that vanish for classical materials. The dimension of κ is force/length², and α, β, γ have dimension of forces (couple/length). Two characteristic lengths can be extracted from the constitutive law, equation (2.40), corresponding to the bending ($m_{ij}, i \neq j$), or torsion-like ($m_{ij}, i = j$) couple-stress components. These two characteristic lengths can be computed from the torsion of circular cylinder and plate bending, respectively. They are related to the micro-polar elastic constants as follows (Lakes, 1995):

$$\ell_t = \left(\frac{\beta + \gamma}{2\mu^* + \kappa} \right)^{1/2}; \ell_b = \left(\frac{\gamma}{2(2\mu^* + \kappa)} \right)^{1/2} \tag{2.42}$$

The stress and couple-stress vectors are combined into a single generalized vector $\boldsymbol{\sigma}^C = [\boldsymbol{\sigma}, \mathbf{m}]^T$, with

$$\begin{aligned}
\boldsymbol{\sigma} &= [\sigma_{xx}, \sigma_{yy}, \sigma_{zz}, \sigma_{xy}, \sigma_{yx}, \sigma_{yz}, \sigma_{zy}, \sigma_{zx}, \sigma_{xz}]^T \\
\mathbf{m} &= [m_{xx}, m_{yy}, m_{zz}, m_{xy}, m_{yx}, m_{yz}, m_{zy}, m_{zx}, m_{xz}]^T
\end{aligned} \tag{2.43}$$

in which the components m_{xx}, m_{yy}, m_{zz} are the torsion couple-stresses. Similarly, the strains and micro-curvatures are combined into a single generalized strain vector $\boldsymbol{\epsilon}^C = [\boldsymbol{\epsilon}, \boldsymbol{\chi}]^T$, where $\boldsymbol{\epsilon}$ and $\boldsymbol{\chi}$ are the following vectors

$$\begin{aligned}
\boldsymbol{\epsilon} &= [\epsilon_{xx}, \epsilon_{yy}, \epsilon_{zz}, \epsilon_{xy}, \epsilon_{yx}, \epsilon_{yz}, \epsilon_{zy}, \epsilon_{zx}, \epsilon_{xz}]^T \\
\boldsymbol{\chi} &= [\chi_{xx}, \chi_{yy}, \chi_{zz}, \chi_{xy}, \chi_{yx}, \chi_{yz}, \chi_{zy}, \chi_{zx}, \chi_{xz}]^T
\end{aligned} \tag{2.44}$$

After removing the interaction between the stress and couple-stress components due to centro-symmetry (we restrict to media endowed with this symmetry in the present contribution), the constitutive relation for an elastic Cosserat medium can be written as $\boldsymbol{\sigma}^C = \mathbf{D}\boldsymbol{\epsilon}^C$, where \mathbf{D} (18×18 matrix) is the elastic Cosserat constitutive matrix defined by

$$\mathbf{D} = \begin{bmatrix} \mathbf{E} & \mathbf{0} \\ \mathbf{0} & \mathbf{K} \end{bmatrix} \tag{2.45}$$

Hence, the constitutive equations can be recast into the form

$$\boldsymbol{\sigma} = \mathbf{E}\boldsymbol{\epsilon}, \quad \mathbf{m} = \mathbf{K}\boldsymbol{\chi} \tag{2.46}$$

where, according to the orthotropic nature of the problem, the matrix representation of \mathbf{E} is

$$\mathbf{E} = \begin{bmatrix} E_{11} & E_{12} & E_{13} & 0 & 0 & 0 & 0 & 0 & 0 \\ E_{21} & E_{22} & E_{23} & 0 & 0 & 0 & 0 & 0 & 0 \\ E_{31} & E_{32} & E_{33} & 0 & 0 & 0 & 0 & 0 & 0 \\ 0 & 0 & 0 & E_{44} & E_{45} & 0 & 0 & 0 & 0 \\ 0 & 0 & 0 & E_{54} & E_{55} & 0 & 0 & 0 & 0 \\ 0 & 0 & 0 & 0 & 0 & E_{66} & E_{67} & 0 & 0 \\ 0 & 0 & 0 & 0 & 0 & E_{76} & E_{77} & 0 & 0 \\ 0 & 0 & 0 & 0 & 0 & 0 & 0 & E_{88} & E_{89} \\ 0 & 0 & 0 & 0 & 0 & 0 & 0 & E_{98} & E_{99} \end{bmatrix} \quad (2.47)$$

The curvature tensor \mathbf{K} in (2.46) has the same structure.

Note that the isotropic case is recovered when the following relations are taken into account

$$\begin{aligned} E_{11} &= E_{22} = E_{33} = \lambda + 2\mu^* + \kappa; \\ E_{12} &= E_{13} = E_{23} = \lambda; \quad E_{45} = E_{67} = E_{89} = \mu^*; \\ E_{44} &= E_{55} = E_{66} = E_{77} = E_{88} = E_{99} = \mu^* + \kappa; \\ K_{11} &= K_{22} = K_{33} = \alpha + \beta + \gamma; \\ K_{12} &= K_{13} = K_{23} = \alpha; \quad K_{45} = K_{67} = K_{89} = \beta; \\ K_{44} &= K_{55} = K_{66} = K_{77} = K_{88} = K_{99} = \gamma. \end{aligned} \quad (2.48)$$

Using the symmetry properties of the lattice, one can further simplify the expressions of the Cauchy stress $\boldsymbol{\sigma}$ and (Cauchy) couple stress \mathbf{m} . The general form of the constitutive equations of linear micropolar elasticity, equation (2.39), can presently be identified from the expressions of the homogenized stress and couple stress tensors together with \mathbf{S}^i and $\boldsymbol{\mu}^i$ expressions:

$$\begin{aligned} \boldsymbol{\sigma} &= \frac{1}{g} \mathbf{S}^i \otimes \frac{\partial \mathbf{R}}{\partial \lambda^i} = \frac{1}{g} (\mathbf{S}_1^i + \varepsilon \mathbf{S}_2^i) \otimes \frac{\partial \mathbf{R}}{\partial \lambda^i} = \underbrace{\frac{1}{g} \mathbf{S}_1^i \otimes \frac{\partial \mathbf{R}}{\partial \lambda^i}}_{[E]\{\varepsilon\}} + \underbrace{\frac{1}{g} \varepsilon \mathbf{S}_2^i \otimes \frac{\partial \mathbf{R}}{\partial \lambda^i}}_{[B]\{\chi\}} \\ \mathbf{m} &= \frac{1}{g} \boldsymbol{\mu}^i \otimes \frac{\partial \mathbf{R}}{\partial \lambda^i} = \frac{1}{g} (\varepsilon \boldsymbol{\mu}_1^i + \varepsilon^2 \boldsymbol{\mu}_2^i) \otimes \frac{\partial \mathbf{R}}{\partial \lambda^i} = \underbrace{\frac{1}{g} \varepsilon \boldsymbol{\mu}_1^i \otimes \frac{\partial \mathbf{R}}{\partial \lambda^i}}_{[B]\{\varepsilon\}} + \underbrace{\frac{1}{g} \varepsilon^2 \boldsymbol{\mu}_2^i \otimes \frac{\partial \mathbf{R}}{\partial \lambda^i}}_{[K]\{\chi\}} \end{aligned} \quad (2.49)$$

with g the Jacobean of the transformation from Cartesian to curvilinear coordinates and \mathbf{R} the position vector of any material point.

Accordingly, the constitutive equations for the equivalent micropolar continuum can be written from equation (2.46) in 3D matrix format as

$$\begin{aligned}
& \left\{ \sigma_{xx}, \sigma_{yy}, \sigma_{zz}, \sigma_{xy}, \sigma_{yx}, \sigma_{yz}, \sigma_{zy}, \sigma_{zx}, \sigma_{xz} \right\}^T \\
& = [\mathbf{E}] \left\{ \frac{\partial u_x}{\partial x}, \frac{\partial u_y}{\partial y}, \frac{\partial u_z}{\partial z}, \frac{\partial u_y}{\partial x} - \phi_z, \frac{\partial u_x}{\partial y} + \phi_z, \frac{\partial u_z}{\partial y} - \phi_x, \frac{\partial u_y}{\partial z} + \phi_x, \frac{\partial u_x}{\partial z} - \phi_y, \frac{\partial u_z}{\partial x} + \phi_y \right\}^T; \\
& \left\{ m_{xx}, m_{yy}, m_{zz}, m_{xy}, m_{yx}, m_{yz}, m_{zy}, m_{zx}, m_{xz} \right\}^T \\
& = [\mathbf{K}] \left\{ \frac{\partial \phi_x}{\partial x}, \frac{\partial \phi_y}{\partial y}, \frac{\partial \phi_z}{\partial z}, \frac{\partial \phi_y}{\partial x}, \frac{\partial \phi_x}{\partial y}, \frac{\partial \phi_z}{\partial y}, \frac{\partial \phi_y}{\partial z}, \frac{\partial \phi_x}{\partial z}, \frac{\partial \phi_z}{\partial x} \right\}^T
\end{aligned} \tag{2.50}$$

Focusing herewith on centro-symmetrical lattices, the previous constitutive equation then implies that the vectors $\boldsymbol{\mu}_1^i$ and \mathbf{S}_2^i should vanish; this leads to an important simplification of the stress and couple stress vectors, which receive the simplified expressions

$$\begin{aligned}
\mathbf{S}^i = \mathbf{S}_1^i &= \sum_{b \in B_R} \left(\frac{(t^b)^2 E_s}{L^b} (\mathbf{e}_x \cdot \Delta \mathbf{U}_1^b) \mathbf{e}_x + \frac{E_s (t^b)^4}{(L^b)^3 \left(1 + \frac{E_s (t^b)^2}{G_s k_s (L^b)^2} \right)} \left(\mathbf{e}_y \cdot \Delta \mathbf{U}_1^b - \frac{L^b}{2} (\mathbf{e}_z \cdot (\phi_0^{O_{R(b)}} + \phi_0^{E_{R(b)}})) \right) \right) \mathbf{e}_y \\
&+ \left(\frac{E_s (t^b)^4}{(L^b)^3 \left(1 + \frac{E_s (t^b)^2}{G_s k_s (L^b)^2} \right)} \left(\mathbf{e}_z \cdot \Delta \mathbf{U}_1^b + \frac{L^b}{2} (\mathbf{e}_y \cdot (\phi_0^{O_{R(b)}} + \phi_0^{E_{R(b)}})) \right) \right) \mathbf{e}_z \Bigg) \delta^{ib} \\
&= \sum_{b \in B_R} (F_{x1}^b \mathbf{e}_x + F_{y1}^b \mathbf{e}_y + F_{z1}^b \mathbf{e}_z) \\
\boldsymbol{\mu}^i = \boldsymbol{\mu}_2^i &= \sum_{b \in B_R} \left(\frac{G_s (t^b)^4}{7L^b} \left(\mathbf{e}_x \cdot \left(\phi_1^{E_{R(b)}} - \phi_1^{O_{R(b)}} + \frac{\partial \phi_0}{\partial \lambda^i} \delta^{ib} \right) \right) \mathbf{e}_x \right) \\
&+ \frac{E_s (t^b)^4}{12L^b} \left(\left(\mathbf{e}_y \cdot \left(\phi_1^{E_{R(b)}} - \phi_1^{O_{R(b)}} + \frac{\partial \phi_0}{\partial \lambda^i} \delta^{ib} \right) \right) \mathbf{e}_y + \left(\mathbf{e}_z \cdot \left(\phi_1^{E_{R(b)}} - \phi_1^{O_{R(b)}} + \frac{\partial \phi_0}{\partial \lambda^i} \delta^{ib} \right) \right) \mathbf{e}_z \right) \Bigg) \delta^{ib} \\
&= \sum_{b \in B_R} \left(M_{2x}^{E(b)} \mathbf{e}_x + \frac{1}{2} (M_{2y}^{E(b)} - M_{2y}^{O(b)}) \mathbf{e}_y + \frac{1}{2} (M_{2z}^{E(b)} - M_{2z}^{O(b)}) \mathbf{e}_z \right) \delta^{ib}
\end{aligned} \tag{2.51}$$

with F_{x1}^b , F_{y1}^b , F_{z1}^b , M_{2x}^n , M_{2y}^n , and M_{2z}^n respectively, the first order normal and transverse efforts and the second order moment about axes x' , y' , and z' . Those expressions still involve the unknown displacements u_1^n , u_2^n and rotations ϕ_0^n , ϕ_1^n , which are determined for all nodes by solving the equilibrium equations (2.24) and (2.31). After solving for the first order rotation unknowns ϕ_0^n , it appears that those variables are function of the deformation tensor $[\boldsymbol{\epsilon}]$; one then splits the deformation into a symmetrical and an antisymmetrical part, respectively denoted $\boldsymbol{\epsilon}^{(s)}$ and $\boldsymbol{\epsilon}^{(a)}$. The homogenized microrotation $\boldsymbol{\phi}(\phi_x, \phi_y, \phi_z)$ is identified to the antisymmetrical part of the strain tensor, hence this gives

$$\phi_0^n = \underbrace{c_i \epsilon_i^{\{ \}}}_{\phi_{\{0\}0}^n} + \underbrace{d_i \epsilon_i^{\} \{}}_{\phi = \phi_{\{0\}0}} \quad (2.52)$$

One shall note that the antisymmetrical part of the microrotation $\phi_{\{0\}0}(\lambda)$ is independent of the considered node in the unit cell; hence, it represents the equivalent (homogenized) microrotation of the unit cell. The first order rotation $\phi_{\{0\}0}(\lambda)$ is obtained by identifying afterwards the variable micropolar rotation $\phi_{\{0\}0} = \phi$ in the first order solution for the micropolar rotation variable. The micropolar rotation $\phi = (\phi_x, \phi_y, \phi_z)$ is identified as

$$\phi_x = \frac{1}{2} \left(\frac{\partial u_z}{\partial y} - \frac{\partial u_y}{\partial z} \right); \quad \phi_y = \frac{1}{2} \left(\frac{\partial u_x}{\partial z} - \frac{\partial u_z}{\partial x} \right); \quad \phi_z = \frac{1}{2} \left(\frac{\partial u_y}{\partial x} - \frac{\partial u_x}{\partial y} \right) \quad (2.53)$$

2.4 Conclusions

In this chapter, the discrete homogenization method is employed as a mathematical technique to derive the equivalent continuous medium behavior of a repetitive discrete structure made of elementary cells. The discrete homogenization method consists of assuming asymptotic series expansions of both static and kinematic parameters in the successive powers of a small parameter labeled ε , defined as the ratio of a characteristic length of the basic cell to a characteristic length of the lattice structure. Those expansions are then inserted into the equilibrium equations, conveniently expressed in weak form. The discrete sums are finally converted in the limit of a continuous density of beams into Riemann integrals, thereby highlighting continuous stress and strain measures. A three-dimensional micropolar effective continuum model has been constructed using asymptotic homogenization of 3D discrete media considering axial, shear, flexural and torsional deformations of the cell struts. The effective anisotropic classical and micropolar behaviors are identified with the constitutive equations of a continuous (anisotropic) micropolar continuum.

CHAPTER 3: COMPUTATION OF THE EFFECTIVE MECHANICAL PROPERTIES OF TEXTILES

This chapter addresses the issue of predicting the mechanical behavior of different woven fabric architectures using a discrete homogenization approach, through which the initially discrete architecture is transformed into an equivalent homogeneous effective medium. The determination of the effective mechanical moduli of textiles from mechanical measurements is usually difficult due to their discrete architecture, which makes micromechanical analyses a relevant alternative to access those properties. Micropolar continuum models describing the effective mechanical behavior of woven fabric monolayers are constructed from the homogenization of an identified repetitive pattern of the textile within a representative unit cell. The interwoven yarns within the textile are represented as a network of trusses connected by nodes at their crossover points. These trusses have extensional and bending rigidities to allow for yarn stretching and flexion, and a transverse shear deformation is additionally considered. Interactions between yarns at the crossover points are captured by beam segments connecting the nodes. The woven fabric is modeled after homogenization as an anisotropic planar continuum with two preferred material directions in the mean plane of the textile. Based on the developed methodology, the effective mechanical properties of plain weave and twill are evaluated, including their bending moduli and characteristic flexural lengths. A satisfactory agreement is obtained between the effective moduli obtained by homogenization and numerical values obtained by finite element simulations performed over periodic unit cells.

3.1 Introduction

Over the past decade, considerable attention from the composite manufacturing sector has been devoted to textile composites and especially woven fabrics. These materials have many advantages over unidirectional fibers reinforced composites, such as enhanced dimensional stability over a large range of temperatures (Tabiei and Yi, 2002), more balanced properties in the fabric plane, and better impact resistance.

The mechanical behavior of woven fabrics is of interest in numerous applications, including apparel, fabric reinforced composites, and body armor for ballistic protection. The development of these technologies requires a thorough understanding of the mechanical behavior of woven fabrics. Such fabrics are produced by the assembly of two or more fiber bundles (called yarns) in a specific architecture defining the armor (e.g. plain weave, twill, satin). Their fabrication involves interlacing two series of yarns, known as warps and wefts. From a modeling point of view, woven fabrics may be studied at different length scales as shown in Figure 3.1.

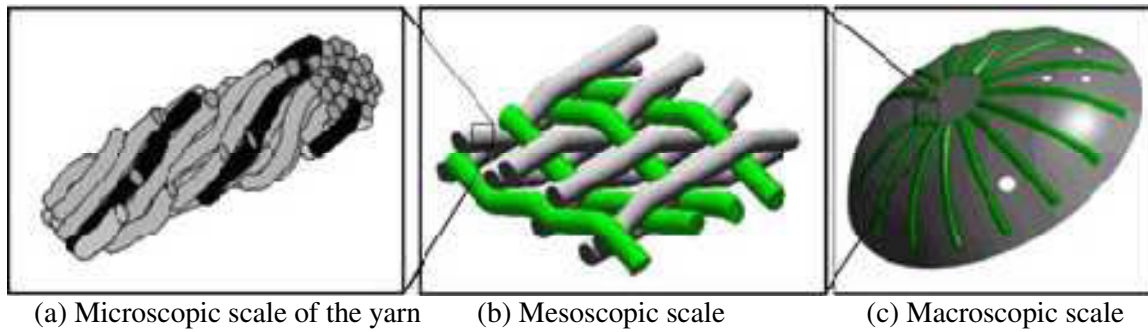


Figure 3.1: Multiscale modelling of woven fabrics.

The mechanical behavior of fabrics is clearly a multi-scale problem: at the macroscopic scale, the fabric consists of an assembly of yarns in the armor (meso-scale), themselves composed of fibers (micro-scale), leading overall to a complex mechanical behavior. Micro-scale approaches take the distribution and the contact between thousands of fibers into account. Some studies have been performed at this scale (Durville, 2002), but the analyses of the mechanical behavior of the woven unit cell at this scale is very difficult accounting for the number of fibers (some thousands) in a unit cell. In macro-scale approaches, fabrics are modeled as membranes (or shells if bending is taken into account). These approaches are used in forming simulations. Macroscale analyses focus on the characterization of fabric behavior without explicitly modeling the geometric structure of the textile. Usually the fabric is modeled as a homogeneous continuum which obeys a certain constitutive relation. Crimp and interlacement effects are important features of the fabric reinforcement behavior, but it is difficult to incorporate those effects into continuum analyses and continuum models. The analyses at meso-scale consider the geometry of the woven unit cell but consider the yarns as continuous domains. Single yarn interactions are also taken into account in analyses on the mesoscale. These analyses ensure a good compromise between realism and complexity.

To this end, woven fabrics can be considered as structured, hierarchical materials, having the three structural levels previously described (Lomov et al., 2007). The mechanical behavior of woven fabrics is complex due to the intricate interactions of the yarns that constitute the fabric “mesostructure”. Despite many attempts to develop effective models for fabric behavior, there is currently no widely accepted modeling approach that can accurately describe all the important aspects of the fabric mechanical behavior. This is due in part to the variability of requirements for fabric models in different applications (Parsons et al., 2010). A number of these models are next reviewed.

3.2 Review of unit-cell models for woven fabrics

The unit cell to be modeled is described as being the smallest unit of textile that, when tiled, will generate the full scale textile. The fibers within a yarn are not modeled individually; instead, yarns are represented as solid volumes representing the approximate bounds of the fibers they are made of. There are several reasons for this: first of all it is much easier to represent the yarn as a solid volume, and secondly this kind of representation is much more

useful in view of the computational analysis of textile properties. Many modeling approaches have been used while studying the mechanical behavior of fabrics, which can be classified into analytical and numerical models. Most of them are based on the repetitive unit cell technique, the principle consisting in analyzing the mechanical behavior in the smallest geometrical repetitive unit of the textile material. The resulting RUC properties are considered to be representative for the material.

A lot of mesostructurally based analytical models have been developed for the study of woven fabrics behaviors. Such analytical models use mathematical relations to predict the mechanical response of the fabric and its component yarns in specific modes of deformation. In addition, these models can be used to quantify the homogenized material properties for use in continuum models. [Hearle et al. \(1969\)](#) described a number of classical analytical fabric models. In the early 21st century, the same author [Hearle et al. \(2001\)](#) and [Sagar et al. \(2003\)](#) developed models for fabric based on energy minimization. [Kawabata et al. \(1973a; 1973b; 1973c\)](#) presented general models for uniaxial, biaxial and shear deformation properties of plain weave fabrics based on a simplified model representing the structure of the fabric unit cells. The basic geometry used in these models is based on one dimensional stiffness elements (bars) representing yarns, and the connecting stiffness elements at intersection of yarns to model the compression between yarns. Other researchers have developed improved analytical models, including [Realf et al. \(1997\)](#), who modify Kawabata's uniaxial model to include more complex behaviors such as yarn flattening and consolidation. [Kato et al. \(1999\)](#) proposed an analytical model for predicting the constitutive behavior of a coated fabric composite that is based on the pin-joined lattice-type geometry. Recently, [Ben Boubaker et al. \(2007a,b,c\)](#) developed a meso-level discrete model for a woven structure. The woven structure was considered as being organized in two sets of intertwined yarns, the warp yarns and the weft yarns. Each subsystem is considered as a sum of n single yarns. One single yarn is discretized and consists of a set of point masses mutually connected by extensional springs. Each node (point mass) is provided with rotational stiffness. Moreover, [Ben Boubaker et al. \(2007d\)](#) proposed a discrete model of woven textile in which the basic pattern is represented by stretching springs, connected at nodes where a rotational stiffness is represented by flexional springs. More recently, [Assidi et al. \(2011\)](#) developed mesostructurally-based continuum model, relating the fabric behavior at the macroscopic continuum scale to the response and geometry of the fabric's mesostructure (geometrical configuration of the weave and the yarn properties). For a more detailed description of several other analytical models, see [Realf \(1992\)](#).

Analytical models of the fabric mesostructure can be incorporated into anisotropic continuum formulations to yield models that track the fabric mesostructure as the continuum deforms. A number of authors have presented models for woven fabrics with continuum properties calculated from a deforming unit cell. [Boisse et al. \(1997, 2001\)](#) constructed a three-dimensional unit cell like that of Kawabata for quasi-static and dynamic simulations of composite forming, but did not incorporate the resistance to yarn rotation or the inertia of uncrimping. [Rattensperger et al. \(2003\)](#) take a similar approach for modeling fabric-reinforced hydraulic hoses, with fabric lattice geometry similar to that used by Kato, and use a

conventional finite element formulation with rebar reinforcements. [Tanov and Brueggert \(2003\)](#) presented a mesostructurally based continuum model that includes shear and locking resistance through diagonal spar elements within the assumed unit cell network. [Boisse et al. \(2005, 2006\)](#) later used a planar unit cell for dynamic simulations by incorporating shear resistance at the cross-over point, but they did not include cross-locking. [Hamila et al. \(2009\)](#) extended this approach to a shell finite element which includes the resistance to bending of the yarns. Some models are specific to the ballistic impact of woven fabrics. [Ivanov and Tabiei \(2004\)](#) constructed a Kawabata type unit cell for the simulation of ballistic impact but did not consider transverse compression, cross-locking, or the inertia of uncrimping. [Shahkarami and Vaziri \(2007\)](#) also used the Kawabata geometry in the simulation of ballistic impact.

There are also alternative approaches suitable for simulating general fabric deformations and take one of two finite element approaches: either they discretely model in three dimensions every yarn in the weave or they homogenize the response of the yarns, typically by treating the fabric as an anisotropic continuum. The discrete approach, used by [Shockey et al. \(1999a,b, 2001\)](#), [Ng et al. \(1998\)](#), [Duan et al. \(2006b\)](#), [Zhang et al. \(2008\)](#), and [Talebi et al. \(2009\)](#), among others, has the advantage of capturing all yarn interactions and it provides a detailed description of all mechanisms of fabric deformation. It is thus valuable for studying the various modes of deformation of the yarns and the effects of parameters such as weave style and yarn properties on macroscopic deformation. However, building these elaborate finite element meshes is tedious, and simulating actual structures or events of significant duration is computationally prohibitive in most cases. On the other hand, the homogenized, continuum approaches used by [Peng and Cao \(2000, 2002, 2005\)](#), [Xue et al. \(2003, 2005\)](#), and [Baseau \(2003\)](#), among others, allow greater computational efficiency and are easily integrated into multi-component system models. Although these approaches can accurately represent the macroscopic response of woven fabrics, they do not explicitly model the modes of deformation or interactions of the yarns, and therefore cannot predict all of the necessary yarn-level aspects of deformation. [Peng and Cao \(2000, 2002\)](#) applied a dual homogenization technique to predict the mechanical behavior of woven fabrics from a sequence of models for fibers. In the first step, a unit cell is built for the yarn section to estimate the effective elastic constants of fiber yarn. Then, another unit cell in meso-level is constructed to represent the periodic structure of woven fabric. [Peng and Cao \(2005\)](#) developed a continuum mechanics-based non-orthogonal constitutive model to characterize the anisotropic material behavior of woven composite fabrics undergoing large deformations. Moreover, [Xue et al. \(2005\)](#) developed an integrated meso-macro model for the prediction of the mechanical properties of woven fabrics in the range of large deformations. Those authors previously suggested a non-orthogonal constitutive model for the prediction of mechanical properties in macro scale ([Xue et al. 2003](#)), relying on experimental measurements to identify the constants of their model. [Baseau \(2003\)](#) developed continuum formulations for "filamentary networks" appropriate for non-reinforced fabrics. [King et al. \(2005\)](#) also proposed a new approach for continuum modeling of fabrics by selecting a geometric model for the fabric weave coupled with

constitutive models for the yarns behavior. They used energy minimization method to relate the fabrics structural configuration to the macroscopic deformation.

The initially discrete material is substituted by an equivalent dense (continuous) Cosserat solid. A specific homogenization method is developed for this purpose and implemented for the generation of micropolar continuum equivalent models of the woven structure; those generalized continuum models highlight internal length scales traducing the impact of the internal architecture of the considered textile. The proposed method allows evaluating the effective classical and micropolar elastic constants. Such a technique is exploited to get the macroscopic elastic properties of fabrics by taking into account axial, transverse shearing, flexural and torsional deformations of the yarns building the fabrics. The consideration of couple stresses interpreted as moments enables to compute the flexural rigidities of textile monolayers, which is a challenging task considering their small thickness. Furthermore, the strain energy-based method is adopted as an efficient approach for the homogenization and effective elastic properties are obtained numerically based on the sequential homogenization from the fiber scale to the tow scale.

The cornerstone of the method is the mesomechanical analysis performed over an identified textile unit cell for the evaluation of the apparent properties. The woven reinforcement made of an orthogonal interlacing of yarns (warp and weft) can be realistically modeled as a periodic medium (or quasi periodic). The studied domain (Representative Unit Cell, in short RUC) has to be the smallest possible so as to reduce the size of the calculations. As the medium is periodic, an elementary domain called the pattern exists from which the whole fabric can be constructed by the repetitive translations of this pattern. Two typical textile patterns are considered, [Figure 3.2](#) shows the hierarchical structure of periodic unit cells for plain weave and twill fabrics, highlighting the macroscopic level of woven fabrics and the intermediate level of the periodic macro-unit cells.

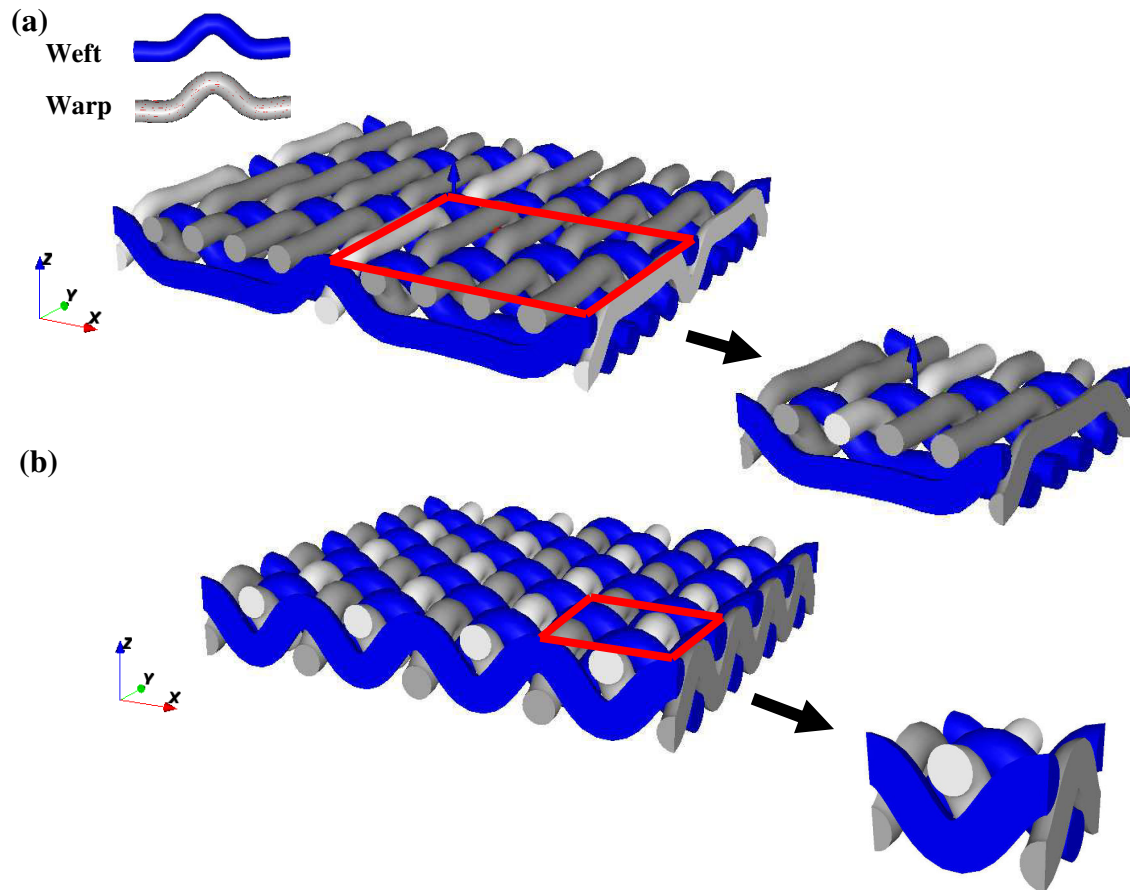


Figure 3.2: Periodic reinforcement and Representative Unit Cell (RUC): (a) Macrostructure of twill fabric and its periodic macro-unit cell (b) Macrostructure of plain weave fabric and its periodic macro-unit cell.

3.3 Discrete homogenization of textile monlayers

The main idea of homogenization methods in a broad sense is to replace a real heterogeneous structure with an equivalent homogeneous one endowed with the same average macroscopic behavior. The homogenization method assumes that all physical quantities vary at both local and global scales, and that those quantities are periodic with respect to the local scale, due to the periodicity of the existing microstructure. As the woven fabrics have a periodic structure based on the RVE, it is possible to apply the asymptotic expansion homogenization method. Its mathematical basis was elaborated by [Bensoussan et al. \(1978\)](#), [Sanchez-Palencia \(1980\)](#), and [Bakhvalov and Panasenko \(1989\)](#). This method applies an asymptotic expansion of the displacement and stress fields on the “natural length parameter”, which is the ratio of a characteristic size of the heterogeneities and a measure of the macrostructure, see, e.g. [Tolnado and Murakami \(1987\)](#); [Devries et al. \(1989\)](#); [Guedes and Kikuchi \(1990\)](#); [Hollister and Kikuchi \(1992\)](#); [Fish et al. \(1999\)](#). Recent reviews on the asymptotic expansion homogenization method applied to composites can be found in [Kanouté et al. \(2009\)](#) and [Oliveira et al. \(2009\)](#). Such an asymptotic homogenization approach provides the overall effective properties as well as local stress and strain values. In this work, the discrete asymptotic homogenization method proposed by ([Mourad, 2003](#); [Caillerie et al., 2006](#); [Raoult](#)

et al., 2008; Dos Reis and Ganghoffer, 2012) in view of the calculation of the effective behavior of periodic lattices, are exploited for construction of micropolar continua from elastic fabric lattices endowed with translational and rotational degrees of freedom. Micropolar elasticity incorporates local rotations of material points in addition to displacements in the kinematic description. As a consequence, the material can transmit both Cauchy stresses and couple stresses. As will be shown, the method allows the treatment of elementary cells, including internal nodes; it is based on the asymptotic development of the kinematic and static variables under consideration, at an arbitrary order a priori. The method relies on the connectivity of the studied structures and the mechanical equilibrium at each node. Here, two geometrical parameters need an asymptotic expansion, namely the beam length l^{eb} and beam radius r^{eb} . In the same way, two kinematic variables should be expanded, the nodal displacement u^{en} (u_x, u_y, u_z), and the nodal microrotation ϕ^{en} (ϕ_x, ϕ_y, ϕ_z) defined at the origin and extremity of each beam. For a large enough fabric structure, the ratio of the elementary cell's length to a macroscopic fabric's length constitutes a small parameter $\varepsilon=l/L$, versus which all geometrical and kinematic variables will be expanded, hence $l^{eb} = \varepsilon L^b$.

A dedicated code has been constructed from the proposed homogenization algorithms for the calculation of the effective classical and micropolar elastic constants of general repetitive fabric unit cells endowed with an arbitrary topology. The code uses an input file including the fabric topology and mechanical properties within a selected unit cell, and delivering as an output the homogenized mechanical properties (classical and micropolar moduli). The previous developments lead to an implementation best summarized by the following algorithm:

Algorithm for the discrete homogenization towards a micropolar continuum for textiles

1. Initialization of the tables of initial data. Definition of the function \mathbf{R} such that $\mathbf{x} = \mathbf{R}(\lambda^1, \lambda^2, \lambda^3)$.

2. Transformation of the expressions $\left(\frac{\partial U}{\partial \lambda_i}\right)_{(Y_1, Y_2, Y_3)} \mapsto \left(\frac{\partial U}{\partial \lambda_i}\right)_{(i,j,k)}$ and $\left(\frac{\partial \phi}{\partial \lambda_i}\right)_{(Y_1, Y_2, Y_3)} \mapsto \left(\frac{\partial \phi}{\partial \lambda_i}\right)_{(i,j,k)}$.

3. For each beam in the fabric elementary cell (weft, warp and contact) $b \in B_R$, define

(a) The origin and end node of a beam respectively, $O=O_R(b)$, $E=E_R(b)$.

(b) Express the displacement difference between extremity and origin node at first order: $\Delta U_1^b = u_1^E - u_1^O + \frac{\partial U}{\partial \lambda^i} \delta^i$, tensile rigidity: $k_t = A^b E_s^b / L^b$, flexural rigidity: $k_{ty} = 12 E_s^b I_z^b / (L^b)^3$, $k_{tz} = 12 E_s^b I_y^b / (L^b)^3$,

torsional rigidity: $k_r = G_s^b J^b / L^b$, and $\Phi_{y,z} = 12 E_s^b I_{y,z} / G_s^b A^b k_s (L^b)^2$.

(c) Express the first order efforts:

$$F_{x1} = k_t \left(\mathbf{e}_x \cdot (\Delta U_1^b) \right), F_{y1} = \frac{k_{ty}}{(1+\Phi_y)} \left(\mathbf{e}_y \cdot (\Delta U_1^b) - \frac{L^b}{2} \left(\mathbf{e}_z \cdot (\phi_0^O + \phi_0^E) \right) \right), F_{z1} = \frac{k_{tz}}{(1+\Phi_z)} \left(\mathbf{e}_z \cdot (\Delta U_1^b) + \frac{L^b}{2} \left(\mathbf{e}_y \cdot (\phi_0^O + \phi_0^E) \right) \right).$$

(d) Express the first order moments:

$$M_{1y}^O = k_{tz} \frac{L^b}{12(1+\Phi_z)} \left(6 \mathbf{e}_z \cdot (\Delta U_1^b) + L^b \left(\mathbf{e}_y \cdot ((4+\Phi_z)\phi_0^O + (2-\Phi_z)\phi_0^E) \right) \right), M_{1y}^E = k_{tz} \frac{L^b}{12(1+\Phi_z)} \left(6 \mathbf{e}_z \cdot (\Delta U_1^b) + L^b \left(\mathbf{e}_y \cdot ((2-\Phi_z)\phi_0^O + (4+\Phi_z)\phi_0^E) \right) \right),$$

$$M_{1z}^O = k_{ty} \frac{L^b}{12(1+\Phi_y)} \left(-6 \mathbf{e}_y \cdot (\Delta U_1^b) + L^b \left(\mathbf{e}_z \cdot ((4+\Phi_y)\phi_0^O + (2-\Phi_y)\phi_0^E) \right) \right), M_{1z}^E = k_{ty} \frac{L^b}{12(1+\Phi_y)} \left(-6 \mathbf{e}_y \cdot (\Delta U_1^b) + L^b \left(\mathbf{e}_z \cdot ((2-\Phi_y)\phi_0^O + (4+\Phi_y)\phi_0^E) \right) \right).$$

4. Calculate the unknowns displacement and rotation u_1^n and ϕ_0^n from (2.24) and (2.31).
 5. Identify the homogenized microrotation ϕ_0 to the antisymmetrical part of the strain tensor

$$\phi_x = \frac{1}{2} \left(\frac{\partial u_z}{\partial y} - \frac{\partial u_y}{\partial z} \right), \quad \phi_y = \frac{1}{2} \left(\frac{\partial u_x}{\partial z} - \frac{\partial u_z}{\partial x} \right), \quad \phi_z = \frac{1}{2} \left(\frac{\partial u_y}{\partial x} - \frac{\partial u_x}{\partial y} \right).$$

6. Express the second order forces and moments as:

$$(a) \Delta U_2^b = u_2^E - u_2^O \quad (b) F_{x2} = k_l \left(\mathbf{e}_x \cdot (\Delta U_2^b) \right), \quad F_{y2} = \frac{k_{ly}}{(1+\Phi_y)} \left(\mathbf{e}_y \cdot (\Delta U_2^b) - \frac{L^b}{2} \left(\mathbf{e}_z \cdot \left(\phi_1^O + \phi_1^E + \frac{\partial \phi}{\partial \lambda^i} \delta^i \right) \right) \right),$$

$$F_{z2} = \frac{k_{tz}}{(1+\Phi_z)} \left(\mathbf{e}_z \cdot (\Delta U_2^b) + \frac{L^b}{2} \left(\mathbf{e}_y \cdot \left(\phi_1^O + \phi_1^E + \frac{\partial \phi}{\partial \lambda^i} \delta^i \right) \right) \right)$$

$$(c) M_{2x}^O = k_r \left(\mathbf{e}_x \cdot \left(\phi_1^O - \left(\frac{\partial \phi}{\partial \lambda^i} \delta^i + \phi_1^E \right) \right) \right), \quad M_{2x}^E = k_r \left(\mathbf{e}_x \cdot \left(\phi_1^E - \phi_1^O + \frac{\partial \phi}{\partial \lambda^i} \delta^i \right) \right),$$

$$M_{2y}^O = k_{tz} \frac{L^b}{12(1+\Phi_z)} \left(6\mathbf{e}_z \cdot (\Delta U_2^b) + L^b \left(\mathbf{e}_y \cdot \left((4+\Phi_z)\phi_1^O + (2-\Phi_z)\phi_1^E + (2-\Phi_z) \frac{\partial \phi}{\partial \lambda^i} \delta^i \right) \right) \right), \quad M_{2y}^E = k_{tz} \frac{L^b}{12(1+\Phi_z)} \left(6\mathbf{e}_z \cdot (\Delta U_2^b) + L^b \left(\mathbf{e}_y \cdot \left((2-\Phi_z)\phi_1^O + (4+\Phi_z)\phi_1^E + (4+\Phi_z) \frac{\partial \phi}{\partial \lambda^i} \delta^i \right) \right) \right),$$

$$M_{2z}^O = k_{ty} \frac{L^b}{12(1+\Phi_y)} \left(-6\mathbf{e}_y \cdot (\Delta U_2^b) + L^b \left(\mathbf{e}_z \cdot \left((4+\Phi_y)\phi_1^O + (2-\Phi_y)\phi_1^E + (2-\Phi_y) \frac{\partial \phi}{\partial \lambda^i} \delta^i \right) \right) \right), \quad M_{2z}^E = k_{ty} \frac{L^b}{12(1+\Phi_y)} \left(-6\mathbf{e}_y \cdot (\Delta U_2^b) + L^b \left(\mathbf{e}_z \cdot \left((2-\Phi_y)\phi_1^O + (4+\Phi_y)\phi_1^E + (4+\Phi_y) \frac{\partial \phi}{\partial \lambda^i} \delta^i \right) \right) \right).$$

Solve for variables u_2^n and ϕ_1^n from (2.24) and (2.31).

7. Construct the stress and couple stress vectors, $S^i = \sum_{b \in B_R} (F_{x1}^b e_x + F_{y1}^b e_y + F_{z1}^b e_z) \delta^{ib}$ and

$$\mu^i = \sum_{b \in B_R} \left(M_{2x}^{E(b)} e_x + \frac{1}{2} (M_{2y}^{E(b)} - M_{2y}^{O(b)}) e_y + \frac{1}{2} (M_{2z}^{E(b)} - M_{2z}^{O(b)}) e_z \right) \delta^{ib} \text{ respectively.}$$

8. Construct the stress tensor $\sigma = \frac{1}{g} S^i \otimes \frac{\partial R}{\partial \lambda^i}$ and couple stress tensor $m = \frac{1}{g} \mu^i \otimes \frac{\partial R}{\partial \lambda^i}$, such that

$$\begin{Bmatrix} \sigma \\ m \end{Bmatrix} = \begin{bmatrix} K^S & 0 \\ 0 & K^\mu \end{bmatrix} \begin{Bmatrix} \epsilon \\ \chi \end{Bmatrix}.$$

9. Compute the effective mechanical properties $E_x^*, E_y^*, \nu_{xy}^*, G_{xy}^*, K_{55}^\mu, K_{66}^\mu$.

3.4 Effective mechanical properties of woven fabrics

A woven fabric consists of two sets of interwoven yarns, called warp and weft. From a geometrical point of view and without considering a specific pattern, each of these yarn elements can be considered to be either inclined (as it passes from top to bottom of the fabric) or straight (as it passes over or under another yarn), as depicted earlier in Figure 3.2. In this section, we apply the discrete homogenization technique exposed in the previous section to two important types of woven fabrics, plain weave and twill (Figure 3.2) to calculate their equivalent effective properties. For this purpose, simplified models based on a 3D geometrical description of the unit cell at the mesoscopic scale are proposed, in which the yarns are assumed to be a composition of beams linked by articulations. The main assumption made throughout the construction of these models is that the yarn section remains constant along the curvilinear trajectory. The curvilinear trajectory, namely the mean line of the yarn, is modeled as straight segments of beams by which the 3D yarns of the fabric are constructed.

The first step is to build a geometrical model that is consistent and able to take into account the diversity of fabric geometries. For this intention, yarns are represented as a network of beams connected by nodes at their crossover points. These beams do not lie in the

plane of the fabric but are interwoven to capture crimp interchange; they have axial and bending rigidities to allow for yarn stretch and flexion. Yarn-yarn interactions at the yarns crossing points clearly influence the effective properties of the material at the meso-level. Interactions between warp and weft yarns at the crossover points are here captured by beam segments connecting the nodes (see Figures 3.3 and 3.4). The crossover beams also have two modes of deformation, namely extension and flexion.

The proposed geometric description therefore is adequate for capturing the relevant behaviors and is more computationally efficient for effective mechanical behaviors than more sophisticated geometrical descriptions. Its chief limitation is that the yarns are modeled as straight beams with sharp corners at the crossover points, whereas they warp around the crossing yarns with a smooth radius of curvature in reality. This geometry consequently permits configurations that are incompatible because of interpenetrations between the yarns, and cannot capture complex behaviors that are controlled by yarn wrapping.

3.4.1 Unit cell of plain weave fabric

The plain weave is the most common weaving (and also the simplest one); the weft and warp tows are interlaced in an “one under–one over” pattern that generates a chessboard pattern with equally exposed weft and warp tows on both faces of the fabric. The basis of the present model is the assumed geometry of the unit cell of the fabric. The unit cell approximates the mesoscale modes of deformation that underlie the macroscopic response of the fabric. The configuration of the unit cell geometry model and the corresponding periodicity vectors (the vectors $\mathbf{Y}_1(1,0,0)$, $\mathbf{Y}_2(0,1,0)$, and $\mathbf{Y}_3(0,0,1)$ are the translation vectors that generate the whole fabric by periodicity in 3D) are described by the parameters shown in Figure 3.3. Note that the structure is only homogenized in the (x, y) plane, but the third vector is nevertheless required. The lengths of the periodicity vectors are $L_1 = 2L_{f1}\cos\theta_f$, $L_2 = 2L_{p1}\cos\theta_p$, and $L_3 = 1$. The subscripts f and p stand for the weft and warp yarns, respectively. We denote by θ_f and θ_p the crimp angles of the weft and warp yarns respectively.

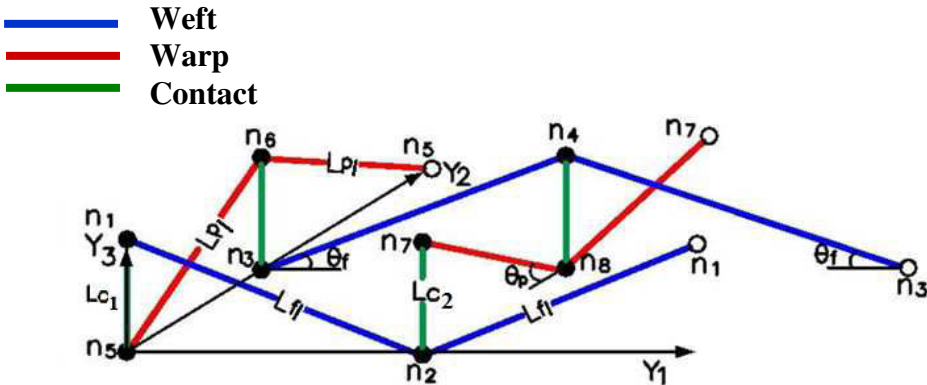


Figure 3.3: A 3D lattice model of 2D plain weave.

The following geometrical parameters and material properties for plain weave are here considered. The geometrical parameters of fiber tows are chosen as follows:

Table 3.1: Plain weave fabric configuration parameters.

Weft	$L_{f1} = 0.618 \text{ mm}$	$\theta_f = 40^\circ$	$d_f = 0.27 \text{ mm}$
Warp	$L_{p1} = 0.56 \text{ mm}$	$\theta_p = 40^\circ$	$d_p = 0.25 \text{ mm}$

The mechanical properties of weft and warp made of PES are given in Table 3.2; we intentionally choose very different moduli to represent an unbalanced fabric, leading to an expected anisotropic behavior.

Table 3.2: Elastic properties of weft and warp yarns.

Weft	$E_{sf} = 1889 \text{ MPa}$	$G_{sf} = 756 \text{ MPa}$	$\nu_f = 0.25$
Warp	$E_{sp} = 13853 \text{ Mpa}$	$G_{sp} = 5541 \text{ Mpa}$	$\nu_p = 0.25$

Relying on the previous geometrical and material data, the tensile, flexural, and torsion rigidities of the beam segments building the fabric lattice, which are used as an input for the homogenization, are quantified as follows:

$$\text{Tensile rigidities: } k_{lf1} = E_{sf} A_f / L_{f1}, k_{lp1} = E_{sp} A_p / L_{p1}, k_{lc1,2} = E_{sc} A_c / L_{c1,2} .$$

$$\text{Flexural rigidities: } k_{tf1} = 12E_{sf} I_f / (L_{f1})^3, k_{tp1} = 12E_{sp} I_p / (L_{p1})^3, k_{tc1,2} = 12E_{sc} I_c / (L_{c1,2})^3 .$$

$$\text{Torsion rigidities: } k_{rf1} = G_{sf} J_f / L_{f1}, k_{rp1} = G_{sp} J_p / L_{p1}, k_{rc1,2} = G_{sc} J_c / L_{c1,2} .$$

Furthermore, the coefficients $\Phi_y = \Phi_z = \Phi$ (the ratio of beam bending to shear stiffness) are

$$\text{calculated as } \Phi_f = 12E_{sf} I_f / G_{sf} A_{sf} k_s L_f^2, \Phi_p = 12E_{sp} I_p / G_{sp} A_{sp} k_s L_p^2 .$$

$$\text{with } L_{c1,2} = L_{f1} \sin \theta_f, L_{p1} \sin \theta_p, r_c = (r_f + r_p) / 2, G_{sc} = (G_{sf} + G_{pf}) / 2, \text{ and } E_{sc} = (E_{sf} + E_{pf}) / 2$$

where $L_{c1,2}$, r_c , I_c , J_c , G_{sc} , and E_{sc} , respectively, represent the lengths, radius, second moment of area, torsional constant, shear and Young's modulus of the contact beams (beams connecting the warp and weft yarns at their crossing points).

After homogenization, the equivalent stiffness matrix is next obtained as a function of geometrical and mechanical parameters of plain weave fabric. The equivalent form of the constitutive law corresponding to stress component, $\{\sigma\} = [K^s] \{\epsilon\}$ can be written as

$$\begin{Bmatrix} \sigma_x \\ \sigma_y \\ \sigma_{xy} \\ \sigma_{yx} \end{Bmatrix} = [K^s] \begin{Bmatrix} \frac{\partial u_x}{\partial x} \\ \frac{\partial u_y}{\partial y} \\ \frac{\partial u_y}{\partial x} - \phi_z \\ \frac{\partial u_x}{\partial y} + \phi_z \end{Bmatrix} \quad (3.1)$$

with the stiffness matrix

$$[K^s] = \begin{bmatrix} 121.7 & 49.70 & 0 & 0 \\ 49.7 & 302.2 & 0 & 0 \\ 0 & 0 & 25.7 & -9.9 \\ 0 & 0 & -58.1 & 78.4 \end{bmatrix} \text{MPa} \quad (3.2)$$

In the same manner, the equivalent stiffness matrix corresponding to the couple stress component is determined from the micropolar constitutive equation $\{m\} = [K^\mu]\{\chi\}$ as follows

$$\begin{Bmatrix} m_x \\ m_y \\ m_{xy} \\ m_{yx} \\ m_{xz} \\ m_{yz} \end{Bmatrix} = [K^\mu] \begin{Bmatrix} \frac{\partial \phi_x}{\partial x} \\ \frac{\partial \phi_y}{\partial y} \\ \frac{\partial \phi_y}{\partial x} \\ \frac{\partial \phi_x}{\partial y} \\ \frac{\partial \phi_z}{\partial x} \\ \frac{\partial \phi_z}{\partial y} \end{Bmatrix} \quad (3.3)$$

with $[K^\mu]$ computed as

$$[K^\mu] = \begin{bmatrix} 1.22 & 0 & 0 & 0 & 0 & 0 \\ 0 & 6.24 & 0 & 0 & 0 & 0 \\ 0 & 0 & 2.00 & 0 & 0 & 0 \\ 0 & 0 & 0 & 5.04 & 0 & 0 \\ 0 & 0 & 0 & 0 & 1.69 & 0 \\ 0 & 0 & 0 & 0 & 0 & 6.92 \end{bmatrix} \text{N} \quad (3.4)$$

As for non polar media, one derives the homogenized traction moduli from the effective compliance matrix $[S^{eff}] = [K^s]^{-1}$ as $E_x^* = [1/S_{11}^{eff}] = 113.5 \text{ MPa}$ and $E_y^* = [1/S_{22}^{eff}] = 281.9 \text{ MPa}$. Furthermore, the effective Poisson's ratios are computed as $\nu_{xy}^* = -S_{21}^{eff} E_x^* = 0.16$ and $\nu_{yx}^* = -S_{12}^{eff} E_y^* = 0.40$. The effective shear modulus is computed using the micropolar moduli $\mu^* + \kappa = K_{33}^s$ and $\mu^* = K_{34}^s$ as $G_{xy}^* = \mu^* + \kappa/2 = 7.90 \text{ MPa}$. The additional bending effects present in a micropolar continuum is characterized by additional parameters (Lakes, 1995), such as the characteristic lengths. The two characteristic lengths of the anisotropic micropolar behavior are calculated from the rigidities as $l_{b1} = \sqrt{K_{55}^\mu / 2(K_{33}^s + K_{34}^s)} = 0.23 \text{ mm}$ and $l_{b2} = \sqrt{K_{66}^\mu / 2(K_{43}^s + K_{44}^s)} = 0.41 \text{ mm}$.

Those lengths are comparable in magnitude to the yarn diameter, but smaller by a factor 3 to the beam length, quantity L_{f1} in Table 3.1. Nevertheless, as will become apparent later on,

the internal length is by itself not sufficient to conclude about the importance of micropolar effects.

3.4.2 Unit cell of twill fabric

The twill weave is characterized by continuous rib diagonals on the faces of the fabric. Regarding its geometry and architecture, a twill fabric is made from the quasi periodic repetition of a given elementary pattern, which repeats by translation in both warp and weft directions. The unit cell model is taken as the smallest periodic repeating geometry pattern with orthogonal periodicity vectors, whose lengths are $L_1 = 2L_{f1}\cos\theta_f + 3L_{f2}$, $L_2 = 2L_{p1}\cos\theta_p + 3L_{p2}$, and $L_3 = 1$. The configuration of this unit cell geometry is described by the parameters shown in Figure 3.4.

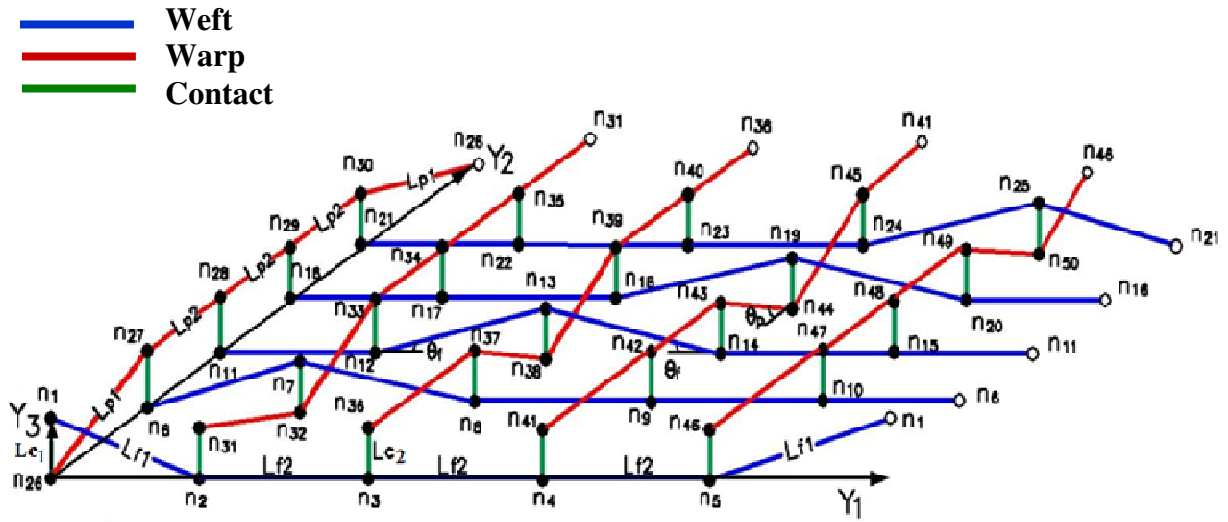


Figure 3.4: Geometrical model of an elementary cell of twill.

The geometrical parameters of the twill unit cell are introduced in Table 3.3.

Table 3.3: Twill fabric configuration parameter

Weft	$L_{f1} = 0.618 \text{ mm}$	$L_{f2} = 0.487 \text{ mm}$	$\theta_f = 40^\circ$	$d_f = 0.27 \text{ mm}$
Warp	$L_{p1} = 0.56 \text{ mm}$	$L_{p2} = 0.41 \text{ mm}$	$\theta_p = 40^\circ$	$d_p = 0.25 \text{ mm}$

The mechanical properties of the yarns are the same as for the plain weave unit cell. The tensile, flexural, and torsion rigidities of the beam segments of twill are quantified as follows:

Tensile rigidities: $k_{lf1} = E_{sf} A_f / L_{f1}$, $k_{lf2} = E_{sf} A_f / L_{f2}$, $k_{lp1} = E_{sp} A_p / L_{p1}$,
 $k_{lp2} = E_{sp} A_p / L_{p2}$, $k_{lc1,2} = E_{sc} A_c / L_{c1,2}$.

Flexural rigidities: $k_{ff1} = 12E_{sf} I_f / (L_{f1})^3$, $k_{ff2} = 12E_{sf} I_f / (L_{f2})^3$,
 $k_{fp1} = 12E_{sp} I_p / (L_{p1})^3$, $k_{fp2} = 12E_{sp} I_p / (L_{p2})^3$, $k_{fc1,2} = 12E_{sc} I_c / (L_{c1,2})^3$.

Torsional rigidities: $k_{rf1} = G_{sf} J_f / L_{f1}$, $k_{rf2} = G_{sf} J_f / L_{f2}$, $k_{rp1} = G_{sp} J_p / L_{p1}$,
 $k_{rp2} = G_{sp} J_p / L_{p2}$, $k_{rc1,2} = G_{sc} J_c / L_{c1,2}$.

The coefficients $\Phi_y = \Phi_z = \Phi$ therein are calculated as

$$\Phi_{f1} = 12E_{sf} I_f / G_{sf} A_{sf} k_s L_{f1}^2, \Phi_{f2} = 12E_{sf} I_f / G_{sf} A_{sf} k_s L_{f2}^2, \Phi_{p1} = 12E_{sp} I_p / G_{sp} A_{sp} k_s L_{p1}^2, \\ \Phi_{p2} = 12E_{sp} I_p / G_{sp} A_{sp} k_s L_{p2}^2.$$

The equivalent stiffness matrix $[K^s]$ is then calculated as

$$[K^s] = \begin{bmatrix} 194.7 & 93.6 & 0 & 0 \\ 93.6 & 360.6 & 0 & 0 \\ 0 & 0 & 34.5 & -15.6 \\ 0 & 0 & -89.4 & 115.6 \end{bmatrix} \text{MPa} \quad (3.5)$$

and $[K^\mu]$ is computed as

$$[K^\mu] = \begin{bmatrix} 3.25 & 0 & 0 & 0 & 0 & 0 \\ 0 & 10.72 & 0 & 0 & 0 & 0 \\ 0 & 0 & 3.64 & 0 & 0 & 0 \\ 0 & 0 & 0 & 8.37 & 0 & 0 \\ 0 & 0 & 0 & 0 & 4.0 & 0 \\ 0 & 0 & 0 & 0 & 0 & 10.45 \end{bmatrix} \text{N} \quad (3.6)$$

From the effective compliance matrix of the twill (the inverse of $[S^{eff}] = [K^s]^{-1}$), the effective homogenized moduli and Poisson's ratios are obtained as

$$E_x^* = 170.4 \text{ MPa}; E_y^* = 315.6 \text{ MPa}; \nu_{xy}^* = 0.26; \nu_{yx}^* = 0.48$$

In addition, the effective shear modulus is computed using the micropolar moduli as

$$G_{xy}^* = \mu^* + \frac{\kappa}{2} = 9.44 \text{ MPa} . \text{ The two characteristic micropolar lengths are calculated as}$$

$$l_{b1} = \sqrt{K_{55}^\mu / 2(K_{33}^s + K_{34}^s)} = 0.33 \text{ mm}; l_{b2} = \sqrt{K_{66}^\mu / 2(K_{43}^s + K_{44}^s)} = 0.45 \text{ mm} .$$

Those lengths are here comparable in magnitude to the length of a beam within the lattice, the quantity L_{f2} in [Table 3.3](#). Those microstructural effects will be further assessed in the forthcoming section, based on the bending behavior of a microstructured beam.

3.4.3 Flexural rigidity on the basis of a micropolar effect

Based on previous fabrics homogenized properties, one shall next construct a lattice presenting a noticeable micropolar effect, due to its internal microstructure. We will compare the simplified equation of a micropolar beam under pure bending to the standard equation of the classical beam, in the plane stress case; the geometrical parameters of the macrobeam are indicated on [Figure 3.5](#): H and W are the beam height and width respectively. The beam

incorporates either a plain weave or a twill microstructure, giving rise to a micropolar effective behavior.

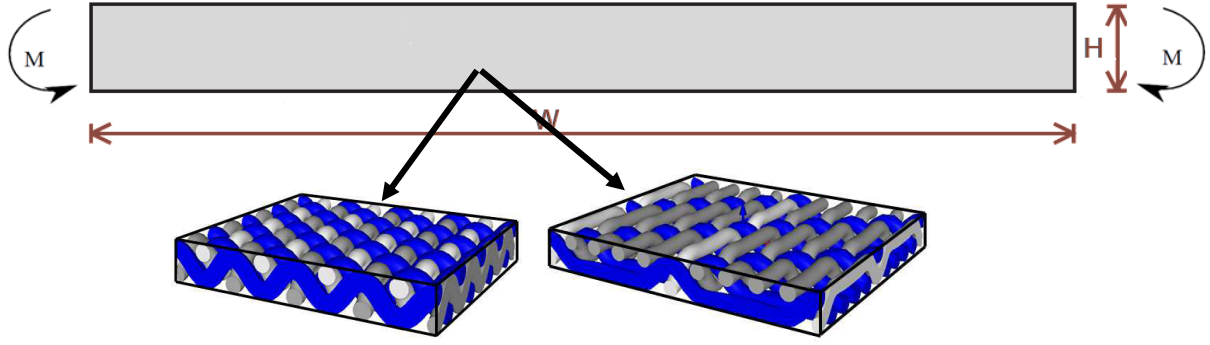


Figure 3.5: Geometrical parameters of a micropolar beam subjected to a pure bending moment.

We employ the following procedure to analyze the deformation of an initially straight micropolar elastic beam subjected to a pure bending moment: the bending stiffnesses K_{xz}^μ and K_{yz}^μ of such a beam are defined from the simplified equilibrium equation of a micropolar beam of anisotropic material, submitted to a uniform bending moment M as

$$\underbrace{\left(E_x^* I_z^* + K_{55}^\mu H\right)}_{K_{xz}^\mu} \frac{\partial \phi_z}{\partial x} = -M \quad ; \quad \underbrace{\left(E_y^* I_z^* + K_{66}^\mu H\right)}_{K_{yz}^\mu} \frac{\partial \phi_z}{\partial y} = -M \quad (3.7)$$

with E_x^* and E_y^* the effective homogenized moduli of the macroscopic equivalent beam, I_z^* the quadratic moment of the macroscopic beam along z , given by $I_z^* = H^3/12$, and K_{55}^μ and K_{66}^μ the homogenized micropolar moduli corresponding to the couple stress components m_{xz} and m_{yz} .

The previous equation can be written with the characteristic micropolar length l_b using the previous expressions of the characteristic lengths, as

$$\underbrace{\left(E_x^* I_z^* + 2l_{b1}^2 \left(K_{33}^s + K_{34}^s\right) H\right)}_{K_{xz}^\mu} \frac{\partial \phi_z}{\partial x} = -M \quad ; \quad \underbrace{\left(E_y^* I_z^* + 2l_{b2}^2 \left(K_{43}^s + K_{44}^s\right) H\right)}_{K_{yz}^\mu} \frac{\partial \phi_z}{\partial y} = -M \quad (3.8)$$

We then define K_{xz}^c and K_{yz}^c , the classical bending stiffnesses (without micropolar effect) from the moment equilibrium of a classical homogenous beam (without micropolar effects) as

$$\underbrace{\left(E_x^* I_z^*\right)}_{K_{xz}^c} \frac{\partial \phi_z}{\partial x} = -M \quad ; \quad \underbrace{\left(E_y^* I_z^*\right)}_{K_{yz}^c} \frac{\partial \phi_z}{\partial y} = -M \quad (3.9)$$

The effective mechanical properties of the (homogenized) macroscopic beam obtained for the two fabrics allow calculating the stiffnesses K^μ and K^c involved in equations (3.7)

and (3.9) respectively (see Table 3.4). We adopt the macroscopic parameter $H=0.52$ mm for the fabric thickness. The gain in flexural rigidity due to the micropolar effect is next defined for a microstructured beam by the parameter $\%gr = ((K^\mu - K^c)/K^c) \times 100$. Results are summarized in Table 3.4: important gains in the bending stiffness are obtained in comparison to a standard beam made of an equivalent continuum material for both fabric types. This shows that micropolar effects are important for those fabrics; the gain in rigidity gr_{xz} is 66.2% for plain weave compared to 104.0% for twill, and gr_{yz} is 108.7% for plain weave compared to 147.0% for twill. Overall, the gain in bending rigidity due to the micropolar effect is higher for twill than for plain weave, a trend that is in agreement with the computed internal bending lengths for both types of textiles.

A microstructural model of the microstructured beam has been developed in the framework of micropolar elasticity. The model contains a material length scale parameter to account for the microstructural effect (plain weave and twill), unlike classical beam theory. The inclusion of this additional material constant enables the model to capture size effects; the intrinsic size dependence decreases the static beam deflections and hence increases the effective bending stiffness.

Table 3.4: Effective bending stiffness of a homogeneous beam made of a microstructure of plain weave and twill fabrics. gr is the gain in stiffness due to the micropolar effect.

	Plain weave	Twill
E_x^* (MPa)	113.5	170.4
E_y^* (MPa)	281.9	315.6
K_{55}^μ (N)	1.69	4.00
K_{66}^μ (N)	6.92	10.45
K_{xz}^μ (N.mm)	2.21	4.08
K_{xz}^c (N.mm)	1.33	2.00
$\%gr_{xz}$	66.2	104.0
K_{yz}^μ (N.mm)	6.91	9.14
K_{yz}^c (N.mm)	3.31	3.70
$\%gr_{yz}$	108.7	147.0

3.4.4 Nonlinearities due to crimping

Due to the interlacing of the warp and weft threads in the weaving process, a certain amount of waviness is imparted to the warp and weft threads of a woven fabric, called the crimp. The crimp interchange in fabrics is a major source of nonlinear deformation (King et al., 2005).

The amount of waviness in a yarn due to the over/under weaving is the amount of crimp content. Crimp interchange, which is a coupling mechanism analogous to Poisson's effect in traditional materials, produces substantial nonlinearities in the constitutive behavior of woven fabrics. These nonlinearities are generally less significant for matrix reinforced fabrics because the matrix limits the amount of yarn slip and rotation that occur at the yarn crossover regions. The crimp content, which characterizes the degree of out-of-plane waviness of a yarn, is obtained by measuring the length of a yarn in a fabric state, the variable L_{fabric} , and the length of the yarn after extraction from the fabric, quantity L_{yarn} , and the straightening, defined from the previous two lengths as $\%CR = \left((L_{\text{yarn}} - L_{\text{fabric}}) / L_{\text{fabric}} \right) \times 100$.

Relying on the yarns data of plain weave and twill fabrics introduced in Sections 3.4.1 and 3.4.2 respectively, we obtain values of the effective mechanical properties and of the crimp interchange percentages in warp and weft directions calculated from the crimp angle (see Table 3.5); those properties are evaluated as a function of the decreasing crimp angle of the tows in the range of angles $5^\circ < \theta < 40^\circ$. The effective elastic moduli as well as Poisson's ratio are plotted against the crimp content (Figure 3.6); note that the crimp is decreasing during loading.

Table 3.5: Effective mechanical properties and crimp amounts of plain weave and twill at different crimp angles.

Crimp angle $\theta_f = \theta_p$	Plain weave							
	L_1 (mm)	L_2 (mm)	Weft crimp $\%CR_1 = \frac{L_{1\theta_0} - L_{1\theta_i}}{L_{1\theta_i}}$	Warp crimp $\%CR_2 = \frac{L_{2\theta_0} - L_{2\theta_i}}{L_{2\theta_i}}$	E_x^* (MPa)	E_y^* (MPa)	G_{xy}^* (MPa)	ν_{xy}^*
40°	0.947	0.858	30.52	30.54	113.5	281.9	7.90	0.164
35°	1.012	0.917	22.13	21.14	133.2	332.6	8.31	0.159
30°	1.070	0.969	15.51	15.58	155.6	399.4	8.71	0.145
25°	1.120	1.015	10.36	10.34	180.4	487.8	9.07	0.122
20°	1.161	1.052	6.46	6.46	206.6	603.6	9.34	0.092
15°	1.194	1.082	3.52	3.51	232.3	749.0	9.55	0.059
10°	1.217	1.103	1.56	1.54	254.6	913.0	9.67	0.029
5°	1.231	1.116	0.41	0.36	269.6	1057.0	9.73	0.007
Crimp angle $\theta_f = \theta_p$	Twill							
	L_1 (mm)	L_2 (mm)	Weft crimp $\%CR_1 = \frac{L_{1\theta_0} - L_{1\theta_i}}{L_{1\theta_i}}$	Warp crimp $\%CR_2 = \frac{L_{2\theta_0} - L_{2\theta_i}}{L_{2\theta_i}}$	E_x^* (MPa)	E_y^* (MPa)	G_{xy}^* (MPa)	ν_{xy}^*
40°	2.408	2.088	12.00	12.55	170.4	315.6	9.44	0.259
35°	2.474	2.147	9.01	9.46	189.3	370.8	9.83	0.234
30°	2.532	2.199	6.52	6.87	209.8	444.3	10.25	0.20
25°	2.582	2.245	4.45	4.68	231.8	542.7	10.67	0.159
20°	2.623	2.282	2.82	2.98	254.8	673.7	11.00	0.114
15°	2.655	2.312	1.58	1.64	277.5	841.0	11.31	0.071
10°	2.678	2.333	0.71	0.73	298.3	1034.0	11.49	0.034
5°	2.693	2.346	0.15	0.17	313.8	1206.0	11.56	0.009

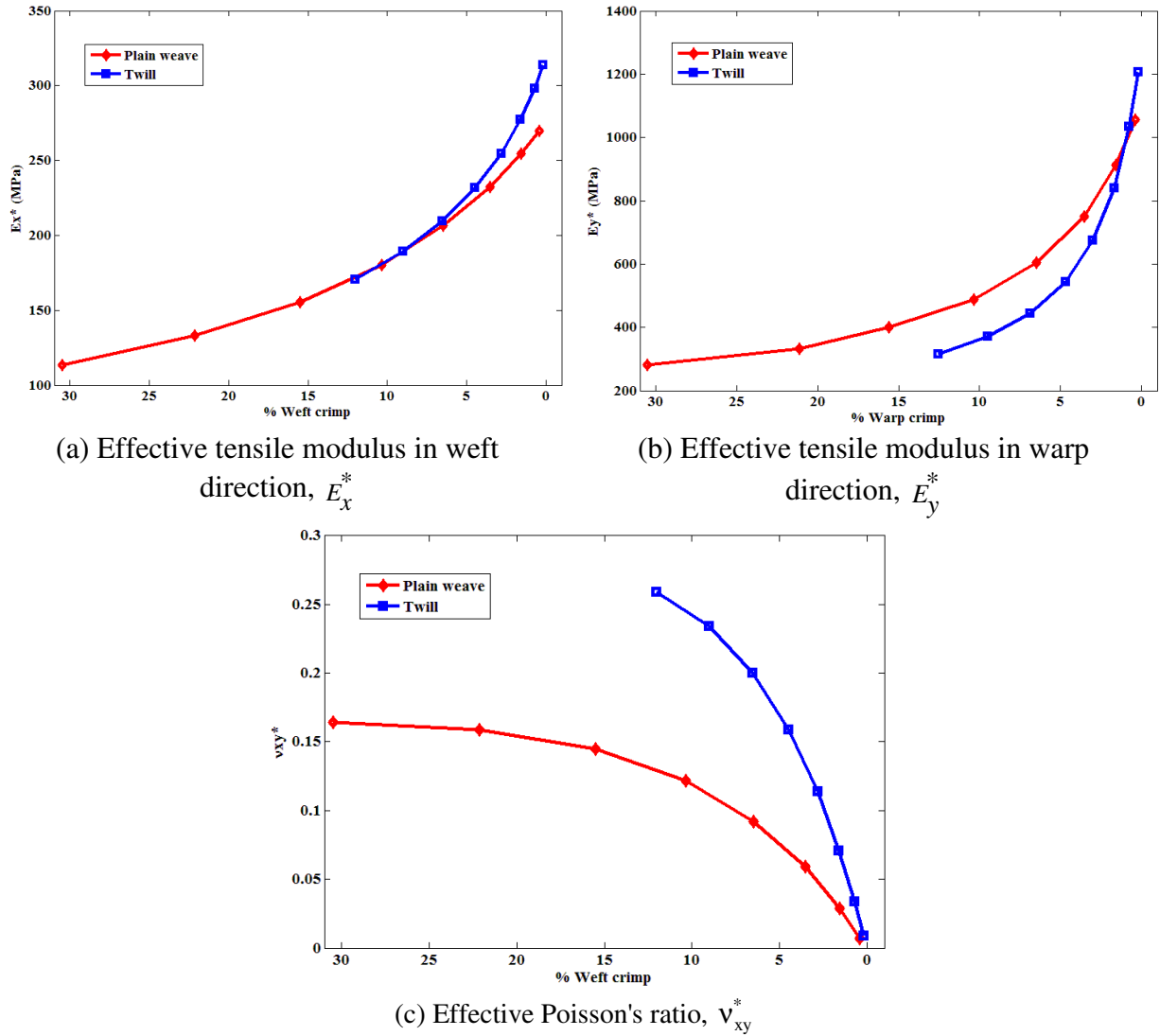


Figure 3.6: Evolution versus crimp interchanges of effective elastic properties of plain weave and twill fabrics. (a), (b) tensile moduli E_x^* , E_y^* and (c) Poisson's ratio v_{xy}^* .

It is noted that the crimp interchanges in both warp and weft yarns of twill (maximum about 12%) are much lower than the crimp interchanges in warp and weft yarns of plain weave (maximum about 30%). Both initial values of the crimp interchange correspond to the same initial crimp angle of 40° .

As evidenced on [Figure 3.6](#), crimp variations have a significant impact on the predicted effective moduli. The main effect of decreasing the crimp angle from $\theta = 40^\circ$ to $\theta = 5^\circ$ (or crimp percentage) of the tows is a nonlinear increase in the effective tensile moduli in both weft or warp direction. The maximum increase is 137.5% in weft direction and 275% in warp direction for plain weave, and 84% in weft direction and 282% in warp direction for twill. Poisson's ratio decreases considerably (again non-linearly), but it is more influenced by the tow crimp. Finally, the shear modulus is decreased by about 23% for both plain weave and twill as a result of tow crimp, this decrease being nearly independent of the crimp angle. The Poisson's ratio as well depends on the crimp angle, as it nonlinearly decreases with the corresponding decrease of the crimp interchange.

3.5 Comparison of homogenized moduli with finite element results

In the current section, 3D finite element models of woven fabrics at meso-level are developed to assess the accuracy of the effective properties predicted from discrete homogenization. The FE model is capable of simulating elementary cells under simultaneous axial loading along the yarn directions and fabric shearing. The effective elastic properties are calculated using the strain energy-based method, based on the relationship established between the strain energy of the microstructure and that of the homogenized equivalent model under specific boundary conditions. The homogenized material properties macroscopically account for the heterogeneity in the tows.

The finite element procedure at the meso-level involves the modelling of a single unit cell instead of modelling the whole fabric structure. In defining such a unit cell, it should be noted that it is not isolated from the adjacent cells in the fabric. Subsequently, the boundary effects from the adjacent cells should be taken into account: this is done by imposing a specific type of geometric constraints known as ‘‘periodic boundary conditions’’ on the unit cells. The boundary surfaces of the unit cell must always appear in parallel pairs; the displacements on a pair of parallel opposite boundary surfaces can be written as

$$u_i^{k+} = \tilde{\epsilon}_{ij} x_j^{k+} + u_i^*, \quad u_i^{k-} = \tilde{\epsilon}_{ij} x_j^{k-} + u_i^* \quad (3.10)$$

where indices ‘‘ k^+ ’’ and ‘‘ k^- ’’ identify the k^{th} pair of two opposite parallel boundary surfaces of a repeated unit cell. Note that u_i^* is the same at the two parallel boundaries (periodicity), thus the difference between the above two equations gives

$$u_i^{k+} - u_i^{k-} = \tilde{\epsilon}_{ij} (x_j^{k+} - x_j^{k-}) = \tilde{\epsilon}_{ij} \Delta x_j^k \quad (3.11)$$

with $\tilde{\epsilon}_{ij}$ the macroscopic (average) strains of the unit cell. Since the quantities Δx_j^k are constants for each pair of the parallel boundary surfaces, for a specified macro strain $\tilde{\epsilon}_{ij}$, the right-hand side in (3.11) becomes constant. The constraint equations are applied as nodal displacement constraint equations, instead of giving equation (3.10) directly as boundary conditions.

Table 3.6 provides a complete and detailed description of the geometrical parameters required to construct the FE models; they are also representative of the micro architectures of plain weave and twill used in the discrete homogenization scheme. On the basis of these parameters, the entire geometry of the unit cell is constructed. The mechanical properties of fabric yarns are listed in Table 3.2.

Table 3.6: Geometrical parameters of plain weave and twill fabrics.

	Plain weave	Twill
L_{f1} (mm)	0.60	0.60
L_{f2} (mm)	--	0.48
L_{p1} (mm)	0.52	0.52
L_{p2} (mm)	--	0.42
θ_f (Deg)	36	36
θ_p (Deg)	38	38
d_f (mm)	0.27	0.27
d_p (mm)	0.25	0.25

The eight-node solid linear hexahedral element (ABAQUS element type C3D8I) is employed to mesh the woven fabrics; a total of 58,042 elements are used to model the plain weave and 78,268 elements for twill. In order to account for the possible displacements between the yarns, the contact with friction is introduced with a master/slave approach. Contact is considered to be an intrinsic character of woven fabrics and cannot be neglected during the meso-level analysis. Contact conditions are prescribed between the possible interlacing surfaces of the yarns under loading and are the same for all loading cases. The tangential behavior at the contact surfaces is defined using the penalty method with a friction coefficient selected here as 0.05, relying on (Peng and Cao, 2002).

3.5.1 Strain energy-based method

A strain energy-based method is proposed to evaluate effective elastic properties with specific boundary conditions imposed on the microstructure. The total strain energy stored in the unit cell is equated with the energy of an equivalent homogeneous continuum, which is obtained by the prescribed strain/stress fields.

In the elastic regime, the macroscopic behaviors of a unit cell can be characterized by the effective stress tensor $\tilde{\sigma}_{ij}$ and strain tensor $\tilde{\epsilon}_{ij}$ over the homogeneous equivalent model. They are interrelated by the effective, also termed homogenized stiffness matrix K^s as

$$\tilde{\sigma}_{ij} = K^s \tilde{\epsilon}_{ij} \quad (3.12)$$

where $\tilde{\sigma}_{ij} = \frac{1}{V_u} \int_{V_u} \sigma_{ij} dV_u$ and $\tilde{\epsilon}_{ij} = \frac{1}{V_u} \int_{V_u} \epsilon_{ij} dV_u$ are the volume averaging of the microscopic stress and strain tensors, σ_{ij} and ϵ_{ij} respectively, and V_u is the volume of the unit cell.

In a 2D plane stress state, equation (3.12) can be rewritten as follows

$$\begin{Bmatrix} \tilde{\sigma}_x \\ \tilde{\sigma}_y \\ \tilde{\sigma}_{xy} \end{Bmatrix} = \begin{bmatrix} K_{11}^s & K_{12}^s & 0 \\ K_{12}^s & K_{22}^s & 0 \\ 0 & 0 & K_{66}^s \end{bmatrix} \begin{Bmatrix} \tilde{\epsilon}_x \\ \tilde{\epsilon}_y \\ \tilde{\epsilon}_{xy} \end{Bmatrix} \quad (3.13)$$

Adopting the periodic boundary conditions imposed over a unit cell of domain Ω with boundary $\partial\Omega$, the components of the stiffness tensor for the unit cell can be evaluated. We perform for this purpose the following four elementary tests:

Load case 1: Prescribed unit strain state in x-direction

$$\tilde{\epsilon}_x = 1, \tilde{\epsilon}_y = \tilde{\epsilon}_{xy} = 0 \quad (3.14)$$

The corresponding displacement boundary conditions are

$$u = x, v = 0, \text{ on } \partial\Omega \quad (3.15)$$

This yields $K_{11}^s = 2U_{\text{cell}} / V_u$.

where U_{cell} is the strain energy over the unit cell.

Load case 2: Prescribed unit strain state in y-direction

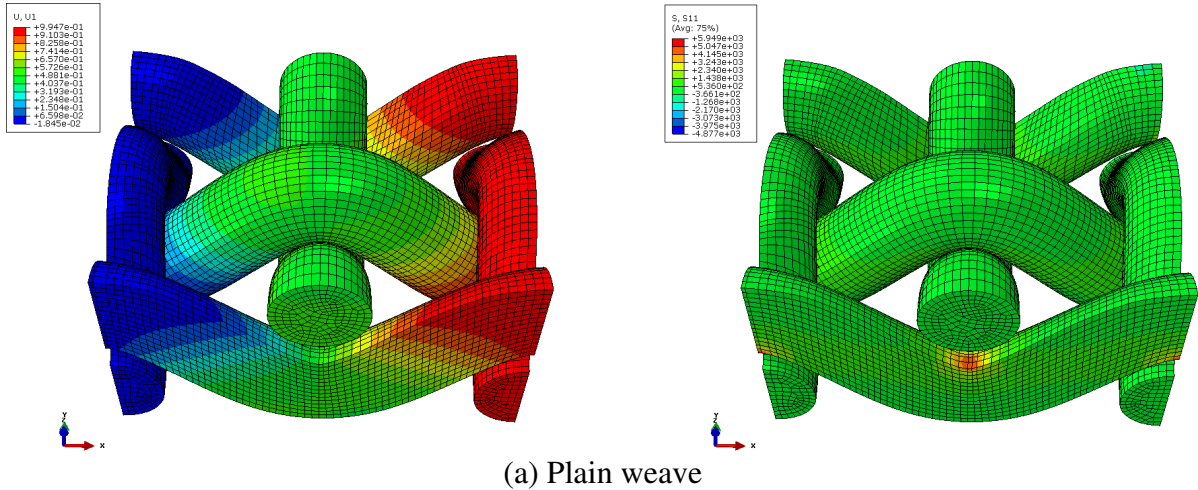
$$\tilde{\epsilon}_x = \tilde{\epsilon}_{xy} = 0, \tilde{\epsilon}_y = 1 \quad (3.16)$$

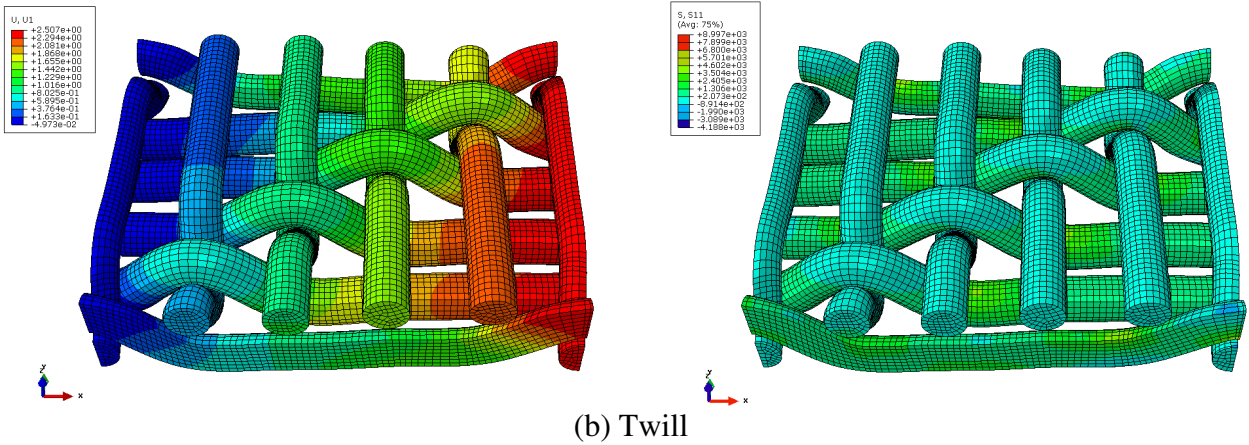
The corresponding displacement boundary conditions are

$$u = 0, v = y, \text{ on } \partial\Omega \quad (3.17)$$

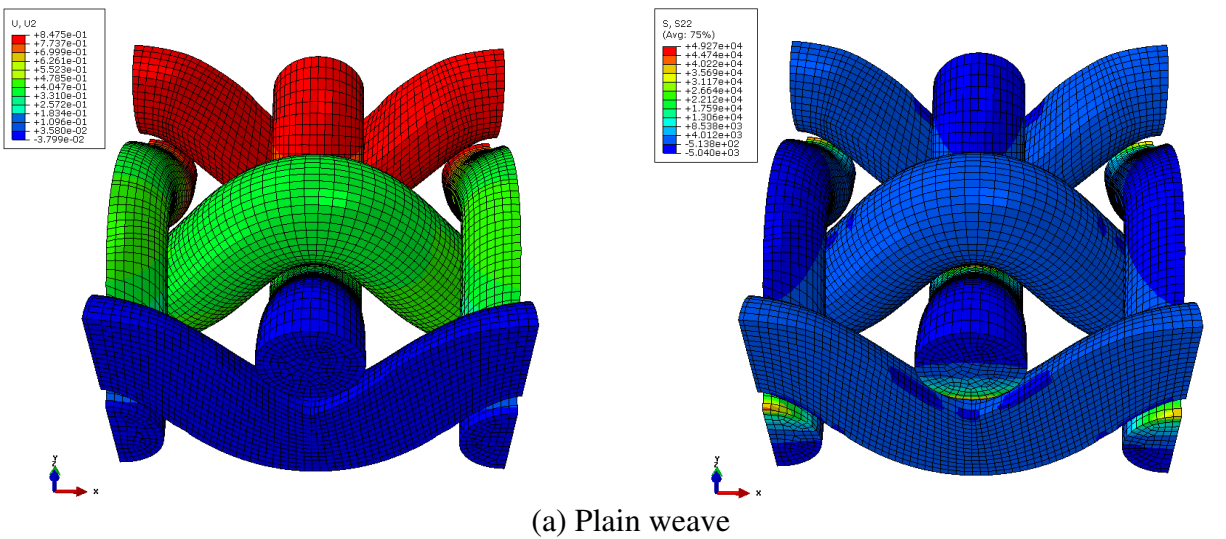
This yields $K_{22}^s = 2U_{\text{cell}} / V_u$.

The displacement and stress distributions over the unit cells of plain weave and twill fabrics for the above two tests under the corresponding displacement boundary conditions are shown in [Figures 3.7](#) and [3.8](#).

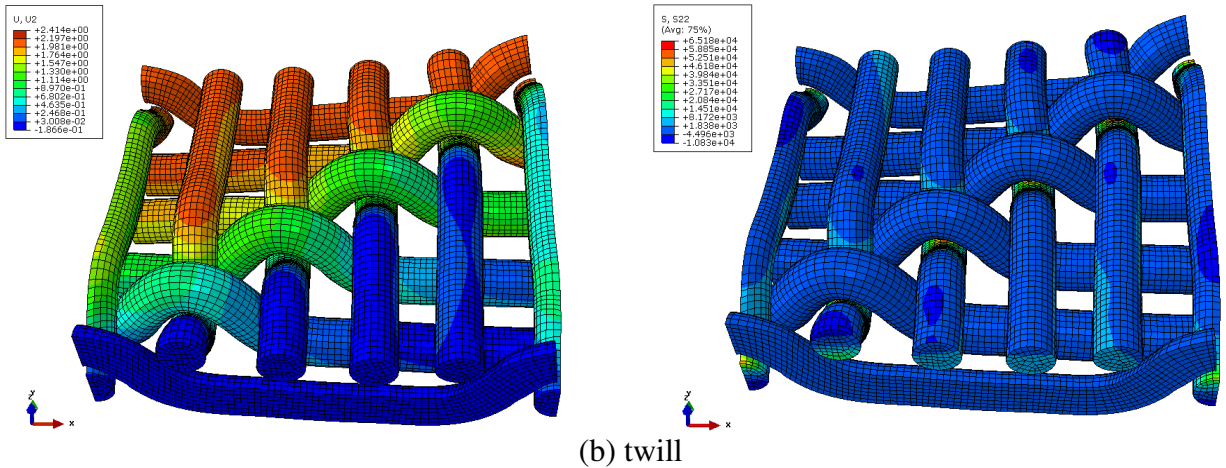




(b) Twill
 Figure 3.7: Displacement (left) and stress (right) distributions over. (a) plain weave and (b) twill tows due to uniaxial extension in x-direction.



(a) Plain weave



(b) twill

Figure 3.8: Displacement (left) and stress (right) distributions over. (a) plain weave and (b) twill tows due to uniaxial extension in y-direction.

Load case 3: Prescribed biaxial strain state

$$\tilde{\epsilon}_x = \tilde{\epsilon}_y = 1, \tilde{\epsilon}_{xy} = 0 \tag{3.18}$$

The corresponding displacement boundary conditions are

$$u = x, v = y, \text{ on } \partial\Omega \quad (3.19)$$

This gives $K_{12}^s = (2U_{\text{cell}} / V_u - K_{11}^s - K_{22}^s) / 2$.

Load case 4: Prescribed shear strain state

$$\tilde{\epsilon}_x = \tilde{\epsilon}_y = 0, \quad \tilde{\epsilon}_{xy} = 1 \quad (3.20)$$

The corresponding kinematic boundary conditions are

$$u = y/2, v = x/2, \text{ on } \partial\Omega \quad (3.21)$$

This yields $K_{66}^s = 2U_{\text{cell}} / V_u$.

The displacement and stress distributions for the last two tests under the corresponding displacement boundary conditions are shown in Figures 3.9 and 3.10.

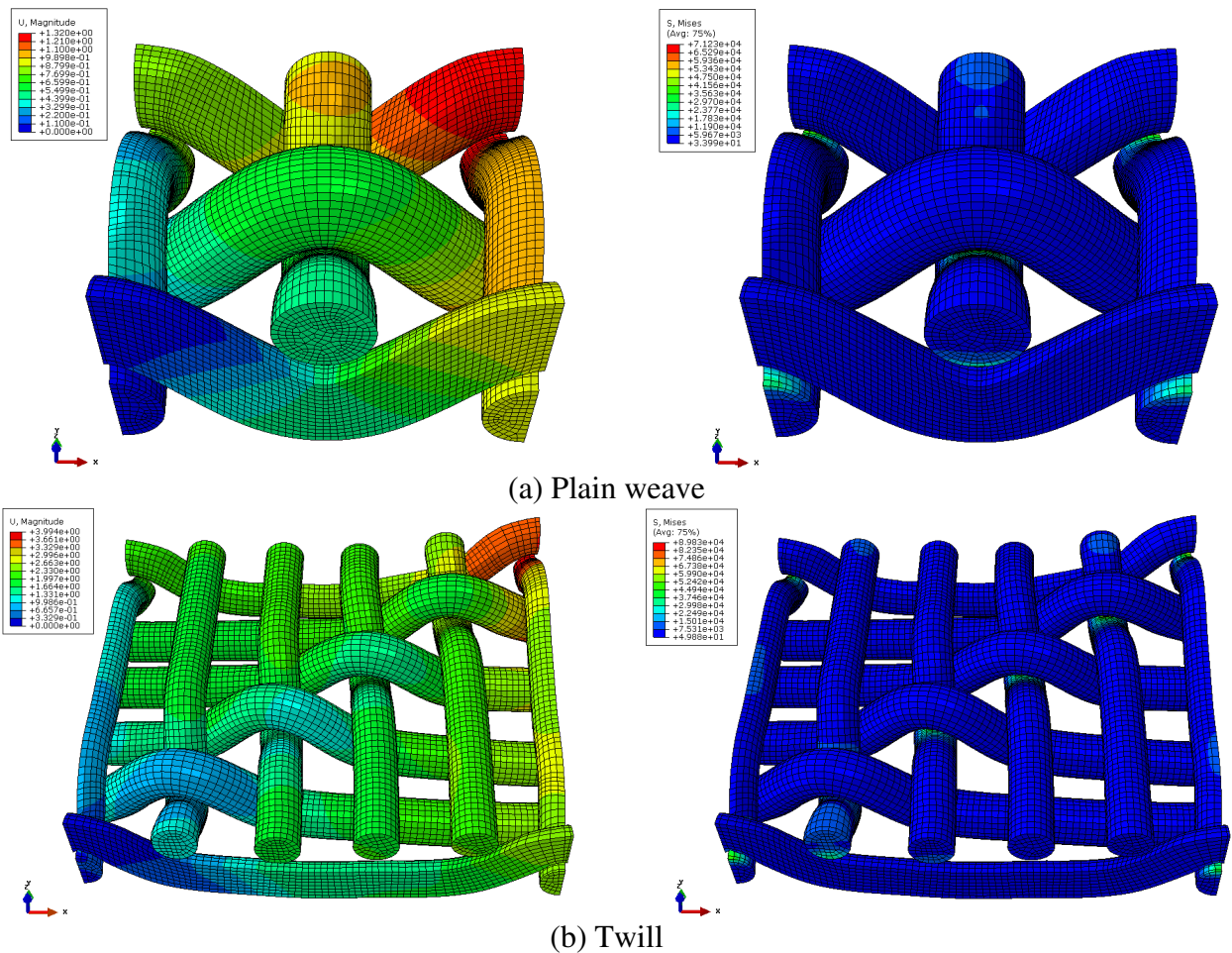


Figure 3.9: Displacement (left) and stress distributions (right) over (a) plain weave and (b) twill tows due to biaxial extension.

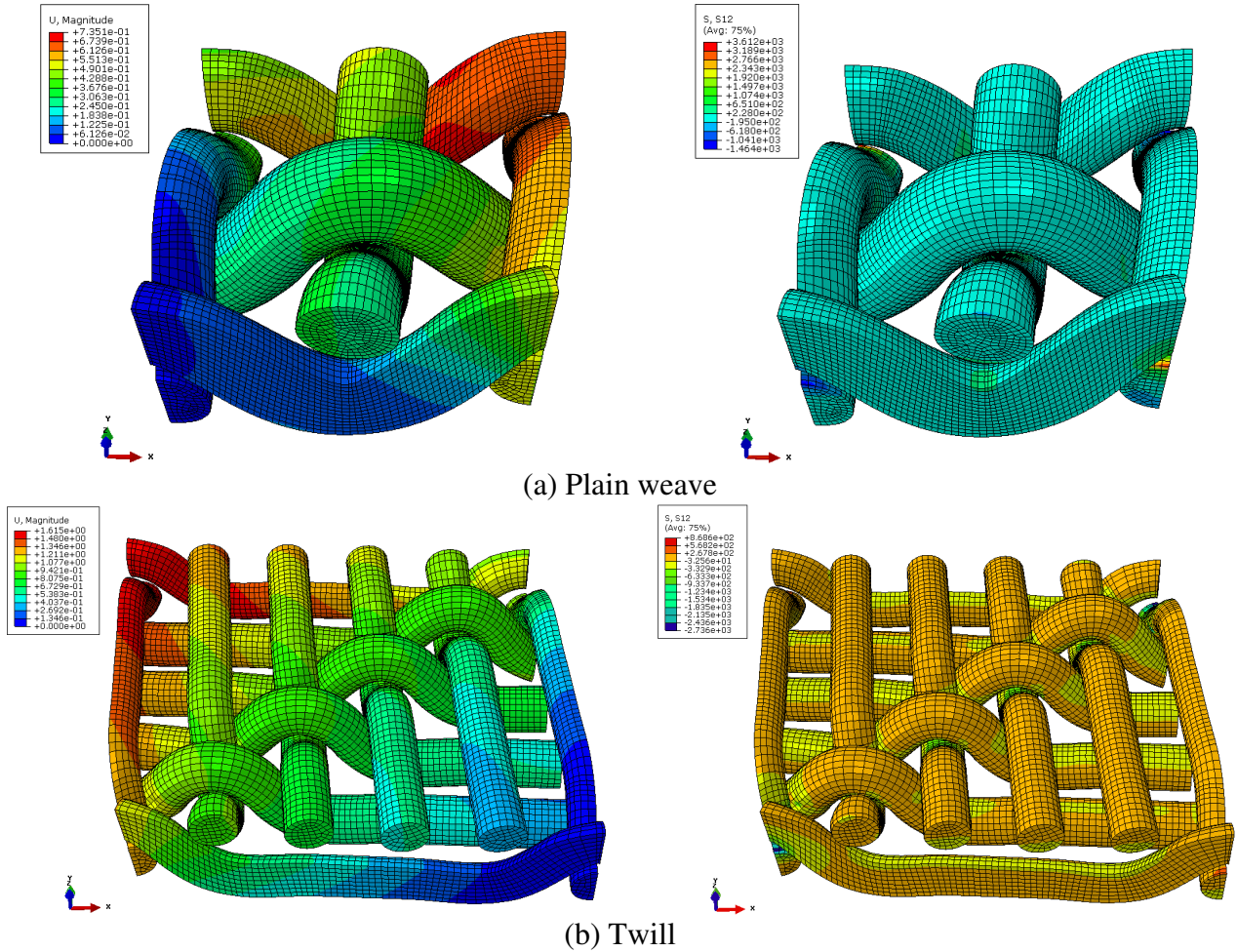


Figure 3.10: Displacement and stress distributions over (a) plain weave and (b) twill tows due to shearing.

The components of the effective stiffness matrix, quantities K_{11}^S , K_{22}^S , K_{12}^S , K_{66}^S , as well as the equivalent moduli and Poisson's ratio are computed from the above numerical analyses and summarized for both fabric types in [Table 3.7](#). The overall behavior appears to be unbalanced (the ratio of effective moduli in warp and weft directions is close to three), thereby reflecting the anisotropy at the yarn level.

Table 3.7: Effective elastic constants of unbalanced plain weave and twill fabrics from discrete homogenization and finite element simulations.

	Discrete homogenization		Finite element simulation	
	Plain weave	Twill	Plain weave	Twill
K_{11}^s (MPa)	156	220	140	197
K_{12}^s (MPa)	53	92	50	87
K_{22}^s (MPa)	341	416	405	516
K_{66}^s (MPa)	9.7	10.5	11	8.5
E_x^* (MPa)	147.7	199.7	134	182
E_y^* (MPa)	323	378	387	477
ν_{xy}^*	0.15	0.22	0.12	0.17
ν_{yx}^*	0.34	0.41	0.36	0.44

Overall, a satisfactory agreement between the homogenized moduli and their numerical counterpart is obtained, with a greater discrepancy (close to 20%) for E_y^* and ν_{xy}^* .

As a matter of completeness, we also evaluate the effective properties for the balanced fabric of plain weave type. The entire geometry of the unit cell is constructed based on the geometrical and mechanical micro parameters of weft yarns (Tables 3.2 and 3.6). The components of the effective stiffness matrix and equivalent effective moduli show a good agreement with their numerical counterpart obtained by unit cell FE simulations (Table 3.8), with 15% maximum difference. The overall behavior appears to be nearly balanced, thus reflecting the isotropy at the yarn level. The stress distributions over the balanced plain weave fabric for axial and shear tests under the corresponding displacement boundary conditions are shown in Figure 3.11 (an isotropic behavior is obtained).

Table 3.8: Effective elastic constants of balanced plain weave fabrics from homogenization and finite element simulations.

	Discrete homogenization	Finite element simulation
$K_{11}^s = K_{22}^s$ (MPa)	82.5	96
K_{12}^s (MPa)	26.3	28
K_{66}^s (MPa)	4.85	4.53
$E_x^* = E_y^*$ (MPa)	74.2	86.7
$\nu_{xy}^* = \nu_{yx}^*$	0.318	0.292

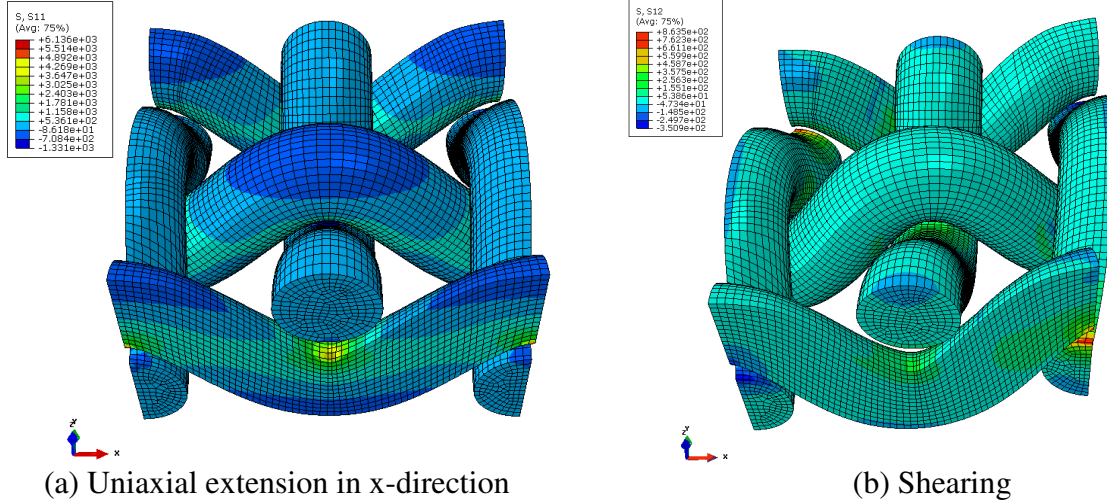


Figure 3.11: Stress distributions over balanced plain weave tows.

These differences may be attributed to several factors, the most important being next reviewed. A first factor is the rigidities of the contact beams connecting warp and weft yarns at the crossing points in the discrete homogenization, which are calculated as $k_{lc1,2} = E_{sc}A_c / L_{c1,2}$, $k_{tc1,2} = 12E_{sc}I_c / (L_{c1,2})^3$, and $k_{rc1,2} = G_{sc}J_c / L_{c1,2}$. Such rigidities depend on different parameters, such as E_{sc} , G_{sc} , L_c , and r_c , computed from the relations

$$E_{sc} = (E_{sf} + E_{pf}) / 2, \quad G_{sc} = (G_{sf} + G_{pf}) / 2, \quad L_{c1,2} = Lf_1 \sin\theta_f, Lp_1 \sin\theta_p, \quad r_c = (r_f + r_p) / 2.$$

These relations are based on the considered model of the fabric topology, and are thus endowed with approximations. As another source of discrepancy, the geometrical representation of fabrics unit cells in the discrete homogenization scheme has some limitations. In finite element simulations, the curvilinear trajectories of the yarns (the middle line) in the 3D model have been identified using Bezier splines (thus having a smooth radius of curvature), while in the discrete homogenization the yarns trajectories are modeled by piecewise straight lines with sharp corners at the crossover points, so the line will not precisely follow the trajectory. This implies that the crimp of the yarn will be slightly different than in the finite element model, which will in turn impact the macroscopic properties.

3.6 Sensitivity analysis on meso-level

The previous sections have addressed the modeling of the mechanical behavior of woven fabrics at the meso-scale using discrete homogenization and finite element simulations performed over representative unit cells. The main objective of this section is to identify the sensitivity of this modeling to uncertainty factors that may exist in real fabrics, and examine their influence on the response of fabric at the macro-level. Uncertainty factors studied here fall into two separate categories: factors that pertain to the discrete homogenization model (yarn transverse shear, beams connecting warp and weft yarns at the crossing points) and other factors related to the finite element simulation setting, such as the friction coefficient between yarns.

3.6.1 Effect of yarns transverse shear

In order to analyze the impact of yarns (warp and weft) transverse shear deformations on the effective properties of woven fabrics, the homogenized properties (tensile and shear moduli and Poisson's ratio) of plain weave and twill fabrics obtained with Timoshenko and Euler Bernoulli beam models are plotted against the crimp content (defined as $\%CR = \left(\frac{L_{\text{yarn}} - L_{\text{fabric}}}{L_{\text{fabric}}} \right) \times 100$), considering the geometrical and mechanical microparameters presented in 3.4.1 and 3.4.2 (Figure 3.12). Note that the crimp content is decreasing (from left to right on Figure 3.12) under loading. The obtained results show that the absence of transverse shear leads to overestimate Young's moduli along weft and warp (moduli E_x^* and E_y^* respectively), as well as the shear moduli G_{xy}^* , and underestimate the in-plane Poisson's ratio ν_{xy}^* .

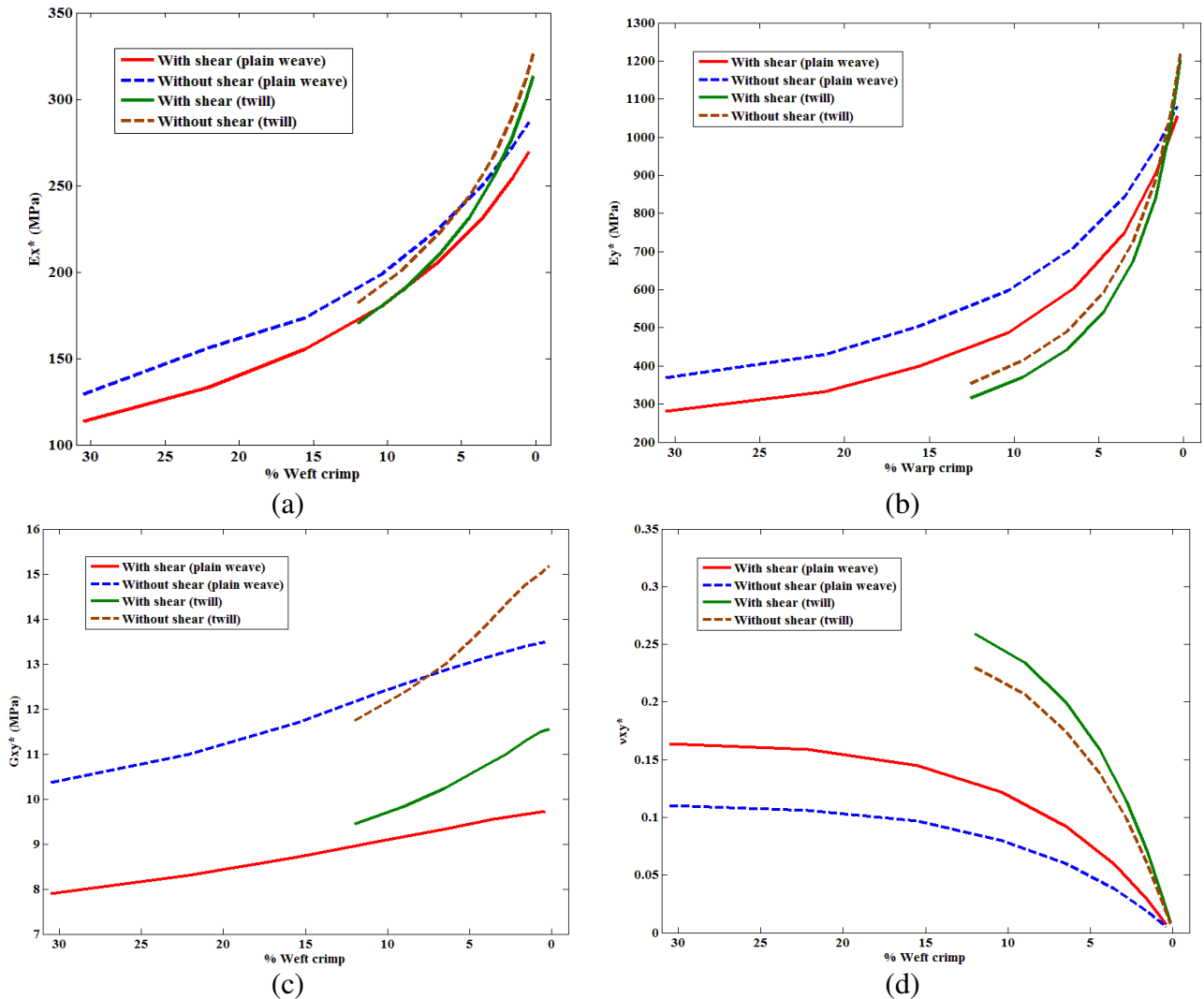


Figure 3.12: Effect of yarn transverse shear deformations on the effective homogenized mechanical properties of plain weave and twill fabrics. (a), (b) Young's moduli E_x^* and E_y^* respectively, (c) Shear modulus G_{xy}^* , and (d) Poisson's ratio ν_{xy}^* .

3.6.2 Effect of friction between yarns on the FE simulated response

The friction coefficient between yarns adopted in FE tests borrows from the work of Peng and Cao (2002), which used a friction coefficient of 0.05 for glass/PP fabrics in the FE modeling. However, one important question is “what is the appropriate range for this factor?” Here, for the sake of the numerical procedure, noticing that the friction behavior is likely to impact the numerical results, the range of variation of the friction coefficient has been considered as 0–0.2. We observe that under axial and biaxial loadings over the plain weave, the effect of friction in the considered range of variation (0–0.2) is very small (almost zero), whereas it generates a variation of the shear modulus G_{xy}^* of about 11.8% (the shear modulus G_{xy}^* is changed from 11 MPa to 12.3 MPa). In the case of twill, the influence of friction under uniaxial and biaxial loadings is relatively small (the variations of Young's moduli do not exceed 2%); under shear loading, the shear modulus is increased by 8%. In the shear mode, friction clearly plays an important role, before and after the formation of side contacts (inducing locking phenomena) in the yarns. In the first stage of deformation, when yarns are rotating over each other, friction plays an important role in generating a reaction force. In the second stage, when yarns are in side contact and a severe pressure acts between yarns, the effect of friction becomes even more important. In the discrete homogenization model, the warp and weft yarns are connected by a vertical beam (contact beam) at the yarn crossing points. Additional locking beams (inclined) shall be required to simulate the shear locking phenomenon.

3.6.3 Effect of contact beam rigidities

The contact between warp and weft in the discrete homogenization models is accounted for by vertical beams connecting both sets of yarns, located at intersection of the yarns. The tensile, flexural, and torsion rigidities of the contact beam are considered, and are quantified respectively as follows: $k_{lc1,2} = E_{sc}A_c / L_{c1,2}$, $k_{tc1,2} = 12E_{sc}I_c / (L_{c1,2})^3$, and $k_{rc1,2} = G_{sc}J_c / L_{c1,2}$. We presently conduct a sensitivity analysis by varying the contact beam rigidities to evaluate their effects on the global behavior of plain weave and twill fabrics (see Table 3.9). The upper and lower bounds of the rigidities are chosen based on the values calculated using the data presented in Sections 3.4.1 and 3.4.2 for plain weave and twill respectively. The upper values will be 10 times and the lower values will be 0.1 times the calculated values (reference values).

From the obtained results (Table 3.9), the following conclusions can be drawn: increasing the extensional rigidity k_{lc} of the contact beam in the range $(0.1–10) \times k_{lc}$ leads to a significant increase of the effective young's modulus E_x^* (44.7% for plain weave and 40.7% for twill), a slight change in E_y^* (5.6% for plain weave and 4.2 % for twill), and almost no

change in shear modulus G_{xy}^* , as well as in bending stiffnesses K_{55}^μ and K_{66}^μ for the two types of fabrics. In addition, a noticeable sensitivity of E_x^* and G_{xy}^* to the flexural rigidity k_{tc} of the contact beam in is obtained, in the range $(0.1-10) \times k_{tc}$: the Young's modulus in weft-direction E_x^* is changed by 24.2% for plain weave and by 20.6% for twill, whereas E_y^* is changed (in warp direction) by about 5% for both fabrics types. An important sensitivity is also obtained for the shear modulus G_{xy}^* , about 167.7% for plain weave and 150% for twill; contrary to that, no effect is detected for the bending stiffnesses. Finally, the torsional rigidity k_{rc} influences the bending stiffnesses K_{55}^μ and K_{66}^μ : the variation $(0.1-10) \times k_{rc}$ results in a clear change in K_{55}^μ (132.6% for plain weave and 205.6% for twill) and in K_{66}^μ (103.5% for plain weave and 148.5% for twill). There is in contrast no effect on the other macroscopic properties E_x^* , E_y^* , and G_{xy}^* . It is therefore clear that the selected properties of the contact beams have overall an important effect on the effective mechanical properties, and may by themselves explain the differences observed between the homogenized moduli and FE simulated values.

Table 3.9: Effect of extensional, flexural, and torsion rigidities of the contact beam on the fabric effective moduli.

		Contact beam rigidities		
		Lower value	Reference value	Upper value
		$0.1 \times k_{lc}$	$k_{lc} = E_{sc} A_c / L_c$	$10 \times k_{lc}$
E_x^* (MPa)	PW	84.6	113.5	122.5
	Twill	123.4	170.4	173.7
E_y^* (MPa)	PW	269.6	281.9	284.7
	Twill	303.7	315.6	316.6
		$0.1 \times k_{tc}$	$k_{tc} = 12 E_{sc} I_c / (L_c)^3$	$10 \times k_{tc}$
E_x^* (MPa)	PW	96.6	113.5	120
	Twill	147.6	170.4	178
E_y^* (MPa)	PW	271.3	281.9	285
	Twill	302	315.6	319.6
G_{xy}^* (MPa)	PW	3.4	7.9	9.1
	Twill	4.4	9.50	11
		$0.1 \times k_{rc}$	$k_{rc} = G_{sc} J_c / L_c$	$10 \times k_{rc}$
K_{55}^μ (N)	PW	0.98	1.84	2.28
	Twill	1.78	4.0	5.44
K_{66}^μ (N)	PW	4.48	7.50	9.12
	Twill	5.85	10.45	14.54

3.7 Measurements of the tensile moduli of plain weave fabric

The characterization of the tensile behavior of plain weave fabric is performed according to the standard EN IS13934-1 by means of the traction machine MTS/20M (Jeguirim and Fontaine, 2008). These tests were carried out on samples of initial length of 200 mm and 50 mm width with a constant elongation rate equal to 20 mm/min. The measured responses are used to determine the elastic initial moduli of the tested samples, which are then compared to the moduli obtained by discrete homogenization. The parameters of the tested samples at both yarn and fabric levels are reported in Table 3.10; the weft has undergone a specific heat treatment.

Table 3.10: Characteristics of the plain weave tested samples.

Yarns	Weft	Warp
Material	PET	PET
Type	Monofilament	Multifilament
Diameter (mm)	0.45	0.403
Average Young's modulus (MPa)	8260	7940
Fabric		
Surface weight (g/m ²)	440	
Density in warp	14 yarns/cm	
Density in weft	8.5 yarns/cm	

Figures 3.13 and 3.14 show the evolution of the recorded force versus the relative elongation (%) in the weft and warp directions, respectively. Six tests were performed in each direction in order to quantify the variability of the tested samples. In order to derive the engineering stresses from the forces provided by the tensile test, the measured width (50 mm) and the calculated thickness based on Peirce model (0.86 mm) are used (Peirce, 1937); this results in a cross-sectional area of 43mm².

The stress–strain curves in the weft and warp directions over the strain range from 0 to 1.2% and from 1.2% to 2.4% respectively are exploited (the tendency is nearly linear in those ranges, and we avoided the initial toe region in warp direction for strains below 1.2%) to calculate the equivalent tensile moduli in weft and warp directions respectively as (means±standard deviations) 1316±46 MPa and 373±94 MPa.

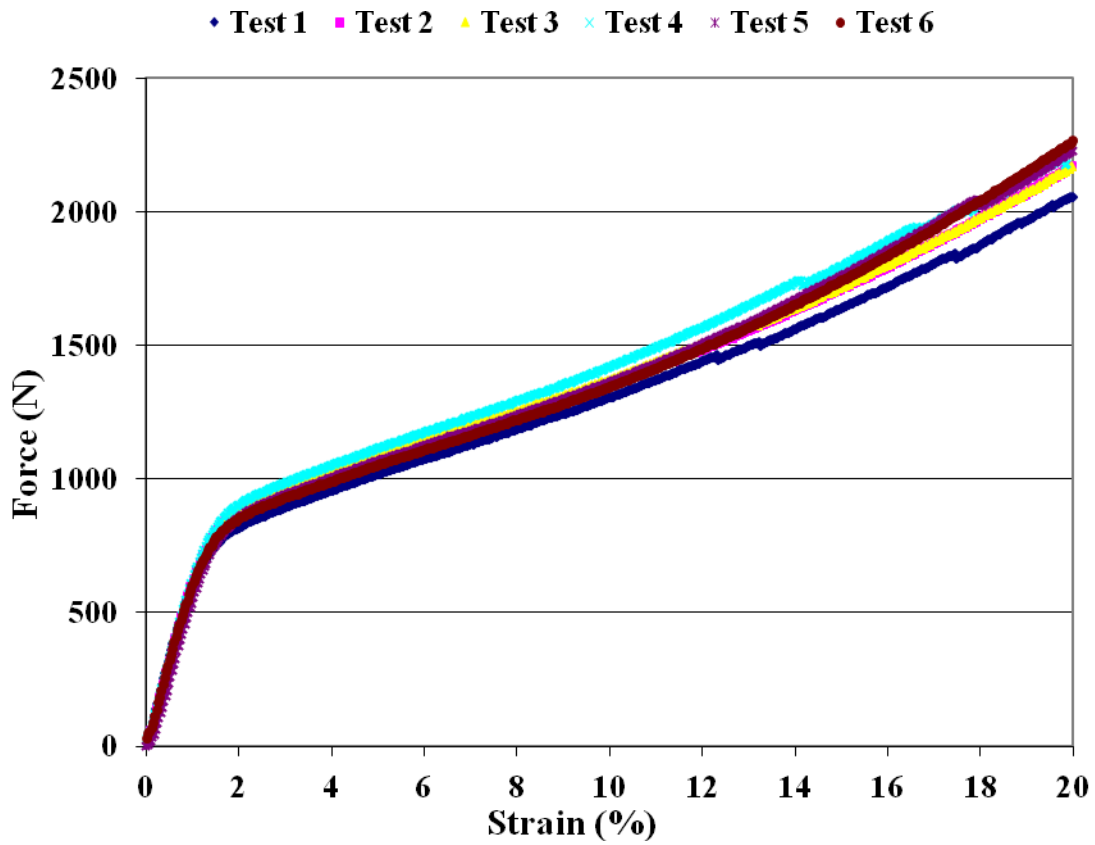


Figure 3.13: Experimental tensile tests of plain weave samples along the weft direction. (Jeguirim and Fontaine, 2008).

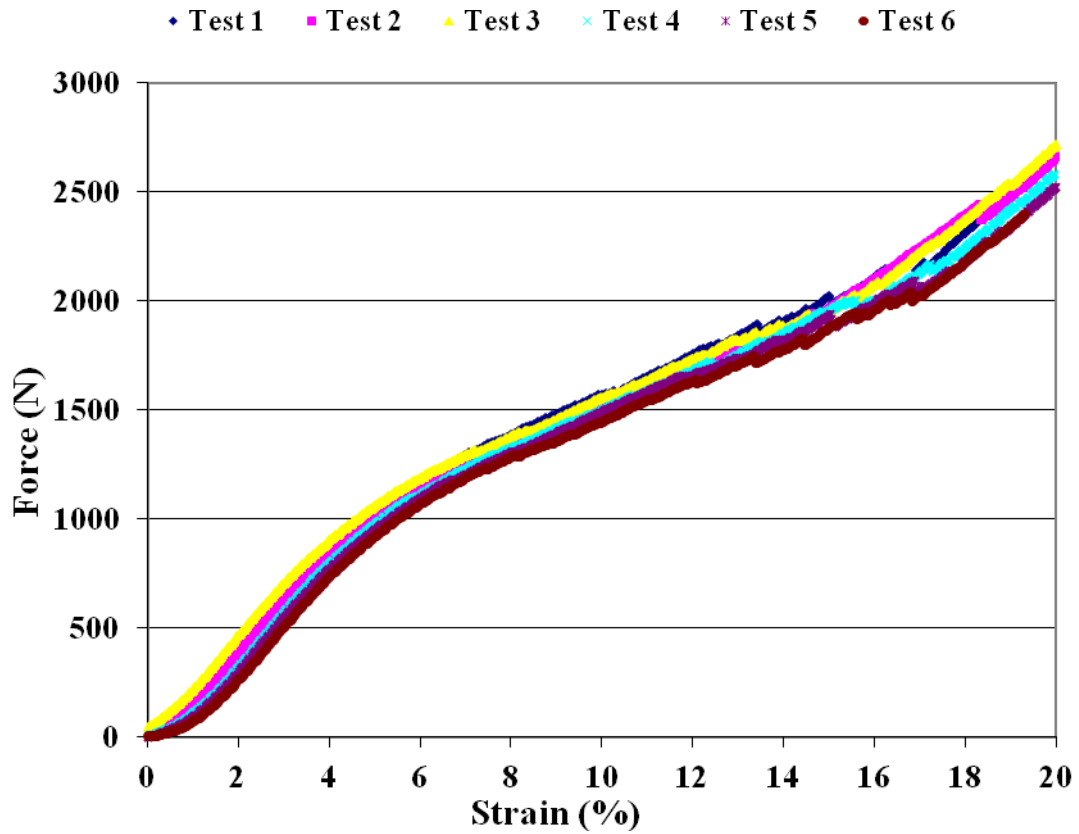


Figure 3.14: Experimental tensile tests of plain weave samples along the warp direction. (Jeguirim and Fontaine, 2008).

The discrete homogenization model is used to predict the mechanical properties, based on the analysis of a representative unit cell (determined from Table 3.10). The geometrical parameters of the unit cell, required as input data, are estimated as: $L_{f1}=1.25$ mm, $\theta_f =20^\circ$, $L_{p1}= 0.83$ mm, $\theta_p =30^\circ$. The computed homogenized moduli along the weft and warp are respectively 1139 MPa and 331 MPa. The elastic moduli determined by discrete homogenization show a satisfactory agreement with the measured values obtained in the elastic region of the uniaxially tested samples, with average discrepancies of 13% in weft and 11% in warp directions.

3.8 Conclusions

Meso-level analyses of the mechanical behavior of textile monolayers have been performed to construct effective anisotropic micropolar continuum models. The discrete asymptotic homogenization method delivers a micropolar effective medium at the mesoscopic level, from the description of the textile as a lattice of beams. Each yarn within the textile is modeled as a Timoshenko beam at the microscopic scale. The micropolar models have been constructed from the fabric topology and mechanical properties as input data, delivering as an output the classical and micropolar elastic effective constants. The derivation of such effective mechanical properties of textile from micromechanical analyses is quite interesting, since those properties haven't been measured up to now, due to the discrete nature of textiles. Furthermore, the micropolar effect proves to be important for both types of fabric as witnessed by the gain of bending rigidity for a macroscopic beam tested virtually in flexion and endowed with such a fabric texture.

A relatively good agreement has been obtained between the effective properties determined from discrete homogenization and those computed numerically by the sequential FE homogenization from the fiber scale to the tow scale. It has further been shown that the effective initial moduli (for small strains) are representative of the moduli measured on PET plain weave fabric samples.

The effect of the textile microstructure on the bending stiffness has been examined for both plain weave and twill tows, by comparing a classical macrobeam model to a model based on micropolar elasticity theory. The micropolar model contains a material length scale parameter to account for the microstructural effect, namely a bending stiffness depending on two additional material constants, K_{55}^μ and K_{66}^μ . A consequence of this is the prediction of an increased bending stiffness, which becomes measurable at the scale of a few millimeters.

Sensitivity analysis has been performed to uncertainty factors that may exist in real fabrics. They fall into two separate categories: factors that pertain to the discrete homogenization model (yarn transverse shear, beams connecting warp and weft yarns at the crossing points) and other factors related to the finite element simulation setting, which is the friction coefficient between yarns. The obtained results show that the absence of transverse shear leads to overestimate Young's moduli along weft and warp, as well as the shear moduli,

and underestimate the in-plane Poisson's ratio. The influence of friction under uniaxial and biaxial loadings is found to be relatively small, while in the case of shear loadings the influence is high. When we came across the sensitivity analysis conducted for the contact beams, we found that increasing the extensional rigidity of the contact beams leads to a significant increase of the Young's modulus along the weft, a slight change along warp, and almost no change in shear modulus as well as in bending stiffnesses. While, increasing the flexural rigidity leads to a noticeable increase of the Young's modulus along the weft, a slight change along the warp, and a significant increase in shear modulus. Finally, the torsional rigidity has great influences on the bending stiffnesses and there is in contrast no effect on the other properties.

CHAPTER 4: MICROPOLAR CONSTITUTIVE MODELS OF TRABECULAR BONE

This chapter deals with the construction of Cosserat models of trabecular bone in 2D and 3D situations, based on micromechanical approaches to investigate microstructure-related scale effects on the macroscopic properties of bone. The cell walls of the bone microstructure are modeled as Timoshenko thick beams. Closed form expressions of the equivalent properties are obtained versus the geometrical and mechanical microparameters, accounting for the effects of bending, axial, and transverse shear deformations; torsion is additionally considered for a 3D geometry. The classical and micropolar effective moduli and the internal flexural and torsional lengths are identified versus the micropolar material constants. The scaling laws of the effective moduli versus density are determined in situations of low and high effective densities to assess the impact of the transverse shear deformation. Finite element models over the local architecture of the trabeculae and also over the whole lattice are performed to validate the results from homogenization. The stress distribution in a cracked 2D bone sample is also computed based on the effective micropolar model, highlighting the regularizing effect of the Cosserat continuum in comparison to a classical elasticity continuum model.

4.1 Introduction

Bone is a particularly complex multiscale material, which is hierarchically organized to provide maximum performance with a minimum amount of material (Figure 4.1). At the nanoscale, bone is composed of collagen fibers, apatite crystals and water; at the sub-microscale (1–10 μm), the arrangements of collagen fibers reinforced with crystals form lamellas. These lamellas are packed and organized in different orientations to form cylindrical struts called trabecula at the microscale (several hundred of micrometers). At the mesoscale, the complex and very organized network of trabeculae forms the cancellous bone. The macro scale represents the whole bone which is constituted by both the cancellous (trabecular) bone and the cortical (compact) bone. The location of these bone types in the femur is further illustrated in Figure 4.2; cortical bone is a dense material with a specific gravity of almost two in humans and a little over two in cattle; it forms most of the outer shell of a whole bone, a shell of variable thickness. Cancellous (porous) bone generally exists only within the confines of the cortical bone coverings; it is composed of short struts of bone material called trabeculae. The connected trabeculae give cancellous bone a spongy appearance, and it is consequently often called spongy bone.

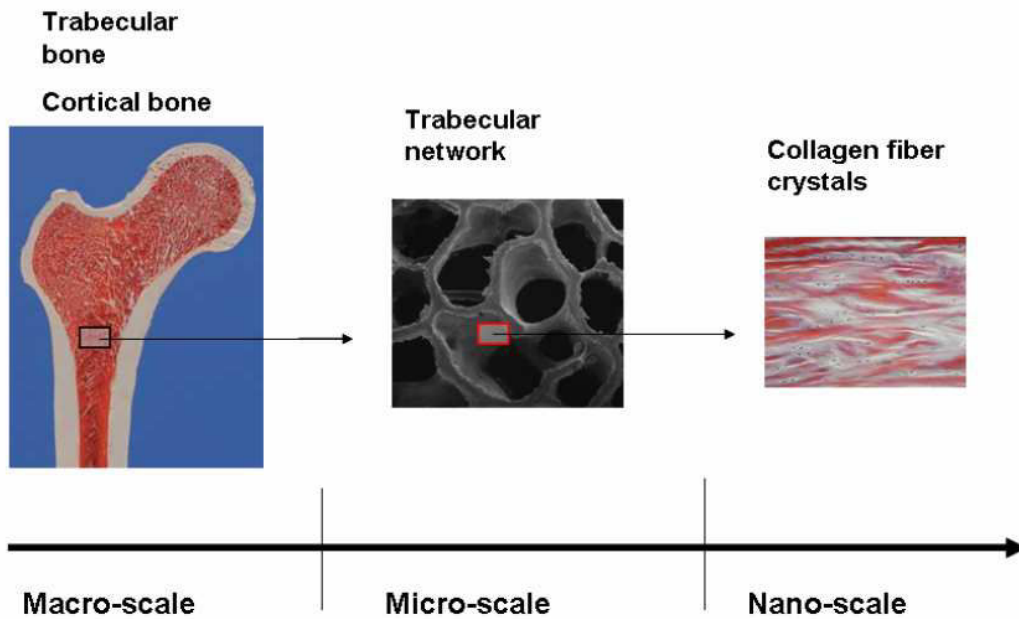


Figure 4.1: Multiscale aspects of bone structure.

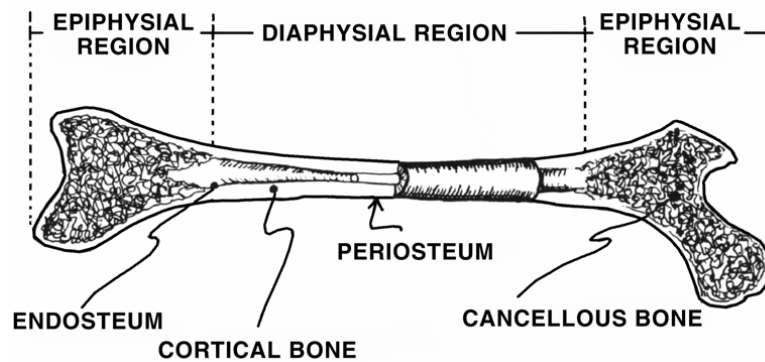


Figure 4.2: Longitudinal section of the femur illustrating cancellous and cortical bone types (Cowin and Doty, 2007).

Trabecular bone is very complex due to its randomness and spatial heterogeneity. In order to simplify the forthcoming analysis, one can choose to represent bone as having an idealized periodic microstructure. This work addresses the modeling of trabecular bone as hexagonal periodic structures, considering successively 2D and 3D geometries

4.2 Review of trabecular bone models

Considering first microstructural modeling approaches, Gibson (1985) proposed to model cancellous bone by a periodic network of cubic or hexagonal cells; this model was used to estimate the compressive behavior of cancellous bone as a function of mechanical properties of the cell material and dimensions of the cell (thickness t , length l). Guo et al. (1994) studied the compressive fatigue of trabecular bone modeled by a 2-D hexagonal honeycomb structure. Silva and Gibson (1997) developed a two-dimensional finite element model of the human vertebral trabecular bone using a technique based on Voronoï diagrams to investigate its mechanical behavior. Silva and Gibson (1997) also showed that the variability in the

arrangement of cell walls creates a small amount of variability in the elastic constants of honeycombs, but that overall the relationship between the microstructure and the elastic properties for isotropic and anisotropic non-periodic honeycombs are no different from periodic honeycombs. This result lends some evidence in utilizing periodic unit cells in modeling the random geometry of trabecular bone. Analytical models were also developed to investigate the strength asymmetry observed in trabecular bone (Keaveny et al., 1994; Kaplan et al., 1985). The geometrical formulations include a two dimensional honeycomb. The models were loaded under a remote uniaxial stress and the unit cells were aligned with the direction of loading (Ford and Gibson, 1998). Visual inspection of several representative cross sections suggested that a choice of 60° for the parameter θ was reasonable to represent, on the average, the relatively steep angle at which the oblique trabeculae lies relative to the horizontal direction. Also, a value that results in a degree of material anisotropy that is consistent with previous measurements for this type of trabecular bone was chosen, namely $h/l = 0.5$ for the geometry of that model (h is the vertical cell length).

Conventional continuum mechanical models do not incorporate any intrinsic characteristic lengths. However, real materials such as cellular solids and biological tissues often exhibit a number of important length scales, which must be included in any realistic model.

Although there have been many continuum models of bone developed over the last two decades on the basis of classical elasticity (Taylor et al., 2002; Bowman et al., 1998), those models ignore microstructure-related scale effects on the macroscopic mechanical properties. Consequently, they do not provide a complete description of the mechanical behavior when the microstructural size of bone approaches the macroscopic length scale. The structural hierarchy of materials with microstructures such as bones plays an important role in determining their macroscopic mechanical behavior as well as the stress and strain distribution. Such microstructural effects are most pronounced near bone-implant interfaces and in areas of high strain gradients. This issue is presently investigated by studying generalized continuum mechanics theories which account for the influence of microstructure-related scale effects on the macroscopic properties of bone. Bone is a strongly heterogeneous material with microstructural features, requiring generalized continuum mechanics theories when the macroscopic length scale (identified as the smallest length scale of the deformation pattern) becomes comparable or smaller than the typical microstructural length scale, such as the size of trabeculae in cancellous bone. Especially, the classical assumption inherent to classical elasticity is no more valid under such conditions, which occur in zones of high stress and strain gradients, for instance in the vicinity of cracks or within a bone prosthesis region.

The incorporation of the microstructural scale within the continuum framework involves the relaxation of the local action hypothesis, and the introduction of a spatial interaction and typical length scales to account for the influence of neighboring points in the formulation of constitutive equations. Such enhanced continuum formulations aim at incorporating information related to the microstructure, and they follow three possible main strategies, namely integral nonlocal models, higher-order gradient models and micropolar (otherwise coined Cosserat) theories. All three models share the fact that a characteristic length inherent

to the material is introduced in the field equations. Second order models for bones have emerged recently in the literature (Gitman et al. 2010), in which the authors evidence the stress reduction close to the crack line in contrast to classical continuum elasticity which shows a stress peak.

In the class of micropolar models developed in this work, independent rotational degrees of freedom are considered in addition to the translational degrees of freedom (the displacement vector), in the form of a microrotation vector field. This entails that the material can transmit couple stresses in addition to tractions; those couple stresses develop internal work in the variation of microcurvatures, defined as the spatial gradients of the microrotation, a second order tensor. From a historical perspective, the Cosserat Brothers, who introduced the concept bearing their name (Cosserat and Cosserat, 1909), developed the theory of non-symmetric elasticity, and further developments emerged in the sixties (Eringen, 1968; Mindlin, 1964; Mindlin and Tiersten, 1962). Based on the generalized continuum theory established by the Cosserat brothers about 100 years ago, Eringen (1966, 1968, 1976, 1999) formulated a general theory of Cosserat continuum coined the micropolar theory, adequate for materials possessing microstructures, such as bones, but also for granular composites, amorphous metals/ceramics, polymers. This theory can well explain the discrepancies between experiments and the classical theory of elasticity in cases when the effects of material microstructures are known to contribute significantly to the body's overall deformation, for example, in materials with a granular microstructure such as human bones (Lakes et al., 1990; Lakes, 1995; Shmoylova et al., 2007). A special case of Cosserat theory is the *couple-stress* theory, in which the microrotation and macrorotation coincide, Koiter (1964). Micropolar theory assumes that the interaction between continuum particles through a surface element dA occurs not only through a force vector ($F_i dA$) but also through a moment vector ($M_i dA$). This establishes the “force-stress” tensor expressed as force per unit area, σ_{ij} , and the “couple-stress” tensor expressed as moment per unit area, m_{ij} , from the Euler-Cauchy equilibrium principle. In terms of kinematics, material particles have additional rotational degrees of freedom ϕ_i allowing to better capture the behavior of heterogeneous materials like bone, which have microstructural dimensions comparable to the size of specimen.

The existence of couple stress was first evidenced by Yang and Lakes (1981), who measured the effect of the size of a bone specimen on the apparent stiffness of cortical bone in quasi-static torsion; they further obtained the characteristic length scales for torsion and bending for cortical bone in the context of couple stress theory. Bone trabeculae are modelled as isotropic micropolar materials in Lakes (1993). Lakes and co-workers conducted a series of experiments on bone and other cellular materials, in which they observed a stiffening effect in such materials in bending and in torsion (Park and Lakes 1987) and a tougher notched bone Lakes et al. (1990) than expected from classical Cauchy-type elasticity. Those last authors found that Cosserat elasticity provides better predictions of the response of bone than classical elasticity theory. Tanaka and Adachi (1999) represented the trabeculae as beam elements in a lattice structure in which the lattice elements are rigidly interconnected to each other, for the

purpose of bone remodeling. The microstructure was then embedded in the continuum in the context of the couple stress theory. The issue of application of higher-order continuum theories to mechanical analysis of bone (both cortical and cancellous) was addressed by [Fatemi et al. \(2002\)](#), who analyzed a simplified two-dimensional bone-prosthesis configuration using a micropolar-based FE formulation. The stress and strain intensities they calculated at the bone-prosthesis interface are different from those predicted by classical elasticity. In addition, [Fatemi et al. \(2003\)](#) identified the micropolar elastic constants of cancellous bone in the context of micromechanical analyses. In this approach, it is assumed that at the microscopic level the bone tissue is an isotropic, Cauchy-type elastic material, whereas cancellous bone behaves as a homogeneous, anisotropic micropolar-type continuum at the macroscopic level. The effective elastic constants for the micropolar continuum were determined from the response of a bone specimen, whose microstructure was obtained from micro-CT scans. This, in addition to experimental evidence reported by, e.g., [Lakes \(1993\)](#), makes Cosserat theory a suitable candidate for the continuum modeling of cellular materials, because it contains rotations as degrees of freedom. Moreover ([Lakes et al. 1990](#); [Shmoylova et al. 2007](#)) found that Cosserat elasticity gave better predictions of the response of bone and cellular materials than classical elasticity theory.

The evaluation of the effective mechanical properties of trabecular bone and their relationships to microstructural parameters is a critical issue when analysing stresses and strains in bone tissues and simulating their remodelling. The known limitations of experimental methods make the homogenization of "equivalent" trabecular microstructures an advantageous tool for this task. Many papers reporting results of mechanical or acoustical tests of trabecular bone have been published, e.g. [Ashman et al. \(1986\)](#), [Ashman et al. \(1989\)](#), [Rho et al. \(1995\)](#), [Kopperdahl and Keaveny \(1998\)](#), [Cendre et al. \(1999\)](#), and recent contributions [Hellmich et al. \(2004\)](#) and [Diamant et al. \(2007\)](#). They however are limited most of the time to the identification of a few mechanical properties; especially, anisotropic properties are difficult to access, thus pointing towards the need for predictive models of cancellous bone based on its architecture. Moreover, due to the variation of bone architecture (geometry) according to location, such predictive models will exhibit the advantage of their versatility, in the sense they are able to provide quantitative estimates of bone mechanical properties versus the bone architectural and micromechanical parameters.

This chapter focuses on the modeling of the micropolar elastic response of trabecular bone using 2D and 3D geometric models.

4.3 Construction of two-dimensional anisotropic Cosserat bone models

We adopt the viewpoint of trabecular bone as a cellular solid consisting of a quasi periodical lattice of cells having an hexagonal topology, the cell walls being modeled as thick beams. The characteristics of many periodic cellular structures are discussed in detail in the well-known contribution of [Gibson and Ashby \(1997\)](#), wherein the equivalent mechanical properties of honeycomb lattices are derived by analyzing strain and stress states in unit cells

through the application (in most cases) of beam theory. Taking bending as the sole deformation mechanism, [Gibson et al. \(1982\)](#) derived the in-plane elastic constants for regular honeycombs with cell walls of uniform thickness; their normalized results are consequently independent of the honeycomb relative density. Taking bending and stretching as the main deformation mechanisms, [Warren and Kraynik \(1987\)](#) also developed a model to study the in-plane elastic properties of honeycombs. Considering the transverse shear as an additional deformation mechanism, [Silva et al. \(1995\)](#) and [Zhu \(2010\)](#) obtained the closed form in-plane elastic constants of regular honeycombs. Taking bending, stretching and hinging the deformation mechanisms, [Masters and Evans \(1996\)](#) theoretically analyzed the in-plane elastic constants of honeycombs. The normalized in-plane elastic constants of honeycombs generally depend on the honeycomb relative density ([Silva et al., 1995](#); [Zhu et al., 2001](#); [Zhu, 2010](#)), because the axial stretching/compression and transverse shear play an important role in the deformation.

A two-dimensional micropolar continuum model equivalent to the initial lattice is next constructed relying on discrete homogenization, and its mechanical properties are identified versus the microbeams geometry and mechanical behavior.

The adopted beam model includes transverse shear, which is necessary for thick beams. In a local coordinate systems attached to each beam element, the normal (tension) and transverse efforts adopt the expressions in asymptotic expansion forms as

$$N^{b\varepsilon} = E_s \eta \left(\mathbf{e}^b \cdot \left(\varepsilon \Delta U_1^b + \varepsilon^2 \Delta U_2^b \right) \right) = \varepsilon N_1^b + \varepsilon^2 N_2^b \quad (4.1)$$

$$\begin{aligned} T_t^{b\varepsilon} &= \frac{E_s \eta^3}{\left(1 + \frac{E_s \eta^2}{(G_s k_s)}\right)} \left(\mathbf{e}^{b\perp} \cdot \left(\varepsilon \Delta U_1^b + \varepsilon^2 \Delta U_2^b \right) - \varepsilon \frac{L^b}{2} \left(\phi_0^{O_{R(b)}} + \phi_0^{E_{R(b)}} + \varepsilon \left(\phi_1^{O_{R(b)}} + \phi_1^{E_{R(b)}} + \frac{\partial \phi_0}{\partial \lambda^i} \delta^{ib} \right) \right) \right) \\ &= \varepsilon T_{t1}^b + \varepsilon^2 T_{t2}^b \end{aligned} \quad (4.2)$$

and the moments at both extremities of the beam are expressed as:

$$\mathbf{M}^{O(b)\varepsilon} = \varepsilon^2 \mathbf{M}_1^{O(b)} + \varepsilon^3 \mathbf{M}_2^{O(b)}; \quad \mathbf{M}^{E(b)\varepsilon} = \varepsilon^2 \mathbf{M}_1^{E(b)} + \varepsilon^3 \mathbf{M}_2^{E(b)} \quad (4.3)$$

with

$$\begin{aligned} M_1^{O(b)} &= \frac{E_s \eta^3 L^b}{2 \left(1 + \frac{E_s \eta^2}{(G_s k_s)}\right)} \left(-e^{b\perp} \cdot \Delta U_1^b \right) + \frac{E_s \eta^3 (L^b)^2}{12 \left(1 + \frac{E_s \eta^2}{(G_s k_s)}\right)} \left(\left(4 + \frac{E_s \eta^2}{(G_s k_s)} \right) \phi_0^{O_{R(b)}} + \left(2 - \frac{E_s \eta^2}{(G_s k_s)} \right) \phi_0^{E_{R(b)}} \right) \\ M_2^{O(b)} &= \frac{E_s \eta^3 L^b}{2 \left(1 + \frac{E_s \eta^2}{(G_s k_s)}\right)} \left(-e^{b\perp} \cdot \Delta U_2^b \right) + \frac{E_s \eta^3 (L^b)^2}{12 \left(1 + \frac{E_s \eta^2}{(G_s k_s)}\right)} \left(\left(4 + \frac{E_s \eta^2}{(G_s k_s)} \right) \phi_1^{O_{R(b)}} + \left(2 - \frac{E_s \eta^2}{(G_s k_s)} \right) \phi_1^{E_{R(b)}} + \left(2 - \frac{E_s \eta^2}{(G_s k_s)} \right) \frac{\partial \phi_0}{\partial \lambda^i} \delta^{ib} \right) \\ M_1^{E(b)} &= \frac{E_s \eta^3 L^b}{2 \left(1 + \frac{E_s \eta^2}{(G_s k_s)}\right)} \left(-e^{b\perp} \cdot \Delta U_1^b \right) + \frac{E_s \eta^3 (L^b)^2}{12 \left(1 + \frac{E_s \eta^2}{(G_s k_s)}\right)} \left(\left(2 - \frac{E_s \eta^2}{(G_s k_s)} \right) \phi_0^{O_{R(b)}} + \left(4 + \frac{E_s \eta^2}{(G_s k_s)} \right) \phi_0^{E_{R(b)}} \right) \\ M_2^{E(b)} &= \frac{E_s \eta^3 L^b}{2 \left(1 + \frac{E_s \eta^2}{(G_s k_s)}\right)} \left(-e^{b\perp} \cdot \Delta U_2^b \right) + \frac{E_s \eta^3 (L^b)^2}{12 \left(1 + \frac{E_s \eta^2}{(G_s k_s)}\right)} \left(\left(2 - \frac{E_s \eta^2}{(G_s k_s)} \right) \phi_1^{O_{R(b)}} + \left(4 + \frac{E_s \eta^2}{(G_s k_s)} \right) \phi_1^{E_{R(b)}} + \left(4 + \frac{E_s \eta^2}{(G_s k_s)} \right) \frac{\partial \phi_0}{\partial \lambda^i} \delta^{ib} \right) \end{aligned}$$

with the non-dimensional factor $\Phi_y = 12E_s I_z / G_s k_s L^2$ vanishing when transverse shear is neglected, \mathbf{e}^b the unit director for each beam, and $\mathbf{e}^{b\perp}$ the transverse unit vector. The coefficients E_s , G_s are respectively the Young's modulus and shear modulus of the trabecular struts, A , L are respectively, the cross-sectional area and the length of the strut, I_z is the second moment of area of the strut cross-section, and k_s is the shear correction factor.

The kinematic and static variables for any beam in the lattice are represented in the local coordinate system associated to the Timoshenko beam element in Figure 4.3.

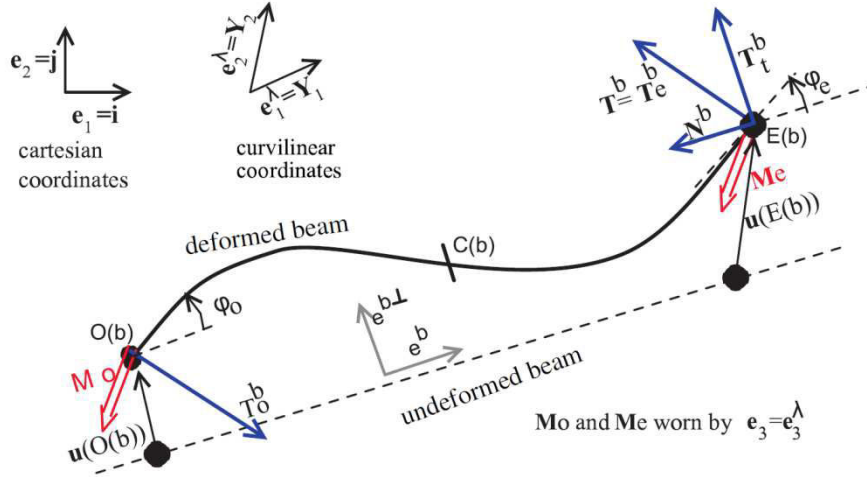


Figure 4.3: Kinematic and static parameters of a beam element.

The constitutive behavior of the equivalent anisotropic micropolar continuum is obtained in the present 2D context in matrix format as

$$\begin{Bmatrix} \sigma_x \\ \sigma_y \\ \sigma_{xy} \\ \sigma_{yx} \\ m_{xz} \\ m_{yz} \end{Bmatrix} = \begin{bmatrix} [\mathbf{E}] & [\mathbf{B}] \\ [\mathbf{C}] & [\mathbf{K}] \end{bmatrix} \begin{Bmatrix} \epsilon_x \\ \epsilon_y \\ \epsilon_{xy} \\ \epsilon_{yx} \\ \chi_{xz} \\ \chi_{yz} \end{Bmatrix} \quad (4.4)$$

This constitutive law can further be simplified basing on symmetry properties of the studied lattices: it has indeed been shown that for centro-symmetrical lattices, the pseudo-tensors $[\mathbf{B}]$ and $[\mathbf{C}]$ vanish.

The previous form of the continuum constitutive law can presently be identified from the expressions of the homogenized stress \mathbf{S}_1^i and couple stress $\boldsymbol{\mu}_2^i$ vectors as

$$\boldsymbol{\sigma} = \underbrace{\frac{1}{g} \mathbf{S}_1^i \otimes \frac{\partial \mathbf{R}}{\partial \lambda^i}}_{[\mathbf{E}]\{\epsilon\}}, \quad \mathbf{m} = \underbrace{\frac{1}{g} \epsilon^2 \boldsymbol{\mu}_2^i \otimes \frac{\partial \mathbf{R}}{\partial \lambda^i}}_{[\mathbf{K}]\{\chi\}} \quad (4.5)$$

The homogenized stress and couple stress vectors are respectively

$$S_1^i = \sum_{b \in B_R} \left(E_s \eta (\mathbf{e}^b \cdot \Delta \mathbf{U}_1^b) \mathbf{e}^b + \left(\frac{E_s \eta^3}{1 + \frac{E_s \eta^2}{(G_s k_s)}} \left(\mathbf{e}^{\perp b} \cdot \Delta \mathbf{U}_1^b - \frac{L^b}{2} (\phi_0^{O_{R(b)}} + \phi_0^{E_{R(b)}}) \right) \right) \mathbf{e}^{b \perp} \right) \delta^{ib} = \sum_{b \in B_R} (N_1^b \mathbf{e}^b + T_{11}^b \mathbf{e}^{b \perp}) \delta^{ib} \quad (4.6)$$

$$\mu_2^i = \sum_{b \in B_R} \left(E_s \eta^3 \frac{(L^b)^2}{12} \left(\phi_1^{E_{R(b)}} - \phi_1^{O_{R(b)}} + \frac{\partial \phi_0}{\partial \lambda^i} \delta^{ib} \right) \right) \delta^{ib} = \sum_{b \in B_R} \left(\frac{1}{2} (M_2^{E(b)} - M_2^{O(b)}) \right) \delta^{ib}$$

with N_1^b , T_{11}^b , and, M_2^n , respectively, the first order normal and transverse effort and the second order moment. Those expressions still involve the unknown displacements \mathbf{u}_1^n , \mathbf{u}_2^n and rotations ϕ_0^n , ϕ_1^n (this defines the so called localization problem over the representative cell), which are determined for all nodes and as a last step by solving the equilibrium equations in translation and rotation.

4.3.1 Effective micropolar properties of bone

The general anisotropic hexagonal unit cell of two-dimensional honeycomb under consideration is pictured in [Figure 4.4](#); it consists of three beams, a vertical beam of length h and two inclined beams of length l . The vertical beams have elastic and shear moduli E_{sI} and G_{sI} , respectively, while the two inclined beams have elastic and shear moduli E_s and G_s , respectively. The dimensionless parameters θ and $\alpha=h/l$ are descriptors of the cell shape, as well as the aspect ratio of the cell walls $\eta=t/l$, a parameter determining the relative density or area fraction of the solid phase. The lattice is called re-entrant when the angle θ between the two inclined beams relative to the horizontal is negative (see [Figure 4.5b](#)). When this angle takes the value 30° , the classical hexagonal lattice is obtained. When $\theta < 0$, $\left(\theta \in \left[-\frac{\pi}{2}, \frac{\pi}{2} \right] \right)$, an auxetic lattice ([Gonella and Ruzzene, 2008](#); [Dos Reis and Ganghoffer, 2012](#)) having a negative Poisson's ratio is obtained. Regular unit cells correspond to the specific geometrical parameters $\alpha=1$ and $\theta=30^\circ$ and anisotropic unit cells correspond to all other values.

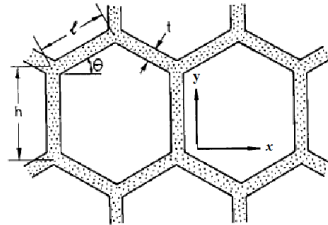


Figure 4.4: General anisotropic unit cell for two dimensional honeycomb models. The geometrical descriptors are the cell angle (θ), the vertical cell length (h), the inclined cell length (l), and the wall thickness (t).

The lengths of the periodicity vectors (norm of \mathbf{Y}_1 and \mathbf{Y}_2 in the Cartesian basis) are $L_1 = L_2 = \sqrt{(l \cos \theta)^2 + (h + l \sin \theta)^2}$; the other features of the lattice are collected in the connectivity [Table 4.1](#).

Table 4.1: Connectivity array for the hexagonal lattice

Beam	1	2	3
O(b)	2	1	1
E(b)	1	2	2
δ_1	0	1	0
δ_2	0	0	1

The representative unit cell is easily identified for the hexagonal lattice ([Figure 4.5](#)).

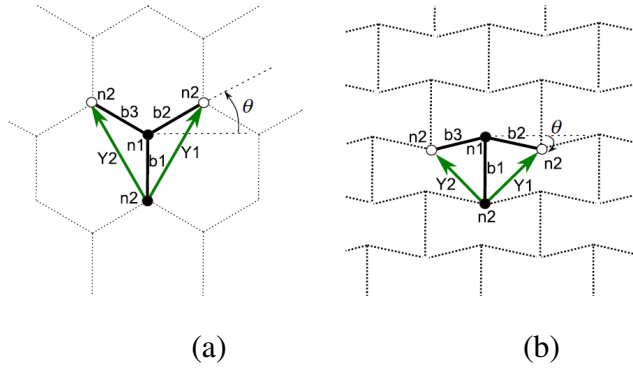


Figure 4.5: Representative unit cell of the investigated lattices: (a) hexagonal lattice, (b) re-entrant lattice ($\theta < 0$).

The homogenization scheme provides the effective mechanical properties (classical and micropolar moduli) versus the geometrical and micromechanical parameters of the considered microstructure. After calculations, we extract the effective homogenized moduli of the hexagonal lattice from the equivalent stiffness matrix, expressed versus the dimensionless parameters η , α , θ , κ_s , and κ_{s1} and the elastic and shear moduli of the solid cell walls E_s , E_{s1} , G_{s1} , and G_s as follows:

$$\begin{aligned}
 E_x^* &= -\frac{E_s \eta^3 C_t}{\left(-1 + C_t^2 - C_t^2 \eta^2 + \frac{C_t^2 E_s \eta^2}{G_s k_s} - \frac{E_s \eta^2}{G_s k_s}\right) (S_t + \alpha)}, \quad E_y^* = \frac{(S_t + \alpha) E_s E_{s1} \eta^3}{\left(C_t^2 E_{s1} + \frac{C_t^2 E_s E_{s1} \eta^2}{G_s k_s} + E_{s1} \eta^2 + 2 E_s \eta^2 \alpha - C_t^2 E_{s1} \eta^2\right) C_t}, \\
 G_{xy}^* &= \frac{(S_t + \alpha) E_s E_{s1} \eta^3 C_t}{\left(\frac{E_s \eta^2 \alpha^2 C_t^2 E_{s1}}{G_s k_s} + \alpha^2 E_{s1} C_t^2 + \frac{2 E_s E_{s1} \eta^2 \alpha C_t^2}{G_{s1} k_{s1}} + 2 \alpha^3 C_t^2 E_s + 2 E_{s1} \eta^2 \alpha S_t + E_{s1} \eta^2 + \alpha^2 E_{s1} \eta^2 - E_{s1} \eta^2 \alpha^2 C_t^2\right)}, \\
 \nu_{xy}^* &= -\frac{\left(\frac{E_s \eta^2}{G_s k_s} - \eta^2 + 1\right) S_t C_t^2}{\left(\frac{C_t^2 E_s \eta^2}{G_s k_s} - C_t^2 \eta^2 + C_t^2 - \frac{E_s \eta^2}{G_s k_s} - 1\right) (S_t + \alpha)}, \quad \nu_{yx}^* = \frac{\left(\frac{E_s \eta^2}{G_s k_s} - \eta^2 + 1\right) S_t (S_t + \alpha) E_{s1}}{\left(\frac{C_t^2 E_s E_{s1} \eta^2}{G_s k_s} + E_{s1} C_t^2 + E_{s1} \eta^2 + 2 E_s \eta^2 \alpha - C_t^2 E_{s1} \eta^2\right)}, \\
 K_{11} &= \frac{1}{12} \frac{E_s \eta^3 l^2 C_t}{\alpha + S_t}, \quad K_{22} = \frac{1}{12} \frac{l^2 E_s \eta^3 E_{s1} (\alpha + S_t)}{(2 E_s \alpha + E_{s1}) C_t}.
 \end{aligned} \tag{4.7}$$

The characteristic length and coupling coefficient receive the following expressions

$$l_b = \frac{1}{12} \sqrt{3} \sqrt{\frac{l^2 \left(\frac{E_s \eta^2 \alpha^2 C_t^2 E_{s1}}{G_s k_s} + E_{s1} \eta^2 + \frac{2\alpha E_s C_t^2 E_{s1} \eta^2}{G_{s1} k_{s1}} + 2\alpha^3 E_s C_t^2 + 2E_{s1} \eta^2 S_t \alpha + \alpha^2 \eta^2 E_{s1} - C_t^2 \alpha^2 \eta^2 E_{s1} + C_t^2 \alpha^2 E_{s1} \right)}{E_{s1} (-2S_t \alpha - \alpha^2 - 1 + C_t^2)}}}$$

$$N_{coupl}^2 = \frac{\left(\frac{E_s \eta^2 \alpha^2 C_t^2 E_{s1}}{G_s k_s} + E_{s1} C_t^2 \alpha^2 + 2\alpha^3 E_s C_t^2 + \frac{2\alpha E_s C_t^2 E_{s1} \eta^2}{G_{s1} k_{s1}} + 2E_{s1} \eta^2 S_t \alpha + \eta^2 E_{s1} + \alpha^2 \eta^2 E_{s1} - C_t^2 \alpha^2 \eta^2 E_{s1} \right)}{\left(4S_t \alpha E_{s1} + 2E_{s1} \alpha^2 + \frac{4S_t \alpha \eta^2 E_s E_{s1}}{G_s k_s} + E_{s1} \alpha^2 \eta^2 + \frac{2E_s E_{s1} \alpha^2 \eta^2}{G_s k_s} - E_{s1} \eta^2 \alpha^2 C_t^2 - 2C_t^2 E_{s1} - \frac{2C_t^2 E_s E_{s1} \eta^2}{G_s k_s} + 2E_{s1} \eta^2 \alpha S_t + \frac{E_s \eta^2 \alpha^2 C_t^2 E_{s1}}{G_s k_s} + 2E_{s1} + E_{s1} C_t^2 \alpha^2 + \frac{2E_s \eta^2 E_{s1}}{G_s k_s} + \frac{2C_t^2 E_s E_{s1} \eta^2 \alpha}{G_{s1} k_{s1}} + 2\alpha^3 E_s C_t^2 + E_{s1} \eta^2 \right)}$$
(4.8)

We next compare the effective properties of irregular hexagonal lattices with the values determined by [Gibson and Ashby \(1997\)](#) for a periodic array of hexagonal cells accounting for bending, axial and shear deformations of the cell walls. The homogenized properties obtained with an Euler Bernoulli beam model are plotted against, cell angle θ for the purpose of assessing the impact of transverse shear (see [Figures 4.6](#) and [4.7](#)). In order to perform this comparison, it is assumed that properties of both vertical and inclined members are the same ($E_s = E_{s1}$, $G_s = G_{s1}$, and $k_s = k_{s1}$).

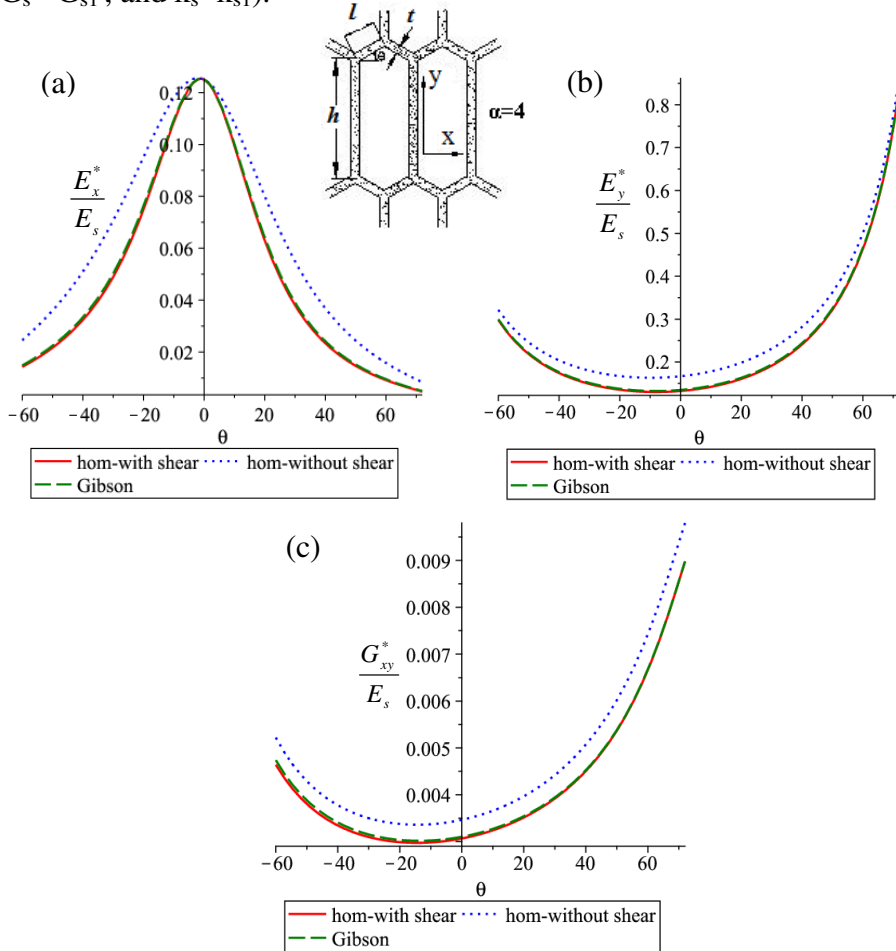


Figure 4.6: Comparison between the homogenized elastic and shear moduli with and without considering shear effects and Gibson model for the hexagonal lattice. $\eta=1/2$, $\alpha=4$.

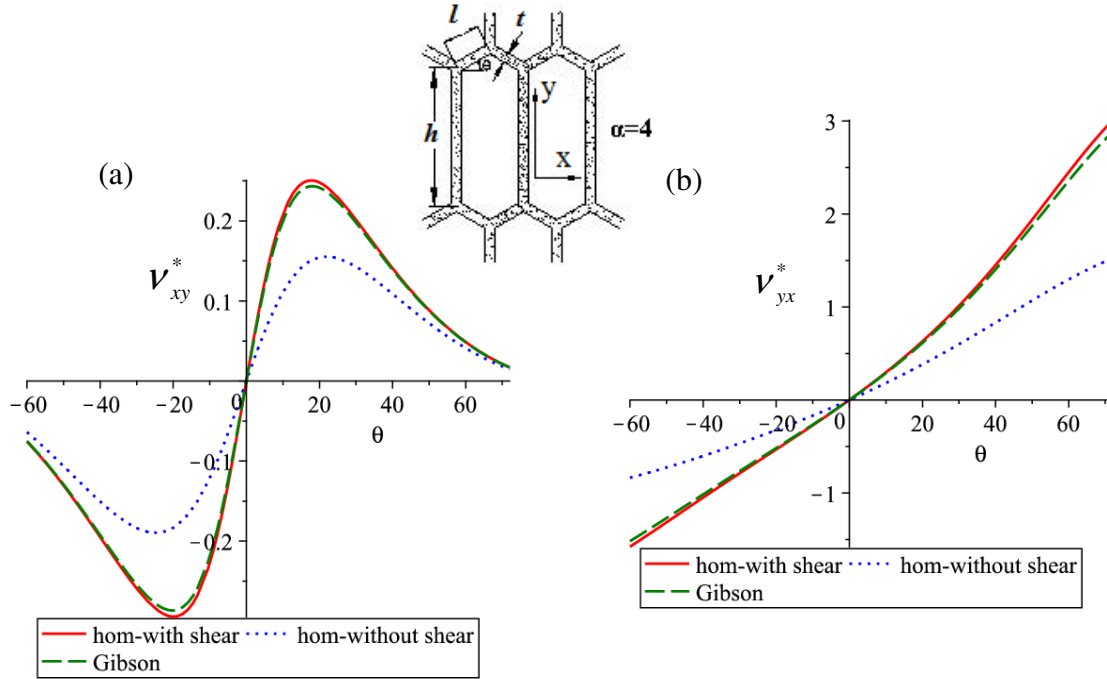


Figure 4.7: Comparison between the homogenized Poisson's ratios ν_{xy}^* and ν_{yx}^* with the values obtained by Gibson for the hexagonal lattice. $\eta=1/2$, $\alpha=4$.

All three moduli show quite similar evolutions versus the cell angle (Figures 4.6), whereas the absence of transverse shear tends to overestimate those moduli, as expected.

Both Poisson's ratios are antisymmetric function of θ (see Figures 4.7), and become negative for re-entrant configurations. The originality of the present approach is the derivation of an anisotropic micropolar model for cellular solids from homogenization of the underlying lattice. Contrary to this, many phenomenologically based generalized continuum models for bone postulate such a behavior. The homogenized properties are close to Gibson and Ashby values as pictured on previous figures with relative difference reaches a maximum of about 4% for the Young's modulus E_x^* and Poisson's ratios ν_{xy}^* and ν_{yx}^* , and about 2% for E_y^* and G_{xy}^* .

The effect of cell geometry on the effective properties is determined by considering a much lower value of $\alpha = 1/2$, leading to a concave evolution of the effective shear modulus versus θ . In this situation, we observe a noticeable difference between the homogenized shear modulus and Gibson model and this difference decreases when increasing the cell angle (Figure 4.8).

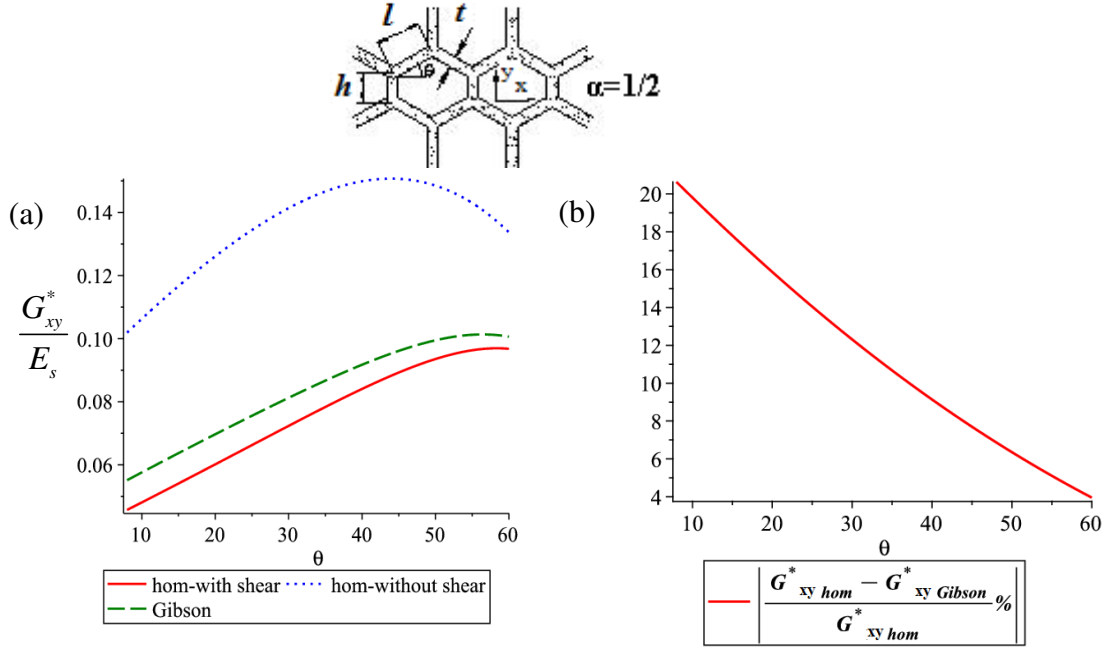


Figure 4.8: (a) Comparison between the homogenized shear modulus G_{xy}^* / E_s (with and without shear effects) with the values obtained by Gibson for the hexagonal lattice. $\eta=1/2$, $\alpha=1/2$. (b) Relative difference (in percent) between the effective modulus G_{xy}^* obtained by homogenization and Gibson model.

To demonstrate the effects of microstructural anisotropy α on the anisotropy of the elastic constants, the relative elastic and shear moduli and effective Poisson's ratios are evaluated at different values of α ranging from 0.25 to 4 (extreme value of anisotropy); they are illustrated in Figures 4.9 and 4.10. The computation is performed by setting slenderness parameter $\eta=0.5$ and $\theta = 30^\circ$. It is observed that the Young's and shear moduli and Poisson's ratios depend strongly on the amount of microstructural anisotropy. The relative Young's and shear moduli E_x^* / E_s and G_{xy}^* / E_s , respectively decreases (Figures 4.9a and 4.9c) whereas the relative modulus E_y^* / E_s increases (Figure 4.9b) when increasing the microstructural anisotropy α . Furthermore, this discrepancy increases when decreasing the cell aspect ratio α . It is observed a noticeable difference between the homogenized shear modulus and Gibson model (see Figure 4.9c), which increases when decreasing the cell aspect ratio α , reaching a maximum of about 30% for $\alpha=0.25$.

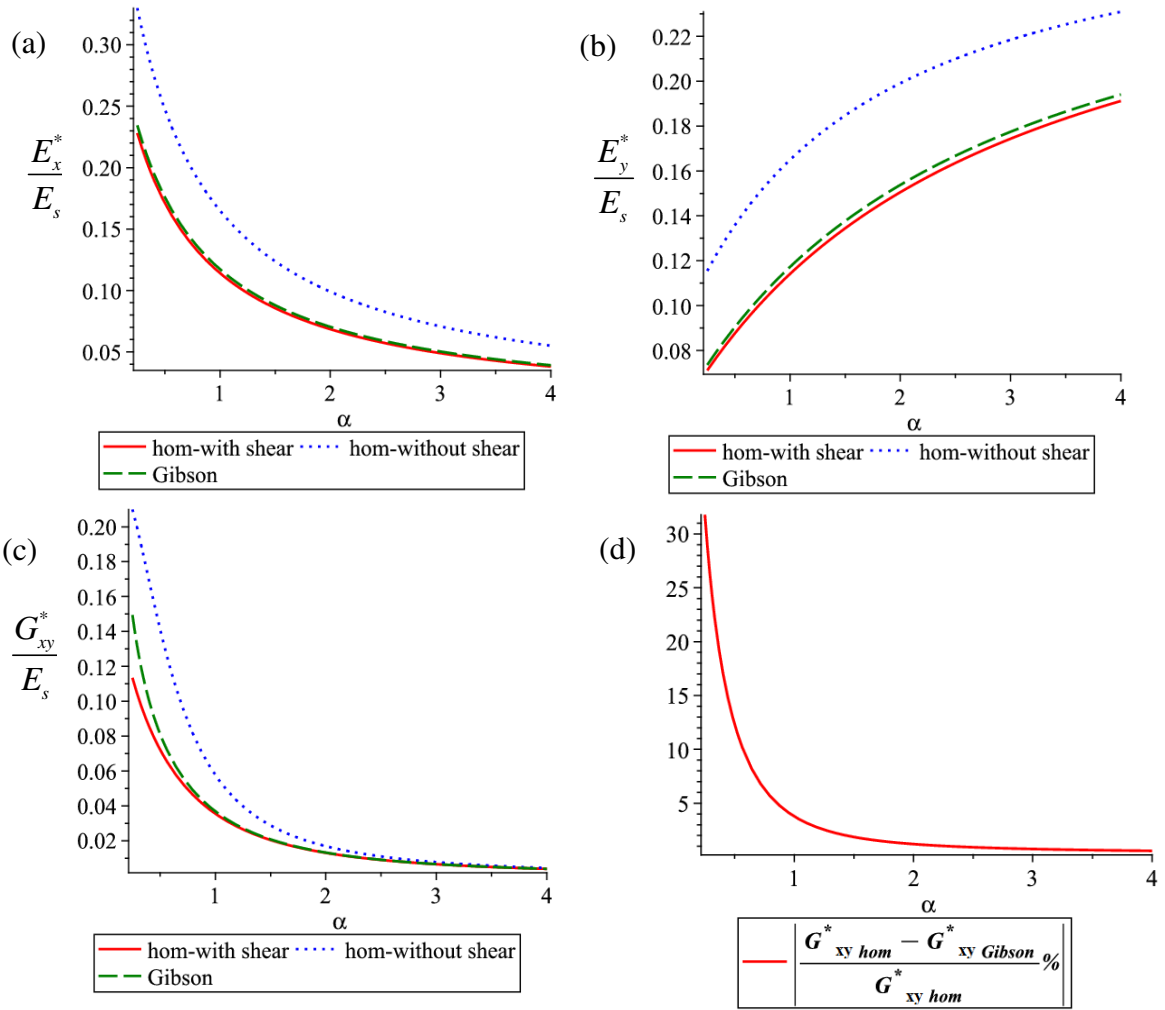


Figure 4.9: (a) and (b) Evolution of the relative tensile moduli versus the geometrical parameter α . (c) Relative shear modulus. (d) Relative difference between the homogenized shear modulus and Gibson model. $\eta=1/2$, $\theta=30$.

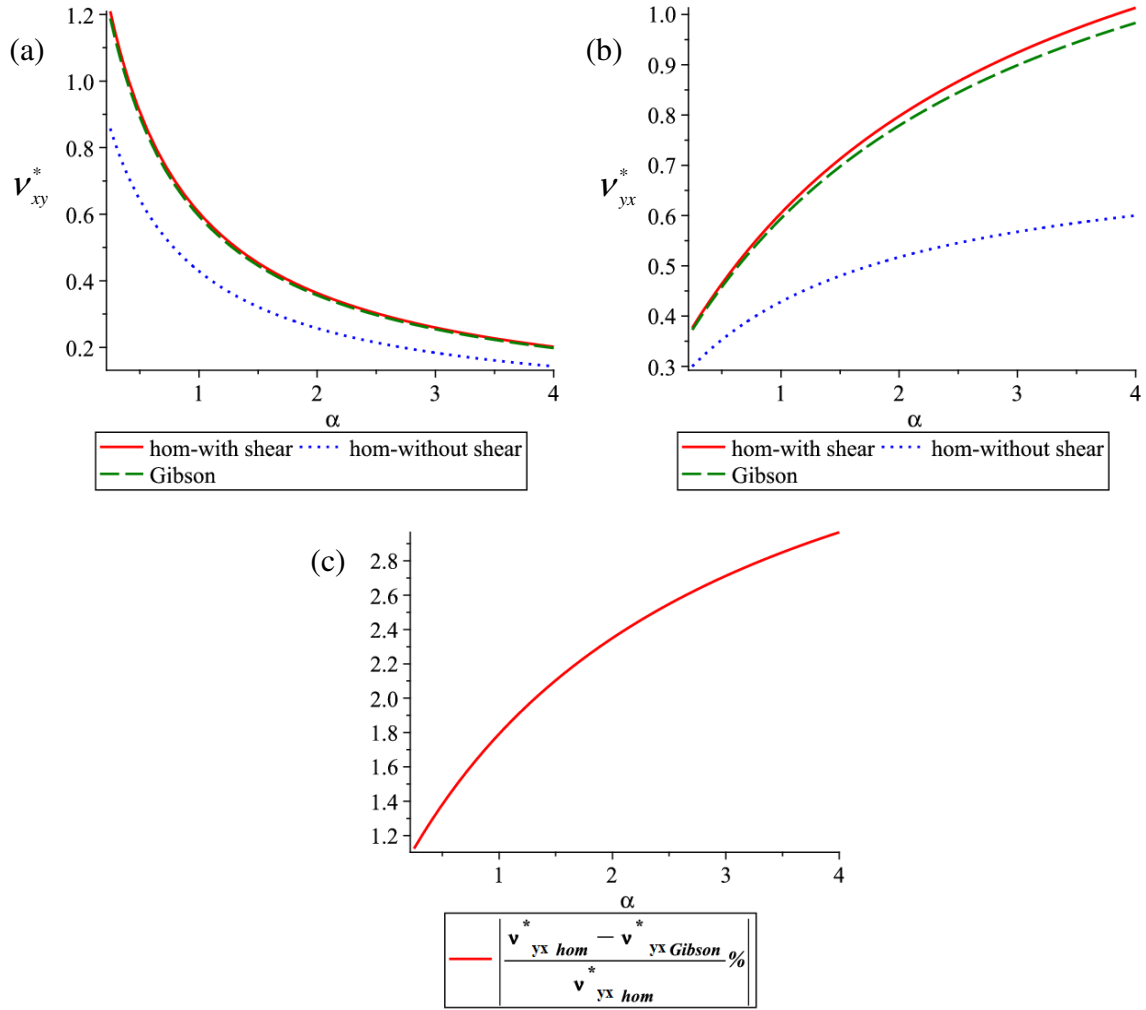


Figure 4.10: (a) and (b) Equivalent Poisson's ratios versus the geometrical parameter α . (c) Relative difference between homogenized Poisson's ratio v_{yx}^* and Gibson model. $\eta=1/2$, $\theta=30$.

4.3.2 Numerical determination of the effective rigidities

In a 2D plane stress situation, the stress tensor has four independent components σ_x , σ_y , σ_{xy} , σ_{yx} and the couple stress tensor (or moment per unit area) has two components m_{xz} , m_{yz} . The deformation and micro-curvature components express versus the displacement gradients and micro-rotations as

$$\begin{aligned} \epsilon_x &= \partial u / \partial x, \quad \epsilon_y = \partial v / \partial y, \quad \epsilon_{xy} = \partial v / \partial x - \phi, \quad \epsilon_{yx} = \partial u / \partial y + \phi \\ \chi_{xz} &= \partial \phi / \partial x, \quad \chi_{yz} = \partial \phi / \partial y \end{aligned} \quad (4.9)$$

In the Cosserat theory, the rotation ϕ is an independent field, whereas in the couple-stress theory is related to displacement gradients as in classical elasticity (equal to the local

rigid rotation) $\phi = (\partial v / \partial x - \partial u / \partial y) / 2$. As a result, in the couple-stress theory, the strain tensor ϵ_{ij} is symmetrical with components defined as $\epsilon_{xy} = \epsilon_{yx} = (\partial v / \partial x + \partial u / \partial y) / 2$.

The equilibrium in translation and rotation, ignoring body forces and body moments, writes as the set of equations

$$\begin{aligned} \partial \sigma_x / \partial x + \partial \sigma_{yx} / \partial y &= 0, \quad \partial \sigma_{xy} / \partial x + \partial \sigma_y / \partial y = 0, \\ \partial m_{xz} / \partial x + \partial m_{yz} / \partial y + \sigma_{xy} - \sigma_{yx} &= 0. \end{aligned} \quad (4.10)$$

The last equation (4.10), implies that the shear stress σ_{xy} differs from σ_{yx} ; Mindlin (1963) suggested then resolving σ_{xy} and σ_{yx} into a symmetric part σ_S and an anti-symmetric part σ_A .

$$\sigma_S = (\sigma_{xy} + \sigma_{yx}) / 2, \quad \sigma_A = (\sigma_{xy} - \sigma_{yx}) / 2. \quad (4.11)$$

The symmetric part of the shear stress produces the usual shear strain ϵ_{xy} , while the anti-symmetric part tends to produce a local rigid rotation. Thus, the constitutive equation can be expressed in the following uncoupled form (for a centrally symmetric unit cell structure) as

$$\begin{Bmatrix} \sigma_x \\ \sigma_y \\ \sigma_S \\ m_{xz} \\ m_{yz} \end{Bmatrix} = \begin{bmatrix} \mathbf{E} & \mathbf{0} \\ \mathbf{0} & \mathbf{K} \end{bmatrix} \begin{Bmatrix} \epsilon_x \\ \epsilon_y \\ \epsilon_{xy} \\ \chi_{xz} \\ \chi_{yz} \end{Bmatrix} \quad (4.12)$$

with

$$\mathbf{E} = \begin{bmatrix} E_{11} & E_{12} & 0 \\ E_{12} & E_{22} & 0 \\ 0 & 0 & E_{66} \end{bmatrix}, \quad \mathbf{K} = \begin{bmatrix} K_{11} & 0 \\ 0 & K_{22} \end{bmatrix}. \quad (4.13)$$

Matrix \mathbf{E} contains the classical moduli, while matrix \mathbf{K} contains the micropolar moduli relating the two couple stress components to the corresponding curvatures.

The discrete homogenization method provides the effective homogenized moduli which are computed from the effective compliance matrix (the inverse of previous stiffness matrix). This includes Young's moduli E_x^* and E_y^* , Poisson's ratios ν_{xy}^*, ν_{yx}^* , shear modulus G_{xy}^* , and micropolar bending moduli K_{11}, K_{22} .

The numerical homogenization technique consists in determining the overall effective mechanical properties (couple-stress moduli and characteristic lengths) over a representative unit cell of trabecular bone, relying on a finite element discretization of the unit cell geometry. Each cell wall is modeled with a three-node beam element (element type B22 in ABAQUS), endowed with bending, stretching and shearing deformation mechanisms. An earlier study by Silva et al. (1995) showed that using such a beam element to model each cell wall is sufficient for convergence.

We presently consider the honeycomb-like structural model of a trabecular bone specimen made of a 2D array of hexagonal cells and we model the trabecular architecture as a two-dimensional lattice (Figure 4.11) with a unit cell geometry of geometrical parameters given from (Ford and Gibson, 1998) as: $\alpha = h/l = 0.5$; $\eta = t/l = 0.25$; $l = 1 \text{ mm}$; $\theta = 60^\circ$ (Figure 4.11a). The bulk mechanical properties of the unit cells wall representative of the behavior of human femur (Gibson and Ashby, 1997) are taken as $E_s = 12000 \text{ MPa}$; $\nu_s = 0.3$.

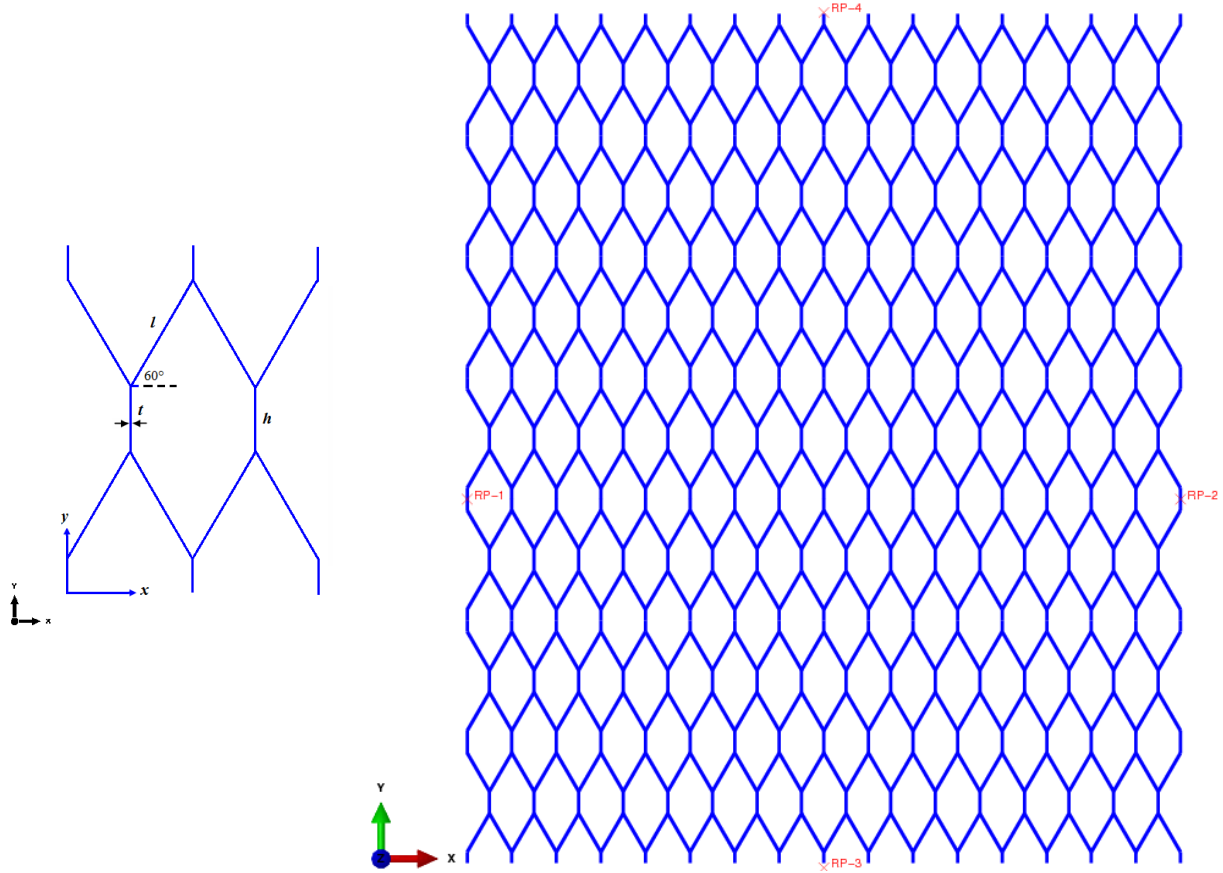


Figure 4.11: (a) Geometrical model of an elementary cell of trabecular bone. (b) Hexagonal honeycomb model representing the trabecular bone lattice.

In order to evaluate the effective Young's moduli E_x^* and E_y^* , Poisson's ratios ν_{xy}^* and ν_{yx}^* , and shear modulus G_{xy}^* , we conduct three finite element simulations over the whole lattice (two tensile tests and one for shear). The uniaxial tensile in the x and y -directions and shear are computed using displacement boundary conditions. In the case of the uniaxial tensile tests, the nodes forming an edge are displaced by a specified amount while the nodes on the opposite edge are prevented from translating in the direction of displacement. The node at the bottom left is also constrained from translating in y -direction when applying tension in x -direction and from translating in x -direction in the case of applying tension in y -direction. The stress-strain curves are then constructed from the reaction forces and displacements captured using the reference points in the displacement directions. The reference points do not belong to the main geometry of the lattice, and they are for adjusting movements on the lattice

surfaces. The effective tensile modulus in x-direction is then estimated from the FE simulation as $E_x^* = \frac{\sigma_x}{\epsilon_x} = 74.4 \text{ MPa}$ and the Poisson's coefficient is computed as

$\nu_{xy}^* = -\frac{\epsilon_y}{\epsilon_x} = 0.2$. The effective tensile modulus in y-direction is also estimated from the FE simulation as $E_y^* = \frac{\sigma_y}{\epsilon_y} = 1247 \text{ MPa}$ and the Poisson's coefficient as $\nu_{yx}^* = -\frac{\epsilon_x}{\epsilon_y} = 3.21$. The

finite element simulation results under uniaxial tension in x and y are respectively presented in Figures 4.12 and 4.13.

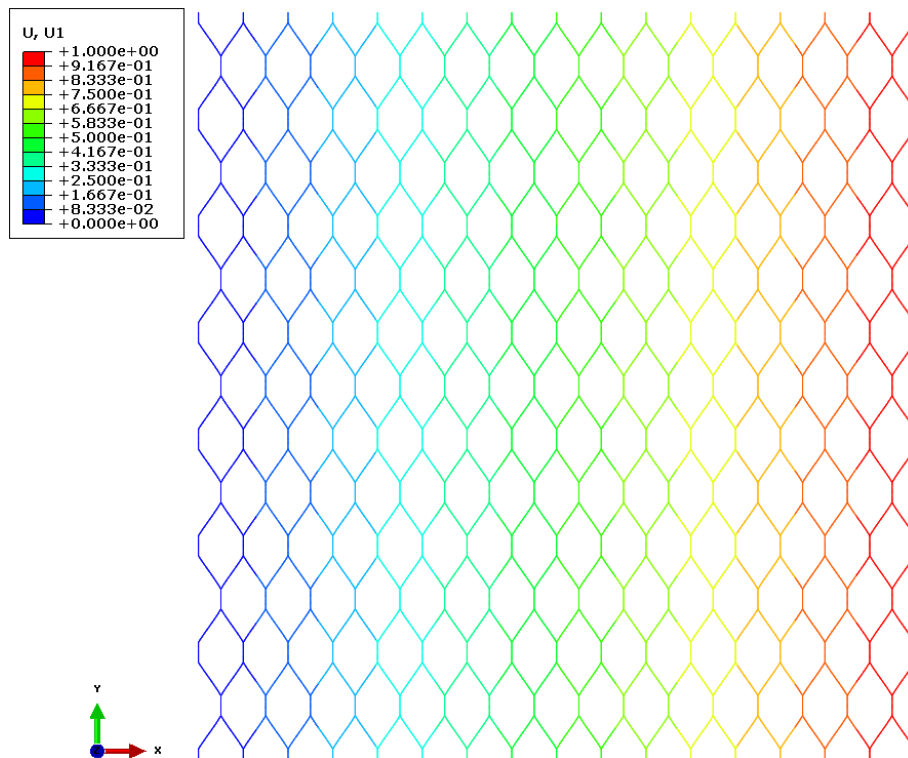


Figure 4.12: Finite element simulation of the hexagonal lattice under tension in x. U1 variable deformation along the x-axis.

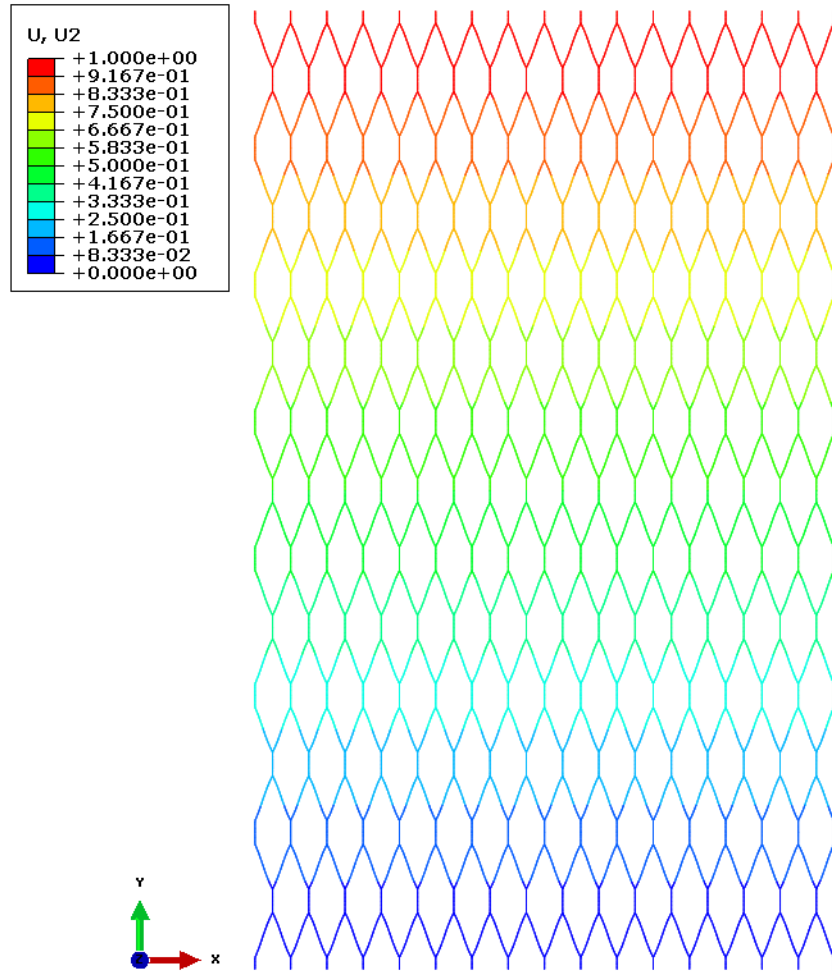


Figure 4.13: Finite element simulation of the hexagonal lattice under tension in y. U2 variable deformation along the y-axis.

A FE simulation for simple shear on trabecular lattice is needed to be performed to construct the shear stress–strain curve, from which the shear modulus is obtained. To perform such simulation, we impose a displacement field on the top surface of the lattice along the x direction, while the bottom surface is constrained in the same direction. Both the left and right surfaces are also prevented from translating in the direction perpendicular to x. Subsequently, we capture the x-component of the resultant reaction force produced on the top surface caused by the applied displacement in the x direction. The shear strain is computed by dividing the displacement on the top surface on the length of the trabecular lattice along the y direction. The shear stress–strain curve is then constructed from the reaction force and displacement and the effective shear modulus is calculated as $G_{xy}^* = \frac{\sigma_{xy}}{\epsilon_{xy}} = 408.5 \text{ MPa}$. The iso-displacements and Von Mises stresses due to simple shear test are shown respectively, in [Figures 4.14](#) and [4.15](#).

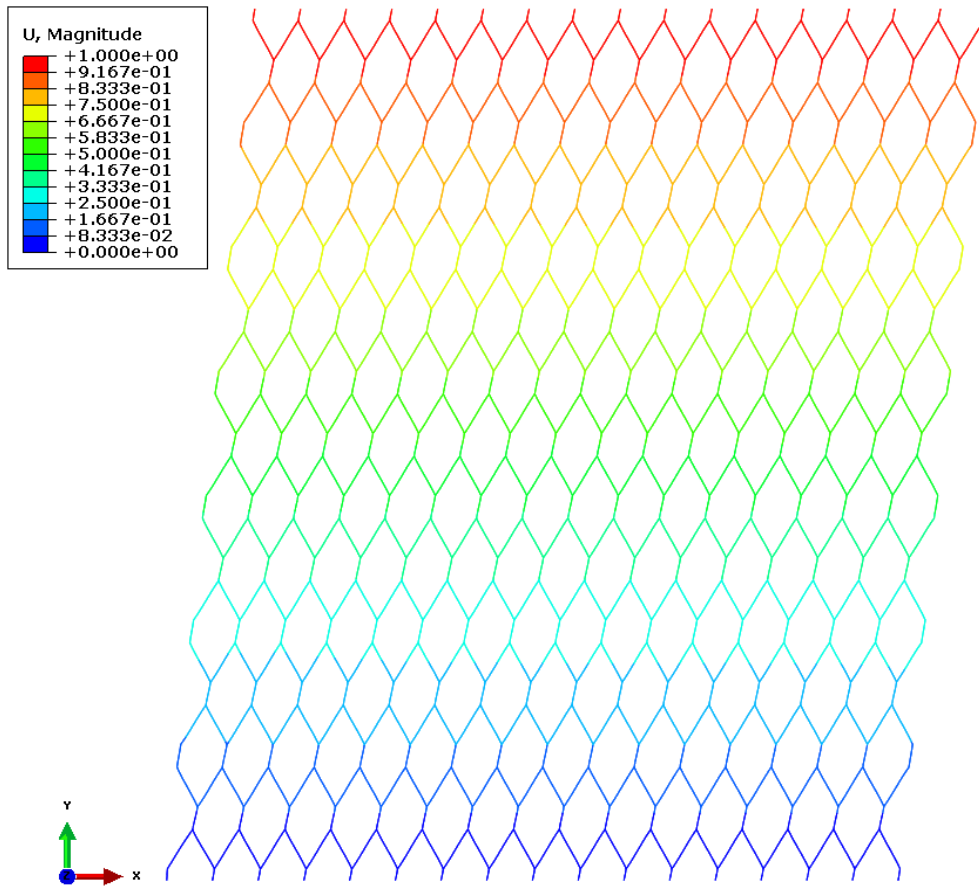


Figure 4.14: Iso-displacement of the hexagonal lattice under shear test.

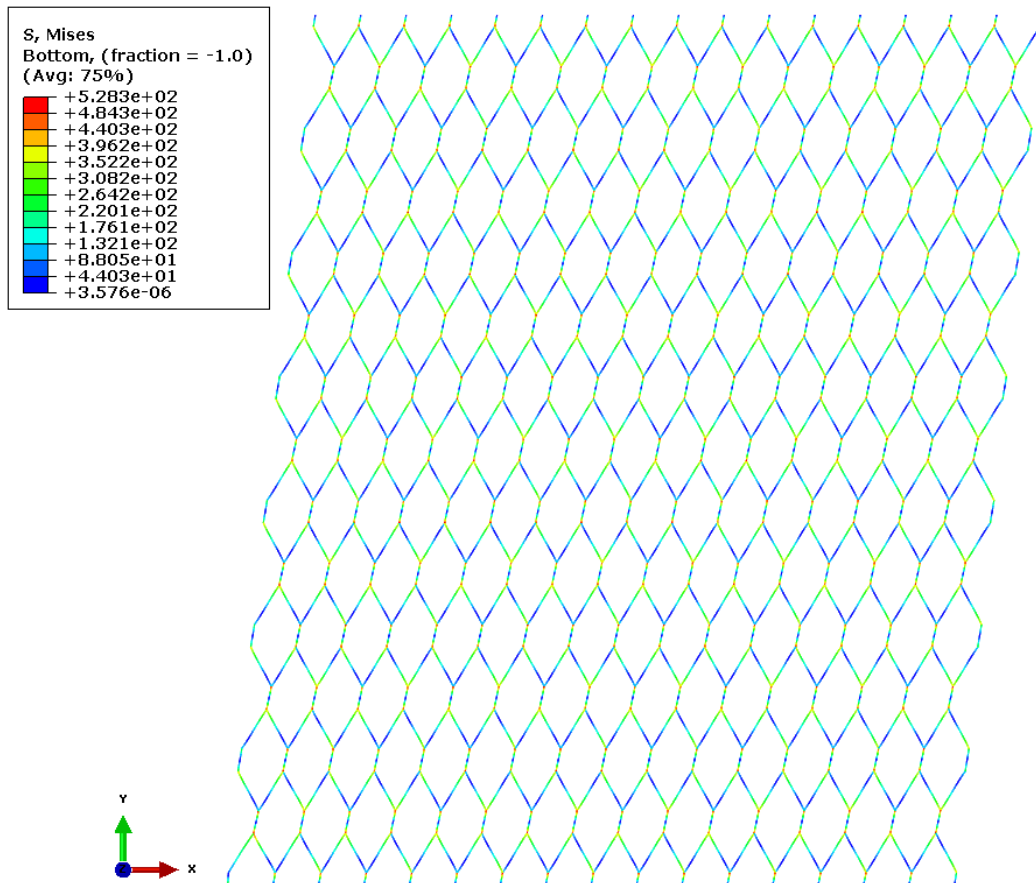


Figure 4.15: Von Mises stress distribution of the hexagonal lattice under shear test.

The values of effective Young's moduli, Poisson's coefficients, and shear modulus computed from FE simulations performed over the whole trabecular lattice are summarized in [Table 4.2](#), showing a very good agreement with those calculated by discrete homogenization. The discrepancies between the results obtained by homogenization and FE simulation is less than 1%, hence one can consider that the predicted homogenized moduli are quite accurate. We seek now to evaluate the components of the bending stiffness matrix \mathbf{K} , thus two separated bending tests shall be performed to identify the micropolar constants K_{11} and K_{22} .

We employ the following equilibrium equations of a micropolar elastic beam of anisotropic material subjected to a uniform bending moment M to define the micropolar bending stiffnesses K_{11} and K_{22} as

$$\underbrace{\left(E_x^* I_z^* + K_{11} H\right)}_{K_{xz}^m} \frac{\partial \phi_z}{\partial x} = -M \quad ; \quad \underbrace{\left(E_y^* I_z^* + K_{22} H\right)}_{K_{yz}^m} \frac{\partial \phi_z}{\partial y} = -M \quad (4.14)$$

with E_x^* and E_y^* the effective homogenized moduli of the macroscopic equivalent beam, I_z^* the quadratic moment of the macroscopic beam along z , given by $I_z^* = H^3 / 12$.

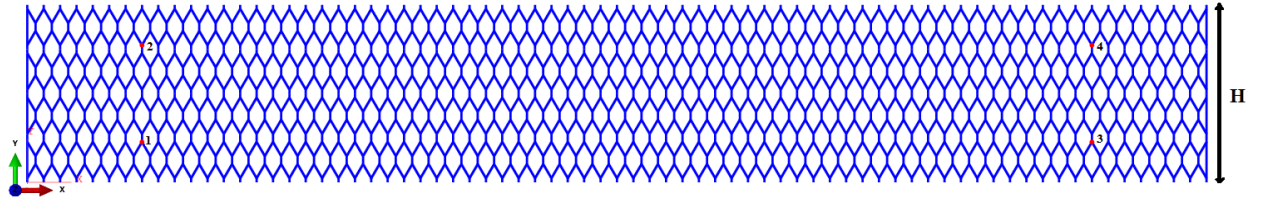


Figure 4.16: Hexagonal honeycomb beam model representing the trabecular bone lattice submitted to pure bending moment.

We calculate the bending stiffness of the beam K_{xz}^m (exhibiting micropolar effect), with the microrotation determined from the displacements of nodes 1-4 ([Figure 4.16](#)). The horizontal and vertical distance separating the points 1-4 are respectively 58 mm and 5.96 mm. The microcurvature of this macrobeam is defined as the relative variation of the microrotation, calculated from the two intermediate variables as

$$\phi_{left} = -(U_{2x} - U_{1x}) / dist(2-1); \quad \phi_{right} = -(U_{4x} - U_{3x}) / dist(4-3) \quad (4.15)$$

therefore the gradient of the microrotation and the bending stiffness are computed successively as

$$\frac{\partial \phi}{\partial x} = (\phi_{left} - \phi_{right}) / dist(3-1); \quad (4.16)$$

$$K_{xz}^m = M / \frac{\partial \phi}{\partial x}$$

The calculation of the reponse of the trabecular lattice under pure bending is achieved by applying a concentrated moment = 0.2 N.mm on the lateral edges. The simulation results are shown in [Figure 4.17](#). The micropolar constant K_{11} is computed from the relation in (4.14) and given in [Table 4.2](#).

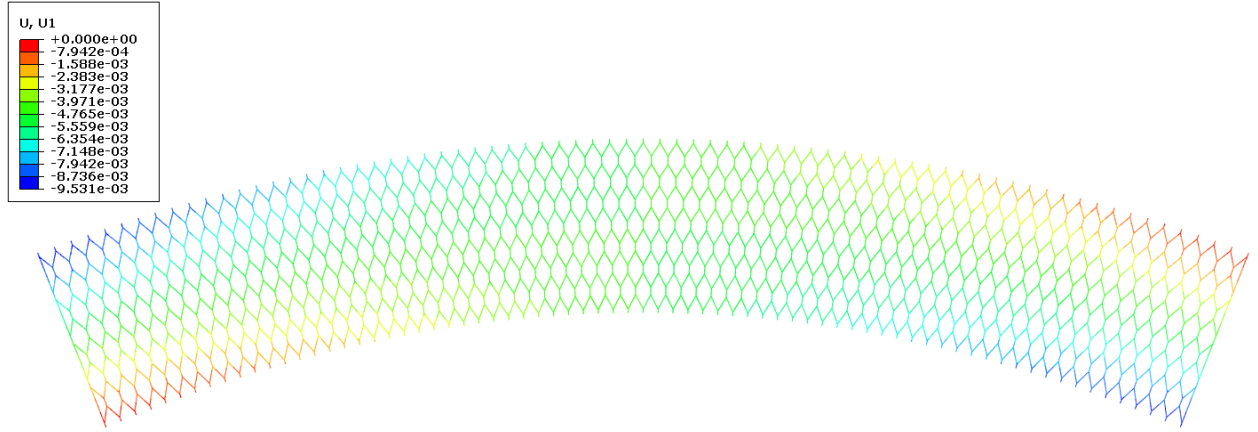


Figure 4.17: Iso-displacements along x-axis under the bending moment.

For the planar orthotropic couple-stress model considered in this work, there are four characteristics lengths which are defined by the following expressions in terms of the engineering constants (Bouyage et al., 2002; Rovati and Veber, 2007)

$$\begin{aligned}
 l_{b1} &= \sqrt{\frac{K_{11}}{4E_{66}}}, \quad l_{b2} = \sqrt{\frac{K_{22}}{4E_{66}}}, \\
 l_{Ex} &= \sqrt{\frac{(1+\nu_{yx}^*)K_{11}}{2E_x^*}}, \quad l_{Ey} = \sqrt{\frac{(1+\nu_{xy}^*)K_{22}}{2E_y^*}}
 \end{aligned} \tag{4.17}$$

The components of the effective elastic constants of trabecular bone evaluated by discrete homogenization and FE simulation are compared in Table 4.2. They are in a very good agreement.

Table 4.2: The couple-stress elastic constants and characteristics lengths of trabecular bone unit cell.

	Discrete homogenization	Finite element simulation
E_x^* (MPa)	75.2	74.4
E_y^* (MPa)	1255	1247
G_{xy}^* (MPa)	407.5	408.5
ν_{xy}^*	0.197	0.2
ν_{yx}^*	3.28	3.21
K_{11} (N)	5.7	6.0
K_{22} (N)	21.3	--
l_{b1} (μm)	59.0	60.6
l_{b2} (μm)	114.0	--
l_{Ex} (μm)	402.7	412.0
l_{Ey} (μm)	100.8	--

In the next section, the established anisotropic micropolar constitutive model for bone is applied to investigate the expected regularizing effect of such an enhanced continuum around a crack present in the bone structure.

4.3.3 Application to bone fracture

Simulations of a square bone sample including a crack are performed, using the previously obtained homogenized anisotropic micropolar model. The results are compared to those obtained by a classical four node finite element called CPS4 within the Abaqus environment.

4.3.3.1 Four node Cosserat finite element

A four node Cosserat finite element has been developed and implemented in the industrial code Abaqus in order to simulate the two dimensional response of the trabecular bone including a crack. The effective trabecular bone behavior has been obtained by the discrete asymptotic homogenization technique described in the previous sections. A simple finite element has been constructed, the four node quadrilateral with three degrees of freedom per node u_{1j}, v_{2j}, ϕ_j at each vertex (there are four nodes: $j=1,2,3,4$), as shown on [Figure 4.18](#).

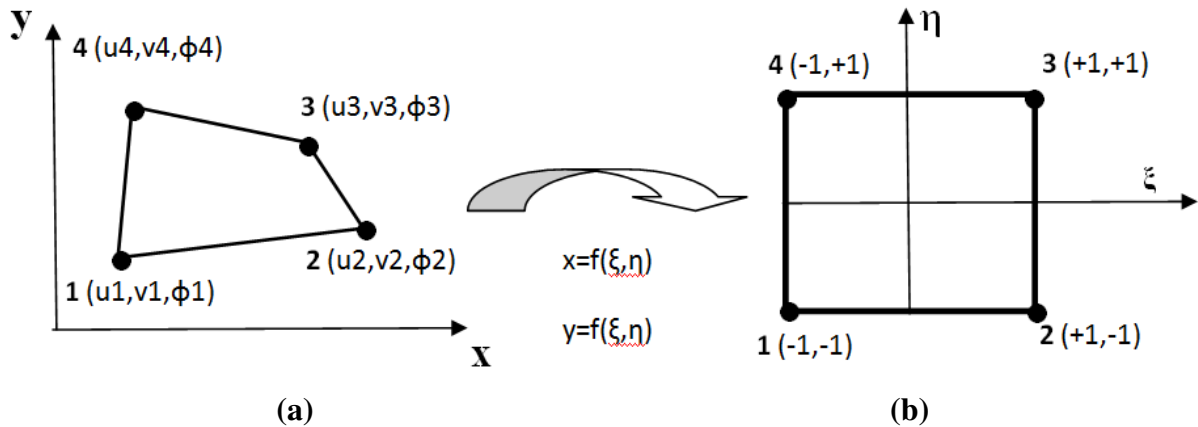


Figure 4.18: Four node linear quadrangle Cosserat FE. (a) Arbitrary four-node quadrilateral FE with three degree of freedom (u,v,ϕ) . (b) Reference element.

The geometrical transformation of the element is given by the following relations:

$$x(\xi, \eta) = \sum_{i=1}^4 N_i(\xi, \eta) x_i; \quad y(\xi, \eta) = \sum_{i=1}^4 N_i(\xi, \eta) y_i; \quad \phi(\xi, \eta) = \sum_{i=1}^4 N_i(\xi, \eta) \phi_i; \quad (4.18)$$

In those expressions, ξ, η are the coordinates of any point of the reference element, $x(\xi, \eta)$, $y(\xi, \eta)$ and $\phi(\xi, \eta)$ successively the position and rotation of one point of the physical element; x_i , y_i and ϕ_i are respectively the coordinates and rotation of node i of the real element and N_i are the shape functions.

The stress-strain relation in a two dimensional plane stress situation can be written as follows:

$$\begin{Bmatrix} \sigma_x \\ \sigma_y \\ \sigma_{xy} \\ \sigma_{yx} \\ m_{xz} \\ m_{yz} \end{Bmatrix} = [\mathbf{D}] \begin{Bmatrix} \epsilon_x \\ \epsilon_y \\ \epsilon_{xy} \\ \epsilon_{yx} \\ \chi_{xz} \\ \chi_{yz} \end{Bmatrix} = [\mathbf{D}] \begin{Bmatrix} \frac{\partial u}{\partial x} \\ \frac{\partial v}{\partial y} \\ \frac{\partial v}{\partial x} - \phi \\ \frac{\partial u}{\partial y} + \phi \\ \frac{\partial \phi}{\partial x} \\ \frac{\partial \phi}{\partial y} \end{Bmatrix} \quad (4.19)$$

with $[\mathbf{D}]$ therein the effective stiffness matrix of the bone, obtained by the discrete asymptotic homogenized method. Introducing the stress and couple stress vector, the constitutive equation for an anisotropy centro-symmetric unit cell can be written in the form given by (4.4). The kinematic relations (4.19) are conveniently written in the matrix form

$$\{\epsilon\} = [B]\{u\} \quad (4.20)$$

The displacement-rotation mixed vector therein is defined as $\{u\} = \{u_1 \ v_1 \ \phi_1 \ u_2 \ v_2 \ \phi_2 \ u_3 \ v_3 \ \phi_3 \ u_4 \ v_4 \ \phi_4\}^T$ and $[B]$ is the matrix defined as:

$$[B] = \begin{bmatrix} B_{11} & 0 & 0 & B_{14} & 0 & 0 & B_{17} & 0 & 0 & B_{110} & 0 & 0 \\ 0 & B_{22} & 0 & 0 & B_{25} & 0 & 0 & B_{28} & 0 & 0 & B_{211} & 0 \\ 0 & B_{32} & B_{33} & 0 & B_{35} & B_{36} & 0 & B_{38} & B_{39} & 0 & B_{311} & B_{312} \\ B_{41} & 0 & B_{43} & B_{44} & 0 & B_{46} & B_{47} & 0 & B_{49} & B_{410} & 0 & B_{412} \\ 0 & 0 & B_{53} & 0 & 0 & B_{56} & 0 & 0 & B_{59} & 0 & 0 & B_{512} \\ 0 & 0 & B_{63} & 0 & 0 & B_{66} & 0 & 0 & B_{69} & 0 & 0 & B_{612} \end{bmatrix}$$

The components of this matrix are as follows:

$$\begin{aligned} B_{11} &= \frac{1}{4} j_{11} (-1 + \eta) + \frac{1}{4} j_{12} (-1 + \xi), & B_{14} &= \frac{1}{4} j_{11} (1 - \eta) + \frac{1}{4} j_{12} (-1 - \xi), \\ B_{17} &= \frac{1}{4} j_{11} (1 + \eta) + \frac{1}{4} j_{12} (1 + \xi), & B_{110} &= \frac{1}{4} j_{11} (-1 - \eta) + \frac{1}{4} j_{12} (1 - \xi), \\ B_{22} &= \frac{1}{4} j_{21} (-1 + \eta) + \frac{1}{4} j_{22} (-1 + \xi), & B_{25} &= \frac{1}{4} j_{21} (1 - \eta) + \frac{1}{4} j_{22} (-1 - \xi), \\ B_{28} &= \frac{1}{4} j_{21} (1 + \eta) + \frac{1}{4} j_{22} (1 + \xi), & B_{211} &= \frac{1}{4} j_{21} (-1 - \eta) + \frac{1}{4} j_{22} (1 - \xi), \\ B_{32} &= B_{11}, & B_{33} &= \frac{1}{4} (-1 + \xi + \eta - \xi\eta), & B_{35} &= B_{14}, & B_{36} &= \frac{1}{4} (-1 - \xi + \eta + \xi\eta), \end{aligned}$$

$$\begin{aligned}
B_{38} &= B_{17}, B_{39} = \frac{1}{4}(-1 - \xi - \eta - \xi\eta), B_{311} = B_{110}, B_{312} = \frac{1}{4}(-1 + \xi - \eta + \xi\eta), \\
B_{41} &= B_{22}, B_{43} = \frac{1}{4}(1 - \xi - \eta + \xi\eta), B_{44} = B_{25}, B_{46} = \frac{1}{4}(1 + \xi - \eta + \xi\eta), B_{47} = B_{28}, \\
B_{49} &= \frac{1}{4}(1 + \xi + \eta + \xi\eta), B_{410} = B_{211}, B_{412} = \frac{1}{4}(1 - \xi + \eta - \xi\eta), \\
B_{53} &= B_{11}, B_{56} = B_{14}, B_{59} = B_{17}, B_{512} = B_{110}, \\
B_{63} &= B_{22}, B_{66} = B_{25}, B_{69} = B_{28}, B_{612} = B_{211}, \\
&\text{and } j_{ij}, i, j=1, 2 \text{ are the coefficients of the Jacobean matrix.}
\end{aligned}$$

4.3.3.2 Simulation results

The stress distribution across the crack is compared with the corresponding distribution obtained for a classical Cauchy continuum, relying on the developed special finite element. Especially, the anisotropy reflected in the equivalent stiffness matrix is shown to act on both the classical and the micropolar parts of the overall constitutive behavior; the directions of anisotropy are here dictated by the underlying cellular structure, which is distributed over the considered bone sample, although represented in an average sense in this specific application. The principal directions of anisotropy (here orthotropy) are supposed to be aligned with the fiber directions within the selected bone sample, which by definition coincide with the X and Y directions of the representative volume element (the unit cell).

The specimen dimensions correspond to 1mm width and 1 mm height. The effective material properties calculated by the discrete homogenization technique are summarized in the following matrix:

$$[\mathbf{D}] = \begin{bmatrix} 212.7 & 698.3 & 0 & 0 & 0 & 0 \\ 698.3 & 3547.4 & 0 & 0 & 0 & 0 \\ 0 & 0 & 436.2 & 378.8 & 0 & 0 \\ 0 & 0 & 271.6 & 543.4 & 0 & 0 \\ 0 & 0 & 0 & 0 & 5.7 & 0 \\ 0 & 0 & 0 & 0 & 0 & 21.3 \end{bmatrix} \quad (4.21)$$

The two characteristic lengths of this anisotropic micropolar behavior are calculated from the rigidities in (4.21), as $l_{b1} = \sqrt{K_{55} / 2(K_{33} + K_{34})} = 60\mu\text{m}$ and $l_{b2} = \sqrt{K_{66} / 2(K_{43} + K_{44})} = 115\mu\text{m}$. A horizontal crack representing 14% of the total specimen width is introduced to represent longitudinal fracture, as viewed on [Figure 4.19](#). The bottom edge of the specimen (1 x 1 mm) is simply supported in Y-direction (the corner node at the origin is fixed), and the top edge is submitted to a uniaxial displacement magnitude equal to 0.25 mm in the vertical direction.

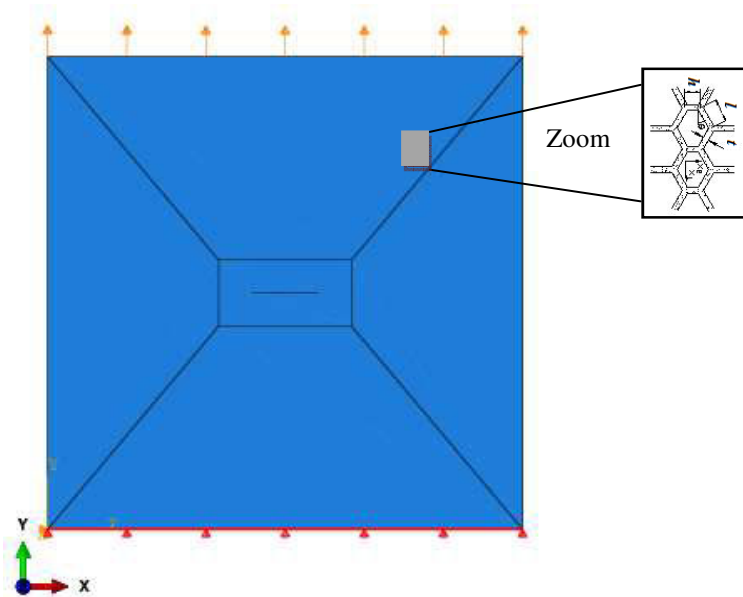


Figure 4.19: Applied loading and boundary conditions of the 2D bone specimen with bone fracture. Zoom of the material specimen on two hexagonal unit cells.

In these simulations, three different meshes referred to as Coarse, Medium and Fine are used; those meshes contain respectively 128, 489 and 1188 elements. We checked that using a finer mesh (than the mesh referred to as Fine) does not lead to different stress distributions. The spatial distribution of the in-plane stress components S_{11} , S_{12} , and S_{22} is pictured below for those three mesh sizes, in [Figures 4.20](#), [4.21](#), [4.22](#), corresponding successively to the coarse, medium and fine meshes for both the Cauchy and the Cosserat anisotropic continuum models for the purpose of assessing the effect of enhancement of the Cauchy continuum by microrotations. As a matter of clarity of the presentation of the results and despite the existence of two orthogonal symmetry planes, we choose to plot stress distributions over the complete sample including the whole crack. We observe as a general tendency that the peak stress is reduced by the enhancement of the Cauchy model by micropolar degrees of freedom, for all three mesh sizes, at the exception of the vertical component S_{22} in the case of the coarse mesh ([Figures 4.20e](#) and [f](#)). One observes that a stress peak is obtained for both models close to the crack tip, a fact which is well known in the field of fracture mechanics ([Broek, 1974](#)). However, the amplitude of the peak stress is significantly reduced when the Cosserat continuum model is employed; the percentage of reduction is evaluated for each stress component (and each mesh size) in [Table 4.3](#). It reaches up to 50% for the fine mesh, a value in agreement with the amount of reduction of the stress concentration factor obtained for sharp cracks using a linear isotropic Cosserat behavior in [Lakes et al \(1990\)](#). Note that the reduction of the stress concentration depends on the Cosserat characteristic length, which is fixed in present analysis, since it is a byproduct of the effective moduli.

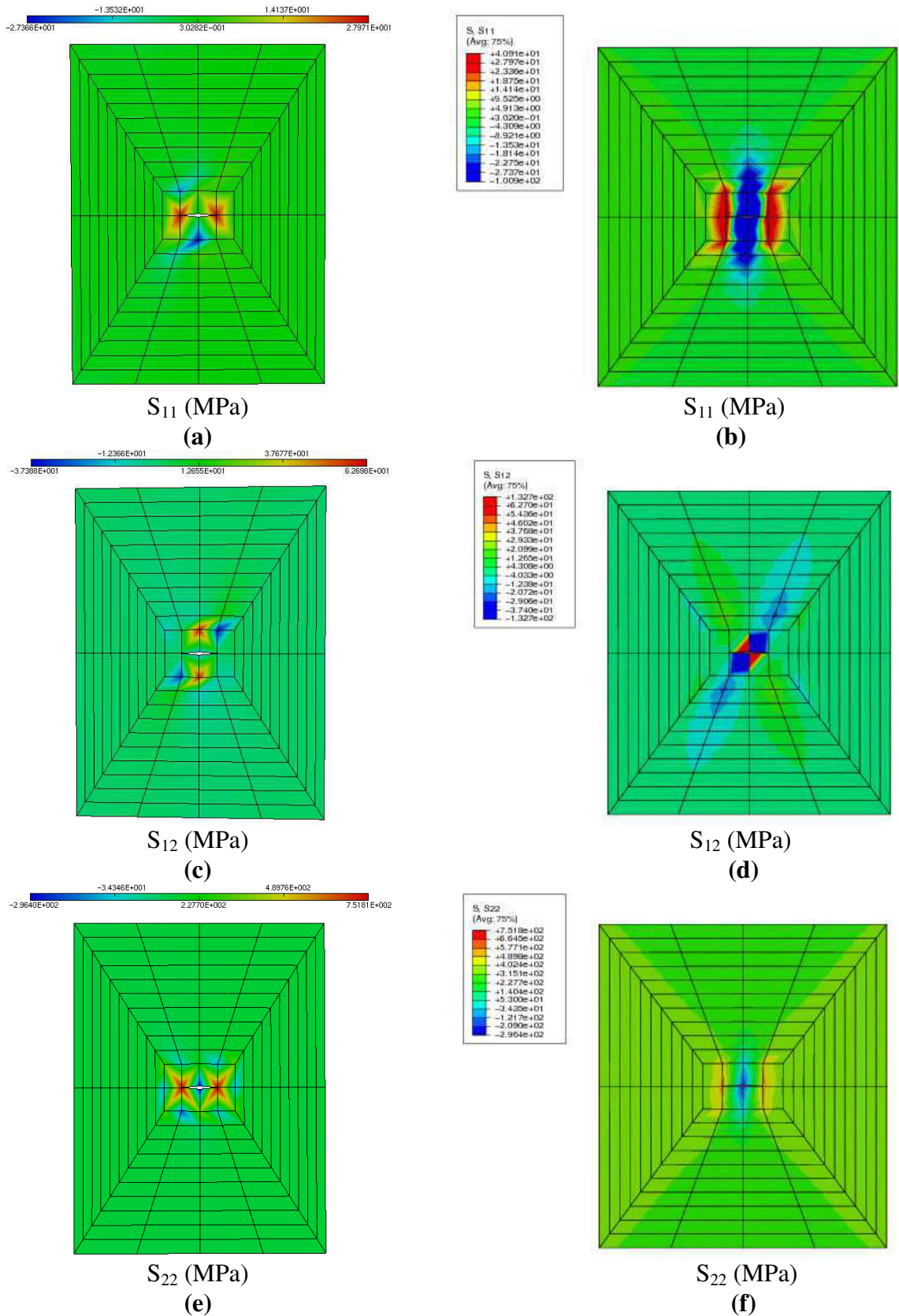
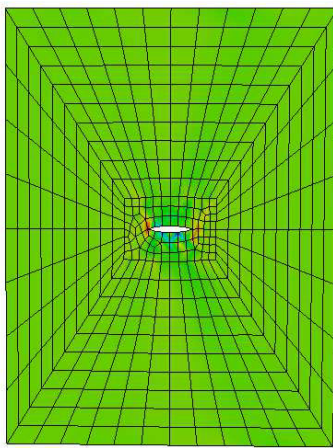
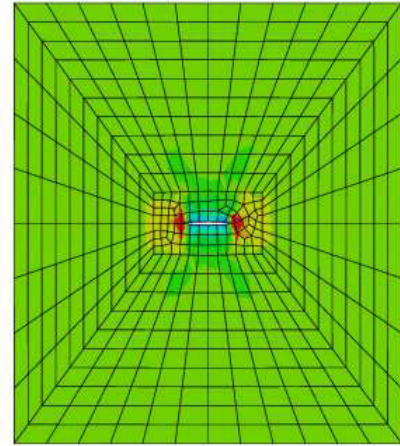
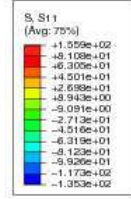


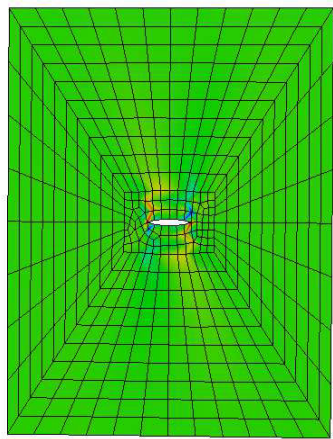
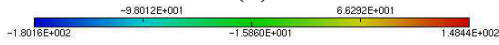
Figure 4.20: Spatial stress distribution obtained by extrapolation of stresses from the integration points to the nodal points. (a), (c), and (e) correspond to Cosserat finite element results and (b), (d), and (f) correspond to the classical four node finite element. Coarse mesh (128 elements).



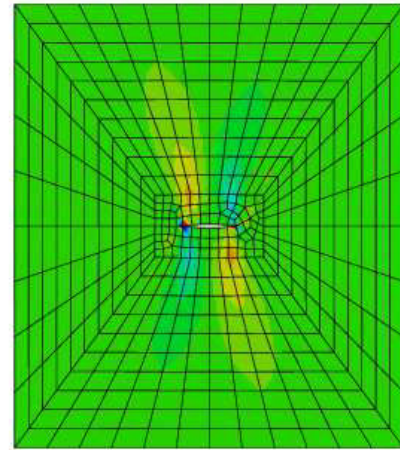
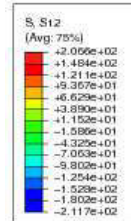
S_{11} (MPa)
(a)



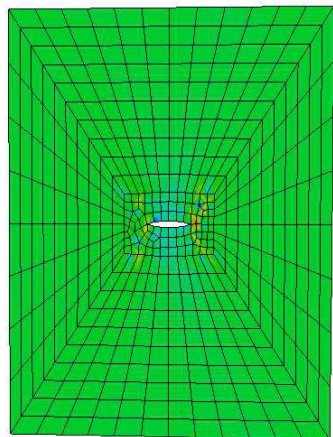
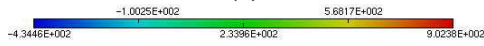
S_{11} (MPa)
(b)



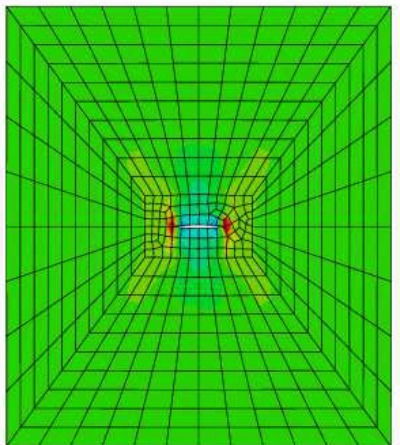
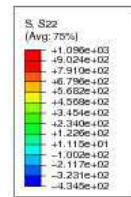
S_{12} (MPa)
(c)



S_{12} (MPa)
(d)



S_{22} (MPa)
(e)



S_{22} (MPa)
(f)

Figure 4.21: Spatial stress distribution obtained by extrapolation of the stresses from integration points to the nodal points. (a), (c), and (e) correspond to Cosserat finite element results and (b), (d), and (f) correspond to the classical four node finite element. Medium mesh (489 elements).

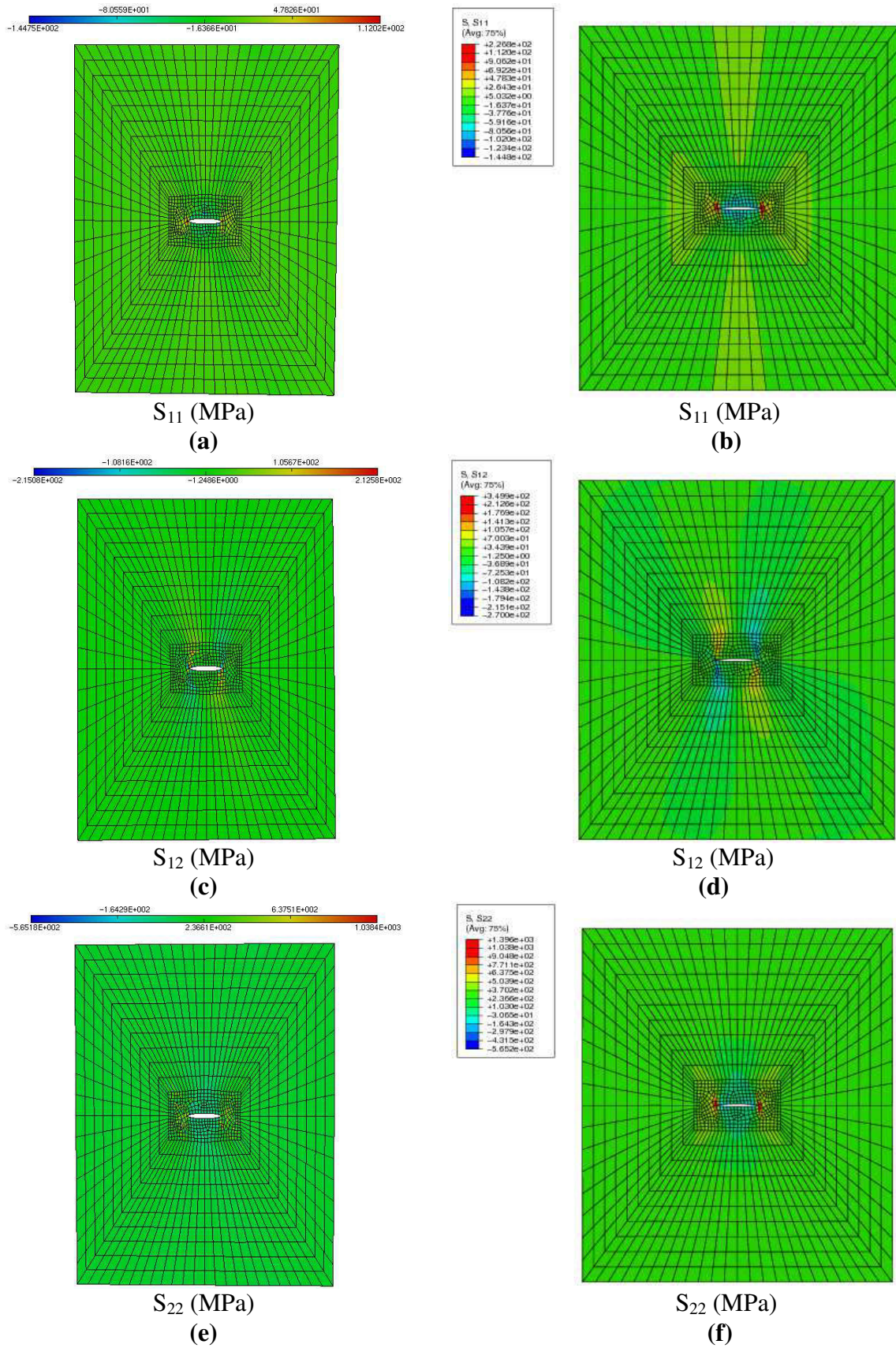


Figure 4.22: Spatial stress distribution obtained by extrapolation of stresses from the integration points to nodal points. (a), (c), and (e) correspond to Cosserat finite element results and (b), (d), and (f) correspond to the classical four node finite element. Fine mesh (1188 elements).

Table 4.3: Comparison of peak stress values for the two models (Cauchy and micropolar).

	Cosserat finite element			CPS4 finite element (Abaqus)			% of stress reduction $\frac{S_{\text{Cauchy}} - S_{\text{Cosserat}}}{S_{\text{Cauchy}}} \times 100$		
	S11	S12	S22	S11	S12	S22	S11	S12	S22
Coarse	28	63	752	41	133	752	31.7	52.6	0
Medium	81	148	902	156	206	1096	48.1	28.2	17.7
Fine	112	213	1038	227	350	1396	50.7	39.2	25.6

We further plot the isovalues of the two in-plane displacement components, U_1 and U_2 (Figure 4.23); we observe a more diffuse displacement field when Cosserat model is employed, in comparison to Cauchy continuum, for which steep stress gradients are obtained. This confirms the regularizing effect of the Cosserat continuum model.

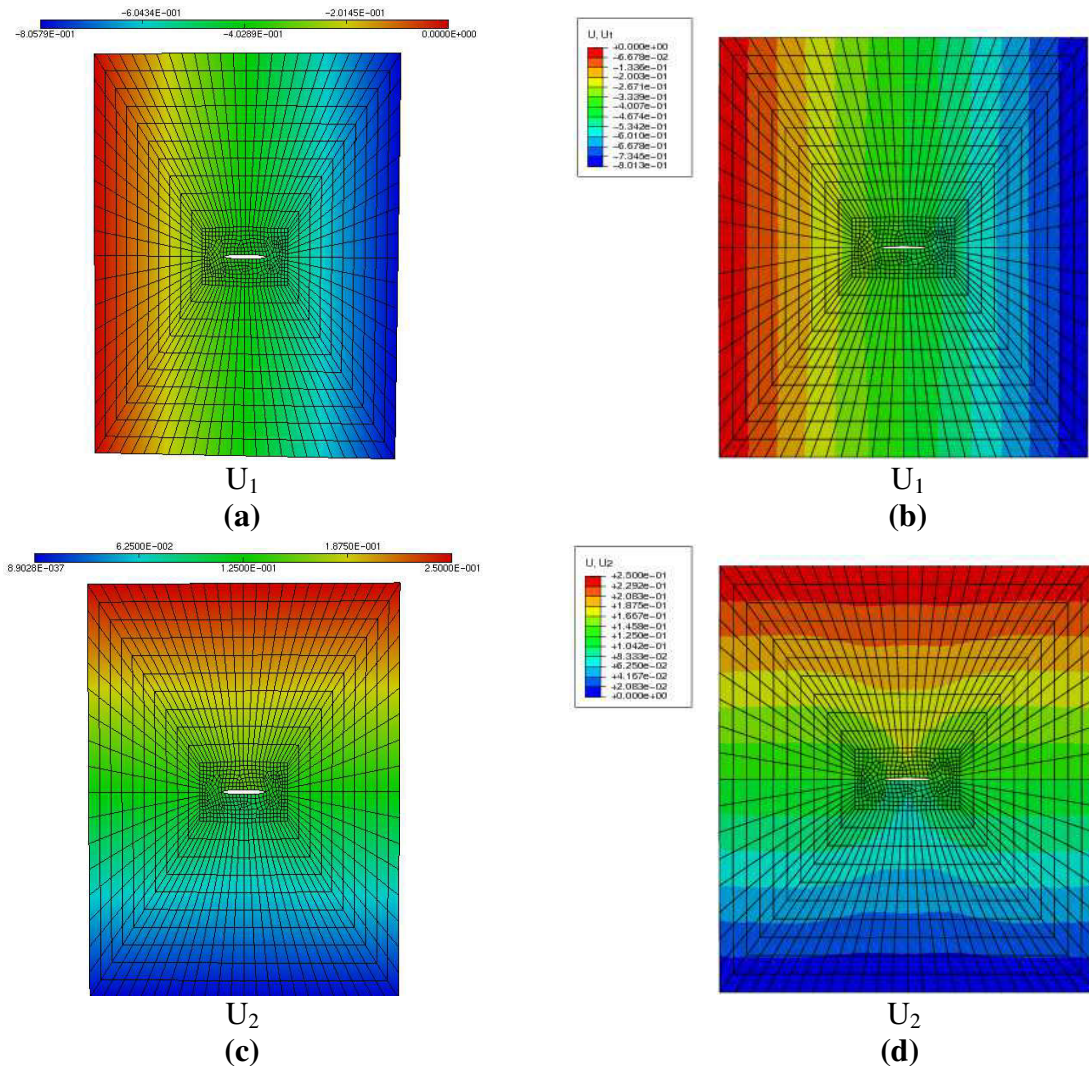


Figure 4.23: Displacement distribution. (a), (c) correspond to Cosserat finite element results and (b), (d) correspond to the classical four node finite element (CPS4 from Abaqus). Fine mesh (1188 elements).

4.4 Effective mechanical properties of vertebral trabecular bone

Trabecular bone, or spongy bone, is a highly porous biological tissue with an open-celled cellular structure, which accounts for up to 20% of the bone mass in humans. It is found in vertebrae; [Figure 4.24](#) shows lumbar vertebra in superior and lateral view with x and y are the lateral directions while z is oriented in the superior direction. The individual trabeculae that make up the trabecular tissue tend to have one of two basic shapes, either slender rods (or beam like struts) or relatively thin and flat plates. These struts and plates form a three-dimensional scaffolding within the cortical shell. Structurally, trabecular bone helps to distribute loading from the articular surfaces to the cortical shell. Trabecular tissue is also very important for the stability and fixation of joint implants and other fixation devices placed into bone. At microscopic scale, trabecular bone contains small trabecular struts connecting in a way that generates a three-dimensional porous structure. In the vertebral body, cancellous bone appears to contain a somewhat regular array of trabecular struts ([Figure 4.24](#)), and thus can be idealized as a cellular solid. It is reported that the predominant arrangement of vertebral bone is that of vertically oriented columns with reinforcing horizontal struts, and the structure can be assumed to be columnar with cylindrical symmetry ([Gibson, 1985](#); [Overaker, 1997](#); [Kim & Al-Hassani, 2002](#)). Therefore, we consider the idealized shape of trabecular bone as a hexagonal cellular structure comprised of a doubly prism shape unit cell, as will be described later on.

In order to be specific to the considered application to vertebral trabecular bone, a general 3D anisotropic hexagonal lattice with horizontal struts of lengths L and h (lengths of in-plane struts) and vertical struts of length L_v (out-of-plane) is considered, both struts being endowed with uniform circular cross-section of diameter d . The whole lattice is generated from the repetition of the unit cell shown in [Figure 4.25](#) thanks to three periodicity vectors defined in the Cartesian basis. The considered hexagonal unit cell is composed of five beams; three horizontal beams b_1 , b_2 , and b_3 and the vertical beams b_4 and b_5 . The horizontal beams b_2 and b_3 have the same length L and are inclined by the angle θ with the horizontal direction, while b_1 has length h . The two vertical beams b_4 and b_5 have the same length L_v .

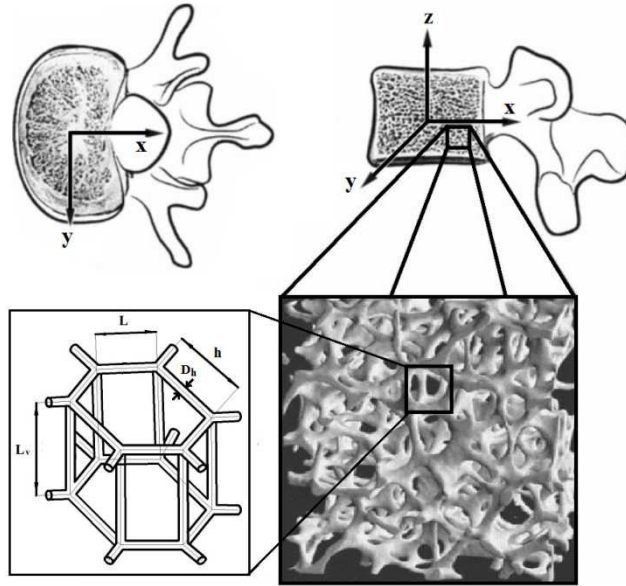


Figure 4.24: General anisotropic unit cell for 3D hexagonal models. The geometric parameters include the cell angle θ , the in-plane strut lengths (L, h) , and the vertical length L_v .

This geometry is representative of the unit cell of vertebral trabecular bone. The lengths of the periodicity vectors (the norm of the periodicity vectors \mathbf{Y}_1 , \mathbf{Y}_2 , and \mathbf{Y}_3 in the Cartesian basis) are $L_1 = L_2 = \sqrt{(L \cos \theta)^2 + (h + L \sin \theta)^2}$ and $L_3 = L_v$. The connectivity Table 4.4 gives the numbering of beams and nodes within the chosen representative unit cell.

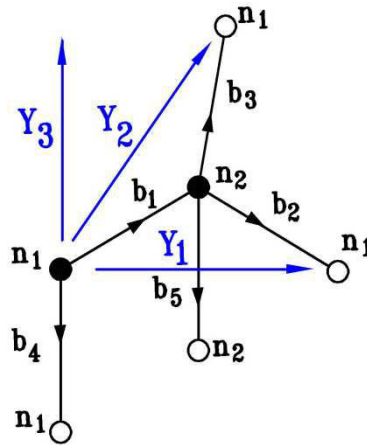


Figure 4.25: Reference unit cell of vertebral trabecular bone and its periodicity vectors \mathbf{Y}_1 , \mathbf{Y}_2 , and \mathbf{Y}_3 .

Table 4.4: Connectivity array for the 3D hexagonal lattice.

Beam	1	2	3	4	5
O(b)	1	2	2	1	2
E(b)	2	1	1	1	2
δ_1	0	1	0	0	0
δ_2	0	0	1	0	0
δ_3	0	0	0	-1	-1

The lattice is called re-entrant when the angle θ between the horizontal direction and the strut with length L (in-plane) is negative. Regular unit cells correspond to geometrical parameters $L = h$ and $\theta = 30^\circ$ and anisotropic unit cell correspond to all other values.

The relative density of the general 3D anisotropic hexagonal is computed in terms of the geometrical parameters L, h, L_v, r and θ as

$$\frac{\rho^*}{\rho_s} = \frac{1}{2} \frac{\pi r^2 (h + 2L + 2L_v)}{LL_v \cos \theta (h + L \sin \theta)} \quad (4.22)$$

where ρ^* is the equivalent density of the lattice, and ρ_s the density of the bulk material. After homogenization, the equivalent orthotropic stiffness matrix for the 3D hexagonal lattice is finally obtained in terms of the geometrical and mechanical lattice parameters by rearranging equation (2.45) in matrix format as

$$\mathbf{D} = \begin{bmatrix} \mathbf{E} & \mathbf{0} \\ \mathbf{0} & \mathbf{K} \end{bmatrix} = \begin{bmatrix} E_{11} & E_{12} & E_{13} & 0 & 0 & 0 & 0 & 0 & 0 & 0 & 0 & 0 & 0 & 0 & 0 & 0 & 0 & 0 & 0 & 0 & 0 \\ E_{21} & E_{22} & E_{23} & 0 & 0 & 0 & 0 & 0 & 0 & 0 & 0 & 0 & 0 & 0 & 0 & 0 & 0 & 0 & 0 & 0 & 0 \\ E_{31} & E_{32} & E_{33} & 0 & 0 & 0 & 0 & 0 & 0 & 0 & 0 & 0 & 0 & 0 & 0 & 0 & 0 & 0 & 0 & 0 & 0 \\ 0 & 0 & 0 & E_{44} & E_{45} & 0 & 0 & 0 & 0 & 0 & 0 & 0 & 0 & 0 & 0 & 0 & 0 & 0 & 0 & 0 & 0 \\ 0 & 0 & 0 & E_{54} & E_{55} & 0 & 0 & 0 & 0 & 0 & 0 & 0 & 0 & 0 & 0 & 0 & 0 & 0 & 0 & 0 & 0 \\ 0 & 0 & 0 & 0 & 0 & E_{66} & E_{67} & 0 & 0 & 0 & 0 & 0 & 0 & 0 & 0 & 0 & 0 & 0 & 0 & 0 & 0 \\ 0 & 0 & 0 & 0 & 0 & E_{76} & E_{77} & 0 & 0 & 0 & 0 & 0 & 0 & 0 & 0 & 0 & 0 & 0 & 0 & 0 & 0 \\ 0 & 0 & 0 & 0 & 0 & 0 & 0 & E_{88} & E_{89} & 0 & 0 & 0 & 0 & 0 & 0 & 0 & 0 & 0 & 0 & 0 & 0 \\ 0 & 0 & 0 & 0 & 0 & 0 & 0 & E_{98} & E_{99} & 0 & 0 & 0 & 0 & 0 & 0 & 0 & 0 & 0 & 0 & 0 & 0 \\ 0 & 0 & 0 & 0 & 0 & 0 & 0 & 0 & 0 & K_{11} & K_{12} & K_{13} & 0 & 0 & 0 & 0 & 0 & 0 & 0 & 0 & 0 \\ 0 & 0 & 0 & 0 & 0 & 0 & 0 & 0 & 0 & K_{21} & K_{22} & K_{23} & 0 & 0 & 0 & 0 & 0 & 0 & 0 & 0 & 0 \\ 0 & 0 & 0 & 0 & 0 & 0 & 0 & 0 & 0 & K_{31} & K_{32} & K_{33} & 0 & 0 & 0 & 0 & 0 & 0 & 0 & 0 & 0 \\ 0 & 0 & 0 & 0 & 0 & 0 & 0 & 0 & 0 & 0 & 0 & 0 & K_{44} & K_{45} & 0 & 0 & 0 & 0 & 0 & 0 & 0 \\ 0 & 0 & 0 & 0 & 0 & 0 & 0 & 0 & 0 & 0 & 0 & 0 & K_{54} & K_{55} & 0 & 0 & 0 & 0 & 0 & 0 & 0 \\ 0 & 0 & 0 & 0 & 0 & 0 & 0 & 0 & 0 & 0 & 0 & 0 & 0 & 0 & K_{66} & K_{67} & 0 & 0 & 0 & 0 & 0 \\ 0 & 0 & 0 & 0 & 0 & 0 & 0 & 0 & 0 & 0 & 0 & 0 & 0 & 0 & K_{76} & K_{77} & 0 & 0 & 0 & 0 & 0 \\ 0 & 0 & 0 & 0 & 0 & 0 & 0 & 0 & 0 & 0 & 0 & 0 & 0 & 0 & 0 & 0 & K_{88} & K_{89} & 0 & 0 & 0 \\ 0 & 0 & 0 & 0 & 0 & 0 & 0 & 0 & 0 & 0 & 0 & 0 & 0 & 0 & 0 & 0 & K_{98} & K_{99} & 0 & 0 & 0 \end{bmatrix} \quad (4.23)$$

The rigidity constants therein are lengthy expressions of the lattice descriptors and microbeams moduli, given in the [Appendix A](#). From the effective compliance matrix (the inverse of previous stiffness matrix), one is able to identify the classical and micropolar effective moduli as closed form expressions of the lattice geometrical and mechanical parameters. The effective elastic constants are given in terms of the geometrical parameters L, h, L_v, r and θ , the shear correction k_s , and the elastic moduli of the solid cell walls E_s, G_s , as follows:

$$E_x^* = -\frac{3\pi r^4 C_t G_s k_s E_s}{\begin{pmatrix} -3C_t^2 r^2 G_s k_s L S_t - S_t L^3 G_s k_s - 3S_t E_s r^2 L \\ + S_t L^3 C_t^2 G_s k_s + 3S_t E_s r^2 C_t^2 L + L^2 C_t^2 h G_s k_s \\ -3C_t^2 r^2 h G_s k_s - L^2 h G_s k_s - 3h E_s r^2 + 3C_t^2 h E_s r^2 \end{pmatrix}}; E_y^* = \frac{3\pi r^4 (h + L S_t) G_s k_s E_s}{L_v L C_t \begin{pmatrix} 3L C_t^2 r^2 E_s + L^3 C_t^2 G_s k_s + 3r^2 L G_s k_s \\ + 6r^2 h G_s k_s - 3L r^2 C_t^2 G_s k_s \end{pmatrix}};$$

$$E_z^* = \frac{\pi r^2 E_s}{L C_t (h + L S_t)};$$

$$\begin{aligned}
G_{xy}^* &= \frac{E_{45} + E_{44}}{2} = \frac{E_{54} + E_{55}}{2} = \frac{3\pi r^4 C_t (h + LS_t) G_s k_s E_s}{L_v \left(6LhS_t r^2 G_s k_s + 3h^2 C_t^2 E_s r^2 + L^2 h^2 C_t^2 G_s k_s + 3r^2 h^2 G_s k_s \right. \\
&\quad \left. + 2C_t^2 h^3 L G_s k_s + 6C_t^2 L h r^2 E_s + 3L^2 r^2 G_s k_s - 3C_t^2 h^2 r^2 G_s k_s \right)}; \\
G_{yz}^* &= \frac{E_{66} + E_{67}}{2} = \frac{E_{76} + E_{77}}{2} = \frac{3\pi r^4 (h + LS_t) G_s k_s E_s}{LC_t \left(2LhL_v^2 S_t G_s k_s + 6LhS_t E_s r^2 + L^3 G_s k_s L_v + 3h^2 E_s r^2 + 3L^2 E_s r^2 + 3E_s r^2 L L_v \right. \\
&\quad \left. + 2h^3 L_v G_s k_s + 6hE_s r^2 L_v + h^2 L_v^2 G_s k_s + L^2 L_v^2 G_s k_s - 3L^2 C_t^2 E_s r^2 - L^2 C_t^2 L_v^2 G_s k_s \right)}; \\
G_{xz}^* &= \frac{E_{88} + E_{89}}{2} = \frac{E_{98} + E_{99}}{2} = \frac{3\pi r^4 C_t G_s k_s E_s}{(h + LS_t) \left(3C_t^2 L r^2 E_s + C_t^2 L_v^2 L G_s k_s + L^2 G_s k_s L_v + 3E_s r^2 L_v \right)}; \\
\nu_{xy}^* &= -\frac{\left(L^2 G_s k_s + 3r^2 E_s - 3r^2 G_s k_s \right) LC_t^2 S_t}{\left(-3r^2 C_t^2 G_s k_s L S_t - L^3 S_t G_s k_s - 3L S_t r^2 E_s + S_t L^3 C_t^2 G_s k_s + 3S_t E_s r^2 C_t^2 L \right. \\
&\quad \left. + L^2 C_t^2 h G_s k_s - 3r^2 C_t^2 h G_s k_s - L^2 h G_s k_s - 3h E_s r^2 + 3C_t^2 h E_s r^2 \right)}; \\
\nu_{yx}^* &= \frac{S_t (h + LS_t) \left(L^2 G_s k_s + 3r^2 E_s - 3r^2 G_s k_s \right)}{\left(3C_t^2 r^2 L E_s + L^3 C_t^2 G_s k_s + 3r^2 L G_s k_s + 6r^2 h G_s k_s - 3C_t^2 L r^2 G_s k_s \right)}; \\
\nu_{xz}^* &= \nu_{zx}^* = \nu_{yz}^* = \nu_{zy}^* = 0.
\end{aligned} \tag{4.24}$$

E_x^* and E_y^* are the in-plane effective Young's moduli; E_z^* is the out-of-plane effective Young's modulus; G_{xy}^* is the in-plane effective shear modulus; G_{xz}^* and G_{yz}^* are the out-of-plane effective shear moduli; ν_{xy}^* and ν_{yx}^* are the in-plane effective Poisson's ratios and $\nu_{xz}^*, \nu_{zx}^*, \nu_{yz}^*, \nu_{zy}^*$ the out-of-plane effective Poisson's ratios. C_t and S_t stand for $\cos \theta$ and $\sin \theta$, respectively.

The present 3D micropolar model substantiates additional material constants. The micropolar shear constant κ couples the rotation of particles to shear stresses; if $\kappa = 0$ (coupling number (N) = 0) the Cauchy stress does not depend on the rotational degree of freedom. The limit $\kappa \rightarrow \infty$ is a condition energetically admissible, similar to "incompressibility" in classical elasticity, and corresponds to $N = 1$ (upper bound) which is called "couple stress theory". The modulus γ sets the intensity of the couple stresses and is proportional to the characteristic lengths for bending and torsion, quantities l_b and l_t respectively. In Cauchy solids, the internal characteristic length is of the order of the atomic distance and moments of forces and consequently do not produce any macroscopic effect. However, in microstructured solids such as hard biological tissues having a cellular structure where an intrinsic internal length of the order of several microns may be detected, couple stresses may influence the macroscopic behaviour. In the limit situation when $\gamma = 0$, Cauchy elasticity is recovered.

The micropolar moduli κ and μ^* are further identified from the effective stiffness matrix (4.23) as closed form expressions of the geometrical and micromechanical parameters of the hexagonal unit cell as follows:

$$\begin{aligned}
\kappa_{xy} &= \frac{3\pi r^4 C_t E_s}{L^2 L_v \left(\frac{3S_t r^2 E_s}{G_s k_s L} + LS_t + h + \frac{3hr^2 E_s}{G_s k_s L^2} \right)}; \kappa_{yx} = \frac{3\pi r^4 S_t E_s}{L^3 L_v C_t \left(1 + \frac{3r^2 E_s}{G_s k_s L^2} \right)}; \\
\kappa_{yz} &= \frac{3\pi r^4 S_t E_s}{L^3 L_v C_t \left(1 + \frac{3r^2 E_s}{G_s k_s L^2} \right)}; \kappa_{zy} = \frac{3\pi r^4 E_s}{LL_v^2 C_t \left(\frac{3S_t r^2 L E_s}{G_s k_s L_v^2} + LS_t + h + \frac{3hr^2 E_s}{G_s k_s L_v^2} \right)}; \\
\kappa_{zx} &= \frac{3\pi r^4 E_s}{LL_v^2 C_t (h + LS_t) \left(1 + \frac{3r^2 E_s}{G_s k_s L_v^2} \right)}; \kappa_{xz} = \frac{3\pi r^4 C_t E_s}{L^2 L_v (h + LS_t) \left(1 + \frac{3r^2 E_s}{G_s k_s L^2} \right)}; \\
\mu_{xy}^* &= -\frac{3}{2} \frac{\pi r^4 C_t E_s \left(-4S_t h L^3 + C_t^2 L^2 h^2 - \frac{12S_t L h r^2 E_s}{G_s k_s} + 6S_t r^2 h L + 3L^2 r^2 + 2C_t^2 L h^3 + \frac{3C_t^2 h^2 r^2 E_s}{G_s k_s} + \frac{6C_t^2 h L r^2 E_s}{G_s k_s} \right)}{L^2 L_v \left(1 + \frac{3r^2 E_s}{G_s k_s L^2} \right) \left(\frac{9S_t r^2 L h^2 - 3L h^2 r^2 S_t C_t^2 + 2S_t h^3 L^2 C_t^2 + C_t^2 S_t L^3 h^2 + 3S_t L^3 r^2 + \frac{6S_t L^2 h C_t^2 r^2 E_s}{G_s k_s} + \frac{3S_t L h^2 C_t^2 r^2 E_s}{G_s k_s}}{-3C_t^2 h^3 r^2 + \frac{6h^2 L C_t^2 r^2 E_s}{G_s k_s} + 9h L^2 r^2 + 2h^4 L C_t^2 - 6h L^2 r^2 C_t^2 + 3h^3 r^2 + \frac{3h^3 C_t^2 r^2 E_s}{G_s k_s} + h^3 L^2 C_t^2} \right)}; \\
\mu_{yx}^* &= \frac{3}{2} \frac{\pi r^4 E_s \left(-\frac{6S_t C_t^2 h L r^2 E_s}{G_s k_s} - \frac{3C_t^2 S_t h^2 r^2 E_s}{G_s k_s} + \frac{6C_t^2 S_t L^2 r^2 E_s}{G_s k_s} - 2C_t^2 S_t L h^3 - L^2 C_t^2 S_t h^2 - 3L^2 r^2 S_t \right.}{\left. + 3h^2 r^2 C_t^2 S_t + 2C_t^2 S_t L^4 - 3S_t h^2 r^2 + 6C_t^2 r^2 h L - 6L h r^2 + 2L^3 C_t^2 h + \frac{6L C_t^2 h r^2 E_s}{G_s k_s} \right)}{L^3 L_v C_t \left(1 + \frac{3r^2 E_s}{G_s k_s L^2} \right) \left(\frac{6S_t r^2 L h + C_t^2 L^2 h^2 + \frac{3C_t^2 h^2 r^2 E_s}{G_s k_s} + 3h^2 r^2}{+ \frac{6C_t^2 h L r^2 E_s}{G_s k_s} + 2C_t^2 L h^3 + 3L^2 r^2 - 3C_t^2 h^2 r^2} \right)}; \\
\mu_{yz}^* &= \frac{3}{2} \frac{\pi r^4 E_s \left(S_t L^3 - \frac{6S_t h E_s r^2}{G_s k_s} + \frac{3S_t L E_s r^2}{G_s k_s} + S_t C_t^2 L^2 L_v - 2S_t h^3 + \frac{3S_t L^2 C_t^2 E_s r^2}{L_v G_s k_s} - S_t L_v L^2 - \frac{3S_t h^2 E_s r^2}{L_v G_s k_s} \right.}{\left. - \frac{3S_t L^2 E_s r^2}{L_v G_s k_s} - L_v S_t h^2 + 2L^2 h + 2C_t^2 L_v L h + \frac{6C_t^2 L h E_s r^2}{L_v G_s k_s} + \frac{6h E_s r^2}{G_s k_s} - \frac{6h L E_s r^2}{L_v G_s k_s} - 2L_v h L \right)}{L^3 L_v C_t \left(1 + \frac{3r^2 E_s}{G_s k_s L^2} \right) \left(\frac{-C_t^2 L_v L^2 - \frac{3L^2 C_t^2 E_s r^2}{L_v G_s k_s} + \frac{3L r^2 E_s}{G_s k_s} + 2L h L_v S_t + \frac{6L h S_t E_s r^2}{L_v G_s k_s}}{\frac{6h E_s r^2}{G_s k_s} + \frac{3h^2 E_s r^2}{L_v G_s k_s} + L^2 L_v + L^3 + \frac{3L^2 E_s r^2}{L_v G_s k_s} 2h^3 + h^2 L_v} \right)}; \\
\mu_{zy}^* &= -\frac{3}{2} \frac{\pi r^4 E_s \left(-2L L_v h S_t - \frac{6L h S_t E_s r^2}{L_v G_s k_s} + 2h^3 - \frac{3L^2 E_s r^2}{L_v G_s k_s} + \frac{3L E_s r^2}{G_s k_s} + L^3 \right.}{\left. + \frac{6h E_s r^2}{G_s k_s} - L^2 L_v - \frac{3h^2 E_s r^2}{L_v G_s k_s} - L_v h^2 + \frac{3L^2 C_t^2 E_s r^2}{L_v G_s k_s} + L_v L^2 C_t^2 \right)}{\left(\frac{-3S_t C_t^2 L^3 E_s r^2}{L_v G_s k_s} - \frac{9C_t^2 h L^2 E_s r^2}{L_v G_s k_s} - S_t C_t^2 L^3 L_v - 3C_t^2 h L_v L^2 + \frac{3S_t L^3 E_s r^2}{L_v G_s k_s} \right.} \\
&\quad \left. + \frac{9S_t h^2 E_s r^2 L}{L_v G_s k_s} + \frac{9h L^2 E_s r^2}{L_v G_s k_s} + \frac{3h^3 E_s r^2}{L_v G_s k_s} + 2S_t L h^3 + S_t L^3 L_v + 3h L_v L^2 + 3S_t h^2 L_v L \right. \\
&\quad \left. + \frac{3h L E_s r^2}{G_s k_s} + 2h^4 + \frac{6S_t h L E_s r^2}{G_s k_s} + h L^3 + S_t L^4 + \frac{6h^2 E_s r^2}{G_s k_s} + \frac{3S_t L^2 E_s r^2}{G_s k_s} + L_v h^3 \right)
\end{aligned}$$

$$\begin{aligned}
\mu_{zx}^* &= -\frac{3}{2} \frac{\pi r^4 E_s \left(-\frac{3C_t^2 r^2 E_s}{G_s k_s L_v} - C_t^2 L_v + \frac{3E_s r^2}{G_s k_s L} + L \right)}{L_v^2 L C_t (h + L S_t) \left(\frac{9r^4 E_s^2}{L L_v^2 G_s^2 k_s^2} + C_t^2 L_v + \frac{3E_s r^2 L}{G_s k_s L_v} + \frac{6C_t^2 r^2 E_s}{G_s k_s L_v} + \frac{9C_t^2 E_s^2 r^4}{G_s^2 k_s^2 L_v^3} + L + \frac{3r^2 E_s}{L G_s k_s} \right)}; \\
\mu_{xz}^* &= \frac{3}{2} \frac{\pi r^4 C_t E_s \left(-\frac{3C_t^2 r^2 E_s}{G_s k_s L_v} - C_t^2 L_v + \frac{3E_s r^2}{G_s k_s L} + L \right)}{L_v L^2 (h + L S_t) \left(\frac{3C_t^2 r^2 E_s}{L_v G_s k_s} + C_t^2 L_v + \frac{9C_t^2 E_s^2 r^4}{G_s^2 k_s^2 L^2 L_v} + \frac{3C_t^2 L_v r^2 E_s}{G_s k_s L^2} + L + \frac{6r^2 E_s}{L G_s k_s} + \frac{9r^4 E_s^2}{L^3 G_s^2 k_s^2} \right)}.
\end{aligned} \tag{4.25}$$

The characteristic lengths for bending and torsion are next identified from the homogenized stiffness matrix as

$$\begin{aligned}
l_{b_{xy}}^2 &= \frac{K_{99}}{2(E_{45} + E_{44})}; \quad l_{b_{yx}}^2 = \frac{K_{66}}{2(E_{54} + E_{55})}; \quad l_{b_{yz}}^2 = \frac{K_{55}}{2(E_{67} + E_{66})}; \\
l_{b_{zy}}^2 &= \frac{K_{88}}{2(E_{76} + E_{77})}; \quad l_{b_{zx}}^2 = \frac{K_{77}}{2(E_{89} + E_{88})}; \quad l_{b_{xz}}^2 = \frac{K_{44}}{2(E_{98} + E_{99})}; \\
l_{t_{xy}}^2 &= \frac{K_{99} + K_{98}}{E_{44} + E_{45}}; \quad l_{t_{yx}}^2 = \frac{K_{66} + K_{67}}{E_{54} + E_{55}}; \quad l_{t_{yz}}^2 = \frac{K_{55} + K_{54}}{E_{66} + E_{67}}; \\
l_{t_{zy}}^2 &= \frac{K_{88} + K_{89}}{E_{76} + E_{77}}; \quad l_{t_{zx}}^2 = \frac{K_{77} + K_{76}}{E_{88} + E_{89}}; \quad l_{t_{xz}}^2 = \frac{K_{44} + K_{45}}{E_{98} + E_{99}}.
\end{aligned} \tag{4.26}$$

One additional micropolar constant, the coupling number N , determines the strength of the micropolar behavior; it is calculated for the three planes x-y, y-z and x-z as

$$\begin{aligned}
N_{xy}^2 &= \frac{E_{44} - E_{45}}{2E_{44}}; \quad N_{yx}^2 = \frac{E_{55} - E_{54}}{2E_{55}}; \quad N_{yz}^2 = \frac{E_{66} - E_{67}}{2E_{66}}; \\
N_{zy}^2 &= \frac{E_{77} - E_{76}}{2E_{77}}; \quad N_{zx}^2 = \frac{E_{88} - E_{89}}{2E_{88}}; \quad N_{xz}^2 = \frac{E_{99} - E_{98}}{2E_{99}}.
\end{aligned} \tag{4.27}$$

The micropolar material constants, the characteristic lengths in bending and torsion l_b and l_t , respectively, and the coupling number N , indicate the nature and significance of non-classical phenomena in the response of a medium with microstructure. The coupling number $0 \leq N \leq 1$ indicates the mechanisms producing micro-rotations and the contribution of the skew-symmetric part of the stress tensor or non classical effects (Eringen, 1999). The two extreme cases $N = 0$ and $N = 1$ denote classical-elasticity behavior and the coincidence of micro-rotations with macro-rotations respectively. The latter is known as couple-stress or Mindlin theory (Eringen, 1999), and it is a special case of micropolar elasticity with constrained micro-rotations which occurs when $\gamma \rightarrow \infty$. A value of N between zero and unity ($0 < N < 1$) denotes a micropolar behavior (Cowin, 1970).

4.4.1 Results and discussion

The anisotropic mechanical behavior of vertebral trabecular bone is largely determined by its trabecular architecture. The precise determination of the mechanical behavior requires the

determination of the geometrical and mechanical features of the micro-architecture of bone. Although detailed architectural measurements are not available for three-dimensional specimens, we suggest from visual inspection of several representative cross sections that the range of $\theta \in [10^\circ - 80^\circ]$ is reasonable to represent, on average, the relatively steep angle at which the oblique trabeculae lies relative to the horizontal. By contrast to the parameter θ , which could be reasonably estimated by visual inspection of the strut alignment, the geometrical model parameter h/L could not be reasonably estimated (from simple visual inspection). However, this parameter does affect the degree of anisotropy of the material. Therefore, to determine an appropriate value of h/L , we choose a value that results in a degree of material anisotropy consistent with previous measurements for the type of trabecular bone presented in (Ford and Keaveny 1996); specifically, we choose $h/L = 0.5$. Hence, a combination of $h/L = 0.5$ and $L_v/L = 1$ is used to simulate the anisotropic vertebral trabecular bone. We consider all struts (trabeculae) with identical cross-section geometry of diameter $d = 0.25\text{mm}$ and strut lengths $L = 1\text{mm}$ (Miller and Fuchs 2005). The mechanical parameters of the trabeculae building structure are: $G_s = 0.5 * E_s / (1 + \nu_s)$, with Poisson's ratio $\nu_s = 0.3$ (Yoo and Jasiuk 2006). The shear correction coefficient is $k_s = 9/10$. We plot the calculated homogenized elastic properties previously obtained for vertebral trabecular bone versus the geometrical parameter θ (Figures 4.26, 4.27, and 4.28), with a range of variation chosen in the interval $[10^\circ, 80^\circ]$; this range is also supported by Liu et al. (2009), who scanned specimens of vertebral trabecular bone using microcomputed tomography. Here and in the sequel, the ratio of the effective properties to the bulk value is recorded.

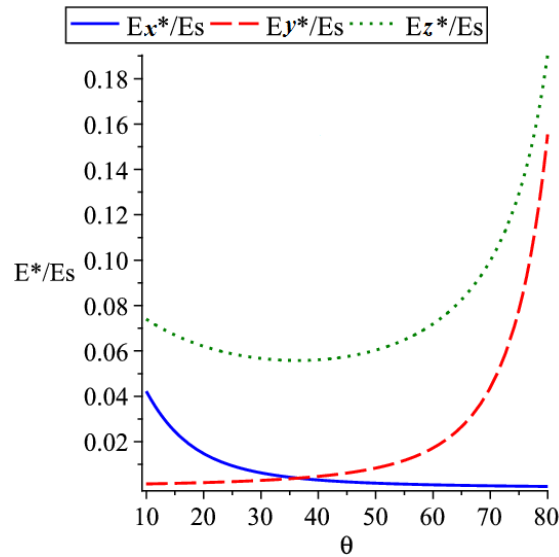


Figure 4.26: Effective elastic moduli E_x^* , E_y^* , and E_z^* of vertebral trabecular bone versus the geometrical parameter θ .

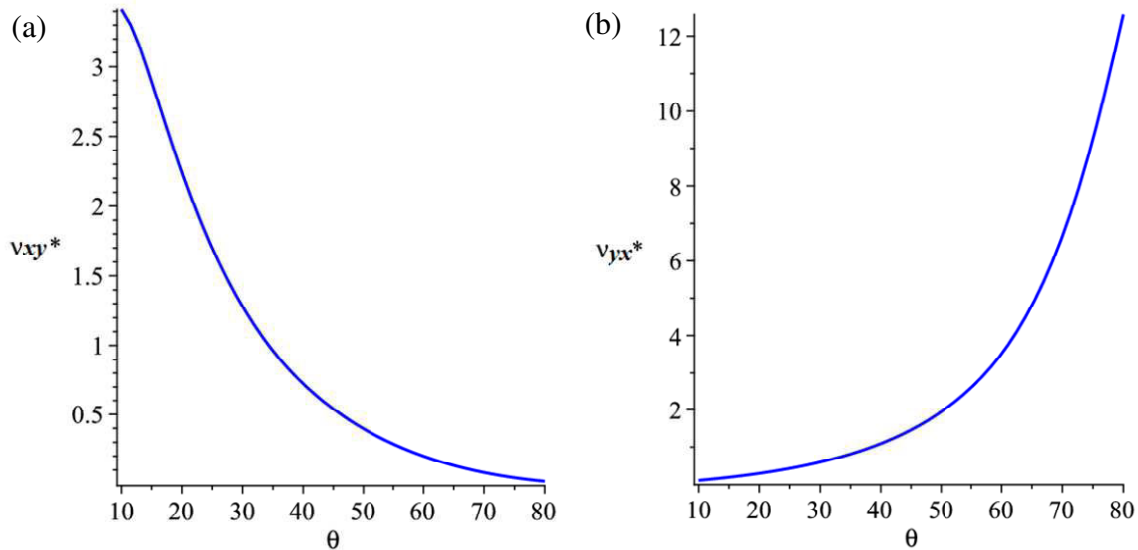


Figure 4.27: Effective in-plane Poisson's ratios of vertebral trabecular bone versus θ (a) ν_{xy}^* and (b) ν_{yx}^* .

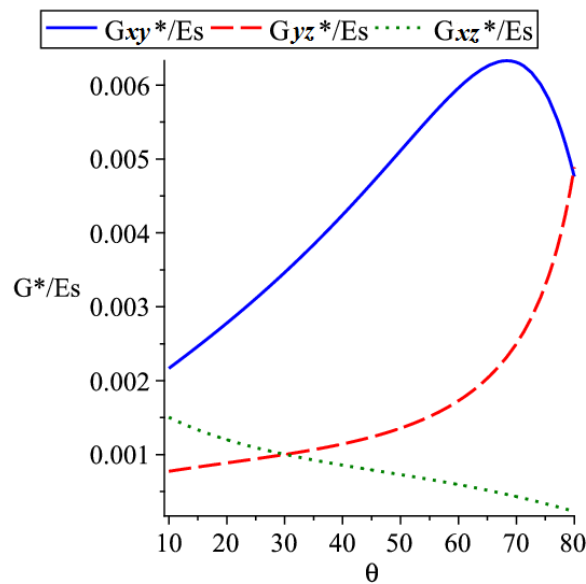


Figure 4.28: Effective shear moduli G_{xy}^* , G_{yz}^* , and G_{xz}^* of vertebral trabecular bone versus angle θ .

As can be seen on [Figure 4.26](#), the equivalent tensile modulus E_x^* exhibits a maximum for θ close to 10° and a minimum at 80° ; it shows strong variations around those two cell angle values. It is obvious that the Young's modulus E_y^* increases gradually with increasing θ , contrary to E_x^* ; it exhibits a maximum for θ close to 80° and a minimum at 10° maximum for θ close to 10° . Those evolutions can be explained as follows: when the inclination angle θ gets closer to zero (θ is nil), the bone architecture becomes close to a tetragonal topology, thus the equivalent tensile modulus along the x-direction (E_x^*) exhibits a maximum (the tensile modulus along the y-direction shows a minimum). The opposite situation occurs when the

angle θ gets closer to 90° . At about $\theta=35^\circ$, we note that the bone structure appears as isotropic ($E_x^* = E_y^*$). In addition, the Young's modulus E_z^* decreases slightly with θ to reach a minimum at about 40° and then further increases up to 80° . We note from Figure 4.28 that the effective in-plane shear modulus G_{xy}^* gradually increases with the inclination angle up to a maximum at about 70° , and then rapidly decreases. The out-of-plane shear moduli G_{yz}^* , G_{xz}^* have behaviours similar to those of E_y^* and E_x^* .

In order to reflect the impact of transverse shear deformations on the effective properties of vertebral trabecular structure, the scaling behavior of the equivalent elastic and shear moduli as well as of Poisson's ratios versus effective density is determined, considering the following geometrical parameters: $L_v = 0.5L$; $h = 0.5L$; $\theta = 30^\circ$ (Figures 4.29, 4.30, and 4.31). The obtained results show that the absence of transverse shear leads to overestimate Young's moduli (E_x^* and E_y^*) and the shear moduli (G_{xy}^* , G_{yz}^* , and G_{xz}^*) of vertebral trabecular bone; there is no such effect of transverse shear on E_z^* . We also note that neglecting shear deformation leads to underestimate the in-plane Poisson's ratios ν_{xy}^* and ν_{yx}^* .

The equivalent properties are obviously dependent on the relative densities of vertebral trabecular bone, as next results show. The elastic (E_x^* and E_y^*) and shear moduli (G_{xy}^* , G_{yz}^* , and G_{xz}^*) exhibit a power law dependency on the relative density (Figures 4.29 and 4.30 respectively); there is a linear dependence for E_z^* . Observe that the effective density takes high values (up to 0.3) due to the consideration of thick beams.

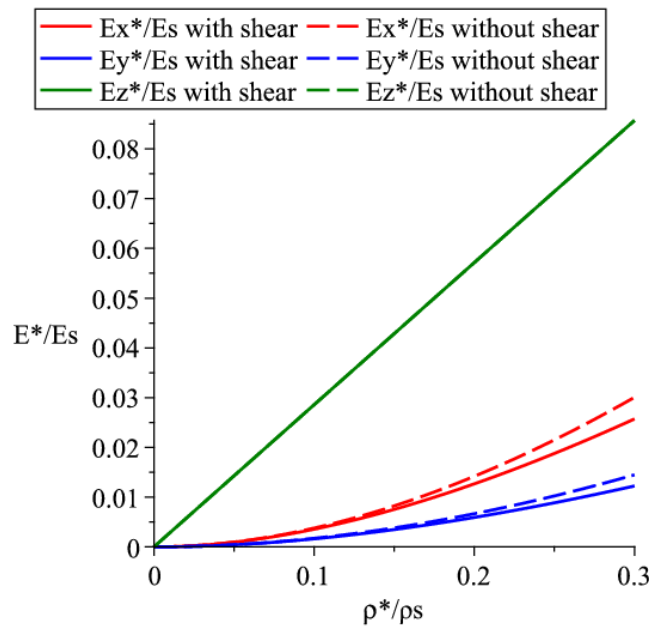


Figure 4.29: Effective elastic moduli E_x^* , E_y^* , and E_z^* of vertebral trabecular bone versus the relative density ρ^* / ρ_s and impact of transverse shear.

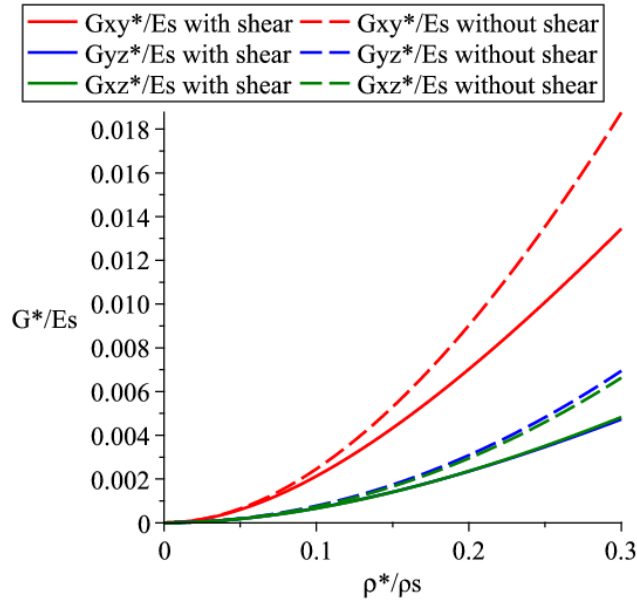


Figure 4.30: Effective shear moduli G_{xy}^* , G_{yz}^* , and G_{xz}^* of vertebral trabecular bone versus the relative density ρ^* / ρ_s and impact of transverse shear.

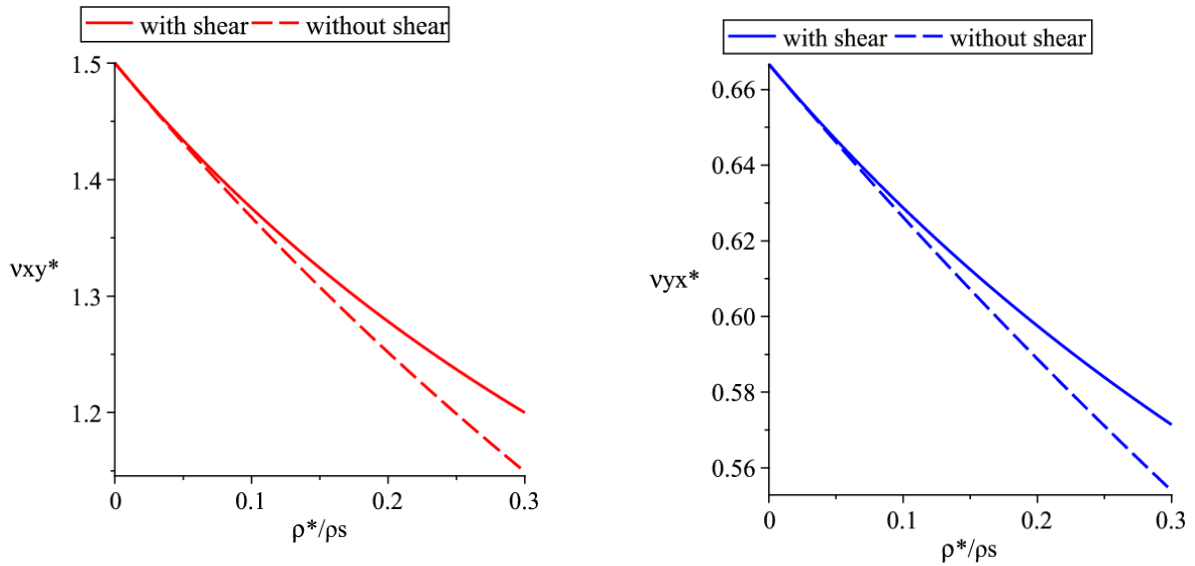


Figure 4.31: Effective Poisson's ratios ν_{xy}^* and ν_{yx}^* of vertebral trabecular bone versus the relative density ρ^* / ρ_s and impact of transverse shear.

Two main aspects of the homogenization method and effective micropolar bone model shall be analyzed in the sequel: the justification of the micropolar effects and the validation of the method in terms of the accuracy of the predicted effective properties.

4.4.1.1 Relevance of the choice of a micropolar effective continuum

In order to assess the relevance of a micropolar continuum model, the characteristic lengths and coupling number for the micropolar behaviour respectively described by equations (4.26)

and (4.27), are evaluated versus the angle θ . The ratio of the characteristic internal micropolar lengths for bending and torsion, quantities l_b and l_t , to the characteristic unit cell size, the factor $2L\cos(\theta)$, are plotted to assess the strength of the micropolar effect (Figures 4.32a-c). It appears that those ratio reach values close to unity (and higher than unity for $l_{b_{zx}}, l_{t_{zx}}$), indicating that micropolar effects indeed impact the continuum behavior.

Furthermore, the coupling number N is plotted against the angle θ , to point out the nature and significance of non-classical phenomena in the response of bone considered as a medium with a microstructure (Figure 4.32d). It is recognized that values of the coupling number between zero and one ($0 < N < 1$) indicate a micropolar behaviour: this appears to be the case for the three planes, and for all values of the cell angle θ in the considered range.

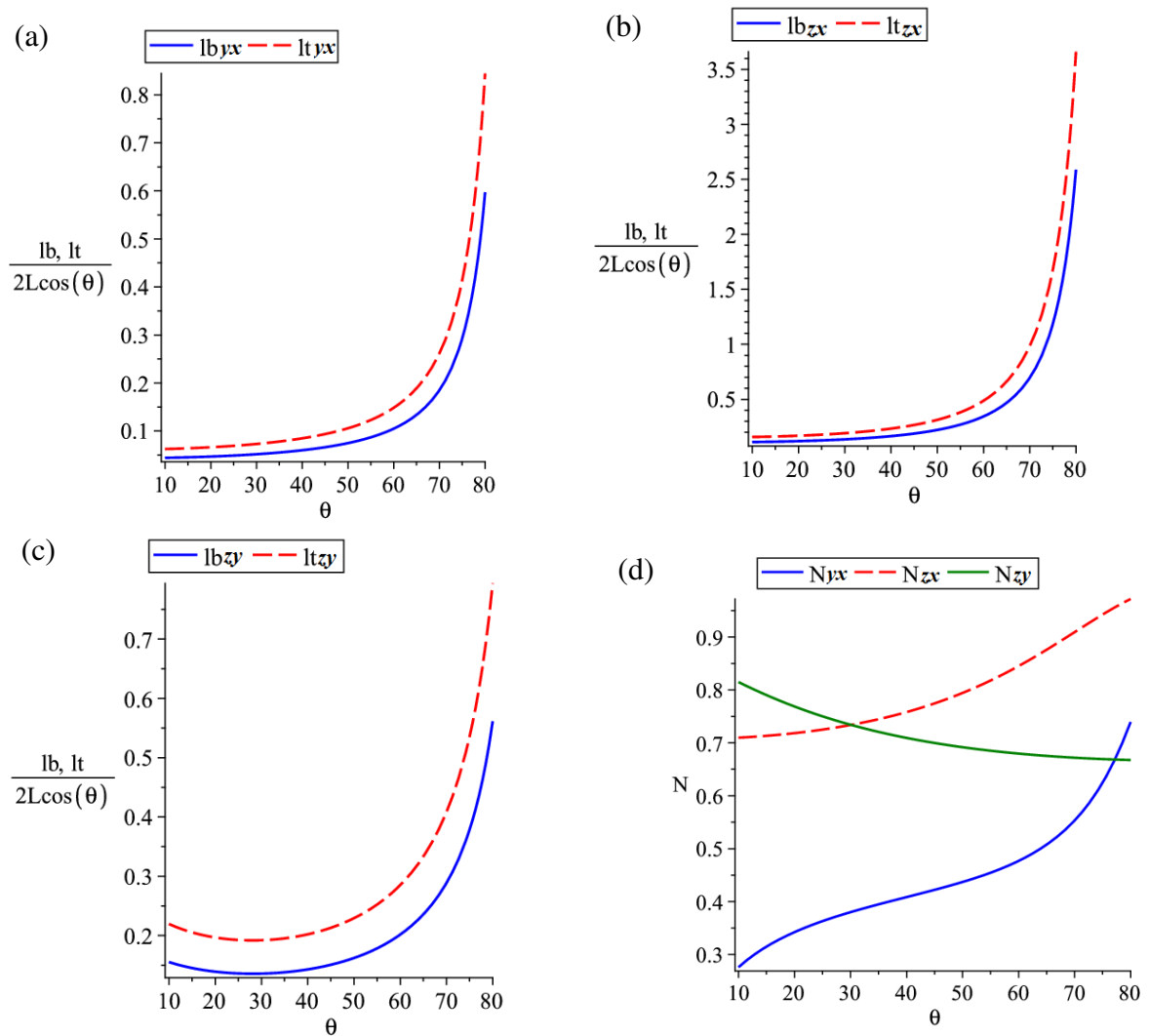


Figure 4.32: (a), (b), (c) Ratio of the characteristic micropolar lengths in bending and torsion to the unit cell size of vertebral trabecular bone and (d) Micropolar coupling number versus the angle $\theta \in [10^\circ - 80^\circ]$.

As mentioned earlier, the classical and micropolar shear moduli, respectively quantities G^* and μ^* , are related by $G^* = \mu^* + \kappa/2$; the coefficient $2\mu^* + \kappa$ in micropolar elasticity

replaces the term $2G^*$ in classical elasticity. The case $\kappa = 0$ corresponds to a decoupling of the rotational and translational degrees of freedom, hence the solid becomes classically elastic; the coupling number N then vanishes and the shear modulus μ^* is identical to the classical continuum theory ($\mu^* = G^*$). One observes (Figure 4.33) a correlative increase of the micropolar shear constant κ and of the coupling number N . We also notice the negative values of μ_{yz}^*/G_{yz}^* in the range $\theta = 60^\circ \sim 80^\circ$ in which the coupling number is greater than 0.7. As mentioned by (Jeong et al. 2008), values of the coupling number larger than $1/\sqrt{2}$ lead to negative μ^* . Subsequently, in order to preserve the positive definiteness of strain-energy density, upper and lower bounds for the coupling number should be chosen such that $0.1 \leq N \leq 1/\sqrt{2}$.

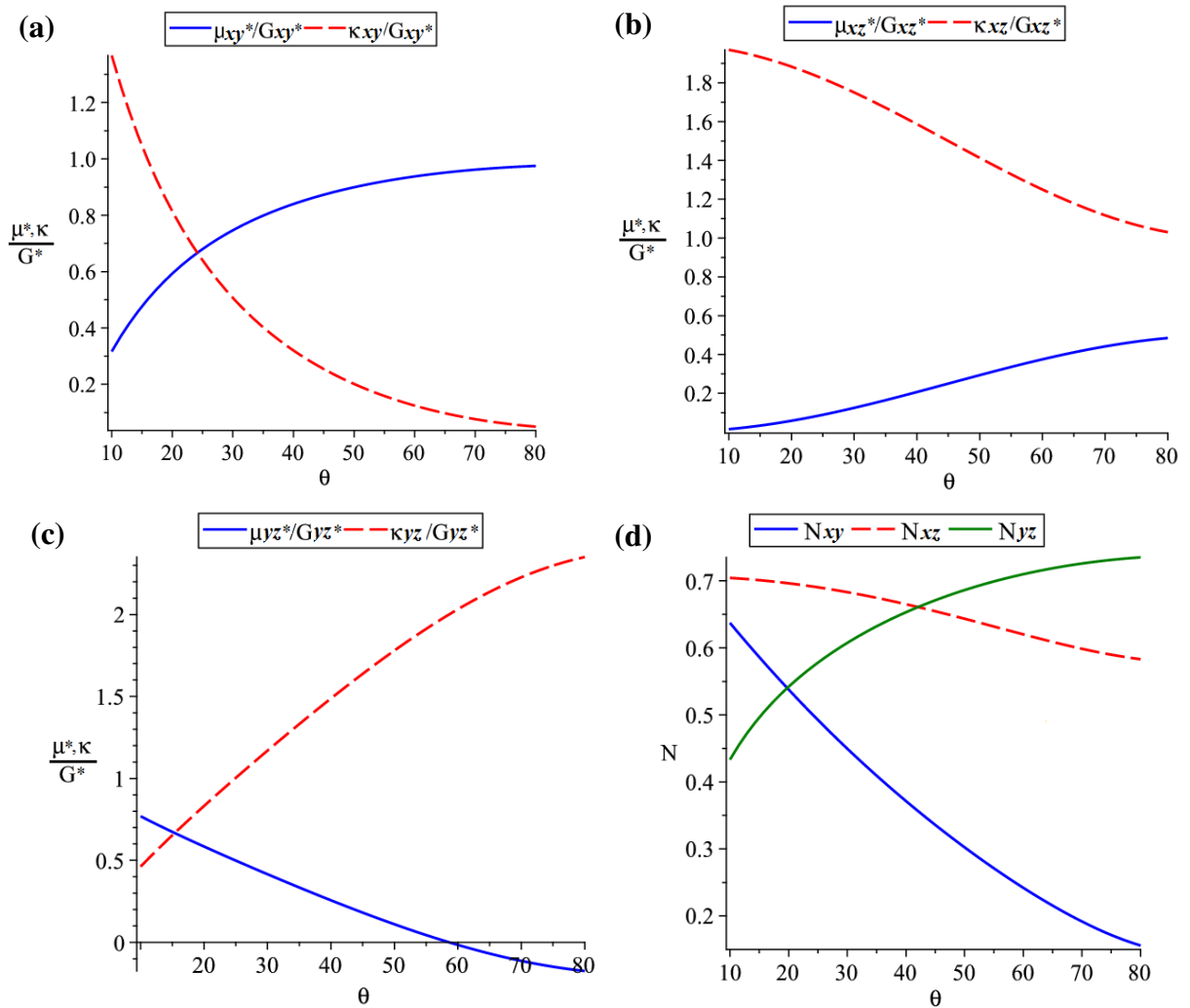


Figure 4.33: Non dimensional micropolar anisotropic linear media material constants of vertebral trabecular bone: μ^*/G^* and κ/G^* variations and its corresponding coupling number N versus the geometrical parameter $\theta \in [10^\circ - 80^\circ]$.

In order next to assess the accuracy of the calculated effective properties, numerical simulations are performed to calculate those properties from a micromechanical model of vertebral trabecular bone.

4.4.1.2 Finite element validation

In this subsection, a numerical homogenization approach is applied to evaluate the accuracy of the effective properties predicted by the homogenization scheme. The finite element simulations presented here are performed over a representative volume element of the bone structure, equivalent to the unit cell of vertebral trabecular bone previously used in the analytical homogenization. The moduli are compared with those issued from the discrete homogenization analysis developed in the previous sections. Only the classical moduli will be computed and compared with those obtained from discrete homogenization.

The developed finite element model consists of three basic steps. Firstly, appropriate periodic boundary conditions are applied to the representative unit cell. Subsequently, the non-homogenous strain fields obtained from the analysis are integrated to define volume averaged strains. Finally, the effective elastic coefficients of the vertebral trabecular bone structure are obtained as the ratio of the average stress to the average strain. The average stresses and strains in the unit cell are defined by

$$\bar{\sigma}_{ij} = \frac{1}{V_u} \int_{V_u} \sigma_{ij} dV_u ; \quad \bar{\epsilon}_{ij} = \frac{1}{V_u} \int_{V_u} \epsilon_{ij} dV_u \quad (4.28)$$

where V_u is the volume of the periodic unit cell, and σ_{ij} and ϵ_{ij} are the local (microscopic) stresses and strains (in the unit cell). The average strain $\bar{\epsilon}_{ij}$ can be related to the periodic boundary displacements of the unit cell by means of the divergence theorem (Lai et al., 1993) as follows:

$$\bar{\epsilon}_{ij} = \frac{1}{V_u} \int_{V_u} \epsilon_{ij} dV_u = \frac{1}{2V_u} \int_S (u_i n_j + u_j n_i) dS \quad (4.29)$$

where S is the boundary surface of the unit cell, u_i the displacement and n_j the unit exterior normal to S . Since the analysis is based on the RVE, periodical boundary conditions should be applied in the model to obtain a reasonable stress distribution. Two continuity conditions must be satisfied at the boundary surfaces of the neighbouring unit cells: the displacements must be continuous, and the traction distribution at the opposite parallel boundaries of the unit cell must be uniform.

As previously mentioned, the equivalent vertebral trabecular microstructure model consists of repeatable cells within the 3D space; Figure 4.34 depicts the geometry of vertebral trabecular unit cell. Since the microstructure is repeatable, only one cell needs to be analysed, with periodic boundary conditions. A condition of continuity of the displacement has been prescribed to the boundaries of the unit cell, in terms of periodic displacement boundary conditions. Hence, opposite surfaces of the unit cell are constrained to have an equivalent deformation state.

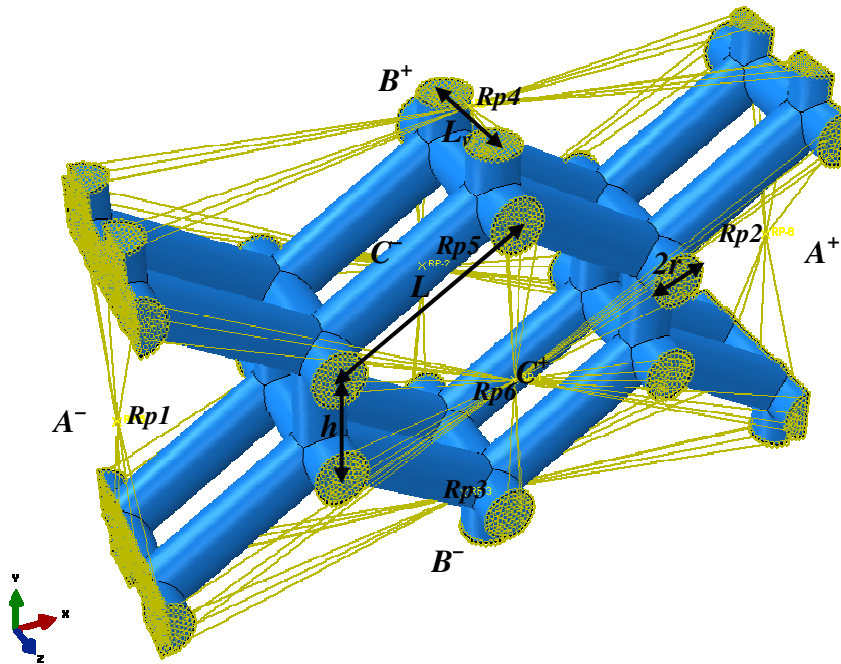


Figure 4.34: Geometry of a repeatable vertebral trabecular structural unit cell with periodic boundary conditions.

The periodic boundary conditions must be applied on the boundary of the unit cell model shown in Figure 4.34, to ensure that there is no separation or overlap between the neighbouring unit cells. We apply the nodal displacement constraint equations (3.11) in the finite element procedure directly as the boundary conditions.

To this end, the unit cell has been meshed by the so called C3D10 element, a 10-nodes quadratic tetrahedral finite element, used in ABAQUS environment and the analysis has been performed using a linear perturbation analysis. We have performed simulations with different number of elements; results are here presented for the finer meshes (88,574 elements and 137,091 nodes). In order to apply the constraint equations (3.11), the six side surfaces are defined as sets, which are actually the boundaries and then the nodal degree of freedom on each surface (set) is constrained by an equation written for the degree of freedom of a reference point (six reference points are defined, labelled Rp1, Rp2, ... Rp6). The reference point does not belong to the main geometry of the unit cell for adjusting movements on the unit cell surface (to implement the periodic and loading boundary conditions). This mechanical constraint enforces all the nodes on the plane to have the same displacement in the specified direction, which means those nodes remain in the same plane. Because of the different kinematic conditions for applying the loading on the unit cell in axial and shear tests, separate sets of interactions will be defined. However, it should be noted that both of these interaction sets are designed in a way to satisfy the periodic boundary conditions when applying the macroscopic displacement field on the unit cell. The coupling here is quite similar to the equation constraint defined for the axial loadings.

In order to calculate the effective properties of vertebral trabecular bone, the general strain–stress relationship for an orthotropic material is expressed in matrix format as

$$\left[\tilde{\epsilon}_{ij} \right] = \left[S_{ij}^{eff} \right] \left[\tilde{\sigma}_{ij} \right] \quad (4.30)$$

where $\left[S_{ij}^{eff} \right]$ is the effective compliance matrix, written as

$$\left[S_{ij}^{eff} \right] = \begin{bmatrix} S_{11}^{eff} & S_{12}^{eff} & S_{13}^{eff} & 0 & 0 & 0 \\ S_{12}^{eff} & S_{22}^{eff} & S_{23}^{eff} & 0 & 0 & 0 \\ S_{13}^{eff} & S_{23}^{eff} & S_{33}^{eff} & 0 & 0 & 0 \\ 0 & 0 & 0 & S_{44}^{eff} & 0 & 0 \\ 0 & 0 & 0 & 0 & S_{55}^{eff} & 0 \\ 0 & 0 & 0 & 0 & 0 & S_{66}^{eff} \end{bmatrix} \quad (4.31)$$

According to the relationship between the engineering elastic constants and the compliance matrix S_{ij} , nine independent effective elastic constants of 3D vertebral trabecular bone can be calculated as

$$\begin{aligned} E_x^* &= \frac{1}{S_{11}^{eff}}; \nu_{xy}^* = -\frac{S_{12}^{eff}}{S_{11}^{eff}}; G_{xy}^* = \frac{1}{S_{44}^{eff}}; \\ E_y^* &= \frac{1}{S_{22}^{eff}}; \nu_{xz}^* = -\frac{S_{13}^{eff}}{S_{11}^{eff}}; G_{xz}^* = \frac{1}{S_{55}^{eff}}; \\ E_z^* &= \frac{1}{S_{33}^{eff}}; \nu_{yz}^* = -\frac{S_{23}^{eff}}{S_{22}^{eff}}; G_{yz}^* = \frac{1}{S_{66}^{eff}}. \end{aligned} \quad (4.32)$$

A Python programming subroutine has been written within the ABAQUS environment, in order to get the effective properties automatically.

By assuming a set of the global strain, $\tilde{\epsilon}_{ij}$, and applying the periodic boundary conditions in the form of equation (3.11), we obtain a unique stress distribution of the unit cell. Then the global stress, $\tilde{\sigma}_{ij}$, corresponding to this set of global strain, is obtained; the effective compliance matrix S_{ij} is evaluated from equation (4.30).

We consider to be specific a unit cell of vertebral trabecular bone with the following geometrical parameters: $r=0.125\text{mm}$, $L=1\text{mm}$, $L_v=0.5\text{mm}$, $h=0.5\text{mm}$, and $\theta=30^\circ$; the bulk modulus of the trabeculae is chosen as $E_s=12000\text{MPa}$, Poisson's ratio $\nu_s=0.3$, and density 2000kg/m^3 (Gibson, 2005). We do not take into account the heterogeneity of properties inside the trabeculae, although researchers showed that properties of trabecular bone at the tissue level are heterogeneous (e.g. Harrison et al., 2008). Also, some experimental data indicates anisotropy in the properties of trabeculae; bone tissue stiffness depends on direction (e.g. van Eijden et al. 2004). We follow here instead most of the works which assume a homogeneous and isotropic behaviour of the trabeculae, e.g. Kim and Al-Hassani (2002), Gibson (2005), Yoo and Jasiuk (2006), and Liu et al. (2009).

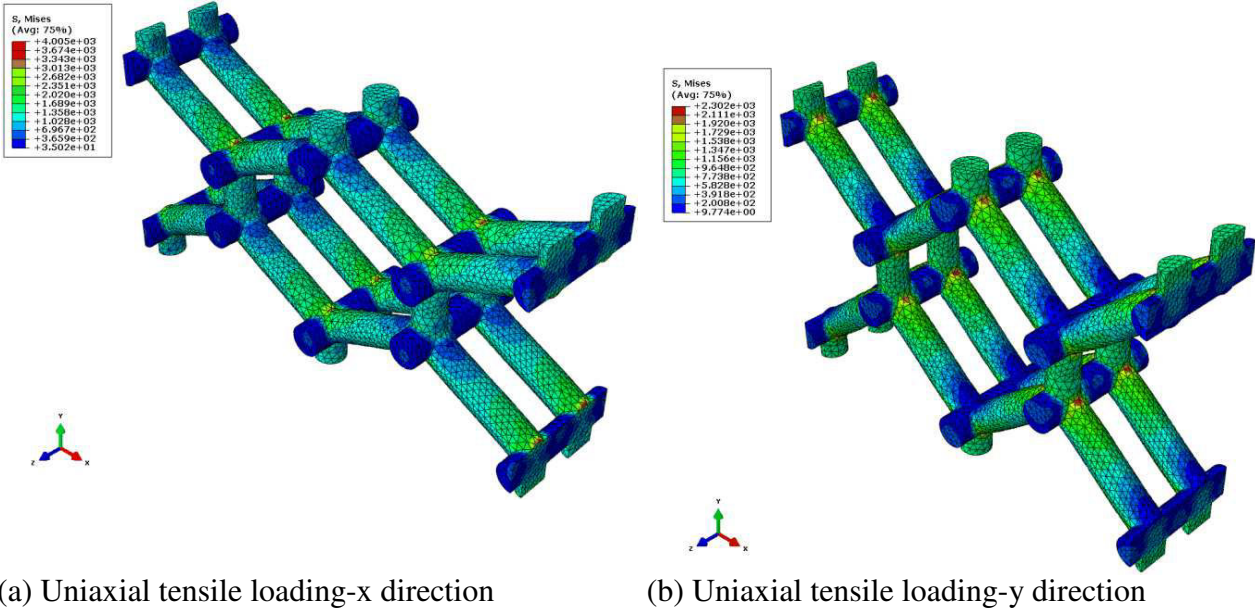
As shown in Table 4.5, a relatively good agreement is obtained between the moduli predicted by finite elements and those calculated by discrete homogenization. In Figures 4.35a-c, the contour plots of the von Mises effective stress within the unit cells are shown for uniaxial tensile loadings in x, y directions, as well as for shear loading in the y-z plane.

Table 4.5: Normalized elastic constants predicted by homogenization and FE simulations.

Non-dimensional elastic constants	ABAQUS	Discrete homogenization	%	Abaqus – Hom
				Abaqus
E_x^* / E_s	0.014	0.013		7.1
E_y^* / E_s	0.0067	0.0059		11.9
E_z^* / E_s	0.059	0.057		3.3
G_{xy}^* / E_s	0.0056	0.0069		23.2
G_{xz}^* / E_s	0.0030	0.0024		20.0
G_{yz}^* / E_s	0.0027	0.0023		14.8
ν_{xy}^*	1.27	1.28		0.8
ν_{yx}^*	0.57	0.59		3.5

The relative density $\rho^* / \rho_s = 0.19$, so the apparent density = 380 kg/m³

The more pronounced differences (up to 23%) between both moduli occur under shear (the homogenized tensile moduli are predicted with a better accuracy) can be explained by the occurrence of stress gradients appearing at the articulation of beams within the unit.



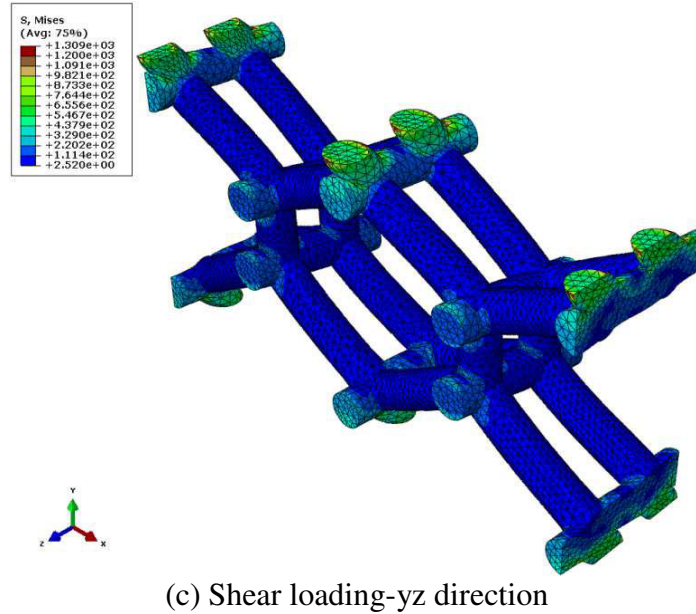


Figure 4.35: Contour plot of von Mises effective stress after uniaxial tensile ((a) and (b)) and shear (c) loading.

4.4.1.3 Discussion and limitations

There is a limitation of our microstructural models that should be discussed when extrapolating the results to real trabecular bone: simple observations indeed reveal that the trabeculae are most of the time not perfectly uniform, but have a certain degree of non uniformity due to the natural variance in trabecular thickness for real vertebral bones. Models for such a variation of cross-section have been proposed such as the double-tapered shape model in (Kim and Al-Hassani, 2002), with a cross-section area minimal at the center and maximum at the base (Figure 4.36, right view). A correction of this approximation by the trabeculae thickening could recover the part of the reduction due to considering the idealized uniform cross-sectional area. Detailed information on the strut morphology near the strut joints is not available in the literature and experimental measurements of the variation in strut thickness are lacking as well. Gefen et al. 2008 reported that the maximal thickness at the ends of the bases of a trabecula d_{max} (at the junctions of the lattice) is proportional to the minimal thickness at the center of a trabecula d_{min} , adopting the relation $d_{max} = 0.9922d_{min} + 60.174$ (μm). This linear proportion is observed by measuring the d_{max} and d_{min} dimensions of the trabeculae of canine cancellous bone from digital optical micrographs.

We next consider an extension of our model in order to compensate the thickening near the strut joints by an additional thickness of the strut. The diameter of the strut midway between large and small diameters shall be adopted as the average thickness of an equivalent uniform trabecula, $d = (d_{max} + d_{min}) / 2$, as pictured on Figure 4.36.

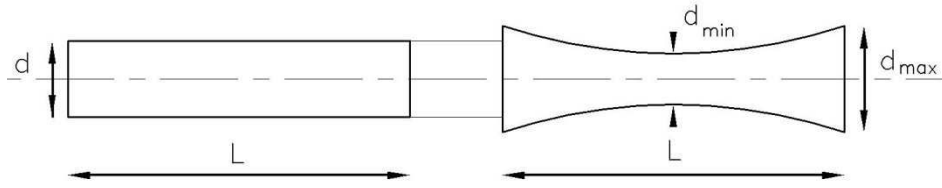


Figure 4.36: Geometric dimensions of rod-like trabecula: Right: base thickness (d_{\max}) and minimum thickness at the centre (d_{\min}). Left: Equivalent uniform strut with diameter $d = (d_{\max} + d_{\min}) / 2$.

The mechanical properties of trabecular bone according to this enhanced geometrical model will be modified, due to the increase of the relative density of trabecular bone. The scaling behavior of the equivalent elastic and shear moduli versus the effective relative density is next obtained to highlight the effect of increasing trabeculae thickness; we adopt the following geometrical microparameters: $d_{\min} = 0.25\text{mm}$; $L_y = 0.5L$; $h = 0.5L$; $\theta = 30^\circ$ (see Figures 4.37-4.39). The relative elastic and shear moduli vary as power law functions of the relative density ρ^* / ρ_s (except for E_z^* / E_s varies linearly) for both geometric dimensions of the initial and extended model, based respectively on d_{\min} and $d = (d_{\max} + d_{\min}) / 2$, given in Table 4.6.

Table 4.6: Relationships between the relative Young's and shear moduli as well as Poisson's ratios versus relative density for two types of trabecular geometry.

	d_{\min} (at the centre)	$d = (d_{\max} + d_{\min}) / 2$
Young's moduli	$E_x^* / E_s = 0.26 (\rho^* / \rho_s)^{1.89} \quad R^2=0.99$	$E_x^* / E_s = 0.38 (\rho^* / \rho_s)^{1.87} \quad R^2=0.99$
	$E_y^* / E_s = 0.13 (\rho^* / \rho_s)^{1.91} \quad R^2=0.99$	$E_y^* / E_s = 0.19 (\rho^* / \rho_s)^{1.89} \quad R^2=0.99$
	$E_z^* / E_s = 0.285 (\rho^* / \rho_s) \quad R^2=1$	$E_z^* / E_s = 0.357 (\rho^* / \rho_s) \quad R^2=1$
Shear Moduli	$G_{xy}^* / E_s = 0.13 (\rho^* / \rho_s)^{1.81} \quad R^2=0.99$	$G_{xy}^* / E_s = 0.17 (\rho^* / \rho_s)^{1.78} \quad R^2=0.99$
	$G_{yz}^* / E_s = 0.048 (\rho^* / \rho_s)^{1.87} \quad R^2=0.99$	$G_{yz}^* / E_s = 0.068 (\rho^* / \rho_s)^{1.85} \quad R^2=0.99$
	$G_{xz}^* / E_s = 0.05 (\rho^* / \rho_s)^{1.89} \quad R^2=0.99$	$G_{xz}^* / E_s = 0.07 (\rho^* / \rho_s)^{1.88} \quad R^2=0.99$
Poisson's ratio	$\nu_{xy}^* = -0.098 (\rho^* / \rho_s) + 1.48 \quad R^2=0.99$	$\nu_{xy}^* = -1.15 (\rho^* / \rho_s) + 1.47 \quad R^2=0.98$
	$\nu_{yx}^* = -0.32 (\rho^* / \rho_s) + 0.66 \quad R^2=0.99$	$\nu_{yx}^* = -0.37 (\rho^* / \rho_s) + 0.66 \quad R^2=0.99$

The Young's moduli (E_x^*, E_y^*) and shear moduli ($G_{xy}^*, G_{yz}^*, G_{xz}^*$) are approximately 50% higher than those of trabeculae with minimum thickness at the centre, while E_z^* shows an increase by about 25%, as shown on [Figures 4.37](#) and [4.38](#).

There is no comprehensive experimental evidence to fully verify the predicted homogenized mechanical behavior by comparison with real cancellous bone, due to an insufficient amount of experimental data: in most cases, only the longitudinal stiffness modulus is determined. Experimental studies generally neglect the issue of principal directions of orthotropy: the specimens are cut in arbitrary directions and the measured data are thus not sufficient to determine the principal directions. A number of authors have measured the elastic modulus of vertebral trabecular bone. [Kopperdahl et al. \(2002\)](#) tested human vertebral trabecular bone and obtained a mean elastic modulus of 319 ± 189 MPa with apparent density in the range 0.09-0.38 g/cm³. [Keaveny et al. \(1997\)](#) measured the Young's modulus of human vertebral bone by compression tests as 165 ± 110 MPa with a mean value of apparent density of 0.14 ± 0.06 g/cm³. [Kopperdahl and Keaveny \(1998\)](#) reported the elastic moduli from compression of human vertebral specimens to be 291 ± 113 MPa, with a wet apparent density of 0.17 ± 0.04 g/cm³. Moreover, [Cendre et al. \(1999\)](#) measured by compression tests an average Young's modulus of human lumbar cancellous bone of 134 ± 81 MPa, for a bone volume fraction of $17.77 \pm 5.65\%$. [Banse et al. \(2002\)](#) measured the average elastic modulus of human vertebral cancellous bone of 352 ± 145 MPa and the mean apparent density of the samples as 0.174 ± 0.052 g/cm³, while [Morgan and Keaveny \(2001\)](#) measured a similar value of 344 ± 148 MPa from compression tests of human vertebral trabecular bone specimens, with a mean apparent density of 0.18 ± 0.05 g/cm³. [Morgan et al. \(2003\)](#) reported power-law regressions between modulus E^* (in MPa) and apparent density ρ^* (in g/cm³) as $E^* = 4730\rho^{*1.56}$, from tension and compression tests of human vertebral trabecular bone; the mean measured value of apparent density is 0.18 g/cm³. [Wolfram et al. \(2010\)](#) performed non-destructive macroscopic mechanical compression and tension tests on human vertebral bones, reporting apparent Young's moduli of 424 MPa in compression and 439 MPa in tension; morphological analysis of the samples yielded volume fraction of $11 \pm 0.03\%$. [Havill et al. \(2010\)](#) reported a mean elastic modulus of $813.10 \pm 419.28\%$ MPa for vertebral trabecular bone of baboons, with bone volume fraction of $29.93 \pm 8.16\%$.

[Hu et al. \(2002\)](#) performed nondestructive compression tests in the lumbar vertebral specimens of dogs in the anteroposterior (AP) and left-right (LR) directions, and destructive compression tests are performed in the cephalocaudal (CC) direction: the measured Young's moduli are respectively 209 ± 54 MPa, 269 ± 96 MPa, and 967 ± 83 MPa in (AP), (LR), and (CC), with an apparent density of 0.35 ± 0.03 g/cm³, a tissue density of 2.05 ± 0.01 g/cm³ and bone volume fraction of $19 \pm 2\%$; those moduli are normalized with respect to the mean value $E_s = 19.9 \pm 2.5$ GPa, computed by [Jorgensen and Kundu \(2002\)](#) from a canine distal femur using a 1 GHz acoustic microscope.

Shear properties of trabecular bone received limited attention, perhaps due to the experimental and conceptual difficulties encountered when testing such highly anisotropic porous structures. The shear moduli for cancellous bone are rarely measured; e.g. in (Ashman et al., 1986), the mean shear modulus is measured using an ultrasonic technique in the range 58-89 MPa. Wolfram et al. (2010) reported apparent shear modulus of 85 MPa by performing non-destructive macroscopic mechanical torsion tests on human vertebral trabecular samples with volume fraction of $11 \pm 0.03\%$. Kasra and Gryn timer (2007) performed torsion testing on ovine vertebral cancellous bones, reporting shear modulus of $282 \pm 81 \text{ MPa}$ and a mean apparent density of $0.69 \pm 0.07 \text{ g/cm}^3$; the shear is normalized with respect to the Young's modulus of a single trabecula for sheep, measured by Lorenzetti (2006) as $15.0 \pm 1.4 \text{ GPa}$. Moreover, Wang et al. (2005) measured the mean shear modulus as $183 \pm 75 \text{ MPa}$ by conducting torsion tests on bovine tibial trabecular bone samples of volume fraction $26.3 \pm 0.041\%$.

We have plotted on Figures 4.37 and 4.38 the variation of the effective mechanical properties obtained by our model, together with previously mentioned measurements. The computed values of Young's and shear moduli compare well with the reported experimental values; however, measurements are dispersed around our anisotropic computed values, partially due to the arbitrary directions in which specimens are cut (the principal directions are undetermined). Another source of discrepancy is the variation of the geometry (the tested struts have different lengths and thicknesses, which are in most cases not described) and location of the tested samples.

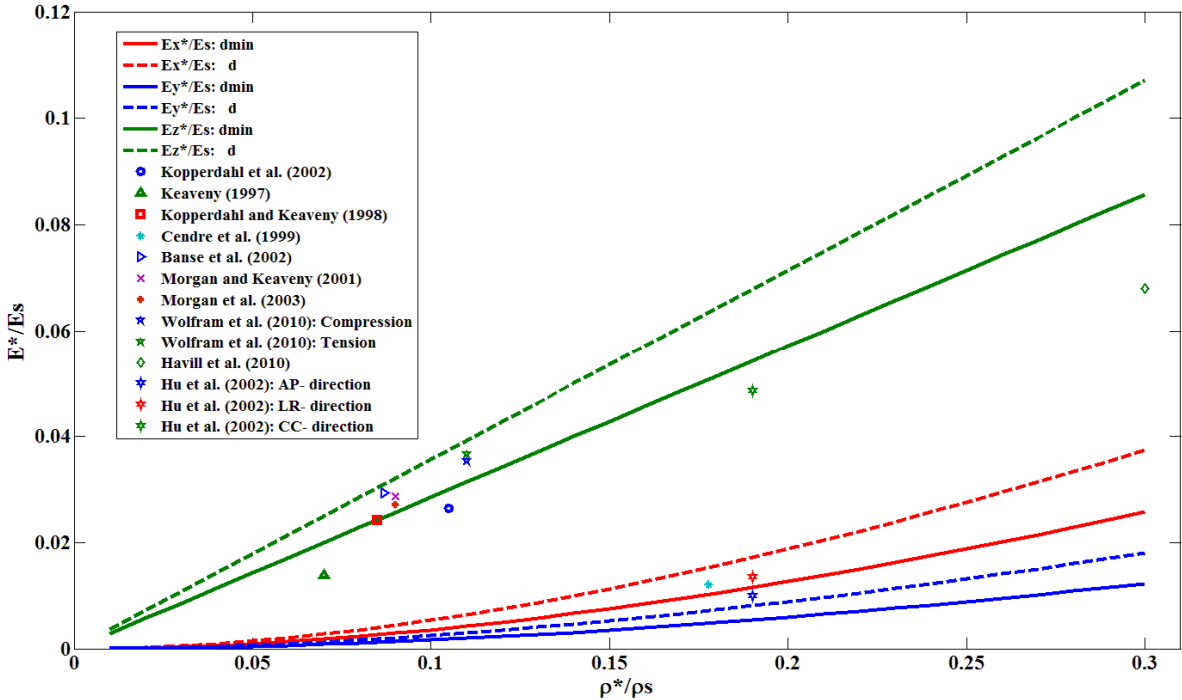


Figure 4.37: Normalized homogenized effective Young's moduli of vertebral trabecular bone and experimental values from literature plotted against relative density.

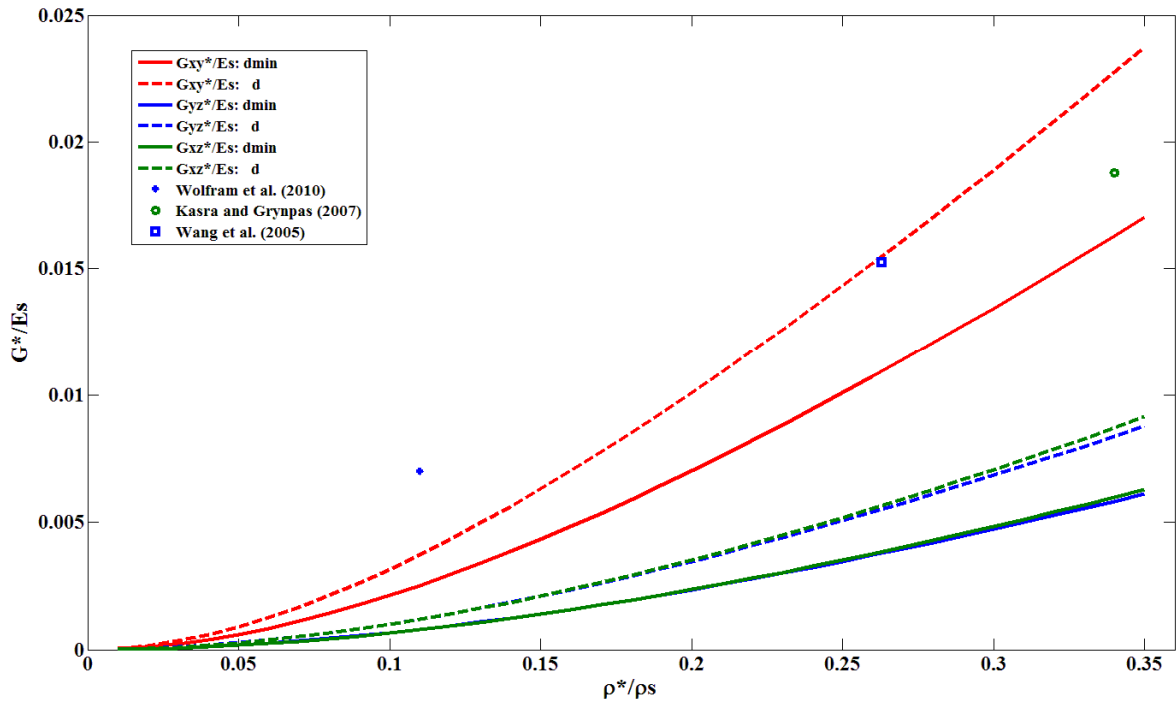


Figure 4.38: Normalized homogenized effective shear moduli of trabecular bone and experimental values from literature plotted against relative density.

Finally, the anisotropic Poisson coefficients are never reported to be investigated experimentally. The calculated Poisson's ratios are shown to only weakly depend on relative density (Figure 4.39).

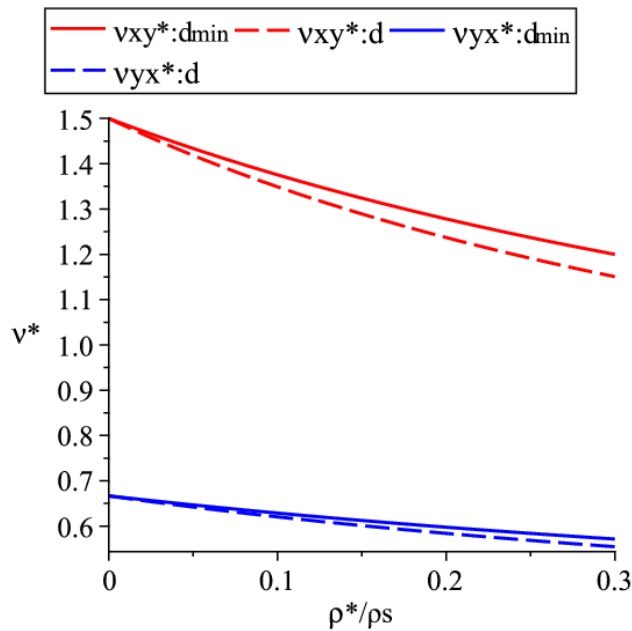


Figure 4.39: In-plane Poisson's ratios of vertebral trabecular bone plotted against relative density.

4.5 Conclusions

A micromechanical approach of microstructural effects of trabecular bone has been developed. As a main novelty, a Cosserat anisotropic continuum model has been developed from the discrete homogenization of a quasi periodical lattice model of the cancellous bone microstructure, whereby the effective mechanical properties of bone are directly related to the lattice micro-geometry and micromechanical elastic properties. The cell walls of this cellular material are modeled as linear elastic Timoshenko beams, accounting for the transverse shear occurring in thick beams in the regime of high bone density. The first stiffness tensor and the second couple stress stiffness tensor have been evaluated, allowing in turn the identification of the micropolar (non classical) constants of cancellous bone (in addition to the classical moduli), including internal flexural lengths. The equivalent moduli have been recorded versus the geometrical descriptors of the unit cell. A planar linear Cosserat finite element model of a cracked bone sample has been developed on the basis of the constructed effective Cosserat continuum, in order to illustrate the microstructural effects on the macroscopic response of cancellous bone. The FE analysis of the cracked configuration evidence an important reduction of the stress concentration in the vicinity of the crack; this feature reflects the trabecular architecture of cancellous bone and the regularizing effect of the employed Cosserat elasticity model. The effective micropolar rigidities properties obtained from discrete homogenization are in very good agreement with corresponding rigidities provided by FE simulations over a unit cell.

Such micromechanically based enhanced continuum models developed at the mesoscopic scale pave the way towards realistic simulations of the mechanical response of complete bone structures submitted to complex loadings.

The developed homogenization model constitutes an interesting tool for an efficient virtual experimentation of the mechanical behavior of lattices endowed with diverse topologies, and can therefore next be adapted to model many repetitive representative cells of bone by which the main structural features of the trabecular microstructure can be characterized, such as tapered hexagonal and tetrakaidecahedral morphologies, or topologies acquired from microcomputed tomography.

CHAPTER 5: IDENTIFICATION OF COUPLE-STRESS MODULI OF VERTEBRAL TRABECULAR BONE: FINITE ELEMENT STUDY

The purpose of this chapter is to develop a homogeneous, orthotropic couple-stress continuum model as a substitute of the 3D periodic heterogeneous cellular solid model of vertebral trabecular bone. Vertebral trabecular bone is presently modeled as a porous material with an idealized periodic structure made of 3D open cubic cells, which is effectively orthotropic. The effective properties are obtained based on the response of the representative volume element under prescribed boundary conditions. Mixed boundary conditions comprising both traction and displacement boundary conditions are applied on the structure boundaries. The effective mechanical constants of the effective couple-stress continuum are deduced by an equivalent strain energy method. The characteristic lengths for bending and torsion are identified from the resulting homogenized orthotropic moduli. We conduct this study computationally using a finite element approach. Vertebral trabecular bone is modeled either as a cellular solid or as a two-phase material consisting of bone tissue (stiff phase) forming a trabecular network, and surrounding soft tissue referring to the bone marrow present in the pores. Both the bone tissue forming the network and the pores are assumed to be homogeneous linear elastic, and isotropic media. The effects of scale and boundary conditions on the predicted couple stress moduli of these networks are investigated by varying the size of the bone specimens over which the boundary conditions are applied. The analysis using mixed boundary conditions gives results that are independent of unit cell size when computing the first couple stress tensor, while it is dependent on the cell size as to the second couple stress tensor moduli. This study provides overall guidance on how the size of the trabecular specimen influence couple stresses elastic moduli of cellular materials, with focus on bones. The developed approach is quite general and applicable to any heterogeneous cellular and composite materials.

5.1 Introduction

As introduced earlier, micropolar theory assumes that the interaction between continuum particles through a surface element dA occurs not only through a force vector ($F_i dA$) but also through a moment vector ($M_i dA$). This establishes the “force-stress” tensor expressed as force per unit area, σ_{ij} , and the “couple-stress” tensor expressed as moment per unit area. Balance of angular momentum shows that the stress tensor in the micropolar media is no longer symmetric as in the classical theory. A special case of Cosserat theory is the couple-stress theory, in which the microrotation and macrorotation coincide, [Koiter \(1964\)](#). In comparison with a classical continuum, a couple stress continuum is obtained by adding a rotation (dependent of displacement vector) to each point of the continuum; it is based on the assumption that micromoments exist at each point of the continuum. The appealing aspect of the couple-stress theory is that a physically meaningful link can be made between the kinetic

and kinematic variables of the couple-stress theory and the behavior of materials with microstructure like trabecular bone.

Adachi et al. (1998) proposed finite element methods applied to the 2D-lattice continuum, which is a continuous model of discrete lattice structure obeying couple stress theory such as cancellous bone with trabecular architecture, to analyze the dependence of the stress concentration factor on the microstructural parameters. Ostoja-Starzewski et al., 1999; Bouyge, 2000; Bouyge et al., 2001, 2002 used the couple-stress theory and strain energy based RVE method to evaluate couple-stress constants of planar, periodic, effectively isotropic or orthotropic, two-phase composites with linear elastic constituents of classical Cauchy type. Yoo and Jasiuk, 2006 computed the apparent couple-stress moduli of 3D trabecular bone using displacement and traction boundary conditions, which respectively gives upper and lower bounds of effective couple-stress moduli. The apparent couple-stress moduli obtained using displacement boundary conditions and those obtained using traction boundary conditions show very large differences. Additionally, the same authors reported that the apparent moduli depend on the size of the domain and boundary conditions on which they are evaluated, without however showing any underlying analysis. The questions arise here by how large the domain size and boundary conditions affect the predicted apparent moduli and for what size of the RVE the obtained moduli converge. These issues related to scale effects and the nature of boundary conditions are addressed in this work.

As far as trabecular bone is concerned, understanding the effects of trabecular micro-architecture on the mechanics of effective trabecular bone under diverse loading conditions may provide some insight into bone quality. In this regard, the overall goal of this work is to predict the effective couple-stress elastic moduli of vertebral trabecular bone, which is represented by a three-dimensional periodic porous network relying on relationships between the bone morphology and bone age.

To our knowledge, the present study is the first attempt to predict and evaluate in a complete manner the effective couple-stress moduli, from a finite element strategy for a three dimensional representative orthotropic vertebral trabecular bone micro-architecture. Mixed boundary conditions including both traction and displacement boundary conditions shall be applied along the outer boundaries of the considered bone domain; they are very important since they are similar to the loadings used in experiments to obtain the mechanical properties. Computationally, using finite elements based homogenization approaches, the effective 3D orthotropic couple-stress rigidity tensor is fully determined by an equivalent energy method. In addition, the characteristic lengths for bending and torsion are subsequently identified from the orthotropic homogenized stiffness matrix.

We address the issue of the size of the specimen and the nature of the boundary conditions to be applied, which are expected to affect the effective properties. Mixed boundary conditions demonstrate that the predicted components of the first couple-stress stiffness tensor (giving the effective normal and shear stresses components of trabecular bone) are independent of the bone domain size. Contrary to this, the predicted second couple-stress stiffness tensor shows a dependency on the specimen size. The present approach is particularly interesting and novel, due to the difficulty to measure such effective properties for

3D trabecular bone considering their discreteness. It is thus the main objective of this contribution to circumvent the experimental difficulty in accessing effective properties of such architected materials endowed with size effect by means of predictive models.

5.2 Basic equations of couple stress elasticity

In the micropolar continuum the deformation is described by the displacement vector \mathbf{u} and an independent rotation vector $\boldsymbol{\phi}$, whereas in the couple stress theory, the rotation vector $\boldsymbol{\phi}$ is not independent of the displacement vector but, rather, fully described by the displacement vector.

In the couple-stress theory, the rotation ϕ_i is related to displacement gradients (equal to the local rigid rotations) as:

$$\phi_x = (\partial u_z / \partial y - \partial u_y / \partial z) / 2; \phi_y = (\partial u_x / \partial z - \partial u_z / \partial x) / 2; \phi_z = (\partial u_y / \partial x - \partial u_x / \partial y) / 2 \quad (5.1)$$

The kinematic variables to be taken into account within the linear modified couple-stress theory (Yang et al., 2002) are the strain ϵ_{ij} and the gradient of rotation χ_{ij} , they are defined, respectively, as

$$\epsilon_{ij} = 1/2(u_{i,j} + u_{j,i}) = \epsilon_{ji}; \chi_{ij} = 1/2(\phi_{i,j} + \phi_{j,i}) = \chi_{ji} \quad i,j=x,y,z \quad (5.2)$$

The strain tensor ϵ_{ij} is symmetric, with components depending upon the displacements gradients as

$$\begin{aligned} \epsilon_{xx} &= \partial u_x / \partial x; \epsilon_{yy} = \partial u_y / \partial y; \epsilon_{zz} = \partial u_z / \partial z; \epsilon_{xy} = \epsilon_{yx} = (\partial u_y / \partial x + \partial u_x / \partial y) / 2; \\ \epsilon_{xz} &= \epsilon_{zx} = (\partial u_z / \partial x + \partial u_x / \partial z) / 2; \epsilon_{yz} = \epsilon_{zy} = (\partial u_z / \partial y + \partial u_y / \partial z) / 2 \end{aligned} \quad (5.3)$$

In the same way, the curvature tensor is symmetrical (Yang et al., 2002); its components are explicitly written from the gradient of rotations (5.1) as

$$\begin{aligned} \chi_{xx} &= \frac{\partial \phi_x}{\partial x} = \frac{1}{2} \left(\frac{\partial^2 u_z}{\partial x \partial y} - \frac{\partial^2 u_y}{\partial z \partial x} \right); \chi_{yy} = \frac{\partial \phi_y}{\partial y} = \frac{1}{2} \left(\frac{\partial^2 u_x}{\partial y \partial z} - \frac{\partial^2 u_z}{\partial x \partial y} \right); \chi_{zz} = \frac{\partial \phi_z}{\partial z} = \frac{1}{2} \left(\frac{\partial^2 u_y}{\partial x \partial z} - \frac{\partial^2 u_x}{\partial y \partial z} \right); \\ \chi_{xy} &= \frac{\partial \phi_y}{\partial x} = \frac{1}{2} \left(\frac{\partial^2 u_x}{\partial z \partial x} - \frac{\partial^2 u_z}{\partial x^2} \right); \chi_{yz} = \frac{\partial \phi_z}{\partial y} = \frac{1}{2} \left(\frac{\partial^2 u_y}{\partial x \partial y} - \frac{\partial^2 u_x}{\partial y^2} \right); \chi_{xz} = \frac{\partial \phi_z}{\partial x} = \frac{1}{2} \left(\frac{\partial^2 u_y}{\partial x^2} - \frac{\partial^2 u_x}{\partial x \partial y} \right) \end{aligned} \quad (5.4)$$

For orthotropic solids endowed with central symmetry, the constitutive equations of the effective couple stress continua can be expressed in a compact form as follows

$$\boldsymbol{\sigma} = \mathbf{C} : \boldsymbol{\epsilon}; \mathbf{m} = \mathbf{D} : \boldsymbol{\chi} \quad (5.5)$$

with the stiffness matrix \mathbf{C} relating stresses to strains and the curvature tensor \mathbf{D} relating couple stresses to curvatures.

The stress and couple-stress for the effective 3D couple stress continuum can be defined in vector format as

$$\boldsymbol{\sigma} = [\sigma_{xx}, \sigma_{yy}, \sigma_{zz}, \sigma_{xy}, \sigma_{yz}, \sigma_{xz}]^T, \mathbf{m} = [m_{xx}, m_{yy}, m_{zz}, m_{xy}, m_{yz}, m_{xz}]^T \quad (5.6)$$

in which the components m_{xx} , m_{yy} , m_{zz} are the torsion couple-stresses and m_{xy} , m_{yz} , m_{xz} are the bending couple stresses.

Hence, the constitutive equations for orthotropic materials can be recast into the form

$$\begin{bmatrix} \sigma_{xx} \\ \sigma_{yy} \\ \sigma_{zz} \\ \sigma_{xy} \\ \sigma_{yz} \\ \sigma_{xz} \end{bmatrix} = \begin{bmatrix} C_{11} & C_{12} & C_{13} & 0 & 0 & 0 \\ C_{12} & C_{22} & C_{23} & 0 & 0 & 0 \\ C_{13} & C_{23} & C_{33} & 0 & 0 & 0 \\ 0 & 0 & 0 & C_{44} & 0 & 0 \\ 0 & 0 & 0 & 0 & C_{55} & 0 \\ 0 & 0 & 0 & 0 & 0 & C_{66} \end{bmatrix} \begin{bmatrix} \epsilon_{xx} \\ \epsilon_{yy} \\ \epsilon_{zz} \\ \epsilon_{xy} \\ \epsilon_{yz} \\ \epsilon_{xz} \end{bmatrix} ; \begin{bmatrix} m_{xx} \\ m_{yy} \\ m_{zz} \\ m_{xy} \\ m_{yz} \\ m_{xz} \end{bmatrix} = \begin{bmatrix} D_{11} & D_{12} & D_{13} & 0 & 0 & 0 \\ D_{12} & D_{22} & D_{23} & 0 & 0 & 0 \\ D_{13} & D_{23} & D_{33} & 0 & 0 & 0 \\ 0 & 0 & 0 & D_{44} & 0 & 0 \\ 0 & 0 & 0 & 0 & D_{55} & 0 \\ 0 & 0 & 0 & 0 & 0 & D_{66} \end{bmatrix} \begin{bmatrix} \frac{1}{2} \left(\frac{\partial^2 u_z}{\partial x \partial y} - \frac{\partial^2 u_y}{\partial z \partial x} \right) \\ \frac{1}{2} \left(\frac{\partial^2 u_x}{\partial y \partial z} - \frac{\partial^2 u_z}{\partial x \partial y} \right) \\ \frac{1}{2} \left(\frac{\partial^2 u_y}{\partial x \partial z} - \frac{\partial^2 u_x}{\partial y \partial z} \right) \\ \frac{1}{2} \left(\frac{\partial^2 u_x}{\partial z \partial x} - \frac{\partial^2 u_z}{\partial x^2} \right) \\ \frac{1}{2} \left(\frac{\partial^2 u_y}{\partial x \partial y} - \frac{\partial^2 u_x}{\partial y^2} \right) \\ \frac{1}{2} \left(\frac{\partial^2 u_y}{\partial x^2} - \frac{\partial^2 u_x}{\partial x \partial y} \right) \end{bmatrix} \quad (5.7)$$

In the next section, 3D finite element models of vertebral trabecular bone are developed to evaluate the first and second couple-stress stiffness tensors introduced in equation (5.7). The effective couple-stress elastic properties are calculated using the strain energy-based method, based on the relationship established between the strain energy of the microstructure and that of the homogenized equivalent model under specific boundary conditions. The numerical homogenization technique consists in determining the overall effective couple-stress elastic coefficients over a representative unit cell of trabecular bone with different sizes, relying on a finite element discretization of the unit cell geometry.

5.3 Effective couple stress continuum model of vertebral trabecular bone

The main purpose of this section is to determine the effective constitutive coefficients of the couple-stress continuum from the unit cell response of trabecular structure. We design different boundary conditions for the determination of the components of the constitutive (rigidity) constants over various unit cell domain Ω (Figure 5.1) with boundary $\partial\Omega$. In each case, we force the unit cell in 3D context to bear the designed specific deformations ϵ_{ij} , χ_{ij} and compute numerically the total elastic strain energy U_{cell} stored in the unit cell under the corresponding boundary conditions.

The numerical procedure used here relies on equating the total elastic strain energy stored in the unit cell to the energy of an equivalent homogeneous couple-stress continuum, thus

$$U_{cell} = U_{couple-stress} = \frac{V_u}{2} \left[\epsilon_{ij} C_{ijkl} \epsilon_{kl} + \chi_{ij} D_{ijkl} \chi_{kl} \right] \quad (5.8)$$

where $V_u = |\Omega|$ is the volume of the unit cell. The left-hand side in (5.8) is the total elastic strain energy stored in the unit cell of the trabecular bone, while the right-hand side is the energy of a couple-stress continuum, which is a function of volume-average strains ϵ_{ij} and curvatures χ_{ij} of the unit cell.

We aim at the prediction of the effective couple-stress moduli of a 3D periodic unit cell of trabecular bone using mixed traction and displacement boundary conditions involving applied displacements and tractions along the borders. The motivation behind the application of such boundary conditions rather than periodic ones - although we have a periodic microstructure - lies in the fact that periodic boundary conditions cannot be employed for the loadings needed to evaluate the second couple-stress stiffness \mathbf{D} , since it gives a deformation which is non-periodic.

As a heterogeneous porous cellular solid, trabecular bone has anisotropic mechanical properties that depend on the porosity of the specimen as well as the architectural arrangement of the individual trabeculae. Its effective (whole-specimen) level properties depend on the tissue-level geometrical and material properties of the individual trabeculae. It is well-known that trabecular bone consists of an interconnected network of rods. The micro-architecture of trabecular bone makes it extremely difficult to characterize. We model the rod-like architecture of vertebral bone as a three-dimensional cubic lattice with a unit cell geometry whose its micro-architecture (thick with longer vertical columns and thinner with shorter horizontal struts) is based on studies of samples taken from the central part of vertebral bodies (Figure 5.1a). The architecture of the model (thick vertical columns and thinner horizontal struts) is based on studies of samples taken from the central part of vertebral bodies from normal Individuals aged from 30 to 90 years (Mosekilde, 1988, 1989). Four indices are used to describe the morphology of the unit cell (Figure 5.1b): the horizontal trabecular thickness (D_h), the vertical trabecular thickness (D_v), and the mean distance between the horizontal trabeculae (L_h) as well as between the vertical trabeculae (L_v). From the morphological indices (D_h , D_v , L_h , L_v) an idealized model of trabecular microarchitecture is constructed – the cubic shape. The age-related change of vertebral bone architecture (the changes in trabecular thickness and spacing that occur with aging) has been described using the relations in Table 5.1.

Table 5.1: Micro-structural parameters for vertebral bone based on morphology–age relationships by Mosekilde (1988), age is measured in years.

Parameter	Relation
Horizontal trabeculae thickness (μm)	$D_h = -1.03 \times \text{Age} + 189$
Vertical trabeculae thickness (μm)	$D_v = 0.14 \times \text{Age} + 208$
Distance between horizontal trabeculae (μm)	$L_h = 13.74 \times \text{Age} + 288$
Distance between vertical trabeculae (μm)	$L_v = 6.74 \times \text{Age} + 456$

As a consequence, 3D effective orthotropic couple-stress moduli will be produced. On the contrary, [Yoo and Jasiuk, 2006](#) used a geometric parameters based on a simplified cubic unit cell whose its micro-architectures are identical, which entails an effective isotropic behavior.

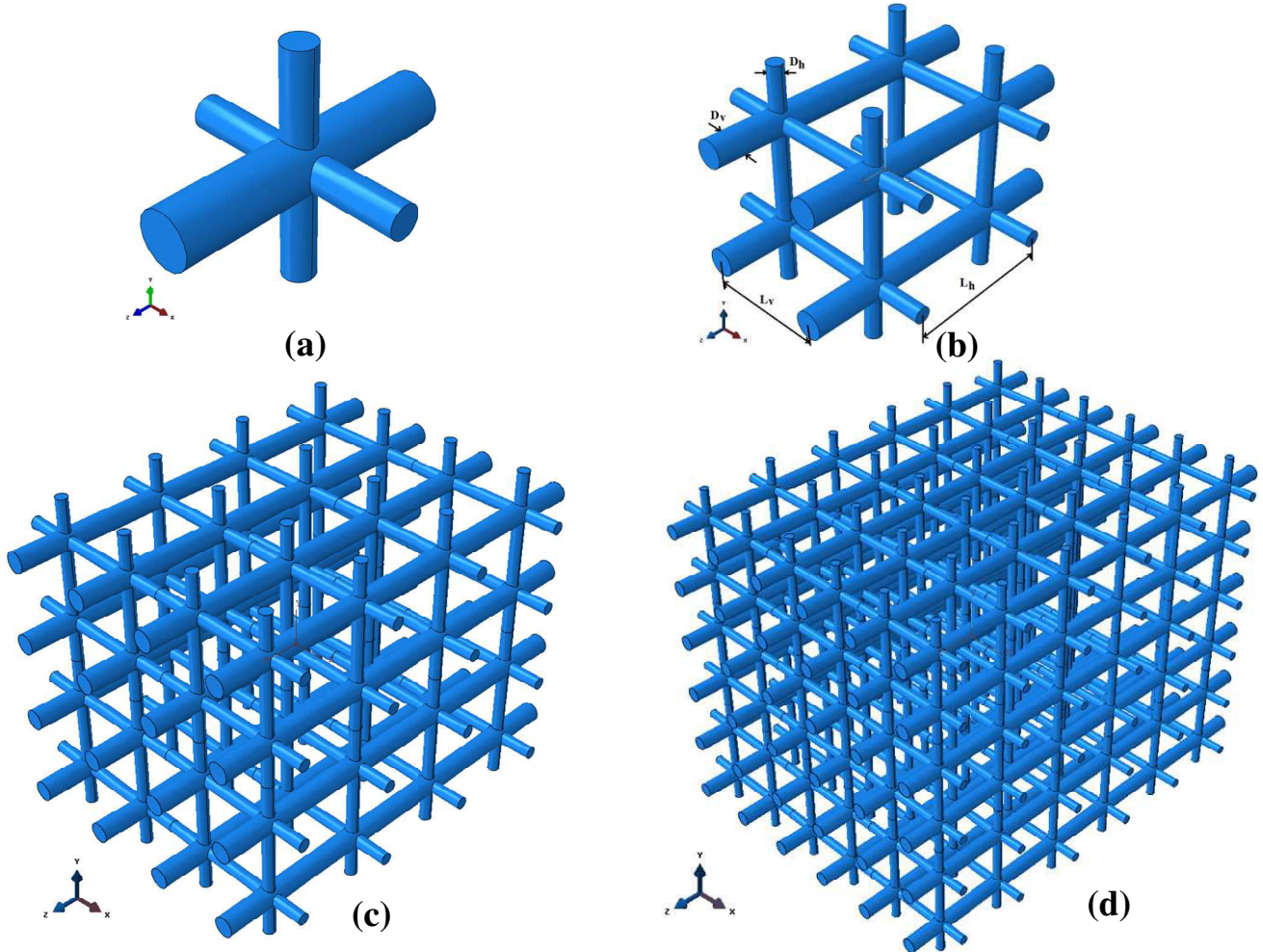


Figure 5.1: Four different 3D periodic model representation of vertebral trabecular bone with (a) a single unit cell denoted 1, (b) $2 \times 2 \times 2$ unit cells, (c) $4 \times 4 \times 4$ unit cells, and (d) $6 \times 6 \times 6$ unit cells. Note that both vertical and horizontal trabeculae are idealized as a circular beam with diameter D_v and D_h , respectively.

The bulk mechanical properties of the unit cells wall representative of the behavior of human vertebral trabecular bone are taken as $E_s = 12000$ MPa; $\nu_s = 0.3$.

The loadings applied to obtain the couple-stress coefficients include uniaxial extension tests, biaxial extension tests, and in-plane and out-of plane shear tests to evaluate stiffness matrix components \mathbf{C} and uniaxial twist (or torsion) tests, biaxial twist tests, and in plane and out-of plane curvature (or bending moment) tests to evaluate stiffness matrix components \mathbf{D} . Nine tests are subsequently constructed to determine the components of stiffness matrix \mathbf{C} and additional nine tests are performed to determine the components of stiffness matrix \mathbf{D} . For each loading case, we compute by the finite element method the total strain energy stored in

the unit cell and then equate this energy with the energy of an equivalent homogeneous couple-stress continuum.

In order to evaluate the components of the first couple-stress stiffness tensor \mathbf{C} for the unit cell, we conduct the following nine elementary tests:

1. Test 1- Mixed uniaxial extension for C_{11} : we apply a uniform strain $\epsilon_{xx} = 1$ and shear stress $\sigma_{xy} = \sigma_{yz} = \sigma_{xz} = 0$ on the unit cell's boundary, the corresponding mixed boundary conditions are then written as

$$\begin{aligned} u_x = x, \quad t_2 = \sigma_{xy} n_1 = 0, \quad t_3 = \sigma_{xz} n_1 = 0 \quad \text{on } n_1 \text{ face} \\ u_y = 0, \quad t_1 = \sigma_{xy} n_2 = 0, \quad t_3 = \sigma_{yz} n_2 = 0 \quad \text{on } n_2 \text{ face} \\ u_z = 0, \quad t_1 = \sigma_{xz} n_3 = 0, \quad t_2 = \sigma_{yz} n_3 = 0 \quad \text{on } n_3 \text{ face} \end{aligned} \quad (5.9)$$

which leads to identify C_{11}

$$C_{11} = 2U_{cell} / V_u \quad (5.10)$$

2. Test 2- Mixed uniaxial extension for C_{22} : we apply a uniform strain $\epsilon_{yy} = 1$ and shear stress $\sigma_{xy} = \sigma_{yz} = \sigma_{xz} = 0$ on the unit cell's boundary, the corresponding mixed boundary conditions are then written as

$$\begin{aligned} u_x = 0, \quad t_2 = 0, \quad t_3 = 0 \quad \text{on } n_1 \text{ face} \\ u_y = y, \quad t_1 = 0, \quad t_3 = 0 \quad \text{on } n_2 \text{ face} \\ u_z = 0, \quad t_1 = 0, \quad t_2 = 0 \quad \text{on } n_3 \text{ face} \end{aligned} \quad (5.11)$$

which gives

$$C_{22} = 2U_{cell} / V_u \quad (5.12)$$

3. Test 3- Mixed uniaxial extension for C_{33} : we apply a uniform strain $\epsilon_{zz} = 1$ and shear stress $\sigma_{xy} = \sigma_{yz} = \sigma_{xz} = 0$ on the unit cell's boundary, the corresponding mixed boundary conditions are then written as

$$\begin{aligned} u_x = 0, \quad t_2 = 0, \quad t_3 = 0 \quad \text{on } n_1 \text{ face} \\ u_y = 0, \quad t_1 = 0, \quad t_3 = 0 \quad \text{on } n_2 \text{ face} \\ u_z = z, \quad t_1 = 0, \quad t_2 = 0 \quad \text{on } n_3 \text{ face} \end{aligned} \quad (5.13)$$

this gives

$$C_{33} = 2U_{cell} / V_u \quad (5.14)$$

4. Test 4- Mixed biaxial extension for C_{12} : we apply a uniform strain $\epsilon_{xx} = \epsilon_{yy} = 1$ and shear stress $\sigma_{xy} = \sigma_{yz} = \sigma_{xz} = 0$ on the unit cell's boundary, the corresponding mixed boundary conditions are then written as

$$\begin{aligned} u_x = x, \quad t_2 = 0, \quad t_3 = 0 \quad \text{on } n_1 \text{ face} \\ u_y = y, \quad t_1 = 0, \quad t_3 = 0 \quad \text{on } n_2 \text{ face} \\ u_z = 0, \quad t_1 = 0, \quad t_2 = 0 \quad \text{on } n_3 \text{ face} \end{aligned} \quad (5.15)$$

which yields

$$C_{12} = (2U_{cell} / V_u - C_{11} - C_{22}) / 2 \quad (5.16)$$

5. Test 5- Mixed biaxial extension for C_{23} : we apply a uniform strain $\epsilon_{yy} = \epsilon_{zz} = 1$ and shear stress $\sigma_{xy} = \sigma_{yz} = \sigma_{xz} = 0$ on the unit cell's boundary, the corresponding mixed boundary conditions are then written as

$$\begin{aligned} u_x = 0, t_2 = 0, t_3 = 0 & \text{ on } n_1 \text{ face} \\ u_y = y, t_1 = 0, t_3 = 0 & \text{ on } n_2 \text{ face} \end{aligned} \quad (5.17)$$

$$u_z = z, t_1 = 0, t_2 = 0 \text{ on } n_3 \text{ face}$$

which yields

$$C_{23} = (2U_{cell} / V_u - C_{22} - C_{33}) / 2 \quad (5.18)$$

6. Test 6- Mixed biaxial extension for C_{13} : we apply a uniform strain $\epsilon_{xx} = \epsilon_{zz} = 1$ and shear stress $\sigma_{xy} = \sigma_{yz} = \sigma_{xz} = 0$ on the unit cell's boundary, the corresponding mixed boundary conditions are then written as

$$\begin{aligned} u_x = x, t_2 = 0, t_3 = 0 & \text{ on } n_1 \text{ face} \\ u_y = 0, t_1 = 0, t_3 = 0 & \text{ on } n_2 \text{ face} \end{aligned} \quad (5.19)$$

$$u_z = z, t_1 = 0, t_2 = 0 \text{ on } n_3 \text{ face}$$

which yields

$$C_{13} = (2U_{cell} / V_u - C_{11} - C_{33}) / 2 \quad (5.20)$$

7. Test 7- Mixed shear deformation for C_{44} : we apply a uniform shear strain $\epsilon_{xy} = 1$ and normal stress $\sigma_{xx} = \sigma_{yy} = \sigma_{zz} = 0$ on the unit cell's boundary, the corresponding mixed boundary conditions are then written as

$$\begin{aligned} u_x = y / 2, t_2 = \sigma_{yy} n_2 = 0, t_3 = \sigma_{zz} n_3 = 0 & \text{ on } n_2 \text{ face} \\ u_y = x / 2, t_1 = \sigma_{xx} n_1 = 0, t_3 = \sigma_{zz} n_3 = 0 & \text{ on } n_1 \text{ face} \\ u_z = 0, t_1 = \sigma_{xx} n_1 = 0, t_2 = \sigma_{yy} n_2 = 0 & \text{ on } n_3 \text{ face} \end{aligned} \quad (5.21)$$

which yields

$$C_{44} = 2U_{cell} / V_u \quad (5.22)$$

8. Test 8- Mixed shear deformation for C_{55} : we apply a uniform shear strain $\epsilon_{yz} = 1$ and normal stress $\sigma_{xx} = \sigma_{yy} = \sigma_{zz} = 0$ on the unit cell's boundary, the corresponding mixed boundary conditions are then written as

$$\begin{aligned} u_x = 0, t_2 = 0, t_3 = 0 & \text{ on } n_1 \text{ face} \\ u_y = z / 2, t_1 = 0, t_3 = 0 & \text{ on } n_3 \text{ face} \\ u_z = y / 2, t_1 = 0, t_2 = 0 & \text{ on } n_2 \text{ face} \end{aligned} \quad (5.23)$$

which yields

$$C_{55} = 2U_{cell} / V_u \quad (5.24)$$

9. Test 9- Mixed shear deformation for C_{66} : we apply a uniform shear strain $\epsilon_{xz} = 1$ and normal stress $\sigma_{xx} = \sigma_{yy} = \sigma_{zz} = 0$ on the unit cell's boundary, the corresponding mixed boundary conditions are then written as

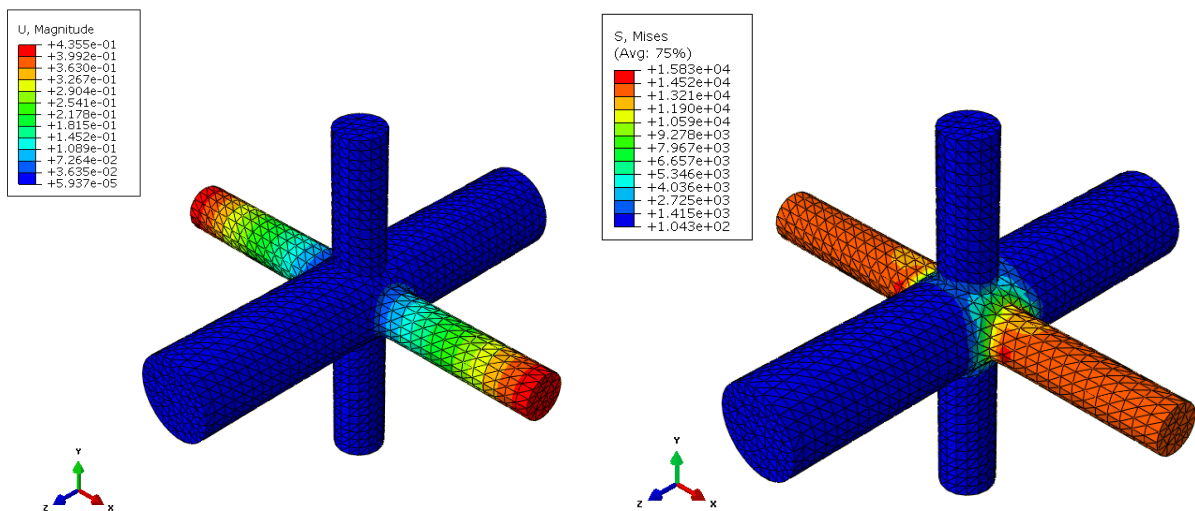
$$\begin{aligned} u_x &= z/2, \quad t_2 = 0, \quad t_3 = 0 && \text{on } n_3 \text{ face} \\ u_y &= 0, \quad t_1 = 0, \quad t_3 = 0 && \text{on } n_2 \text{ face} \\ u_z &= x/2, \quad t_1 = 0, \quad t_2 = 0 && \text{on } n_1 \text{ face} \end{aligned} \quad (5.25)$$

which yields

$$C_{66} = 2U_{cell} / V_u \quad (5.26)$$

The couple-stress elastic moduli of 3D trabecular bone are derived computationally using the finite element method. The unit cells have been meshed by the so-called C3D4H first-order tetrahedral element, used in ABAQUS environment. The micro-architecture parameters L_v , L_h , D_h , and D_v of the trabecular are selected for a person at the age of 60, resulting in a relative density of about 7.2%. The analysis includes four different unit cell sizes representing the vertebral trabecular bone samples; we consider the same mesh sizes for bone tissue for all trabecular networks under study, with an approximate global size of 0.03.

The iso-displacements and stress distributions within the first two trabecular bone unit cells 1 and $2 \times 2 \times 2$ due to uniaxial strains loadings $\epsilon_{xx} = 1$ and $\epsilon_{zz} = 1$, biaxial strain loadings $\epsilon_{xx} = \epsilon_{yy} = 1$ and $\epsilon_{xx} = \epsilon_{zz} = 1$, and shear loadings $\epsilon_{xy} = 1$ and $\epsilon_{xz} = 1$ under the corresponding boundary conditions are exposed respectively in Figures 5.2-5.7. Note that we keep the same mesh size for both unit cells.



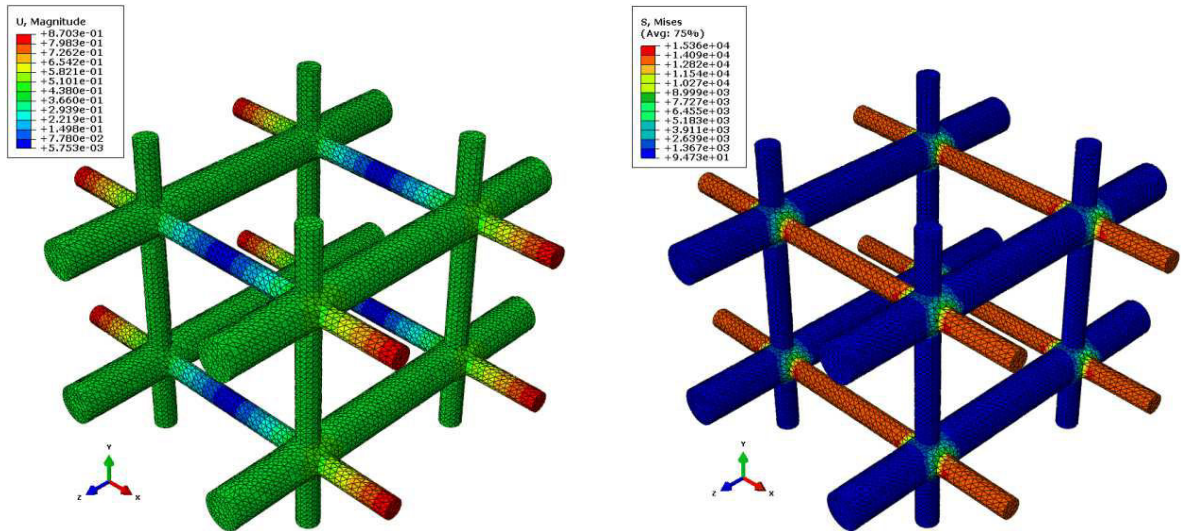


Figure 5.2: Displacements and Von Mises stress distributions due to uniaxial tensile test in x-direction ($\epsilon_{xx} = 1$).

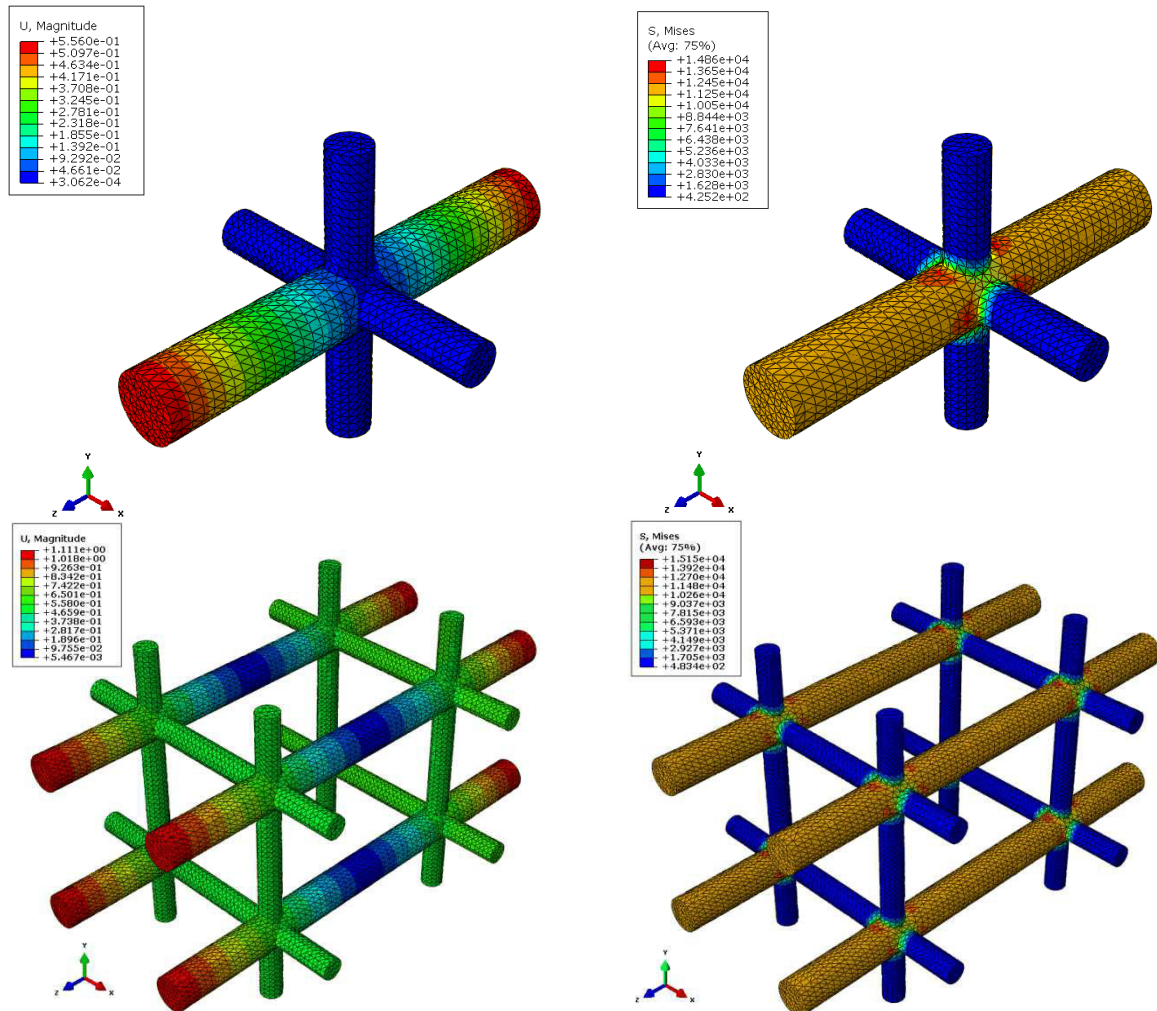


Figure 5.3: Displacements and Von Mises stress distributions due to uniaxial tensile test in z-direction ($\epsilon_{zz} = 1$).

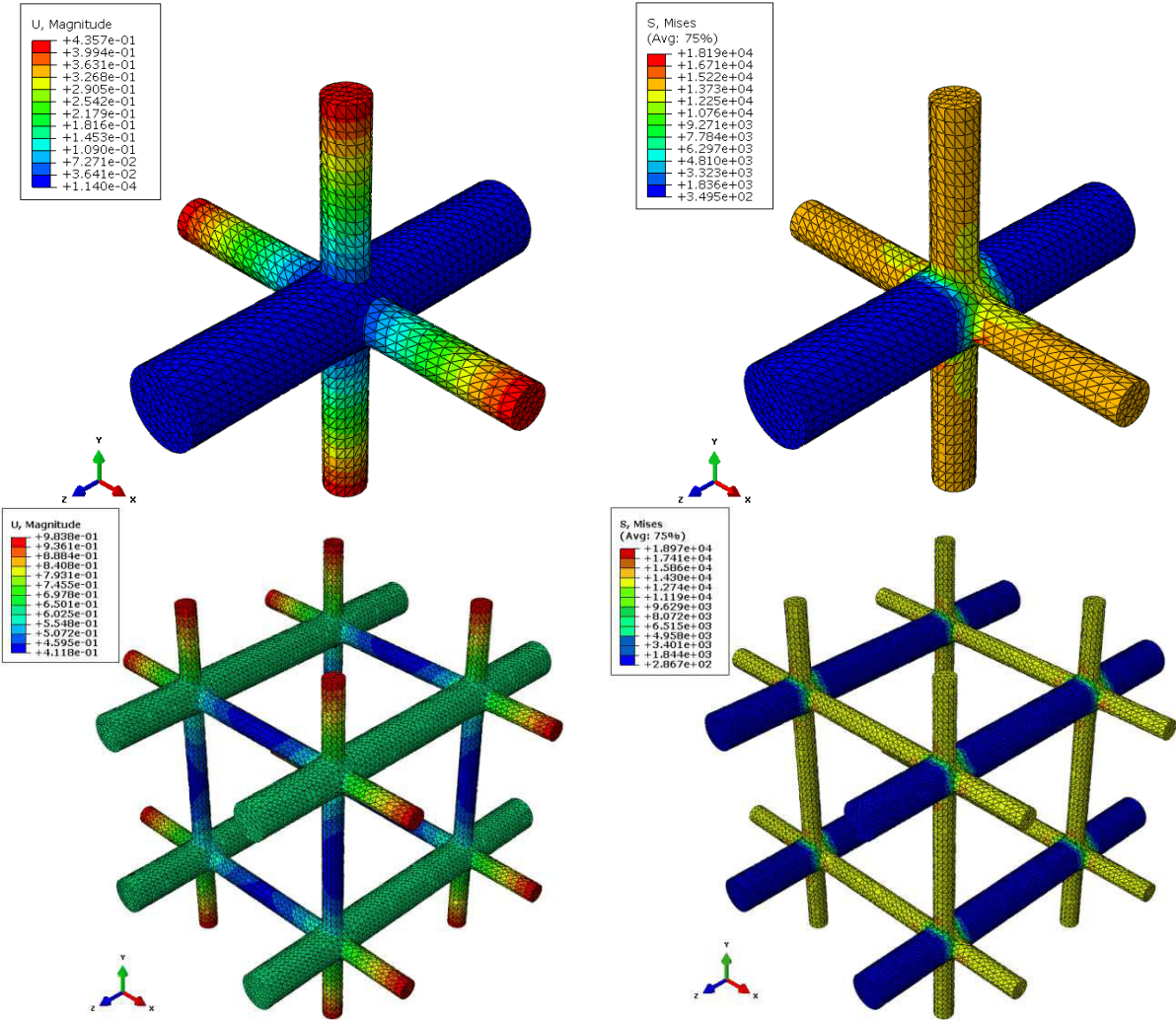
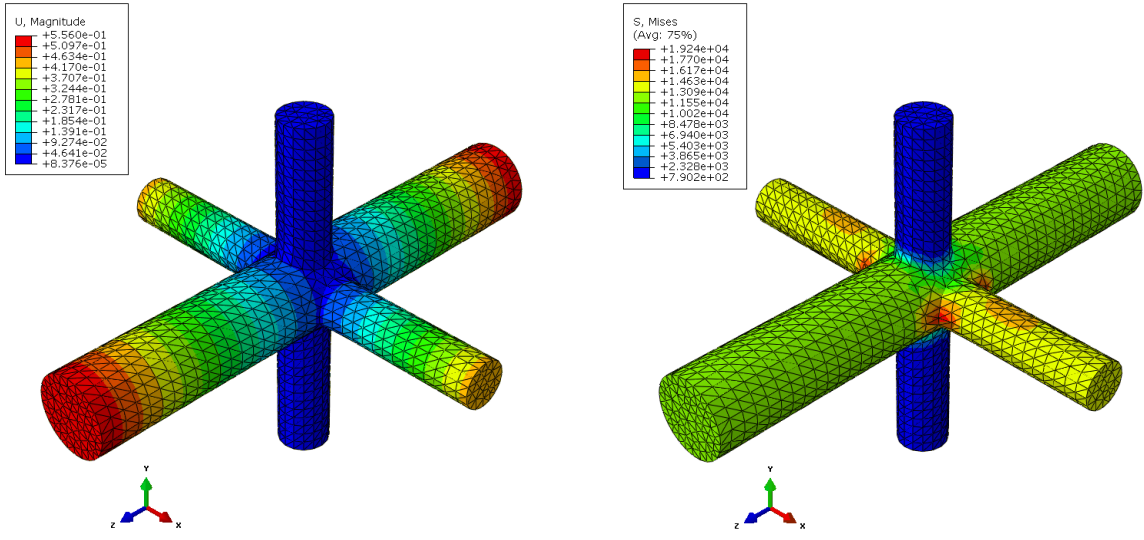


Figure 5.4: Displacements and Von Mises stress distributions due to biaxial tensile test ($\epsilon_{xx} = \epsilon_{yy} = 1$).



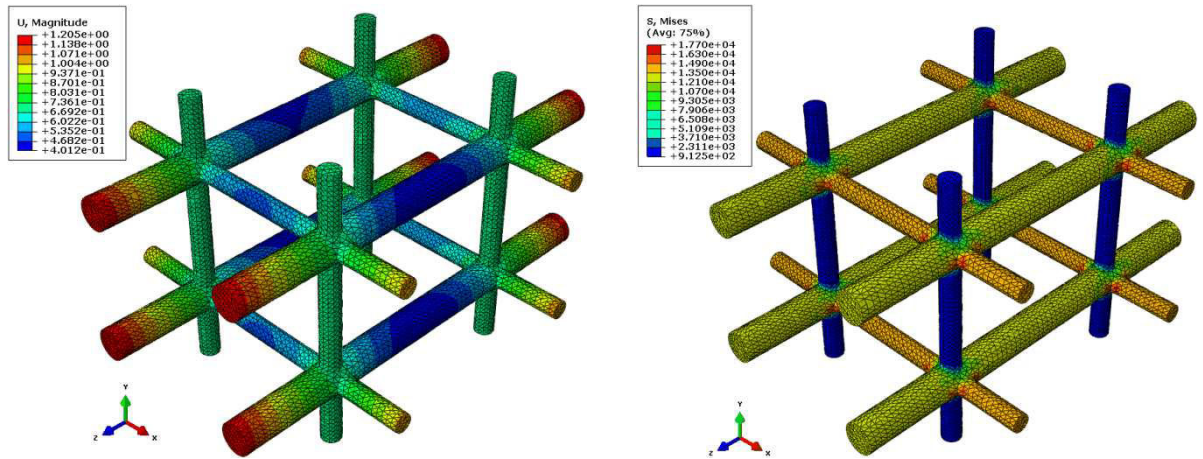
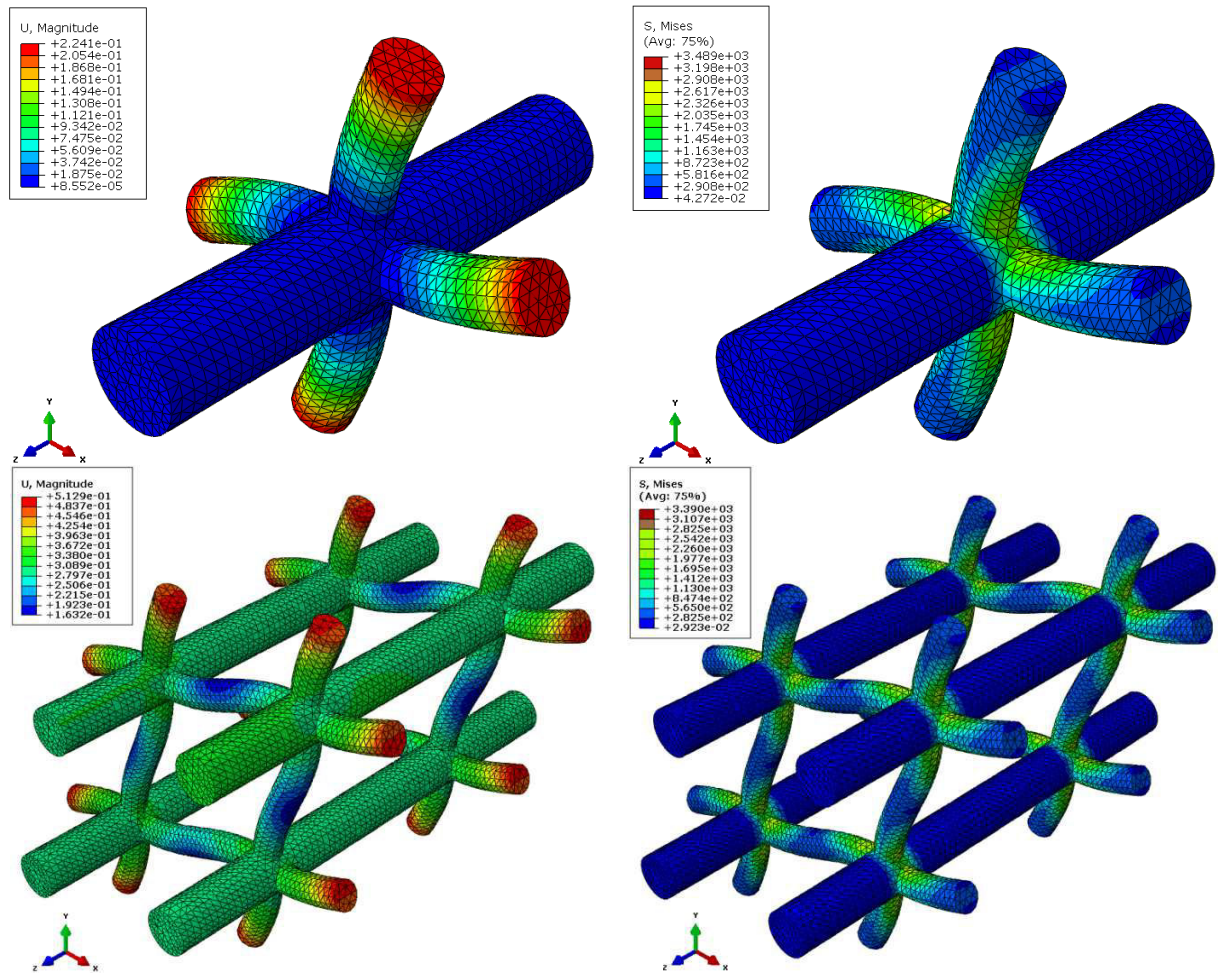


Figure 5.5: Displacements and Von Mises stress distributions due to biaxial tensile test ($\epsilon_{xx} = \epsilon_{zz} = 1$).



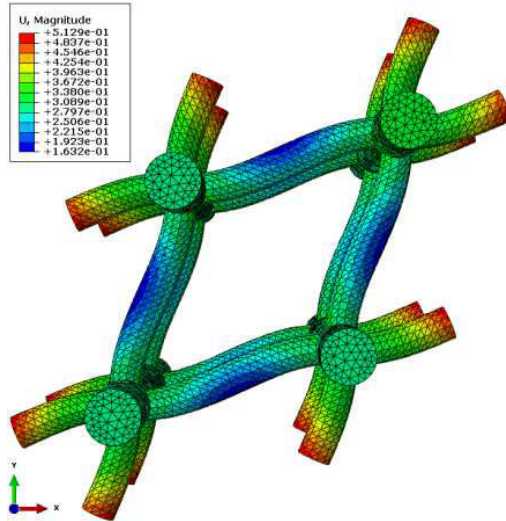
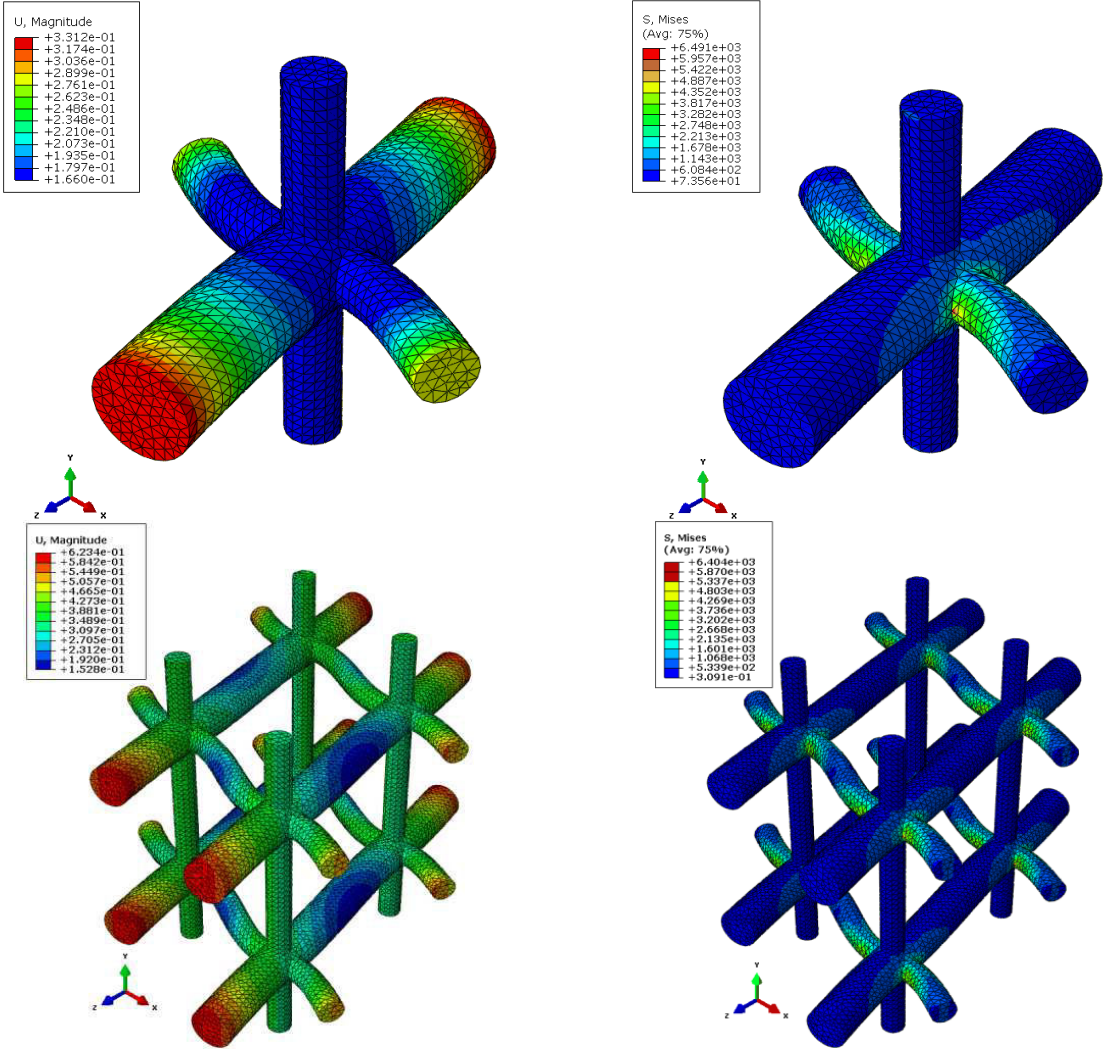


Figure 5.6: Displacements and Von Mises stress distributions due to shear test in xy ($\epsilon_{xy} = 1$).



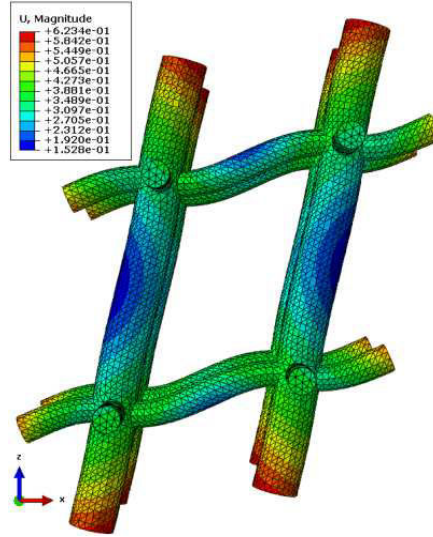


Figure 5.7: Displacements and Von Mises stress distributions due to shear test in xz ($\epsilon_{xz} = 1$).

We next evaluate the components of the couple-stress stiffness tensor \mathbf{D} ; for this purpose, we perform the following nine elementary tests:

1. Test 1- Mixed uniaxial torsional rotation for D_{11} : we apply a uniform torsional rotation $\chi_{xx} = 1$ and specify zero shear tractions on the unit cell's boundary, thus the corresponding mixed boundary conditions are written as

$$u_x = 0, u_y = -xz, u_z = xy \quad \text{on } n_1 \text{ face} \quad (5.27)$$

which gives

$$D_{11} = 2U_{cell} / V_u \quad (5.28)$$

1. Test 2- Mixed uniaxial torsional rotation for D_{22} : we apply a uniform torsional rotation $\chi_{yy} = 1$ and specify zero shear tractions on the unit cell's boundary, thus the corresponding mixed boundary conditions are written as

$$u_x = yz, u_y = 0, u_z = -xy \quad \text{on } n_2 \text{ face} \quad (5.29)$$

which gives

$$D_{22} = 2U_{cell} / V_u \quad (5.30)$$

3. Test 3- Mixed uniaxial torsional rotation for D_{33} : we apply a uniform torsional rotation $\chi_{zz} = 1$ and specify zero shear tractions on the unit cell's boundary, thus the corresponding mixed boundary conditions are written as

$$u_x = -yz, u_y = xz, u_z = 0 \quad \text{on } n_3 \text{ face} \quad (5.31)$$

which gives

$$D_{33} = 2U_{cell} / V_u \quad (5.32)$$

4. Test 4- Mixed biaxial torsional rotation for D_{12} : we apply a uniform torsional rotation $\chi_{xx} = \chi_{yy} = 1$ and specify zero shear tractions on the unit cell's boundary, thus the corresponding mixed boundary conditions are written as

$$\begin{aligned} u_y = -xz, u_z = xy & \quad \text{on } n_1 \text{ face} \\ u_x = yz, u_z = -xy & \quad \text{on } n_2 \text{ face} \end{aligned} \quad (5.33)$$

which gives

$$D_{12} = (2U_{cell} / V_u - D_{11} - D_{22}) / 2 \quad (5.34)$$

5. Test 5- Mixed biaxial torsional rotation for D_{23} : when we apply a uniform torsional rotation $\chi_{yy} = \chi_{zz} = 1$ on the unit cell's boundary, the corresponding mixed boundary conditions are then written as

$$\begin{aligned} u_x = yz, u_z = -xy & \quad \text{on } n_2 \text{ face} \\ u_x = -yz, u_y = xz & \quad \text{on } n_3 \text{ face} \end{aligned} \quad (5.35)$$

which yields

$$D_{23} = (2U_{cell} / V_u - D_{22} - D_{33}) / 2 \quad (5.36)$$

6. Test 6- Biaxial torsional rotation for D_{13} : when we apply a uniform torsional rotation $\chi_{xx} = \chi_{zz} = 1$ on the unit cell's boundary, the corresponding mixed boundary conditions are then written as

$$\begin{aligned} u_y = -xz, u_z = xy & \quad \text{on } n_1 \text{ face} \\ u_x = -yz, u_y = xz & \quad \text{on } n_3 \text{ face} \end{aligned} \quad (5.37)$$

which yields

$$D_{13} = (2U_{cell} / V_u - D_{11} - D_{33}) / 2 \quad (5.38)$$

7. Test 7- Uniform curvature for D_{44} : when we apply a uniform curvature $\chi_{xy} = 1$ on the unit cell's boundary, the corresponding boundary conditions are then given as

$$\begin{aligned} u_x = xz & \quad \text{on } n_1 \text{ face} \\ u_y = 0 & \quad \text{on } n_2 \text{ face} \\ u_z = -x^2 / 2 & \quad \text{on } n_3 \text{ face} \end{aligned} \quad (5.39)$$

which yields

$$D_{44} = 2U_{cell} / V_u - C_{11}z^2 \quad (5.40)$$

8. Test 8- Uniform curvature for D_{55} : when we apply a uniform curvature $\chi_{yz} = 1$ on the unit cell's boundary, the corresponding boundary conditions are then given as

$$\begin{aligned}
u_x &= -y^2 / 2 && \text{on } n_1 \text{ face} \\
u_y &= xy && \text{on } n_2 \text{ face} \\
u_z &= 0 && \text{on } n_3 \text{ face}
\end{aligned} \tag{5.41}$$

which gives

$$D_{55} = 2U_{cell} / V_u - C_{22}x^2 \tag{5.42}$$

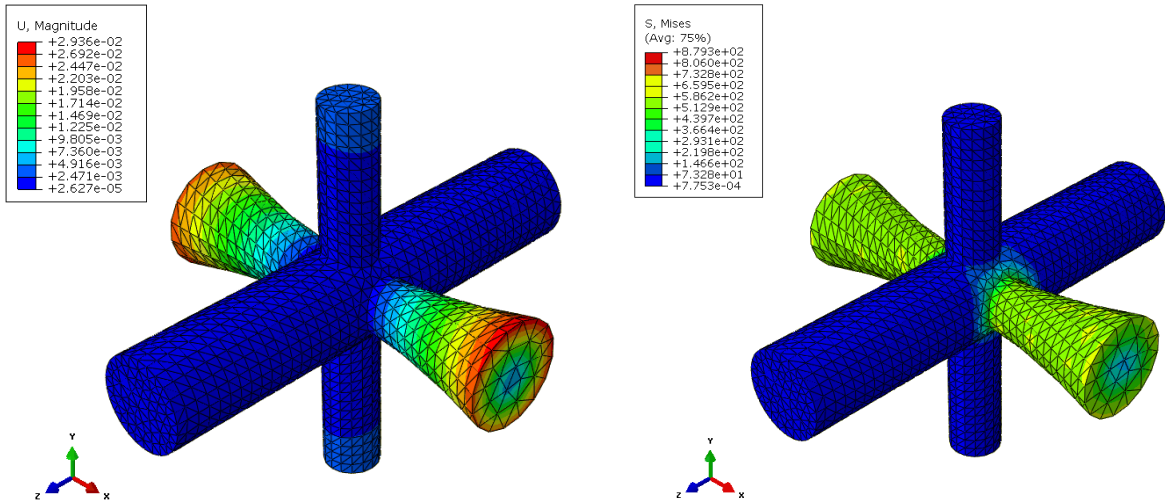
9. Test 9- Uniform curvature for D_{66} : when we apply a uniform bending curvature $\chi_{xz} = 1$ on the unit cell's boundary, the corresponding mixed boundary conditions are then written as

$$\begin{aligned}
u_x &= -xy && \text{on } n_1 \text{ face} \\
u_y &= x^2 / 2 && \text{on } n_2 \text{ face} \\
u_z &= 0 && \text{on } n_3 \text{ face}
\end{aligned} \tag{5.43}$$

which yields

$$D_{66} = 2U_{cell} / V - C_{11}y^2 \tag{5.44}$$

The deformation modes including displacements and stress distributions within trabecular bone unit cell 1 and $2 \times 2 \times 2$ for the uniaxial torsion ($\chi_{xx} = 1$ and $\chi_{zz} = 1$), biaxial torsion ($\chi_{xx} = \chi_{yy} = 1$), and bending ($\chi_{xy} = 1$ and $\chi_{yz} = 1$) under the corresponding boundary conditions are illustrated on [Figures 5.8-5.12](#).



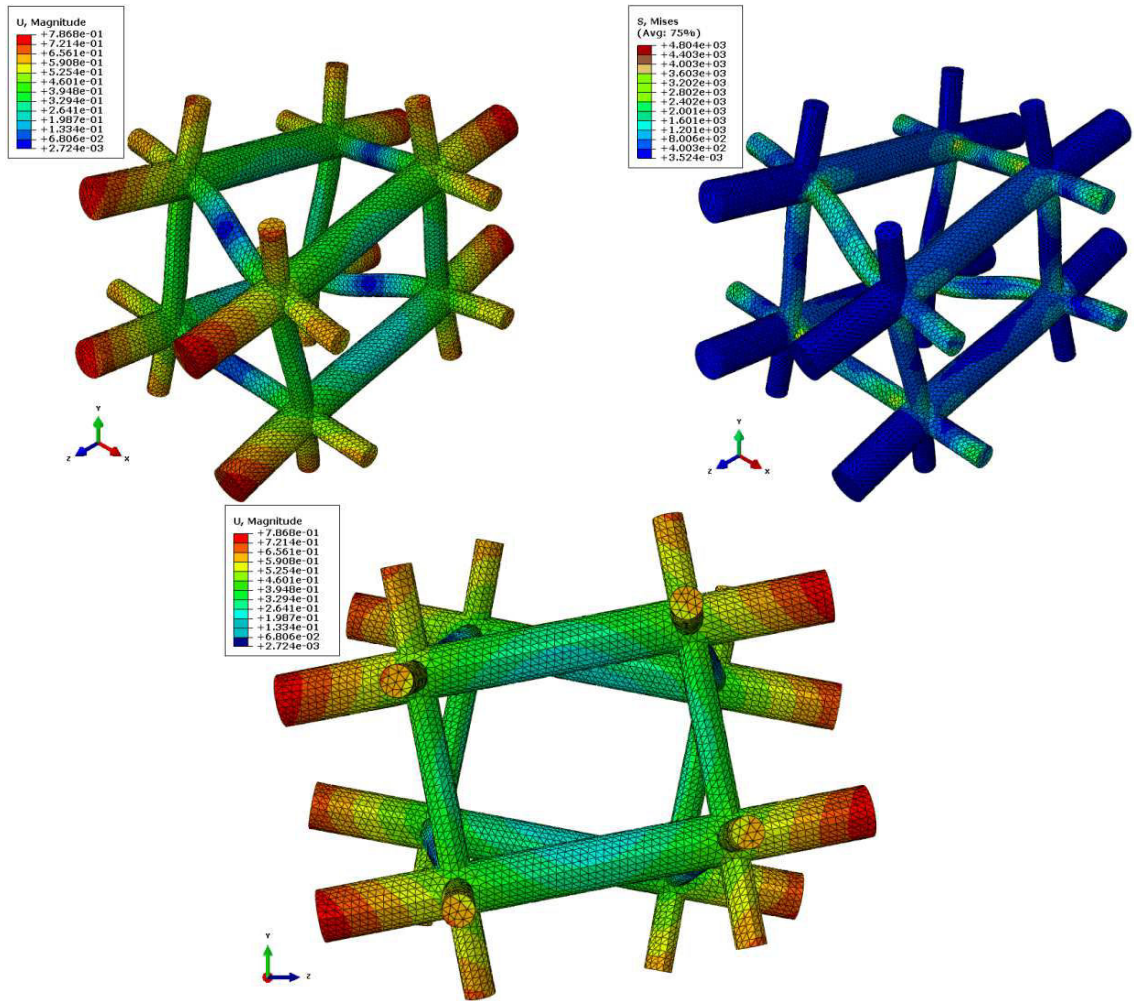
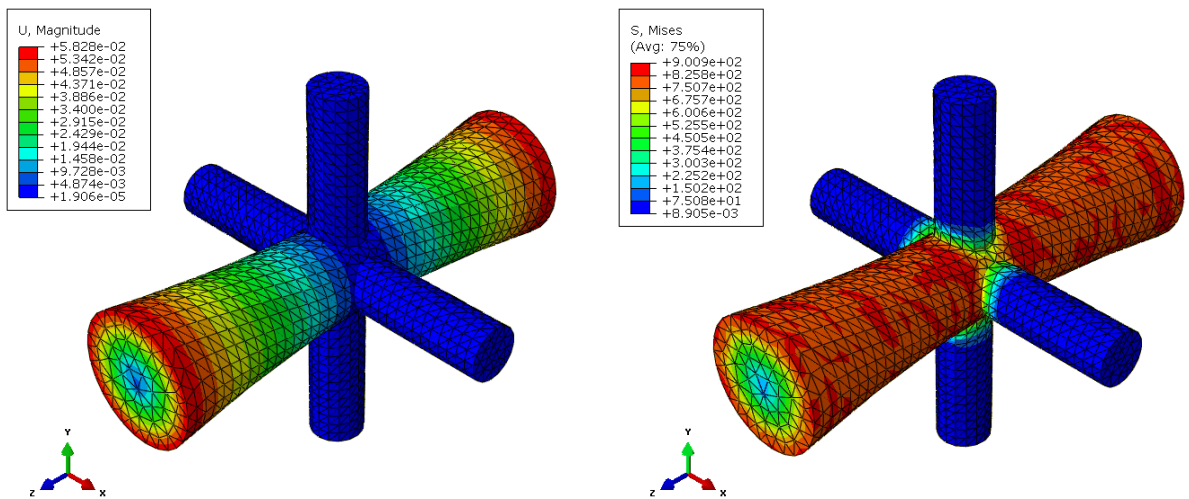


Figure 5.8: Displacements and Von Mises stress distributions due to torsional rotation about x-axis ($\chi_{xx} = 1$).



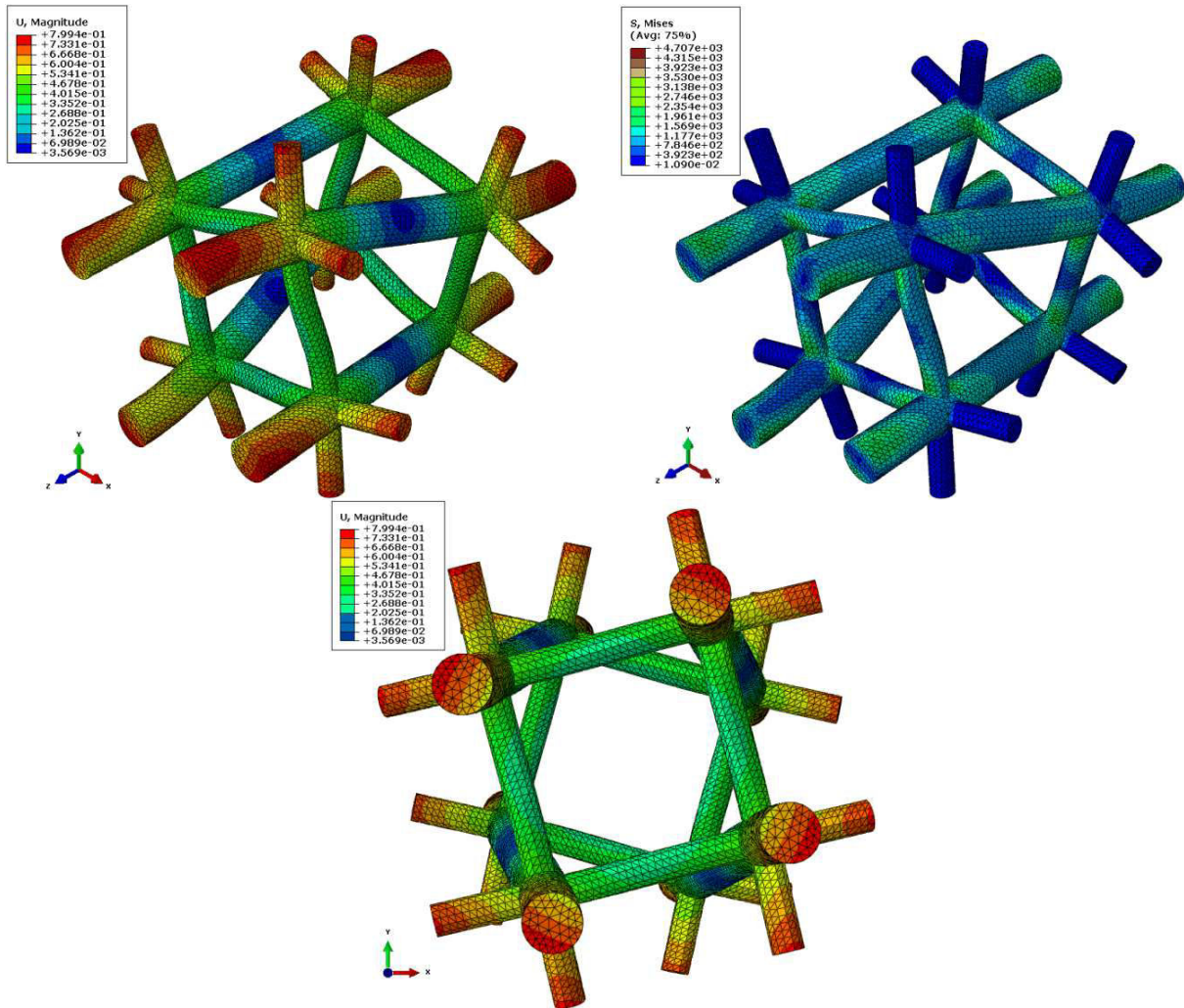
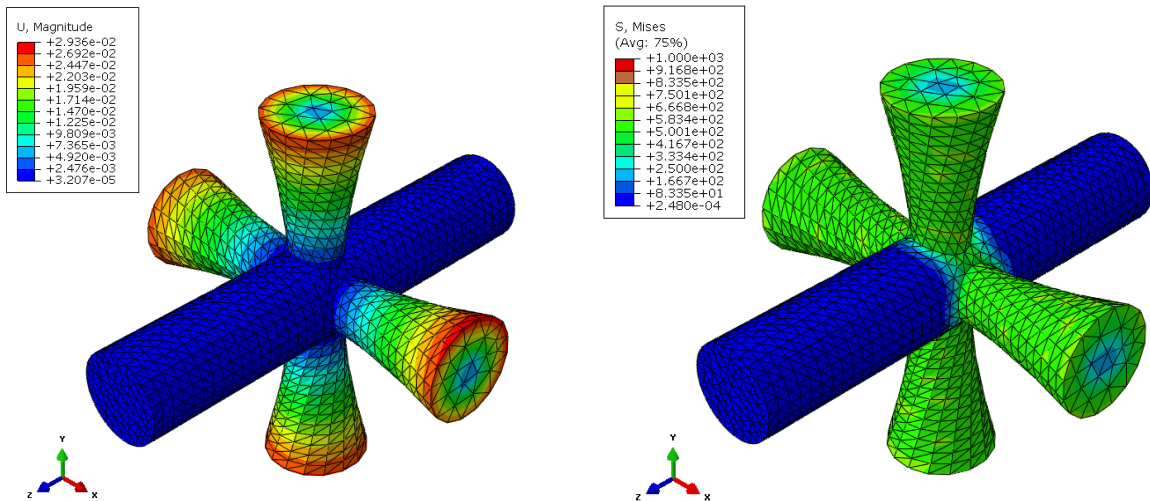


Figure 5.9: Displacements and Von Mises stress distributions due to torsional rotation about z-axis ($\chi_{zz} = 1$).



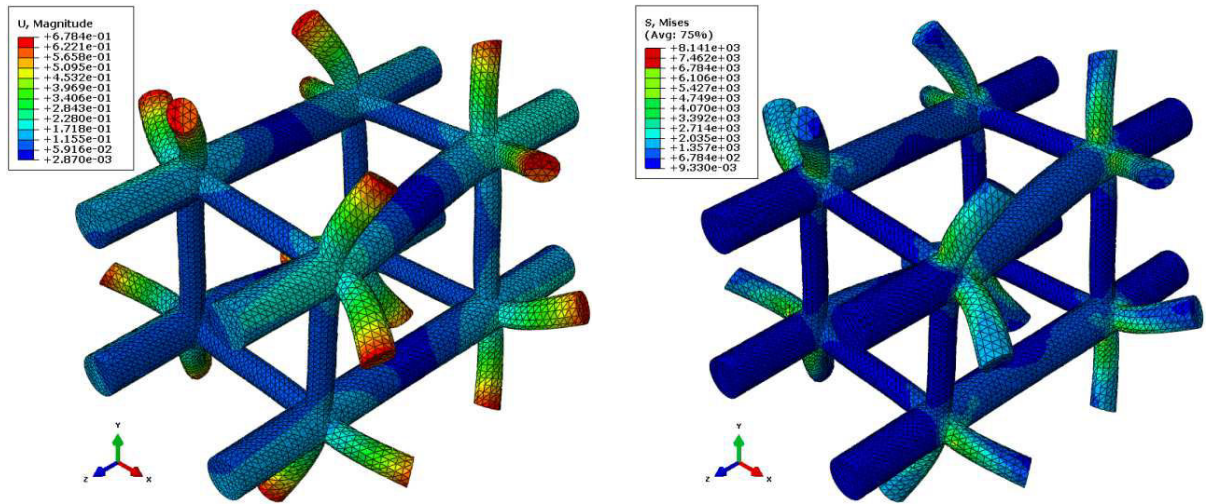


Figure 5.10: Displacements and Von Mises stress distributions due to biaxial torsional rotation in xy ($\chi_{xx} = \chi_{yy} = 1$).

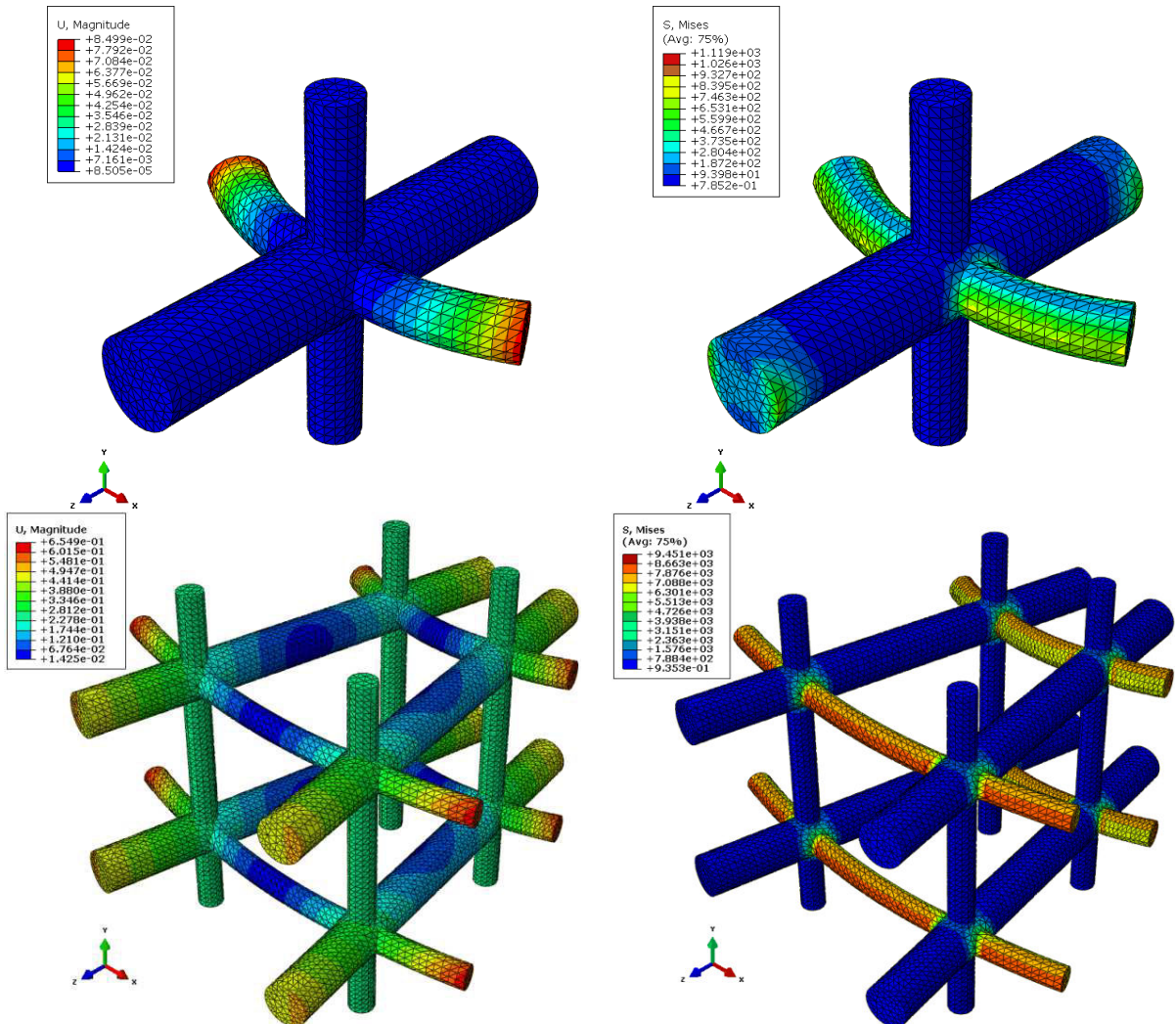


Figure 5.11: Displacements and Von Mises stress distributions due to uniform curvature $\chi_{xy} = 1$.

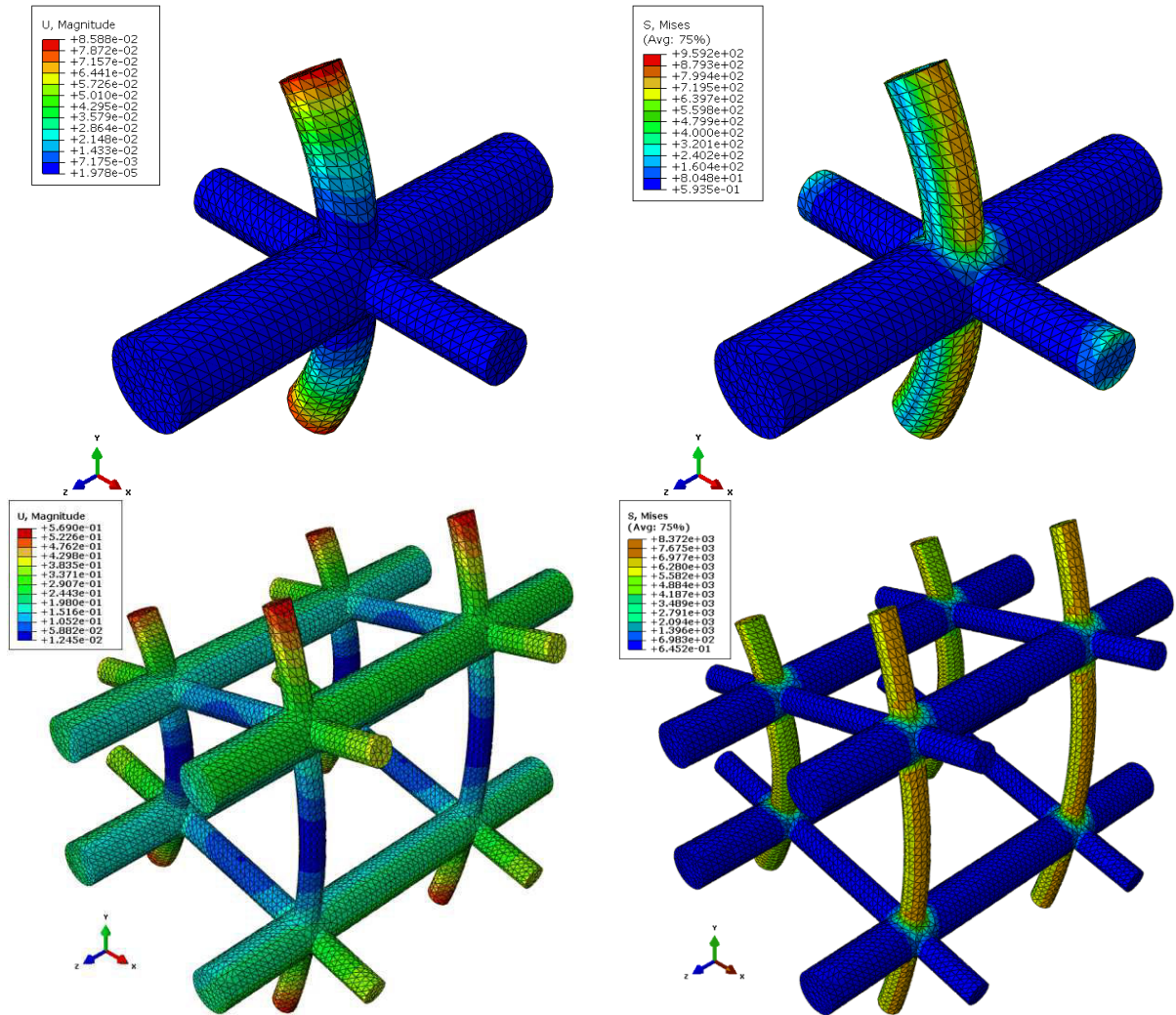


Figure 5.12: Displacements and Von Mises stress distributions due to uniform curvature

$$\chi_{yz} = 1.$$

An essential issue in predicting the effective properties of trabecular bone (but also any other material with a microstructure) is the adequate size of the RVE to be used in calculations or testing so that the boundary conditions effects are minimized.

As described earlier, the 3D periodic model of trabecular bone can be represented by 3D repeating unit cells, [Figure 5.1\(a\)](#), each unit cell being the smallest elementary pattern capable of reproducing the whole structure. Several different periodic cell sizes are exposed on [Figure 5.1](#), including 1, 2×2×2, 4×4×4, and 6×6×6 unit cell sizes. In order to study the effect of scale size, we choose different sample sizes involving the repetition of the smallest unit cell to form different unit cell sizes. Since our objective is studying scale effects, we then presently explore how the effective couple-stress elastic constants obtained using mixed displacement and traction boundary conditions within the elementary cell changes when we increase the size of the repeated unit cell (see [Table 5.2](#)). Computations are performed on 4×4×4, and 6×6×6 unit cell sizes which need a huge powerful machine due to the large computational power required. It was unattainable to further increase the domain size of trabecular bone due to the huge required computational power.

Table 5.2: Calculated effective couple-stress stiffness tensors of trabecular bone with sample 1, 2×2×2, 4×4×4, and 6×6×6.

Stiffness tensor C_{ij} (MPa)	Uniaxial tensile tests		Biaxial tensile tests		Shear tests	
	$C_{11} = C_{22}$	C_{33}	C_{12}	$C_{13} = C_{23}$	C_{44}	$C_{55} = C_{66}$
1, 2×2×2, 4×4×4, 6×6×6	166	554	4.5	13	1.9	3
Couple-stress tensor D_{ij} (N)	Uniaxial torsional test		Biaxial torsional tests		Curvature tests	
	$D_{11} = D_{22}$	D_{33}	D_{12}	$D_{13} = D_{23}$	D_{44}	$D_{55} = D_{66}$
1	0.14	1.26	0.009	0.018	0.21	0.18
	$l_b = 0.15mm ; l_t = 0.30mm$					
2×2×2	2	3.7	0.85	1.7	50	31.5
	$l_b = 2mm ; l_t = 4mm$					
4×4×4	7.4	9.4	--	--	254	157
	$l_b = 4.5mm ; l_t = 9mm$					
6×6×6	16	19	--	--	582	358
	$l_b = 7mm ; l_t = 14mm$					

The iso-displacements and Von Mises stress distributions within 4×4×4 unit cells due to uniaxial tensile in x ($\epsilon_{xx}=1$), shear ($\epsilon_{xz}=1$), uniaxial torsion about z ($\chi_{zz}=1$), and curvature $\chi_{yz}=1$ are respectively shown in [Figures 5.13-5.16](#). Additionally, plots of deformation modes within 6×6×6 unit cells due to uniaxial torsion about x ($\chi_{xx}=1$), and bending curvatures $\chi_{xy}=1$, and $\chi_{yz}=1$ are given respectively in [Figures 5.17-5.19](#). In those simulations, we keep the same size meshes like 1 and 2×2×2 cells.

One can conclude from the results illustrated in [Table 5.2](#) that mixed displacement and traction boundary conditions give effective elastic coefficients C_{ij} which are independently of the unit cell size.

On the other hand, the dependency of the second couple stress moduli D_{ij} on the RVE size is clear due to the fact that these moduli increase with the RVE size. Although the analysis highlights the magnitude of the size effects on the macroscopic behavior, we are not able to determine the converged value of those moduli due to the very slow apparent convergence rate.

Since the characteristic length is an essential parameter in the couple-stress continua, we generalize the definition of this parameter to orthotropic continuum in terms of engineering constants. Two characteristic lengths can be extracted from the micropolar constitutive law, corresponding to the bending or torsion couple-stress components. The characteristic lengths for bending and torsion are then identified from the homogenized orthotropic stiffness matrix components as

$$l_{b_{xy}}^2 = \frac{1}{2} l_{t_{xy}}^2 = \frac{D_{66}}{4C_{44}}; \quad l_{b_{xz}}^2 = l_{t_{xz}}^2 = \frac{1}{2} l_{t_{xy}}^2 = \frac{D_{44}}{4C_{66}} \quad (7.45)$$

The calculated values of characteristic lengths in bending and torsion for different bone sample sizes, including $1,2 \times 2 \times 2$, $4 \times 4 \times 4$, and $6 \times 6 \times 6$, are given in Table 5.2. These lengths are close to the RVE linear dimension, showing that microstructural effects are indeed pronounced, and they further increase with the size of the RVE.

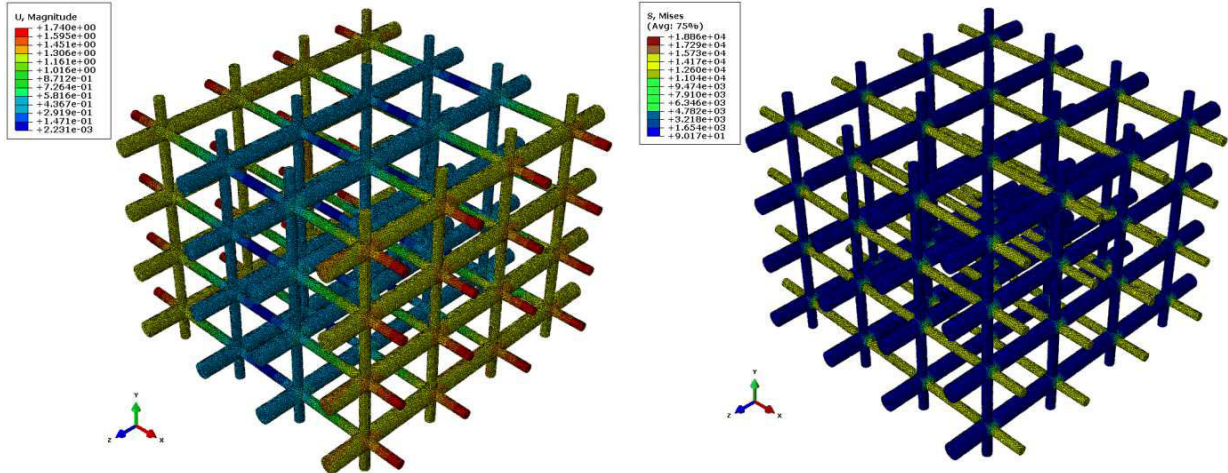


Figure 5.13: Displacements and Von Mises stress distributions due to uniaxial tensile test in x within $4 \times 4 \times 4$ unit cells.

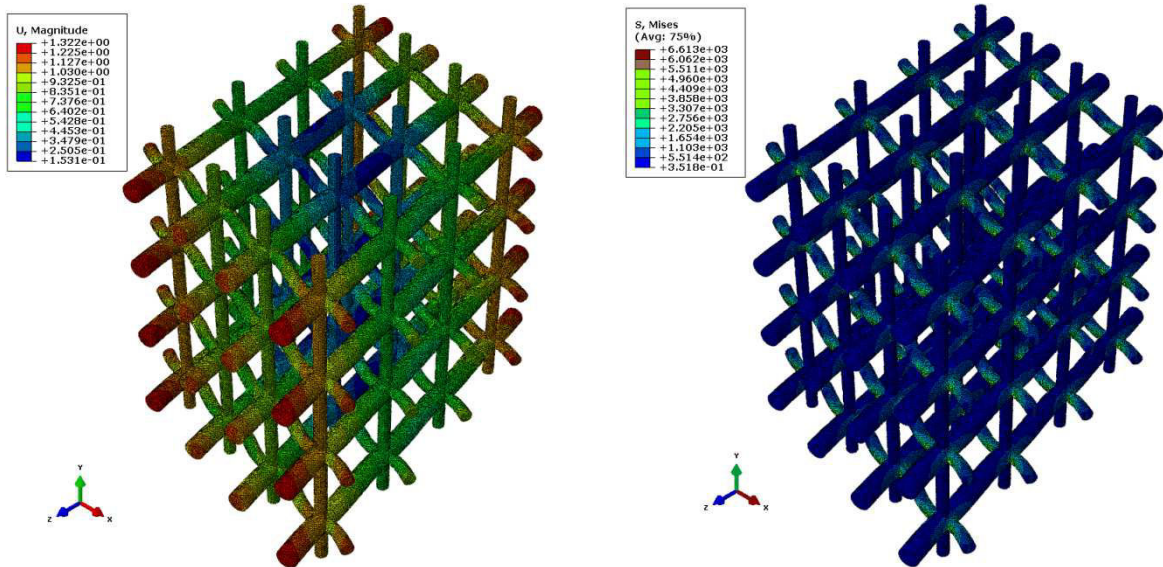


Figure 5.14: Displacements and Von Mises stress distributions due to shear test in xz within $4 \times 4 \times 4$ unit cells.

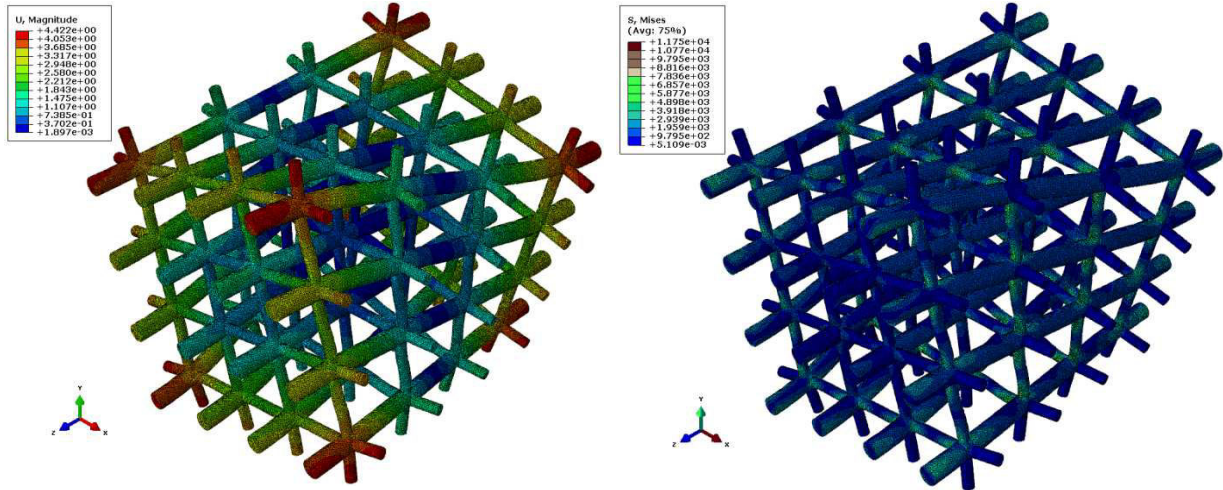


Figure 5.15: Displacements and Von Mises stress distributions due to torsional rotation $\chi_{zz} = 1$ within $4 \times 4 \times 4$ unit cells.

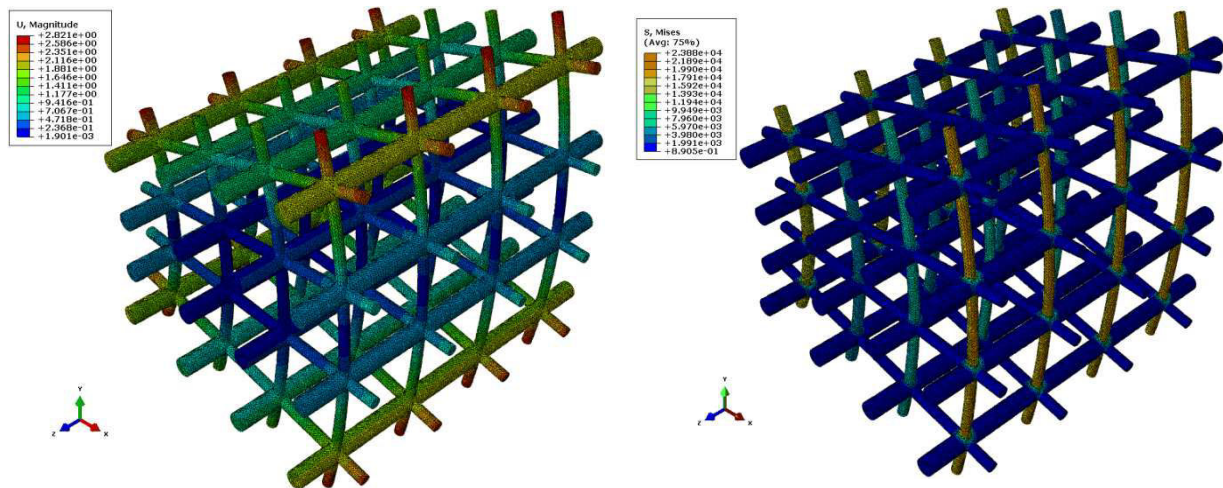


Figure 5.16: Displacements and Von Mises stress distributions due to uniform curvature $\chi_{yz} = 1$ within $4 \times 4 \times 4$ unit cells.

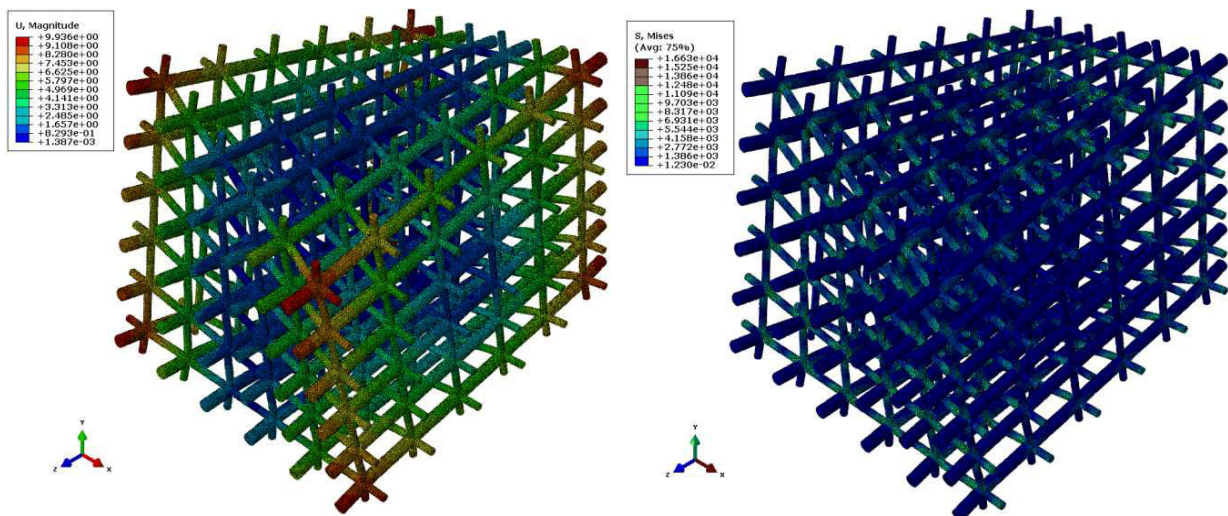


Figure 5.17: Displacement and Von Mises stress distributions due to torsional rotation $\chi_{xx} = 1$ within $6 \times 6 \times 6$ unit cells.

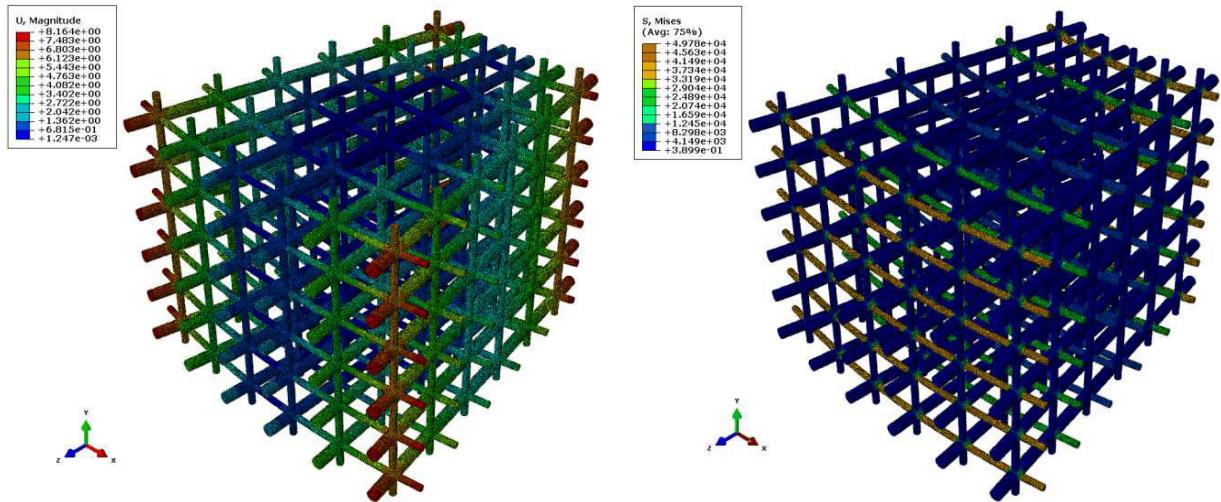


Figure 5.18: Displacement and Von Mises stress distributions due to bending curvature $\chi_{xy} = 1$ within $6 \times 6 \times 6$ unit cells.

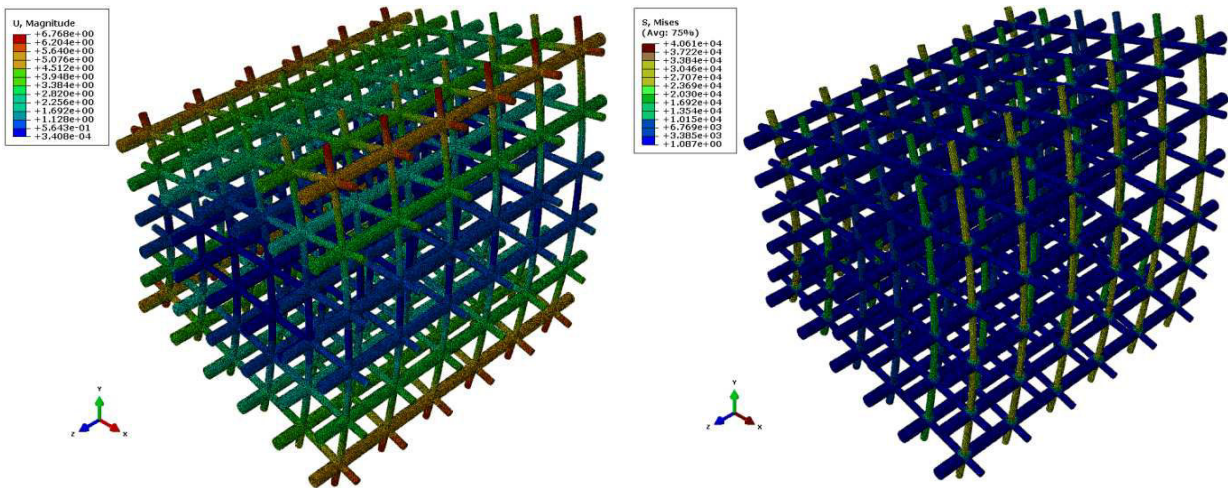


Figure 5.19: Displacement and Von Mises stress distributions due to bending curvature $\chi_{yz} = 1$ within $6 \times 6 \times 6$ unit cells.

5.4 Effective couple stress moduli of a two phase material consisting of bone tissue and marrow

Bone marrow found within the porous structure of trabecular bone provides a specialized environment for numerous cell types, including mesenchymal stem cells (Birmingham et al., 2013). To improve our understanding of the trabecular bone mechanical behavior, especially in bending and torsion, it is interesting to determine the effects of the presence of bone marrow on trabecular bone mechanical properties. The present section focuses on the mechanical behavior analysis of bones at mesoscopic scale under prescribed boundary conditions, paying a special attention to both the trabecular bone and the bone marrow filling the porosities.

The nature of trabecular bone which is composed of bony trabecular struts and marrow-filled cavities can be described in terms of structural and material properties. Trabecular bone is usually represented as open-celled materials, since it has a very low volume fraction. Thus,

the open-celled regular network is chosen as the representative unit cell. We represent trabecular bone as having idealized 3D periodic structures, consisting of hard tissue (bone trabeculae) and soft tissue (bone marrow). In order to explain the bone marrow contribution on the mechanical behavior of trabecular bone, finite element investigations on idealized trabeculae have been performed to capture the interaction between bone and marrow under various loading types.

Based on energetic approach presented in [Section 5.3](#), we evaluate the effective elastic couple-stress moduli of trabecular bone by equating the total elastic strain energy of the heterogeneous elastic medium (periodic trabecular unit cell consisting both bone tissue and marrow) and the elastic strain energy of the equivalent homogeneous couple-stress medium.

5.4.1 Material and geometrical models

Vertebral trabecular bone is modeled as a two phase material consisting of a bone tissue which is the stiff phase forming a trabecular network and pores which is the soft phase. We assume that both phases are homogeneous, linear elastic, and isotropic. Bone tissue is assigned to have a Young's modulus of 12.0 GPa and a Poisson ratio of 0.3 while the cavities are filled with soft material with a Young's modulus of 2 MPa and a Poisson ratio of 0.167 ([Lacroix and Prendergast, 2002](#)).

We model trabecular bone as an idealized 3D periodic network composed of bony struts and marrow, as shown in [Figure 5.20](#); the cellular network represents the bone tissue (a) and the remaining void spaces represent the marrow (b). We select the micro-architecture parameters of the trabecular struts for a person at the age of 60.

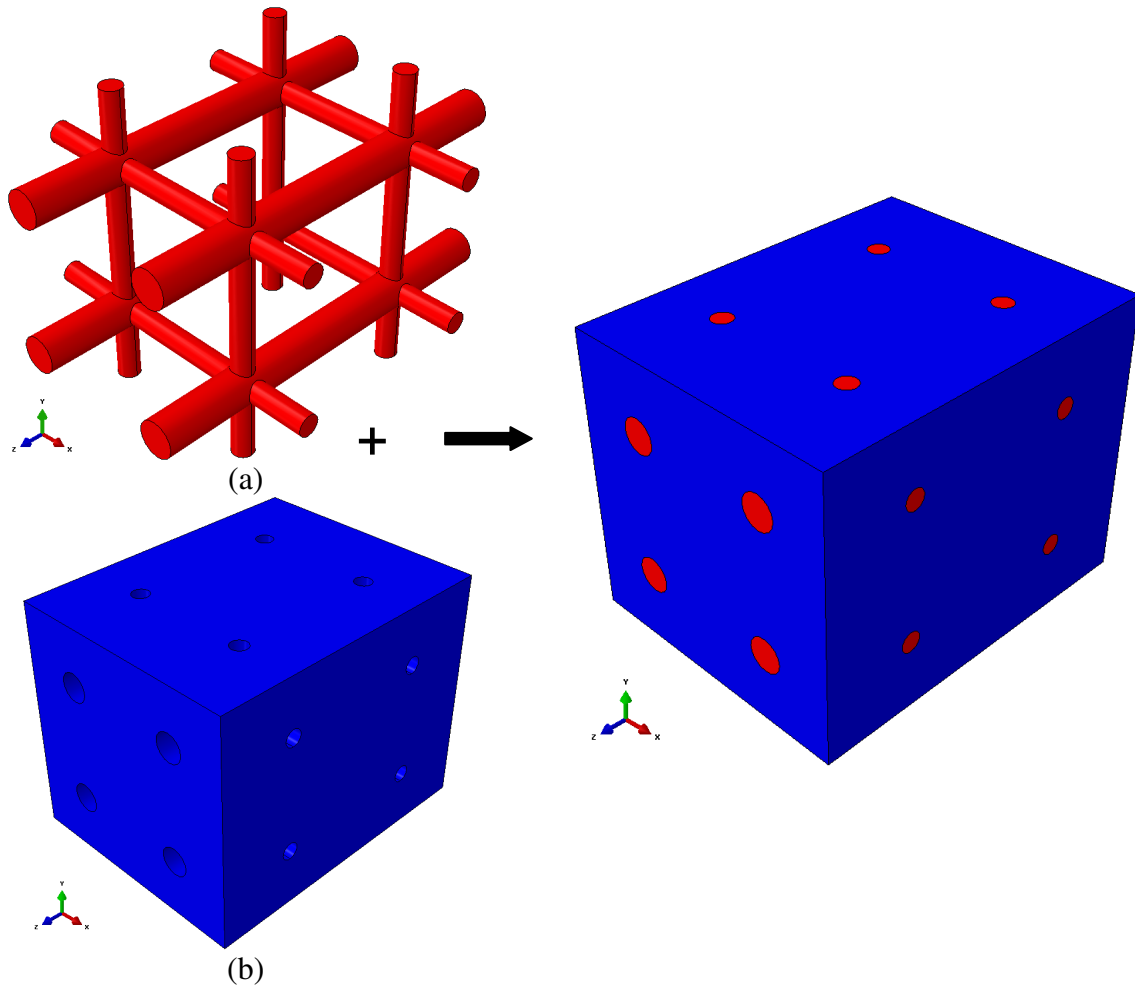


Figure 5.20: Representation of trabecular bone composed of bony trabecular struts and marrow-filled cavities. (a) bone tissue and (b) marrow.

5.4.2 Results of couple stress moduli with and without marrow

Effective couple stress elastic moduli of trabecular bone are analyzed computationally using the finite element software ABAQUS, utilizing the first-order tetrahedral element C3D4H. We keep the same mesh sizes of 0.04 for the stiff bone tissue making up the trabecular bone tissue network and the soft material representing the porosities.

In order to investigate the contribution of bone marrow on the effective mechanical response of trabecular network, finite element investigations have been performed on trabecular bone network of size $2 \times 2 \times 2$ with tensile modulus 2 MPa (as indicated before) and without the presence of bone marrow. From a computational viewpoint, a very low modulus has been adopted ($2 \cdot 10^{-3}$ Pa) for the surrounding matrix phase to simulate the absence of marrow.

The iso-displacement distributions within trabecular bone with marrow under the corresponding loadings applied to obtain the couple-stress coefficients are shown in [Figures 5.21-5.32](#). This includes the deformation modes from uniaxial and biaxial extension tests, in-plane and out-of plane shear tests which have been used to evaluate the stiffness matrix

components **C**, uniaxial and biaxial torsion tests, and the in plane and out-of plane bending tests used to evaluate the second couple stress stiffness matrix components **D**. The calculated components of the effective couple-stress stiffness tensors obtained including and excluding bone marrow are summarized in [Table 5.3](#).

Table 5.3: Effective couple-stress moduli of trabecular bone of sample size $2 \times 2 \times 2$ with and without bone marrow.

Stiffness tensor C_{ij} (MPa)	Uniaxial tensile tests		Biaxial tensile tests		Shear tests	
	$C_{11} = C_{22}$	C_{33}	C_{12}	$C_{13} = C_{23}$	C_{44}	$C_{55} = C_{66}$
Without bone marrow	152	539	4.0	11.0	1.8	3.2
With bone marrow	155	542	4.1	11.1	2.8	4.2
Difference (%)	2	0.5	2	1	35	23
Couple stress stiffness tensor D_{ij} (N)	Uniaxial torsional test		Biaxial torsional tests		Curvature tests	
	$D_{11} = D_{22}$	D_{33}	D_{12}	$D_{13} = D_{23}$	D_{44}	$D_{55} = D_{66}$
Without bone marrow	2.0	3.7	1.0	1.7	46	29
With bone marrow	2.5	4.0	1.1	1.9	47	30
difference (%)	20	7.5	9	10	2	3

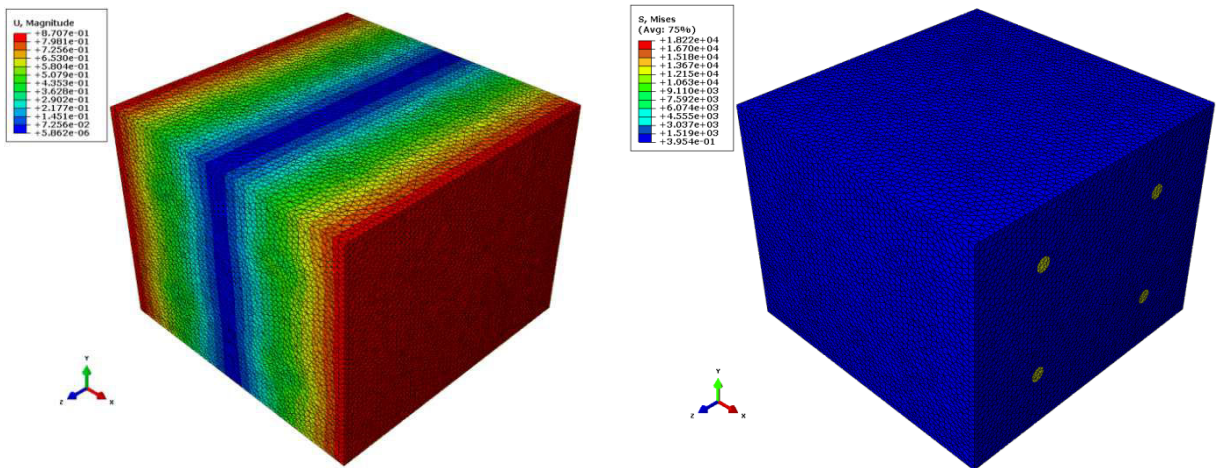


Figure 5.21: Displacements and Von Mises stress due to uniaxial extension ($\epsilon_{xx} = 1$) considering bony trabecular struts and marrow-filled cavities.

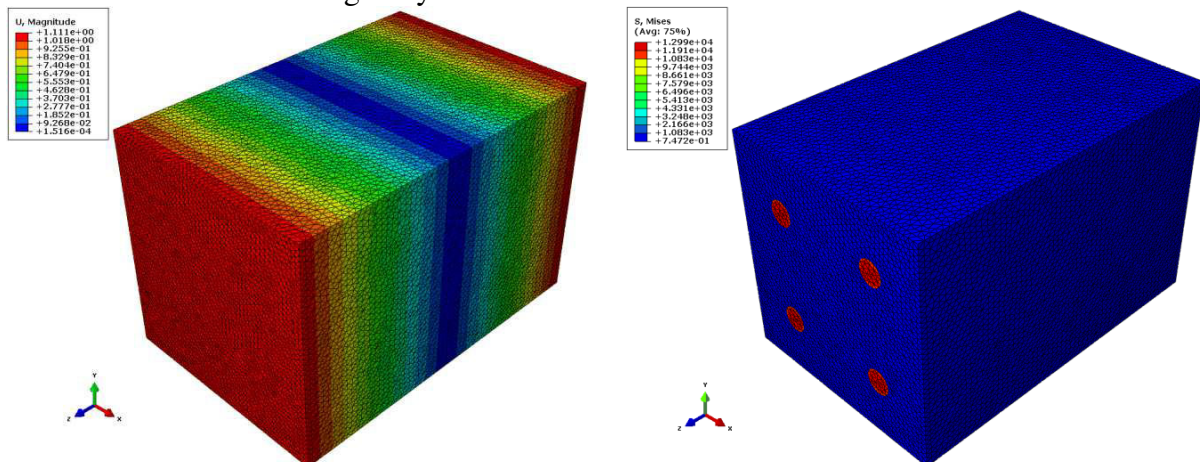


Figure 5.22: Displacements and Von Mises stress due to uniaxial extension ($\epsilon_{zz} = 1$) considering bony trabecular struts and marrow-filled cavities.

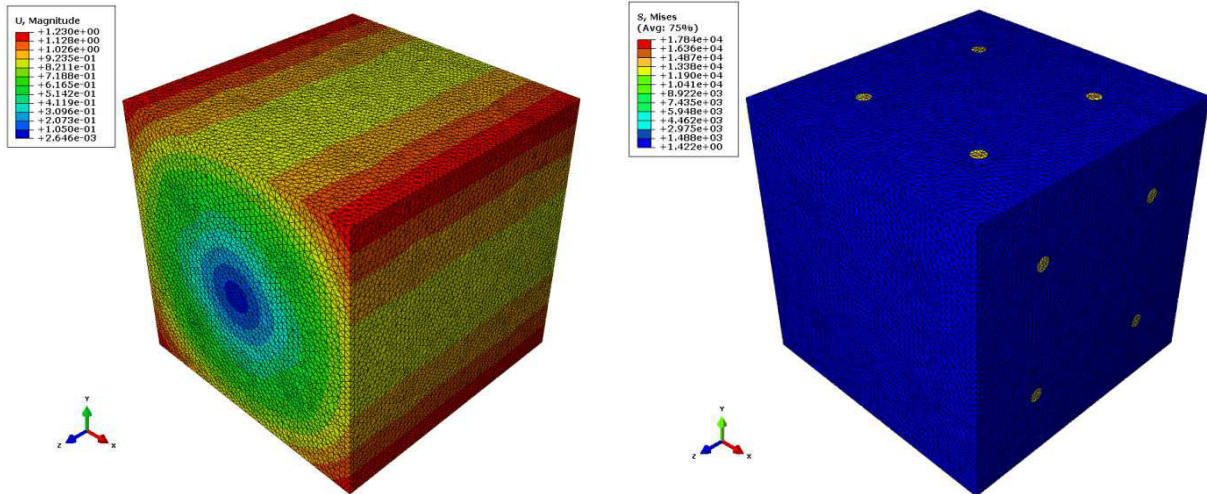


Figure 5.23: Displacements and Von Mises stress distributions due to biaxial extension ($\epsilon_{xx} = \epsilon_{yy} = 1$) considering bony trabecular struts and marrow-filled cavities.

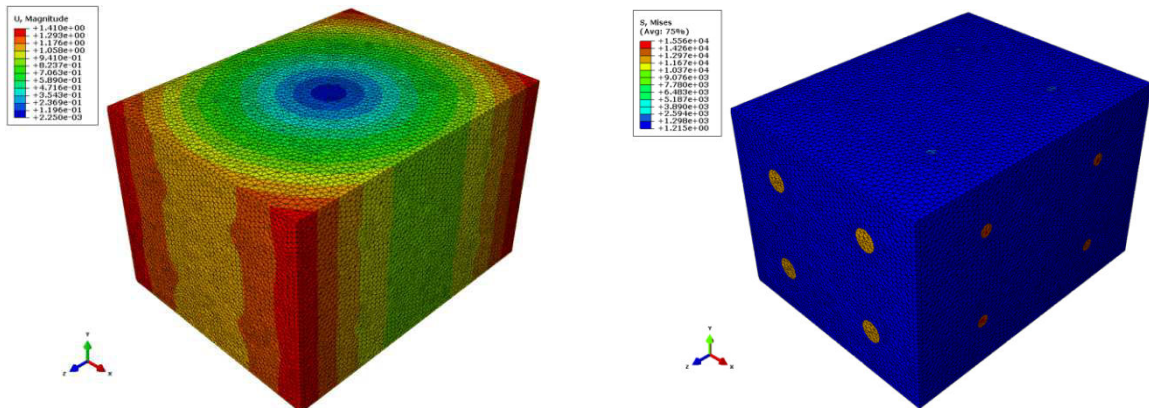


Figure 5.24: Displacements and Von Mises stress distributions due to biaxial extension ($\epsilon_{xx} = \epsilon_{zz} = 1$) considering bony trabecular struts and marrow-filled cavities.

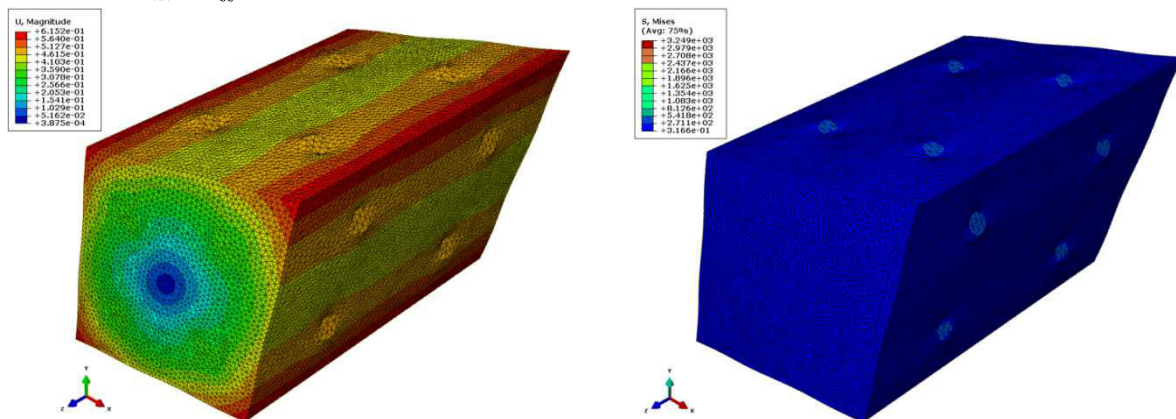


Figure 5.25: Displacements and Von Mises stress due to shear test in xy ($\epsilon_{xy} = 1$) considering bony trabecular struts and marrow-filled cavities.

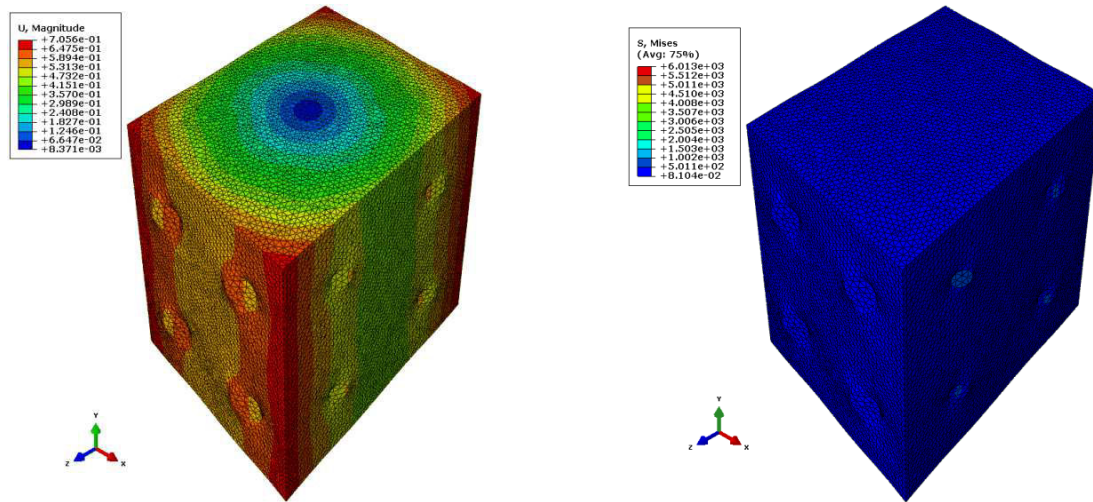


Figure 5.26: Displacements and Von Mises stress due to shear test in xz ($\epsilon_{xz} = 1$) considering bony trabecular struts and marrow-filled cavities.

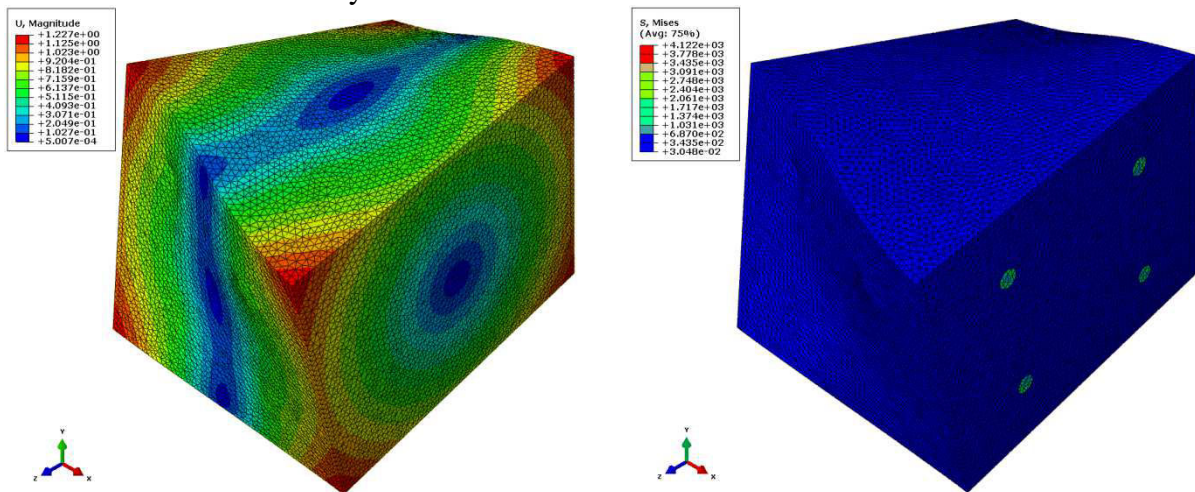


Figure 5.27: Displacements and Von Mises stress due to torsional rotation ($\chi_{xx} = 1$) considering bony trabecular struts and marrow-filled cavities.

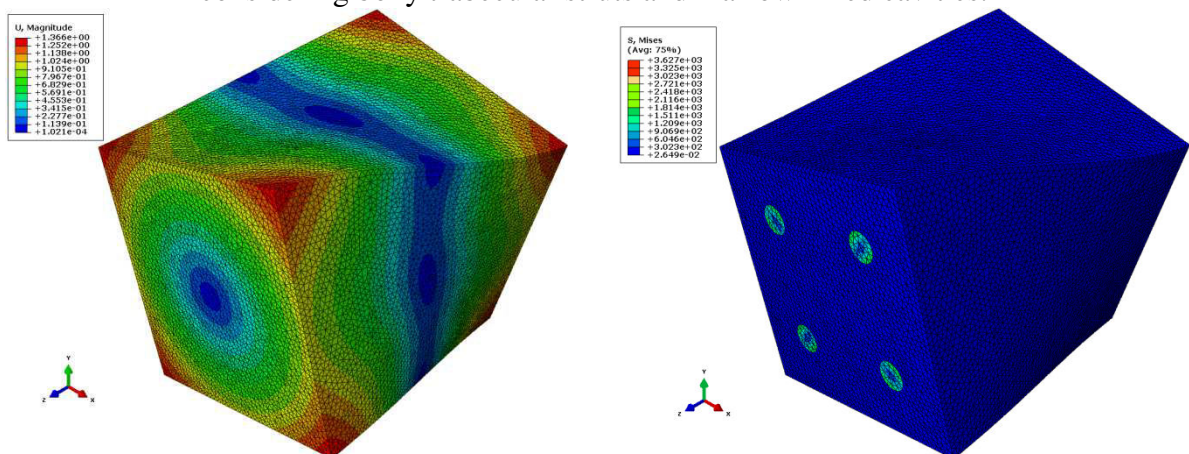


Figure 5.28: Displacements and Von Mises stress due to torsional rotation ($\chi_{zz} = 1$) considering bony trabecular struts and marrow-filled cavities.

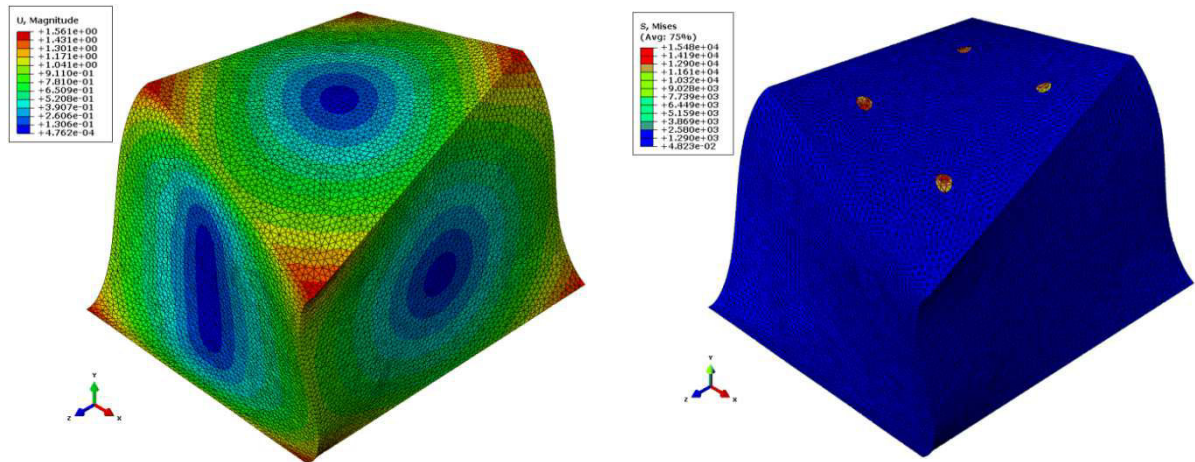


Figure 5.29: Displacements and Von Mises stress due to biaxial torsional rotation ($\chi_{xx} = \chi_{yy} = 1$) considering bony trabecular struts and marrow-filled cavities.

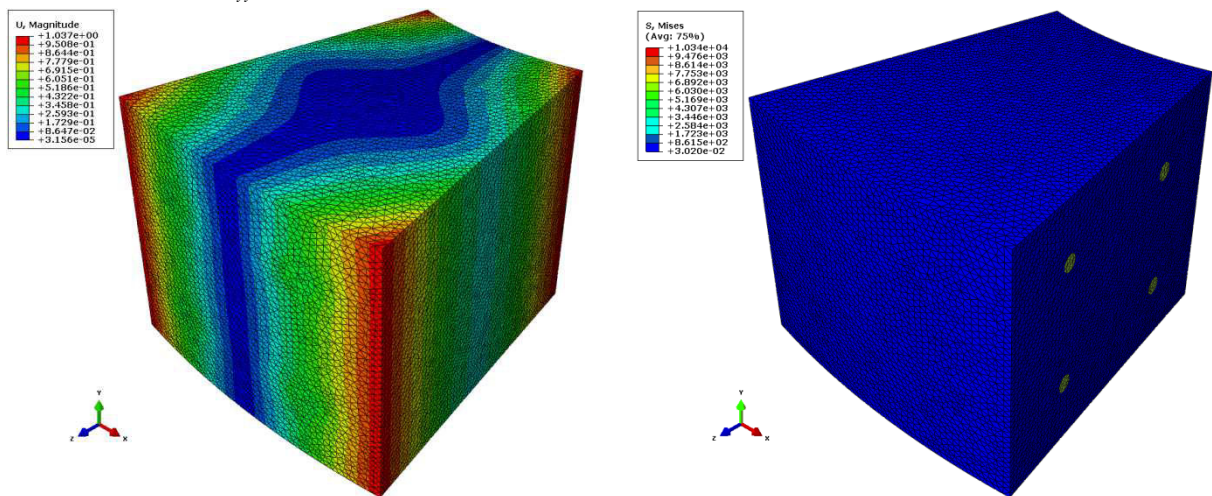


Figure 5.30: Displacements and Von Mises stress due to bending curvature ($\chi_{xy} = 1$) considering bony trabecular struts and marrow-filled cavities.

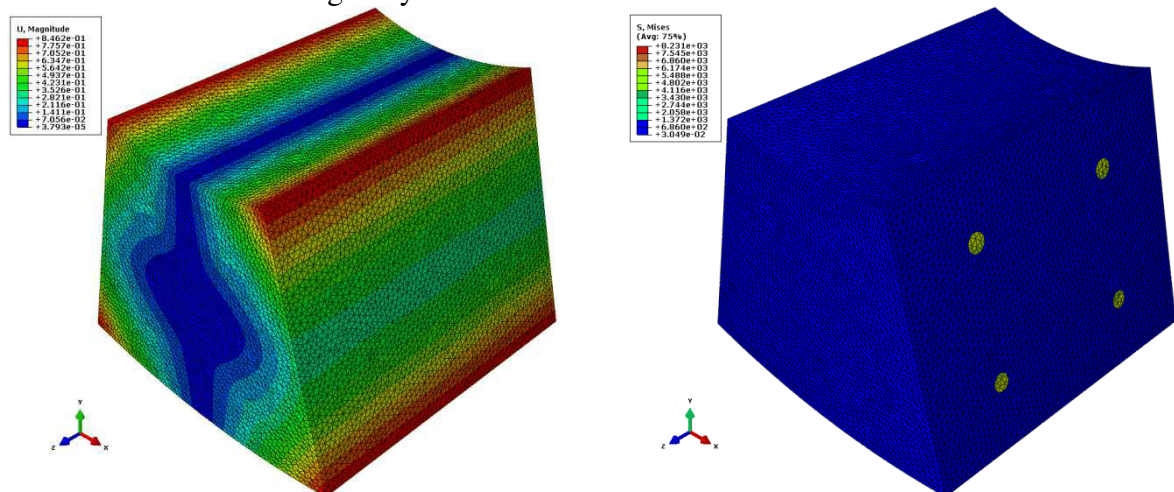


Figure 5.31: Displacement and Von Mises stress due to bending curvature ($\chi_{xz} = 1$) considering bony trabecular struts and marrow-filled cavities.

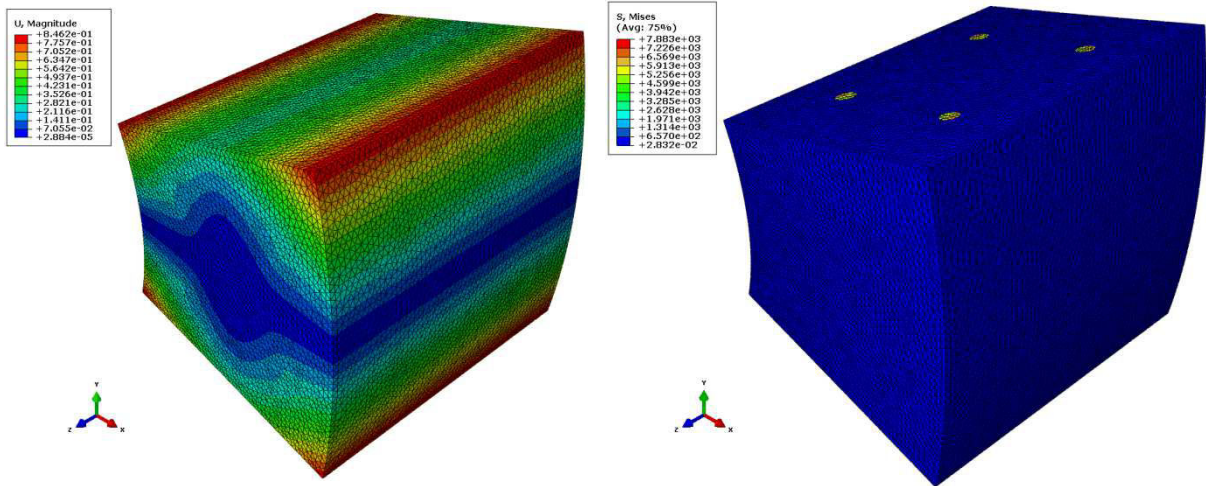


Figure 5.32: Displacement and Von Mises stress due to bending curvature ($\chi_{yz} = 1$) considering bony trabecular struts and marrow-filled cavities.

When we come across the analysis of the previous results focusing on bone marrow effects, we observe that bone marrow contributes to an overall increase of the effective mechanical properties under extension, shearing, twisting, and bending curvature tests. Significant increases of moduli occur for the shearing mode, followed by twisting; this can be explained as the presence of bone marrow causes stiffening effect under these tests.

The maximum increase observed under tensile and bending curvature tests is about 3%; this indicates that the effect of bone marrow in increasing bone stiffness in tension and bending is not significant. On the contrary, the effects of bone marrow in increasing bone shear and torsion stiffnesses become significant: the twisting moments have less stiffening effect than that in shear: the maximum increase in shear stiffness is about 35%, while it is about 23% in torsion.

5.5 Conclusions

In this chapter, we computed from finite element analyses the effective couple-stress continuum properties of vertebral trabecular bone represented by three-dimensional periodic cellular network solid models, based on the equivalent strain energy approach. Boundary conditions based on combinations of displacement and traction boundary conditions applied along the outer boundaries of the bone structure are formulated, leading to the determination of both the classical and non classical components of the effective constitutive matrix. Such boundary conditions demonstrate that the effective elastic tensile and shear coefficients are independent of the bone window size, while the effective torsion and bending moment constants are dependent on the bone structure size.

We further extended the analysis by modeling vertebral trabecular bone as a two-phase material consisting of bone tissue (stiff phase) forming a trabecular network and soft tissue which refer to bone marrow (soft phase) present in pores. The effects of the presence of bone marrow on the effective trabecular bone properties are examined under uniaxial and biaxial tensile and torsion tests, shear tests, as well as bending moment tests.

The present numerical modeling performed on trabecular bone is a useful tool to predict the effective properties of bone and to better understand and interpret experimental results. Furthermore, it can serve as a framework to study the effective couple-stress moduli of other three dimensional composite and cellular materials with orthotropic properties. The obtained results can also provide better insight to researchers involved in the computational modeling of materials and in experimental testing of mechanical properties of bone and other porous structures.

Since trabecular bone consists of a bony network of connecting rods filled with bone marrow which is actually a fluid phase, trabecular bone is likely to exhibit a viscoelastic behavior, which shall depend on the material behavior of the bone tissue as well as on the interaction between bone trabeculae and bone marrow (solid and fluid phases). The prediction of the effective couple stress-moduli demonstrating a viscoelastic behavior will accordingly be more realistic and is planned in future works.

CHAPTER 6: SIZE DEPENDENT STATIC AND DYNAMIC BEHAVIOR OF TRABECULAR BONE

In order to investigate microstructure-related scale effects on bone macroscopic properties, Cosserat models of vertebral trabecular bone are constructed, based on micromechanical approaches. A micropolar equivalent continuum model is firstly constructed, the effective mechanical properties of which are expressed versus the geometrical and mechanical microparameters, accounting for bending, axial, transverse shear deformations, and torsion. The static and dynamic effective behaviors of vertebral trabecular bone in the form of beam structures are next analyzed, in terms of the deflection, torsion and eigenfrequencies of deformations. The governing differential equations of static and dynamic bending and torsion of trabecular bone are derived using variational principles based on non-classical theory, and explicit solutions are derived, accounting for length scale effects. The static bending and torsion behaviors developed by the non-classical theory show significant differences with those obtained by the classical theory, when the ratio of the beam characteristic size to the internal material length scale parameter is small, or for small specimen sizes. The identified static and dynamical effective properties of bone are correlated to physiological factors, such as the age of patient, the effective bone density, and pathologies leading to a modification of the internal architecture.

6.1 Introduction

Classical continuum theory based on the Cauchy-Boltzmann approach is the simplest continuum model in which the stress at a material point depends only on the strain at the same point. As a consequence, it cannot incorporate microstructural size effects and internal lengths, which occur in micron- and sub-micron-scale structures. However, real materials such as biological tissues often exhibit a number of important length scales, which must be included in any realistic model. Although there have been many continuum models of bone developed over the last two decades on the basis of classical elasticity ([Bowman et al. 1998](#); [Taylor et al. 2002](#)), those models ignore microstructure-related scale effects on the macroscopic mechanical properties. The structural hierarchy of materials with microstructures such as bones plays an important role in determining their macroscopic mechanical behavior as well as the stress and strain distribution. This issue is presently investigated by studying generalized continuum mechanics theories which account for the influence of microstructure-related scale effects on the macroscopic properties of bone. Bone is a strongly heterogeneous material with microstructural features, requiring generalized continuum mechanics theories when the macroscopic length scale (identified as the smallest length scale of the deformation pattern) becomes comparable or smaller than the typical microstructural length scale, such as the size of trabeculae in cancellous bone. Especially, the classical assumptions inherent to classical elasticity are no more valid under such conditions.

The generalized continuum mechanics like micro-dilatation theory ([Nunziato and Cowin, 1979](#)), micro-polar or so-called Cosserat theory ([Eringen, 2001](#)), microstretch theory ([Eringen, 2001](#)), micro-strain theory ([Forest and Sievert, 2006](#)) and micromorphic theory

(Eringen, 2001) have inherently the capacity to bridge micro and macro scale using their explicit size effect features. These theories were widely applied for modeling purposes of foams (Diebels and Steeb, 2003), cellular materials and bone (Lakes, 1986) as well as heterogeneous materials (Forest and Sab, 1998; Forest et al., 1999) like sand, soil (Majid and Manzari, 2004; Karimi and Khoei, 2010) and rock (Stefanou and Sulem, 2010). The existence of couple stress in bones was first evidenced by Yang and Lakes (1981), who measured the effect of the size of a bone specimen on the apparent stiffness of cortical bone in quasi-static torsion; they further obtained the characteristic length scales for torsion and bending for cortical bone in the context of couple stress theory. Bone trabeculae are modelled as isotropic micropolar materials in Lakes (1993). Lakes and co-workers conducted a series of experiments on bone and other cellular materials, in which they observed a stiffening effect in such materials in bending and in torsion (Park and Lakes 1987) and a tougher notched bone Lakes et al. (1990) than expected from classical Cauchy-type elasticity. Those last authors found that Cosserat elasticity provides better predictions of the response of bone than classical elasticity theory.

The dynamics of cellular solids obeying a Cosserat behavior such as bones doesn't appear to have received much attention in the literature. Wang and Stronge (2001) used a micropolar theory to calculate displacements and stresses generated by a fundamental boundary value problem in dynamics of elastic continua; namely, a time-harmonic line force acting at a point on the edge of a two-dimensional honeycomb half-space. Baker et al. (1998) studied the effect of impact and energy absorption behaviour of cellular materials. Banerjee and Bhaskar (2005) developed a numerical scheme for reducing the computational expense associated with the free vibration and the response calculations of the cellular structures. Moreover, Banerjee and Bhaskar (2009) investigated the applicability and the limitations of the effective medium theory for dynamics of cellular structures.

6.2 Age-related change of vertebral bone architecture

We model the beam-like architecture of vertebral bone as a three-dimensional lattice with a unit cell geometry shown in Figure 6.1b. The architecture of the model (thick vertical columns and thinner horizontal struts) is based on studies of samples taken from the central part of vertebral bodies from normal Individuals aged from 30 to 90 years (Mosekilde, 1988, 1989). Four indices are used to describe the morphology of the unit cell: the horizontal trabecular thickness (D_h), the vertical trabecular thickness (D_v), and the mean distance between the horizontal trabeculae (L_h) as well as between the vertical trabeculae (L_v). From those morphological indices, an idealized model of trabecular microarchitecture is constructed – the prismatic shape. The age-related change of vertebral bone architecture (the changes in trabecular thickness and spacing that occur with aging) has been described by Mosekilde (1988, 1989), using the relations in Table 6.1.

The whole structure is generated from the repetition of the reference unit cell [Figure 6.1a](#) by means of three periodicity vectors defined in a Cartesian basis. Note that both vertical and horizontal trabeculae are idealized as a circular beam with diameter D_v and D_h , respectively.

Table 6.1: Micro-structural parameters for vertebral bone based on morphology–age relationships by [Mosekilde \(1988\)](#), age is measured in years.

Parameter	Relation
Horizontal trabeculae thickness (μm)	$D_h = -1.03 \times \text{Age} + 189$
Vertical trabeculae thickness (μm)	$D_v = 0.14 \times \text{Age} + 208$
Distance between horizontal trabeculae (μm)	$L_h = 13.74 \times \text{Age} + 288$
Distance between vertical trabeculae (μm)	$L_v = 6.74 \times \text{Age} + 456$

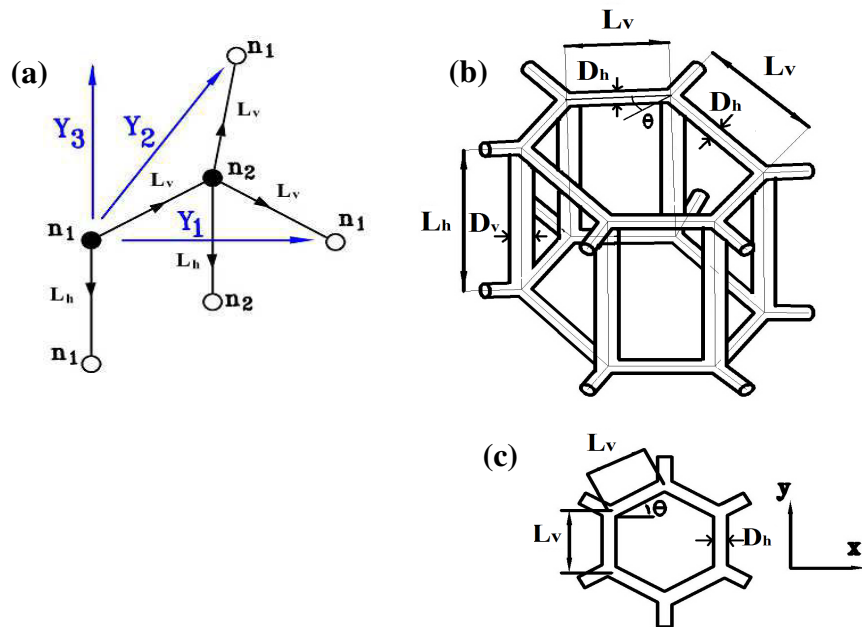


Figure 6.1: Representative model of vertebral trabecular bone and its parameters. (a) Reference unit cell and its periodicity vectors Y_1 , Y_2 , and Y_3 , (b) 3D hexagonal unit cell with thick vertical trabeculae and thinner horizontal ones rendering of human vertebral bone, (c) 2D hexagonal lattice.

A 3D geometric model of a regular hexagonal structure is considered as an idealized representation of vertebral trabecular bone, for which the micropolar elastic constants at the macroscopic level are identified from a micromechanical analysis. The considered hexagonal unit cell is composed of five beams; three horizontal beams have the same length L_v and diameter D_h (two lengths of in-plane struts are inclined by the angle $\theta = 30^\circ$ with the horizontal direction) and two vertical struts of length L_h and diameter D_v (out-of-plane). The lengths of the periodicity vectors are $L_1 = L_2 = \sqrt{3}L_v$ and $L_3 = L_h$.

The relative density of the 3D hexagonal is computed in terms of the geometrical parameters of vertebral trabecular bone architecture L_v , L_h , D_h , and D_v as

$$\frac{\rho^*}{\rho_s} = \frac{1}{18} \frac{\pi (3L_v D_h^2 + 2L_h D_v^2) \sqrt{3}}{L_v^2 L_h} \quad (6.1)$$

The effective density decreases with age, a fact in agreement with physiology (Figure 6.2).

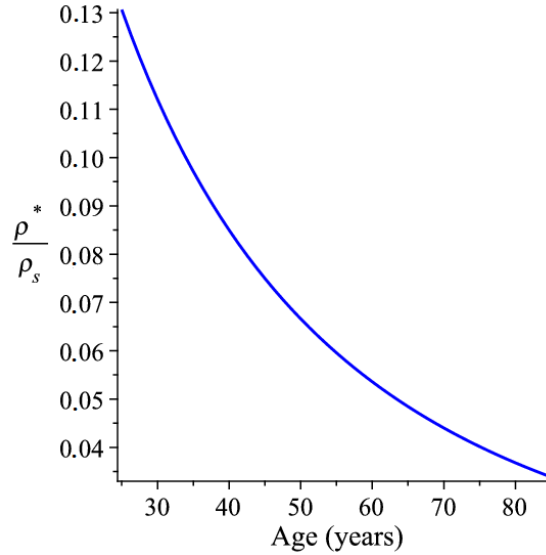


Figure 6.2: Evolution with age of the effective normalized density of trabecular bone.

In the forthcoming sections, microstructure-dependent beam models for vertebral trabecular bone are developed for the purpose of evaluating the bending and torsional behaviors in both the static and dynamic regimes. The derivations are based on the micropolar model and Hamilton's principle. The models contain material length scale parameter and are able to capture size effects, unlike classical beam theory.

6.3 Size dependent static and dynamic bending behaviors

In this section, we identify the static and dynamic response of vertebral cancellous bone beam samples subjected to bending, in relation with their microstructural properties.

6.3.1 Governing equations of the motion of micropolar beams in bending

We consider a straight beam made of a micropolar continuum representative of the homogenized bone architecture, with cross section of height H and width W , subjected to a pure bending moment around the z axis, as shown in Figure 6.3. According to the micropolar theory, the strain energy density is a function of both strain (conjugated to stress) and curvature (conjugated to couple stress). It then follows that the strain energy U in a deformed isotropic linear elastic material occupying a fixed domain Ω is given by

$$U = \frac{1}{2} \int_{\Omega} (\sigma_{ij} \epsilon_{ij} + m_{ij} \chi_{ij}) dV \quad (6.2)$$

The total length (or span) of the beam member is L_m . According to the basic assumptions of Bernoulli–Euler beams and the one-dimensional beam theory, the strain energy writes

$$U = \frac{1}{2} \int_{\Omega} (\sigma_{xx} \epsilon_{xx} + m_{xz} \chi_{xz}) dV \quad (6.3)$$

with $\sigma_{xx} = E_x^* y \frac{\partial^2 v(x,t)}{\partial x^2}$, $\epsilon_{xx} = y \frac{\partial^2 v(x,t)}{\partial x^2}$, and $m_{xz} = \gamma_{xz} \frac{\partial^2 v(x,t)}{\partial x^2}$, hence

$$U = \frac{1}{2} \int_0^{L_m} \int_A (E_x^* y^2 + \gamma_{xz}) \left(\frac{\partial^4 v(x,t)}{\partial x^4} \right) dA dx = \frac{1}{2} \int_0^{L_m} (E_x^* I_z^* + \gamma_{xz} A) \left(\frac{\partial^4 v(x,t)}{\partial x^4} \right) dx \quad (6.4)$$

where I_z^* is the second moment of cross-sectional area defined by $I_z^* = \int_A y^2 dA$ and A the cross-sectional area of the macroscopic beam. The rotation angle of the centroidal axis of the beam is related to the deflection as: $\phi_z(x,t) = \frac{\partial v(x,t)}{\partial x}$.

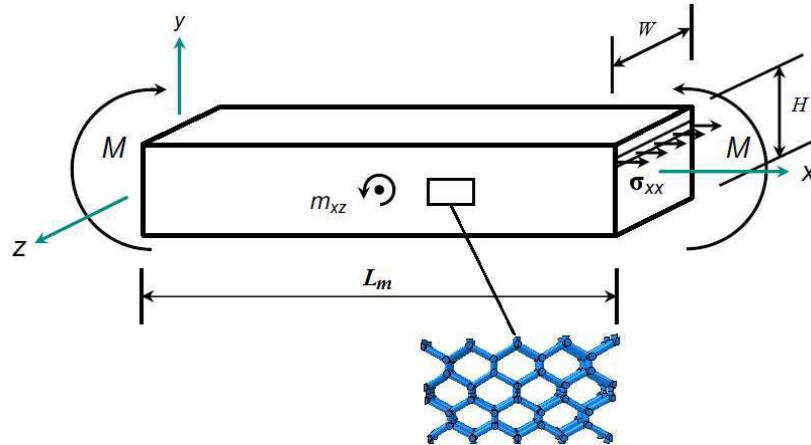


Figure 6.3: Configuration of the micropolar micro-structured beam of the vertebral trabeculae.

The previous expression (6.4) of the strain energy can be written with the characteristic micropolar length (internal material length scale parameter) $l_{b,xy}$ as

$$U = \frac{1}{2} \int_0^{L_m} (E_x^* I_z^* + 2l_{b,xy}^2 (2\mu_{xy}^* + \kappa_{xy}) A) \left(\frac{\partial^4 v(x,t)}{\partial x^4} \right) dx \quad (6.5)$$

On the other hand, the kinetic energy can be written as

$$KE = \frac{1}{2} \int_0^{L_m} \rho^*(x) A(x) \left(\frac{\partial^2 v(x,t)}{\partial t^2} \right) dx \quad (6.6)$$

with $\rho^*(x)$ the effective density of the beam material (for trabecular bone this is equivalent to the volume fraction (BV/TV) or relative density multiplied by the tissue density).

By neglecting the body force and the body couple, the work done by the external forces in the form of lateral forces $q(x,t)$ can be written as

$$W^{ex} = \int_0^{L_m} q(x,t)v(x,t)dx \quad (6.7)$$

The governing equation of motion of the micropolar beam can then be determined thanks to Hamilton's principle

$$\delta \int_{t_1}^{t_2} (KE - U + W^{ex}) dt = 0 \quad (6.8)$$

where δ denotes the variation symbol. Substituting equations (6.5) - (6.7) into (6.8) then leads to

$$\delta \int_{t_1}^{t_2} \int_0^{L_m} \left(\frac{1}{2} \rho^* A \left(\frac{\partial v(x,t)}{\partial t} \right)^2 - \frac{1}{2} (E_x^* I_z^* + 2l_{b_{xy}}^2 (2\mu_{xy}^* + \kappa_{xy}) A) \left(\frac{\partial v^2(x,t)}{\partial x^2} \right)^2 + q(x,t)v(x,t) \right) dx dt = 0 \quad (6.9)$$

The variation in equation (6.9) can be evaluated using integration by parts to obtain

$$\begin{aligned} & \int_{t_1}^{t_2} \int_0^{L_m} \left(-\rho^* A \frac{\partial v^2(x,t)}{\partial t^2} - (E_x^* I_z^* + 2l_{b_{xy}}^2 (2\mu_{xy}^* + \kappa_{xy}) A) \frac{\partial v^4(x,t)}{\partial x^4} + q(x,t) \right) \delta v dx dt + \int_0^{L_m} \rho^* A \frac{\partial v(x,t)}{\partial t} \delta v dx \Big|_{t_1}^{t_2} \\ & - \int_{t_1}^{t_2} (E_x^* I_z^* + 2l_{b_{xy}}^2 (2\mu_{xy}^* + \kappa_{xy}) A) \frac{\partial v^2(x,t)}{\partial x^2} \delta \frac{\partial v(x,t)}{\partial x} dt \Big|_0^{L_m} + \int_{t_1}^{t_2} (E_x^* I_z^* + 2l_{b_{xy}}^2 (2\mu_{xy}^* + \kappa_{xy}) A) \frac{\partial v^3(x,t)}{\partial x^3} \delta v dt \Big|_0^{L_m} = 0 \end{aligned} \quad (6.10)$$

The governing differential equation of motion and boundary conditions follow from previous equation: the Euler–Lagrange equation coincide with the dynamical equation of motion

$$\left(E_x^* I_z^* + 2l_{b_{xy}}^2 (2\mu_{xy}^* + \kappa_{xy}) A \right) \frac{\partial^4 v(x,t)}{\partial x^4} + \rho^* A \frac{\partial^2 v(x,t)}{\partial t^2} = q(x,t) \quad (6.11)$$

Since δv is zero at time t_1 and time t_2 , the boundary conditions follow from (6.10) as

$$\frac{\partial v^2}{\partial x^2} \delta \frac{\partial v}{\partial x} = 0; \quad \frac{\partial v^3}{\partial x^3} \delta v = 0, \quad x = 0 \quad \text{and} \quad x = L_m \quad (6.12)$$

Equation (6.11) shows that the bending deformation of the beam has two contributions: one associated with the normal stress component σ_{xx} , and the second one due to the couple stress component m_{xz} . The bending rigidity of the beam, quantity $E_x^* I_z^* + 2l_{b_{xy}}^2 (2\mu_{xy}^* + \kappa_{xy}) A$, explicitly depends on the internal bending length $l_{b_{xy}}$, itself related to the underlying microstructure of the beam material. This internal bending length enables the incorporation of the material microstructural features in the micropolar model and accounts for the size effect, as will be proven in the next section. Clearly, when the microstructural effect is suppressed by letting $l_{b_{xy}} = 0$, the model defined by equation (6.11) reduces to the classical Bernoulli-Euler beam theory.

6.3.2 Size-dependent static bending behavior

The static size-dependent behavior of micro-structured beams is analyzed by considering a specific case. Figure 6.4 illustrates a micro-structured cantilever with uniform rectangular cross section with height H and width W , subjected to a moment M at its end. From equation (6.11), the static form of the governing (equilibrium) equation can be obtained as

$$\left(E_x^* I_z^* + 2l_{b_{xy}}^2 (2\mu_{xy}^* + \kappa_{xy}) A\right) \frac{\partial^4 v(x)}{\partial x^4} = q(x) \quad (6.13)$$

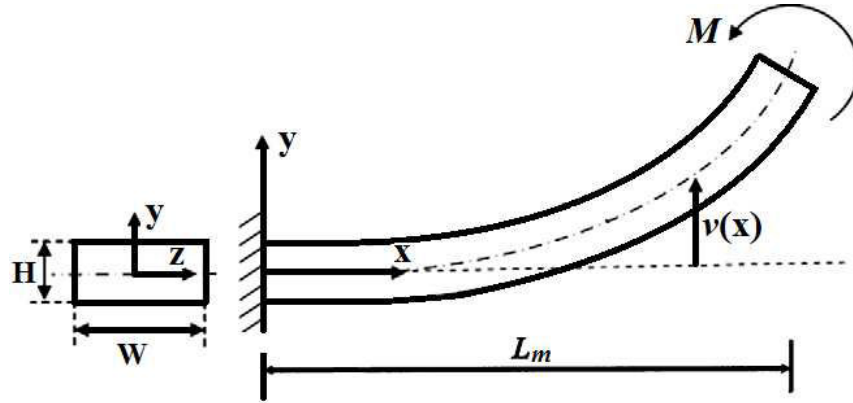


Figure 6.4: Schematic diagram of a micro-structured cantilever beam with rectangular cross section exposed to a moment at its free end.

The boundary conditions are prescribed in terms of the displacement and rotation, variables v and ϕ_z , at $x=0$ and $x=L_m$ as

$$\begin{aligned} v(0) = 0, \quad \phi_z(0) = \frac{\partial v(0)}{\partial x} = 0, \quad \frac{\partial \phi_z^2(L_m)}{\partial x} = \frac{\partial^3 v(L_m)}{\partial x^3} = 0, \\ \left(E_x^* I_z^* + 2l_{b_{xy}}^2 (2\mu_{xy}^* + \kappa_{xy}) A\right) \frac{\partial \phi_z(L_m)}{\partial x}, \quad \frac{\partial^2 v(L_m)}{\partial x^2} = M \end{aligned} \quad (6.14)$$

Integrating the governing equation (6.13) four times with $q(x) = 0$, gives

$$\left(E_x^* I_z^* + 2l_{b_{xy}}^2 (2\mu_{xy}^* + \kappa_{xy}) A\right) v(x) = \frac{C_1}{6} x^3 + \frac{C_2}{2} x^2 + C_3 x + C_4 \quad (6.15)$$

Applying the boundary conditions (6.14) then leads to the four constants

$$C_1 = C_3 = C_4 = 0, \quad C_2 = M \quad (6.16)$$

Summarizing, the following expression for the static deflection is obtained

$$\left(E_x^* I_z^* + 2l_{b_{xy}}^2 (2\mu_{xy}^* + \kappa_{xy}) A\right) v(x) = \frac{M}{2} x^2 \quad (6.17)$$

The closed-form expression for the static deflection of the micropolar beam is then obtained as a function of the geometrical and mechanical micro-parameters (mechanical: E_s , G_s ; geometrical: L_v, L_h, D_h, D_v , and k_s) of vertebral trabeculae as well as a function of geometrical parameters of the macroscopic beam (W and H):

$$v(x) = \frac{32\sqrt{3}L_h L_v (3E_s D_h^2 + 4G_s k_s L_v^2 + 9D_h^2 G_s k_s) M x^2}{\pi D_h^4 W H E_s (16G_s k_s H^2 + 3E_s D_h^2 + 4G_s k_s L_v^2 + 9D_h^2 G_s k_s)} \quad (6.18)$$

The previous equation can be rewritten as a function of the internal material length scale, a parameter describing micro-structure-dependent size effects, as

$$v(x) = \frac{2L_v L_h \sqrt{3} (3E_s D_h^2 + 4G_s k_s L_v^2 + 3D_h^2 G_s k_s) (4G_s k_s L_v^2 + 3E_s D_h^2 + 9D_h^2 G_s k_s) M x^2}{\pi D_h^4 E_s G_s k_s W H (3E_s D_h^2 H^2 + 36E_s D_h^2 l_{b_{xy}}^2 + 3D_h^2 G_s k_s H^2 + 108l_{b_{xy}}^2 G_s k_s D_h^2 + 48l_{b_{xy}}^2 G_s k_s L_v^2 + 4H^2 G_s k_s L_v^2)} \quad (6.19)$$

If the microstructural effect is neglected, by letting $l_{b_{xy}} = 0$, the static deflection formula predicted by the classical theory is recovered as

$$(E_x^* I_z^*) \bar{v}(x) = \frac{M}{2} x^2 \quad (6.20)$$

6.3.3 Size-dependent free flexural vibration behavior

In this subsection, the size-dependent flexural vibration behavior of a micro-structured micropolar beam is analyzed. Many papers appeared in the literature in the last 10 years that develop microstructure-dependent beam models based on nonlocal theories; those models are however by essence phenomenological. For instance, a Timoshenko beam model was considered in (Ma et al., 2008) to investigate the dynamical bending behavior; the authors employ a modified couple stress theory which however does not result from a micromechanical analysis of an underlying microstructure.

According to Hamilton's principle, the dynamic governing equation for the free flexural vibrations of a micro-structured beam in terms of $v(x, t)$ is determined by equation (6.11) as

$$(E_x^* I_z^* + 2l_{b_{xy}}^2 (2\mu_{xy}^* + \kappa_{xy}^*) A) \frac{\partial^4 v(x, t)}{\partial x^4} + \rho^* A \frac{\partial^2 v(x, t)}{\partial t^2} = 0 \quad (6.21)$$

To be specific, we consider the dynamic analysis of a cantilever beam to demonstrate the size dependency of the beams' natural frequencies. The problems of a cantilever beam of length L_m with rectangular cross-sectional shape is next solved; the corresponding boundary conditions are written as

$$v(0, t) = 0, \quad \frac{\partial v(0, t)}{\partial x} = 0, \quad \frac{\partial^2 v(L_m, t)}{\partial x^2} = 0, \quad \frac{\partial^3 v(L_m, t)}{\partial x^3} = 0 \quad (6.22)$$

Using variable separation, the substitution of the ansatz $v(x, t) = V(x) \underbrace{[A \sin(\omega_b t) + B \cos(\omega_b t)]}_{F(t)}$ into equation (6.21) leads to the frequency equation

$$\cos(\zeta L_m) \cosh(\zeta L_m) = -1 \quad (6.23)$$

where $\zeta^4 = \frac{\rho^* A \omega_b^2}{E_x^* I_y + 2l_{b_{xy}}^2 (2\mu_{xy}^* + \kappa_{xy}^*) A}$

The bending natural frequency therein is denoted by ω_b . The solution of equation (6.23) writes

$$(\zeta L_m)_n = 1.875, 4.694, 7.855, 10.996, 14.137, \dots \quad n = (1, 2, 3, 4, 5, \dots) \quad (6.24)$$

The bending natural frequencies are then derived as

$$(\omega_b)_n = (\zeta L_m)_n^2 \sqrt{\frac{E_x^* I_y + 2l_{b_{xy}}^2 (2\mu_{xy}^* + \kappa_{xy}) A}{\rho^* A L_m^4}} \quad (6.25)$$

By replacing the parameters involved in equation (6.25) by their expression from the Appendix B, a closed form solution for the circular bending natural frequency ω_b due to micropolar effect is obtained in terms of the micro-architecture geometrical parameters of vertebral trabecular bone, quantities $L_v, L_h, D_h,$ and D_v , the shear correction k_s , the bulk density ρ_s , the bulk elastic modulus E_s , the shear modulus G_s of the solid tissue struts of vertebral bone, and the macro-size parameters of the macrobeam H, L_m as follows:

$$(\omega_b)_n = (\zeta L_m)_n^2 \frac{\sqrt{6}}{8L_m^2} \sqrt{\frac{D_h^4 E_s (16G_s k_s H^2 + 3E_s D_h^2 + 4G_s k_s L_v^2 + 9D_h^2 G_s k_s) L_v}{\rho_s (3E_s D_h^2 + 4G_s k_s L_v^2 + 9D_h^2 G_s k_s) (3L_v D_h^2 + 2L_h D_v^2)}} \quad (6.26)$$

The previous equation can be written in terms of the characteristic micropolar length $l_{b_{xy}}$ as

$$(\omega_b)_n = (\zeta L_m)_n^2 \frac{\sqrt{6}}{2L_m^2} \sqrt{\frac{G_s k_s E_s D_h^4 (3E_s D_h^2 H^2 + 36E_s D_h^2 l_{b_{xy}}^2 + 3D_h^2 G_s k_s H^2 + 108l_{b_{xy}}^2 G_s k_s D_h^2 + 48l_{b_{xy}}^2 G_s k_s L_v^2 + 4H^2 G_s k_s L_v^2) L_v}{\rho_s (3L_v D_h^2 + 2L_h D_v^2) (3E_s D_h^2 + 4G_s k_s L_v^2 + 3D_h^2 G_s k_s) (4G_s k_s L_v^2 + 3E_s D_h^2 + 9D_h^2 G_s k_s)}} \quad (6.27)$$

Flexural natural frequency in cycles per second can be obtained by the relation $(f_b)_n = (\omega_b)_n / 2\pi$.

6.3.4 Numerical results

To illustrate the derived solution for the static deflection and the free flexural vibration of the fixed-free beam based on micropolar theory, a few numerical results are presented, focusing on the first two natural frequencies. For the purpose of illustration, the beam considered here and thereafter is taken to be made of vertebral cancellous human bone; the material (tissue) properties used in the calculations are selected as $E_s = 12000$ MPa, $G_s = 0.5 * E_s / (1 + \nu_s)$, Poisson's ratio $\nu_s = 0.3$, and density $\rho_s = 2000$ kg / m³ following (Gibson, 2005). The shear correction coefficient is $k_s = 9/10$.

The aforementioned properties hold at the microlevel, while the cross-sectional shape of the macroscopic beam is kept as $W=2H$, with the length $L_m=15H$ (let $H=1$ mm). Figures 6.5 and 6.6 show the change with age (in the range 25-85 years) of the bending deflection at the free end of the beam and of the first two natural frequencies. In the static deflection analysis, the moment at the end of the beam is set to 0.01 N.mm.

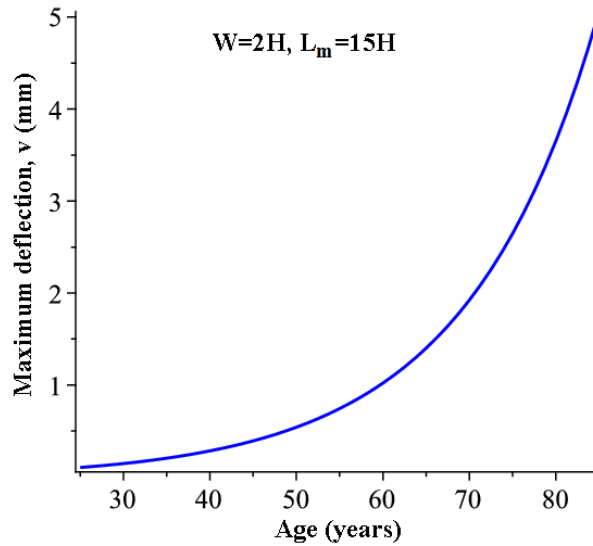


Figure 6.5: Variation of the maximum deflection of the micro-structured cantilever beam with age.

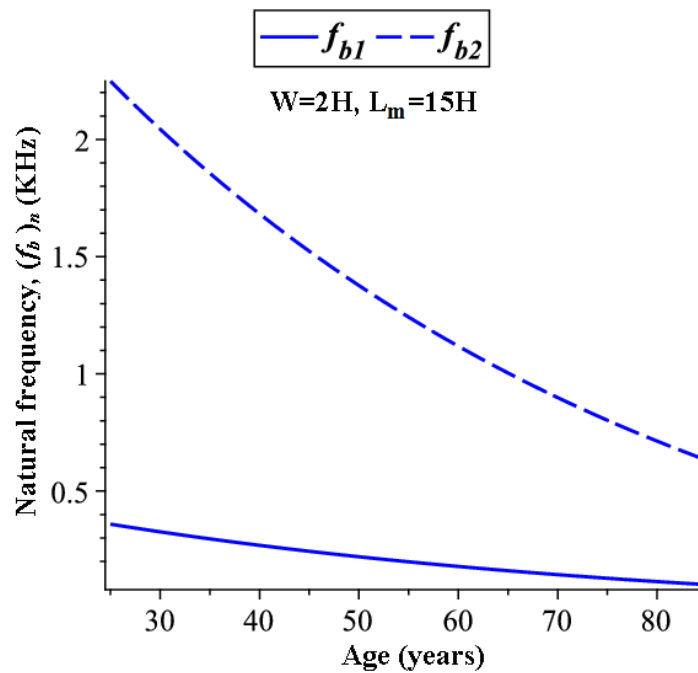


Figure 6.6: Variation of the first two flexural natural frequencies of the micro-structured cantilever beam with age.

Figure 6.7 compares the deflection and rotation caused by an applied moment $M = 0.01$ N.mm at the free end of the cantilevered beam, predicted by the micropolar model and by the classical theory. The geometrical parameters $L_v, L_h, D_h,$ and D_v of the trabeculae building structure are selected (from Table 6.1) for a person at the age of 40. It is clearly observed from Figure 6.7 that the deflection and rotation predicted by the current microstructure-dependent model are always smaller than those predicted by the classical model, along the entire length of the cantilever beam. Hence, the micro-structured beam is predicted from the micropolar theory as stiffer in bending in comparison to the classical beam theory.

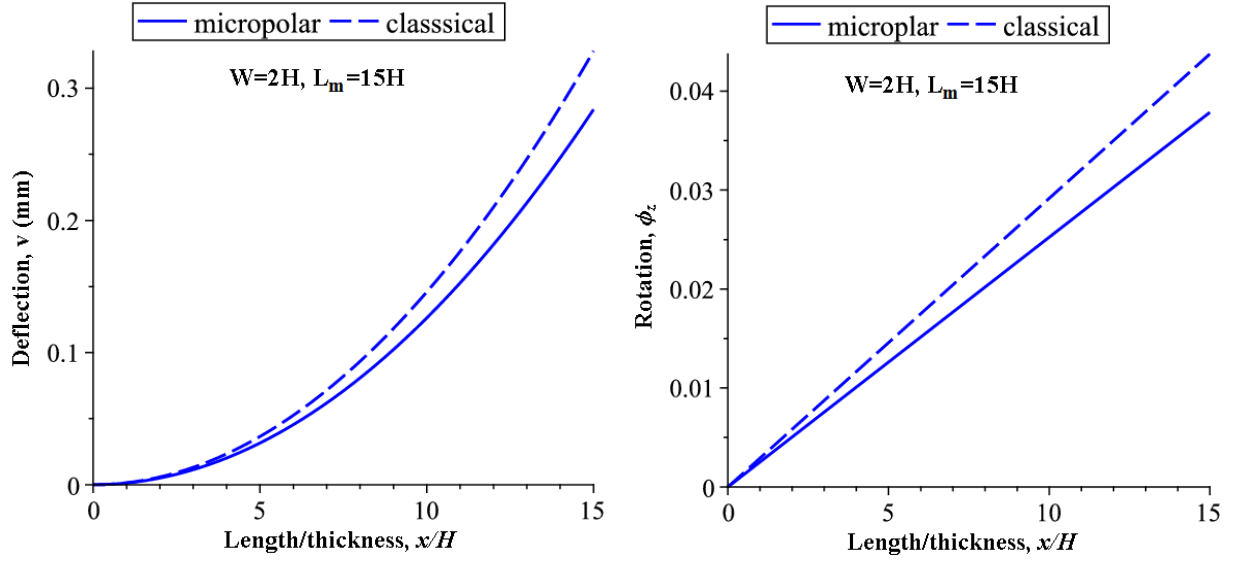


Figure 6.7: Deflection and rotation of the micro-structured cantilever beam.

In order to assess the size-dependent static and vibration behaviours of micro-structured beams, a few numerical case studies are analyzed for both static and vibration situations, basing on the equations established in the previous sections. In order to study the dependence of the size effect on the geometric dimensions of the cantilever beam, we set the definitions of the normalized static deflection (or rotation) as v/\bar{v} (or $\phi_z/\bar{\phi}_z$) and the normalized natural frequency as $(\omega_b)_n/(\bar{\omega}_b)_n$, where \bar{v} and $\bar{\omega}_b$ are respectively the static deflection and bending natural frequency that do not consider the size effect ($l_{b_{xy}} = 0$) as evaluated by the classical theory, and v and ω_b are respectively the bending deflection and natural frequency incorporating the size effect. By this definition, for certain length-scale parameters, the influence of the size effect on mechanical properties is more substantial when the normalized value is smaller.

For the static case, the normalized static deflection of the micro-structured cantilever versus the ratio of the beam thickness to the length scale parameter $H/l_{b_{xy}}$ is depicted in Figure 6.8. The difference between the static deflection predicted by the classical beam theory and by the micropolar theory increases as the macroscopic beam thickness H approaches the characteristic length $l_{b_{xy}}$. As a specific case, for $H/l_{b_{xy}} = 10$, the static deflection of the micro-cantilever predicted by the classical beam theory is about 1.15 greater than the static deflection estimated by micropolar theory. For large ratios, typically $H/l_{b_{xy}} > 20$, the results predicted by classical beam theory are close to the predictions of the micropolar theory.

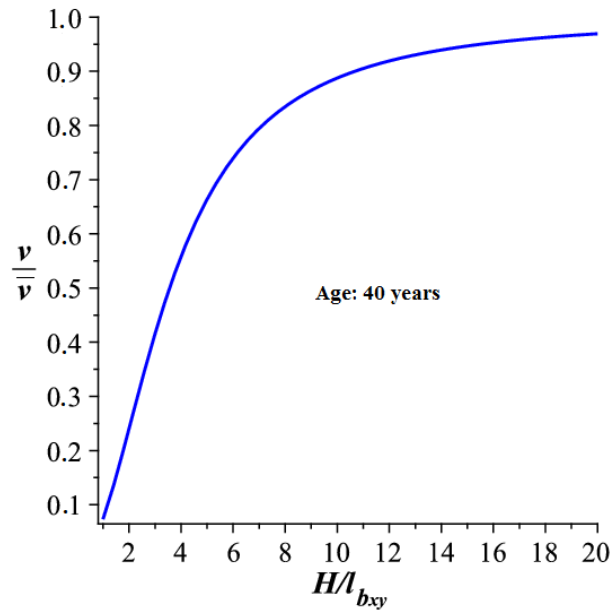


Figure 6.8: Normalized static deflection of a micro-structured-cantilever versus the ratio of the cantilever thickness to the material length scale parameter of trabecular bone.

For the vibration case, the normalized size-dependent natural frequency of the considered micro-structured beam is recorded versus the ratio of the beam characteristic size (thickness) to the internal material length scale parameter H/l_{bxy} in Figure 6.9. For large ratios $H/l_{bxy} > 15$, the classical and micropolar beam theories predict approximately the same results. It is notable that for all values of H/l_{bxy} , the natural frequencies predicted by micropolar theory are greater than those predicted by classical beam theory, thus revealing that the micropolar beam is stiffer than the classical beam.

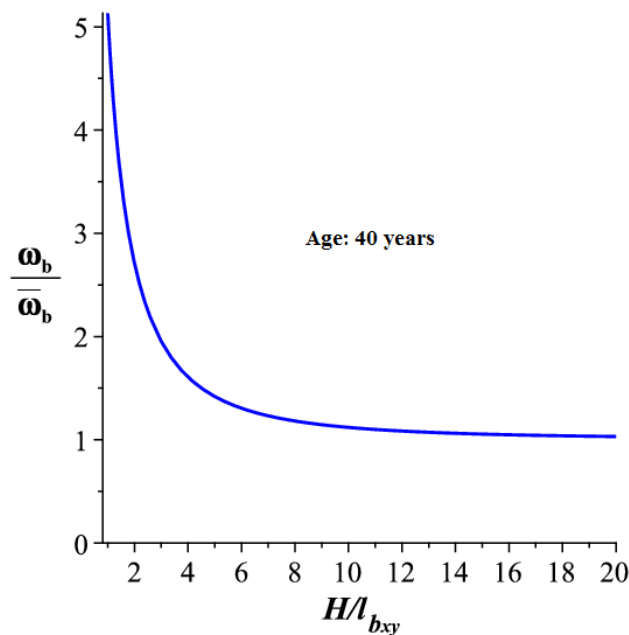


Figure 6.9: Size effect on the flexural natural frequencies with respect to various sizes for micro-structured cantilevered beam.

The numerical results show that the size effect on static deflection and free vibration characteristics is pronounced for micro-structured beam with ratio less than $H/l_{b,xy} < 15$. The static deflection behavior of micro-structured beams is much more affected by the size effect than its natural frequencies; as the length scale parameter $H/l_{b,xy}$ decreases, the deflection decreases due to an increase of bending stiffness, whereas the natural frequencies increase.

We conclude from previous results that the difference between the normalized static deflection and natural frequencies predicted by the micropolar theory with those of the classical theory is significant when the ratio of the beam characteristic size to the internal material length scale parameter is small. The classical theory underestimates the bending stiffness for relatively small thicknesses, due to the absence of any internal length; hence, the use of non-classic theories such as micropolar theory seems to be essential for the analysis in these cases.

In the forthcoming section, the torsion of vertebral trabecular bone in beam samples is formulated based on Cosserat reduced theory. The governing differential equation of torsion is derived employing Hamilton's principle (variational approach) and an explicit analytical solution is derived for the static torsion. The characteristic equation giving the natural frequencies is derived and solved analytically for the free torsional vibrations of beams.

6.4 Size dependent static and dynamic torsional behaviors

6.4.1 Governing equations of motion of a twisted micro-structured beam

The problem of a twisted micro-structured fixed-free beam of total length L_m , thickness H and width W is considered (Figure 6.10). For pure torsion, the components of the displacement of the micro-structured beam can be expressed as (Rao, 2007)

$$u_x(x,t) = 0; u_y(x,t) = -z\phi(x,t); u_z(x,t) = y\phi(x,t) \quad (6.28)$$

where u_x , u_y , and u_z denote the displacement along x , y and z axes, respectively; the field $\phi(x,t)$ stands for the rotation angle about the center of twist (x -axis).

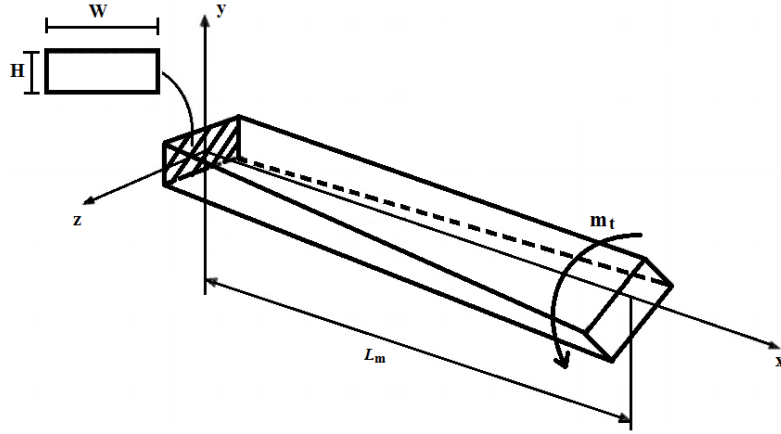


Figure 6.10: Schematic of the micro-structured beam: Geometry, loading, and coordinate system.

In the Cosserat reduced or couple-stress theory, the rotation is related to displacement gradients (equal to the local rigid rotation) as:

$$\phi_x = (\partial u_z / \partial y - \partial u_y / \partial z) / 2; \quad \phi_y = (\partial u_x / \partial z - \partial u_z / \partial x) / 2; \quad \phi_z = (\partial u_y / \partial x - \partial u_x / \partial y) / 2$$

As a result, the strain tensor ϵ_{ij} is symmetrical, with components depending upon the displacements gradients as

$$\epsilon_{xy} = \epsilon_{yx} = (\partial u_y / \partial x + \partial u_x / \partial y) / 2; \quad \epsilon_{xz} = \epsilon_{zx} = (\partial u_z / \partial x + \partial u_x / \partial z) / 2; \quad \epsilon_{yz} = \epsilon_{zy} = (\partial u_z / \partial y + \partial u_y / \partial z) / 2 .$$

Subsequently, the components of the rotation vector are derived as follows:

$$\phi_x = \phi(x, t); \quad \phi_y = -\frac{y}{2} \frac{\partial \phi(x, t)}{\partial x}; \quad \phi_z = -\frac{z}{2} \frac{\partial \phi(x, t)}{\partial x}$$

The components of the strain tensor are then obtained as,

$$\epsilon_{xx} = \epsilon_{yy} = \epsilon_{zz} = \epsilon_{yz} = 0; \quad \epsilon_{xy} = \epsilon_{yx} = -\frac{z}{2} \frac{\partial \phi(x, t)}{\partial x}; \quad \epsilon_{xz} = \epsilon_{zx} = \frac{y}{2} \frac{\partial \phi(x, t)}{\partial x} \quad (6.29)$$

and the nonzero components of the symmetrical part of the curvature (or rotation of gradient) tensor $\chi_{ij} = 1/2(\phi_{i,j} + \phi_{j,i})$ are written as

$$\chi_{xx} = \frac{\partial \phi(x, t)}{\partial x}; \quad \chi_{yy} = -\frac{1}{2} \frac{\partial \phi(x, t)}{\partial x}; \quad \chi_{zz} = -\frac{1}{2} \frac{\partial \phi(x, t)}{\partial x}; \quad \chi_{xy} = \chi_{yx} = -\frac{y}{4} \frac{\partial^2 \phi(x, t)}{\partial x^2}; \quad \chi_{xz} = \chi_{zx} = -\frac{z}{4} \frac{\partial^2 \phi(x, t)}{\partial x^2} \quad (6.30)$$

By substituting the strain components from equation (6.29) into the force stresses σ_{ij} , equation (2.40), the non-zero components of the stress tensor are obtained as

$$\sigma_{xy} = \sigma_{yx} = -\frac{z}{2} (2\mu_{xy}^* + \kappa_{xy}) \frac{\partial \phi(x, t)}{\partial x}; \quad \sigma_{xz} = \sigma_{zx} = \frac{y}{2} (2\mu_{xz}^* + \kappa_{xz}) \frac{\partial \phi(x, t)}{\partial x} \quad (6.31)$$

Proceeding in a similar manner, by substituting equation (6.30) into the couple stresses m_{ij} , we obtain the non zero components of the couple stress tensor as

$$\begin{aligned}
m_{xx} &= E_{tor-x}^* \frac{\partial \phi(x,t)}{\partial x}; \quad m_{yy} = -\frac{1}{2} E_{tor-y}^* \frac{\partial \phi(x,t)}{\partial x}; \quad m_{zz} = -\frac{1}{2} E_{tor-z}^* \frac{\partial \phi(x,t)}{\partial x}; \\
m_{xy} &= -\frac{y}{2} \gamma_{xy} \frac{\partial^2 \phi(x,t)}{\partial x^2}; \quad m_{yx} = -\frac{y}{2} \beta_{yx} \frac{\partial^2 \phi(x,t)}{\partial x^2}; \quad m_{xz} = -\frac{z}{2} \gamma_{xz} \frac{\partial^2 \phi(x,t)}{\partial x^2}; \quad m_{zx} = -\frac{z}{2} \beta_{zx} \frac{\partial^2 \phi(x,t)}{\partial x^2}.
\end{aligned} \tag{6.32}$$

where $E_{tor-x,y,z}^*$ are the homogenized torsional elastic moduli in directions x, y, and z respectively. The additional bending and torsion effects present in the micropolar continuum can be characterized by characteristic lengths for bending and torsion involved in the following micropolar coefficients

$$\begin{aligned}
\gamma_{xy} &= 2 \left(2\mu_{xy}^* + \kappa_{xy} \right) l_{b_{xy}}^2, \quad \gamma_{xz} = 2 \left(2\mu_{xz}^* + \kappa_{xz} \right) l_{b_{xz}}^2, \quad \beta_{yx} = \left(2\mu_{yx}^* + \kappa_{yx} \right) \left(l_{t_{yx}}^2 - 2l_{b_{yx}}^2 \right) \\
\beta_{zx} &= \left(2\mu_{zx}^* + \kappa_{zx} \right) \left(l_{t_{zx}}^2 - 2l_{b_{zx}}^2 \right).
\end{aligned}$$

This entails the expression of the strain energy of the micro-structured beam

$$\begin{aligned}
U &= \frac{1}{2} \int_{\Omega} \left(\sigma_{xy} \epsilon_{xy} + \sigma_{yx} \epsilon_{yx} + \sigma_{xz} \epsilon_{xz} + \sigma_{zx} \epsilon_{zx} + m_{xx} \chi_{xx} + m_{yy} \chi_{yy} + m_{zz} \chi_{zz} + m_{xy} \chi_{xy} + m_{yx} \chi_{yx} + m_{xz} \chi_{xz} + m_{zx} \chi_{zx} \right) dV \\
&= \frac{1}{2} \int_{\Omega} \left(\frac{z^2}{2} (2\mu_{xy}^* + \kappa_{xy}) \frac{\partial^2 \phi(x,t)}{\partial x^2} + \frac{y^2}{2} (2\mu_{xz}^* + \kappa_{xz}) \frac{\partial^2 \phi(x,t)}{\partial x^2} + \left(E_{tor-x}^* + \frac{E_{tor-y}^*}{4} + \frac{E_{tor-z}^*}{4} \right) \frac{\partial^2 \phi(x,t)}{\partial x^2} \right. \\
&\quad \left. + \frac{y^2}{8} \gamma_{xy} \frac{\partial^4 \phi(x,t)}{\partial x^4} + \frac{y^2}{8} \beta_{yx} \frac{\partial^4 \phi(x,t)}{\partial x^4} + \frac{z^2}{8} \gamma_{xz} \frac{\partial^4 \phi(x,t)}{\partial x^4} + \frac{z^2}{8} \beta_{zx} \frac{\partial^4 \phi(x,t)}{\partial x^4} \right) dV \\
&= \frac{1}{2} \int_0^{L_m} \int_A \left(\left(\frac{1}{2} (z^2 (2\mu_{xy}^* + \kappa_{xy}) + y^2 (2\mu_{xz}^* + \kappa_{xz})) + \left(E_{tor-x}^* + \frac{E_{tor-y}^*}{4} + \frac{E_{tor-z}^*}{4} \right) \right) \frac{\partial^2 \phi(x,t)}{\partial x^2} \right. \\
&\quad \left. + \frac{1}{8} ((\gamma_{xy} + \beta_{yx}) y^2 + (\gamma_{xz} + \beta_{zx}) z^2) \frac{\partial^4 \phi(x,t)}{\partial x^4} \right) dA dx
\end{aligned} \tag{6.33}$$

with the moment of inertia about the z-axis and y-axis defined as $I_z^* = \int_A y^2 dA$; $I_y^* = \int_A z^2 dA$; hence,

$$\begin{aligned}
U &= \frac{1}{2} \int_0^{L_m} \left(\left(\frac{1}{2} ((2\mu_{xy}^* + \kappa_{xy}) I_y^* + (2\mu_{xz}^* + \kappa_{xz}) I_z^*) + \left(E_{tor-x}^* + \frac{E_{tor-y}^*}{4} + \frac{E_{tor-z}^*}{4} \right) A \right) \left(\frac{\partial \phi(x,t)}{\partial x} \right)^2 \right. \\
&\quad \left. + \frac{1}{8} ((\gamma_{xy} + \beta_{yx}) I_z^* + (\gamma_{xz} + \beta_{zx}) I_y^*) \left(\frac{\partial^2 \phi(x,t)}{\partial x^2} \right)^2 \right) dx
\end{aligned} \tag{6.34}$$

The total kinetic energy of the micro-structured beam can be expressed as

$$\begin{aligned}
KE &= \frac{1}{2} \int_{\Omega} \rho^*(x) \left(\frac{\partial^2 u_x(x,t)}{\partial t^2} + \frac{\partial^2 u_y(x,t)}{\partial t^2} + \frac{\partial^2 u_z(x,t)}{\partial t^2} \right) dV = \frac{1}{2} \int_0^{L_m} \int_A \rho^*(x) (y^2 + z^2) \left(\frac{\partial^2 \phi(x,t)}{\partial t^2} \right) dx \\
&= \frac{1}{2} \int_0^{L_m} \rho^*(x) I_x^* \left(\frac{\partial \phi(x,t)}{\partial t} \right)^2 dx
\end{aligned} \tag{6.35}$$

with the polar moment of inertia about the x-axis $I_x^* = \int_A (y^2 + z^2) dA$.

The work done by the distributed torque-per-unit length about x-axis, $m_t(x, t)$ can be represented as

$$W^{ex} = \int_0^{L_m} m_t(x, t) \phi(x, t) dx \quad (6.36)$$

The governing equation of motion and the boundary conditions for a microstructured beam undergoing torsional deformation under to an externally applied torque are similarly obtained from Hamilton's principle

$$\int_{t_1}^{t_2} (\delta KE - \delta U + \delta W^{ex}) dt = 0 \quad (6.37)$$

with t_1 and t_2 the times at which the configuration of the system is assumed to be known.

The first variation or virtual change of the strain energy of the beam in the time interval $[t_1, t_2]$ writes

$$\delta U = \int_0^{L_m} \left(\frac{1}{2} \left((2\mu_{xy}^* + \kappa_{xy}) I_y^* + (2\mu_{xz}^* + \kappa_{xz}) I_z^* \right) + \left(E_{tor-x}^* + \frac{E_{tor-y}^*}{4} + \frac{E_{tor-z}^*}{4} \right) A \right) \frac{\partial \phi(x, t)}{\partial x} \delta \frac{\partial \phi(x, t)}{\partial x} dx + \frac{1}{8} \left((\gamma_{xy} + \beta_{yx}) I_z^* + (\gamma_{xz} + \beta_{zx}) I_y^* \right) \frac{\partial^2 \phi(x, t)}{\partial x^2} \delta \frac{\partial^2 \phi(x, t)}{\partial x^2} dx \quad (6.38)$$

Similarly, we obtain the variations of the kinetic energy and external work

$$\delta KE = \int_0^{L_m} \rho^*(x) I_x^* \frac{\partial \phi(x, t)}{\partial t} \delta \frac{\partial \phi(x, t)}{\partial t} dx \quad (6.39)$$

$$\delta W^{ex} = \int_0^{L_m} m_t(x, t) \delta \phi(x, t) dx \quad (6.40)$$

The variation $\int_{t_1}^{t_2} \delta KE dt$ in equation (6.37) can be evaluated by integration by parts with respect to time:

$$\begin{aligned} \int_{t_1}^{t_2} \delta KE dt &= \int_0^{L_m} \left(\int_{t_1}^{t_2} \rho^*(x) I_x^* \frac{\partial \phi(x, t)}{\partial t} \delta \frac{\partial \phi(x, t)}{\partial t} dt \right) dx = \int_0^{L_m} \left(\rho^*(x) I_x^* \frac{\partial \phi(x, t)}{\partial t} \delta \phi \Big|_{t=t_1}^{t=t_2} - \int_{t_1}^{t_2} \rho^*(x) I_x^* \frac{\partial^2 \phi(x, t)}{\partial t^2} \delta \phi dt \right) dx \\ &= - \int_{t_1}^{t_2} \int_0^{L_m} \rho^*(x) I_x^* \frac{\partial^2 \phi(x, t)}{\partial t^2} \delta \phi dx dt \end{aligned} \quad (6.41)$$

It is assumed that the initial and final configurations are known, in terms of the data $\phi(x, t_{1,2})$.

Thus, $\delta \phi(x, t_1) = \delta \phi(x, t_2) = 0$, and the integrated terms on the RHS of equation (6.41) vanishes.

Similarly, for the strain energy, integrating by parts with respect to x leads to

$$\int_{t_1}^{t_2} \delta U dt = \int_{t_1}^{t_2} \left(- \int_0^{L_m} \left[\frac{1}{2} \left((2\mu_{xy}^* + \kappa_{xy}) I_y^* + (2\mu_{xz}^* + \kappa_{xz}) I_z^* \right) + \left(E_{tor-x}^* + \frac{E_{tor-y}^*}{4} + \frac{E_{tor-z}^*}{4} \right) A \right] \frac{\partial^2 \phi(x, t)}{\partial x^2} \delta \phi dx + \frac{1}{8} \left((\gamma_{xy} + \beta_{yx}) I_z^* + (\gamma_{xz} + \beta_{zx}) I_y^* \right) \frac{\partial^3 \phi(x, t)}{\partial x^3} \delta \phi \Big|_{x=0}^{x=L_m} \right) dt + \int_0^{L_m} \frac{1}{8} \left((\gamma_{xy} + \beta_{yx}) I_z^* + (\gamma_{xz} + \beta_{zx}) I_y^* \right) \frac{\partial^4 \phi(x, t)}{\partial x^4} \delta \phi dx \quad (6.42)$$

Substituting the aforementioned expressions in equation (6.37), one obtains the governing equation and boundary conditions in weak form as

$$\begin{aligned}
& \int_{l_1}^{l_2} \int_0^{L_m} \left(\frac{1}{8} \left((\gamma_{xy} + \beta_{yx}) I_z^* + (\gamma_{xz} + \beta_{zx}) I_y^* \right) \frac{\partial^4 \phi(x,t)}{\partial x^4} - \left(\frac{1}{2} \left((2\mu_{xy}^* + \kappa_{xy}) I_y^* + (2\mu_{xz}^* + \kappa_{xz}) I_z^* \right) \right. \right. \\
& \left. \left. + \left(E_{tor-x}^* + \frac{E_{tor-y}^*}{4} + \frac{E_{tor-z}^*}{4} \right) A \right) \frac{\partial^2 \phi(x,t)}{\partial x^2} + \rho^*(x) I_x^* \frac{\partial^2 \phi(x,t)}{\partial t^2} - m_t(x,t) \right) \delta \phi dx dt \\
& + \int_{l_1}^{l_2} \left(\frac{1}{2} \left((2\mu_{xy}^* + \kappa_{xy}) I_y^* + (2\mu_{xz}^* + \kappa_{xz}) I_z^* \right) + \left(E_{tor-x}^* + \frac{E_{tor-y}^*}{4} + \frac{E_{tor-z}^*}{4} \right) A \right) \frac{\partial \phi(x,t)}{\partial x} - \frac{1}{8} \left((\gamma_{xy} + \beta_{yx}) I_z^* + (\gamma_{xz} + \beta_{zx}) I_y^* \right) \frac{\partial^3 \phi(x,t)}{\partial x^3} \Big|_{x=0}^{x=L_m} dt \\
& + \int_{l_1}^{l_2} \frac{1}{8} \left((\gamma_{xy} + \beta_{yx}) I_z^* + (\gamma_{xz} + \beta_{zx}) I_y^* \right) \frac{\partial^2 \phi(x,t)}{\partial x^2} \delta \frac{\partial \phi(x,t)}{\partial x} \Big|_{x=0}^{x=L_m} dt = 0
\end{aligned} \tag{6.43}$$

From (6.43), the governing equation of motion of torsion is obtained in terms of $\phi(x, t)$ as

$$\begin{aligned}
& \frac{1}{8} \left((\gamma_{xy} + \beta_{yx}) I_z^* + (\gamma_{xz} + \beta_{zx}) I_y^* \right) \frac{\partial^4 \phi(x,t)}{\partial x^4} - \left(\frac{1}{2} \left((2\mu_{xy}^* + \kappa_{xy}) I_y^* + (2\mu_{xz}^* + \kappa_{xz}) I_z^* \right) \right. \\
& \left. + \left(E_{tor-x}^* + \frac{E_{tor-y}^*}{4} + \frac{E_{tor-z}^*}{4} \right) A \right) \frac{\partial^2 \phi(x,t)}{\partial x^2} \\
& + \rho^*(x) I_x^* \frac{\partial^2 \phi(x,t)}{\partial t^2} = m_t(x,t)
\end{aligned} \tag{6.44}$$

6.4.2 Size-dependent static torsional behavior

The static torsion of the micro-structured beam is next analyzed; from the relations

$$\frac{\partial \phi(x,t)}{\partial t} = 0 \text{ and } \frac{\partial \phi(x,t)}{\partial x} = \frac{d\phi}{dx}, \text{ equation (6.44) reduces to}$$

$$\underbrace{\frac{1}{8} \left((\gamma_{xy} + \beta_{yx}) I_z^* + (\gamma_{xz} + \beta_{zx}) I_y^* \right)}_{K_{t1}} \frac{d^4 \phi}{dx^4} - \underbrace{\left(\frac{1}{2} \left((2\mu_{xy}^* + \kappa_{xy}) I_y^* + (2\mu_{xz}^* + \kappa_{xz}) I_z^* \right) + \left(E_{tor-x}^* + \frac{E_{tor-y}^*}{4} + \frac{E_{tor-z}^*}{4} \right) A \right)}_{K_{t2}} \frac{d^2 \phi}{dx^2} = m_t(x) \tag{6.45}$$

$$\text{Letting } K_t = \frac{K_{t2}}{K_{t1}} = \frac{\left(\frac{1}{2} \left((2\mu_{xy}^* + \kappa_{xy}) I_y^* + (2\mu_{xz}^* + \kappa_{xz}) I_z^* \right) + \left(E_{tor-x}^* + \frac{E_{tor-y}^*}{4} + \frac{E_{tor-z}^*}{4} \right) A \right)}{\frac{1}{8} \left((\gamma_{xy} + \beta_{yx}) I_z^* + (\gamma_{xz} + \beta_{zx}) I_y^* \right)},$$

one can rewrite (6.45) as

$$\frac{d^4 \phi}{dx^4} - K_t \frac{d^2 \phi}{dx^2} = \frac{1}{K_{t1}} m_t(x) \tag{6.46}$$

This equation is a non-homogenous linear ordinary differential equation with constant coefficients that can be solved analytically; a double integration of equation (6.46) results in:

$$\frac{d^2 \phi}{dx^2} - K_t \phi = (1/K_{t1}) \iint m_t(x) dx dx + C_1 x + C_2 \tag{6.47}$$

The general solution of (6.47) decomposes into

$$\phi(x) = \underbrace{C_3 e^{\sqrt{K_t} x} + C_4 e^{-\sqrt{K_t} x}}_{\phi_h(x)} + \phi_p(x) \tag{6.48}$$

in which $\phi_h(x)$ represents the complementary solution (or homogeneous solution) and $\phi_p(x)$ the particular (or non-homogeneous solution)

$$\phi_p(x) = e^{\sqrt{K_t}x} \int \frac{e^{-\sqrt{K_t}x} \left((1/K_{t1}) \int \int m_t(x) dx dx + C_1 x + C_2 \right)}{2\sqrt{K_t}} dx - e^{-\sqrt{K_t}x} \int \frac{e^{\sqrt{K_t}x} \left((1/K_{t1}) \int \int m_t(x) dx dx + C_1 x + C_2 \right)}{2\sqrt{K_t}} dx \quad (6.49)$$

The general solution of (6.47) can then be written as

$$\phi(x) = C_3 e^{\sqrt{K_t}x} + C_4 e^{-\sqrt{K_t}x} + e^{\sqrt{K_t}x} \int \frac{e^{-\sqrt{K_t}x} (m_t x^2 / 2K_{t1} + C_1 x + C_2)}{2\sqrt{K_t}} dx - e^{-\sqrt{K_t}x} \int \frac{e^{\sqrt{K_t}x} (m_t x^2 / 2K_{t1} + C_1 x + C_2)}{2\sqrt{K_t}} dx \quad (6.50)$$

After simplification, one obtains

$$\phi(x) = -\frac{1}{2} \frac{2K_t K_{t1} C_2 + 2m_t + 2xK_t K_{t1} C_1 + m_t x^2 K_t}{K_t^2 K_{t1}} + C_3 e^{\sqrt{K_t}x} + C_4 e^{-\sqrt{K_t}x} \quad (6.51)$$

with C_1, \dots, C_4 constants that can be obtained by applying the fixed-free boundary conditions, that is from (6.43):

$$\phi(0) = \frac{d\phi(0)}{dx} = 0; \quad \frac{d^2\phi(L_m)}{dx^2} = 0; \quad K_t \frac{d\phi(L_m)}{dx} - \frac{d^3\phi(L_m)}{dx^3} = 0 \quad (6.52)$$

This delivers the constants

$$C_1 = -\frac{m_t L_m}{K_{t1}}; \quad C_2 = -\frac{m_t \left(e^{-\sqrt{K_t}L_m} + e^{\sqrt{K_t}L_m} - 2 - \sqrt{K_t} e^{\sqrt{K_t}L_m} L_m + L_m \sqrt{K_t} e^{-\sqrt{K_t}L_m} \right)}{\left(e^{-\sqrt{K_t}L_m} + e^{\sqrt{K_t}L_m} \right) K_t K_{t1}}; \quad (6.53)$$

$$C_3 = -\frac{m_t \left(L_m \sqrt{K_t} e^{-\sqrt{K_t}L_m} - 1 \right)}{K_t^2 K_{t1} \left(e^{-\sqrt{K_t}L_m} + e^{\sqrt{K_t}L_m} \right)}; \quad C_4 = \frac{m_t \left(1 + \sqrt{K_t} e^{\sqrt{K_t}L_m} L_m \right)}{K_t^2 K_{t1} \left(e^{-\sqrt{K_t}L_m} + e^{\sqrt{K_t}L_m} \right)}$$

The torsion angle of the micro-structured beam is then obtained as

$$\phi(x) = -\frac{1}{2} \frac{2m_t \left(e^{-\sqrt{K_t}L_m} + e^{\sqrt{K_t}L_m} - 2 - \sqrt{K_t} e^{\sqrt{K_t}L_m} L_m + L_m \sqrt{K_t} e^{-\sqrt{K_t}L_m} \right)}{e^{-\sqrt{K_t}L_m} + e^{\sqrt{K_t}L_m}} + \frac{2m_t - 2xK_t m_t L_m + m_t x^2 K_t}{K_t^2 K_{t1}} \quad (6.54)$$

$$-\frac{m_t \left(L_m \sqrt{K_t} e^{-\sqrt{K_t}(-x+L_m)} - e^{\sqrt{K_t}x} - e^{-\sqrt{K_t}x} - L_m \sqrt{K_t} e^{\sqrt{K_t}(-x+L_m)} \right)}{K_t^2 K_{t1} \left(e^{-L_m \sqrt{K_t}} + e^{L_m \sqrt{K_t}} \right)}$$

The maximum torsion angle of the beam occurs at its end (when $x = L_m$), given by

$$\phi(x)_{\max} = \frac{1}{2} \frac{2m_t \left(e^{-\sqrt{K_t}L_m} + e^{\sqrt{K_t}L_m} - 2 - \sqrt{K_t} e^{\sqrt{K_t}L_m} L_m + L_m \sqrt{K_t} e^{-\sqrt{K_t}L_m} \right)}{e^{-\sqrt{K_t}L_m} + e^{\sqrt{K_t}L_m}} + \frac{L_m^2 K_t m_t}{K_t^2 K_{t1}} \quad (6.55)$$

The torsion angle can be derived on the basis of the classical theory from equation (6.54) as

$$\bar{\phi}(x) = \frac{xm_t}{2(G_{xy}^* I_y^* + G_{xz}^* I_z^*)} (2L_m - x) \quad (6.56)$$

6.4.3 Size-dependant free torsional vibration behavior

The governing equation of the free torsional vibration of the micro-structured beam can be written from equation (6.44), considering $m_t(x, t) = 0$, as

$$\underbrace{\frac{1}{8}((\gamma_{xy} + \beta_{yx})I_z^* + (\gamma_{xz} + \beta_{zx})I_y^*)}_{K_{t1}} \frac{\partial^4 \phi(x, t)}{\partial x^4} - \underbrace{\left(\frac{1}{2}((2\mu_{xy}^* + \kappa_{xy})I_y^* + (2\mu_{xz}^* + \kappa_{xz})I_z^*) + \left(E_{tor-x}^* + \frac{E_{tor-y}^*}{4} + \frac{E_{tor-z}^*}{4} \right) A \right)}_{K_{t2}} \frac{\partial^2 \phi(x, t)}{\partial x^2} + \rho^*(x) I_x^* \frac{\partial^2 \phi(x, t)}{\partial t^2} = 0 \quad (6.57)$$

To solve this vibrational problem, we use the separation of variables method, writing

$$\phi(x, t) = \varphi(x) [A \sin(\omega_T t) + B \cos(\omega_T t)] \quad (6.58)$$

Here, ω_T denotes the torsional natural frequency of the micro-structured beam. By substituting equation (6.58) into equation (6.57), we obtain the homogeneous linear ordinary differential equation with constant coefficients

$$K_{t1} \frac{d^4 \varphi}{dx^4} - K_{t2} \frac{d^2 \varphi}{dx^2} - \rho^* I_x^* \omega_T^2 \varphi = 0 \quad (6.59)$$

The analytical solution of (6.59) is given by

$$\varphi(x) = C_1 \cosh S_1 x + C_2 \sinh S_1 x + C_3 \cos S_2 x + C_4 \sin S_2 x \quad (6.60)$$

where

$$S_1 = \sqrt{\frac{K_{t2}}{2K_{t1}} + \sqrt{\frac{K_{t2}^2}{4K_{t1}^2} + \frac{\rho I_x^* \omega_T^2}{K_{t1}}}}; \quad S_2 = \sqrt{-\frac{K_{t2}}{2K_{t1}} + \sqrt{\frac{K_{t2}^2}{4K_{t1}^2} + \frac{\rho I_x^* \omega_T^2}{K_{t1}}}} \quad (6.61)$$

with C_1 - C_4 constants that can be defined by applying appropriate boundary conditions. In additions, S_1 and S_2 are the solutions of the characteristic equation of (6.59).

Applying the boundary conditions mentioned in (6.52) for a fixed-free beam to the general solution (equation (6.60)) gives a homogeneous system of equations for the constants C_1 - C_4 expressed in matrix format as:

$$\begin{bmatrix} 1 & 0 & 1 & 0 \\ 0 & S_1 & 0 & S_2 \\ S_1^2 \cosh(S_1 L_m) & S_1^2 \sinh(S_1 L_m) & -S_2^2 \cos(S_2 L_m) & -S_2^2 \sin(S_2 L_m) \\ (K_{t2} S_1 - K_{t1} S_1^3) \sinh(S_1 L_m) & (K_{t2} S_1 - K_{t1} S_1^3) \cosh(S_1 L_m) & -(K_{t2} S_2 + K_{t1} S_2^3) \sin(S_2 L_m) & (K_{t2} S_2 + K_{t1} S_2^3) \cos(S_2 L_m) \end{bmatrix} \begin{Bmatrix} C_1 \\ C_2 \\ C_3 \\ C_4 \end{Bmatrix} = 0 \quad (6.62)$$

Therefore, for non-trivial solutions to exist, we require the vanishing of the determinant of system (6.62), leading to the relations

$$S_2 L_m \approx (n - 0.5) \pi \quad n = 1, 2, 3, \dots \quad (6.63)$$

By inserting equation (6.63) in (6.61) and after some easy manipulations, the n^{th} natural torsional frequency of the fixed-free micro-structured beam is obtained as

$$\begin{aligned}
(\omega_T)_n &= \frac{(n-0.5)\pi}{L_m} \sqrt{\frac{K_{i2} + K_{i1} \left(\frac{(n-0.5)\pi}{L_m} \right)^2}{\rho^* I_x^*}} \\
&= \frac{(n-0.5)\pi}{L_m} \sqrt{\frac{\left(\frac{1}{2} \left((2\mu_{xy}^* + \kappa_{xy}) I_y^* + (2\mu_{xz}^* + \kappa_{xz}) I_z^* \right) + \left(E_{tor-x}^* + \frac{E_{tor-y}^*}{4} + \frac{E_{tor-z}^*}{4} \right) A \right) + \frac{1}{8} \left((\gamma_{xy} + \beta_{yx}) I_z^* + (\gamma_{xz} + \beta_{zx}) I_y^* \right) \left(\frac{(n-0.5)\pi}{L_m} \right)^2}{\rho^* I_x^*}}
\end{aligned} \quad (6.64)$$

where K_{i1} and K_{i2} are identified from the micropolar constants of vertebral trabecular bone; those coefficients are explicitly written in terms of the geometrical and mechanical microparameters of trabeculae as well as geometrical macrostructure of the beam as

$$\begin{aligned}
K_{i1} &= \frac{1}{8} \left[\frac{\sqrt{3} \pi D_h^4 E_s (3D_h^4 E_s^2 D_v^2 + 18D_h^4 E_s D_v^2 G_s + 24L_h^2 D_h^4 G_s^2 k_s + 24E_s D_v^4 L_v L_h G_s k_s + 4L_h^2 D_h^4 E_s G_s k_s + 16L_v G_s^2 k_s D_v^4 L_h)}{384 L_h L_v (6D_h^4 E_s D_v^2 G_s + 3D_h^4 E_s^2 D_v^2 + 8L_h^2 D_h^4 G_s^2 k_s + 4L_h^2 D_h^4 E_s G_s k_s + 16E_s D_v^4 L_v L_h G_s k_s)} \right. \\
&\quad \left. \frac{\sqrt{3} \pi D_h^4 E_s (3D_h^4 E_s D_v^2 + 24D_v^4 L_v L_h G_s k_s + 4L_h^2 D_h^4 G_s k_s) (E_s - 2G_s)}{384 L_h L_v (6D_h^4 E_s D_v^2 G_s + 3D_h^4 E_s^2 D_v^2 + 8L_h^2 D_h^4 G_s^2 k_s + 4L_h^2 D_h^4 E_s G_s k_s + 16E_s D_v^4 L_v L_h G_s k_s)} \right] I_z^* + \frac{1}{1152} \frac{\sqrt{3} \pi D_h^4 E_s I_y^*}{L_v^2}; \\
K_{i2} &= \frac{1}{4} \frac{\sqrt{3} \pi D_h^4 E_s G_s k_s I_y^*}{L_v L_h (3E_s D_h^2 + 4G_s k_s I_v^2 + 3D_h^2 G_s k_s)} + \frac{D_h^4 D_v^4 \sqrt{3} \pi E_s G_s k_s I_z^*}{L_v (9D_h^4 D_v^2 E_s L_v + 12L_h^2 D_h^4 G_s k_s L_v + 12D_h^4 E_s D_h^2 L_h + 16D_v^4 L_h^2 L_h G_s k_s)} \\
&\quad + \frac{1}{24} \frac{\sqrt{3} \pi D_h^4 E_s G_s}{(3E_s + 2G_s) L_v L_h} + \frac{1}{96} \frac{\left(3E_s D_v^4 L_v + \frac{3}{4} \frac{D_h^4 E_s D_v^2}{L_h k_s} + L_h D_h^4 G_s \right) \sqrt{3} \pi G_s E_s D_h^4}{L_v L_h \left(6E_s L_v G_s D_v^4 + E_s^2 D_v^4 L_v + \frac{9}{4} \frac{D_h^4 E_s^2 D_v^2}{L_h k_s} + 3L_h D_h^4 E_s G_s + \frac{3}{2} \frac{D_h^4 G_s E_s D_v^2}{L_h k_s} + 2L_h D_h^4 G_s^2 \right)} + \frac{1}{288} \frac{\sqrt{3} \pi G_s D_v^4}{L_v^2}.
\end{aligned} \quad (6.65)$$

An examination of equation (6.64) shows that the classical torsional frequency can be recovered by letting the micropolar constants vanish (couple stress constants)

$$(\bar{\omega}_T)_n = \frac{(n-0.5)\pi}{L_m} \sqrt{\frac{G_{xy}^* I_y^* + G_{xz}^* I_z^*}{\rho^* I_x^*}} \quad (6.66)$$

The torsional natural frequency in cycles per second can be obtained by the following relation

$$(f_T)_n = (\omega_T)_n / 2\pi.$$

6.4.4 Numerical results

We consider here the geometry of a micro-structured cantilever beam with circular cross-sectional shape (diameter (d) = 1 mm, $L_m = 15d$) for the purpose of numerical illustration. The maximum torsion angle and the first torsion natural frequency versus age (25-85 years) are depicted in Figures 6.11 and 6.12 respectively. The torque acting on the end of the beam in the static case is taken as 0.0001 N.mm.

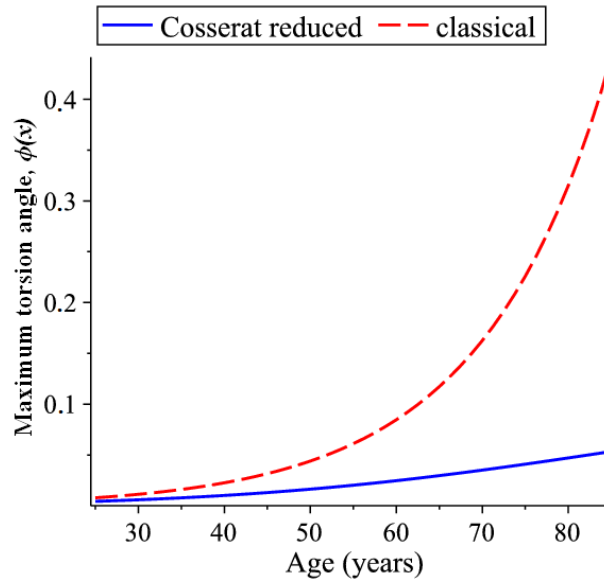


Figure 6.11: Variation with age of the maximum static torsion angle of the micro-structured cantilever beam.

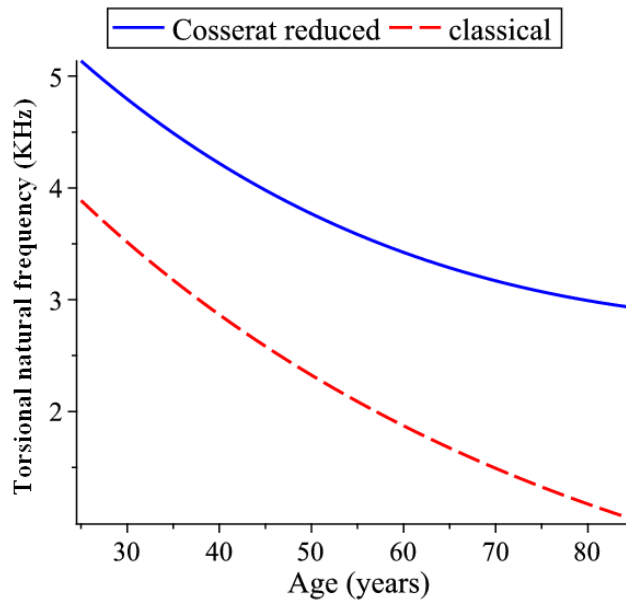


Figure 6.12: Variation with age of the first torsional natural frequencies of the micro-structured cantilever beam.

It appears in [Figure 6.11](#) that the maximum static torsional angle increases gradually with age, contrary to the torsional natural frequency. One can also observe from [Figure 6.11](#) that the static torsion angle predicted by the current microstructural model is always smaller than that predicted by the classical model; this confirms that the micro-structured beams modeled by Cosserat theory are stiffer than those modeled by the classical theory.

From the responses recorded in [Figure 6.12](#), it can be seen that the first torsional natural frequencies predicted by the classical theory are about (1.5-2.5) times lower than that predicted by the Cosserat reduced theory.

In Figure 6.13, we examine the static torsion angle versus the diameter of vertebral trabecular bone specimen of age 40 years; the difference between the Cosserat reduced model and the classical theory becomes significant for specimens of small diameters. The normalized maximum torsion angle of the vertebral trabecular bone beam specimen of age 40 years, variable $\phi / \bar{\phi}$, is recorded versus the beam diameter in Figure 6.13b; it is observed that the static torsional behavior of the beam is size-dependent.

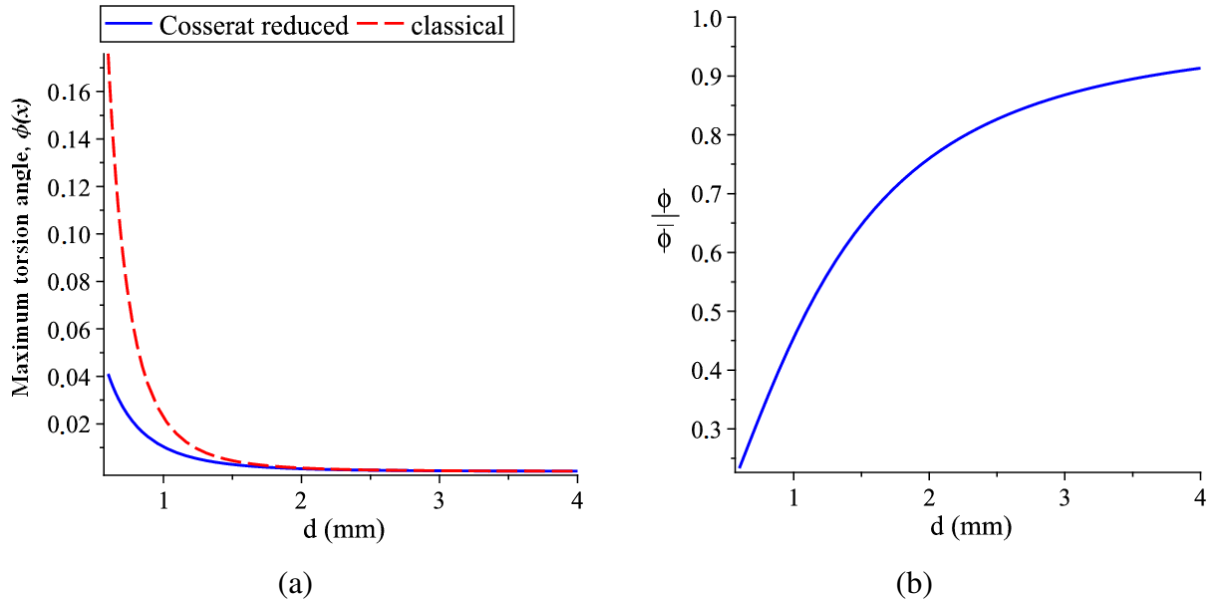


Figure 6.13: (a) Effect of specimen size on the maximum torsion angle, (b) The normalized maximum torsion angle versus beam diameter. Age is 40 years.

Numerical results for the free torsional vibration of size-dependent are depicted in Figure 6.14, which compares the torsional natural frequencies predicted by the present model and by the classical theory. Differences are significant especially for small beam diameters; this indicates that the size dependence of the material properties increases the torsional stiffness and hence it increases the torsional frequencies. The normalized torsional frequency of the vertebral trabecular bone beam specimen of age 40 years, variable $\omega_t / \bar{\omega}_t$, is recorded versus the beam diameter in Figure 6.14b; an increase in the beam dimensions leads to a decreasing size effect which become evanescent for large diameters.

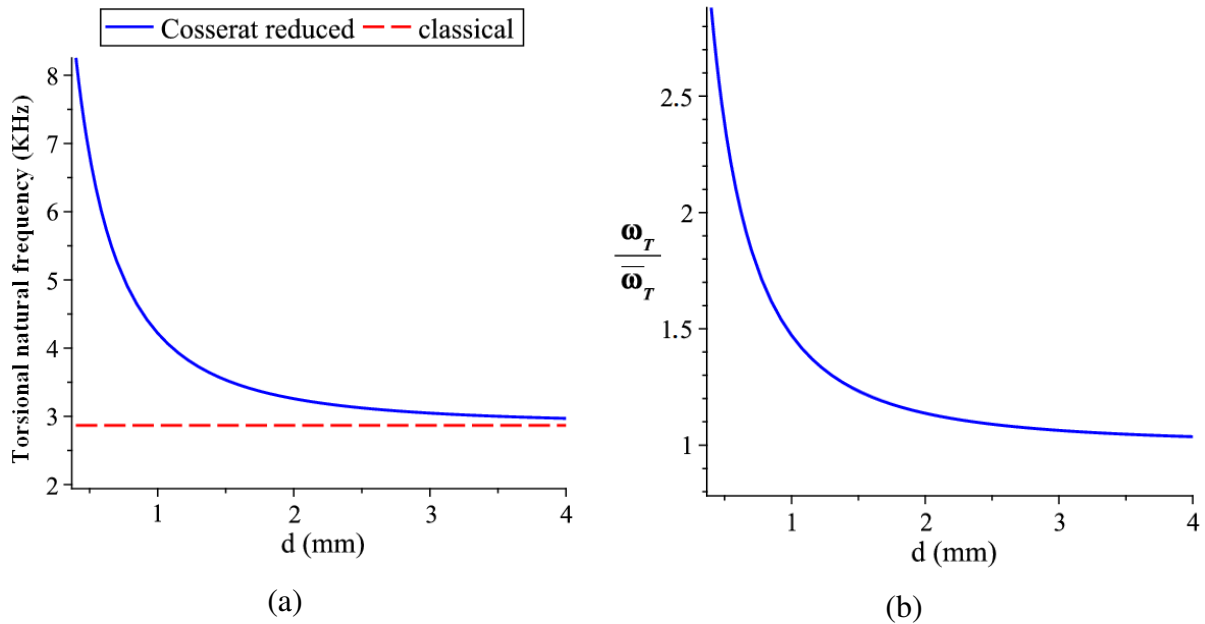


Figure 6.14: (a) Effect of specimen size on the torsional natural frequency, (b) The first normalized torsional natural frequency versus beam diameter. Age is 40 years.

6.5 Conclusions

The bending and torsion of the vertebral trabecular bone beam specimens have been formulated based on the Cosserat theory, a non-classical theory capable of capturing the size-effects. Employing Hamilton principle, the governing equations of motions for both bending and torsional have been obtained. The results obtained for the static bending problem reveal that both the deflection and rotation predicted by the micropolar model are smaller than those predicted by the classical model. Those differences are very large when the beam thickness is small. Similar trends are observed for the free vibration problem, where it is shown that the natural frequency predicted by the micropolar model is higher than the frequency resulting from the classical model, the difference being significantly large only for very thin beams. This work further outlines that the static and dynamic torsional behavior of vertebral bone is size-dependent, with the non-classical theory predicting a stiffer behavior than does the classical theory, especially when the specimen dimensions are reduced.

CHAPTER 7: PLASTIC COLLAPSE AND BRITTLE FRACTURE SURFACE MODELS OF TRABECULAR BONE

The plastic yield and failure properties of trabecular bone are of key interest in understanding and predicting the fracture of bones and bone implant systems. The objective of this chapter is therefore to develop 3D models for describing the multiaxial yield and failure behavior of trabecular bone based on micromechanical approaches. The homogenization technique is presently developed as a convenient micromechanical approach to construct the plastic yield surfaces of 2D and 3D bending-dominated periodic lattices of articulated beams considered as prototype topologies for cancellous bones. The effective strength of trabecular bone is evaluated in the two situations of fully brittle (fracture with no tissue ductility) and fully ductile failure (yield with no tissue fracture) of the trabecular tissue. Finite element simulations are performed to validate the plastic collapse stresses of trabecular bone in a 2D situation under uniaxial, shear, and biaxial tensile loadings. An adaptation and extension of the discrete homogenization method towards a micropolar effective medium are next introduced to construct the plastic yield surfaces for which the material point supports couple stresses in addition to Cauchy-type stresses. As a consequence, the plastic yield surfaces of trabecular bone are determined under the external applied couple stresses. We finally develop a size-dependent non-classical plastic yield criterion relying on the reduced Cosserat theory to capture the size-dependency of the trabecular bone structures.

7.1 Introduction

The fracture of cancellous bone is worth considering in the context of aging due to the fact that the main types of osteoporotic bone fracture in humans are hip fractures. Those fractures usually involve the neck of the femur, which is filled spongy bone, or the collapse of vertebrae, which contain very thin cortical shells and are also primarily spongy bone ([Ritchie et al., 2009](#)). It is known that with age, the density and diameter of the bone struts decrease. Fractures on vertebrae, wrist and hip tend to start in the regions of trabecular bone that show a decreased bone mass and changes in the microarchitecture, which are probably affected by a disease. Trabecular bone microarchitecture plays an important role in trabecular bone mechanics. Osteoporosis leads to a conversion from a plate-like to a more rod-like trabecular morphology, which may contribute to fracture risk beyond that predicted by changes in density ([Shi et al., 2011](#)). Trabecular bone is routinely subjected to a variety of loads during various activities of daily life, and the orientation of the applied stresses with respect to the trabecular orientation plays an important role in trabecular tissue yielding.

The characterization of trabecular bone tissue material and the determination of its failure characteristics and role in the trabecular bone mechanical behavior is of significant clinical importance. From a clinical aspect, the knowledge of the elastic and failure properties of trabecular tissue could be used to investigate the effects of aging and diseases at the tissue level. Obviously, the trabecular bone plays a role in osteoporotic fracture events since the

most common fracture sites, such as vertebral body and proximal femur are rich in trabecular bone. Tissue-level elastic and yield properties are also required as input for both computational (van Rietbergen et al., 1995; Niebur et al., 1999; Yeh and Keaveny, 1999), and analytical (Gibson, 1985) models, and subsequently represent a significant foundation for micromechanical analysis of trabecular bone.

Understanding the effects of trabecular microarchitecture on the mechanics of trabecular bone under various loading conditions should provide insight into bone quality, which will be useful in the development and evaluation of osteoporosis. The osteoporosis, or porous bone, is a skeletal disorder characterized by low bone mass and deterioration the trabecular bone structural, leading to bone fragility and an increased susceptibility to fractures, especially of the hip, spine and wrist. The trabecular bone is a major load-bearing biological tissue in human bone (Eswaran et al., 2006). Its strength properties play a critical role in determining the load-bearing capacity. It is involved in bone vertebral and femoral fractures and is the primary site for the insertion of orthopedic implants. Therefore, its effective mechanical properties are of great clinical and research interest to find proper treatment strategies to strengthen the vertebrae and femur bones in order to prevent such fractures and design better implants (Niebur et al., 2000; Bayraktar and Keaveny, 2004). Furthermore, trabecular bone within the proximal femur experiences multiaxial loads which can lead to entire bone fracture during traumatic activities such as a fall (Lotz et al., 1991). Formulation of a multiaxial failure criterion for such trabecular bone type can enable continuum level models of whole bones and bone-implant systems to mechanistically predict failure loads under various loading scenarios. This could in turn improve hip fracture prediction with osteoporosis (Ford et al., 1996). A multiaxial failure criterion is also of basic bioengineering interest, since it represents a fundamental structure-function biomechanical characteristic of trabecular bone and as such may provide insight into biomimetic design principles of artificial materials (Bayraktar et al., 2004). In this context, the overall goal of this work is to establish a complete strength criterion under multiaxial loads for human trabecular bone based on relationships between the morphology and multiaxial failure properties of bone.

Trabecular bone is less dense in comparison to compact bone, and is made up of an array of microstructural struts or trabeculae that form an open-cell foam, the pores of which are filled in by marrow. The trabeculae enclose a three-dimensional, interconnected, open porous space, resulting in a cellular solid type of material. As dictated by fundamental principles of physics, a fracture occurs when the external load applied to a bone exceeds its strength. It is reported that at lower length to thickness (slenderness) ratio, wet individual trabeculae yield plastically while dry ones fracture in a brittle manner (Townsend et al., 1975; Gibson, 1985). We are here concerned with both wet and dry individual trabecular struts.

One key issue in bone biomechanics is the influence of the microarchitecture strut ductility on the overall strength of trabecular bone. With aging and disease, the individual trabeculae become more brittle, so the question arises as to how does this influence the strength of the apparent trabecular bone? In the present work, we analyze the structural behavior of trabecular bone failure by investigating two extremes behaviors, known as fully ductile and fully brittle. For both strut level behaviors, we investigate failed tissue amount and

reactive strength evaluated at the trabecular bone scale at yield or ultimate point, respectively for ductile or brittle tissue level material behavior. The yield point corresponds to the stress at which a material begins to deform plastically, and the ultimate point corresponds to the highest point of the stress-strain curve. For the entirely ductile case, we consider tissue level failure by plastic yielding, whereas in the brittle case the yielding is not allowed (break without significant deformation or failed by fracture). Furthermore, when determining the plastic yield strength of trabecular bone structure, bone struts are assumed to be made of elastic perfectly plastic material (Gibson, 1985; Keaveny et al., 1994; McDonald et al., 2010). Basically, once the ultimate yielding (plastic collapse) occurs, the structure cannot bear extra loads any more. It is demonstrated that after the onset of initial yielding, the unit cell of bone structure is still capable of withstanding further loading and continuously increasing the loads results in at least one more pair of struts also yielding. Accordingly, the structural unit cell will become a mechanism and ultimately collapses.

In addition, observations by (Nawathe et al., 2013) suggest a possible interaction between bone volume fraction and ductility. At high bone volume fraction, the real strut-level ductility is sufficiently high to effectively be fully ductile; therefore the real behavior mimics that of a perfectly ductile behavior. But at low bone volume fraction, the real behavior falls between the ductile and brittle behaviors.

The main objective advocated in this chapter is the development of a three-dimensional model for describing the multiaxial plastic yielding and brittle fracture behavior of trabecular bone based on micromechanical approaches. As a second aspect, accounting for the moments will allow the homogenization towards the more complete micropolar framework, incorporating a microrotation in addition to the displacement as kinematic descriptors at the continuum level. Such extension and adaptation towards a micropolar effective medium lead to construct the plastic yield surfaces for which the material point supports couple stresses in addition to Cauchy-type stresses. The couple stresses develop internal work in the variation of microcurvatures, defined as the spatial gradients of the microrotation. Consequently, the plastic yield surfaces of trabecular bone will be determined under the external applied couple stresses. The principal thrust in this chapter is also the construction of a size-dependent non-classical plastic yield criterion relying on micromechanical model on the basis of the reduced Cosserat theory in order to capture the size-dependency of trabecular bone structures.

7.2 Homogenization scheme for plastic yield and brittle fracture

7.2.1 3D elementary unit cell for trabecular bone

The microstructural struts that make up a specimen of vertebral trabecular bone are composed of trabecular tissue material. The trabeculae enclose a three-dimensional, interconnected, open porous space, resulting in a cellular solid type material. Accordingly, we will consider the

idealized shape of trabecular bone as a hexagonal cellular structure comprised of double prismatic shape unit cell as shown in [Figure 6.1b](#).

The equilibrium of forces over the entire trabecular unit cell writes in virtual power format as

$$\sum_{b \in B_R} \mathbf{F}^b \cdot \mathbf{v}^{E(b)} - \mathbf{F}^b \cdot \mathbf{v}^{O(b)} = 0 \quad (7.1)$$

We can also add the discrete equilibrium of moments, which is useful for the resolution of the unknowns expressed as the following sum over all unit cell nodes

$$\sum_{b \in B_R} \left(\mathbf{M}^{O(b)} \cdot \mathbf{w}^{O(b)} + \mathbf{M}^{E(b)} \cdot \mathbf{w}^{E(b)} \right) = 0 \quad (7.2)$$

The beam resultant \mathbf{F}^b in equation (7.1) is the sum of the extensional force F_x^b and transversal forces, F_y^b and F_z^b , expressing respectively as

$$\begin{aligned} F_x^b &= \frac{E_s A^b}{L^b} \left(e_x \cdot (\Delta U_1^b) \right) = \frac{E_s A^b}{L^b} \left(e_x \cdot \left(u^{E(b)} - u^{O(b)} + \frac{\partial u}{\partial \lambda^i} \delta^{ib} \right) \right) \\ F_y^b &= \frac{12 E_s^b I_z^b}{(L^b)^3 (1 + \Phi_y)} \left(e_y \cdot (\Delta U_1^b) - \frac{L^b}{2} \left(e_z \cdot (\phi^{O(b)} + \phi^{E(b)}) \right) \right) = \frac{12 E_s^b I_z^b}{(L^b)^3 (1 + \Phi_y)} \left(e_y \cdot \left(u^{E(b)} - u^{O(b)} + \frac{\partial u}{\partial \lambda^i} \delta^{ib} \right) - \frac{L^b}{2} \left(e_z \cdot (\phi^{O(b)} + \phi^{E(b)}) \right) \right) \\ F_z^b &= \frac{12 E_s^b I_y^b}{(L^b)^3 (1 + \Phi_z)} \left(e_z \cdot (\Delta U_1^b) + \frac{L^b}{2} \left(e_y \cdot (\phi^{O(b)} + \phi^{E(b)}) \right) \right) = \frac{12 E_s^b I_y^b}{(L^b)^3 (1 + \Phi_z)} \left(e_z \cdot \left(u^{E(b)} - u^{O(b)} + \frac{\partial u}{\partial \lambda^i} \delta^{ib} \right) + \frac{L^b}{2} \left(e_y \cdot (\phi^{O(b)} + \phi^{E(b)}) \right) \right) \end{aligned} \quad (7.3)$$

Note that the displacement difference ΔU_1^b between the extremity and origin node of each beam is written at first order expansion as $\Delta U_1^b = u^{E(b)} - u^{O(b)} + \frac{\partial u}{\partial \lambda^i} \delta^{ib}$, and the asymptotic expansion of the rotation is accordingly limited to the zeroth order.

The bending moments at both extremities $\mathbf{M}^{O(b)}$ and $\mathbf{M}^{E(b)}$ of the beam introduced in equation (7.2) can be expressed as $\mathbf{M}^{O(b)} = M_y^{O(b)} e_y + M_z^{O(b)} e_z$ and $\mathbf{M}^{E(b)} = M_y^{E(b)} e_y + M_z^{E(b)} e_z$.

with

$$\begin{aligned} M_y^{O(b)} &= \frac{6 E_s^b I_y^b}{(L^b)^2 (1 + \Phi_z)} \left(e_z \cdot \left(u^{E(b)} - u^{O(b)} + \frac{\partial u}{\partial \lambda^i} \delta^{ib} \right) \right) + \frac{E_s^b I_y^b}{L^b (1 + \Phi_z)} \left(e_y \cdot \left((4 + \Phi_z) \phi^{O(b)} + (2 - \Phi_z) \phi^{E(b)} \right) \right) \\ M_y^{E(b)} &= \frac{6 E_s^b I_y^b}{(L^b)^2 (1 + \Phi_z)} \left(e_z \cdot \left(u^{E(b)} - u^{O(b)} + \frac{\partial u}{\partial \lambda^i} \delta^{ib} \right) \right) + \frac{E_s^b I_y^b}{L^b (1 + \Phi_z)} \left(e_y \cdot \left((2 - \Phi_z) \phi^{O(b)} + (4 + \Phi_z) \phi^{E(b)} \right) \right) \\ M_z^{O(b)} &= \frac{6 E_s^b I_z^b}{(L^b)^2 (1 + \Phi_y)} \left(-e_y \cdot \left(u^{E(b)} - u^{O(b)} + \frac{\partial u}{\partial \lambda^i} \delta^{ib} \right) \right) + \frac{E_s^b I_z^b}{L^b (1 + \Phi_y)} \left(e_z \cdot \left((4 + \Phi_y) \phi^{O(b)} + (2 - \Phi_y) \phi^{E(b)} \right) \right) \\ M_z^{E(b)} &= \frac{6 E_s^b I_z^b}{(L^b)^2 (1 + \Phi_y)} \left(-e_y \cdot \left(u^{E(b)} - u^{O(b)} + \frac{\partial u}{\partial \lambda^i} \delta^{ib} \right) \right) + \frac{E_s^b I_z^b}{L^b (1 + \Phi_y)} \left(e_z \cdot \left((2 - \Phi_y) \phi^{O(b)} + (4 + \Phi_y) \phi^{E(b)} \right) \right) \end{aligned} \quad (7.4)$$

The equilibrium equation of the equivalent Cauchy continuum is then written in virtual power form, in order to highlight the stress tensor as the dyadic product of the force vector \mathbf{S}^i with the gradient of the position vector \mathbf{R} with respect to the curvilinear coordinates. The transformation from the Cartesian to the curvilinear coordinates λ^i is expressed as

$$\frac{\partial \mathbf{v}}{\partial \lambda^i} = \nabla_x \cdot \mathbf{v} \cdot \frac{\partial \mathbf{R}}{\partial \lambda^i} \quad (7.5)$$

This leads to the following expression of the equilibrium equation of the equivalent Cauchy continuum

$$\int_{\Omega} S^i \cdot \frac{\partial v}{\partial \lambda^i} d\lambda = \int_{\Omega} S^i \cdot \left(\nabla_x v \cdot \frac{\partial R}{\partial \lambda^i} \right) d\lambda = \int_{\Omega} \left(S^i \otimes \frac{\partial R}{\partial \lambda^i} \right) : \frac{1}{g} (\nabla_x v) dx = \int_{\Omega} (\sigma \cdot \nabla_x) \cdot v dx = 0 \quad (7.6)$$

with the force vectors S^i expressed as the following sums over all struts of the reference unit cell

$$S^i = \sum_{b \in B_R} F^b \delta^{ib} \quad (7.7)$$

From the comparison of the homogenized equilibrium to the equilibrium of a postulated continuum Cauchy medium, it is natural to set the following definition of the macroscopic (apparent) Cauchy stress

$$\sigma = \frac{1}{g} S^i \otimes \frac{\partial R}{\partial \lambda^i} \quad (7.8)$$

It should be noticed that the terms $\frac{\partial u}{\partial \lambda^i}$ appearing in equations (7.3) and (7.4) are strain functions, and all displacements and rotations unknowns are also functions of the strain tensor $[\epsilon]$, which are determined by solving the equilibrium equations in translation and rotation. Accordingly, the constitutive equation for the equivalent continuum writes in 3D matrix format as

$$\{\sigma_x, \sigma_y, \sigma_z, \sigma_{xy}, \sigma_{yz}, \sigma_{xz}\} = [K] \left\{ \frac{\partial u_x}{\partial x}, \frac{\partial u_y}{\partial y}, \frac{\partial u_z}{\partial z}, \frac{\partial u_y}{\partial x}, \frac{\partial u_z}{\partial y}, \frac{\partial u_x}{\partial z} \right\} \quad (7.9)$$

with $[K]$ the equivalent rigidly matrix; the corresponding compliance matrix can be built as

$$[S^{eff}] = [K]^{-1} \quad (7.10)$$

7.2.2 Determination of the plastic yield and fracture surfaces in stress space

Trabeculae form a 3D porous lattice in cancellous bone, whose micro-architecture determines its mechanical performance including the macroscopic strength. Therefore, a 3D geometric model of a hexagonal structure is currently considered as an idealized representation of vertebral trabecular bone, for which the initial yield domain and fracture surface at the macroscopic level are identified from a micromechanical analysis. This study examines the plastic collapse and brittle failure of a hexagonal model of rod-like columnar structure.

We have two different types of analysis to be performed in the so-called ductile and brittle analysis in order to assess effects of tissue level material behavior on the apparent trabecular bone behavior. In the case of ductile, tissue failure occurs by yielding, while in the brittle case, tissue failure occurs via brittle fracture. The terminology "failed tissue" is adopted

here to denote failed tissue regardless of whether it failed by yielding or fracture. Accordingly, we aim at the determination of overall ultimate failure envelopes of trabecular bone in order to give insight into failed tissues. For this purpose, we expose a sequence of equations written in stress space based on homogenization method in order to determine the onset of plastic yielding of trabecular bone and the fracture surface under multiaxial loading conditions, relying on a micromechanical analysis.

7.2.2.1 Microscopic stresses versus the macroscopic deformation tensor

In this subsection, the homogenization method previously described is used to analytically determine the matrix relating the microscopic stress tensor to the apparent (effective) stress tensor. We first construct a vector of the forces that gather all resultants (axial and transverse) and moments acting on each beam b of the reference unit cell considered as an idealized representation prototype vertebral trabecular.

Let $(F_x^b, F_{y,z}^b, M_{y,z}^{O(b)}, M_{y,z}^{E(b)})$ denote the microscopic stress components of beam b , $b=1,2,3,\dots$. Recall that F_x^b is the axial force, $F_{y,z}^b$ the shearing forces and $M_{y,z}^{O(b)}$, $M_{y,z}^{E(b)}$ the bending moments with respect to y and z at both beam extremities. Therefore, the vector of the forces is written lengthily as

$$[F] = \begin{bmatrix} F_x^1 \\ F_y^1 \\ F_z^1 \\ M_y^{O(1)} \\ M_y^{E(1)} \\ M_z^{O(1)} \\ M_z^{E(1)} \\ F_x^2 \\ \dots \end{bmatrix} \quad (7.11)$$

Previous expressions of resultants and moments still involve the unknown displacements u^n and rotations ϕ^n , which are determined for all nodes by solving the equilibrium of efforts and moments equations (7.1) and (7.2). As a consequence, these expressions are functions of the macroscopic strain tensor $[\epsilon]$; then one can construct a matrix $[Q_e]$ relating the force vector on the unit cell to the homogenized strain, so that

$$[F] = [Q_e][\epsilon] \quad (7.12)$$

Additionally, we can relate the effective homogenized strain and stress tensors by the following relation $[\epsilon] = [S^{eff}][\sigma]$, leading in turn to a relation between the stresses at the micro (forces and moments) and macro levels,

$$[F] = [Q_e][S^{eff}][\sigma] \quad (7.13)$$

The previous expression of the microscopic stress is next involved in defining the criteria of onset of plastic yielding and fracture surface for vertebral bone under triaxial and shear loadings.

The overall goal of this work is then to develop models for the plastic yielding and brittle fracture of trabecular bone in stress space incorporating natural anisotropy of bone and multiaxial yield criterion.

7.2.2.2 Plastic collapse and yield surface

It is reported that the post-yield behavior of trabecular bone has been shown to exhibit remarkable similarities to that of open-celled plastic foams (Carter and Hayes, 1976; Hayes and Black, 1979; Gibson, 1985). In the case of wet trabecular bone, the tissue fails in a fully ductile manner; it collapses plastically when loaded beyond the linear-elastic regime (Burstein et al., 1975; Gibson, 1985). Yielding in the struts of such cellular materials type is concentrated in small zones. When a section becomes completely plastic, it is usually referred to as formation of plastic hinges. The initial yield strength is based on the first cell strut(s) to reach the fully plastic limit moment of the cell struts, representing complete loss to carry additional load.

We here consider a uniform strut thickness of trabecular bone; hence, the plastic hinge occurs at a cross-section of maximum bending moment. Based on the plastic hinge concept, trabecular bone collapses plastically when the bending moment exerted by the loads on the individual trabeculae reaches the fully plastic moment, creating plastic hinges at the corners. The fully plastic moment for a perfectly plastic beam under combined bending moment and extensional stress receives the expression (Stronge and Yu, 1993)

$$|M^b| = \sigma_{ys} Z_{\lambda b} \left(1 - \left(\frac{\sigma_a^b}{\sigma_{ys}} \right)^2 \right) \quad (7.14)$$

with M^b the bending moment at the beam extremity nodes with respect to y or z axis, σ_{ys} the initial yield strength of the individual trabecular struts (bulk material), $Z_{\lambda b}$ the plastic section modulus at the plastic hinge section of the trabeculae, which is adopted as $Z_{\lambda b} = D_b^3 / 6$ assuming a circular cross sectional area of the trabeculae. We here consider a 3D geometry of the circular struts, hence the extensional stress acting on them is elaborated as $\sigma_a^b = \frac{F_x^b}{A^b}$. Therefore, the criterion that defines the failure surface for plastic yield is described from (7.14) as

$$\frac{6|M^b|}{\sigma_{ys} D_b^3} + \left(\frac{F_x^b}{A^b \sigma_{ys}} \right)^2 = 1 \quad (7.15)$$

with M^b the bending moments and F_x^b the axial forces within trabecular struts arising from the external applied normal ($\sigma_x, \sigma_y, \sigma_z$) and shear stresses ($\sigma_{xy}, \sigma_{yz}, \sigma_{xz}$) acting on the unit cell.

Introducing the homogenized stress components of $[\sigma]$ after normalization by the initial yield strength of the trabeculae material σ_{ys} into equation (7.13) leads to the following relation

$$[F / \sigma_{ys}] = [F^N] = \begin{bmatrix} F_x^1 \\ F_y^1 \\ F_z^1 \\ M_y^{O(1)} \\ M_y^{E(1)} \\ M_z^{O(1)} \\ M_z^{E(1)} \\ F_x^2 \\ \dots \end{bmatrix}^N = [Q_e][S^{eff}][\sigma / \sigma_{ys}] = [Q_e][S^{eff}] \begin{bmatrix} \sigma_x / \sigma_{ys} \\ \sigma_y / \sigma_{ys} \\ \sigma_z / \sigma_{ys} \\ \sigma_{xy} / \sigma_{ys} \\ \sigma_{yz} / \sigma_{ys} \\ \sigma_{xz} / \sigma_{ys} \end{bmatrix} \quad (7.16)$$

As a final step, the system of previous equations in (7.15) then rewrites for the set of struts b that belong to the reference unit cell by which the whole vertebral bone structure is generated as

$$\frac{6|M^{bN}|}{D_b^3} + \left(\frac{F_x^{bN}}{A^b} \right)^2 = 1 \quad (7.17)$$

The plastic collapse strength domain of the structure is then the surface delimited by previous equality in the normalized stress space. As a consequence, the criteria of plastic collapse for hexagonal cellular considered as a morphological model of vertebral trabecular are derived in three dimensional stress states; addressing the criteria for in-plane and out-of-plane yielding: In-plane stresses σ_x and σ_y combined with out-of-plane normal stress σ_z in addition to in-plane σ_{xy} and out-of-plane shears σ_{yz} , σ_{xz} are considered in the analysis. Note that the normalized axial forces and moments, quantities F_x^{bN} and M^{bN} are extracted from $[F^N]$ in equation (7.16).

7.2.2.3 Brittle failure and fracture surfaces

Structures like vertebra, having trabecular bone as the dominating load carrying biological tissue, are exposed to the risk of fracture in daily activities. The bones of elderly people with osteoporosis are characterized by alteration of micro architecture (thinner, longer individual trabeculae), which results in increased bone fragility and increased risk of fracture. Identification of the point where bone fracture initiates is extremely important to understand failure of bone. We seek to assess the effect of tissue level material behavior as perfectly brittle on the apparent strength of trabecular bone.

As stated earlier that at very low bone volume fraction (high slenderness ratios of trabeculae), trabecular bone may fail in a brittle mode. Additionally, at low slenderness ratios dry individual trabeculae can also fracture in a brittle way (fracture with no tissue ductility);

the stress reaches the ultimate point very quickly (only a small amount of plastic strain can be sustained, and consequently only a very small amount of load is enough to break the whole specimen). The trabecular bone may be subjected to multiaxial stresses; it is then required to set a failure criterion to estimate the combination of stresses leading to failure. When plotted in stress space, this combination defines the brittle failure surface, which is a convenient representation of the criterion for the brittle rupture of bone.

Brittle failure occurs when the maximum stress in a cell strut of trabecular bone subjected to both bending and axial loads exceeds the modulus of rupture σ_{fs} of the cell bone materials. This criterion has been used by (Gibson and Ashby, 1997). The moment that causes the maximum stress writes as

$$\sigma_{\max} = M^b / S_E^b \quad (7.18)$$

with S_E^b the elastic section modulus adopted as $S_E^b = \pi D_b^3 / 32$ for circular trabeculae. Therefore, failure occurs when the previous stress cumulated to the axial stress is equal to σ_{fs} ,

$$\sigma_{fs} = \sigma_a^b + M^b / S_E^b \quad (7.19)$$

where σ_a^b is the axial stress in the cell strut adopted as $\sigma_a^b = \frac{F_x^b}{A^b}$, M^b the bending moment at the strut ends either with respect to y or z axis. The brittle failure condition now becomes

$$\frac{F_x^b}{\sigma_{fs} A^b} + \frac{M^b}{\sigma_{fs} S_E^b} = 1 \quad (7.20)$$

Inserting the macroscopic stress components $[\sigma]$ normalized by the modulus of rupture of trabecular strut σ_{fs} into (7.13) yields the following relation

$$\left[F / \sigma_{fs} \right] = \left[F^N \right] = \begin{bmatrix} F_x^1 \\ F_y^1 \\ F_z^1 \\ M_y^{O(1)} \\ M_y^{E(1)} \\ M_z^{O(1)} \\ M_z^{E(1)} \\ F_x^2 \\ \dots \end{bmatrix}^N = [Q_e][S^{eff}][\sigma / \sigma_{fs}] = [Q_e][S^{eff}] \begin{bmatrix} \sigma_x / \sigma_{fs} \\ \sigma_y / \sigma_{fs} \\ \sigma_z / \sigma_{fs} \\ \sigma_{xy} / \sigma_{fs} \\ \sigma_{yz} / \sigma_{fs} \\ \sigma_{xz} / \sigma_{fs} \end{bmatrix} \quad (7.21)$$

It is obvious that the combination of applied normal and shear stresses required to cause tensile failure in the cell strut is found from the applied moments and the axial stresses acting on the cell struts.

Finally, based on the system of previous equations (7.20), the failure surface of trabecular bone under multiaxial stress conditions accounting for bone anisotropy is described by a

brittle failure criterion condition rewritten for the set of struts b that belong to the reference unit cell as

$$\frac{F_x^{bN}}{A^b} + \frac{32M^{bN}}{\pi D_b^3} = 1 \quad (7.22)$$

A dedicated code has been constructed from the previous developments for the calculation of the plastic yield and brittle fracture surfaces in the stress states of trabecular bone modeled as 3D porous open-celled structure. The code uses an input file including the bone topology and mechanical properties within a selected unit cell, and delivering as an output the plastic collapse and brittle fracture stresses. A summary of the homogenization steps and the determination of the plastic yield and brittle fracture domains are exposed in the following algorithm.

Algorithm for the determination of the plastic yield and brittle fracture surfaces based on classical Cauchy medium from 3D lattice homogenization of trabecular bone microstructure

1. Initialize the data tables. Definition of the coordinates transformation function \mathbf{R} such that $\mathbf{x} = \mathbf{R}(\lambda^1, \lambda^2, \lambda^3)$.

2. For each beam in the trabecular bone elementary cell $b \in B_R$, define the following quantities

(a) The origin and end node of the beam respectively $O(b)$, $E(b)$

(b) The non-dimensional transverse shear factor $\Phi_{y,z}^b = 12E_s^b I_z^b / G_s^b A^b k_s (L^b)^2$

(c) The displacement difference ΔU_1^b between the extremity and origin node of each beam

$$\Delta U_1^b = \mathbf{u}^{E(b)} - \mathbf{u}^{O(b)} + \frac{\partial \mathbf{u}}{\partial \lambda^i} \delta^{ib}$$

with displacements and rotations unknowns $\mathbf{u}^n = [u_x^n \ u_y^n \ u_z^n]$, $\phi^n = [\phi_x^n \ \phi_y^n \ \phi_z^n]$

(d) Express the extensional force F_x^b and transversal forces, F_y^b and F_z^b :

$$F_x^b = \frac{E_s^b A^b}{L^b} (e_x \cdot (\Delta U_1^b)), F_y^b = \frac{12E_s^b I_z^b}{(L^b)^3 (1 + \Phi_y^b)} \left(e_y \cdot (\Delta U_1^b) - \frac{L^b}{2} (e_z \cdot (\phi^{O(b)} + \phi^{E(b)})) \right), F_z^b = \frac{12E_s^b I_y^b}{(L^b)^3 (1 + \Phi_z^b)} \left(e_z \cdot (\Delta U_1^b) + \frac{L^b}{2} (e_y \cdot (\phi^{O(b)} + \phi^{E(b)})) \right)$$

(e) Express the bending moments:

$$M_y^{O(b)} = \frac{6E_s^b I_y^b}{(L^b)^2 (1 + \Phi_z^b)} (e_z \cdot (\Delta U_1^b)) + \frac{E_s^b I_y^b}{L^b (1 + \Phi_z^b)} (e_y \cdot ((4 + \Phi_z^b) \phi^{O(b)} + (2 - \Phi_z^b) \phi^{E(b)})),$$

$$M_y^{E(b)} = \frac{6E_s^b I_y^b}{(L^b)^2 (1 + \Phi_z^b)} (e_z \cdot (\Delta U_1^b)) + \frac{E_s^b I_y^b}{L^b (1 + \Phi_z^b)} (e_y \cdot ((2 - \Phi_z^b) \phi^{O(b)} + (4 + \Phi_z^b) \phi^{E(b)})),$$

$$M_z^{O(b)} = \frac{6E_s^b I_z^b}{(L^b)^2 (1 + \Phi_y^b)} (-e_y \cdot (\Delta U_1^b)) + \frac{E_s^b I_z^b}{L^b (1 + \Phi_y^b)} (e_z \cdot ((4 + \Phi_y^b) \phi^{O(b)} + (2 - \Phi_y^b) \phi^{E(b)})),$$

$$M_z^{E(b)} = \frac{6E_s^b I_z^b}{(L^b)^2 (1 + \Phi_y^b)} (-e_y \cdot (\Delta U_1^b)) + \frac{E_s^b I_z^b}{L^b (1 + \Phi_y^b)} (e_z \cdot ((2 - \Phi_y^b) \phi^{O(b)} + (4 + \Phi_y^b) \phi^{E(b)}))$$

(f) $\text{equ1}[E(b)] = \text{equ1}[E(b)] + F_x^b e_x + F_y^b e_y + F_z^b e_z$; $\text{equ1}[O(b)] = \text{equ1}[O(b)] - F_x^b e_x - F_y^b e_y - F_z^b e_z$

(g) $\text{equ2}[E(b)] = \text{equ2}[E(b)] + M_y^{E(b)} e_y + M_z^{E(b)} e_z$; $\text{equ2}[O(b)] = \text{equ2}[O(b)] + M_y^{O(b)} e_y + M_z^{O(b)} e_z$

3. Construct the two systems of equilibrium equations of efforts and moments

$$[\text{equ1}] = [0]; [\text{equ2}] = [0]$$

4. Solve the systems of equilibrium equations in (3) for the kinematic unknowns

$$u^n = \begin{bmatrix} u_x^n & u_y^n & u_z^n \end{bmatrix}, \quad \phi^n = \begin{bmatrix} \phi_x^n & \phi_y^n & \phi_z^n \end{bmatrix}$$

5. Construct the matrix $[Q_e]$ that relates the forces vector on bone unit cell $[F]$ to the homogenized macroscopic strain $[\epsilon]$ as $[F] = [Q_e][\epsilon]$. The vector of forces writes

$$[F] = \begin{bmatrix} F_x^1 & F_y^1 & F_z^1 & M_y^{O(1)} & M_y^{E(1)} & M_z^{O(1)} & M_z^{E(1)} & F_x^2 & \dots \end{bmatrix}^T$$

6. Construct the stress vectors $S^i = \sum_{b \in B_R} (F_{x1}^b e_x + F_{y1}^b e_y + F_{z1}^b e_z) \delta^{ib}$

7. Construct the apparent homogenized Cauchy stress tensor $\sigma = \frac{1}{g} S^i \otimes \frac{\partial R}{\partial \lambda^i}$

8. Construct the equivalent stiffness matrix $[K]$, such that $[\sigma] = [K][\epsilon]$. In 3D format, it writes

$$\{\sigma_x, \sigma_y, \sigma_z, \sigma_{xy}, \sigma_{yz}, \sigma_{xz}\} = [K] \left\{ \frac{\partial u_x}{\partial x}, \frac{\partial u_y}{\partial y}, \frac{\partial u_z}{\partial z}, \frac{\partial u_y}{\partial x}, \frac{\partial u_x}{\partial y}, \frac{\partial u_z}{\partial x} \right\}$$

9. Construct the compliance matrix $[S^{eff}] = [K]^{-1}$

10. Construct a relation between the microscopic force vector and the macroscopic stress tensor, such that $[F] = [Q_e][S^{eff}][\sigma]$

11. Normalize the equation in step 10 by the initial yield strength of the trabecular strut material, so that $[F^N] = [Q_e][S^{eff}][\sigma / \sigma_{ys}]$

12. The failure surface due to plastic yielding is defined by writing for each strut b in the reference unit cell of trabecular bone the following criterion $\frac{6|M^{bN}|}{D_b^3} + \left(\frac{F_x^{bN}}{A^b}\right)^2 = 1$

The plastic yield domain is then the surface delimited by the criterion defined in step 12 which will be exposed in the normalized stress space.

13. Repeat steps 1 to 10.

14. Normalize the relation in step 10 by the modulus of rupture of trabecular strut σ_{fs} , thus

$$[F^N] = [Q_e][S^{eff}][\sigma / \sigma_{fs}]$$

15. The failure surface due to brittle fracture is described by a brittle failure criterion by rewriting for the set of struts b that belong to the reference bone unit cell $\frac{F_x^{bN}}{A^b} + \frac{32M^{bN}}{\pi D_b^3} = 1$

The failure envelope delineating the brittle fracture is then the intersection of the surfaces defined by previous equality in the normalized stress space.

7.3 Numerical results

In such porous open-celled structures, the apparent density is generally the most important factor affecting the failure behavior. The apparent density (ρ^*) is the density of a volume of the porous material, including voids, whereas the material density (ρ_s) is the density of the structural matrix itself. For both ductile and brittle analyses, there is a strong correlation between strength and bone volume fraction. The ductile strength of bone will be expressed later on in terms of the relative density to give insights about the bone volume fraction dependence.

The vertebral fractures will be related to the relative density of vertebral trabecular bone expressed in terms of trabecular bone architecture, itself changing with age. The relative density is then computed in terms of geometrical parameters of the bone unit cell D_h , D_v , L_h , and L_v as

$$\frac{\rho^*}{\rho_s} = \frac{1}{8} \frac{\pi (3L_v D_h^2 + 2L_h D_v^2)}{L_v^2 L_h \cos \theta (1 + \sin \theta)} \quad (7.23)$$

If we consider an inclination angle of in-plane trabeculae $\theta = 60^\circ$, the relation between the effective density of vertebral bone and age writes

$$\frac{\rho^*}{\rho_s} = \frac{0.0148(\text{Age} + 44.24)(\text{Age}^2 - 262.95\text{Age} + 75848.2)}{(\text{Age} + 67.66)^2 (\text{Age} + 20.96)} \quad (7.24)$$

From the last relations, it is obvious that the trabecular thickness and density both decrease with age. In particular, the horizontal trabeculae thickness and density values decrease more rapidly than the vertical ones. Vertical trabeculae are in general thicker and denser than the horizontal ones at all ages in view of the fact that the vertical trabeculae more importantly contribute to the bone load bearing ability.

In the forthcoming sections, the proposed failure criterion for trabecular bone due to yielding (ductile behavior) and by brittle fracture (ultimate strength) are evaluated numerically under multiaxial stress states.

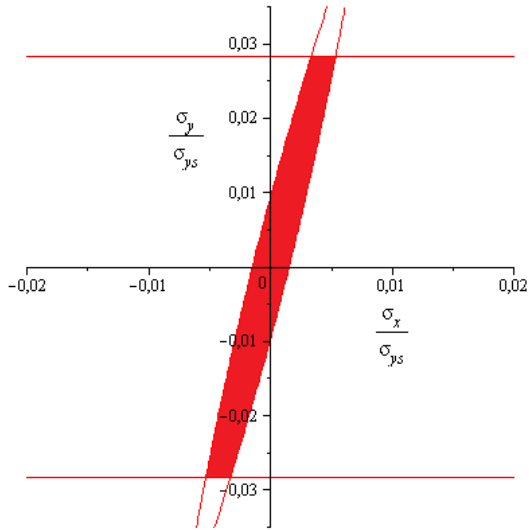
7.3.1 Plastic yield surface calculations under multiaxial loading

The overall collapse surface in the macroscopic stress space consists of intersecting collapse surfaces which are associated with particular collapse modes. In this section, we detail the calculations of the collapse surfaces for six essential practical combinations of macroscopic stress loadings.

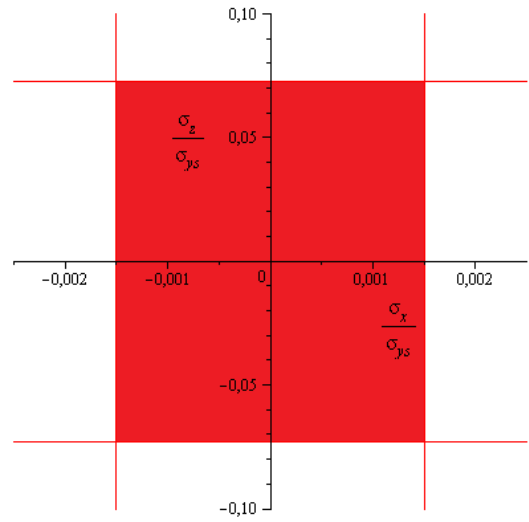
The initial yield strength of periodic trabecular structure is based on the first cell wall(s) reaching the fully plastic limit moment of the cell walls in either tension or compression. We develop a yield surface descriptive of the plastic collapse mechanism of vertebral bone. The initial yield surface is the inner envelope of the intersecting surfaces for the plastic collapse mechanism. Such mechanism is characterized by a failure surface, namely a surface in stress-space describing the combination of stresses causing failure via plastic collapse.

We seek to define the onset of plastic yielding under multiaxial state of stress for vertebral trabecular bones relying on the algorithm established in the previous section with the plasticity criterion defined by equality equation (7.17). The micro-architecture parameters L_v , L_h , D_h , and D_v of the trabecular are selected for a person at the age of 40, with an inclination angle of the oblique trabeculae $\theta = 60^\circ$, hence a relative density of about 12%. The combination of the applied normal and shear stresses which causes plastic collapse, plotted on stress axes σ_{ij} ($i = x, y, z$), is a closed surface called the yield surface for the vertebral trabecular bone as illustrated on Figure 7.1. Initial yield surfaces are plotted according to equation (7.17) in various stress sub-spaces, with all stress components σ_x/σ_{ys} , σ_y/σ_{ys} , σ_z/σ_{ys} , σ_{xy}/σ_{ys} , σ_{yz}/σ_{ys} , and σ_{xz}/σ_{ys} normalized by σ_{ys} , the trabecula yield strength. In Figures 7.1a, b, c, d, e, and f, the yield surfaces are pictured in the subspaces $(\sigma_x, \sigma_y) \Big|_{\sigma_z, \sigma_{xy}, \sigma_{yz}, \sigma_{xz}=0}$,

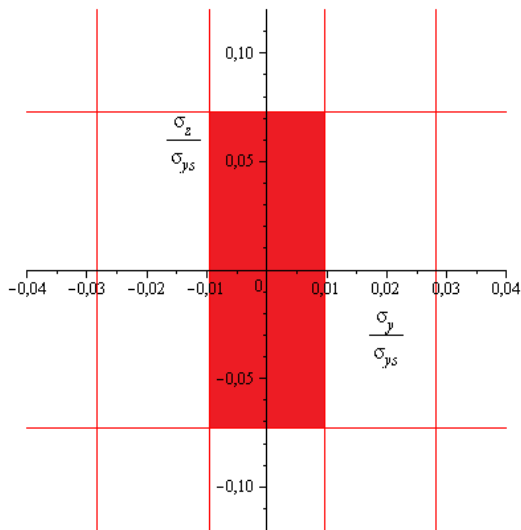
$(\sigma_x, \sigma_z) \Big|_{\sigma_y, \sigma_{xy}, \sigma_{yz}, \sigma_{xz}=0}$, $(\sigma_y, \sigma_z) \Big|_{\sigma_x, \sigma_{xy}, \sigma_{yz}, \sigma_{xz}=0}$, $(\sigma_{xy}, \sigma_{xz}) \Big|_{\sigma_x, \sigma_y, \sigma_z, \sigma_{yz}=0}$, $(\sigma_{xy}, \sigma_{yz}) \Big|_{\sigma_x, \sigma_y, \sigma_z, \sigma_{xz}=0}$, and $(\sigma_{xz}, \sigma_{yz}) \Big|_{\sigma_x, \sigma_y, \sigma_z, \sigma_{xy}=0}$, respectively.



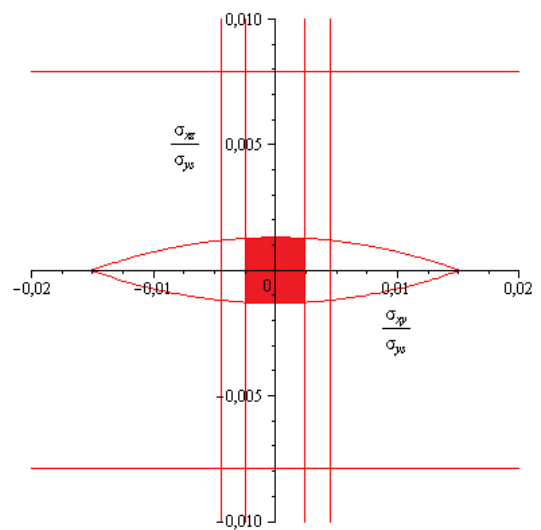
(a)



(b)



(c)



(d)

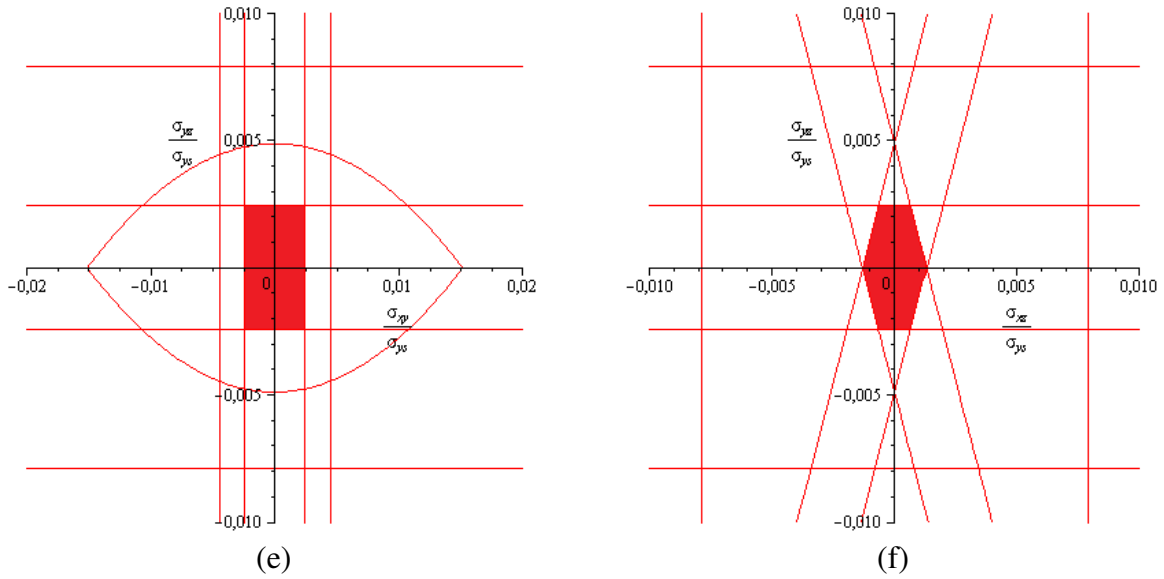


Figure 7.1: Plastic yield surfaces in the stress spaces of (a) $\sigma_x - \sigma_y$, (b) $\sigma_x - \sigma_z$, (c) $\sigma_y - \sigma_z$, (d) $\sigma_{xy} - \sigma_{xz}$, (e) $\sigma_{xy} - \sigma_{yz}$, and (f) $\sigma_{xz} - \sigma_{yz}$, all the stresses are normalized with respect to the yield strength of the bulk material. Age is 40 years with relative density $\rho^*/\rho_s = 0.12$.

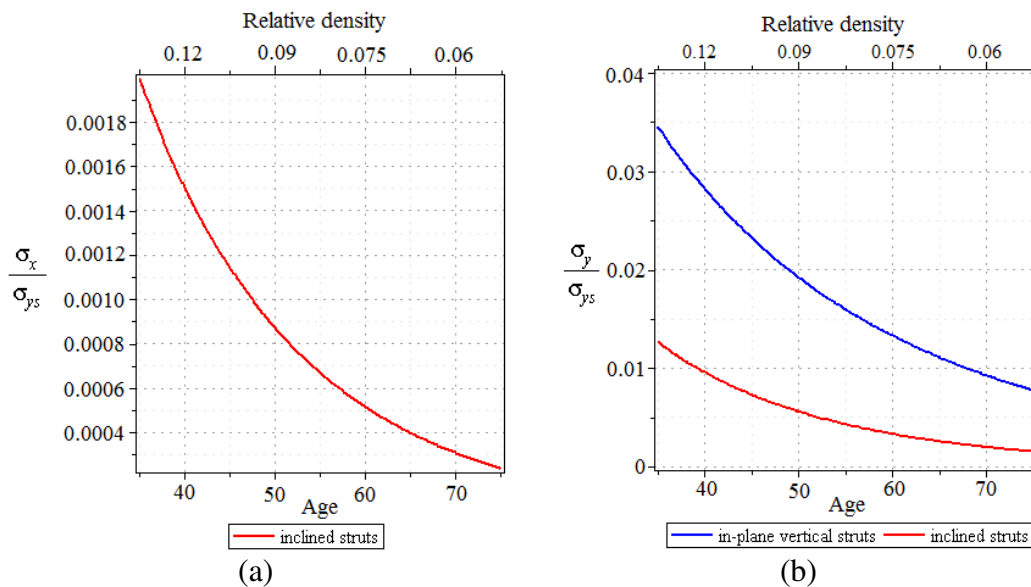
From the results illustrated in Figure 7.1, some key points shall be noticed: the plastic yield domains are closed, anisotropic, and consist of several convex curved surfaces, with some planar facets. All the plastic failure envelopes are symmetrical with respect to tensile and compressive loadings. This may derive from the fact that the initial yield is based on the first cell strut to collapse in bending or reaching yield by extension. If we would consider the post-buckling behavior past initial yield, the behavior would exhibit a tension-compression asymmetry (in this study, we assume that the first compressive buckling load is greater than the initial yield limit of any strut within the lattice, so that no buckling will arise). In the in-plane stress space $\sigma_x - \sigma_y$, the strength domain is truncated in the tensile and compression zone by the axial yielding of in-plane vertical struts aligned to the applied loading direction-y.

We shall further consider the separate effect of individually applying each of the macroscopic stress components σ_{ij} on the periodic vertebral unit cell, in order to determine the plastic collapse strength (i.e. the value of each of these stresses which produces full plasticity at any section); we summarize the plastic collapse criteria defined by expressions adopted for bone aged 40 years in Table 7.1.

Table 7.1: Summary of plastic collapse criteria for 3D vertebral trabecular bone (aged 40 years) unit cell.

Category	Plastic yield strength
In-plane vertical trabeculae	$1254.8 \left(\frac{\sigma_y}{\sigma_{ys}} \right)^2 = 1; 409.8 \left \frac{\sigma_{xy}}{\sigma_{ys}} \right = 409.8 \left \frac{\sigma_{yz}}{\sigma_{ys}} \right = 1;$
Inclined trabeculae	$1092.3 \left(\frac{\sigma_x}{\sigma_{ys}} \right)^2 + 662.2 \left \frac{\sigma_x}{\sigma_{ys}} \right = 1; 253.3 \left(\frac{\sigma_y}{\sigma_{ys}} \right)^2 + 102.4 \left \frac{\sigma_y}{\sigma_{ys}} \right = 1;$ $4369.4 \left(\frac{\sigma_{xy}}{\sigma_{ys}} \right)^2 + 204.9 \left \frac{\sigma_{xy}}{\sigma_{ys}} \right = 1; 764.6 \left \frac{\sigma_{xz}}{\sigma_{ys}} \right = 1; 204.9 \left \frac{\sigma_{yz}}{\sigma_{ys}} \right = 1;$
Vertical trabeculae	$187.9 \left(\frac{\sigma_z}{\sigma_{ys}} \right)^2 = 1; 126.7 \left \frac{\sigma_{xz}}{\sigma_{ys}} \right = 126.7 \left \frac{\sigma_{yz}}{\sigma_{ys}} \right = 1.$

Additionally, for ductile or plastic collapse strength, there is a strong correlation between the strength of vertebral trabecular bone and bone age and its bone volume fraction as well. To give insight into the age dependence with the stress characteristics, for the representative trabecular lattice, we obtain the effective yield strength normalized by the trabecula strength as a function of the bone age or bone relative density. Figure 7.2 shows the yield strength as a function of age. The results are obtained by applying six loading conditions (uniaxial load in the x, y, z directions Figure 7.2a-c, and in-plane and out-of-plane shear loads Figure 7.2d-f to determine the maximum stress in the cell walls and the plastic yield strength. It is clear from the plots that the effective plastic yield strengths decrease with age and increases with the relative density.



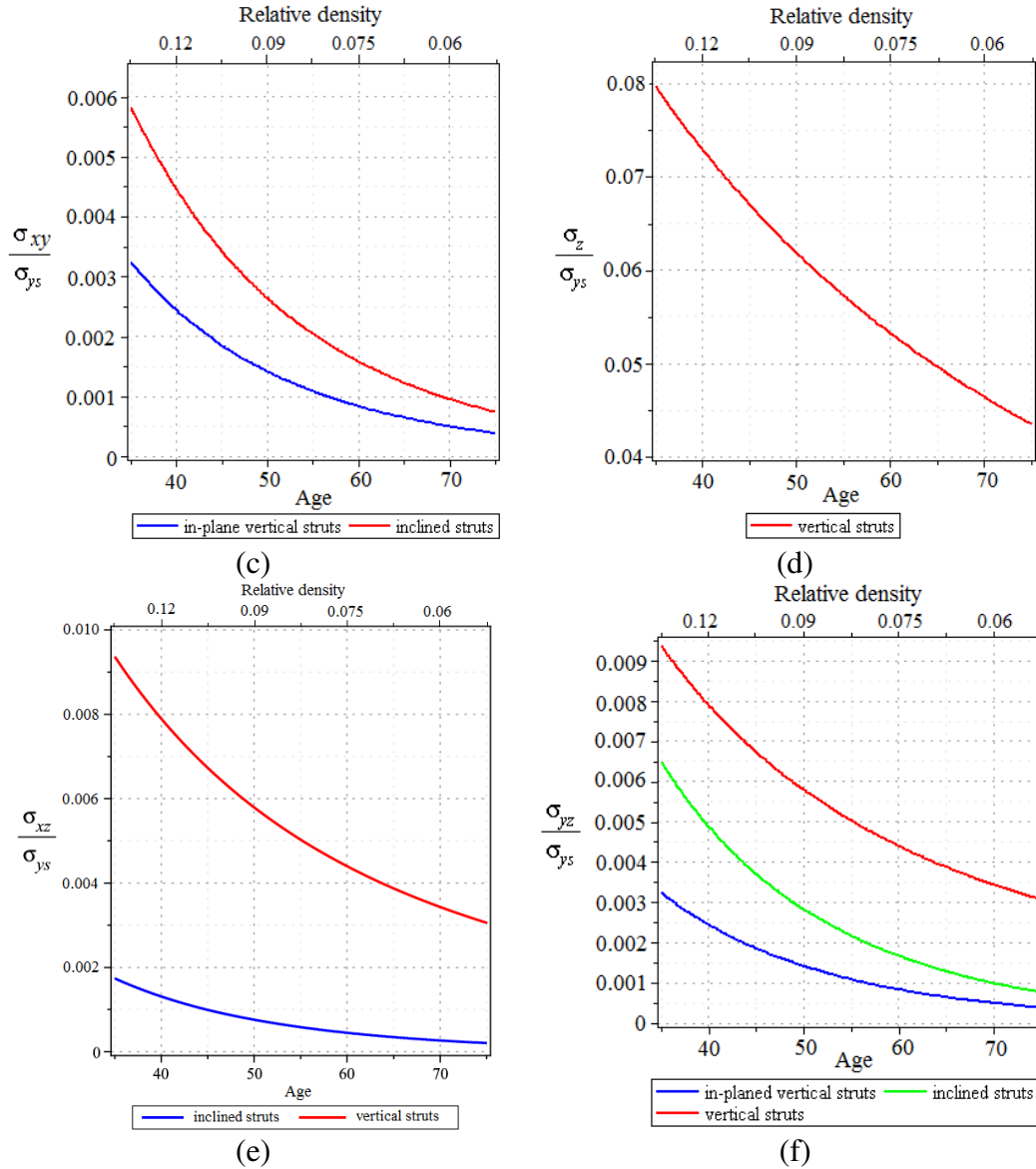


Figure 7.2: The relationship between yield strength and bone age (or bone relative density) for: (a) uniaxial stress -x, (b) uniaxial stress -y, (c) uniaxial stress -z, (d) in-plane shear x-y, (e) out-of-plane shear x-z, and (f) out-of-plane shear y-z.

We observe from the previous results that the remote or external in-plane normal stress σ_x applied to the structure makes the slanted or inclined trabecular struts tend to yield first. In addition, under an in-plane normal stress σ_y , plastic collapses are characterized by two modes: collapses of inclined and in-plane vertical struts depending on which strut fails. According to Table 7.1 and Figures 7.2b, failure does not occur in the in-plane vertical strut, but in the slanted struts because the collapse stress of in-plane vertical struts exceeds the collapse stress of the inclined struts. Furthermore, the collapse modes under in-plane shear σ_{xy} are also characterized by two states (collapse of the in-plane vertical and inclined struts), depending on which strut fails. Relying on Table 7.1 and Figures 7.2c, we find the plastic in-plane shear collapse of vertebral bone from the criteria of yielding of in-plane vertical struts. Going to the out-of-plane stresses, we find that the out-of-plane stress σ_z produces an axial

stress on the vertical struts in the periodic unit cell, so when the axial stress of the vertical struts lies above the yield strength of the bulk material σ_{ys} , the vertical struts will yield axially under σ_z . Under the out-of-plane shear stress σ_{xz} , there will be two collapse modes: the plastic collapses in the inclined struts and in the vertical struts, also depending on which strut fails. The results show that failure of inclined struts occurs first since the equation of plastic yield of inclined struts go before the equation of vertical ones. Lastly, the plastic collapses under out-of-plane shear stress σ_{yz} are characterized by three states including collapses in inclined, in-plane vertical, and vertical struts, depending on which strut fails. These results highlight that the in-plane vertical struts fail first, followed sequentially by the inclined and vertical struts under the shear σ_{yz} .

7.3.2 Brittle fracture surface under triaxial stress state

The combination of applied normal stresses required to cause tensile failure in the trabecular strut is found from the applied moment and the axial stress acting on the cell struts using equation (7.22). A set of trabecular dimensions is used corresponding to a typical lattice for a person aged 85 years. Such an old trabecular lattice is selected since it has a low relative density of about 5% and at very low bone relative density, trabecular bone can fail in a brittle manner.

We analyze the brittle failure of this lattice under a multiaxial loading by determining the brittle fracture surfaces, to provide the complete failure envelope. Typical failure envelopes for biaxial stress states, showing the intersection of the surfaces for the vertebral bone unit cell, are plotted in Figure 7.3 in various stress sub-spaces, considering all normal stress components normalized by σ_{fs} , the rupture strength of solid cell strut material. It is obvious that the brittle fracture in tension is quite different from that in compression and the whole failure surface is not completely defined, due to the fact that all failure mechanisms are not considered (the failure surface does not close in the compression quadrant). If we wanted to do this, we should consider additional failure mechanisms like elastic buckling in compression (compressive buckling is not considered here).

Some key points should be addressed: from Figure 7.3a (in-plane stress state) it can be seen that the fracture surface is elongated in the direction of tension and it is truncated in the biaxial tension zone because of the brittle fracture of in-plane vertical trabeculae under axial stress σ_y . Moreover, the fracture surfaces in stress spaces $\sigma_x - \sigma_z$, and $\sigma_y - \sigma_z$ are composed of several planar facets; they exhibit anisotropic properties and are closed in the tension - tension zone.

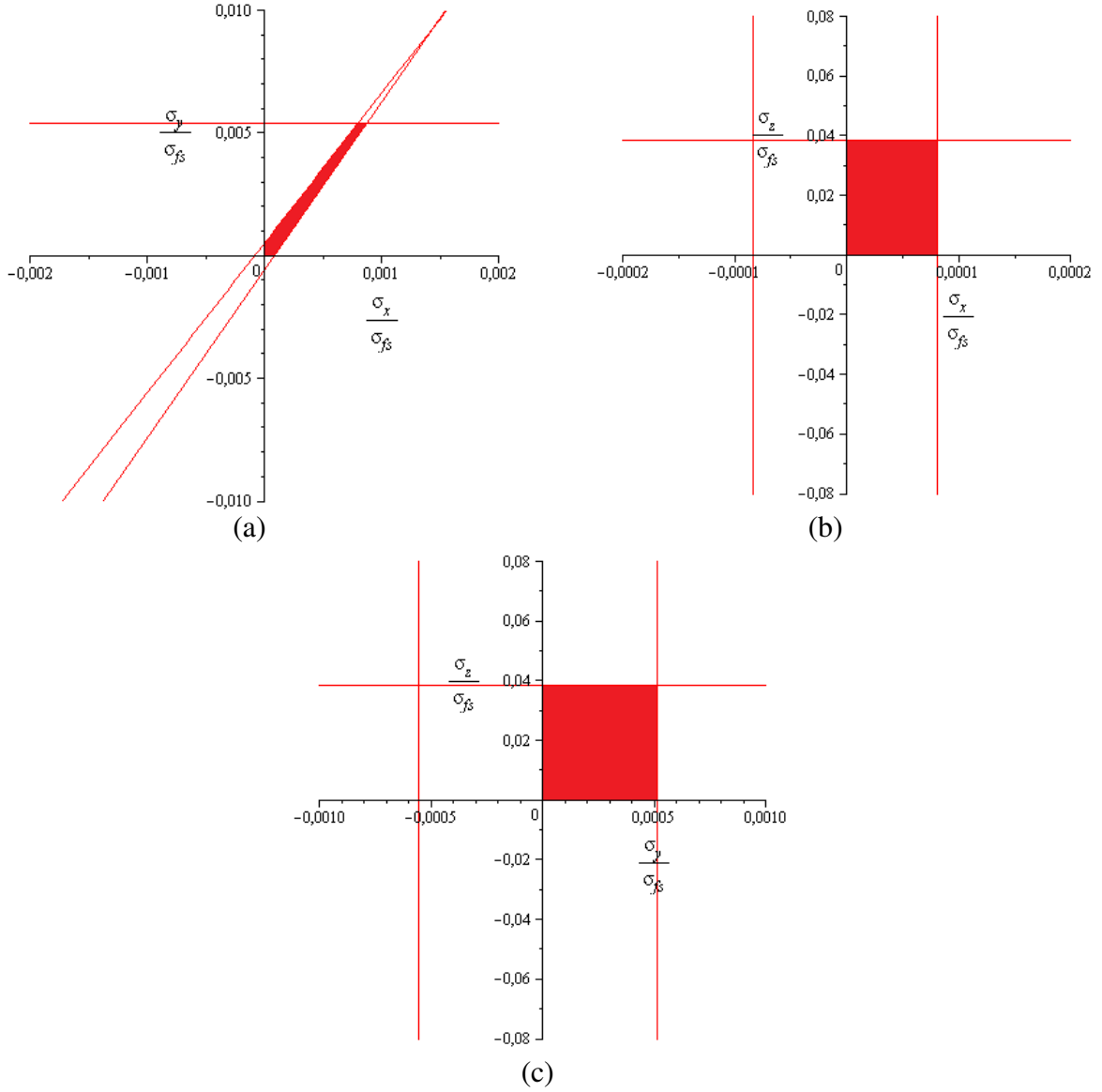


Figure 7.3: Brittle fracture surfaces in the stress spaces of (a) $\sigma_x - \sigma_y$, (b) $\sigma_x - \sigma_z$, and (c) $\sigma_y - \sigma_z$ for a person aged 85 years with bone relative density $\rho^*/\rho_s = 0.05$. The tension–tension quadrant is colored.

7.4 2D trabecular lattice

Upon substitution for the plastic section modulus $Z_{\lambda b} = wt^2/4$, the elastic section modulus $S_E^b = wt^2/6$, vertical length $L_h = w$, and area $A^b = wt$, the in-plane criteria for plastic and brittle failure reduce to those for the 2D hexagonal trabecular lattice. Here, w is the depth of the hexagonal cell (reduces to unit in a planer situation), and t the width of the cell walls. As a result, the in-plane yield surface and brittle failure criteria for the trabecular lattice with uniform rectangular cross-section write for a generic trabecula b respectively as

$$|M^b| = \frac{t^2}{4} \sigma_{ys} \left(1 - \left(\frac{\sigma_a^b}{\sigma_{ys}} \right)^2 \right), \quad \frac{\sigma_a^b}{\sigma_{fs}} + \frac{6M^b}{\sigma_{fs} t^2} = 1; \quad \text{with } \sigma_a^b = \frac{F_x^b}{t} \quad (7.25)$$

Under a general in-plane loading in the 2D situation, the cell struts will be subjected to bending moments and axial forces arising from the external applied stresses σ_x , σ_y , and σ_{xy} .

7.4.1 Plastic collapse validation by the finite element approach

In this section, we consider the honeycomb-like structural model of a trabecular bone specimen made of a 2D array of hexagonal cells, and we model the trabecular architecture as a two-dimensional lattice with a unit cell geometry, as illustrated in [Figure 6.1c](#).

We here demonstrate the use of the unit cell approach in finite element analyses to compute the uniaxial, biaxial, and shear plastic collapse properties of trabecular bone in 2D situation. A comparison to finite element results shall then enable to evaluate the effectiveness of the discrete homogenization approach. The finite element method consists in determining the overall effective plastic yield strength over a representative unit cell of trabecular bone, relying on a finite element discretization of the unit cell geometry. Each cell strut is modeled with a three-node beam element (ABAQUS beam type B22), endowed with bending, stretching and shearing deformation mechanisms. The geometrical parameters of the 2D trabecular lattice are selected as follows: the trabecular separation and trabecular thickness are respectively 0.726 and 0.148 mm. All finite elements are assigned the same material properties of an isotropic elastic modulus of 12.0 GPa, a Poisson's ratio of 0.3, and a yield strength 136 MPa based on the values reported in the literature ([Gibson, 2005](#)). In order to evaluate the post-yield behavior (plastic collapse), we assume a linear elastic-perfectly plastic constitutive relation for the cell wall of the trabecular. The uniaxial yield strengths in tension via x and y-directions, shear, and biaxial tension are computed using displacement boundary conditions from the stress-strain curves shown in [Figures 7.4-7.7](#), respectively. The yield strengths are taken as the peak values of the stress on the stress-strain curve. Additionally, the FE code is used to compute the maximum stress (von-Mises stress) on the strut surface and the equivalent plastic strain.

The uniaxial tensile yield strengths in x and y directions are determined using displacement boundary conditions. The nodes forming an edge are displaced by a specified amount while the nodes on the opposite edge are prevented from translating in the direction of displacement. Rotations in the x-y plane are prevented at the internal nodes to reproduce the behavior of a unit cell in a hexagonal arrangement. The node at the bottom left is also constrained from translating in y- direction when performing tension in x-direction and from translating in x-direction in the case of applying tension in y- direction to ensure uniform deformation of the unit cell (or the nodes of one of the two sides in the direction normal to the displacement direction are prevented from translating in the direction normal to the displacement direction). The stress-strain curves are then constructed from the reaction forces and displacements captured at each increment in the displacement directions ([Figures 7.4 and 7.5](#)).

It is clearly shown from the contour plots of von Mises stress and plastic strain distribution shown in [Figures 7.4b and c](#) that the maximum stress is generated on the inclined

trabecular struts under an applied uniaxial stress σ_x and plastic hinges are produced as well on the inclined struts. This result supports findings from the discrete homogenization that the plastic collapse occurs due to failure of oblique struts. In the same manner, [Figures 7.5b](#) and [c](#) shows the von Mises stress and plastic strain distributions under uniaxial stress in y-direction. It is noticed that the maximum stress and plastic hinges are visibly formed in the oblique struts. As a result of discrete homogenization, there will be two plastic collapse modes under uniaxial stress σ_y , one related to the vertical struts ($\sigma_y = 0.203\sigma_{ys}$) and the other to the inclined ones ($\sigma_y = 0.082\sigma_{ys}$) depending on which strut fails first. Since the value of plastic collapse in vertical struts exceeds the collapse in inclined struts, failure does not occur in the vertical struts but arises in the inclined ones, as confirmed by finite element simulations ($\sigma_y = 0.085\sigma_{ys}$).

The stress-strain curves under biaxial loading conditions are constructed by displacing the nodes forming the edge by a specified amount, while the nodes of the opposite edge are prevented from translating in the direction of the displacement. The displacements are imposed at the two sides, which means that boundary conditions are imposed at all four sides (x and y directions). [Figures 7.7c](#) and [d](#) shows contour plots for the stress factors and equivalent plastic strain under biaxial loading.

The overall yield surface determined by discrete homogenization under a biaxial stress state has been shown to consist of the intersection of the surfaces of two collapse modes: the collapse due to plastic hinges by axial and bending stresses in the inclined struts and the collapse mechanism due to axial yielding of the vertical struts. Typical yield surfaces for biaxial stress states, showing the truncation of the surfaces, are plotted in [Figure 7.7b](#); they are closed convex sets of σ_x and σ_y . It is clear that the plastic yield surface has to be truncated by the collapse of struts aligned with the applied stress in y direction; this means that the plastic collapse under biaxial loading occurs not only in the oblique struts but also in the vertical ones. The bounds of the yield strength defined by the circles ([Figure 7.7b](#)) give the values of stresses which are determined by the intersection of the two plastic yield surfaces of inclined and vertical struts.

As a result from the stress-strain curves obtained under biaxial loading condition by FE simulation ([Figure 7.7a](#)), the first peak gives the yield strength in y-direction with the corresponding two stresses in x-direction. The plastic collapses of inclined and vertical struts do not occur simultaneously since they do not have the same stress values.

As a final test, a FE simulation for simple shear on trabecular lattice is performed to construct shear stress-strain curve for each displacement loading step, from which the plastic shear strength is obtained in order to validate the result from discrete homogenization. To perform such simulation, we impose a displacement field on the top surface of the unit cell along the x direction, while the bottom surface is constrained in the same direction. Both the left and right surfaces are also prevented from translating in the direction perpendicular to x. Subsequently, we capture the x-component of the resultant reaction force produced on the top surface caused by the applied displacement in the x direction. The shear strain is computed by dividing the displacement on the top surface on the length of the trabecular lattice along the y

direction. The shear stress-strain curve is then constructed from the reaction force and displacement at each increment. The yield strength is taken as the value of the stress on the shear stress strain curve as illustrated on Figure 7.6a.

Based on discrete homogenization (DH) results, the plastic collapses under shear stress σ_{xy} are characterized by two failure modes, depending on which strut fails. Since the value of shear collapse stress of inclined struts $\sigma_{xy} = 0.0367\sigma_{ys}$ exceeds the value of the stress of the vertical beam, $\sigma_{xy} = 0.021\sigma_{ys}$, then the failure does not occur in the inclined struts but in the vertical struts. This outcome is supported by FE shear simulation which gives $\sigma_{xy} = 0.022\sigma_{ys}$ from the shear stress strain plot shown on Figure 7.6a; additionally the von Mises stress and plastic strain have significantly values for the vertical struts.

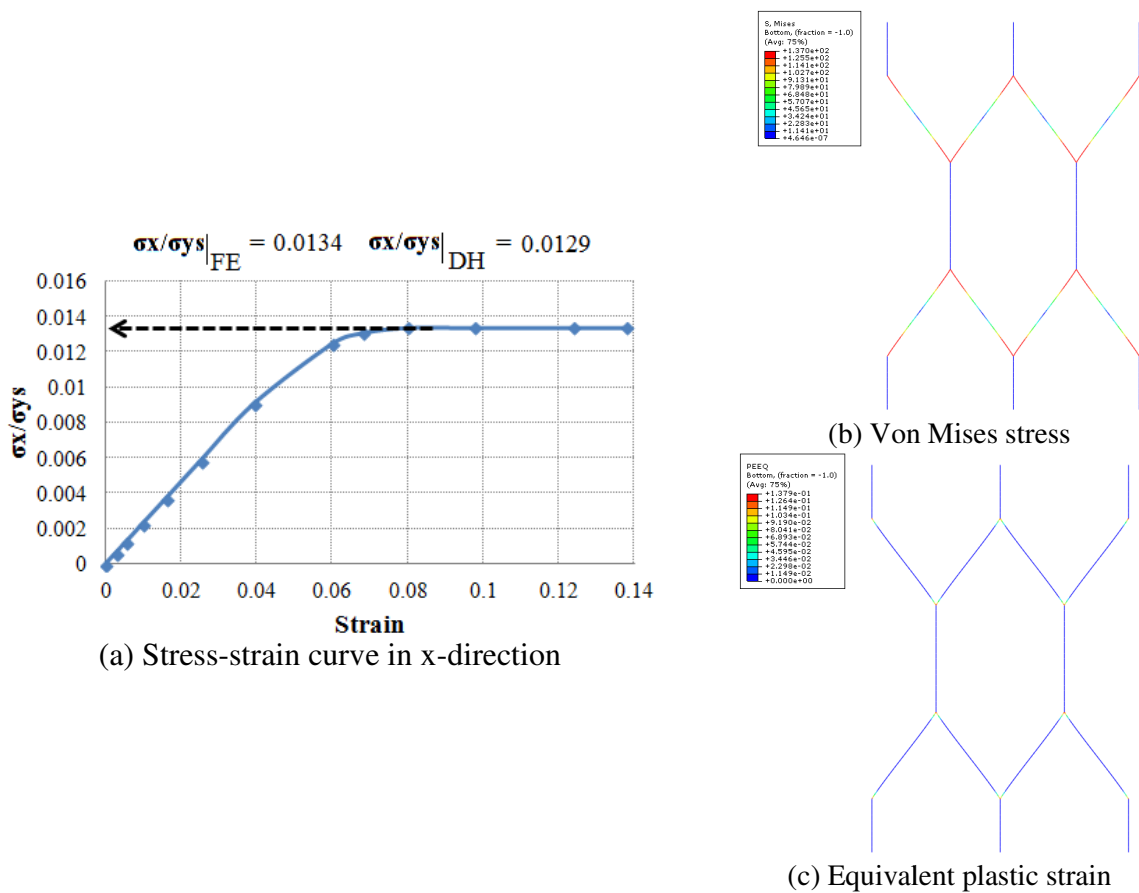
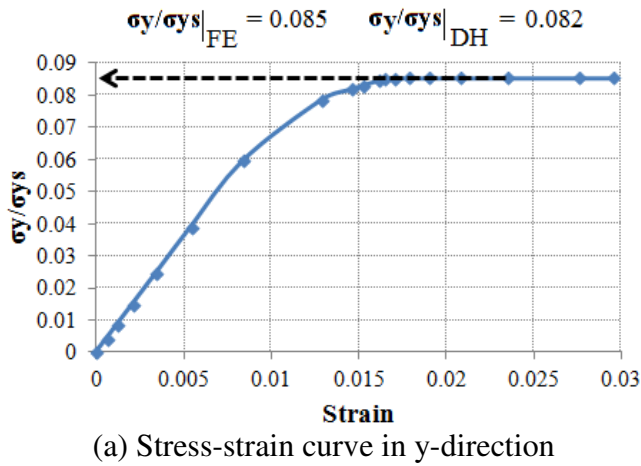
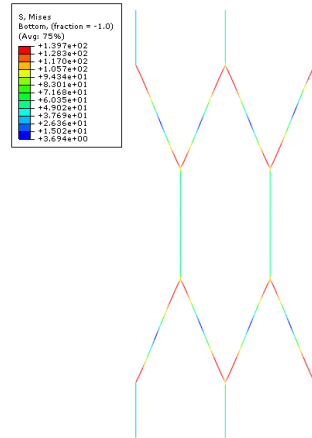


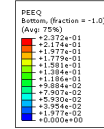
Figure 7.4: Plastic yield stress determined by FE model from the stress-strain curve during tension in x-direction for the trabecular bone lattice. (b) Von Mises stress and (c) Equivalent plastic strain.



(a) Stress-strain curve in y-direction

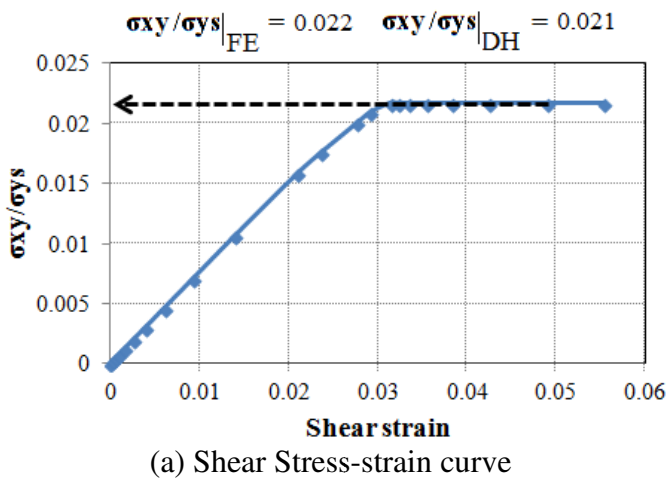


(b) Von Mises stress

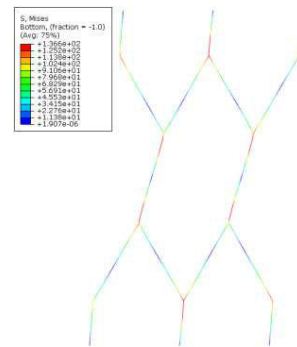


(c) Equivalent plastic strain

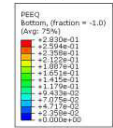
Figure 7.5: Plastic yield stress determined by FE model from the stress-strain curve during tension in y-direction for trabecular bone lattice. (b) Von Mises stress and (c) Equivalent plastic strain.



(a) Shear Stress-strain curve

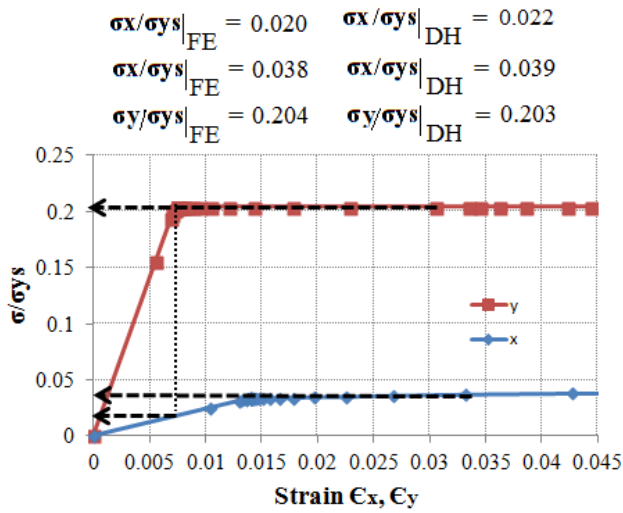


(b) Von Mises stress

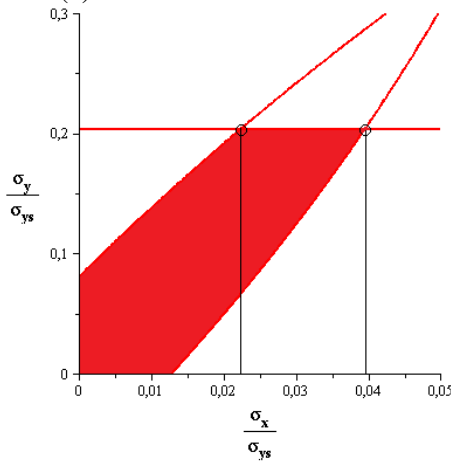


(c) Equivalent plastic strain

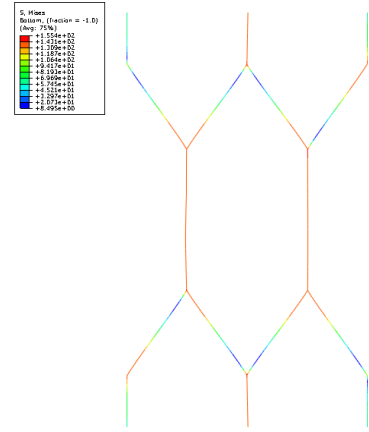
Figure 7.6: Shear yield stress determined by FE model from the shear stress-strain curve during shearing test for trabecular bone lattice. (b) Von Mises stress and (c) Equivalent plastic strain.



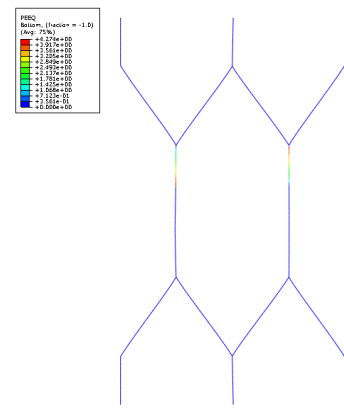
(a) Biaxial stress-strain curve



(b) The plastic yield surface



(c) Von Mises stress



(d) Equivalent plastic strain

Figure 7.7: Biaxial plastic yield stress determined by FE model from biaxial tension test for trabecular bone lattice. (b) Plastic yield surface (c) Von Mises stress and (d) Equivalent plastic strain.

7.4.2 Plastic yield surface based on micropolar theory

In previous analyses, the considered effective continuum medium was selected as a classical Cauchy continuum. Accounting for the moments would allow the homogenization towards more general effective media, such as micropolar continua, a more complete equivalent continuum incorporating a microrotation in addition to the displacement as kinematic descriptors at the continuum level. This entails that the material can transmit couple stresses in addition to tractions (classical stresses); those couple stresses develop internal work in the variation of microcurvatures, defined as the spatial gradients of the microrotation. In the micropolar continua, the material point support couple stresses in addition to the usual Cauchy-stress; however, micropolar theory is different than the couple stress theory or the reduced Cosserat theory in which the rotational degree of freedom is not independent, but is the anti-symmetric part of the displacement gradient tensor. As a consequence, the second order development of the displacement is taken into account in this specific theory to capture

the micropolar effect and hence the asymptotic expansion of the rotation is limited to the first order. The moments are then expressed at both ends as:

$$\begin{aligned}
M^{O(b)\varepsilon} &= \frac{6E_s^b I_z^{eb}}{(L^{eb})^2 (1+\Phi^\varepsilon)} \left(-e_y \cdot (\varepsilon \Delta U_1^b + \varepsilon^2 \Delta U_2^b) \right) + \frac{E_s^b I_z^{eb}}{L^{eb} (1+\Phi^\varepsilon)} \left(\begin{aligned} &(4+\Phi^\varepsilon)\phi_0^{O(b)} + (2-\Phi^\varepsilon)\phi_0^{E(b)} \\ &+ \varepsilon \left((4+\Phi^\varepsilon)\phi_1^{O(b)} + (2-\Phi^\varepsilon)\phi_1^{E(b)} + (2-\Phi^\varepsilon) \frac{\partial \phi_0}{\partial \lambda^i} \delta^{ib} \right) \end{aligned} \right) \\
M^{E(b)\varepsilon} &= \frac{6E_s^b I_z^{eb}}{(L^{eb})^2 (1+\Phi^\varepsilon)} \left(-e_y \cdot (\Delta U_1^b + \Delta U_2^b) \right) + \frac{E_s^b I_z^{eb}}{L^{eb} (1+\Phi^\varepsilon)} \left(\begin{aligned} &(2-\Phi^\varepsilon)\phi_0^{O(b)} + (4+\Phi^\varepsilon)\phi_0^{E(b)} \\ &+ \varepsilon \left((2-\Phi^\varepsilon)\phi_1^{O(b)} + (4+\Phi^\varepsilon)\phi_1^{E(b)} + (4+\Phi^\varepsilon) \frac{\partial \phi_0}{\partial \lambda^i} \delta^{ib} \right) \end{aligned} \right)
\end{aligned} \tag{7.26}$$

with ΔU_2^b the second order displacement difference between the ends of each beam, defined as $\Delta U_2^b = u_2^{E(b)} - u_2^{O(b)}$. The unknown displacements u_1^n , u_2^n and rotations ϕ_0^n , ϕ_1^n , are determined for all nodes by solving the equilibrium equations (2.24) and (2.31). The solutions lead to u_1^n and ϕ_0^n expressed versus the displacement gradient or deformation tensor, while ϕ_1^n and u_2^n express versus the gradient of micro-rotation or the micro-curvature tensor.

The homogenization of the discrete equilibrium of forces leads to the construction of the stress vectors (equation (7.7)) therein $F^b = F_x^b + F_y^b$ in the 2D case; this in turn leads to the homogenized Cauchy stress σ in equation (7.8). In order to get the couple stress components, local the equilibrium of each individual strut is considered for the purpose of homogenization, written at the centre of each strut. After some developments and simplifications, the moment equilibrium equation after homogenization takes the following virtual power form

$$\int_{\Omega} \mu^i \cdot \frac{\partial w}{\partial \lambda^i} d\lambda = \int_{\Omega} \mu^i \cdot \left(\nabla_x w \cdot \frac{\partial R}{\partial \lambda^i} \right) d\lambda = \int_{\Omega} \left(\mu^i \otimes \frac{\partial R}{\partial \lambda^i} \right) : \frac{1}{g} (\nabla_x w) dx = \int_{\Omega} (m \cdot \nabla_x) \cdot w dx = 0 \tag{7.27}$$

with m the macroscopic (effective) couple stress and w the virtual rotational velocity. The identification of the couple stress vectors μ^i leads in turn to the expression of the homogenized couple stress according to

$$m = \frac{1}{g} \mu^i \otimes \frac{\partial R}{\partial \lambda^i} \tag{7.28}$$

with μ^i therein expressed as the following sum over all struts forming the lattice

$$\mu^i = \sum_{b \in \tilde{B}_R} \frac{1}{2} \left(M_2^{E(b)} - M_2^{O(b)} \right) \delta^{ib} \tag{7.29}$$

After solving for all unknowns displacements and rotations, we obtain the effective constitutive equations according to equations (7.8) and (7.28), written in a 2D context in matrix format

$$\underbrace{\begin{Bmatrix} \sigma_x \\ \sigma_y \\ \sigma_{xy} \\ m_{xz} \\ m_{yz} \end{Bmatrix}}_{\Sigma^\Pi} = [K^\Pi] \underbrace{\begin{Bmatrix} \epsilon_x \\ \epsilon_y \\ \epsilon_{xy} \\ \chi_{xz} \\ \chi_{yz} \end{Bmatrix}}_{\Pi} \quad (7.30)$$

where $[K^\Pi]$ is the effective (homogenized) stiffness matrix, σ_{ij} the symmetric part of Cauchy stress tensor and m_{ij} the couple stress tensor.

We consider here the reduced Cosserat theory, where the rotation is related to the displacement gradients $\phi = (\partial u_y / \partial x - \partial u_x / \partial y) / 2$. As a result, the strain tensor ϵ_{ij} is symmetrical, with components defined as $\epsilon_{xy} = \epsilon_{yx} = (\partial u_y / \partial x + \partial u_x / \partial y) / 2$. The couple stress tensor (or moment per unit area) has two components m_{xz} , m_{yz} (Figure 7.8) and the corresponding micro-curvatures express versus the micro-rotations as $\kappa_{xz} = \partial \phi / \partial x$, $\kappa_{yz} = \partial \phi / \partial y$.

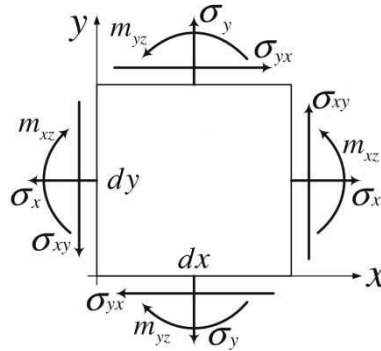


Figure 7.8: Rectangular components of stress and couple stress.

We can next construct the matrix relating the microscopic stress tensor to the macroscopic stress tensor; one first elaborates the force vector gathering all resultants and moments for all struts of the reference unit cell

$$[F] = \begin{bmatrix} F_x^1 \\ F_y^1 \\ M^{O(1)} \\ M^{E(1)} \\ F_x^2 \\ \dots \end{bmatrix} \quad (7.31)$$

After solving for all kinematic unknowns in the localization problem, we can obtain the individual expressions for all forces and moments. These expressions involve the macroscopic deformation tensor Π , allowing to build the following relation between the microscopic stress and the macroscopic deformation

$$[F]=[Q][\Pi] \quad (7.32)$$

This in turn entails the following relation between the microscopic stress and the macroscopic stress

$$[F]=[Q][K^\Pi]^{-1}[\Sigma^\Pi] \quad (7.33)$$

On the basis of the previous calculation of the microscopic stress, we can use the criterion of plasticity initiation in equation (7.25) to define the boundary of the elastic domain of the micropolar continuum medium.

By inserting the macroscopic Cauchy and couple stresses Σ^N normalized by the initial yield strength of strut material σ_{ys} equation (7.33), the following relation is obtained

$$[F^N] = \begin{bmatrix} F_x^1 \\ F_y^1 \\ M^{O(1)} \\ M^{E(1)} \\ F_x^2 \\ \dots \end{bmatrix}^N = [Q][K^\Pi]^{-1}[\Sigma^{\Pi N}] = [Q][K^\Pi]^{-1} \begin{bmatrix} \sigma_x / \sigma_{ys} \\ \sigma_y / \sigma_{ys} \\ \sigma_{xy} / \sigma_{ys} \\ m_{xz} / \sigma_{ys} \\ m_{yz} / \sigma_{ys} \end{bmatrix} \quad (7.34)$$

The plastic yield surface domain of the trabecular lattice is then the surface delimited by the yield criterion; the system of previous equation (7.34) rewrites for the set of struts that belong to the reference unit cell forming the lattice as

$$\left((F_x^{bN})^2 + 4|M^{bN}| \right) / t^2 = 1 \quad (7.35)$$

We next plot the plastic yield surfaces of the trabecular bone lattice adopting the micro-architecture and mechanical parameters of bone cell already presented in Section 7.4.1. In order to assess the overall plastic yield strength for the micropolar continuum, we plot the plastic yield surfaces under the shear stress combined with the couple stress in x-z plane and the couple stress state in both x-z and y-z planes as well (Figure 7.9); we assume $\sigma_x = \sigma_y = m_{yz} = 0$, and $\sigma_x = \sigma_y = \sigma_{xy} = 0$, respectively. The plastic yield surface consists of the intersection surfaces of collapse of vertical and inclined struts.

We shall also consider the separate effect of individually applying each of the couple stresses indicated on Figure 7.8 to determine the couple plastic collapse strengths m_{xz} and m_{yz} , i.e. the value of each of these which produces full plasticity of any section. Under the couple stress m_{yz} , assuming that the other Cauchy and couple stress components are zero, the collapse modes are characterized by the failure of the vertical and inclined struts, depending on which one first fails. The results indicate that failure occurs in the vertical struts and not in the inclined ones, since the couple collapse stresses of inclined struts ($m_{yz} = 0.0046\sigma_{ys}$) exceeds the values of the vertical ones ($m_{yz} = 0.0023\sigma_{ys}$). We also find that the collapse under

couple stress m_{xz} is characterized only by a failure mode of the inclined struts, which occurs when the couple stress is $m_{yz} = 0.0011\sigma_{ys}$.

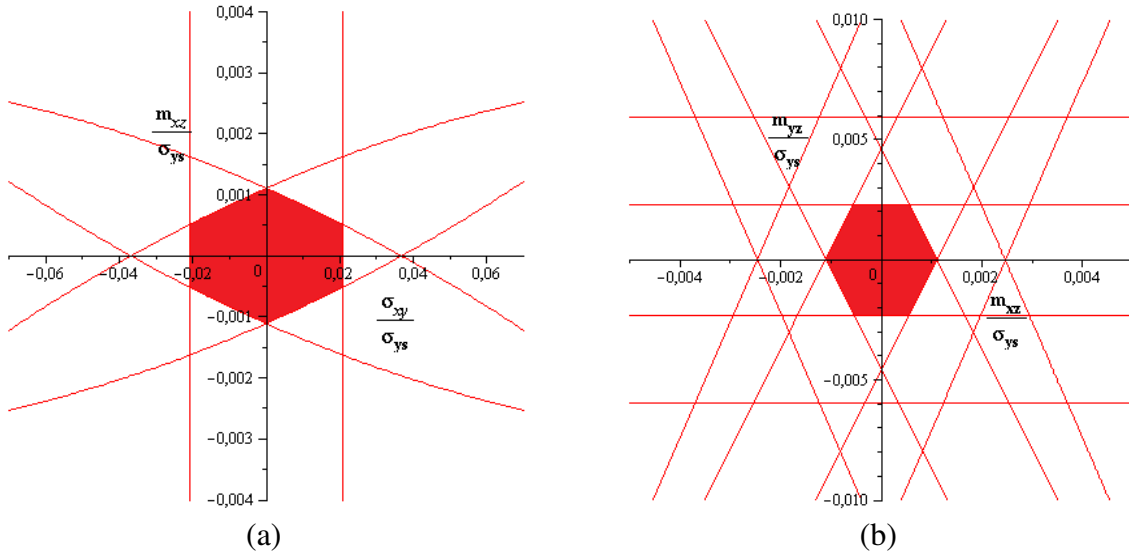


Figure 7.9: Plastic yield surfaces of the trabecular lattice under combined shear and couple stress state (σ_{xy} , m_{xz} , and m_{yz}).

7.4.3 Size dependent plastic yield criterion based on micropolar theory

The classical yield criterion does not describe the yield size dependency that has been observed in microstructured structures such as trabecular bone, and thus it may underestimate the yield loads of structures. So, we would suggest a specific size-dependent plastic yield criterion relying on micromechanical model on the basis of the micropolar theory. In order to develop the micropolar yield criterion, the deviatoric part of the strain energy density of the microscale structure including both classical and non-classical parts is calculated based on this theory and equated to the deviatoric strain energy of a macro-sample subjected to its yielding tensile load. For the bending of microstructured beams, the yielding load is derived in closed-form expression and will be compared with the results calculated based on the classical criterion.

According to the micropolar theory, the strain energy density is a function of both strain (conjugated to stress) and curvature (conjugated to couple stress); this entails that the strain energy U of a micropolar elastic continuum is given by

$$U = \frac{1}{2} (\sigma_{ij} \epsilon_{ij} + m_{ij} \chi_{ij}) \quad (7.36)$$

where σ_{ij} , ϵ_{ij} , m_{ij} , and χ_{ij} refer to the components of the classical stress and strain tensors, the couple stress tensor and the curvature (or rotation gradient) tensor respectively. The strain

energy of a micropolar continuum consists of two parts: a classical part, i.e. $1/2\sigma_{ij}\epsilon_{ij}$ and a non-classical part $1/2m_{ij}\chi_{ij}$.

The strain energy density consists of one part due to dilation (volume changes) and a second one accounting for distortion (change of shape). The former is called the dilatational strain energy (hydrostatic part) and the latter the distortional energy (deviatoric part). From this decomposition, the hydrostatic and deviatoric energy densities take the forms

$$U = \frac{1}{2}(\sigma_{ij}\epsilon_{ij} + m_{ij}\chi_{ij})\Big|_H + \frac{1}{2}(\sigma_{ij}\epsilon_{ij} + m_{ij}\chi_{ij})\Big|_D \quad (7.37)$$

The hydrostatic stress tensor writes as follows $\sigma_{ij}\Big|_H = \frac{1}{3}\delta_{ij}\sigma_{kk}$, which entails the hydrostatic stress components

$$\sigma_{xx} = \sigma_{yy} = \sigma_{zz} = \underbrace{(\sigma_{xx} + \sigma_{yy} + \sigma_{zz})}_{\sigma_{kk}}/3, \quad \sigma_{xy} = \sigma_{xz} = \sigma_{yz} = 0$$

In this case, the corresponding hydrostatic strain will be $\epsilon_{ij}\Big|_H = \frac{1}{3}\delta_{ij}\epsilon_{kk} = \frac{(1-2\nu)}{3E}\delta_{ij}\sigma_{kk}$ in accordance with the Hooke's law of isotropic materials, relating the strain tensor to the stress tensor by, i.e. $\epsilon_{ij} = \frac{1}{E}((1+\nu)\sigma_{ij} - \nu\delta_{ij}\sigma_{kk})$. Here, the hydrostatic components of the couple stress and curvature tensors will vanish; however, they will appear later on in the distortional part. Accordingly, the dilatational part of the strain energy can be obtained as

$$U_H = \frac{1-2\nu}{6E}(\sigma_{kk})^2 \quad (7.38)$$

The deviatoric stress tensor can be obtained by subtracting the hydrostatic stress from the total stress tensor as $\sigma_{ij}\Big|_D = \sigma_{ij} - \frac{1}{3}\delta_{ij}\sigma_{kk}$. In the same manner, the deviatoric strain is obtained

$$\text{as } \epsilon_{ij}\Big|_D = \epsilon_{ij} - \frac{1}{3}\delta_{ij}\epsilon_{kk} = \frac{1}{E}((1+\nu)\sigma_{ij} - \nu\delta_{ij}\sigma_{kk}) - \frac{(1-2\nu)}{3E}\delta_{ij}\sigma_{kk} = \frac{(1+\nu)}{E} \underbrace{\left(\sigma_{ij} - \frac{1}{3}\delta_{ij}\sigma_{kk}\right)}_{\sigma_{ij}\Big|_D}$$

The non-classical part of the strain energy due to the couple stress and curvature tensors will have a deviatoric nature as will be shown next; therefore, the distortional part of the strain energy can be evaluated by subtracting the dilatational term from the total strain density as follows

$$U_D = \frac{1}{2}(\sigma_{ij}\epsilon_{ij} + m_{ij}\chi_{ij}) - \frac{1-2\nu}{6E}(\sigma_{kk})^2 = \frac{1}{2}\left(\frac{\sigma_{ij}}{E}((1+\nu)\sigma_{ij} - \nu\delta_{ij}\sigma_{kk}) + m_{ij}\chi_{ij}\right) - \frac{1-2\nu}{6E}(\sigma_{kk})^2 \quad (7.39)$$

After simplification, the distortional strain energy of the micro-scale structure receives

$$U_D = \frac{1+\nu}{2E}\left(\sigma_{ij}\sigma_{ij} - \frac{(\sigma_{kk})^2}{3}\right) + \frac{1}{2}m_{ij}\chi_{ij} \quad (7.40)$$

where the Young's modulus E is related to Lamé's shear constant G by the relation $E=2G(1+\nu)$.

According to von Mises's yield theory, a ductile solid will yield when the distortional energy density reaches a critical value for that material; this critical value of the distortional energy can be estimated from a uniaxial tensile test. At the instance of yielding, $\sigma_{xx} = \sigma_Y$ (yield stress), all other normal and shear stresses will vanish; therefore, the distortion energy density associated with yielding is

$$U_D|_Y = \frac{1+\nu}{3E} \sigma_Y^2 \quad (7.41)$$

The material under multi-axial loading will yield when the distortional energy U_D is equal to or greater than the critical value for the material $U_D|_Y$. We then equate the distortional strain energy density of the micro-level structure which incorporates both the classical and non-classical terms to the distortional strain energy stored in a macro-level sample at the yield point during tensile test, as follows

$$\left(\sigma_{ij} \sigma_{ij} - \frac{(\sigma_{kk})^2}{3} \right) + \frac{E}{\underbrace{1+\nu}_{2G}} m_{ij} \chi_{ij} = \frac{2}{3} \sigma_Y^2 \quad (7.42)$$

Consequently, yielding will occur when the stresses and couple stresses produced by loadings satisfy the previous equality. We can also define an equivalent stress σ_{eq} based on the previous relation to show the failure condition under which yield occurs, $\sigma_{eq} \geq \sigma_Y$ as

$$\sigma_{eq} = \sqrt{\frac{1}{2} \left(3\sigma_{ij} \sigma_{ij} - (\sigma_{kk})^2 \right) + 3G m_{ij} \chi_{ij}} \quad (7.43)$$

It is obvious that when the non-classical term in equation (7.43) vanishes, the classical von Mises yield criterion will be recovered.

Consistent with the basic assumptions of Bernoulli–Euler beam and the one-dimensional beam theory (Figure 7.10), the nonzero components of the static and kinematic variables write

$$\sigma_{xx} = E_x^* y \frac{\partial^2 v(x,t)}{\partial x^2}, \quad \chi_{xz} = \frac{\partial \phi_z(x,t)}{\partial x} = \frac{\partial^2 v(x,t)}{\partial x^2}, \quad \text{and} \quad m_{xz} = \gamma_{xz} \frac{\partial^2 v(x,t)}{\partial x^2} \quad (7.44)$$

where v represents the lateral deflection of the beam in y -direction, x and y refer respectively to the longitudinal and lateral coordinates, and γ_{xz} is the homogenized micropolar bending constant. The rotation angle of the centroidal axis of the beam is related to the deflection as:

$$\phi_z(x,t) = \frac{\partial v(x,t)}{\partial x}.$$

Upon substitution of non-zero components of stress, couple stress, and curvature from equation (7.44) into equation (7.43), the equivalent or yield stress of the microstructured beam writes

$$\sigma_Y^* = \sqrt{\left(E_x^* y \frac{\partial^2 v(x,t)}{\partial x^2}\right)^2 + 3G_{xy} \gamma_{xz} \frac{\partial^4 v(x,t)}{\partial x^4}} \quad (7.45)$$

The external bending moment acting on a beam based on the micropolar theory can be written as

$$\begin{aligned} M^* &= M_\sigma^* + M_m^* = \int_A (\sigma_{xx} y + m_{xz}) dA = \int_A \left(E_x^* y^2 \frac{\partial^2 v(x,t)}{\partial x^2} + \gamma_{xz} \frac{\partial^2 v(x,t)}{\partial x^2} \right) dA \\ &= (E_x^* I_z^* + \gamma_{xz} A) \frac{\partial^2 v(x,t)}{\partial x^2} \end{aligned} \quad (7.46)$$

where M_σ^* and M_m^* are the components of the bending moment due to the classical stress and couple stress, respectively. I_z^* refers to the second moment of cross-sectional area defined by $I_z^* = \int_A y^2 dA$, with A the cross-sectional area of the macroscopic beam and y the perpendicular distance to the neutral axis.

By substituting the second displacement gradient from equation (7.46) into equation (7.45), one can obtain after simplification a relation for the yielding load in the following form

$$(\sigma_Y^*)^2 = \frac{(M^*)^2 \left((E_x^* y)^2 + 3G_{xy} \gamma_{xz} \right)}{(E_x^* I_z^* + \gamma_{xz} A)^2} \quad (7.47)$$

The size-dependent yielding behavior of the micro-structured beams is analyzed by considering a micro-structured cantilever with uniform rectangular cross section with height H and width W , subjected to a concentrated force F acting on the free end as shown on Figure 7.10. For this beam, the maximum bending moment happens at the clamped end based on the relation $M_{\max}^* = FL$, and the maximum distance on the beam section from the neutral axis is $y_{\max} = H/2$. Hence, the yield moment is determined as $M_{\max}^* = FL$. Rewriting equation (7.47) leads to the following yielding moment of the micro-structured beam

$$M_Y^* = M_{\max}^* = \frac{\sigma_Y^* (E_x^* I_z^* + \gamma_{xz} A)}{\sqrt{(E_x^* y)^2 + 3G_{xy} \gamma_{xz}}} \quad (7.48)$$

The previous relation (7.48) can be written with the characteristic micropolar bending length l_b using the relation $l_b = \sqrt{(\gamma_{xz})/2(2\mu^* + k)}$ (Lakes, 1995), as

$$M_Y^* = \frac{\sigma_Y^* (E_x^* I_z^* + 4l_b^2 G_{xy} A)}{\sqrt{(E_x^* y)^2 + 12G_{xy}^2 l_b^2}} \quad (7.49)$$

The internal bending length enables the incorporation of the material micro-structural features in the model and accounts for the size effect; when the micro-structural effect is

suppressed by letting $l_b = 0$; the yielding moment defined by equation (7.49) then reduces to the yielding moment predicted by classical yield criterion, viz $M_y^* = \sigma_y^* I_z^* / y$.

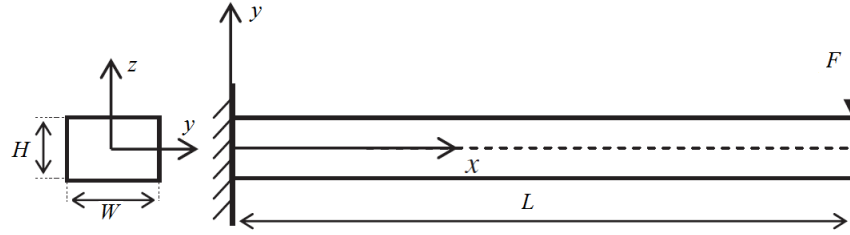


Figure 7.10: Schematic diagram of a micro-structured cantilever beam with rectangular cross section exposed to a concentrated force at its free end.

The yielding bending moment defined in the abovementioned equations corresponds to the first yield moment. To this extent, the applied moment is just sufficient that the yield stress of the material is reached at the outermost fibers of the cross-section. All other stresses in the cross section are lower than the yield stress. This defines the limit of applicability of an elastic analysis: as the load continues to increase, more and more fibers reach the yield stress. Ultimately, the whole of the cross section reaches the yield stress and the moment corresponding to this state is known as the plastic moment of the cross section, a quantity denoted by M_p^* . We here focus on the fully plastic moment of a yielded section of a beam, wherein the plastic moment M_p^* is always greater than the yielding moment. Therefore, beams have an ability to carry loads beyond the initial yielding of the beam. The ratio of the fully plastic moment to the yield moment is known as the shape factor since it depends on the shape of the cross section. Thus, for a rectangular section the plastic moment M_p^* is about 1.5 times greater than the elastic moment capacity M_y^* . Rewriting equation (7.49) leads to the fully homogenized plastic moment of a beam with rectangular cross-section as

$$M_p^* = \frac{3}{2} \frac{\left(\frac{E_x^* H^3}{12} + 4l_b^2 G_{xy} H \right)}{\sqrt{\left(\frac{E_x^* H}{2} \right)^2 + 12G_{xy}^2 l_b^2}} \sigma_y^* \quad (7.50)$$

We note that when the length scale bending parameter l_b is negligible, the plastic yield load of a classical cantilever beam can be obtained from equation (7.50) as $\frac{FL}{H^2} = \frac{M_p^*}{H^2} = \frac{1}{4} \sigma_y^*$. This also means that the size-dependent plastic yield criterion reduces to the classical criterion when the size of the beam increases.

We recall that I_z^* in (7.49) is the quadratic moment of the macroscopic beam along z , given by $I_z^* = H^3 / 12$ (a unit width is considered here in a planar situation), and E_x^* and G_{xy} respectively stand for the effective homogenized elastic and shear moduli of the macroscopic equivalent beam of trabecular bone. We here select the inclined angle of the hexagonal

trabecular cell to be 30° . Such configuration delivers the following relations for E_x^* and G_{xy} in terms of the geometrical and mechanical micro-parameters of trabecular bone struts as

$$E_x^* = \frac{4\sqrt{3}}{3} \frac{E_s G_s k_s D_h^3}{(E_s D_h^2 + 3D_h^2 G_s k_s + G_s k_s L_v^2) L_v}; G_{xy}^* = \frac{\sqrt{3}}{3} \frac{E_s G_s k_s D_h^3}{(E_s D_h^2 + G_s k_s L_v^2 + D_h^2 G_s k_s) L_v} \quad (7.51)$$

Additionally, it should be noted that σ_Y^* in (7.50) refers to the effective homogenized initial yield strength of the beam material. It is determined based on the micromechanical model using the maximum elastic bending moment criteria and expressed (normalized by initial yield strength of bone tissue material) in a closed form expression in terms of the micro-architecture parameter of bone as

$$\frac{\sigma_Y^*}{\sigma_{ys}} = \frac{2}{9} \frac{-3L_v + \sqrt{9L_v^2 + 12D_h^2}}{L_v} \quad (7.52)$$

In order to assess the size-dependent plastic yield of micro-structured beams, we consider the microbeams to be made of human trabecular bone; the geometrical parameters of 2D trabecular lattice are selected as follows: the trabecular separation and trabecular thickness are respectively 0.726 and 0.148 mm. Bone tissue is represented as an isotropic material with an elastic modulus $E_s = 12$ GPa and a shear modulus $G_s = 0.5E_s / (1 + \nu_s)$, selecting a Poisson's ratio $\nu_s = 0.3$. The plastic moment M_p^* / H^2 normalized by the initial yield stress of bulk material σ_{ys} is evaluated on the basis of the size effect plastic yield criterion (equation (7.50)) and compared to the classical plastic moment (Figure 7.11).

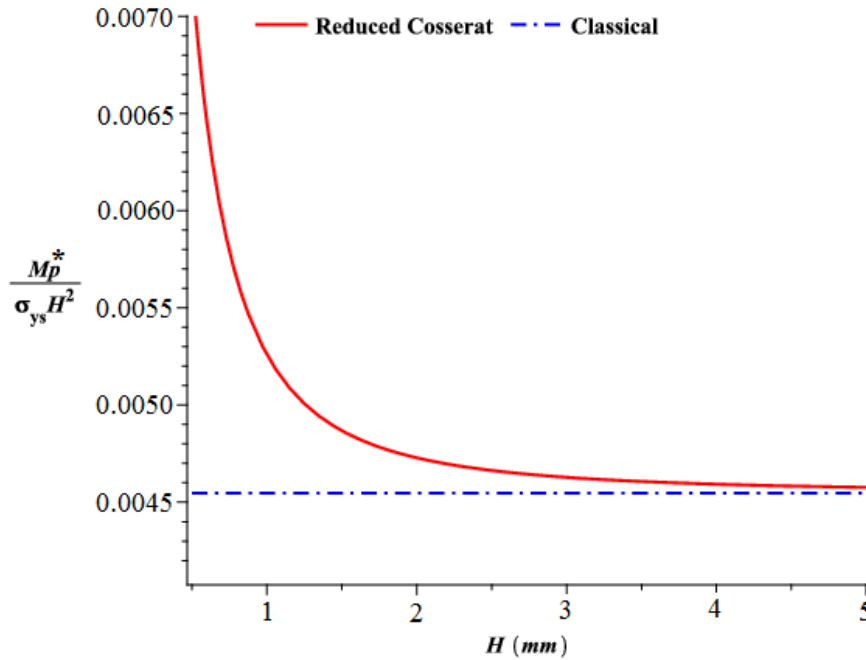


Figure 7.11: Effect of bone specimen size on the plastic yield moment of the beam. $l_b = 0.12$ mm.

From [Figure 7.11](#), we observe that contrary to the classical plastic yield criterion, the present non-classical plastic yield criterion is able to capture the size dependency. It is indicated that when the characteristic size of the microscale structure is comparable to the length scale of the structure material, there will be a considerable gap between the results of the classical criterion and the results of the micropolar based criterion. Conversely, the size yield criterion approaches the classical ones as the size of the beam increases.

7.5 Conclusions

In this chapter, the overall plastic yield and brittle failure behaviors of three-dimensional vertebral trabecular bone has been investigated by microstructural modeling based on the homogenization of the initially discrete microstructure of trabecular bone at the level of the trabeculae. The multiaxial yield behavior of trabecular bone has been analyzed to formulate a multiaxial plastic yield criterion. In addition, the brittle fracture of trabecular bone has been modeled under triaxial stress states to construct the failure surfaces, defined in the tension-tension quadrant.

In plastic yielding, the analyses are performed assuming on an elastic perfectly plastic lattice of hexagonal cells which provides a surrogate model for trabecular bone with open cells. A micromechanical model based on homogenization scheme is applied to a representative unit cell to determine the macroscopic plastic yield surfaces in stress space. The comparison of the plastic collapse stress obtained from discrete homogenization with their counterpart evaluated by finite element shows overall an excellent agreement.

An adaptation and extension of the discrete homogenization method towards a micropolar effective medium has been introduced in order to construct the plastic yield surfaces for which the material point supports couple stresses in addition to Cauchy-type stresses. As a consequence, the plastic yield surfaces of trabecular bone are determined under the external applied couple stresses. The size effects in the ductile fracture mode have been addressed by considering a micropolar behavior of trabecular bone, reflecting the influence of additional degrees of freedom and internal bending lengths effects on the initiation of plasticity. It is worth noted that, when the size of the beam samples increases, one recovers the plastic yielding moment predicted by the classical criterion.

CHAPTER 8: COMBINED INTERNAL AND EXTERNAL REMODELING AT MESOSCOPIC, MICROSCOPIC AND MACROSCOPIC SCALES

Models for the internal and external bone remodeling are developed in this chapter in the framework of the thermodynamics of irreversible processes. Internal remodeling is essentially accounted for by an evolution of the internal bone density versus the trace of the Eshelby stress. The growing surface is endowed by a specific mechanical behavior elaborated from a surface potential, depending upon the elastic surface strain and the external normal. The surface remodeling velocity is related to the driving force for growth identified as the surface divergence of Eshelby stress. The developed formalism is applied to simulate bone internal and external remodeling for 2D geometries, showing the influence of external mechanical stimuli on the evolution of the external shape of bone. Simulations of the evolution of the shape and density of bone structures are carried out successively at mesoscopic, microscopic and macroscopic levels, the former representing cellular level simulations of the trabecular unit cell. At the macroscopic level, a linear elastic constitutive law for trabecular bone is derived, relying on the discrete homogenization approach, whereby the continuum parameters such as stiffness evolve with morphology as remodeling occurs within bone. The developed numerical platform is able to simulate combined bone internal and external remodeling at both trabecular and macroscopic scales.

8.1 Introduction

Bone tissue is an adaptable living structure, having the capacity to adapt its internal structure and external shape to variations in its mechanical environment. Bone tissue adapts its density and hence its mechanical properties in such a way that its structure is optimized in some sense. It aims at preserving the mechanical properties and adapting its structure in response to the mechanical and physiological environments it experiences. This adaptive capacity of bone tissue to the mechanical forces and their history is called bone remodeling, with a classification as either internal or external remodeling (Cowin and Van Buskirk, 1979). External or surface remodeling results in a change of the external shape of the overall bone structure, and occurs by the resorption or apposition of bone material on the surfaces. On the contrary, internal remodeling refers to the resorption or deposition of bone material only, accompanied by the removal and densification of the architecture of cancellous bone.

Obviously, since these processes have a tremendous impact on the overall behavior and health of the entire body, bone remodeling simulations are of great importance. The need for bone-remodeling models is especially marked in applications dealing with bone adaptivity, such as bone implants and scaffold design (see, e.g., Sanz-Herrera et al., 2009; Fernandes et al. 2002), and also to predict the outcome of dental or orthodontic treatment (see, e.g., Field et al. 2012; Wang et al., 2012).

Bone remodeling plays an important role in the processes of formation, maintenance and repair of bone tissues. It largely determines the internal microstructure of the bone and has an essential influence on its strength and mechanical properties.

The main objective advocated in this chapter is the setting up of a multiscale modeling framework relying on the thermodynamics of irreversible processes for the simulation of the evolution of the external bone surface (external remodeling) jointly with internal bone adaptation, resulting in changes in local density (material properties) induced by mechanical stimulations. An increase of mechanical stimuli is found to cause bone formation, whereas a decrease in load leads to bone resorption (Chen et al, 2007).

Two types of bone functional adaptation may then occur simultaneously: internal adaptation and external adaptation. Most of the efforts have been paid to internal bone adaptation in the literature: indeed, numerous models are developed to simulate bone density evolution, where various mechanical stimuli have been proposed as triggers for bone adaptation, including stresses (Beaupré et al., 1990; van der Meulen et al., 1993; Carter et al., 1996; Doblaré and Garcia, 2002; Garijo et al., 2014), strains (Cowin and Hegedus, 1976; Fernandes et al., 1999), strain rate (Negus and Impelluso, 2007), strain energy density (Weinans et al., 1992; Huiskes et al., 2000; Kuhl et al., 2003; Fernandez et al., 2010; Kaczmarczyk and Pearce, 2011), and tissue damage (McNamara et al., 1992; Prendergast and Taylor, 1994; Martin, 1995; Levenston and Carter, 1998; Ramtani and Zidi, 1999, 2001). Conversely, only a few models are developed for external adaptation (see, Huiskes et al., 1987, 2000; Cowin and Firoozbakhsh, 1981). It is clear that most of the efforts have been driven to study internal remodeling, and fewer one to external remodeling. This difference of interest maybe due to the external remodeling (change of shape) occurring more slowly and for being less important than internal remodeling (Fridez et al., 1998); this is true especially for adult persons. However, external bone remodeling is significant in the bone healing process, and it is essential to predict the bone external shape in the design of artificial bone grafts (Chen et al., 2007).

A bone undergoes morphological changes in response to applied mechanical loads by modifying its external geometry as well as its internal structure, i.e., external and internal remodelling occurs simultaneously. Remodeling processes take place in order to adjust the amount of tissue and its geometrical shape.

Incorporating in a coupled approach both external and internal remodeling into an integrated model including both processes is a challenging task we propose to address in the present contribution. We accordingly propose a two-dimensional mathematical model of trabecular bone remodeling at both microscopic and macroscopic scales that simulates the surface-based addition or removal of bone tissue material, combined with bone density alterations induced by the mechanical loads it experiences.

We call internal remodeling, the reorganization of trabecular bone resulting in changes of bone density, while external remodeling refers to the processes occurring at the external surface of bone resulting in geometrical changes. Total remodeling denotes both processes; in addition to the redistribution of bone mineral content, the external remodeling or the change in shape (surface remodeling) is of great interest in order to understand the adjustment of bone

to a new mechanical environment. Therefore, the objective of the present study is to develop a numerical model capable of simulating both internal and external bone adaptation.

The function of internal remodeling is the renewal of the tissue with alteration of the bone mechanical properties either at the strut level or at macroscopic level. Bone formation occurs in overloaded conditions, in order to reinforce bone where needed, while resorption occurs when disuse is observed. This resorption tends to reduce the amount of bone at locations where it is not needed from a mechanical viewpoint. Bone therefore adapts its density in such a way as to attain a homeostatic state of a given mechanical stimulus. Besides density changes, remodeling also occurs to modify bone topology, mainly in trabecular tissue, since the trabeculae tend to align along the load directions.

External bone adaptation at macro and micro-levels is defined as the bone capacity to form or destroy bone surface in response to mechanical loadings. Moreover, throughout this study, the external geometries of the proximal femur and trabecular strut are considered to be variable, so that changes in the external shape are allowed during bone local adaptation (surfaces move freely). As we shall demonstrate later, the divergence and trace of Eshelby stress are adopted as feedback control variables to determine the shape and bone density adaptations. In the case of femur bone remodeling, both types of bone remodeling (internal and external) occur simultaneously, but the most important mechanism which determines the outer geometry and the rate of boundary movement is external bone remodeling. Therefore, in order to determine the rate of bone remodeling, external bone remodeling is mathematically modeled and simulated jointly with internal remodeling.

8.2 Volumetric and surface growth model

We consider a solid body Ω with external boundary $\partial\Omega$; in the continuum macroscopic formulation of growth, those boundaries are only external, whereas internal boundaries are likely to exist when we later on adopt a micromechanical viewpoint.

Part of the external boundary of the solid body is submitted to an evolution due to new mass being added or removed, leading to an overall shape change of the body. This process is called external remodeling in the literature, as illustrated on [Figure 8.1](#). Internal remodeling generally also occurs during the life time of a bone, due to the dynamical equilibrium between bone resorbing units (specialized cells called osteoclasts) and bone generating units (the osteoblasts), leading to a morphological evolution of the trabecular structure.

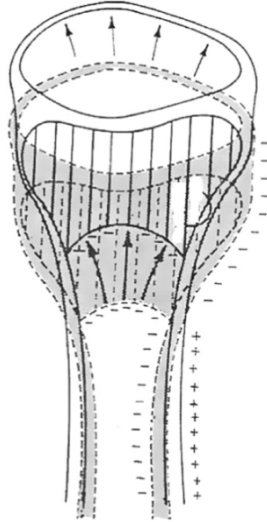


Figure 8.1: External remodeling of a bone. + (resp. -) zones indicate bone apposition (resp. resorption). From Weiss (1988).

Regarding notations, any field $A(\mathbf{x})$ (scalar valued or tensorial valued) having its domain within the growing volume Ω_g shall have a counterpart (that can be envisaged as its trace) on the growing surface S_g , using the same variable with a tilde \tilde{A} , and a line trace on the edge of S_g ∂S_g , when the surface is not closed), noted with a double tilde $\tilde{\tilde{A}}$. The transpose of a second order tensor is denoted \mathbf{A}^T . The curvature tensor is defined as $\mathbf{K}_r = -\nabla \mathbf{N}$, with \mathbf{N} the unit exterior normal to the considered surface. The double contraction of two second order tensors is defined as $\mathbf{A} : \mathbf{B} := A_{ij} B_{ij}$ in a Cartesian coordinate system. The dot over any quantity denotes its material derivative, viz $\dot{a} := Da / Dt$.

8.2.1 Bulk growth model

8.2.1.1 Local dissipation and growth laws involving Eshelby stress

In order to set the stage for the construction of the bulk growth model, we shall first express the local dissipation in order to highlight the duality between the growth velocity gradient and a conjugated driving force for bulk growth. Although bone mechanics involves small strains, one has to consider large shape changes that will be induced by growth, thus it is convenient to adopt in full generality a large strains framework.

Since the number of particles is the same in any configuration, a motion that connects all configurations can be defined: a multiplicative decomposition of the total transformation gradient \mathbf{F} is adopted, in line with the pioneering work of Rodriguez et al. (1994), relating the reference, intermediate and actual configurations, respectively the set of material points $\Omega_0, \Omega_a, \Omega_t \equiv \Omega$ as:

$$\mathbf{F} = \mathbf{F}_a \mathbf{F}_g \quad (8.1)$$

with \mathbf{F}_g the growth transformation and \mathbf{F}_a the mapping accounting for growth accommodation (see Figure 8.2); observe that neither of these two mappings are compatible in general. The kinematic decomposition (8.1) induces the similar decomposition of the Jacobean

$$J_g = \text{Det}(\mathbf{F}_g); J_a = \text{Det}(\mathbf{F}_a) \rightarrow J = J_a J_g \quad (8.2)$$

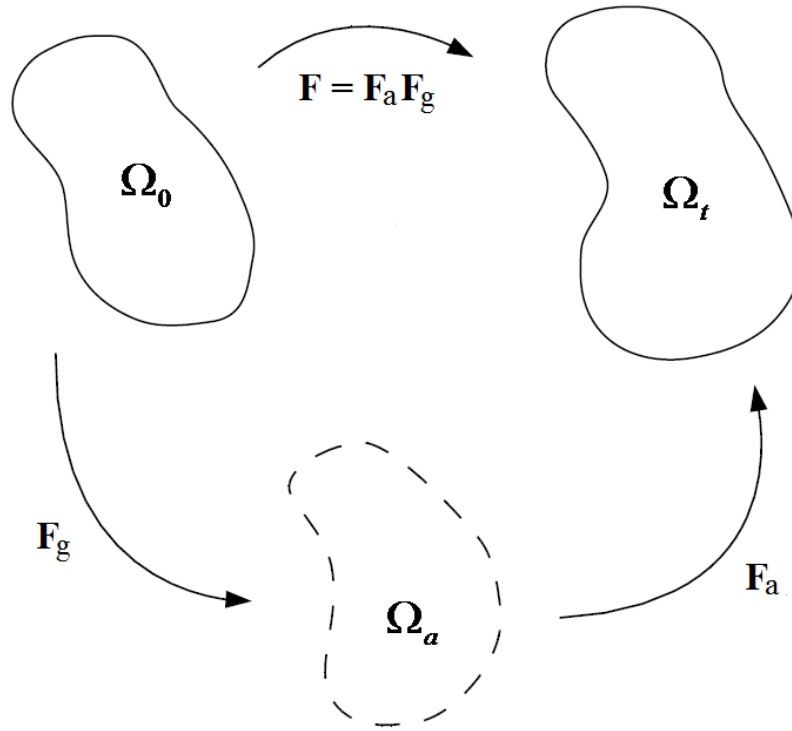


Figure 8.2: Schematic representation of the multiplicative decomposition of deformation gradient into its elastic and growth parts.

Assuming mass is preserved between the natural (intermediate) and the actual configuration, and that the density does not change from the reference to the natural configuration (following the theory of multiple natural configurations), and in line with Ambrosi and Guana (2007), the continuity equation is obtained as

$$\rho_0 = J_a \rho \quad (8.3)$$

The local dissipation expresses in the presence of transport of chemical species as follows, recalling the inequality obtained in Ganghoffer and Haussy (2005) in the initial configuration, and considering first in full generality a large strains framework:

$$J \rho \sigma_s = \mathbf{J} \boldsymbol{\sigma} : \mathbf{D} - \frac{d}{dt} (\rho_0 \psi) \geq 0 \quad (8.4)$$

with σ_s the intrinsic dissipation. Here, $\psi = \psi(\mathbf{F}_a; \mathbf{X})$ is the energy density per unit mass in the reference configuration, related to the referential volumetric strain energy density $W_0 = W_0(\mathbf{F}_a; \mathbf{X})$ by the relation $W_0(\mathbf{F}_a; \mathbf{X}) = \rho_0 \psi(\mathbf{F}_a; \mathbf{X})$; the second order tensor \mathbf{D} is the

symmetrical part of the velocity gradient $\mathbf{L} := \text{grad}\mathbf{V}$. The assumed dependencies of the potential $W_0 = W_0(\mathbf{F}_a)$ for a supposedly uniform body (we can then drop the dependency on the coordinate \mathbf{X}) then lead to the writing of the second law, dropping the thermal and chemical dissipation to focus on the purely mechanical dissipation:

$$\begin{aligned} \mathbf{J}\boldsymbol{\sigma} : (\dot{\mathbf{F}}\mathbf{F}^{-1}) - \frac{dW_0(\mathbf{F}_a)}{dt} \geq 0 \Rightarrow & \left(\mathbf{J}_a \boldsymbol{\sigma} \mathbf{F}_a^{-T} - \frac{\partial W_0(\mathbf{F}_a)}{\partial \mathbf{F}_a} \right) : \delta \mathbf{F}_a \\ & + \left(\mathbf{J}_a \mathbf{F}_a^T \cdot \boldsymbol{\sigma} \mathbf{F}_a^{-T} - \rho_0 \psi \mathbf{I} \right) : (\delta \mathbf{F}_g \cdot \mathbf{F}_g^{-1}) \geq 0 \end{aligned} \quad (8.5)$$

substituting therein variations to the material derivatives, and dividing both members of the inequality by ρJ , using the relation $\frac{1}{\rho} = \frac{J_a}{\rho_0}$. The arbitrariness of the variations $\delta \mathbf{F}_a$ then leads to the vanishing of the multiplicative factor therein, viz

$$\mathbf{J}_a \boldsymbol{\sigma} \mathbf{F}_a^{-T} - \frac{\partial W_0(\mathbf{F}_a)}{\partial \mathbf{F}_a} = 0 \rightarrow \frac{\partial W_0(\mathbf{F}_a)}{\partial \mathbf{F}_a} = \mathbf{J}_a \boldsymbol{\sigma} \mathbf{F}_a^{-T} \quad (8.6)$$

Inserting this expression into the previous local dissipation then gives

$$\left(\mathbf{F}_a^T \cdot \frac{\partial W_0(\mathbf{F}_a)}{\partial \mathbf{F}_a} - W_0(\mathbf{F}_a) \mathbf{I} \right) : (\delta \mathbf{F}_g \cdot \mathbf{F}_g^{-1}) \geq 0 \quad (8.7)$$

thereby identifying the Eshelby stress attached to the intermediate configuration, second order tensor

$$\boldsymbol{\Sigma}_a := W_0(\mathbf{F}_a; \mathbf{X}) \mathbf{I} - \mathbf{F}_a^T \cdot \frac{\partial W_0(\mathbf{F}_a; \mathbf{X})}{\partial \mathbf{F}_a} \quad (8.8)$$

with the second order tensor \mathbf{I} therein denoting the identity mapping.

The nominal stress $\mathbf{P}_a := \frac{\partial W_0}{\partial \mathbf{F}_a}$ (adopting identical notations as in previous paragraph) appearing in Eshelby stress is dual to the accommodation (elastic) mapping \mathbf{F}_a . From the dependency $W_0(\mathbf{F}_a)$, previous derivations lead to the expression of Cauchy stress in the actual configuration as

$$\boldsymbol{\sigma} = \rho \frac{\partial W_0(\mathbf{F}_a)}{\partial \mathbf{F}_a} \cdot \mathbf{F}_a^T \quad (8.9)$$

Hence, the dissipation rewrites in terms of the highlighted Eshelby stress in (8.8) as

$$\mathbf{J} \rho \boldsymbol{\sigma}_s = -\boldsymbol{\Sigma}_a : (\delta \mathbf{F}_g \cdot \mathbf{F}_g^{-1}) \geq 0 \Leftrightarrow -\boldsymbol{\Sigma}_a : \mathbf{L}_g \geq 0 \quad (8.10)$$

defining therein the growth velocity gradient

$$\mathbf{L}_g := \dot{\mathbf{F}}_g \cdot \mathbf{F}_g^{-1} \quad (8.11)$$

Evolution laws for the flux variables can be written from the formulation of the second law: simple linear growth models may be obtained, in line with [Ambrosi and Guana \(2007\)](#), considering a quadratic dissipation (versus \mathbf{L}_g), whence

$$\mathbf{L}_g = -A \boldsymbol{\Sigma}_a, \quad A \geq 0 \quad \text{A being a non negative constant} \quad (8.12)$$

In view of the application to bone structures, the small strain version of previous dissipation inequality can be adopted for bone due to the fact that peak strains are of the order of 2-3%; it clearly writes:

$$-\Sigma_a : \dot{\epsilon}_g \geq 0 \quad (8.13)$$

with $\dot{\epsilon}_g$ the growth strain rate and the small strains version of Eshelby stress expressing as

$$\Sigma_a := W_0(\epsilon_a) \mathbf{I} - \epsilon_a^T \cdot \frac{\partial W_0(\epsilon_a)}{\partial \epsilon_a} \quad (8.14)$$

Here, $W_0(\epsilon_a)$ is the strain energy density per unit volume depending upon the small elastic strains ϵ_a , the form of which will be obtained later on from the discrete homogenization of the trabecular architecture considered as a repetitive unit cell of prismatic shape.

The small strains kinematics here relies on an additive decomposition of the total strain into a grown strain and an elastic strain necessary to restore the kinematic integrity at each material point of the evolving body; it writes in rate form:

$$\dot{\epsilon} = \dot{\epsilon}_a + \dot{\epsilon}_g \quad (8.15)$$

with $\dot{\epsilon}_a$ given by the elastic constitutive law, and the growth strain rate $\dot{\epsilon}_g$ satisfying the positive character of the local dissipation in (8.13); a sufficient condition for this writes

$$\dot{\epsilon}_g = -A \Sigma_a, \quad A \geq 0 \quad (8.16)$$

with the small strains version of the Eshelby stress Σ_a .

Note that the intermediate configuration is needed since the grown strains are in fact cumulative, thus they induce a change of the initial reference configuration, from which elastic strains have to be measured. The introduced intermediate configuration can be viewed as the configuration obtained by unloading any material point from the physical configuration.

Integrating the previously written local dissipation on an arbitrary volume Ω_g and considering that the growth strain rate arises from the volumetric growth velocity field \mathbf{v}_g further entails

$$-\int_{\Omega_g} \Sigma_a : \nabla \mathbf{v}_g \geq 0 \Rightarrow \int_{\Omega_g} \nabla \cdot \Sigma_a \cdot \mathbf{v}_g - \int_{\partial \Omega_g} \mathbf{N} \cdot \Sigma_a \cdot \mathbf{v}_g \geq 0 \quad (8.17)$$

Although the growth velocity \mathbf{v}_g is normally not globally integrable (compatible), one assumes it is locally an integrable field, thus permitting integration by part in (8.17); this is further allowed since we consider both internal bulk growth and surface growth as fully irreversible phenomena.

Thereby, and focusing on the volume integral in previous inequality, a sufficient condition for the local dissipation to be non-negative is

$$\mathbf{v}_g = \mathbf{K}_g \nabla \cdot \Sigma_a, \quad \mathbf{K}_g \geq 0 \quad (8.18)$$

The involvement of the fully material Eshelby stress tensor relies on the belief that configurational changes due to internal or external remodeling occur in the reference configuration, and have to be distinguished from the motion problem *per se* (see [Ganghoffer, 2013](#)).

Since the newly apposed or resorbed material on the surface of bone leads from a kinematic point of view to a purely irreversible growth deformation, one has to update the shape continuously since the variation of the amount of material on the surface of the solid body under external remodeling leads to a permanent change of shape. Since apposition or removal of bone material is presently considered as being fully irreversible, it means that the removal of the external load will lead to the shape induced by the growth velocity field and associated growth velocity gradient computed from the previous step of the growth sequence.

In a second stage, one has to redistribute the existing stresses and (elastic) strains to the new shape of the (new) bone sample subjected to the same external loads, by interpolating the mechanical fields to the new domain (a remeshing is possibly done based on an indicator of mesh distortions). This evolution in two successive steps (a growth phase followed by an elastic computation) is achieved thanks to some operator splitting method explained into more details in the forthcoming sections.

8.2.1.2 Evolution of bulk density

Two alternative growth schemes can be considered from a kinematic point of view: constant-density growth is usually coupled with the assumption of an incompressible tissue, so that $J_a = 1$ and thus density does only change due to growth, but it remains constant when elastic accommodation is considered. For constant-volume growth, the change in volume from the initial body to the unstressed body is neglected, so that $J_g = 1$. Bone tissue growth then occurs by densification only, a viewpoint advocated in this contribution; accordingly, the balance of mass expresses the rate of change of the material density versus the growth mapping

$$\frac{d\rho}{dt} = \Gamma^g \rho \quad (8.19)$$

In a biological context, the growth rate Γ^g appearing in the mass balance equation receives the following expression versus the growth mapping

$$\Gamma^g = \text{Tr}(\dot{\mathbf{F}}_g \mathbf{F}_g^{-1}) \quad (8.20)$$

In the present context, various authors (e.g., [Ganghoffer, 2010, 2012](#), [Ambrosi and Guana, 2007](#)) argued based on thermodynamic principles that the driving force behind growth is the Eshelby stress. [Ganghoffer \(2010\)](#) introduced general balance laws for solid bodies undergoing growth phenomena in the framework of irreversible thermodynamics of open systems. The growth is viewed as a multiphysical phenomenon coupling the transport of nutrients with mechanical factors promoting a local variation of the density, at constant number of particles. The growing continuum body is endowed with a general hyperelastic constitutive behavior encapsulated into a strain energy function $W(\mathbf{u})$, expressed per unit referential volume.

Relying on that the growth rate depends on the Eshelby-like tensor, we propose a constitutive relation for the mass source, wherein the growth rate is proportional to the trace of the Eshelby tensor

$$\Gamma^g = \frac{B_c}{\rho^2} \text{Tr}(\Sigma_a(\boldsymbol{\varepsilon}_a) - \Sigma_0) \quad (8.21)$$

where B_c is a proportionality constant measuring the rate of the adaptation process (it governs the velocity of the adaptation process), $\Sigma_a(\boldsymbol{\varepsilon}_a)$ is the actual volumetric Eshelby stress tensor receiving the expression

$$\Sigma_a(\boldsymbol{\varepsilon}_a) = W_0(\boldsymbol{\varepsilon}_a) \mathbf{I} - \boldsymbol{\varepsilon}_a \cdot \frac{\partial W_0(\boldsymbol{\varepsilon}_a)}{\partial \boldsymbol{\varepsilon}_a} \quad (8.22)$$

and Σ_0 the threshold value for the volumetric Eshelby stress stimulus (reference value).

The evolution equation of the density (8.19) combined with the definition of the mass source Γ^g in (8.21) then delivers

$$\frac{d\rho}{dt} = \frac{B_c}{\rho} \text{Tr}(\Sigma_a(\boldsymbol{\varepsilon}_a) - \Sigma_0) \quad (8.23)$$

This equation describes bone adaptation, and more precisely whether the stress stimulus within bone tissue will induce bone formation, bone resorption or equilibrium, according to the sign and value of the rate of change of the apparent bone density. Equilibrium is reached when the Eshelby stress attains the homeostatic value Σ_0 , supposed to be known at each point. The present model describes density changes at constant volume, so that $J_g = 1$.

It is noteworthy that the trace of Eshelby stress is the strain energy density

$$\text{Tr}(\Sigma_a(\boldsymbol{\varepsilon}_a)) = 3W_0(\boldsymbol{\varepsilon}_a) - \boldsymbol{\varepsilon}_a : \boldsymbol{\sigma}(\boldsymbol{\varepsilon}_a) = 3W_0(\boldsymbol{\varepsilon}_a) - 2W_0(\boldsymbol{\varepsilon}_a) = W_0(\boldsymbol{\varepsilon}_a) \quad (8.24)$$

Accordingly, the volumetric strain energy density (or the trace of Eshelby stress) is the mechanical stimulus that triggers bone adaptation locally, a scalar quantity that incorporates on an equal footing local stress and strain tensors. We then propose a formulation for internal bone adaptation utilizing the strain energy density function as the remodeling signal representing the deformational energy at any point, taking the following form:

$$\frac{d\rho}{dt} = B_c \left(\frac{W_0(\boldsymbol{\varepsilon}_a)}{\rho} - \frac{W_t}{\rho_m} \right) \equiv f(t, \rho) \quad (8.25)$$

This modified evolution equation ensures a good stability behavior of the time-dependent remodeling. The driving mechanism for adaptive activity is then the deviation between the actual energy per unit mass $W_0(\boldsymbol{\varepsilon}_a)/\rho$ from a site-specific homeostatic equilibrium W_t/ρ_m ; the scalar ρ_m therein is the maximum density. The internal remodeling process in (8.25) is considered to have converged when the rate $d\rho/dt$ tends to zero (equilibrium is then reached) or when the density secures a minimal or maximal value. The baseline value of strain energy, quantity W_t , is determined based on the relation $W_t = 1/2\sigma_0\varepsilon_0$, wherein a constant reference value for bone formation of the order of 2000 microstrain (variable ε_0) is

considered (McNamara and Prendergast, 2007). The remodeling rate B_c is chosen from Chen et al. (2007) to be $1.0 \text{ (kg m}^{-3}\text{)}^2\text{/(Pa.time)}$ in the simulation at the macroscopic level.

The rate of change of the local density of the trabecular bone at a particular location, quantity dp/dt , introduced in the last equation is evaluated by the finite difference method. The improved Euler's method known as Crank-Nicolson scheme is a modified method used instead of Euler forward method in order to improve the solution of the differential equation satisfied by density, using the average of the slopes of the solution curves; it is presently involved to estimate the density of bone tissue at the considered region, based on a first order non-linear ordinary differential equation (8.25); the internal adaptation is updated according to

$$\rho_{n+1} = \rho_n + \frac{\Delta t}{2} [f(t_n, \rho_n) + f(t_{n+1}, \rho_{n+1})] \quad (8.26)$$

involving the function $f(t_n, \rho_n)$ defined in equation (8.25), evaluated at the discrete point (t_n, ρ_n) . This scheme contains the implicit terms, $f(t_{n+1}, \rho_{n+1})$; in order to make it explicit, we approximate ρ_{n+1} using a forward Euler method, so that $\rho_{n+1} = \rho_n + \Delta t f(t_n, \rho_n)$, with $\Delta t = t_{n+1} - t_n$ the time step size (iteration).

A surface growth model is next elaborated, in a manner that mimics the developed bulk growth model.

8.2.2 Surface growth model

Surface growth is based on the framework elaborated in Ganghoffer (2010, 2012) ; hence we only provide the main thrust of the kinematics, referring the reader to those two contributions for more details.

From a kinematic viewpoint, and adopting unless otherwise stated a large deformation formalism, the surface deformation gradient is split multiplicatively into a surface growth mapping $\tilde{\mathbf{F}}_g$ and an accommodation mapping $\tilde{\mathbf{F}}_a$ needed to restore the kinematic compatibility, hence

$$\tilde{\mathbf{F}} = \tilde{\mathbf{F}}_a \tilde{\mathbf{F}}_g \quad (8.27)$$

The surface mapping $\tilde{\mathbf{F}} := \mathbf{F} \cdot \mathbf{\Pi}$ represents the projection of the bulk transformation gradient onto the tangent plane of $\partial\Omega$; it is obtained by projecting the transformation gradient onto the local tangent plane \mathbf{N} , with $\mathbf{\Pi} = \mathbf{I}_s - \mathbf{N} \otimes \mathbf{N}$ the corresponding projector, with the second order tensor \mathbf{I}_s denoting the surface identity tensor, mapping any vector in the tangent plane to the surface to itself. A generic point on the boundary is denoted \mathbf{X}_s . Note that $\tilde{\mathbf{F}}$ is in general not invertible, but it has a pseudo inverse $\tilde{\mathbf{f}}$ such that

$$\tilde{\mathbf{F}} \tilde{\mathbf{f}} = \mathbf{i}_s ; \tilde{\mathbf{f}} \tilde{\mathbf{F}} = \mathbf{I}_s \quad (8.28)$$

This multiplicative decomposition mimics a similar one that holds for volumetric growth; it induces a decomposition of the Jacobean of the total transformation, viz

$$\tilde{\mathbf{J}} = \tilde{\mathbf{J}}_a \tilde{\mathbf{J}}_g \quad (8.29)$$

with $\tilde{\mathbf{J}}_a := \det(\tilde{\mathbf{F}}_a)$; $\tilde{\mathbf{J}}_g := \det(\tilde{\mathbf{F}}_g)$ respectively the growth and accommodation Jacobean, such that the surface densities in the reference and actual configurations, quantities ρ_{0s}, ρ_s respectively, are related by

$$\rho_{0s} = \tilde{\mathbf{J}}_a \rho_s \quad (8.30)$$

One here assumes that mass is preserved between the intermediate and actual configurations (growth of mass only occurs between the initial and intermediate configuration), thereby following a similar assumption made classically in the case of volumetric growth.

The mechanical equilibrium is obtained by requiring the vanishing of the first variation of the elastic energy of the growing surface, described from a surface potential energy $W^s(\tilde{\mathbf{F}}, \mathbf{N})$ defined per unit reference surface; the surface energy potential is built from the surface part of the transformation gradient and the normal to the surface under remodeling. The dependency on the normal accounts for curvature effects not being present in the bulk growth model. The elastic surface energy density is simply the projection of the bulk energy density onto the surface under external remodeling.

The surface nominal stress is defined as the partial derivative $\tilde{\mathbf{T}} := \partial_{\tilde{\mathbf{F}}} W^s$. The surface is submitted to a surface force field \mathbf{f}_s , a driving force for surface growth. The stationnarity condition of the total potential energy writes (Ganghoffer, 2010):

$$\nabla_s \cdot \tilde{\Sigma}_a - \mathbf{\Pi} \cdot \mathbf{K}_r \cdot \partial_N W^s + \left(\partial_{X_s} W^s \right)_{\text{expl}} + \tilde{\mathbf{F}}^T \cdot \mathbf{f}_s = \mathbf{0} \quad (8.31)$$

with $\mathbf{K}_r := -\nabla_R \mathbf{N}$ the curvature tensor of the surface. Previous balance equation represents mechanical equilibrium in terms of the surface Eshelby stress

$$\tilde{\Sigma}_a := W^s \mathbf{I}_s - \tilde{\mathbf{F}}_a^t \cdot \tilde{\mathbf{T}} \quad (8.32)$$

with the second order surface tensor \mathbf{I}_s therein denoting the identity mapping with support included in S_g .

One further shows that the tangential projection of Eshelby stress is obtained as the introduced surface Eshelby stress $\tilde{\Sigma}_a$. Due indeed to the involution of the projection operator $\mathbf{\Pi}$ and its symmetry, on obtains the projection of the volumetric Eshelby stress on the tangent plane at any point on the boundary

$$\Sigma_a \cdot \mathbf{\Pi} := W_0(\mathbf{F}_a; \mathbf{X}) \mathbf{\Pi} - \mathbf{F}_a^T \cdot \frac{\partial W_0(\mathbf{F}_a; \mathbf{X})}{\partial \mathbf{F}_a} \cdot \mathbf{\Pi} \equiv W_0(\mathbf{F}_a \cdot \mathbf{\Pi}; \tilde{\mathbf{X}}) \mathbf{\Pi} - (\mathbf{F}_a^T \cdot \mathbf{\Pi}) \cdot \left(\frac{\partial W_0(\mathbf{F}_a; \mathbf{X})}{\partial \mathbf{F}_a} \cdot \mathbf{\Pi} \right) \quad (8.33)$$

in which the strain energy density $W_0(\mathbf{F}_a \cdot \mathbf{\Pi}; \tilde{\mathbf{X}})$ has to be evaluated for boundary points $\tilde{\mathbf{X}}$ and for the projected elastic mapping $\tilde{\mathbf{F}}_a := \mathbf{F}_a \cdot \mathbf{\Pi}$.

Note that Eshelby stress is a purely material stress attached to the reference (initial) configuration. It can be obtained by a pull-back of the balance of linear momentum (equilibrium equation) involving the purely spatial Cauchy stress. It also represents the driving force for the change of domain for a general functional. In shape optimization, the shape derivative of the total potential energy is the jump of Eshelby stress over the moving interface. Both last aspects and derivations can be found in the contribution of [Ganghoffer and Sokolowski \(2014\)](#).

The surface position and its variation on S_g are denoted \mathbf{X}_s and $\delta\mathbf{X}_s$ resp. For a surface with local normal \mathbf{N} (to the locally defined tangent plane), the operators $\nabla_s := \mathbf{N} \cdot \nabla$ and $\text{div}_s(\cdot) := \text{Tr}(\nabla_s(\cdot))$ successively denote the surface gradient and the surface divergence.

The surface mass balance equation expresses as

$$\dot{\rho}_s = \Gamma^g \rho_s \quad (8.34)$$

with ρ_s the surface density of nutrients (HA in the case of bone), and Γ^g the rate of mass growth, given by the trace of the surface growth velocity gradient as

$$\Gamma^g = \text{Tr}(\nabla \tilde{\mathbf{V}}_g) \quad (8.35)$$

with $\tilde{\mathbf{V}}_g$ the surface growth velocity, bringing an irreversible contribution to the kinematics.

As only the normal component of the surface growth velocity induces a change of shape, we assume a normal surface growth velocity proportional to the normal driving force for growth (to be identified later on), quantity $\tilde{\Upsilon}_{gN}$

$$\tilde{\mathbf{V}}_N(\tilde{\mathbf{X}}, t) = \tilde{f}(\tilde{\Upsilon}_{gN}) \quad (8.36)$$

The kinematic picture of this surface growth model is then such that mass growth only occurs through surfaces, generating in turn shape changes of the growing body. The new material accumulated (or resorbed) on those surfaces (with a density different from that of the parent material) induces in turn a volumetric growth process, although no internal material point is submitted to growth. This kinematic viewpoint is believed to be physically consistent with the way growth remodeling occurs in bones through a mineralization process localized close to the surface: the thickness of the erosion zone due to the osteoclast activity is about 60 μm in trabecular bone and 100 μm in cortical bone; hence it is realistic to consider this process as surface growth.

The surface growth velocity can be related to driving forces for surface growth identified from the writing of the local surface dissipation (Clausius-Duhem inequality) for growth processes involving simultaneously transport of mass in addition to irreversible deformations due to growth, as

$$\begin{aligned} \tilde{\mathbf{J}}\tilde{\boldsymbol{\sigma}} : \left(\tilde{\mathbf{F}} \tilde{\mathbf{F}}^{-1} \right) - \frac{dW^s(\tilde{\mathbf{F}}_a)}{dt} \geq 0 \Rightarrow & \left(\tilde{\mathbf{J}}_a \tilde{\boldsymbol{\sigma}} \tilde{\mathbf{F}}_a^{-T} - \frac{\partial W^s}{\partial \tilde{\mathbf{F}}_a} \right) : \delta \tilde{\mathbf{F}}_a \\ & + \left(\tilde{\mathbf{J}}_a \tilde{\mathbf{F}}_a^T \cdot \tilde{\boldsymbol{\sigma}} \tilde{\mathbf{F}}_a^{-T} - W^s \mathbf{I}_s \right) : \left(\delta \tilde{\mathbf{F}}_g \tilde{\mathbf{F}}_g^{-1} \right) \geq 0 \end{aligned} \quad (8.37)$$

substituting variations to the material derivatives, and dividing both members of the inequality by $\rho_s \tilde{J}$, using the relation $\frac{1}{\rho_s} = \frac{\tilde{J}_a}{\rho_{0s}}$. The arbitrariness of the variations $\delta \tilde{\mathbf{F}}_a$ in

previous inequality then leads to the expression of surface Cauchy stress

$$\tilde{J}_a \tilde{\boldsymbol{\sigma}} \tilde{\mathbf{F}}_a^{-T} - \frac{\partial W^S}{\partial \tilde{\mathbf{F}}_a} = 0 \rightarrow \frac{\partial W^S}{\partial \tilde{\mathbf{F}}_a} = \tilde{J}_a \tilde{\boldsymbol{\sigma}} \tilde{\mathbf{F}}_a^{-T} \rightarrow \tilde{\boldsymbol{\sigma}} = \frac{1}{\tilde{J}_a} \frac{\partial W^S}{\partial \tilde{\mathbf{F}}_a} \tilde{\mathbf{F}}_a^T \quad (8.38)$$

Hence the surface dissipation (dividing the previous expression by the factor J_a) resumes to

$$\rho_s \left(\tilde{\mathbf{F}}_a^T \cdot \frac{\partial W^S}{\partial \tilde{\mathbf{F}}_a} - W^S \mathbf{I}_S \right) : \tilde{\mathbf{L}}_g = -\rho_s \tilde{\boldsymbol{\Sigma}}_a : \tilde{\mathbf{L}}_g \geq 0 \quad (8.39)$$

thereby recognizing the surface Eshelby stress built from the surface energy

$$\tilde{\boldsymbol{\Sigma}}_a := W^S \mathbf{I}_S - \tilde{\mathbf{F}}_a^T \cdot \frac{\partial W^S}{\partial \tilde{\mathbf{F}}_a} \quad (8.40)$$

The surface growth velocity gradient in previous inequality is defined by

$$\tilde{\mathbf{L}}_g := \dot{\tilde{\mathbf{F}}}_g \tilde{\mathbf{F}}_g^{-1} \quad (8.41)$$

According to Curie principle, couplings between variables are possible only for variables of the same tensorial nature; it follows from the local dissipation that the growth velocity gradient $\tilde{\mathbf{L}}_g$ is coupled to the sole Eshelby stress, viz $\tilde{\mathbf{L}}_g = \mathbf{f}(\tilde{\boldsymbol{\Sigma}}_a)$, thereby defining the general format of the growth model.

One may go one step beyond, assuming that the surface growth velocity is fully irreversible, due to the fact that the source of shape changes of the growing body is the mass flux (hence it will correspond to situations of either growth or resorption); this means that the surface growth velocity gradient can be expressed as the surface gradient of the surface velocity. This does not preclude the existence of elastic surface strains induced by surface growth, thus the surface velocity gradient splits into a growth part and an elastic contribution, which is nevertheless assumed to be negligible.

In the case of a completely irreversible surface growth, $\tilde{\mathbf{L}}_g$ represents the surface (eulerian) gradient of the surface growth velocity field $\tilde{\mathbf{V}}_g$, viz

$$\tilde{\mathbf{L}}_g = \nabla_S \tilde{\mathbf{V}}_g \quad (8.42)$$

Hence, considering the case of a purely mechanical dissipation as a special case of the surface dissipation inequality, integration by part followed by localization of the corresponding weak statement leads to

$$-\int_{S_g} \tilde{\boldsymbol{\Sigma}}_a : \tilde{\mathbf{L}}_g dS \geq 0 \rightarrow \int_{S_g} \nabla_S \cdot (\tilde{\boldsymbol{\Sigma}}_a) \cdot \tilde{\mathbf{V}}_g dS - \text{Boundary terms} \geq 0 \quad (8.43)$$

Note that the surface divergence $\nabla_S \cdot (\cdot)$ is involved in previous inequality as the tensors are attached to the surface. The line (boundary) terms in previous inequality vanish in case of a closed surface.

The last inequality then leads in view of the arbitrariness of the considered surface S_g to the following linear surface growth model

$$\tilde{\mathbf{V}}_g = \tilde{\mathbf{K}}_g \operatorname{div}_S(\tilde{\boldsymbol{\Sigma}}_a), \quad \tilde{\mathbf{K}}_g \geq 0 \quad (8.44)$$

The positive constant $\tilde{\mathbf{K}}_g$ is chosen such that the local surface dissipation is nonnegative.

Thereby, a linear relation between the surface growth velocity and the surface divergence of the (surface) Eshelby stress shall be adopted for simplicity reason in the sequel.

Remark: as for bulk growth, the integration by parts presupposes that one is entitled to derive the surface growth velocity. However, note that the system of coordinates is in general non integrable (surface growth strains are compatible) in the intermediate configuration in which the derivation is performed; we nevertheless assume that is possible to evaluate such a gradient locally in the neighborhood of a material point.

The bone adaptation algorithm relies on the solution of a linear elasticity problem in the bulk bone, coupled to the surface growth problem. Theses two problems are solved in a staggered manner; the solution of bulk problem provides at each time step the stress field on each point in the domain including the surface, leading in turn to an evaluation of the remodeling velocity given versus the divergence of Eshelby stress.

8.3 A coupled bone internal and external remodeling approach

8.3.1 Strong formulation

The previous set of equations is now specialized to treat the growth of hard tissues like bones; in this case, deformations are limited in both the bulk and on the growing surface; hence one may restrict to a small strains framework, leading to the specialization of previous BVP to this simplified context. The algorithms incorporating both internal and external remodeling mechanisms of bone will later on be performed at different mechanical levels.

Following the representation theorems for isotropic scalar valued functions of tensorial arguments, the mechanical part of the surface strain energy density $W^s(\tilde{\boldsymbol{\epsilon}}, \mathbf{N})$ can in general be selected as a function of the invariants of the curvature tensor (the mean and Gaussian curvatures), the invariants of the small strain surface deformation tensor $\tilde{\boldsymbol{\epsilon}}$ and of its square, and the unit exterior normal to the growing surface, vector \mathbf{N} . We choose for simplicity reasons a form linearly dependent on the second invariant of the linearized part of Cauchy Green strain, viz $\tilde{\mathbf{C}} \cong \mathbf{I} + 2\tilde{\boldsymbol{\epsilon}}$, and quadratic in the normal to the growing surface, hence

$$W^s(\tilde{\boldsymbol{\epsilon}}, \mathbf{N}) = \frac{\lambda(\rho)}{2} \operatorname{Tr}(\tilde{\boldsymbol{\epsilon}})^2 + \mu(\rho) \operatorname{Tr}(\tilde{\boldsymbol{\epsilon}}^2) + \mathbf{CN} \cdot \mathbf{K}_r \cdot \mathbf{N} \quad (8.45)$$

with $\tilde{\boldsymbol{\varepsilon}} = \mathbf{\Pi} \boldsymbol{\varepsilon}$ the surface strain (induced by the existing volumetric strain), and $\lambda(\rho), \mu(\rho)$ the surface mechanical properties, expressing versus the surface density and the maximum value of the traction modulus according to

$$\lambda(\rho) = \frac{E(\rho)\nu}{(1-2\nu)(1+\nu)}; \mu(\rho) = \frac{E(\rho)}{2(1+\nu)} \quad (8.46)$$

and C a constant associated to the energy of geometrical curvature of the growing surface; the second order tensor $\mathbf{K}_r = -\nabla \mathbf{N}$ in previous expression is the curvature tensor, defined as the gradient of the unit exterior normal \mathbf{N} . Interactions terms between curvature and mechanical deformation are presently not considered.

The elastic surface stress then results from previous expression of the surface potential in (8.45) as

$$\tilde{\mathbf{T}}^{\text{el}} \equiv \tilde{\boldsymbol{\sigma}}^{\text{el}} := \frac{\partial W^s}{\partial \tilde{\boldsymbol{\varepsilon}}} = \lambda(\rho) \text{tr}(\tilde{\boldsymbol{\varepsilon}}) \mathbf{I}_s + 2\mu(\rho) \tilde{\boldsymbol{\varepsilon}} \quad (8.47)$$

An orthotropic linear elastic constitutive behavior for the bulk may alternatively be considered as a more general model, in agreement with the literature.

Regarding the kinematics, and additive split of the total surface strain into a growth part $\tilde{\boldsymbol{\varepsilon}}_g$ and an elastic part $\tilde{\boldsymbol{\varepsilon}}_a$ needed to restore kinematic compatibility on the surface is performed, according to

$$\tilde{\boldsymbol{\varepsilon}} = \tilde{\boldsymbol{\varepsilon}}_a + \tilde{\boldsymbol{\varepsilon}}_g \quad (8.48)$$

The elastic part $\tilde{\boldsymbol{\varepsilon}}_a$ enters into the constitutive law expressed in (8.45), (8.47). The field variables can be separated into the set of surface variables and the set of volumetric variables.

As a summary of the field equations of the surface growth of hard tissues, the following BVP can be written on the domain $\Omega \cup S_u \cup S_t \cup S_g$, denoting therein S_u (resp. S_t) the portion of the external boundary with kinematic (resp. static) boundary conditions, with $S_u \cap S_t = \emptyset$, and $S_g \subset S_u$ the subsurface on which external remodeling occurs in the sequel:

Surface kinematic variables

$$\begin{cases} \tilde{\boldsymbol{\varepsilon}} = \tilde{\boldsymbol{\varepsilon}}_a + \tilde{\boldsymbol{\varepsilon}}_g = \boldsymbol{\varepsilon} \cdot \boldsymbol{\Pi} = \boldsymbol{\varepsilon} \cdot (\mathbf{I}_S - \mathbf{N} \otimes \mathbf{N}) \\ \tilde{\boldsymbol{\varepsilon}} = \text{Sym}(\nabla \tilde{\mathbf{U}}) \\ \dot{\tilde{\boldsymbol{\varepsilon}}}_g = \frac{1}{2}(\nabla_S \tilde{\mathbf{V}}_g + \nabla^T_S \tilde{\mathbf{V}}_g) \end{cases}$$

Mass preservation between intermediate and current configuration

$$\rho_{0S} = (\text{Tr} \tilde{\boldsymbol{\varepsilon}}_a) \rho_S \quad \text{on } S_g$$

Stationnarity condition of the surface potential energy :

$$\begin{cases} \nabla_S \cdot \tilde{\boldsymbol{\Sigma}}_a - \boldsymbol{\Pi} \cdot \mathbf{K}_r^t \cdot \frac{\partial W^S}{\partial \mathbf{N}} + \tilde{\mathbf{F}}^T \cdot \mathbf{f}_S = \mathbf{0} \quad \text{on } S_g, \text{ surface gradient } \nabla_S := \boldsymbol{\Pi} \cdot \nabla \\ \mathbf{f}_S = \mathbf{0} \quad \text{on } S_g / S_t \end{cases}$$

Constitutive laws from surface energy and Eshelby stress

$$\begin{cases} W^S(\tilde{\boldsymbol{\varepsilon}}_a) = \frac{\lambda(\rho_S)}{2} \text{Tr}(\tilde{\boldsymbol{\varepsilon}}_a)^2 + \mu(\rho_S)(\tilde{\boldsymbol{\varepsilon}}_a : \tilde{\boldsymbol{\varepsilon}}_a) \rightarrow \tilde{\mathbf{T}}^{\text{el}} \equiv \tilde{\boldsymbol{\sigma}}^{\text{el}} := \frac{\partial W^S(\tilde{\boldsymbol{\varepsilon}}_a)}{\partial \tilde{\boldsymbol{\varepsilon}}_a} = \lambda(\rho_S) \text{tr}(\tilde{\boldsymbol{\varepsilon}}_a) \mathbf{I}_S + 2\mu(\rho_S) \tilde{\boldsymbol{\varepsilon}}_a \\ \tilde{\boldsymbol{\Sigma}}_a := W^S(\tilde{\boldsymbol{\varepsilon}}_a) \mathbf{I}_S - \tilde{\boldsymbol{\varepsilon}}_a^T \cdot \frac{\partial W^S}{\partial \tilde{\boldsymbol{\varepsilon}}_a} \quad \text{on } S_g \end{cases}$$

Surface growth velocity

$$\tilde{\mathbf{V}}_g = \tilde{K}_g \text{div}_S(\tilde{\boldsymbol{\Sigma}}_a), \quad \tilde{K}_g = \text{Cte} \quad \text{on } S_g$$

Continuity equation

$$\dot{\rho} = \Gamma^g \rho \quad \text{on } S_g; \Gamma^g := \text{Tr}(\dot{\mathbf{F}}_g \cdot \mathbf{F}_g^{-1}) = \frac{B_c}{\rho^2} \text{Tr}(\boldsymbol{\Sigma}_a(\boldsymbol{\varepsilon}_a) - \boldsymbol{\Sigma}_0); \rho(\mathbf{X}, t=0) = \rho_0(\mathbf{X})$$

Equilibrium equation of bulk stress

$$\begin{cases} \text{div} \boldsymbol{\sigma} + \rho \mathbf{g} = 0 \quad \text{in } \Omega \\ \boldsymbol{\Sigma}_a := W_0 \mathbf{I} - \boldsymbol{\varepsilon}_a^T \cdot \boldsymbol{\sigma} \\ \mathbf{U} = \mathbf{0} \quad \text{on } S_u; \boldsymbol{\sigma} \cdot \mathbf{N} = \mathbf{f}_S \quad \text{on } S_t \\ \boldsymbol{\sigma} = 2\mu(\rho) \boldsymbol{\varepsilon}_a + \lambda(\rho) \text{Tr}(\boldsymbol{\varepsilon}_a) \mathbf{I} \quad \text{in } \Omega \end{cases}$$

The tensor $\tilde{\boldsymbol{\Sigma}}_a := W^S(\tilde{\boldsymbol{\varepsilon}}_a) \mathbf{I}_S - \tilde{\boldsymbol{\varepsilon}}_a^T \cdot \frac{\partial W^S(\tilde{\boldsymbol{\varepsilon}}_a)}{\partial \tilde{\boldsymbol{\varepsilon}}_a}$ represents the small strain Eshelby stress, the

surface divergence of which drives surface growth. Note that in the considered small strains framework, the surface transformation gradient may be approximated to first order by the surface identity mapping, viz one has $\tilde{\mathbf{F}} \equiv \mathbf{I}_S$. The reversible surface strain $\tilde{\boldsymbol{\varepsilon}}_a$ coincides with the surface elastic strain $\tilde{\boldsymbol{\varepsilon}}_e$, obtained from a projection of the volumetric elastic strain onto the tangent plane to the growing surface.

The growth velocity field on S_g coincides with the total velocity field, which accordingly imposes a kinematic boundary conditions; S_t is the subsurface on which tractions \mathbf{t}^d are applied.

Note that the curvature of the surface intervenes in the momentum balance equation through the curvature tensor, and that Eshelby stress $\tilde{\boldsymbol{\Sigma}}_a$ is involved in both the growth model and in the equilibrium equation. Since the surface growth velocity $\tilde{\mathbf{V}}_g$ is imposed on the growing subsurface S_g (in fact as the total surface velocity), it determines a kinematic boundary

condition in terms of a velocity field. This field is however not known a priori, as it is related to Eshelby stress $\tilde{\Sigma}_a$.

Note that the newly generated material on the growing surface accumulates in the bulk (it is ‘pushed’ in some sense to the bulk by the continuously appearing material on the surface), and it does in fact generate volumetric growth: it generates a new domain with new properties (density, elastic moduli), thereby giving rise to internal stresses. Due to this kinematic picture, the newly generated material is ‘transferred’ to the bulk with a purely elastic strain, which defines the total bulk strain (contrary to surface strain that splits into a growth part and an elastic contribution).

The bone structure is defined by its planar geometry, and a preload is applied to the whole structure, in order to mimic physiological conditions of exercise. This determines an initial state of stress (which is elastic as no growth has yet occurred), from which the surface Eshelby stress $\tilde{\Sigma}_a$ can be evaluated.

The solution of the complete BVP involves the knowledge of the kinematic boundary condition on the growing surface (the velocity field on the growing surface is the total velocity field), which itself requires as a first step to solve the surface BVP. The surface and bulk variables are coupled by the growth model, since the surface growth velocity depends on the trace of the elastic deformation (a tangential field).

The numerical solution of previous BVP requires setting up an incremental solution scheme, which involves the following steps:

1. Time discretization of the interval of interest $[0, T] = \cup_{n=0}^N [t_n, t_{n+1}]$: the time derivatives arising in the weak form are accordingly replaced by suitable algorithmic approximations, hence leading to the formulation of a global time-stepping algorithm, which is independent from the constitutive models.
2. At a particular point in $\Omega \cup S_g \cup S_u \cup S_t$ (typically a quadrature point of a finite element), the goal is to compute an approximation of the field variables appearing in the weak form.
3. At the point of interest, the incremental volume and surface displacements successively denoted by $\{\Delta U^{n+1}, \Delta \tilde{U}^{n+1}\}$ are regarded as given.
4. At time t_n , the state at any point in the closed set $\Omega^n \cup S_g^n \cup S_u^n \cup S_t^n$ characterized by the set of variables $\{\rho^n, E^n, \lambda^n, \mu^n, W_0^n, \mathbf{U}^n, \tilde{\mathbf{U}}^n, \boldsymbol{\varepsilon}^n, \tilde{\boldsymbol{\varepsilon}}_g^n, \tilde{\boldsymbol{\varepsilon}}_a^n, \tilde{\mathbf{V}}_g^n, \boldsymbol{\Sigma}_a^n, \tilde{\boldsymbol{\Sigma}}_a^n, \Omega^n \cup S_g^n \cup S_u^n \cup S_t^n\}$ is given and is assumed to be in equilibrium, i.e. it satisfies previous equilibrium equation.
5. One then has to produce an update of the state variables at any point to the new values $\{\rho^{n+1}, E^{n+1}, \lambda^{n+1}, \mu^{n+1}, W_0^{n+1}, \mathbf{U}^{n+1}, \tilde{\mathbf{U}}^{n+1}, \boldsymbol{\varepsilon}^{n+1}, \tilde{\boldsymbol{\varepsilon}}_g^{n+1}, \tilde{\boldsymbol{\varepsilon}}_a^{n+1}, \tilde{\mathbf{V}}_g^{n+1}, \boldsymbol{\Sigma}_a^{n+1}, \tilde{\boldsymbol{\Sigma}}_a^{n+1}, \Omega^{n+1} \cup S_g^{n+1} \cup S_u^{n+1} \cup S_t^{n+1}\}$ at time step t_{n+1} in a manner consistent with the local BVP.

One can set a separate algorithm for the update of the field variables on the growing surface as follows:

1. Initialization of the data

$$\underline{t} = \underline{t}_0 : \rho_0, \nu, \Delta t, \mathbf{g}, \mathbf{f}_s, \mathbf{B}_c, \mathbf{K}, \mathbf{U}^0, \tilde{\mathbf{U}}^0, \tilde{\mathbf{V}}_g^0 = \mathbf{0}, \Omega^0 \cup S_g^0 \cup S_u^0 \cup S_t^0 \text{ data}$$

2. Initialization of the variables at time t_n

$$\underline{t} = \underline{t}_n : \rho^n, E^n, \lambda^n, \mu^n, \mathbf{U}^n, \tilde{\mathbf{U}}^n, \mathbf{W}_0^n, \tilde{\Sigma}_a^n, \mathbf{V}_g^n, \tilde{\boldsymbol{\varepsilon}}_a^n, \tilde{\boldsymbol{\varepsilon}}_g^n, \tilde{\boldsymbol{\varepsilon}}^n, \Omega^n \cup S_g^n \cup S_u^n \cup S_t^n$$

2.1. Computation of lame's coefficients

$$\lambda^n(\rho) = \frac{E^n(\rho)\nu}{(1-2\nu)(1+\nu)}; \mu^n(\rho) = \frac{E^n(\rho)}{2(1+\nu)}$$

2.2. Set up the constitutive law based on strain energy density

$$\mathbf{W}^S = \mathbf{W}^S(\tilde{\boldsymbol{\varepsilon}}_a^n) = \frac{\lambda^n}{2} \text{Tr}(\tilde{\boldsymbol{\varepsilon}}_a^n)^2 + \mu^n (\tilde{\boldsymbol{\varepsilon}}_a^n : \tilde{\boldsymbol{\varepsilon}}_a^n) + \text{CN}^n \cdot \mathbf{K}^n \cdot \mathbf{N}^n$$

2.3. Set up the constitutive laws for Cauchy and Eshelby stress

$$\rightarrow \tilde{\boldsymbol{\sigma}}^n := \frac{\partial \mathbf{W}^S(\tilde{\boldsymbol{\varepsilon}}_a^n)}{\partial \tilde{\boldsymbol{\varepsilon}}_a^n} = 2\mu^n \tilde{\boldsymbol{\varepsilon}}_a^n + \lambda^n \text{tr}(\tilde{\boldsymbol{\varepsilon}}_a^n) \mathbf{I}_S \rightarrow \tilde{\Sigma}^n := \mathbf{W}^S(\tilde{\boldsymbol{\varepsilon}}_a^n) \mathbf{I}_S - \tilde{\boldsymbol{\varepsilon}}_a^n \cdot \frac{\partial \mathbf{W}^S(\tilde{\boldsymbol{\varepsilon}}_a^n)}{\partial \tilde{\boldsymbol{\varepsilon}}_a^n}$$

3. Update variables

$$\underline{t}_{n+1} = \underline{t}_n + \Delta t : \text{update variables according to}$$

3.1. Equilibrium equation for the bulk elasticity

$$\begin{cases} \text{Div} \boldsymbol{\sigma}(\boldsymbol{\varepsilon}_a(\mathbf{U}^{n+1})) + \rho \mathbf{g} = \mathbf{0} \text{ in } \Omega^n \\ \boldsymbol{\sigma}^{n+1} = 2\mu^{n+1} \boldsymbol{\varepsilon}_a^{n+1} + \lambda^{n+1} \text{Tr}(\boldsymbol{\varepsilon}_a^{n+1}) \mathbf{I} \text{ in } \Omega^n \\ \mathbf{u}^{n+1}_{S_u} = \mathbf{0} \text{ on } S_u \\ \mathbf{U}^{n+1}_{S_g} = \tilde{\mathbf{U}}^{n+1} \\ \boldsymbol{\sigma}^{n+1} \cdot \mathbf{N}^{n+1} = \mathbf{f}_s \text{ on } S_t \\ \tilde{\boldsymbol{\sigma}}^{n+1} = 2\mu^{n+1} \tilde{\boldsymbol{\varepsilon}}_a^{n+1} + \lambda^{n+1} \text{tr}(\tilde{\boldsymbol{\varepsilon}}_a^{n+1}) \mathbf{I}_S \end{cases}$$

3.2. Balance of surface momentum

$$\text{On } S_g^n : \begin{cases} \nabla_s \cdot \tilde{\Sigma}_a^{n+1} - \mathbf{\Pi} \cdot (\mathbf{K}^{n+1})^T \cdot \frac{\partial \Psi^S}{\partial \mathbf{N}} + \mathbf{f}_s = \mathbf{0}, \mathbf{f}_s = \mathbf{0} \text{ on } S_g / S_t \\ \mathbf{K}^n := -\nabla \mathbf{N}^n \text{ curvature tensor} \end{cases}$$

3.2.1 Update surface growth velocity and density

$$\text{On } S_g^n : \begin{cases} \tilde{\mathbf{V}}_g^{n+1} = \tilde{\mathbf{K}}(\nabla_s \cdot \tilde{\Sigma}_a^n) \rightarrow \tilde{\mathbf{U}}^{n+1} = \tilde{\mathbf{U}}^n + \mathbf{V}_g^{n+1} \Delta t \\ \rho_s^{n+1} - \rho_s^n = \Gamma^S \Delta t \rho_s^n \rightarrow \rho_s^{n+1} \\ \Gamma^S = \frac{\mathbf{B}_c}{(\rho_s^n)^2} \text{Tr}(\Sigma_a^n(\boldsymbol{\varepsilon}_a) - \Sigma_0) \end{cases}$$

3.2.2 Update surface kinematic variables

$$\text{On } S_g^n : \begin{cases} \dot{\tilde{\boldsymbol{\varepsilon}}}_g^n = \text{sym}(\nabla_s(\mathbf{V}_g^n)) \\ \tilde{\boldsymbol{\varepsilon}}^{n+1} = \text{Sym}(\text{Grad}_s \tilde{\mathbf{U}}^{n+1}) \\ \tilde{\boldsymbol{\varepsilon}}_g^{n+1} = \tilde{\boldsymbol{\varepsilon}}_g^n + \dot{\tilde{\boldsymbol{\varepsilon}}}_g^{n+1} \Delta t \\ \tilde{\boldsymbol{\varepsilon}}_a^{n+1} = \tilde{\boldsymbol{\varepsilon}}^{n+1} - \tilde{\boldsymbol{\varepsilon}}_g^{n+1} \\ \mathbf{K}^{n+1} = -\nabla \mathbf{N}^{n+1} \end{cases}$$

3.4. Update domain and transport all variables to new mesh

$$\Omega_{n+1} = (\mathbf{I} + \Delta t \mathbf{V}_g^n) \Omega_n \rightarrow S_g^{n+1} = (\mathbf{I} + \Delta t \mathbf{V}_g^n) S_g^n$$

4. Loop again

5. Stop when $\rho_s^{n+1} = \rho_{S\text{Max}}$

End

The surface force field \mathbf{f}_s is prescribed on the growing surface, and it is thought that different choices will lead to different grown shapes. The update of the surface velocity field $\tilde{\mathbf{V}}_g$ leads to a shape evolution during the time increment resulting in an updated domain written as

$$\Omega_{n+1} = (\mathbf{I} + \Delta t \tilde{\mathbf{V}}_g^n) \Omega_n \quad (8.49)$$

A new geometry is then generated, and the whole domain splits into the old domain and the new domain generated by the material point created on the growing surface. The density of the material points of the new domain is the surface density, and new material properties are also given for the newly generated material.

The growth process is arrested when a criterion is satisfied (for instance a maximum or minimum density $\rho_{S\text{Max}}(\tilde{\mathbf{X}}, t)$ has been reached); it is clear from the formulation of bone internal remodeling that this process shall stop when the strain energy density (the driving force for internal remodeling) reaches a homeostatic value. A similar condition applies to bone external remodelling, although no homeostatic value of the driving force appears in the model for the surface growth velocity. It is nevertheless clear from the mathematical formulation that external remodeling will stop when the bone material reaches a state of homogeneous stress (or elastic strain).

Remodeling and the computation of a new internal stress distribution is done in a two steps staggered scheme, whereby new bone is being apposed (or resorbed) – based on mechanical stimulus - and both strains and stresses are redistributed in the domain by a subsequent elastic computation. The external load is kept fixed during the remodeling process.

8.3.2 Variational formulation

In most cases, it is not possible to find an analytical solution for these equations (strong-form of the solution) and thus one needs to recourse to an approximation method. In view of the finite element discretization, these equations need to be rewritten weak form, i.e. an integrated variational formulation.

The variational formulation of surface equilibrium (balance of surface momentum) is written for the purpose of finite element discretization by multiplying the strong form by a test function \mathbf{v} chosen to vanish on the domain boundary, viz $\mathbf{v} = \mathbf{0}$ on $\partial\Omega$. The balance of surface momentum is conveniently recalled in order to build the variational form

$$\nabla_s \cdot \tilde{\Sigma}_a - \Pi \cdot \mathbf{K}_r^t \cdot \frac{\partial W^s}{\partial \mathbf{N}} + \mathbf{f}_s = \mathbf{0} \quad (8.50)$$

is further transformed using the selected expression of the surface energy and elaborating the contribution

$$\Pi \cdot \mathbf{K}_r^t \cdot \frac{\partial W^s}{\partial \mathbf{N}} = \Pi \cdot \mathbf{K}_r^t \cdot \text{grad}_s W^s \cdot \mathbf{N} = -(\text{grad} \mathbf{N})^T \cdot \frac{\partial W^s}{\partial \mathbf{N}} = -\text{grad} W^s \quad (8.51)$$

This delivers the following balance equation

$$\nabla_s \cdot \tilde{\Sigma}_a + \text{grad} W^s + \mathbf{f}_s = \mathbf{0} \quad (8.52)$$

The surface divergence of Eshelby stress is further elaborated as

$$\nabla_s \cdot \tilde{\Sigma}_a = \text{div}_s (W^s \mathbf{I}) - \text{div} \left(\boldsymbol{\varepsilon} \cdot \frac{dW^s}{d\boldsymbol{\varepsilon}} \right) \equiv \text{grad}_s W^s - \text{div} \left(\boldsymbol{\varepsilon} \cdot \frac{dW^s}{d\boldsymbol{\varepsilon}} \right) \quad (8.53)$$

Hence, the surface equilibrium writes as the following nonlinear differential equation

$$-\text{div}_s \left(\boldsymbol{\varepsilon} \cdot \frac{dW^s}{d\boldsymbol{\varepsilon}} \right) + 2 \text{grad}_s W^s + \mathbf{f}_s = \mathbf{0} \quad (8.54)$$

Its weak form is obtained as

$$\begin{aligned} 0 &= \int_{\Omega} -\text{div} \left(\boldsymbol{\varepsilon} \cdot \frac{dW}{d\boldsymbol{\varepsilon}} \right) \cdot \mathbf{v} dx + 2 \int_{\Omega} \text{grad}(W) \cdot \mathbf{v} dx + \int_{\Omega} \mathbf{f} \cdot \mathbf{v} dx \\ &\equiv \int_{\Omega} \boldsymbol{\varepsilon} \cdot \frac{dW}{d\boldsymbol{\varepsilon}} : \boldsymbol{\varepsilon}(\mathbf{v}) dx - 2 \int_{\Omega} W \text{div} \mathbf{v} dx - \int_{\Omega} \mathbf{f} \cdot \mathbf{v} dx \end{aligned} \quad (8.55)$$

For the specific form of the energy density, previous writing becomes

$$0 = \int_{\Omega} \boldsymbol{\varepsilon} \cdot [\lambda(\rho) \text{Tr}(\boldsymbol{\varepsilon}) \mathbf{I} + 2\mu(\rho) \boldsymbol{\varepsilon}] \boldsymbol{\varepsilon}(\mathbf{v}) dx - 2 \int_{\Omega} \left\{ \frac{\lambda(\rho)}{2} \{ \text{Tr}(\boldsymbol{\varepsilon}) \}^2 + \mu(\rho) \boldsymbol{\varepsilon} : \boldsymbol{\varepsilon} \right\} \text{div} \mathbf{v} dx - \int_{\Omega} \mathbf{f} \cdot \mathbf{v} dx = 0 \quad (8.56)$$

This nonlinear problem is solved by a relaxation method: consider a given initial strain $\boldsymbol{\varepsilon}_0$, given as the solution of the elasticity problem in the bulk material: the idea is to freeze the actual strain $\boldsymbol{\varepsilon} = \boldsymbol{\varepsilon}_0$, and to solve the resulting linear problem, which writes

$$0 = \int_{\Omega} \boldsymbol{\varepsilon} \cdot [\lambda(\rho) \text{Tr}(\boldsymbol{\varepsilon}_0) \mathbf{I} + 2\mu(\rho) \boldsymbol{\varepsilon}_0] \boldsymbol{\varepsilon}(\mathbf{v}) dx - 2 \int_{\Omega} \left\{ \frac{\lambda(\rho)}{2} \{ \text{Tr}(\boldsymbol{\varepsilon}_0) \}^2 + \mu(\rho) \boldsymbol{\varepsilon}_0 : \boldsymbol{\varepsilon}_0 \right\} \text{div} \mathbf{v} dx - \int_{\Omega} \mathbf{f} \cdot \mathbf{v} dx = 0 \quad (8.57)$$

The strain is then updated, thus $\boldsymbol{\varepsilon}_0 = \boldsymbol{\varepsilon}$, and the loop is continued up to satisfaction of the arrest criterion, for instance when $\left\| \frac{\boldsymbol{\varepsilon}_0 - \boldsymbol{\varepsilon}}{\boldsymbol{\varepsilon}_0} \right\| \leq \text{eps}$, with eps a prescribed tolerancy.

This nonlinear problem is solved by a relaxation method: consider a given initial strain $\boldsymbol{\varepsilon}_0$, given as the solution of the elasticity problem in the bulk material: the idea is to freeze the actual strain $\boldsymbol{\varepsilon} = \boldsymbol{\varepsilon}_0$, and to solve the resulting linear problem, which writes

The variational formulation of the bulk elasticity equilibrium equation is further written for the purpose of the finite element discretization in weak form by multiplying the strong form of equilibrium by a test (vector) function \mathbf{v} chosen to vanish on the domain boundary, viz $\mathbf{v} = \mathbf{0}$ on $\partial\Omega$. The weak form then writes as follows: we seek the displacement field \mathbf{u} satisfying

$$\int_{\Omega} \boldsymbol{\sigma}(\mathbf{u}) : \boldsymbol{\varepsilon}(\mathbf{v}) dx - \int_{\Omega} \rho \mathbf{g} \cdot \mathbf{v} dx = 0, \quad \forall \mathbf{v} / \mathbf{v} = \mathbf{0} \text{ on } \partial\Omega \quad (8.58)$$

After substitution in (8.58) of the constitutive law, this delivers the following variational equation

$$\int_{\Omega} \lambda(\rho) \nabla \cdot \mathbf{u} \nabla \cdot \mathbf{v} + 2\mu(\rho) \boldsymbol{\varepsilon}(\mathbf{u}) : \boldsymbol{\varepsilon}(\mathbf{v}) dx - \int_{\Omega} \rho \mathbf{g} \cdot \mathbf{v} dx = 0 \quad (8.59)$$

8.4 Applications to hard tissues like bone

Trabecular bone is characterized by struts or plates of bone, or both, connected into a lattice-like network; interstitial spaces are filled with marrow. For trabecular bone of low apparent density, the structure is composed entirely of small struts with a thickness of about 250 μm and variable arrangement of lengths of 700-2,000 μm . In the forthcoming sections, the previous algorithms of the coupled bone internal and external adaptation shall be applied to hard tissues like trabecular bone at different mechanical levels. The external bone adaptation process at micro and macro-level is defined as the bone capacity to form or destroy bone surface in response to the mechanical loadings. Moreover, throughout this study, the external geometries of the proximal femur and trabecular strut are considered to be variable, i.e., changes in the external shape are allowed during bone local adaptation. Internal remodeling processes aim at regulating the local trabecular bone density. The divergence and trace of Eshelby stress are adopted as feedback control variables to determine the shape and bone density adaptations.

8.4.1 Micromechanical simulations of the density and morphological changes of the trabecular structure

We elaborate in this section a two-dimensional mathematical model of trabecular bone remodeling at meso and microscale levels to simulate the surface-based addition and removal of material together with density evolution inside the trabeculae. It is essential to remark here that external bone remodeling always goes together with internal bone remodeling. The model at the microscopic scale is based on a finite element representation of individual trabecular struts in which the material properties of the subtrabecular elements are inconstant (they change over time). The remodeling stimulus is based on Eshelby stress, which is developed in the framework of the thermodynamics of irreversible processes. It is also assumed that the marrow spaces surrounding trabeculae do not contribute any stiffness or structural integrity to the region being modeled. The apposition or removal of bone material is described by modifying the external boundary as a function of time, and then the geometry is adapted.

In fact, when determining the stiffness of trabecular bone tissue, the non-uniformity of the mineral distribution within the trabeculae is usually not taken into account. The assumption that the trabecular bone tissue has uniform mechanical properties is not necessarily valid, since the bone tissue stiffness is strongly dependent on the degree of mineralization (van der Linden et al., 2001; van Eijden et al., 2004). The individual trabeculae of trabecular bone are composed of packets of remodeled bone of different ages

and thus different degrees of mineralization. Furthermore, the bone remodeling rate varies and is supposed to be relevant, for instance, to the amount of mechanical loading it experiences. These differences lead to a non-uniform mineral distribution within the trabeculae, which entails a variation of trabecular tissue stiffness.

The surface layer of trabeculae is frequently renewed, but tissue in the middle of any trabeculae can escape from this remodeling (Boyd et al., 1993), and become older than the surface layer; this results in a large difference in mineral content between the core and the surface layer. Such non-uniform mineral distribution has been shown with a variety of techniques (e.g., Gadeleta et al., 2000; Roschger et al., 1997).

Although tissue mineral density (TMD) has been used to quantify changes in bone tissue as related to a variety of factors (see, Boyd et al., 1993; Mulder et al., 2008; Miller et al., 2007), TMD represents only one constituent of bone (i.e., the mineral phase) and it ignores the contributions of the organic and water phases. Recently, alternative micro-scale approaches based on tissue composition have been proposed by Wagner et al. (2011), relating tissue mass densities to elastic properties. Such approaches would allow for the accurate prediction of the mechanical behavior of trabeculae. These authors present a method for estimating the tissue density and the isotropic elastic modulus from micro-computed tomography (microCT) derived tissue mineral density (gHA/cm^3). The derived relationship between micro-computed tomography and tissue density utilizes four parameters: the density of the three bone constituents (water, ash, and organics) and the volume fraction of the organic constituents. The tissue density (g/cm^3) as a function of microCT (mineral) density (gHA/cm^3) is then given by the following relation

$$\rho_t = 0.6667\rho_{\text{HA}} + 1.144 \quad (8.60)$$

The tissue-level bone elastic modulus (GPa) is related to the microCT (mineral) density (gHA/cm^3) as

$$\log_{10}(E_s) = -8.58 + 4.05 \log_{10}\left(400/(1 + 0.504/\rho_{\text{HA}})\right) \quad (8.61)$$

Combining the two previous relations yields the following relation between tissue elastic modulus (GPa) and tissue density (g/cm^3)

$$E_s = e^{4.05 \ln\left(\frac{400(1.49\rho_t - 1.71)}{1.49\rho_t - 1.21}\right) - 19.75} \quad (8.62)$$

The theoretical basics of the current numerical models of bone remodeling are derived from the observations that the bone architecture is related to the mechanical loads experienced and controlled by a regulatory mechanism.

The coupled internal and external growth model is presently applied to simulate the growth of the individual trabeculae of cancellous bone; Figure 8.3a represents the architecture of a two-dimensional trabecular unit cell. Such coupling model takes into account the adapted bone density to adjust the mechanical response of tissues with the external remodeling phenomenological model. Trabecular bone is assumed to be homogeneous, linear elastic and

isotropic at the trabecular level, with mechanical parameters identified by adjusting the previous relation by a second order polynomial, relating tissue elastic modulus (GPa) to tissue density (g/cm^3) as

$$E_s = 6.5\rho_t^2 + 12.3\rho_t - 26.5 \quad (8.63)$$

with a shear modulus also depending on trabeculae material density relying on the relation $G_s = E_s/2(1 + \nu_s)$; Poisson ratio is selected as $\nu_s = 0.3$.

This 2nd order polynomial equation (8.63) is used within the tissue density range $1.5 \leq \rho_t \leq 2$; this defines the minimum and maximum values of trabeculae bone density over all elements in the design domain. Equation (8.63) determines the change in elastic properties versus bone tissue density, itself varying as a function of a given mechanical stimulus according to (8.25).

In order to simplify the representation of the trabeculae geometry, simulations at the scale of the mesoscopic will be performed, considering a repetitive unit cell (with periodic boundary conditions). At the mesoscale, the complex and very organized network of trabeculae forms the cancellous bone. Relying on microstructural modeling approaches, we address the modeling of trabecular bone as having an idealized periodic network of hexagonal cells. The considered hexagonal unit cell is composed of assembly of inclined and vertical trabeculae of lengths 1 mm with uniform trabeculae thickness 0.25 mm and an inclination angle $\theta = 30^\circ$.

We next carry out a series of growth simulations at the scale of trabecular bone cell and then at the scale of the triple junction of the individual trabeculae to investigate the adaptation responses under different mechanical loading conditions.

Simulations are done with the open source finite element (FE) software Freefem++, relying on the variational formulation of the equilibrium equations. Let Ω be the region occupied by the trabecular bone material enclosed by a boundary $\Lambda = \partial\Omega$. The border is decomposed into four disjoint parts Λ_1 , Λ_2 , Λ_3 , and Λ_4 , where Λ_1 is part of the boundary along which the trabecular cell is fixed (bottom edges), and Λ_2 the part of the boundary (top edges) along which the different loading conditions P (P1, P2) are applied (Figures 8.3-8.5). Periodic boundary conditions are then imposed at the left and right edges (Λ_3 and Λ_4) of the hexagonal trabecular unit cell.

In order to illustrate the application of bone adaptation in numerical computations using the FE method, bone internal and external remodeling at trabecular level is predicted, starting from an initial geometry with a uniform density distribution of 1500 kg/m^3 . We consider a static loading as a mechanical stimulus for internal and external bone remodeling. Three loading conditions are then investigated: case I, a compressive load (P1=25 MPa), case II, a shear load (P2=10 MPa), and case III, a combined compressive and shear loadings (P1=5 MPa, P2=10 MPa).

The two proportionality constants (B_c and \tilde{K}_g) that play the role of gain in the adaptation process are chosen as follows: the remodeling rate B_c governing the velocity of the local adaptation process is taken as $0.01 \text{ (kg m}^{-3}\text{)}^2\text{/(Pa.timestep)}$ and the constant \tilde{K}_g measuring the rate of the surface adaptation process is selected as $1.e-16 \text{ (m}^4\text{/N.timestep)}$. The growth time step size is selected small enough, $\Delta t = 1$. After 50 iteration time steps, the growth simulation results are illustrated sequentially in [Figures 8.3-8.5](#), for compressive, shear, and combined compressive to shear loadings.

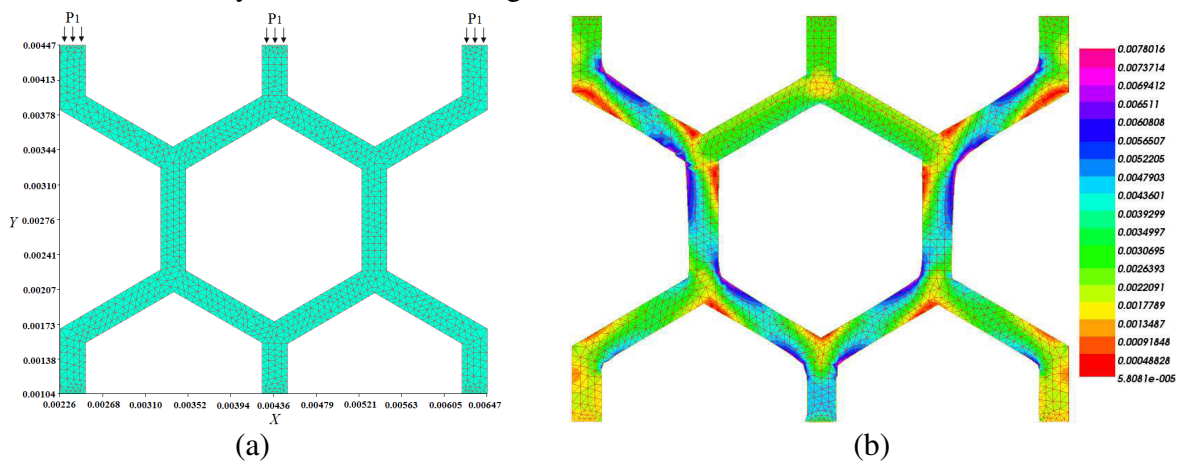
It is important to note that during the bone remodeling process, the external mechanical load is transmitted in the form of stress/strain to the local bone site, which are sensed by osteocytes, which subsequently activate the regulating cells (osteoclasts and osteoblasts) causing changes of bone masses and mechanical properties. External mechanical loads provoke local strains in the bone tissue, and there is a consensus in the literature that the remodeling stimulus depends on the strain magnitude.

The effective strain (which is a scalar value summarizing the strain tensor) of trabecular bone is then computed using the following expression

$$\varepsilon_{eq} = \sqrt{\frac{2}{3} \varepsilon_{ij} \varepsilon_{ij}} \quad (8.64)$$

in which ε_{ij} are the strain tensor components.

The distributions of equivalent strain in the adapted bone are shown in [Figures 8.3b-8.8b](#). In general, one can clearly see that high surface strains give locally rise to significant bone formation (growth). It is also remarkable that when the trabecular structure at the representative unit cell is subjected to alternative load directions, strains in the trabeculae surfaces become very high at the conjunction of the trabecular struts ([Figures 8.3b-8.5b](#)); this induces rapid bone formation along those trabecular edges. Thus, we deduce that bone formation most likely occurs at sites of high mechanical strain.



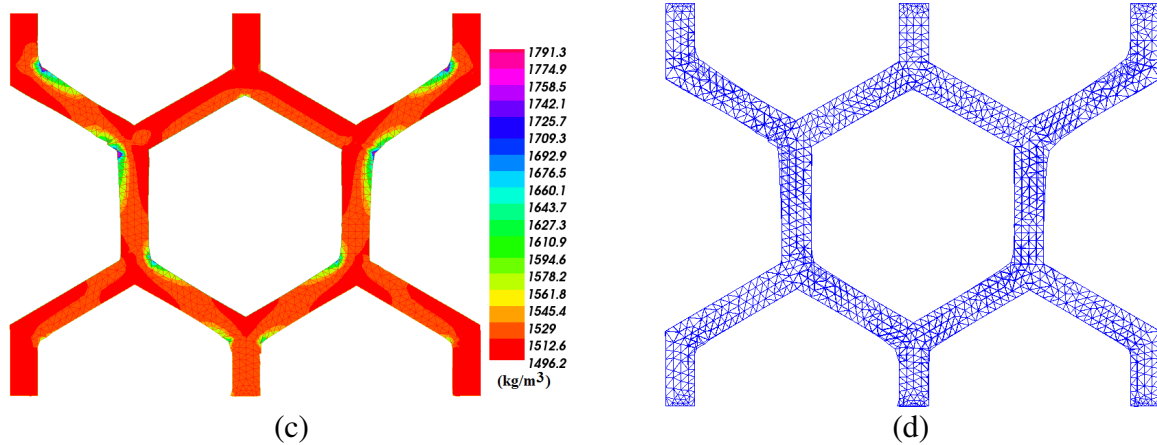


Figure 8.3: Combined internal and external trabecular bone adaptation under compressive load at the top edge: (a) Initial geometry with uniform density of 1500 kg/m^3 submitted to compressive load; (b) Strain distribution; (c) Bone density distribution; and (d) Initial and new grown geometry meshes. The adaptations lasted 50 time steps.

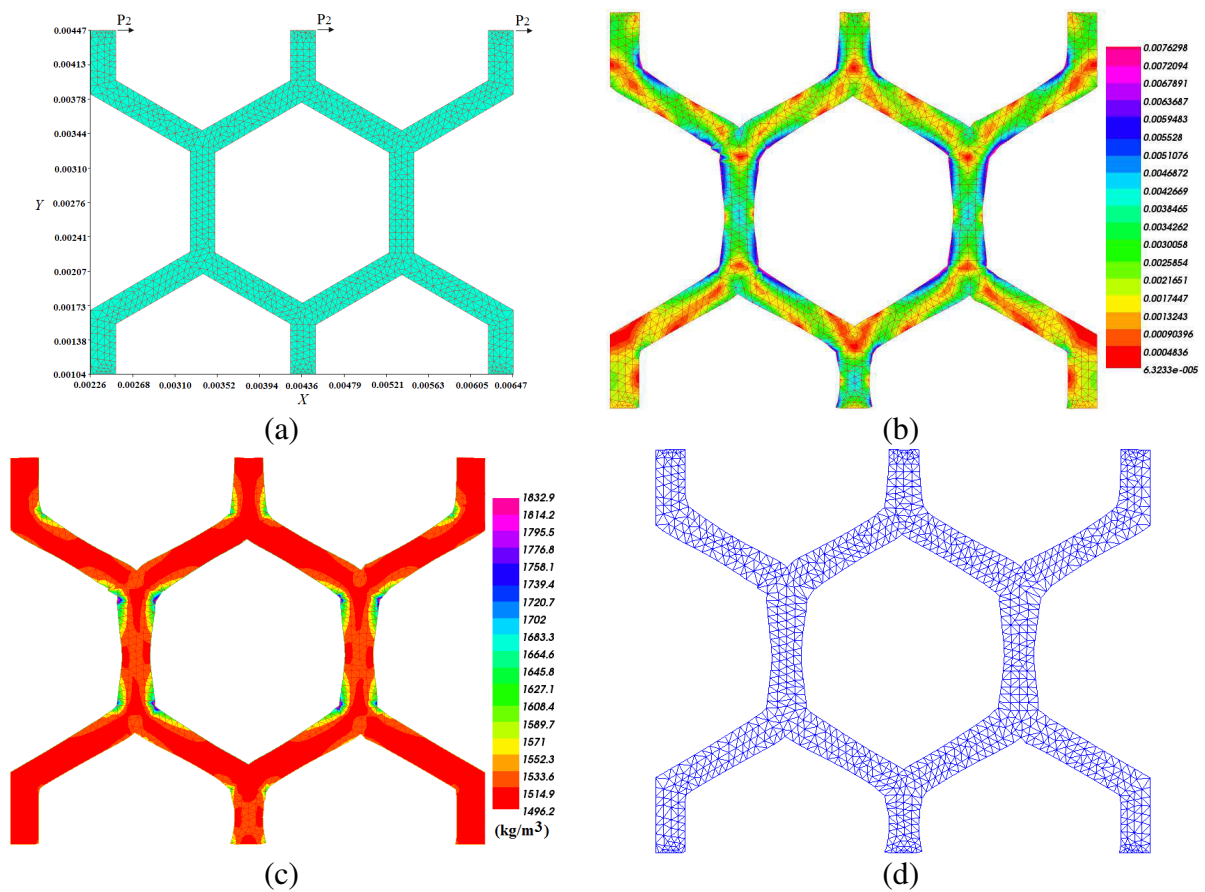


Figure 8.4: Combined internal and external trabecular bone adaptation under shear load at the top edge: (a) Initial geometry with uniform density of 1500 kg/m^3 submitted to shear load; (b) Strain distribution; (c) Bone density distribution; and (d) Meshes of the new grown geometry. The adaptations lasted 50 timesteps.

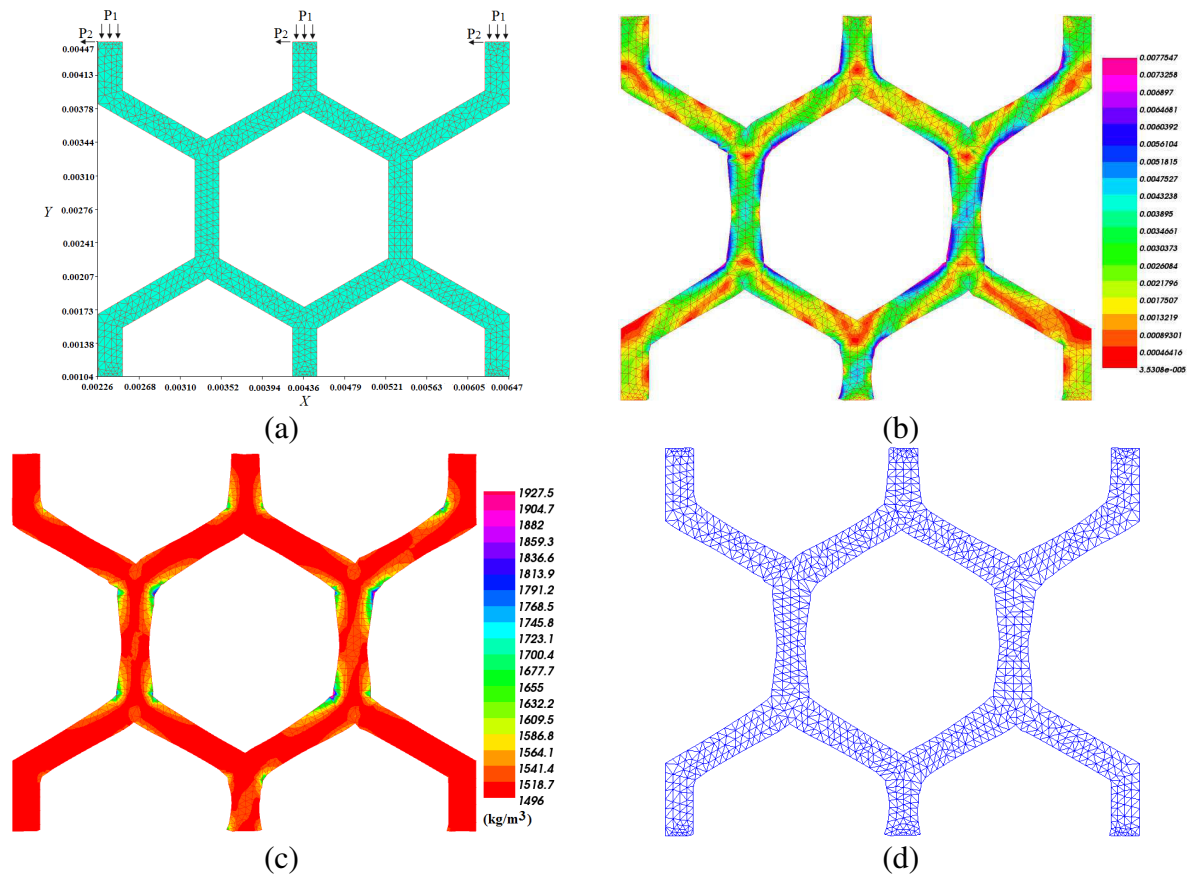


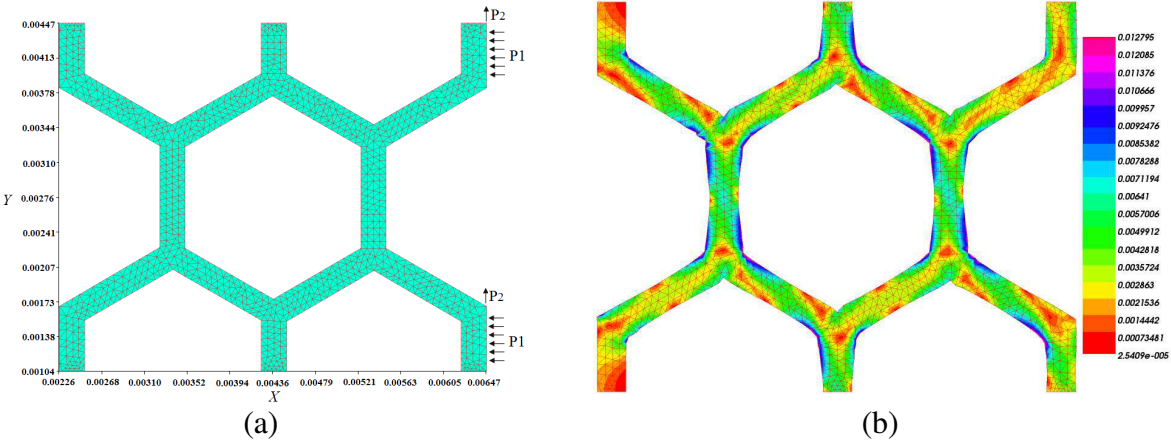
Figure 8.5: Combined internal and external trabecular bone adaptation under compressive and shear loads at the top edge: (a) Initial geometry with uniform density of 1500 kg/m^3 submitted to combined compressive and shear loads; (b) Strain distribution; (c) Bone density distribution; and (d) Meshes of the new grown geometry. The adaptations lasted 50 timesteps.

An additional simulation is performed over the hexagonal trabecular unit cell to give insights into different loading conditions. In this loading case (V), the part of the boundary along which the trabecular cell is fixed is selected to be the left edge, and the part of the boundary along which the loads ($P1=5 \text{ MPa}$, $P2=7 \text{ MPa}$) are applied is the right edge; periodic boundary conditions are then imposed at bottom and top edges. Under those combined compressive and shear loadings, the adaptive response of bone is presented on [Figure 8.6](#) for a fixed number of growth timesteps. The adaptation simulations are also carried out over a maximum of 20 timesteps.

The external bone adaptation process at this level can then be defined as the bone capacity to form or destroy bone surface in response to mechanical stimuli. The tissue response is shown by modifications of the bone shape or its microstructure in addition to a slight reorganization of its material properties. Additionally, as a general remark in simulations of trabecular bone adaptation, one can notice the increasing trabecular thickening near the strut joints. Simple observations indeed reveal that the trabeculae are most of the time not perfectly uniform, but have a certain degree of non uniformity, due to the natural variance in trabecular thickness for real trabecular bones. This in turn illustrates the importance of our obtained results of trabecular thickening near the strut joints; this will enhance the possibility of improving the representation of the topology of the bone unit cell structure. These

computed variations of the trabeculae thickness and information on the strut morphology near the strut joints may indeed help to consider more realistic bone topology prototypes rather than the idealized uniform cross section of the trabeculae.

In order to quantitatively investigate the morphological changes in trabecular bone, we next compute the bone volume fraction or bone relative density. In such porous open-celled structures, the apparent density is generally the most important factor affecting the effective mechanical behavior. The apparent density is the density of a volume of the porous material, including voids, whereas the material density is the density of the structural matrix itself. The relative density is equivalent to BV/TV (bone volume fraction), which stands for bone volume over total volume respectively. The bone volume fraction is presently computed before submitting the trabecular bone to mechanical stimulus and after stimulation to give insights about how much bone volume fraction has been changed due to growth (evolution of the external shape). In order to quantify the external adaptation response, we compute the initial bone volume fraction (original shape geometry) and compare it with the bone volume fraction of the grown geometry; this has been computed for all loading cases. The original bone volume fraction (before evolution occurs) is equal to 0.24. In loading case I, the volume fraction is found equal to 0.25, which means that about 4% increase of bone volume is attained as a result of external growth under compressive load exerted at the top edge. Similarly, in the loading cases II, III, the volume fraction of the grown bone is very similar, about 0.265; this means that about 10.5% of bone volume increase is attained due to the shear and combined compressive and shear loads. As a final growth simulation comparison (case V), it is found that the volume fraction of bone is equal to 0.27; this implies that approximately 12.5% of bone has been added (in terms of volume) to the original geometry.



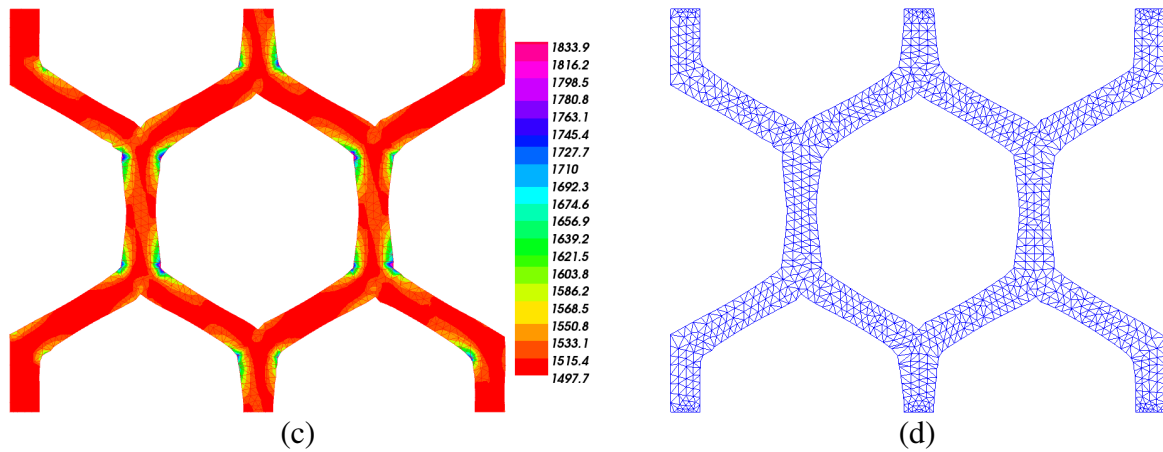


Figure 8.6: Combined internal and external trabecular bone adaptation under compressive and shear loads at the right edge: (a) Original bone geometry with uniform density of 1500 kg/m^3 submitted to combined compressive and shear loads; (b) Strain distribution; (c) Bone density distribution; and (d) Plot of the mesh of the newly grown bone geometry. Bone adaptations are shown after 20 growth-timesteps.

The developed growth model is next applied to simulate the growth of the individual trabeculae of cancellous bone. Simulations at the scale of the triple junction of the individual trabeculae will be performed, considering the same geometrical (strut lengths and thicknesses) and mechanical microparameter as in previous simulations. We simulate separately two static loadings as a mechanical stimulus for external bone adaptation, a compressive load ($P1=10 \text{ MPa}$) and a shear load ($P2=5 \text{ MPa}$); in both cases, the nodes are fixed on the bottom edges.

Bone undergoes morphological changes in response to applied mechanical loads by modifying its external geometry as well as its internal structure, i.e., external and internal remodelling occur simultaneously. At this scale nevertheless, bone remodelling is nearly a purely surface phenomena, traduced by an evolution of the external shape of the individual trabeculae (density variations have been shown to be negligible).

We plot the new external geometrical shape, as indicative of the trend of the external remodeling process. The proportionality constant K_g governing the rate of surface adaptation process in (8.44) is taken as $10^{-11} \text{ (m}^4/\text{N.timestep)}$. The geometry is evolved as a function of time (external remodeling) using the FE method: the adapting process leads to the mesh nodes repositioning without modifying the connectivity or the definition of additional elements (Figures 8.7 and 8.8).

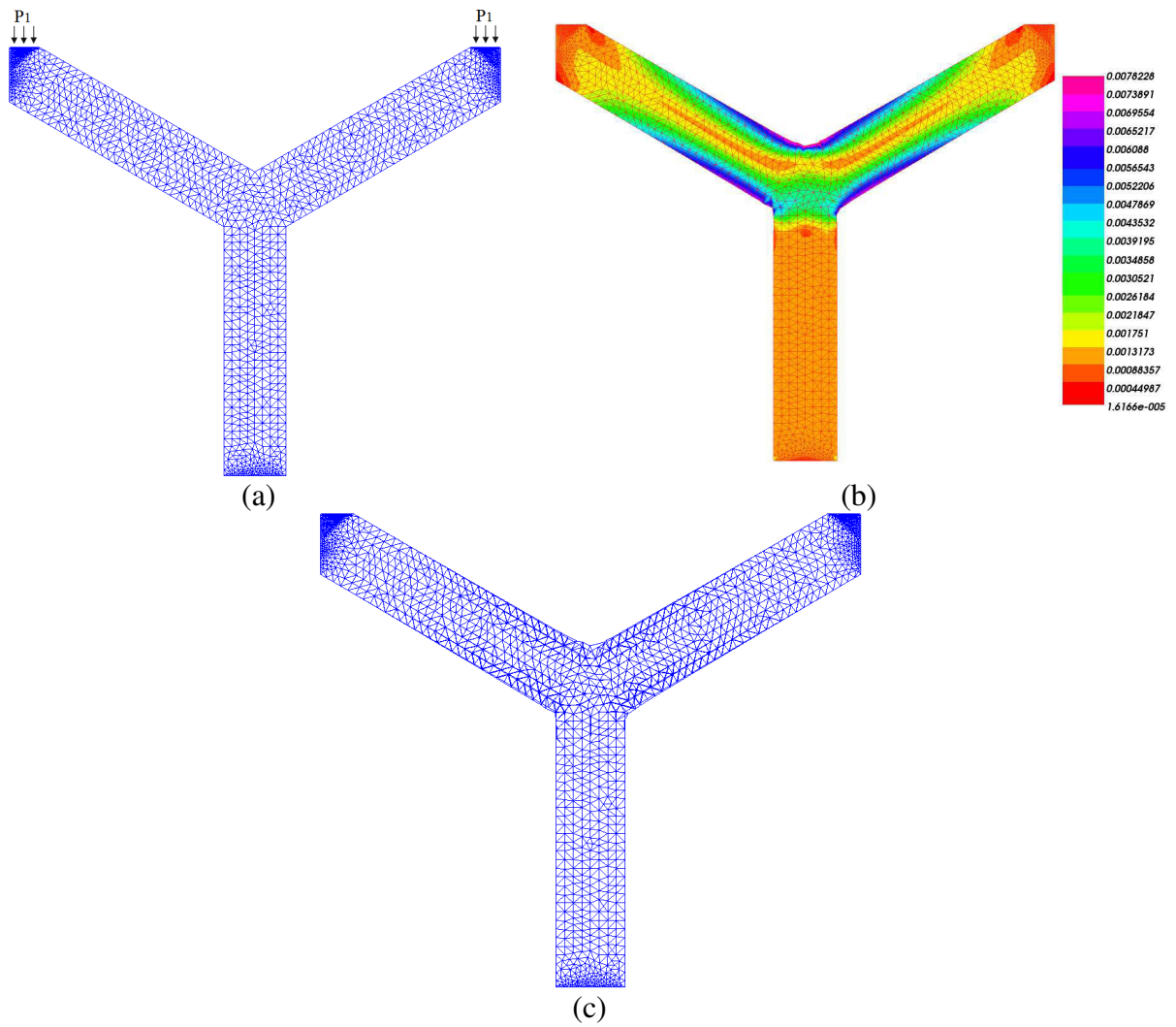
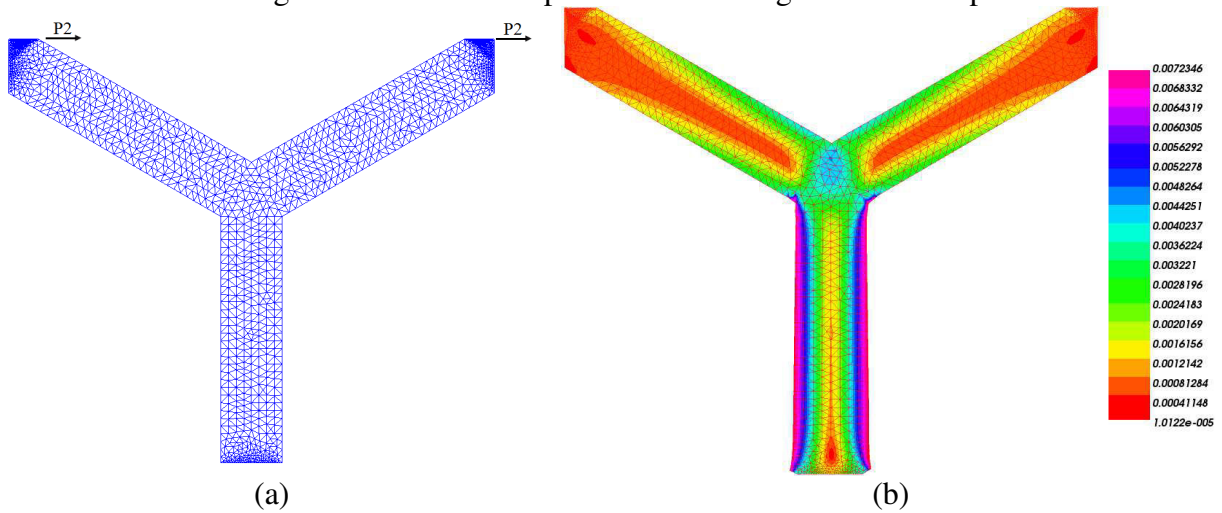


Figure 8.7: External trabecular bone adaptation under compressive: (a) Original configuration submitted to compressive stress; (b) Strain distribution; (c) Overlay plots of the original bone and grown bone. The adaptations lasted 60 growth-timesteps.



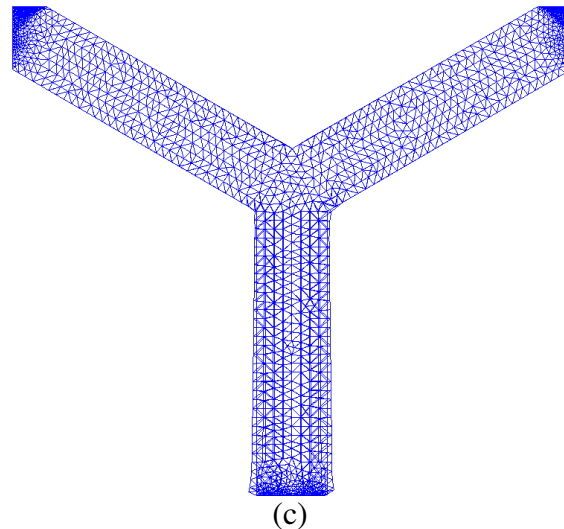


Figure 8.8: External trabecular bone adaptation under shear stress: (a) Original configuration submitted to shear stress; (b) Strain distribution; (c) Overlay plots of the original bone and grown bone meshes. The adaptations lasted 60 growth-timesteps.

8.4.2 Macroscopic viewpoint

We next perform structural remodeling computations of the evolution of the external shape jointly with adaptation of the apparent internal density for a sample of the human femur subjected to physiological loads, in order to illustrate the powerfulness of the developed methodology. Actually, this type of bone remodeling is physiologically caused by the remodeling of the trabecular (spongy) bone.

In order to model surface growth over time, it is necessary to account for internal bone remodeling occurring in the entire bone. Internal remodeling is considered as the mechanism for the redistribution of the apparent trabecular bone density under the action of the physiological loading. The trace of Eshelby stress which identifies to the energy density is adopted as previously as the biomechanical signal that controls internal remodeling of trabecular bone. For external remodeling, the outer geometry of the femur bone adapts due to the applied loads by allowing surfaces to move freely according to a constitutive relation based on the divergence of Eshelby stress. In our structural model, trabecular bone is represented as a cellular structure with the cell walls modeled as a bulk material. Internal and external bone growth shall be expressed in algorithmic format from a variational formulation of the strong form of the field equations, leading to a numerical implementation for 2D situations.

8.4.2.1 Homogenization scheme for trabecular bone

Bone is a particularly complex multiscale material, which is hierarchically organized to provide maximum performance with a minimum amount of material. At the nanoscale, bone is composed of collagen fibers, apatite crystals and water; at the sub-microscale (1–10 μm), the arrangements of collagen fibers reinforced with crystals form lamellas. These latest are

packed and organized in different orientations to form cylindrical struts called trabeculae at the microscale (several hundred of micrometers). At the mesoscale, the complex and very organized network of trabeculae forms the trabecular bone. The macro scale represents the whole bone which is constituted by both the trabecular bone and the cortical bone. Bone is a heterogeneous and anisotropic material normally present into two major forms of bone tissue at the macroscopic level, cortical bone (at the outer surface) and trabecular bone (Figure 8.9). Trabecular bone is very complex due to its randomness and spatial heterogeneity. In order to simplify the forthcoming analysis, one can choose to represent bone as having an idealized periodic microstructure: in this work, we model bone as having a periodic prismatic structure in a two-dimensional context.

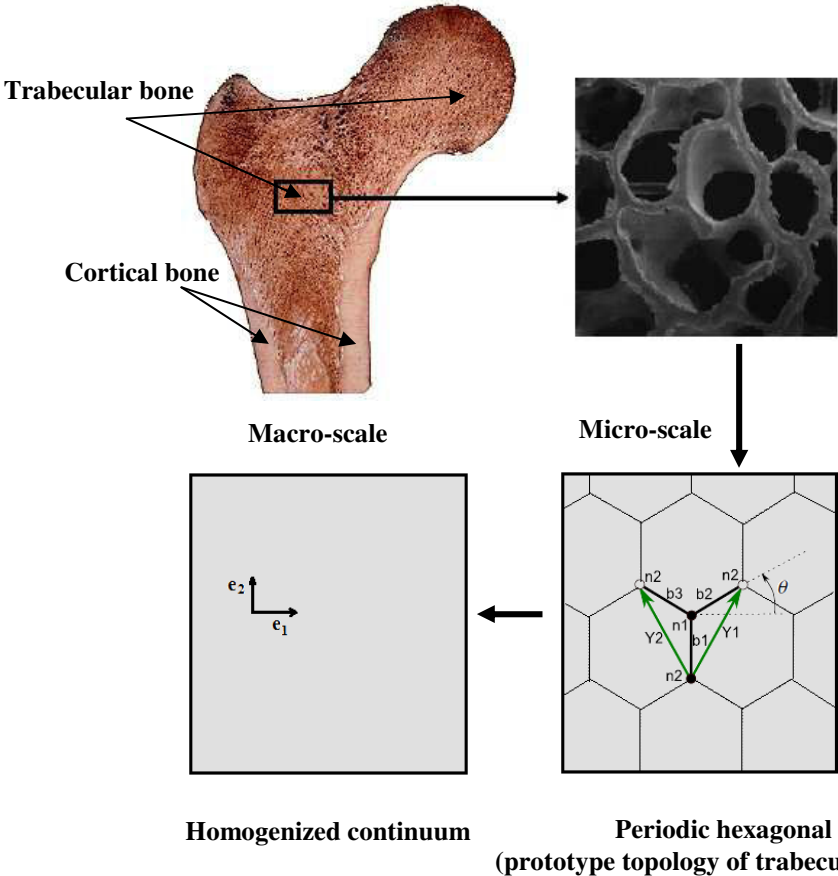


Figure 8.9: Trabecular bone and microstructure homogenization towards an effective continuum.

Discrete homogenization is a tool utilized to determine the effective macroscopic material properties of microstructured materials. Trabecular bone defines the microstructure of bones, mainly located within the confines of the cortical bone coverings. Homogenization aims then at identifying the material properties of trabecular bone at the apparent level; we assume the architecture of trabecular bone consists of an elastically isotropic material.

Following the procedures of discret homogenization introduced in Chapter 2, the constitutive equation for the equivalent Cauchy continuum writes

$$\{\sigma_x, \sigma_y, \sigma_{xy}\} = [C] \left\{ \frac{\partial u_1}{\partial x}, \frac{\partial u_2}{\partial y}, \frac{1}{2} \left(\frac{\partial u_2}{\partial x} + \frac{\partial u_1}{\partial y} \right) \right\} \tag{8.65}$$

with u_1, u_2 the two components of the planar displacement field, and $[C]$ the equivalent rigidity matrix written for an orthotropic material in terms of Young moduli (E_x, E_y), the shear modulus G_{xy} and the two Poisson's ratios (ν_{xy} and ν_{yx}) as

$$[C] = \frac{1}{1 - \nu_{xy}\nu_{yx}} \begin{bmatrix} E_x & \nu_{yx}E_x & 0 \\ \nu_{xy}E_y & E_y & 0 \\ 0 & 0 & 2G_{xy}(1 - \nu_{xy}\nu_{yx}) \end{bmatrix} \quad (8.66)$$

A 2D geometrical model of a hexagonal structure is then considered as an idealized representation of trabecular bone, for which the Young's modulus, shear modulus, are identified at the mesoscopic level from a micromechanical analysis. The model geometry consists of struts of length L for the inclined beams and h for the vertical beams with uniform trabeculae thickness t . The struts of length L are inclined with the angle $\theta = 30^\circ$.

The bony structure has been further assumed to be described by a linear isotropic behavior; this simplifies the previous effective constitutive law in (8.66), which only involves two independent mechanical moduli.

Homogenization results provide the evolution of the effective Young's and shear moduli of trabecular bone versus apparent density. The apparent tensile and shear moduli of trabecular bone are obtained from discrete homogenization as power law functions of the apparent density (kg/m^3),

$$E = 72.5\rho^{2.4}, \quad G = 36.25\rho^{2.4}/(1 + \nu) \quad (8.67)$$

with the effective Poisson ratio assumed to be independent of ρ , $\nu(\rho) = \nu = 0.3$.

We next perform structural remodeling computations of the evolution of the combined internal and external adaptation of bone for a sample of the human femur subjected to physiological load.

8.4.2.2 Simulation of joined internal and external remodeling

The shape of part of the human femur is presented by B-splines, and then meshed; simulations are done with the open source FE software Freefem++, adopting the variational formulation of the equilibrium equations. Let Ω be the region occupied by the effective homogenized isotropic bone material enclosed by a boundary $\Lambda = \partial\Omega$. The border is decomposed into two disjoint parts Λ_1 and Λ_2 , where Λ_1 is the part of the boundary along which the femur is fixed, and Λ_2 the part of the boundary along which the loads P (P_1, P_2) are applied (Figure 8.10). The mechanical load environment for bones is complex, with force components resulting from joint contact, muscles, tendons, and soft tissue, and the load magnitudes and directions vary constantly as a person moves about. The load values and directions are usually corresponding to a static load case representing the stance phase of gait for a person weighing 80 kg. As a representative loading condition, the bone structure is subject to three load cases

(one-legged stance, abduction, and adduction). Remodeling simulations are currently conducted under a single-loading condition. We consider static loading as a mechanical stimulus with the force corresponding to the instant when the foot touches the floor (case 1), which is assumed to be predominant (higher force magnitude than the other load cases). Load values are taken from [Beauré et al., 1990](#), and they are applied at the head of the femur and as the reaction of the muscles located at the great trochanter ([Figure 8.10](#)). The first load condition $P_1=2317$ N is assigned at an angle of $\theta_1 = 24^\circ$ and the second load $P_2= 703$ N is positioned at an orientation of $\theta_2 = 28^\circ$ (the angles are given with respect to the vertical axis).

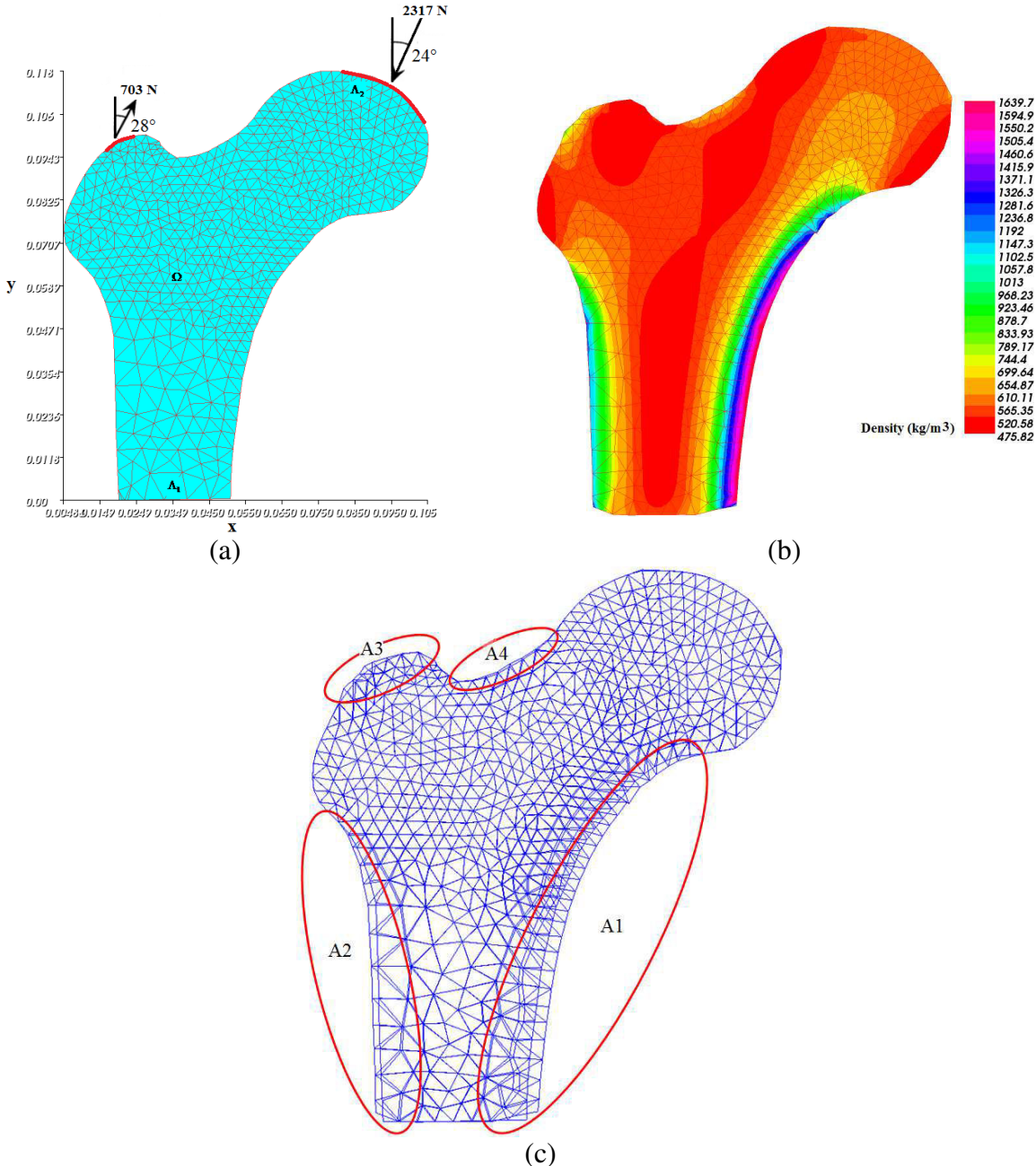


Figure 8.10: Simulations of internal and external bone growth at the macroscopic level. (a) Loading conditions and original structure with uniform distribution at the beginning of simulation: initial density= 800 kg/m^3 , (b) Bone density distribution after 140 growth-timesteps, (c) Overlay plots of the original bone and grown bone meshes after 140 growth-timesteps.

Bone growth results show that the external shape of the femur bone and its internal morphology simultaneously adapt to the surrounding mechanical environment (Figure 8.10). Figure 8.10a shows the geometry of a 2D frontal plane of a proximal femur, which is taken as the initial configuration in our structural internal and external remodeling analysis. The process starts with an assumed uniform density distribution chosen as 800 kg/m³. The time step size (iteration) is selected as $\Delta t = 1$. The combinative algorithms of both adaptive internal and external remodeling lead to changes of both the local bone density and external shape geometry. The adaptation simulations are carried out over a maximum of 140 timestep growth. At the end of the adaptation process, one can observe from the bone density distribution (Figure 8.10b) the formation of two high density external layers along the diaphysis of the femur: a zone of low density corresponding to the medullar channel inside the diaphysis and a complex distribution of density of the femoral head and trochanter including three different density zones with the head surrounded by a lower density zone (low density region on the distal part of the head).

In addition to bone density adaptation and based on surface remodeling, we generated a computational framework for simulating the movement of the surface of femur bone based on the divergence of Eshelby stress. Thereby, the evolution of the whole bone geometry and its shape due to surface growth is simulated. After a maximum of 140 growth timesteps, we observe that most parts of the initial bone show geometrical change during bone remodeling, with however only the periosteal surface on the diaphysis presenting a noticeable change (location A1 and A2). The overlay plots of the original bone and grown bone meshes (Figure 8.10c) show that much of the diaphysis is formed by appositional bone growth. From the assessment of results on Figure 8.10c, we compare the bone outline of the initial structure with that of the final structure. Bone remodeling changes the shape slightly in most regions, except the periosteal surfaces on the diaphysis; growth is more significant on the right surface than on the left. Slight changes occur in regions of great trochanter (A3) and femoral neck cortex (A4).

In conclusion, in this macroscopic point of view, we developed a computational model, based on mechanical loading-induced bone remodeling, which can simulate the changes of internal density (to account for trabecular morphology variations) as well as the simultaneous overall shape changes, especially on the periosteal surfaces in the diaphysis. Simulation results show that the external shape of the femur bone and the internal morphology of the trabecular bone simultaneously adapt to the surrounding mechanical environment. This type of external remodeling simulation platform could be useful for situations like implant surgery, and fracture healing where more important modifications of the external geometry occur.

8.5 Conclusions

Growth phenomena in biological tissues generally affect both changes in density (or rather mass) and changes in volume. Bone tissues are able to adapt their local density and load bearing capacities as well as their size and shape to mechanical stimuli. Such growth

processes result in densification and formation of new material of bone in regions of high mechanically load levels as well as resorption and material removing in regions of low loading levels.

A numerical framework has been developed to simulate the process of external bone adaptation jointly with local adaptation with respect to applied mechanical loading at both the cellular level and the macroscopic level. The underlying mechanical framework is configurational mechanics, with Eshelby stress at the origin of the stimuli for both internal and external remodeling. The implementation of the numerical framework is quite general and can accommodate readily different material models and diverse mechanical stimuli.

Tissue-level mechanical adaptation model is self-trabeculate, wherein the bone tissue is a self-organizing material, and the density distribution within the bone tissue is optimized with respect to the external loads. As a consequence of different kinds of loadings, various patterns of bony morphology arise as simulation results indicate. This model simulates mechanical adaptation of the trabecular structure by adding and removing bone to the surfaces of trabeculae (in which the surfaces move freely according to constitutive relations) in a way that closely approximates physiological bone-remodeling processes.

In simulations at the ultimate macroscopic scale, a two-dimensional model of proximal femur has been simulated under physiological loading conditions. The bone tissue response manifestation is by changing the overall shape of the bone sample and its apparent density, and consequently its microstructure. Bone is modeled as an effective continuum endowed with a linear elastic constitutive law obtained from the homogenization of the underlying microstructure. As a consequence, continuum mechanical parameters such as stiffness evolve with density (and thus morphology) as remodeling occurs within bone tissue. The external surfaces move freely according to constitutive relations, involving the trace of Eshelby stress (the energy density) as the mechanical stimulus driving density evolutions within trabecular bone.

Such a simulation platform for combined bone internal and external remodeling paves the way to multiscale simulations under static and dynamical loading conditions which are aimed to help medical doctors choosing appropriate procedures like implant surgery based on real morphological data.

CHAPTER 9: INTEGRATED REMODELING TO FATIGUE DAMAGE MODEL OF BONE

Bone is a living tissue that continually undergoes damage under normal everyday mechanical loadings. It maintains its structural integrity by a continuous process of damage detection and repair, and by adaptation to changes in the mechanical environment. These adaptive changes are regulated by the so-called process of bone remodeling. The aim of the current chapter is to develop an integrated remodeling-to-fracture model to simulate the bone remodelling process considering the anisotropy of trabecular bone. For this purpose, models for density of continuum solid bodies are developed in the framework of the thermodynamics of irreversible processes, considering bone elasticity with damage properties, in which the damage stimuli is incorporated. The asymptotic homogenization technique is involved to derive the effective anisotropic continuum mechanical properties of the trabecular bone from an initially discrete structure representative of femur bone microstructure, consisting of a piling up of hexagonal planar cells. As a consequence, relationships are established between the apparent density of bone and its effective anisotropic properties, that is the elastic and shear moduli and Poisson's ratio. Damage is directly incorporated into the effective density, the evolution of which is computed versus time. This formalism is involved to simulate bone remodeling for 2D geometries in the context of damaged anisotropic bone elasticity, showing the influence of the external mechanical stimuli on the evolution of the density of bone.

9.1 Introduction

As a result of daily loading activities, fatigue and fracture may be present and grow within bone. On the other hand, bone is a living tissue having the ability to sense damage and repair itself within a certain level of damage. Bone is also able to adapt its mechanical properties to the varying mechanical and physiological environments in a process commonly coined bone remodelling. Accordingly, the analysis of bone remodelling considering bone fatigue and damage is an important issue in biomechanics.

Bone is a living tissue, a remarkable and extremely adaptable substance in the human body. It continuously undergoes processes of growth, reinforcement, and resorption which occur in living situation; these processes are collectively termed bone remodeling. Additionally, bone has the ability to adapt its external shape as well as its internal structure to variations in its mechanical environment. The adaptive response of bones to changes in load history is called bone remodeling (Wolff, 1892), with a classification as either internal or external remodeling (Cowin and Van Buskirk, 1979). External or surface remodeling results in a change of the external geometry of the overall bone structure, and occurs by the resorption or deposition of bone material on the surfaces. To the contrary, internal remodeling refers to the resorption or deposition of bone material only, accompanied by the removal and densification of the cancellous bone, but no change in its overall shape.

Bone remodelling provides a mechanism to repair damage as it is well known that daily activities damage bone; this damage is normally repaired in a continuous remodelling process. During physiological daily activities, bone is regularly subjected to repetitive fatigue loading

and when this load goes beyond a certain level of strain or stress, damage is induced into the bone tissue. The presence of such damage causes a reduction in mechanical properties of the bone material such as stiffness and strength, due to the formation of microcracks. These microcracks have been implicated in physiological phenomena including remodelling ([Mori and Burr, 1996](#)) and bone adaptation ([Prendergast and Taylor, 1994](#); [Lee et al., 1999](#)).

A few researchers considered crack damage and fatigue as the inducer of bone remodeling: ([Carter et al., 1987](#); [Prendergast and Taylor, 1994](#)). [Carter et al. \(1987\)](#) hypothesized that fatigue damage acts to produce a bone maintenance stimulus. [Prendergast and Taylor \(1994\)](#) proposed the hypotheses required to develop damage-adaptive remodelling laws and derived a remodelling law to predict the time course of bone adaptation. Furthermore, [Martin \(1992\)](#) derived an analytical expression for the remodelling equilibrium state of damage based on osteonal repair of cracks. [Prendergast and Huiskes \(1995\)](#) proposed a microstructural finite element analysis to explore the relationship between damage formation and local strain of osteocyte containing lacunae for various types of damage. [Ramtani and Zidi \(2002\)](#) proposed an extension of the adaptive-elasticity theory in order to include the contribution of bone microdamage as a stimulus. [Taylor et al. \(2007\)](#) proposed that bone tissue is a continuous system incorporating the growing and repairing of microcracks. [McNamara and Patrick \(2007\)](#) showed that by incorporating both microdamage and strain as mechano-regulatory stimuli, the creation and refilling of a resorption cavity along the surface of bone trabeculae can be simulated. [Wang et al. \(2011\)](#) proposed a numerical model based on the theory of bone remodeling to predict the evolution of the trabecular bone architecture within the vertebral body. Those authors assumed that the multicellular units activation probability depends on the state of damaged bone tissue (damage accumulation), which is evaluated as to bone fatigue damage.

The resistance of bones to damage by self-repair mechanisms and adaptation to the environmental conditions are the most important bone characteristics. Such adaptive changes are regulated by adaptive physiological process called bone remodeling. A better understanding of such process requires applying the elastic damage theory under the hypothesis of small strain to the bone structure and investigating its mechanical response. From the standpoint of biomechanics, there is a significant need to make an attempt to put some of the theoretical framework in which a hypothetical statement can be made regarding the damage consequence on the process of adaptation of bone. To attain this goal, we use the framework of continuum thermodynamics to introduce and model the presence of microcracks. Thus, the main purpose of this work is to introduce a strategy for modeling the interaction of damage with the remodeling process in bones.

Most of the models consider bone as an isotropic structural material, except for a few works, including ([Watzky and Naili, 2004](#); [Kowalczyk, 2010](#)); this assumption is clearly a shortcoming of the treatment of trabecular bone, ignoring the importance of anisotropic bone material behavior in the remodeling process ([Beaupré et al., 1990](#); [Weinans et al., 1992](#)).

In this work, we couple the material density and bone anisotropy; it is assumed that at the microscopic level, the bone trabeculae consists of an isotropic, Timoshenko type elastic cellular material, whereas cancellous bone behaves as a homogeneous, anisotropic continuum

at the macroscopic level. Anisotropic properties of trabecular bone are difficult to access by observations, thus pointing toward the need for predictive models of cancellous bone, based on its architecture and microstructural properties. Moreover, due to the variation of bone architecture (geometry) according to location, homogenization models will exhibit the advantage of their versatility, in the sense they are able to provide quantitative estimates of bone mechanical properties versus the bone architectural and micromechanical parameters.

The main purpose and originality of this chapter is accordingly to set up a model which combines an anisotropic internal remodeling rule with fatigue damage, based on continuum damage theory. We propose to account for the trabecular structure in the proximal femur by using an orthotropic material model to represent the effective properties of the trabecular bone in a 2D framework on the basis of discrete homogenization. In our structural model, trabecular bone is represented as a cellular structure with the cell walls modeled as a Timoshenko beam. Consequently, at the macroscopic level, the constitutive laws for trabecular bone shall account for morphological effects, including anisotropy as well as damage. Internal growth of bone shall be expressed in algorithmic format from a variational formulation of the strong form of the field equations, leading to a numerical implementation for 2D situations.

9.2 Balance laws and constitutive equations of density growth

Tissue growth associated with changes in volume and mechanical properties (the so-called local evolution of materials) can be interpreted as local material transformations or local deformation measures. In order to describe the deformation of the body due to growth, the balance of mass with source term writes

$$\frac{d}{dt} \int_{V(t)} \rho d^3x = \int_{V(t)} \Gamma^g \rho d^3x \quad (9.1)$$

with $\rho(x, t)$ the mass density, and $\Gamma^g(x, t)$ the rate of mass increase per unit mass (it has the dimension of the inverse of a characteristic time); the volume element therein is denoted d^3x . In a Lagrangian frame of reference, equation (9.1) rewrites

$$\frac{d(J\rho)}{dt} = \Gamma^g \rho J \quad (9.2)$$

where J is the Jacobean of the total deformation gradient, decomposing into

$$J = \det \mathbf{F} = \det \mathbf{F}_a \det \mathbf{F}_g = J_a J_g$$

The mapping \mathbf{F}_g is known as the irreversible growth tensor which corresponds to the deformation from the initial configuration to the grown body (unstressed configuration), while \mathbf{F}_a is referred to as the accommodation tensor or the reversible elastic part of the deformation gradient, corresponding to the deformation between the grown body and the actual

configuration at time t . The scalar quantities J_a and J_g are, respectively, the determinants of the accommodation and growth tensors. In a biological context, it is usual to measure and model the growth rate Γ^g appearing in the mass balance equation rather than the growth mapping (second order tensor) \mathbf{F}_g ; it receives the following expression

$$\Gamma^g = \text{Tr}(\dot{\mathbf{F}}_g \mathbf{F}_g^{-1}) \quad (9.3)$$

Constant-density growth is usually coupled with the assumption of an incompressible tissue, so that $J_a = 1$ and thus density does only change due to growth, but remains constant when elastic accommodation is considered. For constant-volume growth, the change in volume from the initial body to the unstressed body is neglected, so that $J_g = 1$. The bone tissue growth then occurs by densification only; accordingly, the balance of mass expresses the rate of change of the material density versus the growth mapping

$$\frac{d\rho}{dt} = \Gamma^g \rho \quad (9.4)$$

In the present context, various authors (e.g., [Ganghoffer, 2010, 2012](#); [Ambrosi and Guana, 2007](#)) argued based on thermodynamic principles that the driving force behind growth is the Eshelby stress. [Ganghoffer \(2010\)](#) introduced general balance laws for solid bodies undergoing growth phenomena in the framework of irreversible thermodynamics of open systems. The growth is viewed as a multiphysical phenomenon coupling the transport of nutrients with mechanical factors promoting a local variation of the density, at constant number of particles. The growing continuum body is endowed with a general hyperelastic constitutive behavior encapsulate into a strain energy function $W(\mathbf{u})$, expressed per unit referential volume.

Relying on that the growth rate depends on the Eshelby-like tensor, we propose a constitutive relation for the mass source, wherein the growth rate is proportional to the trace of the Eshelby tensor

$$\Gamma^g = \frac{B_c}{\rho^2} \text{Tr}(\boldsymbol{\Sigma}(\mathbf{u}) - \boldsymbol{\Sigma}_0) \quad (9.5)$$

where B_c is a proportionality constant measuring the rate of the adaptation process (it governs the velocity of the adaptation process), $\boldsymbol{\Sigma}(\mathbf{u})$ is the actual volumetric Eshelby stress tensor receiving the expression

$$\boldsymbol{\Sigma}(\mathbf{u}) = W(\mathbf{u})\mathbf{I} - \epsilon(\mathbf{u}) \frac{\partial W(\mathbf{u})}{\partial \epsilon} \quad (9.6)$$

and $\boldsymbol{\Sigma}_0$ the threshold value for the volumetric Eshelby stress stimulus (reference value). The identity tensor is therein denoted \mathbf{I} .

The evolution equation of the density (9.4) combined with the definition of the mass source Γ^g in (9.5) then delivers

$$\frac{d\rho}{dt} = \frac{B}{\rho} \text{Tr}(\boldsymbol{\Sigma}(\mathbf{u}) - \boldsymbol{\Sigma}_0) \quad (9.7)$$

This equation describes bone adaptation, and more precisely whether the tissue stress stimulus will induce bone formation, bone resorption or equilibrium, according to the sign and value of the rate of change of the apparent bone density. Equilibrium is reached when the Eshelby stress attains the homeostatic value $\boldsymbol{\Sigma}_0$, supposed to be known at each point.

It is noteworthy that the trace of Eshelby stress is the strain energy density. Accordingly, the volumetric strain energy density (or the trace of Eshelby stress) is the mechanical stimulus that triggers bone adaptation locally, as a scalar quantity that incorporates local stress and strain tensors. We then propose a formulation for bone adaptation utilizing the strain energy density function as the remodeling signal representing the deformational energy at any point. In particular, the remodeling stimulus is obtained by the calculation of strain energy per unit density (strain energy stored per unit mass of bone) taking the following form:

$$\frac{d\rho}{dt} = B_c \left(\frac{W(\mathbf{u})}{\rho} - \frac{W_t}{\rho_m} \right) \equiv f(t, \rho) \quad (9.8)$$

This modified evolution equation ensures a good stability behavior of the time-dependent remodeling. The driving mechanism for adaptive activity is then the deviation between the actual energy per unit mass $W(\mathbf{u})/\rho$ from a site-specific homeostatic equilibrium W_t/ρ_m ; the scalar ρ_m therein is the maximum density. The internal remodeling process in (9.8) is considered to have converged when the rate $d\rho/dt$ tends to zero (equilibrium is then reached) or when the density secures a minimal (10 kg/m^3) or maximal value (1740 kg/m^3). The remodeling rate B_c is chosen from (Chen et al., 2007) to be $1.0 (\text{kg m}^{-3})^2/(\text{Pa}\cdot\text{time})$.

Although there are many studies (e.g., Hazelwood et al., 2001; Hernandez et al., 2000) considering a constant reference value for bone adaptation of $1000 \mu\epsilon$ (this last notation means microstrain, so that one computes the strain ϵ_0 based on the number of loading cycles), Qin et al. (1998) showed however that the reference value of remodeling strain depends on the daily loading cycles. Based on experimental fitted curves, a continuous nonlinear relation between strain and daily loading cycle is obtained by previous author as

$$\epsilon_0 = 10^{2.28} (5.6 - \log_{10} N)^{1.5} \quad (9.9)$$

where N represents the daily loading cycle number and ϵ_0 is the resultant micro-strain magnitude ($\mu\epsilon$).

Hence, the reference value of W_t can be obtained using relation (9.9), with $W_t(\mathbf{u}) = 1/2\sigma_0\epsilon_0$.

9.3 Elastic damage bone remodeling process

Bone adaptability allows for efficient repair, which in turn helps to prevent fractures. Bone can be remodeled in response to external loads to give denser bone matrix in regions that are subjected to higher levels of stress. These external loads induce changes in the mechanical fields and damage, such as macrocracks or microcracks (Taylor, et al. 2007). A damage-adaptive bone remodeling model is presently developed, wherein microdamage is incorporated as a stimulus.

Bone continuously checks the presence of cracks and other types of damage within its microstructure, and deliberately replaces damaged regions with new material by remodeling processes. In addition to removing fatigue damage, the remodeling process leads to an adjustment of bone mechanical properties in response to imposed loads. The overall aim of the present work is then to numerically simulate the remodeling of femur bone using an elastic-damage theory in the context of small displacements and small strains. In the theory of elastic damage mechanics, the mechanical properties may degrade gradually as damage progresses; combining damage definition and mechanical properties evolution in framework of bone remodeling, the elastic and shear moduli at each location will be calculated from density relying on a micromechanical scheme. Subsequently, we apply the theory of elastic-damage mechanics to the bone remodeling process.

The continuum behavior of bone material is modeled based on the concept of continuum damage mechanics, as an effective elastic anisotropic behavior coupled to fatigue damage. We consider the following rational elastic-damage potential energy based on the physically appealing effective stress concept (Lemaitre and Chaboche, 1978; Lemaitre, 1984; Ju, 1991):

$$W = \frac{1}{2}(1 - D_e)\epsilon : C^0 : \epsilon \quad (9.10)$$

This equation describes the strain energy density function coupled to the fatigue damage, described by the scalar variable D_e (ranging from 0 to 1, $D_e = 0$ corresponding to the undamaged state while $D_e = 1$ physically means the local rupture state or local failure), ϵ is the elastic strain tensor, C^0 the virgin (undamaged) elasticity stiffness tensor.

The effective stress σ incorporates damage as

$$\sigma = (1 - D_e)C^0 : \epsilon \quad (9.11)$$

This last relation entails that the overall elastic-damage stiffness tensor C^D takes the form

$$C^D = (1 - D_e)C^0 \quad (9.12)$$

For simplicity reasons, a homogenized measure of isotropic damage variable D_e is retained coupled with the orthotropic bone behavior that will be obtained later on from a micromechanical analysis of the bone microstructure.

In order to describe the degree of damage D_e , we shall adopt the non-linear damage model for high cycle fatigue under purely elastic strains proposed by [Hambli \(2011\)](#), expressing as

$$D_e = 1 - \left(1 - \left(\frac{N}{N_f} \right)^{1/(1-\alpha_f)} \right)^{1/(1+\beta_f)} \quad (9.13)$$

where $\alpha_f = 0.2$ and $\beta_f = 0.4$ represent the material fatigue parameters of bone ([Hambli et al., 2011](#)), and N/N_f is the proportion of fatigue life with N the cycles per day and N_f the number of cycles to failure. The model expressed in (9.13) is plotted in [Figure 9.1](#); it shows the nonlinear increase of the damage variable (D_e) with the normalized number of cycles (N/N_f); close to final failure, the damage variable increase significantly, representing the critical damage.

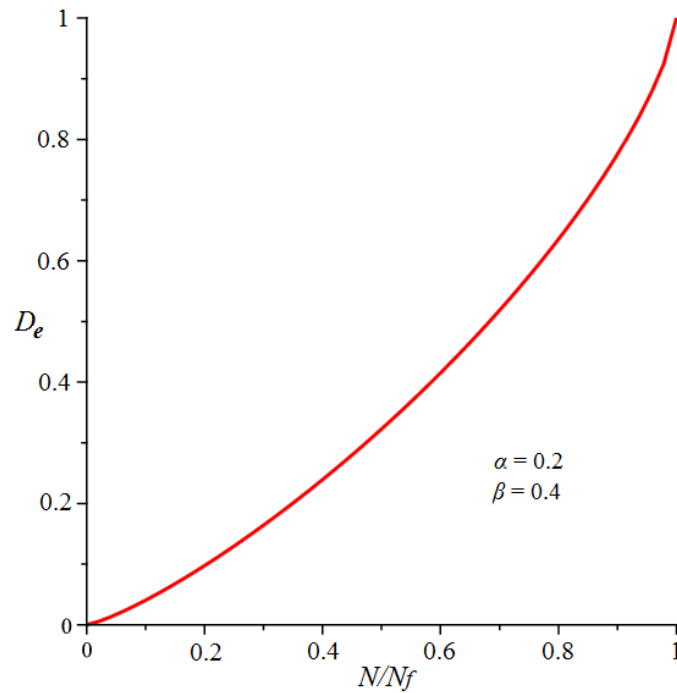


Figure 9.1: Evolution of damage variable (D_e) versus the normalized number of cycles (the ratio of the number of cycles N to the number of cycles to failure N_f).

The strain energy density, considered as the mechanical stimulus controlling the bone adaptation in the presence of damage, is pictured on [Figure 9.2](#), based on (9.10). It is noticed that when the damage density reaches its maximum value ($D_e=1$), the stimulus is set to zero while for a virgin bone tissue ($D_e=0$), the stimulus is maximum because the stiffness of the virgin material is not reduced yet.

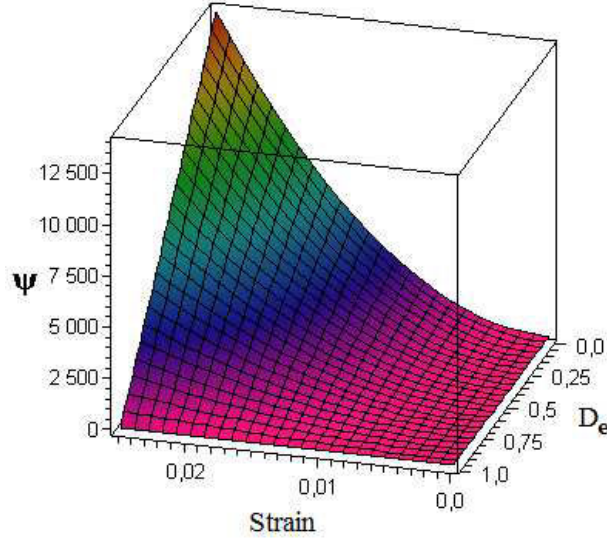


Figure 9.2: 3D plot of strain energy density coupled with damage, function

$$W = \frac{1}{2}(1 - D_e)\sigma\epsilon = \frac{1}{2}(1 - D_e)E^*\epsilon^2 \cdot$$

Under plane stress conditions, it holds that $\sigma_{zz} = \sigma_{zx} = \sigma_{zy} = 0$; Hooke's law for an orthotropic material coupled to fatigue damage then takes the following form, expressed in terms of the homogenized engineering constants (that will be subsequently determined from the trabecular bone architecture), the two Young moduli (E_x^*, E_y^*), the shear modulus G_{xy}^* and the two Poisson's ratios (ν_{xy}^* and ν_{yx}^*).

$$\begin{bmatrix} \sigma_x \\ \sigma_y \\ \sigma_{xy} \end{bmatrix} = \underbrace{(1 - D_e)C^0}_{C^D} : \epsilon = \frac{(1 - D_e)}{1 - \nu_{xy}^*\nu_{yx}^*} \begin{bmatrix} E_x^* & \nu_{yx}^*E_x^* & 0 \\ \nu_{xy}^*E_y^* & E_y^* & 0 \\ 0 & 0 & 2G_{xy}^*(1 - \nu_{xy}^*\nu_{yx}^*) \end{bmatrix} \begin{bmatrix} \epsilon_x \\ \epsilon_y \\ \epsilon_{xy} \end{bmatrix} \quad (9.14)$$

These engineering parameters shall later be computed separately from the proposed micromechanical scheme introduced in [Chapter 4](#).

As the apparent density of bone tissue changes during the process of remodelling, the elastic and shear moduli change accordingly. We next intend to establish relationships between the apparent density and the anisotropic mechanical properties of trabecular bone using a discrete homogenization method. As a consequence, an anisotropic homogenization model of cancellous bone considered as a cellular solid (modeled as two-dimensional lattices of articulated beams) shall be constructed, in order to derive its effective mechanical properties from the trabecular bone microstructural parameters.

Homogenization aims at identifying the material properties of trabecular bone at the apparent level. We adopt the viewpoint of trabecular bone as a cellular solid consisting of a quasi periodical lattice of cells having an hexagonal topology. We assume the architecture of trabecular bone consists of an elastically isotropic material.

Following the procedures exposed in [Section 4.3](#), the constitutive equation for the equivalent continuum of Cauchy stresses writes

$$\{\sigma_x, \sigma_y, \sigma_{xy}\} = [C^0] \left\{ \frac{\partial u_1}{\partial x}, \frac{\partial u_2}{\partial y}, \frac{1}{2} \left(\frac{\partial u_2}{\partial x} + \frac{\partial u_1}{\partial y} \right) \right\} \quad (9.15)$$

with $[C^0]$ the equivalent undamaged rigidity matrix, and u_1, u_2 the two components of the planar displacement field.

A 2D geometrical model of a hexagonal structure is considered as an idealized representation of trabecular bone, for which the Young's modulus, shear modulus, and Poisson's ratio are identified at the mesoscopic level. The model geometry consists of struts of length L for the inclined beams and h ($h=0.5L$) for the vertical beams with uniform trabeculae thickness t . The struts of length L are inclined with the angle $\theta = 30^\circ$. The tensile and shear moduli of trabecular bone express as power law functions of apparent density (kg/m^3), whereas the Poisson's ratio is linearly related to density, viz

$$\begin{aligned} E_x^* &= 7.8\rho^{2.72}, & E_y^* &= 2.7\rho^{2.76}, & G_{xy}^* &= 12.3\rho^{2.55}, \\ \nu_{xy}^* &= -0.0005\rho + 1.57; & \nu_{yx}^* &= -0.0002\rho + 0.69 \end{aligned} \quad (9.16)$$

Those relations are then inserted in (9.14) leading to a formulation of Hooke's law for the orthotropic plane-stress bone material in terms of apparent bone density ρ and fatigue damage D_e .

Furthermore, combining the damage definition and elastic and shear modulus evolutions in the framework of bone remodeling entail the determination of the damaged elastic and shear modulus at each location, based on the knowledge of the density. One can note that the state of anisotropy is evolving in the course of remodeling, due to the evolution of internal density and the distinct scaling laws of the moduli versus density.

We next perform structural remodelling computations of the evolution of the internal density of anisotropic bone for a sample of the human femur subjected to physiological load, in order to illustrate the powerfulness of the developed methodology.

9.4 Simulation of internal bone remodelling with damage

The shape of part of the human femur (shown in Figure 9.3 top-left) is described by B-splines, and then meshed; simulations are done with open source finite element software Freefem++ (Hecht et al. 2005), adopting the variational formulation of equilibrium equations. Let Ω be the region occupied by the effective homogenized anisotropic bone material enclosed by a boundary $\Gamma = \partial\Omega$. The border is decomposed into two disjoint parts Γ_1 and Γ_2 , where Γ_1 is the part of the boundary along which the femur is fixed, and Γ_2 the part of the boundary along which the loads P (P_1, P_2) are applied (Figure 9.3). Indeed, the load environment for bones is complex with force components resulting from joint contact, muscles, tendons, and soft tissue, and the load magnitudes and directions vary constantly as a person moves about. The load values and directions usually correspond to a static load case representing the stance phase of gait for a person weighing 80 kg. As a representative daily loading condition, the bone structure is subject to three load cases (one-legged stance, abduction, and adduction).

Remodeling simulations is presently conducted under single-loading condition. We consider static loading as a mechanical stimulus in bone remodeling with the force corresponding to the time when the foot touches the floor (case 1) which is assumed to be predominant (higher force magnitude than the other load cases). Load values are taken from [Beauré et al., 1990](#), and they are applied at the head of the femur and as the reaction of the muscles located at the great trochanter ([Figure 9.3a](#)). The first load condition $P_1=2317$ N is assigned at an angle of $\theta_1 = 24^\circ$ and the second load $P_2= 703$ N is positioned at an orientation of $\theta_2 = 28^\circ$ (the angles are given with respect to the vertical axis) with a fixed number of $N=6000$ cycles/day.

In the present work, the cycle at failure N_f is assumed to be 15,000, then the fraction of fatigue lifetime cycle is $N / N_f = 0.4$, thus the fatigue damage D_e (which is defined as the loss of stiffness) is computed from the relation in (9.13) to be equal to 0.25.

We recall that the strain tensor is given by $\epsilon(\mathbf{u}) = \frac{1}{2}((\nabla\mathbf{u}) + (\nabla\mathbf{u})^T)$. The linear elastic deformation of anisotropic bone material is described in terms of the stress tensor $\boldsymbol{\sigma}(\mathbf{u})$, the strain tensor $\epsilon(\mathbf{u})$, the displacement vector $\mathbf{u}(u_1, u_2)$, the traction vector \mathbf{P} , and the body force vector $\rho\mathbf{g}_a$ (\mathbf{g}_a is the acceleration due to gravity). Therefore, the governing field equations of the problem are the following

$$\begin{cases} \text{Div}(\boldsymbol{\sigma}(\mathbf{u})) + \rho\mathbf{g}_a = 0 & \text{in } \Omega \\ \mathbf{u} = \mathbf{0} & \text{on } \Gamma_1 \\ \boldsymbol{\sigma} \cdot \mathbf{N} = \mathbf{P} & \text{on } \Gamma_2 \end{cases} \quad (9.17)$$

The constitutive law of stress-strain relation of elasticity based damage mechanics of the anisotropic bone behavior is expressed as

$$\boldsymbol{\sigma}_{ij}(\mathbf{u}) = (1 - D_e) C_{ijkl}^0(\rho) \epsilon_{kl}(\mathbf{u}) \quad (9.18)$$

The variational formulation of the equilibrium equation is written for the purpose of the finite element discretization in weak form by multiplying the strong form of equilibrium by a test (vector) function \mathbf{v} chosen to vanish on the domain boundary, viz $\mathbf{v} = \mathbf{0}$ on $\partial\Omega$. The weak form then writes as follows: we seek the displacement field \mathbf{u} satisfying

$$\int_{\Omega} \boldsymbol{\sigma}(\mathbf{u}) : \epsilon(\mathbf{v}) dx - \int_{\Omega} \rho\mathbf{g}_a \cdot \mathbf{v} dx = \int_{\Gamma_2} \mathbf{P} \cdot \mathbf{v} ds, \quad \forall \mathbf{v}, \mathbf{v} = \mathbf{0} \text{ on } \Gamma_1 \quad (9.19)$$

After substitution in (9.19), this delivers the following variational equation

$$\int_{\Omega} (1 - D_e) \left(\left(C_{11}^0 \frac{\partial u_1}{\partial x} + C_{12}^0 \frac{\partial u_2}{\partial y} \right) \frac{\partial v_1}{\partial x} + \left(C_{21}^0 \frac{\partial u_1}{\partial x} + C_{22}^0 \frac{\partial u_2}{\partial y} \right) \frac{\partial v_2}{\partial y} \right) dx - \int_{\Omega} \rho\mathbf{g}_a \cdot \mathbf{v} dx = 0 \quad (9.20)$$

$$+ \frac{C_{33}^0}{2} \left(\frac{\partial u_1}{\partial y} + \frac{\partial u_2}{\partial x} \right) \left(\frac{\partial v_1}{\partial y} + \frac{\partial v_2}{\partial x} \right)$$

which is the basis for the subsequent FE computations.

In order to illustrate the application of anisotropic internal bone adaptation based on continuum damage mechanics in numerical computations, the proximal femur bone remodeling is predicted, considering an initial geometry with a uniform density distribution of 300 kg/m^3 . The rate of change of the apparent density of the bone at a particular location, quantity $d\rho / dt$, introduced in (9.8) shall be evaluated by the finite difference method.

The improved Euler's method is a modified method used instead of Euler forward method in order to improve the solution of the differential equation satisfied by density, using the average of the slopes of the solution curves; it is presently involved to estimate the apparent density of bone tissue at the considered region, based on a first order non-linear ordinary differential equation (9.8); the density is updated according to

$$\rho_{n+1} = \rho_n + \frac{\Delta t}{2} [f(t_n, \rho_n) + f(t_{n+1}, \rho_{n+1})] \quad (9.21)$$

involving the function $f(t_n, \rho_n)$ defined in equation (9.8), evaluated at the discrete point (t_n, ρ_n) . The second scheme contains the implicit terms, $f(t_{n+1}, \rho_{n+1})$; in order to make the second scheme explicit, we approximate ρ_{n+1} using a forward Euler, so that $\rho_{n+1} = \rho_n + \Delta t f(t_n, \rho_n)$, with $\Delta t = t_{n+1} - t_n$ the time step size (iteration). Consequently, the improved Euler scheme rewrites

$$\rho_{n+1} = \rho_n + \frac{\Delta t}{2} \underbrace{[f(t_n, \rho_n) + f(t_{n+1}, \rho_n + \Delta t f(t_n, \rho_n))]}_{d\rho} \quad (9.22)$$

The mechanical stimulus is computed from the finite element analysis according to (9.10) which rewrites in extended form as

$$W = \frac{1}{2} \left(C_{11}^D \frac{\partial u_1}{\partial x} + C_{12}^D \frac{\partial u_2}{\partial y} \right) \frac{\partial u_1}{\partial x} + \frac{1}{2} \left(C_{12}^D \frac{\partial u_1}{\partial x} + C_{22}^D \frac{\partial u_2}{\partial y} \right) \frac{\partial u_2}{\partial y} + \frac{1}{4} C_{33}^D \left(\frac{\partial u_1}{\partial y} + \frac{\partial u_2}{\partial x} \right)^2 \quad (9.23)$$

Based on the evaluation of expression (9.23), the density increment $d\rho$ for each element can be calculated from equation (9.21), and the element density is then updated as $\rho_{n+1} = \rho_n + d\rho$. As the density changes for each element, the stiffness (elastic and shear modulus and Poisson's ratio) of the continuum is updated at each new iteration as well. At the end of each iteration, the mechanical properties of each element are calculated according to equation (9.16).

In any subsequent iteration, the mechanical stimulus and its proximity to the threshold value are evaluated for each element, with the overall structural response of bone based on the biomechanically adapted stiffness computed from the previous iteration. This iterative process continues until all bone mass is in remodeling equilibrium. The remodeling solution is converged when all elements have reached one of three states: the element reaches the maximum density value, i.e. bone formation; the element density reaches the minimum value, i.e. all bone tissue has fully resorbed, or when the strain energy per unit mass of bone is equal to the reference stimulus, in which case equilibrium is reached.

It should be noted that the aforementioned models of elastic damage bone remodeling are phenomenological in nature; they describe the stimulus and the response, without taking into the very biological mechanisms taking place internally in the bone tissue.

Figure 9.3a shows the geometry and physiological static surface loads of a 2D frontal plane of a proximal femur, which is taken as the initial model in our structural remodeling analysis (the bone sample is simultaneously subjected to its own weight). The process starts with the solution of the elasticity problem, adopting a uniform density distribution chosen as 300 kg/m³. The time step is selected small enough, $\Delta t = 1$, in order not to affect the temporal sequence of the mechanical fields within the bone sample in a significant way. The combinative algorithms of both adaptive and damage remodeling change the local bone density (see Figure 9.3). After 100 iteration steps (Figure 9.3c), one can observe the formation of two high density external layers along the diaphysis of the femur, a zone of low density corresponding to the medullar channel inside the diaphysis, and a complex distribution of density of the femoral head and trochanter including three different density regions with the head surrounded by a lower density zone (low density region on the distal part of the head).

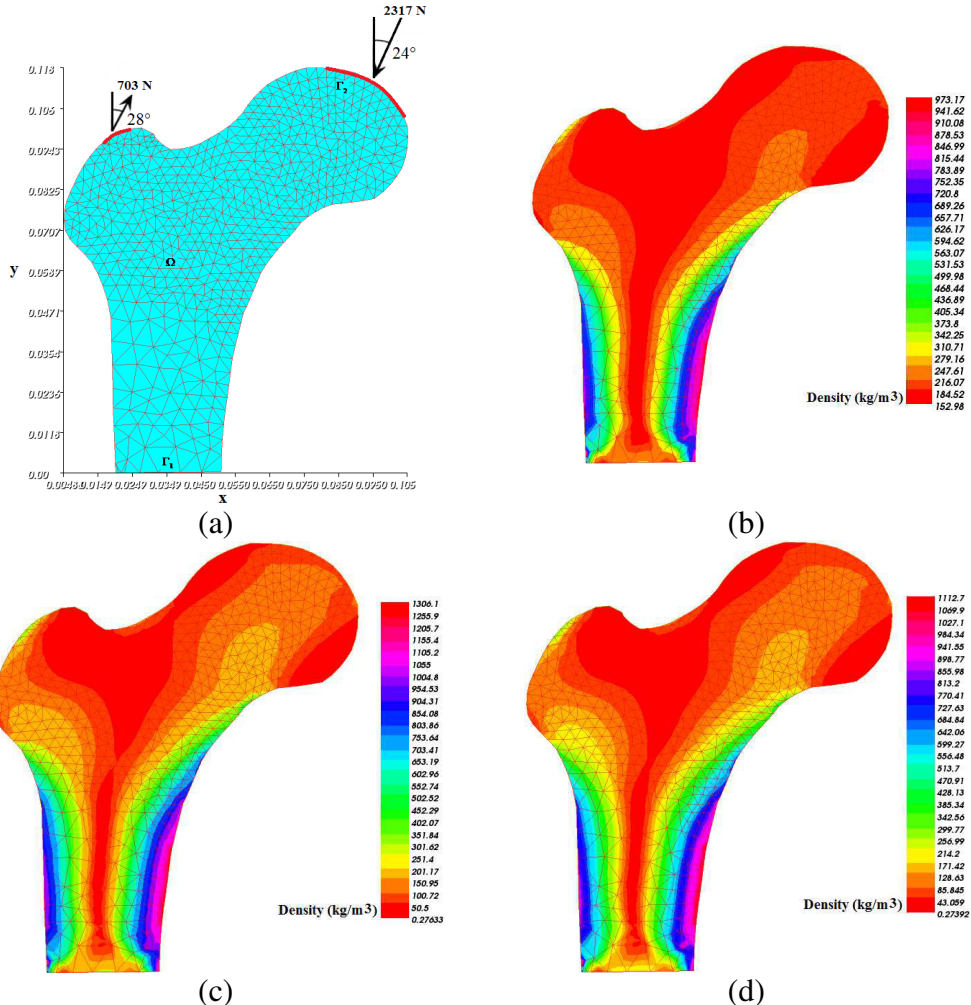


Figure 9.3: Bone density distribution of 2D model of the proximal femur. (a) Loading conditions and uniform distribution at the beginning of simulation: initial density= 300 kg/m³, (b) Bone response to simulated physiological loading after 50 days with D_e=0.25, (c) After 100 days with D_e =0.25, (d) After 100 days with D_e =0.

Density increases with the level of damage, due to the fact that the components of the rigidity matrix will be reduced, resulting in a strain increase, thus to an increase of the mechanical stimulus (strain energy), increasing in turn the driving force for bone adaptation and therefore the density. This is reflected qualitatively in equation (9.18), since damage and density act in opposite manner on the effective mechanical properties, which means that the density increase generated by damage acts as a repair mechanism at the scale of existing microcracks. By analyzing the bone density distribution after a simulation of 100 remodeling days (Figures 9.3c and d), we outline the fact that damaged and undamaged bone density distributions show similar patterns and approximately produce the same spatial distribution; however, they do not show identical values of density. The overall density is increased with the level of damage, e.g., the maximum is 1306 kg/m^3 for the damaged bone and 1112 kg/m^3 for the virgin material. This indicates that the density of undamaged bone never reaches the density of a damaged bone.

Additionally, we observe that the bone density distribution evolves with time; comparing results after 50 days (Figures 9.3b) of application of the loading with the results after 100 remodeling days (Figures 9.3c), an increase of density is observed after 100 days remodeling, with formation of new zones of density as well. Therefore, bone remodeling redistributes the bone material in response to the applied load, leading to a new bone morphology: the bone density is increased wherever the bone is highly loaded (high mechanical stimulus) and is decreased where its presence is not necessary due to less internal stress.

9.5 Conclusions

In this chapter, we developed an anisotropic internal bone remodeling model based on continuum damage mechanics theory and fatigue damage adapted to trabecular bone. The level of damage is related nonlinearly to the number of cycles, so that it is uniform within the bone sample. Trabecular bone is modeled as a cellular structure in 2D with the cell walls described as a solid isotropic material. The objective of the current chapter was then to simulate the internal remodeling within a two-dimensional model of the proximal femur, by considering an elastic-damage constitutive behavior and strain energy density as the mechanical stimulus driving density evolutions. Relying on the discrete homogenization approach, we derived an anisotropic linear elasticity constitutive law for trabecular bone at the continuum mesoscopic level, involving an anisotropic stiffness tensor. The computed stiffness coefficients are determined as explicit power functions of the effective internal density (itself a function of the morphological parameters of the selected unit cell), and they evolve with morphology as remodeling occurs, so that anisotropy changes with ongoing remodeling. The computational simulation of the remodeling process of the proximal femur head coupled to fatigue damage has been subsequently implemented. In the first phase of the simulation, the process starts with a uniform density distribution, and bone subsequently responds to simulated physiological loading over time, producing denser bone at sites of larger mechanical stimulus. One of the main results of these analyses is that an increase of fatigue damage leads to an increase of bone density, so that internal remodeling acts as a mechanism

to compensate for the loss of integrity of trabecular bone. The development of models of distributed damage coupled to internal bone remodeling is one important perspective of this work.

CHAPTER 10: CONCLUSIONS AND PERSPECTIVES

This thesis is concerned with the development of methods for the discrete homogenization of trabecular bone, described as 2D and 3D repetitive quasi-periodic beam lattices, which are substituted by an equivalent continuum with effective mechanical properties. We have successively considered the elastic static and dynamic behavior of trabecular bone. The homogenization models are additionally developed as a convenient micromechanical approach to construct the plastic yield and brittle fracture surfaces of bending-dominated periodic lattices of articulated beams considered as prototype topologies for cancellous bones.

In a second part of the thesis, bone remodeling models are constructed in order to simulate femoral bone remodeling under external physiological loading.

Our contribution focuses on two important issues: firstly, the automation of the homogenization method towards micropolar continuum and its generalization using a Timoshenko beam model rather than a model Bernoulli beam. Secondly, the development of models to simulate both internal and external bone remodeling for 2D geometries in the framework of the thermodynamics of irreversible processes, showing the influence of external mechanical stimuli on the evolution of the external shape of bone. Additionally, internal bone remodeling for 2D geometries is simulated in the context of damaged anisotropic bone elasticity, showing the influence of the external mechanical stimuli on the evolution of bone density.

We first outlined the main steps of the employed discrete homogenization method toward anisotropic micropolar continuum. The discrete asymptotic homogenization approach of centrosymmetric lattices towards a micropolar effective medium is exposed, adopting a Timoshenko beam model at the microscale scale. A three-dimensional micropolar effective continuum model is then constructed using asymptotic homogenization of 3D discrete media considering axial, shear, flexural and torsional deformations of the cell struts. The effective anisotropic classical and micropolar behavior are identified with the constitutive equations of a continuous (anisotropic) micropolar continuum.

As a specific first application of homogenization method, we addressed the issue of predicting the mechanical behavior of different woven fabric architectures using the developed homogenization approach, through which the initially discrete architecture is transformed into an equivalent homogeneous effective medium. In this regard, micropolar continuum models describing the effective mechanical behavior of woven fabric monolayers are constructed from the homogenization of an identified repetitive pattern of the textile within a representative unit cell. The interwoven yarns within the textile are represented as a network of trusses connected by nodes at their crossover points. These trusses have extensional and bending rigidities to allow for yarn stretching and flexion, and a transverse shear deformation is additionally considered. Interactions between yarns at the crossover points are captured by beam segments connecting the nodes. The woven fabric is modeled

after homogenization as an anisotropic planar continuum with two preferred material directions in the mean plane of the textile. Based on the developed methodology, the effective mechanical properties of plain weave and twill are evaluated, including their bending moduli and characteristic flexural lengths.

The core of the thesis which follows this first application to textile monolayers of the developed homogenization technique is the construction of Cosserat models of trabecular bone in 2D and 3D situations, in order to investigate microstructure-related scale effects on the macroscopic properties of bone. The cell walls of the bone microstructure are modeled as Timoshenko thick beams. Closed form expressions of the equivalent properties are obtained versus the geometrical and mechanical microparameters, accounting for the effects of bending, axial, and transverse shear deformations; torsion is additionally considered for a 3D bone geometry. The classical and micropolar effective moduli and the internal flexural and torsional lengths are identified versus the micropolar material constants. Finite element models at the local architecture of the trabeculae and at the trabecular lattice are performed to validate the results obtained from homogenization. The values of effective Young's moduli, Poisson's coefficients, shear modulus, and micropolar bending modulus computed from FE simulations show a very good agreement with those calculated by discrete homogenization. A planar linear Cosserat finite element model of a cracked bone sample has been developed on the basis of the constructed effective Cosserat continuum, in order to illustrate the microstructural effects on the macroscopic response of cancellous bone. The FE analysis of the cracked configuration evidence an important reduction of the stress concentration in the vicinity of the crack; this feature reflects the trabecular architecture of cancellous bone and the regularizing effect of the employed Cosserat elasticity model in comparison to a classical elastic continuum model.

Based on the equivalent strain energy approach, we computed from finite element analyses the effective couple-stress continuum properties of vertebral trabecular bone represented by three-dimensional periodic cellular network solid models. Boundary conditions based on combinations of displacement and traction boundary conditions applied along the outer boundaries of the bone structure are formulated, leading to the determination of both the classical and non classical components of the effective constitutive law. We further extended the analysis by modeling vertebral trabecular bone as a two-phase material consisting of bone tissue (stiff phase) forming a trabecular network and soft tissue which refers to bone marrow (soft phase) present in the pores. The effects of the presence of bone marrow on the effective trabecular bone properties are examined in terms of the computed moduli under various loading types, including uniaxial and biaxial tensile and torsion tests, shear tests, as well as bending moment tests. It is found that bone marrow contributes to reduce the effective mechanical properties of bone in the cases of uniaxial and biaxial extension tests and bending curvature tests as well. Conversely, its presence leads to increase the computed effective shear and torsion coefficients.

The static and dynamic bending and torsion behaviors of vertebral trabecular bone beam specimens have next been formulated based on the Cosserat theory, a non-classical theory capable of capturing the size-effects. Employing Hamilton principle, the governing equations

of motions for both bending and torsional have been obtained. The results obtained for the static bending problem reveal that both the deflection and rotation predicted by the micropolar model are smaller than those predicted by the classical model; the differences are very large when the beam thickness is small. Similar trends are observed for the free vibration problem, where it is shown that the natural frequency predicted by the micropolar model is higher than the frequency resulting from the classical model, the difference being significantly large only for very thin beams.

Three-dimensional models for describing the multiaxial plastic yielding and brittle fracture behavior of trabecular bone have been next developed based on the same micromechanical approaches. Accounting for the moments allows the homogenization towards the more complete micropolar framework, incorporating a microrotation in addition to the displacement, thus leading to an enhancement of the kinematics at the continuum level. Such an extension and adaptation towards a micropolar effective medium leads to the construction of the plastic yield surfaces for which the material point supports couple stresses, in addition to Cauchy-type stresses. The couple stresses develop internal work in the variation of microcurvatures, defined as the spatial gradients of the microrotation. Consequently, the plastic yield surfaces of trabecular bone are determined under the external applied couple stresses. We also constructed a size-dependent non-classical plastic yield criterion relying on micromechanical model on the basis of the reduced Cosserat theory in order to capture the size-dependency of trabecular bone structures. It is pointed out that when the characteristic size of the microscale structure is comparable to the length scale of the structure material, there is a considerable gap between the results of the classical criterion and the results of the micropolar based criterion.

In the last part of the thesis, we came across internal and external bone remodeling issues. A numerical framework has been developed to simulate the process of external bone adaptation jointly with local adaptation with respect to applied mechanical loading at both the trabecular and macroscopic levels. At the macroscopic level, a linear elastic constitutive law for trabecular bone is derived, relying on the discrete homogenization approach, whereby the continuum parameters such as stiffness evolve with morphology as remodeling occurs within bone. Internal remodeling is essentially accounted for by an evolution of the internal bone density versus the trace of the Eshelby stress; regarding external remodeling, the surface remodeling velocity is related to the driving force for growth identified as the surface divergence of Eshelby stress. The implementation of this numerical framework is quite general and can accommodate readily different material models and diverse mechanical stimuli. As a final aspect, an anisotropic internal bone remodeling model has been developed based on continuum damage mechanics theory with fatigue damage adapted to trabecular bone. This has been developed to simulate the evolution of apparent bone density within a two-dimensional model of the proximal femur, by considering an elastic-damage constitutive behavior and strain energy density as the mechanical stimulus driving density evolutions. Relying on the discrete homogenization, an anisotropic linear elasticity constitutive law for trabecular bone is derived at the continuum mesoscopic level, involving an anisotropic stiffness tensor. The computed stiffness coefficients are determined as explicit power

functions of the effective internal density (itself a function of the morphological parameters of the selected unit cell), and they evolve with morphology as remodeling occurs, so that the simulations capture anisotropy changes with ongoing remodeling.

In terms of perspectives, the micromechanical models developed in this work for textiles are particularly interesting and novel, due to the difficulty to measure such effective properties for textiles considering their discreteness. The proposed homogenization technique proves efficient, and it has a great versatility as to the topology of the textile armor, which makes it a suitable tool to explore and compare various textile architectures for both single and multilayer configurations in future developments. Other factors that have been discarded in the textile model can be incorporated in future extensions, like yarn transverse compressibility, a more accurate representation of the shape of the yarn section, and a better description of contact between yarns including friction. Large strains aspects accounting for geometrical nonlinearities have been addressed in another recent thesis in LEMTA and shall be combined with the previously mentioned points.

More importantly, the developed homogenization models for bone constitute an interesting tool for an efficient virtual experimentation of the mechanical behavior of bone internal architectures modeled as lattices endowed with diverse topologies. They can therefore be adapted to model a large diversity of repetitive representative cells of bone by which the main structural features of the trabecular microstructure can be characterized, such as tapered hexagonal and tetrakaidecahedral morphologies, or topologies acquired from microcomputed tomography. Besides these work, since trabecular bone consists of bony network of connecting rods filled with bone marrow which is actually a fluid phase, trabecular bone is likely to exhibit a viscoelastic behavior, which shall depend on the material behavior of the bone tissue as well as on the interaction between the bone trabeculae and bone marrow (solid and fluid phases). The prediction of the effective couple stress-moduli demonstrating a viscoelastic behavior will accordingly be more realistic and is planned in future works. Such micromechanically based enhanced continuum models of textiles and bones developed at the mesoscopic scale pave the way towards realistic simulations of the mechanical response of structures submitted to complex loadings at the macroscopic scale.

Other planned developments aim to improve the generalized homogenization schemes to estimate higher order elastic properties. Taking into account strain gradient effect in the mechanical formulation leads to enhance the constitutive law by a construction of the hyperstress tensor versus the second order gradient of the displacement. It is expected that the continuation of the asymptotic expansion of the kinematic variables up to second (or higher) order will lead to second-order displacement gradients effects; this may prove a convenient strategy to account for the observed stress concentrations and gradient of bone porosity, which are especially relevant at the bone / implant interface.

Moreover, we have elaborated a general methodology based on discrete homogenization to derive the effective dynamical behavior of cellular solids with an arbitrary topology that can be extended to the study of dispersion effects and wave propagation in solids endowed with a microstructure giving rise to micropolar effects. Furthermore, the approach proposed to investigate the local mesoscopic response of trabecular bone in the plastic regime can be

extended to explore the multiaxial response of bone when strain hardening takes place. More generally, developments may be considered in future works regarding the homogenization methods for the purpose of developing multi-scale computational models of elastoplastic, nonlinear viscoelastic, and hyperelastic constitutive laws for various cellular materials.

Finally, the simulations conducted for combined bone internal and external remodeling pave the way to multiscale simulations under static and dynamical loading conditions which are aimed to help medical doctors choosing appropriate procedures like implant surgery based on real morphological data. Additional features shall be mentioned especially when we simulate bone remodeling incorporating damage: the development of models of distributed damage coupled to internal bone remodeling shall prove useful in the context of tissue engineering, especially when considering ligament insertions into bone or bone to implant interfaces.

APPENDICES

Appendix A: Homogenized elastic rigidities of the 3D hexagonal orthotropic lattice

The elastic constants in the homogenized stiffness matrix express versus the geometrical and micromechanical parameters of the unit cell as follows:

$$E_{11} = \frac{E_s \pi r^2 C_t \left(3LE_s r^2 C_t^2 + L^3 C_t^2 G_s k_s + 3Lr^2 G_s k_s + 6hr^2 G_s k_s - 3Lr^2 C_t^2 G_s k_s \right)}{L_v (h + LS_t) \left(6r^2 C_t^2 h G_s k_s + 3E_s r^2 L + G_s k_s L^3 + 2hL^2 G_s k_s + 6hr^2 E_s - 2L^2 h C_t^2 G_s k_s - 6E_s hr^2 C_t^2 \right)};$$

$$E_{12} = E_{21} = \frac{E_s \pi r^2 C_t S_t \left(3E_s r^2 + G_s k_s L^2 - 3r^2 G_s k_s \right)}{L_v \left(6r^2 C_t^2 h G_s k_s + 3E_s r^2 L + G_s k_s L^3 + 2hL^2 G_s k_s + 6hr^2 E_s - 2L^2 h C_t^2 G_s k_s - 6E_s hr^2 C_t^2 \right)};$$

$$E_{22} = -\frac{E_s \pi r^2 (h + LS_t) \left(-G_s k_s L^2 + 3E_s r^2 C_t^2 + G_s k_s L^2 C_t^2 - 3r^2 G_s k_s C_t^2 - 3E_s r^2 \right)}{LL_v C_t \left(6r^2 h G_s k_s C_t^2 + 3E_s r^2 L + G_s k_s L^3 + 2hL^2 G_s k_s + 6hr^2 E_s - 2L^2 h G_s k_s C_t^2 - 6E_s hr^2 C_t^2 \right)};$$

$$E_{13} = E_{31} = E_{23} = E_{32} = 0; \quad E_{33} = \frac{E_s \pi r^2}{LC_t (h + LS_t)};$$

$$E_{44} = \frac{3}{2} \frac{E_s \pi r^4 G_s k_s C_t \left(\begin{array}{l} -6h^2 E_s r^2 - 3r^2 h^2 G_s k_s - 3L^2 r^2 G_s k_s + 6C_t^2 L^2 E_s r^2 - 4S_t h L^3 G_s k_s \\ -2C_t^2 L h^3 G_s k_s - 6C_t^2 L h E_s r^2 - 3C_t^2 h^2 E_s r^2 + 3C_t^2 r^2 h^2 G_s k_s - 6L^2 E_s r^2 \\ + 2L^4 C_t^2 G_s k_s - 2G_s k_s L^4 - 12LhS_t E_s r^2 - 6LhS_t r^2 G_s k_s - L^2 h^2 C_t^2 G_s k_s - 2L^2 h^2 G_s k_s \end{array} \right)}{L_v \left(G_s k_s L^2 + 3E_s r^2 \right) \left(\begin{array}{l} 3S_t L^3 r^2 G_s k_s - 3Lr^2 C_t^2 S_t h^2 G_s k_s + 9S_t Lr^2 h^2 G_s k_s + 6C_t^2 S_t hr^2 L^2 E_s + C_t^2 S_t h^2 L^3 G_s k_s \\ + 3r^2 h^2 LC_t^2 S_t E_s + 2C_t^2 S_t h^3 L^2 G_s k_s - 3C_t^2 h^3 r^2 G_s k_s + h^3 L^2 G_s k_s + 2h^4 LC_t^2 G_s k_s \\ + 3C_t^2 h^3 E_s r^2 + 3h^3 G_s k_s r^2 + 9hL^2 r^2 G_s k_s + 6h^2 LC_t^2 r^2 E_s - 6r^2 C_t^2 hL^2 G_s k_s \end{array} \right)};$$

$$E_{45} = \frac{3}{2} \frac{E_s \pi r^4 G_s k_s C_t \left(\begin{array}{l} -6h^2 E_s r^2 L - 6L^3 E_s r^2 - 3C_t^2 r^2 h^2 LG_s k_s + 2C_t^2 L^2 h^3 G_s k_s + 3C_t^2 h^2 E_s r^2 L - 2L^5 G_s k_s \\ -4S_t h L^4 G_s k_s + 3r^2 h^2 LG_s k_s - 2L^3 h^2 G_s k_s + 3L^3 r^2 G_s k_s + 6h^3 C_t^2 E_s r^2 \\ + 6L^3 C_t^2 E_s r^2 + C_t^2 L^3 h^2 G_s k_s - 12S_t L^2 h E_s r^2 + 6S_t r^2 hL^2 G_s k_s + 2L^5 C_t^2 G_s k_s \end{array} \right)}{L_v \left(G_s k_s L^2 + 3E_s r^2 \right) \left(\begin{array}{l} 3S_t L^3 r^2 G_s k_s - 3Lr^2 C_t^2 S_t h^2 G_s k_s + 9S_t Lr^2 h^2 G_s k_s + 6C_t^2 S_t hr^2 L^2 E_s + C_t^2 S_t h^2 L^3 G_s k_s \\ + 3r^2 h^2 LC_t^2 S_t E_s + 2C_t^2 S_t h^3 L^2 G_s k_s - 3C_t^2 h^3 r^2 G_s k_s + h^3 L^2 G_s k_s + 2h^4 LC_t^2 G_s k_s \\ + 3C_t^2 h^3 E_s r^2 + 3h^3 G_s k_s r^2 + 9hL^2 r^2 G_s k_s + 6h^2 LC_t^2 r^2 E_s - 6r^2 C_t^2 hL^2 G_s k_s \end{array} \right)};$$

$$E_{54} = \frac{3}{2} \frac{E_s \pi r^4 G_s k_s \left(\begin{array}{l} 3S_t C_t^2 r^2 h^2 G_s k_s - 3h^2 r^2 S_t G_s k_s + 2G_s k_s L^4 S_t C_t^2 - 2S_t C_t^2 h^3 LG_s k_s + 6L^2 S_t C_t^2 E_s r^2 - S_t C_t^2 L^2 h^2 G_s k_s \\ - 6S_t C_t^2 hLE_s r^2 - 3S_t C_t^2 h^2 E_s r^2 - 3L^2 r^2 S_t G_s k_s + 6LhC_t^2 r^2 G_s k_s + 2G_s k_s L^3 hC_t^2 + 6LhC_t^2 E_s r^2 - 6Lr^2 hG_s k_s \end{array} \right)}{L_v LC_t \left(G_s k_s L^2 + 3E_s r^2 \right) \left(\begin{array}{l} 6r^2 LhS_t G_s k_s + 3r^2 h^2 C_t^2 E_s + h^2 L^2 C_t^2 G_s k_s + 3r^2 h^2 G_s k_s \\ + 6LhC_t^2 E_s r^2 + 2C_t^2 h^3 LG_s k_s + 3L^2 r^2 G_s k_s - 3C_t^2 h^2 r^2 G_s k_s \end{array} \right)};$$

$$E_{55} = \frac{3}{2} \frac{E_s \pi r^4 G_s k_s \left(\begin{array}{l} C_t^2 S_t L^2 h^2 G_s k_s - 3S_t C_t^2 r^2 h^2 G_s k_s + 2S_t Lh^3 C_t^2 G_s k_s + 6C_t^2 S_t L^2 E_s r^2 + 3r^2 h^2 S_t G_s k_s + 2S_t C_t^2 L^4 G_s k_s \\ + 3L^2 S_t r^2 G_s k_s + 3C_t^2 S_t h^2 E_s r^2 + 6S_t C_t^2 hE_s r^2 L - 6LhC_t^2 r^2 G_s k_s + 2G_s k_s L^3 hC_t^2 + 6LhC_t^2 E_s r^2 + 6Lr^2 hG_s k_s \end{array} \right)}{L_v LC_t \left(G_s k_s L^2 + 3E_s r^2 \right) \left(\begin{array}{l} 6r^2 LhS_t G_s k_s + 3r^2 h^2 C_t^2 E_s + h^2 L^2 C_t^2 G_s k_s + 3r^2 h^2 G_s k_s \\ + 6LhC_t^2 E_s r^2 + 2C_t^2 h^3 LG_s k_s + 3L^2 r^2 G_s k_s - 3C_t^2 h^2 r^2 G_s k_s \end{array} \right)};$$

$$\begin{aligned}
E_{66} &= \frac{3}{2} \frac{E_s \pi r^4 G_s k_s \left(\begin{aligned} &6S_t h E_s r^2 L_v + 9S_t L E_s r^2 L_v + L_v^2 h^2 S_t G_s k_s - 3L^2 S_t C_t^2 E_s r^2 + 2S_t h^3 L_v G_s k_s \\ &+ 3L^3 S_t L_v G_s k_s + 3E_s r^2 h^2 S_t + S_t L^2 L_v^2 G_s k_s - L_v^2 S_t L^2 C_t^2 G_s k_s + 3S_t L^2 E_s r^2 \\ &+ 6h E_s r^2 L_v - 6Lh C_t^2 E_s r^2 - 2Lh L_v C_t^2 G_s k_s + 6Lh E_s r^2 + 2Lh L_v^2 G_s k_s + 2L^2 h L_v G_s k_s \end{aligned} \right)}{L_v L C_t \left(G_s k_s L^2 + 3E_s r^2 \right) \left(\begin{aligned} &2Lh S_t L_v^2 G_s k_s + 6Lh S_t E_s r^2 + L^3 G_s k_s L_v + 3h^2 E_s r^2 + 3L^2 E_s r^2 + 3E_s r^2 L L_v \\ &+ 2h^3 L_v G_s k_s + 6h E_s r^2 L_v + h^2 L_v^2 G_s k_s + L^2 L_v^2 G_s k_s - 3L^2 C_t^2 E_s r^2 - L^2 C_t^2 L_v^2 G_s k_s \end{aligned} \right)}; \\
E_{67} &= \frac{3}{2} \frac{E_s \pi r^4 G_s k_s \left(\begin{aligned} &L^3 S_t L_v G_s k_s - 6S_t h E_s r^2 L_v + 3S_t L E_s r^2 L_v + S_t L_v^2 L^2 C_t^2 G_s k_s - 2S_t h^3 L_v G_s k_s \\ &+ 3S_t L^2 C_t^2 E_s r^2 - S_t L^2 L_v^2 G_s k_s - 3E_s r^2 h^2 S_t - 3S_t L^2 E_s r^2 - L_v^2 h^2 S_t G_s k_s \\ &+ 2L^2 h L_v G_s k_s + 2Lh L_v^2 C_t^2 G_s k_s + 6Lh C_t^2 E_s r^2 + 6h E_s r^2 L_v - 6Lh E_s r^2 - 2Lh L_v^2 G_s k_s \end{aligned} \right)}{L_v L C_t \left(G_s k_s L^2 + 3E_s r^2 \right) \left(\begin{aligned} &2Lh S_t L_v^2 G_s k_s + 6Lh S_t E_s r^2 + L^3 G_s k_s L_v + 3h^2 E_s r^2 \\ &+ 3L^2 E_s r^2 + 3E_s r^2 L L_v + 2h^3 L_v G_s k_s + 6h E_s r^2 L_v \\ &+ h^2 L_v^2 G_s k_s + L^2 L_v^2 G_s k_s - 3L^2 C_t^2 E_s r^2 - L^2 C_t^2 L_v^2 G_s k_s \end{aligned} \right)}; \\
E_{76} &= -\frac{3}{2} \frac{E_s \pi r^4 G_s k_s \left(\begin{aligned} &-2Lh L_v^2 S_t G_s k_s - 6Lh S_t E_s r^2 + 2h^3 L_v G_s k_s - 3L^2 E_s r^2 + 3E_s r^2 L L_v + L^3 G_s k_s L_v \\ &+ 6h E_s r^2 L_v - L^2 L_v^2 G_s k_s - 3h^2 E_s r^2 - h^2 L_v^2 G_s k_s + 3L^2 C_t^2 E_s r^2 + L^2 C_t^2 L_v^2 G_s k_s \end{aligned} \right)}{L C_t \left(G_s k_s L_v^2 + 3E_s r^2 \right) \left(\begin{aligned} &2h^4 L_v G_s k_s + h^3 L_v^2 G_s k_s + S_t L^4 L_v G_s k_s + 9h L^2 E_s r^2 + h L^3 L_v G_s k_s \\ &+ 9S_t h^2 E_s r^2 L + S_t L^3 L_v^2 G_s k_s + 3S_t L^3 E_s r^2 - S_t C_t^2 L^3 L_v^2 G_s k_s - 3S_t C_t^2 L^3 E_s r^2 \\ &- 3C_t^2 h L^2 L_v^2 G_s k_s - 9C_t^2 h L^2 E_s r^2 + 2S_t L h^3 L_v G_s k_s + 3L^2 S_t E_s r^2 L_v + 3h E_s r^2 L L_v \\ &+ 3h^3 E_s r^2 + 3h L^2 L_v^2 G_s k_s + 6Lh S_t E_s r^2 L_v + 3S_t h^2 L_v^2 L G_s k_s + 6E_s L_v r^2 h^2 \end{aligned} \right)}; \\
E_{77} &= \frac{3}{2} \frac{E_s \pi r^4 G_s k_s \left(\begin{aligned} &18Lh S_t E_s r^2 + 6Lh L_v^2 S_t G_s k_s + 3h^2 L_v^2 G_s k_s + L^3 G_s k_s L_v + 3E_s r^2 L L_v + 3L^2 L_v^2 G_s k_s \\ &+ 9h^2 E_s r^2 + 6h E_s r^2 L_v + 2h^3 L_v G_s k_s + 9L^2 E_s r^2 - 3L^2 C_t^2 L_v^2 G_s k_s - 9L^2 C_t^2 E_s r^2 \end{aligned} \right)}{L C_t \left(G_s k_s L_v^2 + 3E_s r^2 \right) \left(\begin{aligned} &2h^4 L_v G_s k_s + h^3 L_v^2 G_s k_s + S_t L^4 L_v G_s k_s + 9h L^2 E_s r^2 + h L^3 L_v G_s k_s \\ &+ 9S_t h^2 E_s r^2 L + S_t L^3 L_v^2 G_s k_s + 3S_t L^3 E_s r^2 - S_t C_t^2 L^3 L_v^2 G_s k_s - 3S_t C_t^2 L^3 E_s r^2 \\ &- 3C_t^2 h L^2 L_v^2 G_s k_s - 9C_t^2 h L^2 E_s r^2 + 2S_t L h^3 L_v G_s k_s + 3L^2 S_t E_s r^2 L_v + 3h E_s r^2 L L_v \\ &+ 3h^3 E_s r^2 + 3h L^2 L_v^2 G_s k_s + 6Lh S_t E_s r^2 L_v + 3S_t h^2 L_v^2 L G_s k_s + 6E_s L_v r^2 h^2 \end{aligned} \right)}; \\
E_{88} &= \frac{3}{2} \frac{E_s \pi r^4 G_s k_s \left(9C_t^2 E_s r^2 L + 3C_t^2 L_v^2 L G_s k_s + L^2 G_s k_s L_v + 3E_s r^2 L_v \right)}{L C_t \left(G_s k_s L_v^2 + 3E_s r^2 \right) (h + L S_t) \left(3C_t^2 E_s r^2 L + C_t^2 L_v^2 L G_s k_s + L^2 G_s k_s L_v + 3E_s r^2 L_v \right)}; \\
E_{89} &= -\frac{3}{2} \frac{E_s \pi r^4 G_s k_s \left(L^2 G_s k_s L_v - C_t^2 L_v^2 L G_s k_s - 3C_t^2 E_s r^2 L + 3E_s r^2 L_v \right)}{L C_t \left(G_s k_s L_v^2 + 3E_s r^2 \right) (h + L S_t) \left(3C_t^2 E_s r^2 L + C_t^2 L_v^2 L G_s k_s + L^2 G_s k_s L_v + 3E_s r^2 L_v \right)}; \\
E_{98} &= \frac{3}{2} \frac{E_s \pi r^4 G_s k_s C_t \left(L^2 G_s k_s L_v - C_t^2 L_v^2 L G_s k_s - 3C_t^2 E_s r^2 L + 3E_s r^2 L_v \right)}{L_v \left(G_s k_s L^2 + 3E_s r^2 \right) (h + L S_t) \left(3C_t^2 E_s r^2 L + C_t^2 L_v^2 L G_s k_s + L^2 G_s k_s L_v + 3E_s r^2 L_v \right)}; \\
E_{99} &= \frac{3}{2} \frac{E_s \pi r^4 G_s k_s C_t \left(3L^2 G_s k_s L_v + 9E_s r^2 L_v + 3C_t^2 E_s r^2 L + C_t^2 L_v^2 L G_s k_s \right)}{L_v \left(G_s k_s L^2 + 3E_s r^2 \right) (h + L S_t) \left(3C_t^2 E_s r^2 L + C_t^2 L_v^2 L G_s k_s + L^2 G_s k_s L_v + 3E_s r^2 L_v \right)}; \\
K_{11} &= -\frac{1}{4} \frac{\pi r^4 C_t G_s \left(\begin{aligned} &-2L_v C_t^2 G_s^2 L k_s - 6E_s L h L_v C_t^2 G_s k_s - 6C_t^2 L E_s r^2 G_s - L E_s L_v^2 G_s k_s - 3L_v E_s^2 L h k_s \\ &- 3L E_s^2 r^2 - 6h E_s^2 r^2 - 2h L_v^2 E_s G_s k_s + L L_v^2 E_s C_t^2 G_s k_s + 3L E_s^2 h C_t^2 L_v k_s + 3L E_s^2 C_t^2 r^2 \end{aligned} \right)}{L_v (h + L S_t) \left(\begin{aligned} &3C_t^2 h E_s^2 r^2 + L_v^2 C_t^2 E_s h G_s k_s + L L_v^2 G_s^2 k_s + 3L_v E_s L h G_s k_s + 3L E_s r^2 G_s \\ &+ 2h L_v^2 G_s^2 k_s + 6h E_s r^2 G_s - 2h L_v^2 G_s^2 C_t^2 k_s - 6h C_t^2 E_s r^2 G_s \end{aligned} \right)};
\end{aligned}$$

$$K_{12} = K_{21} = -\frac{1}{4} \frac{\pi r^4 C_t S_t G_s (E_s - 2G_s) (3E_s r^2 + L_v^2 G_s k_s + 3hL_v E_s k_s)}{L_v \left(3C_t^2 hE_s^2 r^2 + L_v^2 C_t^2 E_s hG_s k_s + LL_v^2 G_s^2 k_s + 3L_v E_s LhG_s k_s + 3LE_s r^2 G_s \right. \\ \left. + 2hL_v^2 G_s^2 k_s + 6hE_s r^2 G_s - 2hL_v^2 G_s^2 C_t^2 k_s - 6hC_t^2 E_s r^2 G_s \right)};$$

$$K_{22} = \frac{1}{4} \frac{\pi r^4 G_s (h + LS_t) (2G_s - 2C_t^2 G_s + C_t^2 E_s) (3E_s r^2 + L_v^2 G_s k_s + 3hE_s k_s L_v)}{LL_v C_t \left(3C_t^2 hE_s^2 r^2 + L_v^2 C_t^2 E_s hG_s k_s + LL_v^2 G_s^2 k_s + 3L_v E_s LhG_s k_s + 3LE_s r^2 G_s \right. \\ \left. + 2hL_v^2 G_s^2 k_s + 6hE_s r^2 G_s - 2hL_v^2 G_s^2 C_t^2 k_s - 6hC_t^2 E_s r^2 G_s \right)};$$

$$K_{13} = K_{31} = K_{23} = K_{32} = 0; K_{33} = \frac{1}{2} \frac{G_s \pi r^4}{LC_t (h + LS_t)};$$

$$K_{44} = \frac{1}{4} \frac{\pi r^4 C_t E_s \left(3LE_s^2 C_t^2 r^2 + LL_v^2 E_s C_t^2 G_s k_s + 6E_s hLC_t^2 L_v G_s k_s + 4hL_v^2 G_s^2 k_s + 6LE_s r^2 G_s + 2LL_v^2 G_s^2 k_s \right. \\ \left. + 12hE_s r^2 G_s + 12hLL_v G_s^2 k_s - 6C_t^2 LE_s r^2 G_s - 2L_v^2 C_t^2 G_s^2 Lk_s - 12LG_s^2 hC_t^2 L_v k_s \right)}{L_v (h + LS_t) \left(4hL_v^2 G_s^2 C_t^2 k_s + 12hC_t^2 E_s r^2 G_s + 6LE_s hL_v G_s k_s + 3LE_s^2 r^2 + 6hE_s^2 r^2 \right. \\ \left. + 2hL_v^2 E_s G_s k_s + LE_s L_v^2 G_s k_s - 6C_t^2 E_s^2 hr^2 - 2L_v^2 C_t^2 E_s hG_s k_s \right)};$$

$$K_{45} = K_{54} = -\frac{1}{4} \frac{\pi r^4 C_t S_t E_s (E_s - 2G_s) (6hL_v G_s k_s + 3E_s r^2 + L_v^2 G_s k_s)}{L_v \left(4hL_v^2 G_s^2 C_t^2 k_s + 12hC_t^2 E_s r^2 G_s + 6LE_s hL_v G_s k_s + 3LE_s^2 r^2 + 6hE_s^2 r^2 \right. \\ \left. + 2hL_v^2 E_s G_s k_s + LE_s L_v^2 G_s k_s - 6C_t^2 E_s^2 hr^2 - 2L_v^2 C_t^2 E_s hG_s k_s \right)};$$

$$K_{55} = -\frac{1}{4} \frac{\pi r^4 E_s (h + LS_t) (C_t^2 E_s - E_s - 2C_t^2 G_s) (6hL_v G_s k_s + 3E_s^2 r^2 + L_v^2 G_s k_s)}{LL_v C_t \left(4hL_v^2 G_s^2 C_t^2 k_s + 12hC_t^2 E_s r^2 G_s + 6LE_s hL_v G_s k_s + 3LE_s^2 r^2 + 6hE_s^2 r^2 \right. \\ \left. + 2hL_v^2 E_s G_s k_s + LE_s L_v^2 G_s k_s - 6C_t^2 E_s^2 hr^2 - 2L_v^2 C_t^2 E_s hG_s k_s \right)};$$

$$K_{66} = \frac{1}{4} \frac{\pi r^4 E_s (h + LS_t)}{LL_v C_t (L + 2h)}; K_{67} = K_{76} = 0; K_{77} = \frac{1}{4} \frac{\pi r^4 E_s}{LC_t (h + LS_t)};$$

$$K_{88} = \frac{1}{4} \frac{\pi r^4 E_s}{LC_t (h + LS_t)}; K_{89} = K_{98} = 0; K_{99} = \frac{1}{4} \frac{\pi r^4 C_t E_s}{L_v (h + LS_t)}.$$

Appendix B: Classical and micropolar elastic constants of bone in terms of parameters based on morphology-age relationships

The homogenized classical and micropolar elastic constants are expressed versus the geometrical and micromechanical parameters of vertebral trabecular bone architecture as follows:

$$E_x^* = E_y^* = \frac{\sqrt{3}\pi D_h^4 E_s}{\left(4L_v^2 + \frac{3E_s D_h^2}{G_s k_s} + 9D_h^2\right) L_v L_h}, E_z^* = \frac{1}{9} \frac{\sqrt{3}\pi D_v^2 E_s}{L_v^2}, G_{xy}^* = G_{yx}^* = \frac{1}{4} \frac{\sqrt{3}\pi D_h^4 E_s G_s k_s}{L_v L_h (3E_s D_h^2 + 4G_s k_s L_v + 3D_h^2 G_s k_s)},$$

$$G_{xz}^* = G_{zx}^* = \frac{(D_h^4 D_v^4 \sqrt{3}\pi E_s G_s k_s)}{L_v (9D_h^4 D_v^2 E_s L_v + 12L_h^2 D_h^4 G_s k_s L_v + 12D_v^4 E_s D_h^2 L_h + 16D_v^4 L_v^2 L_h G_s k_s)},$$

$$E_{tor-x}^* = \frac{1}{24} \frac{\sqrt{3}\pi D_h^4 E_s G_s}{(3E_s + 2G_s) L_v L_h}, E_{tor-y}^* = \frac{1}{24} \frac{\left(3E_s D_v^4 L_v + \frac{3}{4} \frac{D_h^4 E_s D_v^2}{L_h k_s} + L_h D_h^4 G_s\right) \sqrt{3}\pi G_s E_s D_h^4}{L_v L_h \left(6E_s L_v G_s D_v^4 + E_s^2 D_v^4 L_v + \frac{9}{4} \frac{D_h^4 E_s^2 D_v^2}{L_h k_s} + 3L_h D_h^4 E_s G_s + \frac{3}{2} \frac{D_h^4 G_s E_s D_v^2}{L_h k_s} + 2L_h D_h^4 G_s^2\right)},$$

$$E_{tor-z}^* = \frac{1}{72} \frac{\sqrt{3}\pi G_s D_v^4}{L_v^2},$$

$$\kappa_{xy} = \kappa_{yx} = \frac{1}{4} \frac{\sqrt{3}\pi D_h^4 E_s G_s k_s}{(4G_s k_s L_v^2 + 3E_s D_h^2) L_v L_h}, \mu_{xy}^* = \mu_{yx}^* = \frac{1}{8} \frac{\sqrt{3}\pi D_h^4 E_s G_s k_s (3E_s D_h^2 + 4G_s k_s L_v - 3D_h^2 G_s k_s)}{L_v L_h (24E_s D_h^2 G_s k_s L_v^2 + 9E_s^2 D_h^4 + 16L_h^2 G_s^2 k_s^2 + 12D_h^2 G_s^2 k_s^2 L_v + 9D_h^4 E_s G_s k_s)},$$

$$\kappa_{xz} = \frac{1}{4} \frac{\sqrt{3}\pi D_h^4 E_s G_s k_s}{(4G_s k_s L_v^2 + 3E_s D_h^2) L_v L_h}, \kappa_{zx} = \frac{1}{3} \frac{\sqrt{3}\pi D_v^4 E_s G_s k_s}{(4G_s k_s L_h^2 + 3E_s D_v^2) L_v^2},$$

$$\mu_{xz}^* = \frac{1}{8} \frac{\sqrt{3}\pi D_h^4 E_s G_s k_s (-9D_h^4 E_s D_v^2 L_v - 12L_h^2 D_h^4 G_s k_s L_v + 16D_v^4 L_v^2 L_h G_s k_s + 12D_v^4 E_s D_h^2 L_h)}{L_v L_h (36D_h^4 E_s D_v^2 G_s k_s L_v^3 + 48L_h^2 D_h^4 G_s^2 k_s^2 L_v^3 + 96D_v^4 E_s D_h^2 L_h G_s k_s L_v^2 + 64D_v^4 L_v^4 L_h G_s^2 k_s^2 + 27E_s^2 D_h^6 D_v^2 L_v + 36E_s D_h^6 L_h^2 G_s k_s L_v + 36E_s^2 D_h^4 D_v^4 L_h)},$$

$$\mu_{zx}^* = -\frac{1}{6} \frac{\sqrt{3}\pi D_v^4 E_s G_s k_s (-9D_h^4 E_s D_v^2 L_v - 12L_h^2 D_h^4 G_s k_s L_v + 16D_v^4 L_v^2 L_h G_s k_s + 12D_v^4 E_s D_h^2 L_h)}{L_v^2 (72D_h^4 E_s D_v^2 L_h^2 G_s k_s L_v + 48L_h^4 D_h^4 G_s^2 k_s^2 L_v + 48D_v^4 E_s D_h^2 L_h^3 G_s k_s + 64D_v^4 L_v^4 L_h G_s^2 k_s^2 + 27E_s^2 D_h^6 D_v^4 L_v + 36E_s D_v^6 D_h^2 L_h + 48E_s D_v^6 L_v^2 L_h G_s k_s)},$$

$$\gamma_{xy} = \frac{\sqrt{3}}{384} \frac{\pi D_h^4 E_s (24L_h^2 D_h^4 G_s^2 k_s + 18D_h^4 E_s D_v^2 G_s + 16L_v G_s^2 k_s D_v^4 L_h + 3D_h^4 E_s^2 D_v^2 + 24E_s D_v^4 L_v L_h G_s k_s + 4L_h^2 D_h^4 E_s G_s k_s)}{L_h L_v (6D_h^4 E_s D_v^2 G_s + 3D_h^4 E_s^2 D_v^2 + 8L_h^2 D_h^4 G_s^2 k_s + 4L_h^2 D_h^4 E_s G_s k_s + 16E_s D_v^4 L_v L_h G_s k_s)},$$

$$\gamma_{yx} = \frac{\sqrt{3}}{384} \frac{\pi D_h^4 E_s (3D_h^4 E_s D_v^2 + 24D_v^4 L_v L_h G_s k_s + 4L_h^2 D_h^4 G_s k_s) (E_s + 6G_s)}{L_h L_v (6D_h^4 E_s D_v^2 G_s + 3D_h^4 E_s^2 D_v^2 + 8L_h^2 D_h^4 G_s^2 k_s + 4L_h^2 D_h^4 E_s G_s k_s + 16E_s D_v^4 L_v L_h G_s k_s)},$$

$$\beta_{xy} = \beta_{yx} = -\frac{\sqrt{3}}{384} \frac{\pi D_h^4 E_s (3D_h^4 E_s D_v^2 + 24D_v^4 L_v L_h G_s k_s + 4L_h^2 D_h^4 G_s k_s) (E_s - 2G_s)}{L_h L_v (6D_h^4 E_s D_v^2 G_s + 3D_h^4 E_s^2 D_v^2 + 8L_h^2 D_h^4 G_s^2 k_s + 4L_h^2 D_h^4 E_s G_s k_s + 16E_s D_v^4 L_v L_h G_s k_s)},$$

$$\gamma_{yz} = \frac{1}{192} \frac{\sqrt{3}\pi D_h^4 E_s}{L_v L_h}, \gamma_{zy} = \frac{1}{144} \frac{\sqrt{3}\pi D_v^4 E_s}{L_v^2}, \gamma_{zx} = \frac{1}{144} \frac{\sqrt{3}\pi D_v^4 E_s}{L_v^2}, \gamma_{xz} = \frac{1}{192} \frac{\sqrt{3}\pi D_h^4 E_s}{L_v L_h}.$$

$$\beta_{yz} = \beta_{zy} = \beta_{zx} = \beta_{xz} = 0.$$

where $E_{x,y,z}^*$ are the effective Young's moduli extracted from the compliance matrix

$$[S^{eff}] = [E]^{-1} \text{ as } E_x^* = 1/S_{11}^{eff}, E_y^* = 1/S_{22}^{eff}, \text{ and } E_z^* = 1/S_{33}^{eff}, \text{ respectively. The coefficients}$$

$E_{tor-x,y,z}^*$ are the effective homogenized torsional elastic moduli derived from the inverse of

$$\text{the curvature tensor } [S_{tor}^{eff}] = [K]^{-1}, \text{ as } E_{tor-x}^* = 1/S_{tor-11}^{eff}, E_{tor-y}^* = 1/S_{tor-22}^{eff}, \text{ and } E_{tor-z}^* = 1/S_{tor-33}^{eff},$$

respectively.

The characteristic lengths for bending and torsion are given from the homogenized stiffness matrix equation as

$$\begin{aligned}
 l_{b_{xy}} &= \frac{\sqrt{3}}{24} \sqrt{\frac{3E_s D_h^2 + 4G_s k_s L_v^2 + 3D_h^2 G_s k_s}{G_s k_s}}, \quad l_{t_{xy}}^* = \frac{\sqrt{6}}{24} \sqrt{\frac{3E_s D_h^2 + 4G_s k_s L_v^2 + 3D_h^2 G_s k_s}{G_s k_s}}, \\
 l_{b_{xz}} &= \frac{\sqrt{6}}{96} \frac{1}{D_v^2} \sqrt{\frac{(9D_h^4 D_v^2 L_v E_s + 12L_h^2 D_h^4 G_s k_s L_v + 12D_h^4 E_s D_h^2 L_h + 16L_v^2 D_h^4 L_h G k_s)(24E_s D_h^4 L_v L_h G_s k_s + 16L_v G_s^2 D_h^4 L_h k_s + 24L_h^2 D_h^4 G_s^2 k_s + 4L_h^2 D_h^4 E_s G_s k_s + 3D_h^4 E_s^2 D_v^2 + 18D_h^4 E_s D_v^2 G_s)}{L_h G_s k_s (6D_h^4 E_s D_v^2 G_s + 3D_h^4 E_s^2 D_v^2 + 8L_h^2 D_h^4 G_s^2 k_s + 4L_h^2 D_h^4 E_s G_s k_s + 16E_s D_h^4 L_v L_h G_s k_s)}}, \\
 l_{t_{xz}} &= \frac{\sqrt{6}}{24} \frac{1}{D_v^2} \sqrt{\frac{(9D_h^4 D_v^2 L_v E_s + 12L_h^2 D_h^4 G_s k_s L_v + 12D_h^4 E_s D_h^2 L_h + 16L_v^2 D_h^4 L_h G k_s)(8D_h^4 L_v L_h G_s k_s + 4L_h^2 D_h^4 G_s k_s + 3D_h^4 E_s D_v^2)}{L_h k_s (6D_h^4 E_s D_v^2 G_s + 3D_h^4 E_s^2 D_v^2 + 8L_h^2 D_h^4 G_s^2 k_s + 4L_h^2 D_h^4 E_s G_s k_s + 16E_s D_h^4 L_v L_h G_s k_s)}}, \\
 l_{b_{yz}} &= \frac{\sqrt{6}}{96} \frac{1}{D_v^2} \sqrt{\frac{(9D_h^4 D_v^2 L_v E_s + 12L_h^2 D_h^4 G_s k_s L_v + 12D_h^4 E_s D_h^2 L_h + 16L_v^2 D_h^4 L_h G k_s)(6G_s + E_s)(24D_h^4 L_v L_h G_s k_s + 4L_h^2 D_h^4 G_s k_s + 3D_h^4 E_s D_v^2)}{L_h G_s k_s (6D_h^4 E_s D_v^2 G_s + 3D_h^4 E_s^2 D_v^2 + 8L_h^2 D_h^4 G_s^2 k_s + 4L_h^2 D_h^4 E_s G_s k_s + 16E_s D_h^4 L_v L_h G_s k_s)}}, \\
 l_{t_{yz}} &= \frac{\sqrt{6}}{24} \frac{1}{D_v^2} \sqrt{\frac{(9D_h^4 D_v^2 L_v E_s + 12L_h^2 D_h^4 G_s k_s L_v + 12D_h^4 E_s D_h^2 L_h + 16L_v^2 D_h^4 L_h G k_s)(24D_h^4 L_v L_h G_s k_s + 3D_h^4 E_s D_v^2 + 4L_h^2 D_h^4 G_s k_s)}{L_h k_s (6D_h^4 E_s D_v^2 G_s + 3D_h^4 E_s^2 D_v^2 + 8L_h^2 D_h^4 G_s^2 k_s + 4L_h^2 D_h^4 E_s G_s k_s + 16E_s D_h^4 L_v L_h G_s k_s)}}.
 \end{aligned}$$

REFERENCES

- Adachi, T., Tomita, Y., Tanaka, M., 1998. Computational simulation of deformation behavior of 2D-lattice continuum. *International Journal of Mechanical Sciences* 40, 857–866.
- Ambrosi, D., Guana, F., 2007. Stress modulated growth. *Mathematics and Mechanics of Solids* 12(3), 319-342.
- Ashman, R.B., Rho, J.Y., Turner, C.H., 1989. Anatomical variation of orthotropic elastic moduli of the proximal tibia. *Journal of Biomechanics* 22, 895–900.
- Ashman, R.B., Turner, C.H., Cowin, S.C., 1986. Ultrasonic technique for the measurement of the structural elastic modulus of cancellous bone. *Transactions of the Orthopedic Research Society* 43.
- Assidi, M., Ben Boubaker, B., Ganghoffer, J.F., 2011. Equivalent properties of monolayer fabric from mesoscopic modelling strategies. *International Journal of Solids and Structures* 48, 2920–2930.
- Assidi, M., Dos Reis, F., Ganghoffer J.F., 2011. Equivalent mechanical properties of biological membranes from lattice homogenization. *Journal of the Mechanical Behavior of Biomedical Materials* 4(8),1833-1845.
- Badiche, X., Forest, S., Guibert, T., Bienvenu, Y., Bartout, J.-D., Ienny, P., Croset, M., Bernet, H., 2000. Mechanical properties and non-homogeneous deformation of open-cell nickel foams: application of the mechanics of cellular solids and of porous materials. *Materials Science and Engineering A* 289, 276–288.
- Baker, W.E., Togami, T.C., Weydert J.C., 1998. Static and dynamic properties of high density metal honeycombs. *International Journal of Impact Engineering* 21(3), 149–163.
- Bakhvalov, N.S., Panasenko, G.P., 1989. *Homogenization Averaging Processes in Periodic Media*. Kluwer Academic Publishing, Dordrecht.
- Banerjee, S., Bhaskar, A., 2005. Free vibration of cellular structures using continuum modes. *Journal of Sound and Vibration* 287(1–2), 77–100.
- Banerjee, S., Bhaskar, A., 2009. The applicability of the effective medium theory to the dynamics of cellular beams. *International Journal of Mechanical Sciences* 51, 598–608.
- Banse, X., Sims, T.J., Bailey, A.J., 2002. Mechanical properties of adult vertebral cancellous bone: correlation with collagen intermolecular cross-links. *Journal of Bone and Mineral Research* 17(9), 1621-1628.
- Baseau, E., 2003. Finite deformation of elastic–plastic filamentary networks. *International Journal of Nonlinear Mechanics* 38, 1473– 1479.
- Bayraktar, H.H., Gupta, A., Kwon, R.Y., Papadopoulos, P., and Keaveny, T.M., 2004. The Modified Super-Ellipsoid yield criterion for human trabecular bone. *Journal of Biomechanical Engineering* 126(6), 677-684.
- Bayraktar, H.H., Keaveny, T.M., 2004. A computational investigation of the nonlinear behavior of human trabecular bone. *Transactions of the 12th annual Pre-ORS Symposium on Computational Methods in Orthopaedic Biomechanics*, p. 2.

- Beaupré, G.S., Orr, T.E., Carter, D.R., 1990. An approach for time-dependent bone modeling and remodeling-application: a preliminary remodeling simulation. *Journal of Orthopaedic Research* 8(5), 662–670.
- Ben Boubaker, B., Haussy, B., Ganghoffer, J.F., 2007a. Consideration of the yarn-yarn interactions in meso/macro discrete model of the fabric. Part I: Single yarn behavior. *Mechanics Research Communications* 34(4), 359-370.
- Ben Boubaker, B., Haussy, B., Ganghoffer, J.F., 2007b. Consideration of the yarn-yarn interactions in meso/macro discrete model of the fabric, Part II: Woven fabric under uniaxial and biaxial extension. *Mechanics Research Communications* 34(4), 371-378.
- Ben Boubaker, B., Haussy, B., Ganghoffer, J.F., 2007c. Discrete woven structure model: yarn-on-yarn friction. *Comptes Rendus Mécanique* 335, 150-158.
- Ben Boubaker, B., Haussy, B., Ganghoffer, J.F., 2007d. Discrete models of woven structures. Macroscopic approach. *Composites B* 38(4), 498-505.
- Bensoussan, A., Lions, J.L., Papanicolaou, G., 1978. *Asymptotic Analysis for Periodic Structures*. North Holland, Amsterdam.
- Birmingham, E., Grogan, J.A., Niebur, G.L., McNamara, L.M., McHugh, P.E., 2013. Computational Modelling of the Mechanics of Trabecular Bone and Marrow Using Fluid Structure Interaction Techniques. *Annals of Biomedical Engineering* 41(4), 814–826.
- Boisse, P., Borr, M., Buet, K., Cherouat, A., 1997. Finite element simulations of textile composite forming including the biaxial fabric behaviour. *Composites B* 28(4), 453–464.
- Boisse, P., Gasser, A., Hivet, G., 2001. Analyses of fabric tensile behaviour: determination of the biaxial tension-strain surfaces and their use in forming simulations. *Composites A* 32(10), 1395–1414.
- Boisse, P., Zouari, B., Daniel, J., 2006. Importance of in-plane shear rigidity in finite element analyses of woven fabric composite preforming. *Composites A* 37(12), 2201–2212.
- Boisse, P., Zouari, B., Gasser, A., 2005. A mesoscopic approach for the simulation of woven fibre composite forming. *Composites Science and Technology* 65(3-4), 429–436.
- Bouyge, F., 2000. A multiscale model of cancellous bone. M.S. Thesis, Georgia Institute of Technology.
- Bouyge, F., Jasiuk, I., Boccara, S., Ostoja-Starzewski, M., 2002. A micromechanically based couple-stress model of an elastic orthotropic two-phase composite. *European Journal of Mechanics – A/Solids* 21, 465–481.
- Bouyge, F., Jasiuk, I., Ostoja-Starzewski, M., 2001. A micromechanically based couple-stress model of an elastic two-phase composite. *International Journal of Solids Structures* 38, 1721–1735.
- Bowman, S.M., et al., 1998. Creep contributes to the fatigue behavior of bovine trabecular bone. *Journal of Biomechanical Engineering* 120(5), 647–654.
- Boyde, A., Elliot, J.C., Jones, S.J., 1993. Stereology and histogram analysis of backscattered electron images: age changes in bone. *Bone* 14(3), 205–210.
- Broek, D., 1974. *Elementary fracture mechanics*. Noordhoff.

- Burstein, A.H., Zika, J.M., Heiple, K.G., Klein, L., 1975. Contribution of collagen and mineral to the elastic–plastic properties of bone. *Journal of Bone and Joint Surgery* 57-A(7), 956–961.
- Caillerie, D., Mourad, A., Raoult, A., 2006. Discrete homogenization in graphene sheet modeling. *Journal of Elasticity* 84, 33–68.
- Carter, D.R., Fyhrie, D.P., Whalen, R.T., 1987. Trabecular bone density and loading history: regulation of connective tissue biology by mechanical energy. *Journal of Biomechanics* 20(8), 785–794.
- Carter, D.R., Hayes, W.C., 1976. Bone compressive strength: the influence of density and strain rate. *Science* 194, 1174–1176.
- Carter, D.R., Van der Meulen, M.C.H., Beaupré, G.S., 1996. Mechanical factors in bone growth and development. *Bone* 18, S5–S10.
- Cendre, E., Mitton, D., Roux, J.P., Arlot, M.E., Duboeuf, F., Burt-Pichat, B., Rumelhart, C., Peix, G., Meunier, P.J., 1999. High-Resolution Computed Tomography for Architectural Characterization of Human Lumbar Cancellous Bone: Relationships with Histomorphometry and Biomechanics. *Osteoporosis International* 10(5), 353–360.
- Chen, G., Pettet, G., Pearcy, M., McElwain, D.L.S., 2007. Comparison of two numerical approaches for bone remodeling. *Medical Engineering Physics* 29, 134–139.
- Cosserat, E., Cosserat, F., 1909. *Théorie des Corps Déformables*. A. Hermann et Fils, Paris.
- Cowin, S.C., 1970. An incorrect inequality in micropolar elasticity theory. *Zeitschrift für angewandte Mathematik und Physik ZAMP* 21(3), 494–497.
- Cowin, S.C., Doty, S.B., 2007. *Tissue Mechanics*. Springer, New York.
- Cowin, S.C., Firoozbakhsh, K., 1981. Bone remodeling of diaphysial surfaces under constant load: theoretical predictions. *Journal of Biomechanics* 14(7), 471–484.
- Cowin, S.C., Hegedus, D.H., 1976. Bone remodeling I: theory of adaptive elasticity. *Journal of Elasticity* 6(3), 313–325.
- Cowin, S.C., Van Buskirk, W.C., 1979. Surface bone remodeling induced by a medullary pin. *Journal of Biomechanics* 12(4), 269–276.
- Devries, F., Dumontet, H., Duvaut, G., Lene, F., 1989. Homogenization and damage for composite structures. *International Journal for Numerical Methods in Engineering* 27, 285–298.
- Diamant, I., Shahar, R., Masharawi, Y., Gefen, A., 2007. A method for patient-specific evaluation of vertebral cancellous bone strength: In vitro validation. *Clinical Biomechanics* 22, 282–291.
- Diebels, S., Steeb, H., 2003. Stress and couple stress in foams. *Computational Materials Science* 28 (3–4), 714–722.
- Doblaré, M., Garcia, J.M., 2002. Anisotropic bone remodelling model based on a continuum damage-repair theory. *Journal of Biomechanics* 35(1), 1–17.
- Dos Reis, F., 2010. *Homogenization automatique de milieux discrets périodiques. Applications aux mousses polymères et aux milieux auxétiques* (Ph.D. Thesis). I. N. P. L.
- Dos Reis, F., Ganghoffer, J.F., 2012. Equivalent mechanical properties of auxetic lattices from discrete homogenization. *Computational Materials Science* 51(1), 314–321.

- Duan, Y., Keefe, M., Bogetti, T.A., Powers, B., 2006b. Finite element modeling of transverse impact on a ballistic fabric. *International Journal of Mechanical Sciences* 48(1), 33–43.
- Durville, D., 2002. Modélisation par éléments finis des propriétés mécaniques de structures textiles: de la fibre au tissu. *European Journal of Computational Mechanics* 11, 463–477.
- Eringen, A.C., 1966. Linear theory of micropolar elasticity. *Journal of Mathematics and Mechanics* 15, 909–923.
- Eringen, A.C., 1968. Theory of Micropolar Elasticity, in: Liebowitz, H. (ed.), *Fracture*, Vol. II, Academic Press, New York 621–729.
- Eringen, A.C., 1976. *Continuum Physics – Non-local Field Theories*, Academic Press, New York.
- Eringen, A.C., 1999. *Microcontinuum field theories: I foundations and solids*. Springer Verlag, New York.
- Eringen, A.C., 2001. *Microcontinuum field theories II*. New York: Springer.
- Eswaran, S.K., Gupta, A., Adams, M.F., Keaveny, T.M., 2006. Cortical and trabecular load sharing in the human vertebral body. *Journal of Bone and Mineral Research* 21, 307–314.
- Fatemi J, Onck P.R, Poort, G., Van Keulen, F., 2003. Cosserat moduli of anisotropic cancellous bone: a micromechanical analysis. *Journal de Physique IV France*. 105, 273–280.
- Fatemi, J., van Keulen, F. Onck, P.R., 2002. *Generalized Continuum Theories: Application to Stress Analysis in Bone*. *Meccanica* 37, 385–396.
- Fernandes, P., Rodrigues, H., Jacobs, C., 1999. A model of bone adaptation using a global optimisation criterion based on the trajectorial theory of wolff. *Computer Methods in Biomechanics and Biomedical Engineering* 2(2), 125–138.
- Fernandes, P.R., Folgadoa, J., Jacobsb, C., Pellegrini, V., 2002. A contact model with ingrowth control for bone remodelling around cementless stems. *Journal of Biomechanics* 35, 167–176
- Fernandez, J., Garcia-Aznar, J., Martinez, R., Viano, J., 2010. Numerical analysis of a strain-adaptive bone remodelling problem. *Computer Methods in Applied Mechanics and Engineering* 199(23-24), 1549–1557.
- Field, C., Li, Q., Li, W., Thompson, M., Swain, M., 2012. A comparative mechanical and bone remodelling study of all- ceramic posterior inlay and onlay fixed partial dentures. *Journal of Dentistry* 40(1), 48–56.
- Fish, J., Yu, Q., Shek, K., 1999. Computational damage mechanics for composite materials based on mathematical homogenisation. *International Journal for Numerical Methods in Engineering* 45(11), 1657–1679.
- Ford, C. M., Gibson, L.J., 1998. Uniaxial strength asymmetry in cellular materials: an analytical model. *International Journal of Mechanical Sciences* 40(6), 521–531.
- Ford, C.M., Keaveny, T.M., 1996. The dependence of shear failure properties of trabecular bone on apparent density and trabecular orientation. *Journal of Biomechanics* 29(10), 1309–1317.
- Ford, C.M., Keaveny, T.M., Hayes, W.C., 1996. The effect of impact direction on the structural capacity of the proximal femur during falls. *Journal of Bone and Mineral Research* 11(3), 377–383.

- Forest, S., Dendievel, R., Canova, G.R., 1999. Estimating the overall properties of heterogeneous Cosserat materials. *Modelling and Simulation in Materials Science and Engineering* 7, 829-840.
- Forest, S., Sab, K., 1998. Cosserat overall modeling of heterogeneous materials. *Mechanics Research Communications* 25(4), 449–454.
- Forest, S., Sievert, R., 2006. Nonlinear microstrain theories. *International Journal of Solids and Structures* 43(24), 7224–7245.
- Fridez, P., Rakotomanana, L., Terrier, A., Leyvraz, P.F., 1998. Three dimensional model of bone external adaptation. *Computer Methods in Biomechanics and Biomedical Engineering* 2, 189–196.
- Gadeleta, S.J., Boskey, A.L., Paschalis, E., Carlson, C., Menschik, F., Baldini, T., Peterson, Rimnac, C.M., 2000. A physical, chemical, and mechanical study of lumbar vertebrae from normal, ovariectomized, and nandrolone decanoate-treated cynomolgus monkeys (*Macaca fascicularis*). *Bone* 27(4), 541–550.
- Ganghoffer, J.F., 2010. Mechanical modeling of growth considering domain variation Part II: volumetric and surface growth involving Eshelby tensors. *Journal of the Mechanics and Physics of Solids* 58, 1434-1459.
- Ganghoffer, J.F., 2012. A contribution to the mechanics and thermodynamics of surface growth. Application to bone external remodeling. *International Journal of Engineering Science* 50, 166–191.
- Ganghoffer, J.F., 2013. A kinematically and thermodynamically consistent volumetric growth model based on the stress-free configuration. *International Journal of Solids and Structures* 50, 3446–3459.
- Ganghoffer, J.F., Haussy, B., 2005. Mechanical modeling of growth considering domain variation. Part I: constitutive framework. *International Journal of Solids and Structures* 42 (15), 4311–4337.
- Ganghoffer, J.F., Sokolowski, J., 2014. A micromechanical approach to volumetric and surface growth in the framework of shape optimization. *International Journal of Engineering Science* 74, 207–226.
- Garijo, N., Fernández, J.R., Pérez, M.A., García-Aznar, J.M., 2014. Numerical stability and convergence analysis of bone remodeling model. *Computer Methods in Applied Mechanics and Engineering* 271, 253–268.
- Gefen, A., Portnoy, S., Diamant, S., 2008. Inhomogeneity of tissue-level strain distributions in individual trabeculae: Mathematical model studies of normal and osteoporosis cases. *Medical Engineering & Physics* 30, 624–630.
- Gibson, L. J., 1985, The Mechanical behavior of cancellous bone. *Journal of Biomechanics* 18, 317-328.
- Gibson, L.J., 2005. Biomechanics of cellular solids. *Journal of Biomechanics* 38, 377– 399.
- Gibson, L.J., Ashby, M.F., 1997. *Cellular Solids: Structures and Properties*. Cambridge University Press, Cambridge, U.K.
- Gibson, L.J., Ashby, M.F., Schajer, G.S., Robertson, C.I., 1982. The mechanics of two-dimensional cellular materials. *Proceedings of the Royal Society of London A* 382, 25– 42.

Gitman, I.M., Askes, H., Kuhl, K., Aifantis, E.C., 2010. Stress concentrations in fractured compact bone simulated with a special class of anisotropic gradient elasticity. *International Journal of Solids and Structures* 47, 1099-1107.

Gonella, S., Ruzzene, M., 2008. Homogenization and equivalent in-plane properties of two-dimensional periodic lattices. *International Journal of Solids and Structures* 45, 2897–2915.

Guedes, J.M., Kikuchi, N., 1990. Preprocessing and postprocessing for materials based on the homogenization method with adaptive finite element methods. *Computer Methods in Applied Mechanics and Engineering* 83,143–198.

Guo, X-D. E., McMahon, T.A., Keaveny, T.M., Hayes, W.C., and Gibson, L.J., 1994. Finite element modelling of damage accumulation in trabecular bone under cyclic loading. *Journal of Biomechanics* 27, 145-155.

Hambli, R., 2011. Apparent damage accumulation in cancellous bone using neural networks. *Journal of the Mechanical Behavior of Biomedical Materials* 4(6), 868–878.

Hamila, N., Boisse, P., Sabourin, F., Brunet, M., 2009. A semi-discrete shell finite element for textile composite reinforcement forming simulation. *International Journal for Numerical Methods in Engineering* 79, 1443–1466.

Harrison, N.M., McDonnell, P.F., O'Mahoney, D.C., Kennedy, O.D., O'Brien, F.J., McHugh, P.E., 2008. Heterogeneous linear elastic trabecular bone modelling using micro-CT attenuation data and experimentally measured heterogeneous tissue properties. *Journal of Biomechanics* 41, 2589–2596.

Havill, L.M., Allen, M.R., Bredbenner, T.L., Burr, D.B., Nicoletta, D.P., Turner, C.H., Warren, D.M., Mahaney, M.C., 2010. Heritability of lumbar trabecular bone mechanical properties in baboons. *Bone* 46, 835-840.

Hayes, W.C., Black, D., 1979. Post-yield energy absorption characteristics of trabecular bone. In 1979 Biomechanics Symposium, Van Buskirk, W.C., Ed., ASME, New York,177.

Hazelwood, S.J., Martin, R.B., Rashid, M.M., Rodrigo, J.J., 2001. A mechanistic model for internal bone remodeling exhibits different dynamic responses in disuse and overload. *Journal of Biomechanics* 34, 299–308.

Hearle, J.W.S., Grosberg, P., Baker, S., 1969. *Structural Mechanics of Fibers, Yarns, & Fabrics*. 1, John Wiley & Sons, New York, USA.

Hearle, J.W.S., Potluri, P., Thammandra, V.S., 2001. Modelling fabric mechanics. *Journal of Textile Institute* 92(3, No.1), 53-69.

Hecht, F., Pironneau, O., Le Hyaric, A., Ohtsuka, K., 2005. *FreeFem++ Manual*, downloadable at <http://www.freefem.org>

Hellmich, C., Ulm, F.J., Dormieux, L., 2004. Can the diverse elastic properties of trabecular and cortical bone be attributed to only a few tissue-independent phase properties and their interactions? Arguments from a multiscale approach. *Biomechanics and Modeling in Mechanobiology* 2, 219-238.

Hernandez, C.J., Beaupre, G.S., Carter, D.R., 2000. A model of mechanobiologic and metabolic influences on bone adaptation. *Journal of Rehabilitation Research and Development* 37(2), 235-244.

Hollister, S. J., Kikuchi, N., 1992. A comparison of homogenization and standard mechanics analysis for periodic porous composites. *Computational Mechanics* 10, 73–95.

Hu, J.H., Ding, M., Søballe, K., Bechtold, J.E., Danielsen, C.C., Day, J.S., Hvid, I., 2002. Effects of short-term alendronate treatment on the three-dimensional microstructural, physical, and mechanical properties of dog trabecular bone. *Bone* 31(5), 591-597.

Huiskes, R., Ruimerman, R., van Lenthe, G.H., Janssen, J.D., 2000. Effects of mechanical forces on maintenance and adaptation of form in trabecular bone. *Nature* 405, 704– 706.

Huiskes, R., Weinans, H., Grootenboer, H.J., Dalstra, M., Fudala, B., Slooff, T.J., 1987. Adaptive bone-remodeling theory applied to prosthetic-design analysis. *Journal of Biomechanics* 20,1135–1150.

Ivanov, I., Tabiei, A., 2004. Loosely woven fabric model with viscoelastic crimped fibres for ballistic impact simulations. *International Journal for Numerical Methods in Engineering* 61 (10), 1565–1583.

Jeguirim, S., Fontaine, S., 2008. Internal report, LPMT. Université de Haute-Alsace, Mulhouse, France.

Jeong, J., Abid-Ramezani, H., Al-Mukhtar, M., 2008. Numerical simulation of elastic linear micropolar media based on the pore space length scale assumption. *Strength of materials* 40, 425-438

Jorgensen, C.S., Kundu, T., 2002. Measurement of material elastic constants of trabecular bone: a micromechanical analytic study using a 1 GHz acoustic microscope. *Journal of Orthopaedic Research* 20, 151-158.

Ju, J., 1991. Damage mechanics of composite materials: constitutive modeling and computational algorithms. Technical report, DTIC document.

Kaczmarczyk, L., Pearce, C.J., 2011. Efficient numerical analysis of bone remodelling. *Journal of the Mechanical Behavior of Biomedical Materials* 4, 858–867.

Kanouté, P., Boso, D., Chaboche, J., Schrefler, B., 2009. Multiscale methods for composites: a review. *Archives of Computational Methods in Engineering* 16(1), 31–75.

Kaplan, S., Hayes, W., Stone, J. and Beaupre, G., 1985. Tensile strength of bovine trabecular bone. *Journal of Biomechanics* 18, 723-727.

Karimi, K., Khoei, A.R., 2010. On the analysis of simple shear problem using the micropolar hypoelasticity Cosserat theory. *European Journal of Mechanics - A/Solids* 29 (4), 664– 674.

Kasra, M., Grynias, M.D., 2007. On shear properties of trabecular bone under torsional loading: Effects of bone marrow and strain rate. *Journal of Biomechanics* 40, 2898–2903.

Kato, S., Yoshiro, T., Minami, H., 1999. Formulation of constitutive equations for fabric membranes based on the concept of fabric lattice model. *Engineering Structures* 21, 691–708.

Kawabata, S., Niwa, M., Kawai, H., 1973a. The finite-deformation theory of plain-weave fabrics. Part I: The biaxial-deformation theory. *Journal of the Textile Institute* 64, 21–46.

Kawabata, S., Niwa, M., Kawai, H., 1973b. The finite-deformation theory of plain-weave fabrics. Part II: The uniaxial-deformation theory. *Journal of the Textile Institute* 64, 47–61.

Kawabata, S., Niwa, M., Kawai, H., 1973c. The finite-deformation theory of plain-weave fabrics Part III: The shear-deformation theory. *Journal of the Textile Institute* 64, 62–85.

- Keaveny, T.M., Wachtel, E. F., Ford, C. M. and Hayes, W.C., 1994. Differences between the tensile and compressive strengths of bovine tibial trabecular bone depend on modulus. *Journal of Biomechanics* 27, 1137-1146.
- Keaveny, T.M., Pinilla, T.P., Crawford, R.P., Kopperdahl, D.L, Lou, A., 1997. Systematic and random errors in compression testing of trabecular bone. *Journal of Orthopaedic Research* 15(1), 101-110.
- Kim, H.S., Al-Hassani, S.T.S., 2002. A morphological model of vertebral trabecular bone. *Journal of Biomechanics* 35, 1101–1114.
- King, M.J., Jearanaisilawong, P., Socrate, S., 2005. A continuum constitutive model for the mechanical behavior of woven fabrics. *International Journal of Solids and Structures* 42, 3867–3896.
- Koiter, W.T., 1964. Couple stress in the theory of elasticity. *Proceeding of the Koninklijke Nederland Akademie van Wetenschappen B-67*, 17–44.
- Kopperdahl, D.L., Keaveny, T.M., 1998. Yield strain behavior of trabecular bone. *Journal of Biomechanics* 31, 601-608.
- Kopperdahl, D.L., Morgan, E.F., Keaveny, T.M., 2002. Quantitative computed tomography estimates of the mechanical properties of human vertebral trabecular bone. *Journal of Orthopaedic Research* 20, 801–805.
- Kowalczyk, P., 2010. Simulation of orthotropic microstructure remodelling of cancellous bone. *Journal of Biomechanics* 43, 563–569.
- Kuhl, E., Menzel, A., Steinmann, P., 2003. Computational modeling of growth. *Computational Mechanics* 32:71–88.
- Lacroix, D., Prendergast, P.J., 2002. A mechano-regulation model for tissue differentiation during fracture healing: analysis of gap size and loading. *Journal of Biomechanics* 35, 1163–1171.
- Lai, W.M., Rubin, D., Krempl, E., 1993. *Introduction to continuum mechanics*. New York: Pergamon Press.
- Lakes R., 1993. Materials with structural hierarchy. *Nature* 361, 511– 515.
- Lakes, R. S., 1986. Experimental microelasticity of two porous solids. *International Journal of Solids and Structures* 22, 55-63.
- Lakes, R., 1995. Experimental methods for study of Cosserat elastic solids and other generalized elastic continua. In: Muhlhaus, H-B. (ed.), *Continuum Models for Materials with Microstructure*, Wiley, New York 1–22.
- Lakes, R., Nakamura, S., Behiri, J., Bonfield, W., 1990. Fracture mechanics of bone with short cracks. *Journal of Biomechanics* 23, 967–975.
- Lee, T.C., Noelke, L., McMahon, G.T., Mulville, J.P., Taylor, D., 1999. Functional adaptation in bone. in: Pedersen, P. and Bendsoe, M.P. (eds), *Synthesis in Bio Solid Mechanics* , Kluwer Academic Publishers, Dordrecht, 1–10.
- Lemaitre, J., 1984. How to Use Damage Mechanics. *Nuclear Engineering and Design* 80, 233-245.
- Lemaitre, J., Chaboche, J.L., 1978. Aspect Phenomenologique de la Rupture par Endommagement. *Journal de Mécanique Appliquée* 2, 317-365.

- Levenston, M.E., Carter, D.R., 1998. An energy dissipation- based model for damage stimulated bone adaptation. *Journal of Biomech* 31, 579–586.
- Liu, X.S., Zhang, X.H., Guo, X.E., 2009. Contributions of trabecular rods of various orientations in determining the elastic properties of human vertebral trabecular bone. *Bone* 45, 158-163.
- Lomov, S., Ivanov, D., Verpoest, I., Zako, M., Kurashiki, T., Nakai, H., Hirosawa, S., 2007. Meso-FE modelling of textile composites: Road map, data flow and algorithms. *Composites Science and Technology* 67, 1870-1891.
- Lorenzetti, S.R., 2006. New method to determine the Young's modulus of single trabeculae (Ph.D. Thesis). Rutgers University, Swiss Federal Institute of Technology.
- Lotz, J.C., Cheal, E.J., Hayes, W.C., 1991. Fracture prediction for the proximal femur using finite element models: Part I-Linear analysis. *Journal of Biomechanical Engineering* 113, 353-360.
- Ma, H.M., Gao, X.-L., Reddy, J.N., 2008. A microstructure-dependent Timoshenko beam model based on a modified couple stress theory. *Journal of the Mechanics and Physics of Solids* 56, 3379–3391.
- Majid, T., Manzari, 2004. Application of micropolar plasticity to post failure analysis in geomechanics. *International Journal for Numerical and Analytical Methods in Geomechanics* 28 (10), 1011–1032.
- Martin, R.B., 1992. A theory of fatigue damage accumulation and repair in cortical bone. *Journal of Orthopaedic Research* 10, 818-825.
- Martin, R.B., 1995. Mathematical model for repair of fatigue damage and stress fracture in osteonal bone. *Journal of Orthopaedic Research* 13(3), 309-16.
- Masters, I.G., Evans, K.E., 1996. Models for the elastic deformation of honeycombs. *Composite Structures* 35, 403–422.
- McDonald, K., Little, J., Percy, M., Adam, C., 2010. Development of a multi-scale finite element model of the osteoporotic lumbar vertebral body for the investigation of apparent level vertebra mechanics and micro-level trabecular mechanics. *Medical Engineering & Physics* 32, 653–661.
- McNamara, B.P., Prendergast, P.J., Taylor, D., 1992. Prediction of bone adaptation in the ulnar-osteotomized sheep's forelimb using an anatomical finite element model. *Journal of Biomedical Engineering* 14, 209–216.
- McNamara, L. M., Prendergast, P.J., 2007. Bone remodelling algorithms incorporating both strain and microdamage stimuli. *Journal of Biomechanics* 40, 1381–1391.
- Miller, L.M., Little, W., Schirmer, A., Sheik, F., Busa, B., Judex, S., 2007. Accretion of bone quantity and quality in the developing mouse skeleton. *Journal of Bone and Mineral Research* 1037–1045.
- Miller, Z., Fuchs, M.B., 2005. Effect of trabecular curvature on the stiffness of trabecular bone. *Journal of Biomechanics* 38, 1855-1864.
- Mindlin, R.D. and Tiersten, H.F., 1962. Effects of couple stresses in linear elasticity. *Archive for Rational Mechanics and Analysis* 11, 415–448.

- Mindlin, R.D., 1963. Influence of couple-stresses on stress concentrations. *Experimental Mechanics* 3,1-7.
- Mindlin, R.D., 1964. Micro-structure in linear elasticity. *Archive for Rational Mechanics and Analysis* 16, 51–78.
- Morgan, E.F., Bayraktar, H.H., Keaveny, T.M., 2003. Trabecular bone modulus-density relationships depend on anatomic site. *Journal of Biomechanics* 36, 897-904 .
- Morgan, E.F., Keaveny, T.M., 2001. Dependence of yield strain of human trabecular bone on anatomic site. *Journal of Biomechanics* 34, 569–577.
- Mori, S. and Burr, D.B., 1993. Increased intracortical remodelling following fatigue damage. *Bone* 14, 103–109.
- Mosekilde, Li., 1988. Age-related changes in vertebral trabecular bone architecture—assessed by a new method. *Bone* 9, 247–250.
- Mosekilde, Li., 1989. Sex differences in age-related loss of vertebral trabecular bone mass and structure—biomechanical consequences. *Bone* 10, 425–432.
- Mourad, A., 2003. Description topologique de l'architecture fibreuse et modelisation mecanique du myocarde (Ph.D. thesis). I.N.P.L. Grenoble.
- Mourad, A., Caillerie, D.A., Raoult, A., 2003. A nonlinearly elastic homogenized constitutive law for the myocardium. *Computational Fluid and Solid Mechanics* 2, 1779-1781.
- Muhlhaus, H.B., Oka, F., 1996. Dispersion and wave propagation in discrete and continuous models for granular materials. *International Journal of Solids and Structures* 33, 2841–2858.
- Mulder, L., Koolstra, J.H., den Toonder, J.M.J., van Eijden, T.M.G.J., 2008. Relationship between tissue stiffness and degree of mineralization of developing trabecular bone. *Journal of Biomedical Materials Research A* 84(2) 508–515.
- Nawathe, S., Juillard, F., Keaveny, T.M., 2013. Theoretical bounds for the influence of tissue-level ductility on the apparent-level strength of human trabecular bone. *Journal of Biomechanics* 46(7), 1293-1299.
- Negus, C., Impelluso, T., 2007. Continuum remodeling revisited. *Biomechanics and Modeling in Mechanobiology* 6(4), 211–226.
- Ng, S., Tse, P., Lau, K., 1998. Numerical and experimental determination of the in-plane elastic properties of 2/2 Twill weave fabric composites. *Composites B* 29, 735–744.
- Niebur, G.L., Feldstein, M.J., Yuen, J.C., Chen, T.J., & Keaveny, T.M., 2000. High-resolution finite element models with tissue strength asymmetry accurately predict failure of trabecular bone. *Journal of Biomechanics* 33, 1575–1583.
- Niebur, G.L., Yuen, J.C., Hsia, A.C., Keaveny, T.M., 1999. Convergence behavior of high-resolution finite element models of trabecular bone. *Journal of Biomechanical Engineering* 121(6),629–635.
- Nunziato, J.W., Cowin, S.C., 1979. A nonlinear theory of elastic materials with voids. *Archive for Rational Mechanics and Analysis* 72(2), 175–201.
- Oliveira, J.A., Pinho-da-Cruz, J., Teixeira-Dia, F., 2009. Asymptotic homogenisation in linear elasticity. Part II: Finite element procedures and multiscale applications. *Computational Materials Science* 45, 1081–1096.

- Onck, P. R., Andrews, E., Gibson, L.J., 2001. Size effects in ductile cellular solids. Part I: modeling. *International Journal of Mechanical Sciences* 43, 681-699.
- Ostoja-Starzewski, M., Boccara, S., Jasiuk, I., 1999. Couple-stress moduli and characteristic length of composite materials. *Mechanics Research Communications* 26(4), 387-397.
- Overaker, D.W., 1997. Micromechanical modeling of open cell structures with application in finite element analysis of vertebral body mechanics (Ph.D. Thesis). Rutgers University.
- Panasenko, G.P., 1983. Averaging of processes in frame constructions with random properties. *Zh. Vychisl. Mat. Mat. Fiz.* 23, 1098–1109.
- Park, H.C., Lakes, R.S., 1987. Torsion of a micropolar elastic prism of square cross section. *International Journal of Solids and Structures* 23, 485–503.
- Parsons, E. M., Weerasooriya, T., Sarva, S. and Socrate, S., 2010. Impact of woven fabric: Experiments and mesostructure-based continuum-level simulations. *Journal of the Mechanics and Physics of Solids* 58, 1995-2021.
- Peirce, F.T., 1937. The geometry of cloth structure. *Journal of the Textile Institute* 28 (T45), 43-77.
- Peng, X. Cao, J., 2005. A continuum mechanics-based non-orthogonal constitutive model for woven composite fabrics. *Composites A* 36, 859–874.
- Peng, X., Cao, J., 2000. Numerical determination of mechanical elastic constants of textile composites. 15th Annual Technical Conference of the American Society for Composites, College Station TX, Sept., 677–688.
- Peng, X., Cao, J., 2002. A dual homogenization and finite element approach for material characterization of textile composites. *Composites B* 33, 45–56.
- Pradel, F. 1998. Homogénéisation des milieux discrets périodiques orientés. Une application aux mousses (Ph.D. Thesis). Ecole Nationale des Ponts et Chaussées, Champs-sur-Marne.
- Pradel, F., Sab, K., 1998. Cosserat modelling of elastic periodic lattice structures. *Comptes Rendus de l'Académie des Sciences - Series IIB - Mechanics-Physics-Astronomy* 326, 699–704.
- Prendergast, J., Huiskes, R., 1995. Mathematical modeling of microdamage in bone remodeling and adaptation, in: A. Odgaard, H. Weinans (Eds.), *Bone Structure and Remodeling, Recent Advances in Human Biology 2*, World Scientific, Singapore, 213–223.
- Prendergast, P.J., Taylor, D., 1994. Prediction of bone adaptation using damage accumulation. *Journal of Biomechanics* 27, 1067–1076.
- Qin, Y.X., Rubin, C.T., McLeod, K.J., 1998. Nonlinear dependence of loading intensity and cycle number in the maintenance of bone mass and morphology. *Journal of Orthopaedic Research* 16, 482–489.
- Ramtani, S., Zidi, M., 1999. Damaged-bone remodeling theory: thermodynamical approach. *Mechanics Research Communications* 26(6), 701–708.
- Ramtani, S., Zidi, M., 2001. A theoretical model of the effect of continuum damage on a bone adaptation model. *Journal of Biomechanics* 34, 471–479.
- Ramtani, S., Zidi, M., 2002. Damaged-bone adaptation under steady homogeneous stress. *Journal of Biomechanical Engineering* 124(3), 322-7.

- Rao, S.S., 2007. *Vibration of continuous systems*. Hoboken, New Jersey: John Wiley & Sons, Inc.
- Raoult, A., Caillerie, D., Mourad, A., 2008. Elastic lattices: equilibrium, invariant laws and homogenization. *Ann. Univ. Ferrara* 54, 297–318.
- Rattensperger, H., Eberhardsteiner, J., Mang, H.A., 2003. Numerical investigation of high pressure hydraulic hoses with steel wire braid. In: *Proceedings of the IUTAM Symposium on Computational Mechanics of Solid Materials at Large Strains* 407–416.
- Realff, M.L., 1992. *Mechanical properties of fabrics woven from yarns produced by different spinning technologies* (Ph.D. Thesis). Massachusetts Institute of Technology.
- Realff, M.L., Boyce, M.C., Backer, S., 1997. A micromechanical model of the tensile behavior of woven fabric. *Textile Research Journal* 67, 445–459.
- Rho, J.Y., Hobatho, M.C, Ashman, R.B., 1995. Relations of mechanical properties to density and CT numbers in human bone. *Medical Engineering & Physics* 17, 347-355.
- Ritchie, R.O., Buehler, M.J., & Hansma, P., 2009. Plasticity and toughness in bone. *Physics Today* 62(6), 41–47.
- Rodriguez, E.K., Hoger, A., McCulloch, A.D., 1994. Stress-dependent finite growth in soft elastic tissues. *Journal of Biomechanics* 27(4), 455–467.
- Roschger, P., Fratzl, P., Klaushofer, K., Rodan, G., 1997. Mineralization of cancellous bone after alendronate and sodium fluoride treatment: a quantitative backscattered electron imaging study on minipig ribs. *Bone* 20(5), 393–397.
- Rovati, M., Veber, D., 2007. Optimal topologies for micropolar solids. *Structural and Multidisciplinary Optimization* 33, 47–59.
- Sab, K., 1996. Déformations microscopiques et macroscopiques dans un assemblage dense de particules rigides. *C. R. Acad. Sci. Paris, Ser. Iib* 322, 715–721.
- Sab, K., Pradel, F., 2009. Homogenisation of periodic Cosserat media. *International Journal of Computer Applications in Technology* 34, 60–71.
- Sagar, T.V, Potluri, P, Hearle, J.W.S, 2003. Mesoscale modelling of interlaced fibre assemblies using energy method. *Computational Materials Science* 28(1), 49-62.
- Sanchez-Palencia, E., 1980. *Non-homogeneous media and vibration theory*. Springer, Berlin.
- Sanz-Herrera, J., Garcia-Aznar, J., Doblaré, M., 2009. On scaffold designing for bone regeneration: a computational multiscale approach. *Acta Biomaterialia* 5(1), 219–229.
- Shahkarami, A., Vaziri, R., 2007. A continuum shell finite element model for impact simulation of woven fabrics. *International Journal of Impact Engineering* 34, 104–119.
- Shi, X., Liu, X.S., Wang, X., Guo, X.E., Niebura, G.L., 2011. Type and orientation of yielded trabeculae during overloading of trabecular bone along orthogonal directions. *Journal of Biomechanics* 43(13), 2460–2466.
- Shmoylova, E., Potapenko, S., Rothenburg, L., 2007. Stress distribution around a crack in plane micropolar elasticity. *Journal of Elasticity* 86, 19–39.
- Shockey, D.A., Elrich, D.C., Simons, J.W., 1999a. *Improved Barriers to Turbine Engine Fragments: Interim Report I*. DOT/FAA AR-99/8,I.
- Shockey, D.A., Elrich, D.C., Simons, J.W., 1999b. *Improved Barriers to Turbine Engine Fragments: Interim Report II*. DOT/FAA AR-99/8,II.

- Shockey, D.A., Elrich, D.C., Simons, J.W., 2001. Improved Barriers to Turbine Engine Fragments: Interim Report III. DOT/FAA AR-99/8,III.
- Silva, M. J., Gibson, L.J., 1997. Modeling the Mechanical Behavior of Vertebral Trabecular Bone: Effects of Age-Related Changes in Microstructure. *Bone* 21, 191-199.
- Silva, M.J., Hayes, W.C., Gibson, L.J., 1995. The effects of non-periodic microstructure on the elastic properties of two-dimensional cellular solids. *International Journal of Mechanical Sciences* 37, 1161–1177.
- Stefanou, I., Sulem, J., 2010. Continuum modeling of discontinuous rock structures, Homogenization of discrete particle assemblies. *European Journal of Environmental and Civil Engineering* 14 (8–9), 1199–1217.
- Stronge, W.J., Yu, T.X., 1993. *Dynamic models for structural plasticity*. London: Springer-Verlag.
- Suiker, A.S.J., de Borst, R., Chang, C.S., 2001. Micro-mechanical modelling of granular material. Part 1: Derivation of a secondgradient micro-polar constitutive theory. *Acta Mechanica* 149, 161–180.
- Tabiei, A., Yi, W., 2002. Comparative study of predictive methods for woven fabric composite elastic properties. *Composite Structures* 58, 149–164.
- Talebi, H., Wong, S.V., Hamouda, A.M.S., 2009. Finite element evaluation of projectile nose angle effects in ballistic perforation of high strength fabric. *Composite Structures* 87 (4), 314–320.
- Tanaka, M., Adachi, T., 1999. Lattice continuum model for bone remodeling considering microstructural optimality of trabecular architecture. In: Pedersen, P. and Bendsoe, M.P. (eds), *IUTAM Symposium on Synthesis in Bio Solid Mechanics*, Kluwer Academic Publishers, The Netherlands, 43–54.
- Tanov, R.R., Brueggert, M., 2003. Finite element modeling of non-orthogonal loosely woven fabrics in advanced occupant restraint systems. *Finite Elements in Analysis and Design* 39, 357–367.
- Taylor, D., Hazenberg, J.G., Lee, T.C., 2007. Living with cracks: damage and repair in human bone. *Nature materials* 6(4), 263-268.
- Taylor, M., Cotton, J., Zioupos, P., 2002. Finite Element Simulation of the Fatigue Behaviour of Cancellous Bone. *Meccanica* 37, 419–429.
- Tekoglu, C. and Onck, P.R., 2008. Size effects in two-dimensional Voronoi foams: a comparison between generalized continua and discrete models. *Journal of the Mechanics and Physics of Solids* 56, 3541–3564.
- Tolentino, A., Murakami, H., 1987. A high-order mixture model for periodic particulate composites. *International Journal of Solids and Structures* 23, 989–1002.
- Tollenaere, H., Caillerie, D., 1998. Continuous modeling of lattice structures by homogenization. *Advances in Engineering Software* 29, 699–705.
- Townsend, P.R., Rose, R.M., Radin, E.L., 1975. Buckling studies of single human trabeculae. *Journal of Biomechanics* 8, 199-201.

- van der Lindena, J.C., Birkenhager-Frenkelb, D.H., Verhaara, J.A.N., Weinans, H., 2001. Trabecular bone's mechanical properties are affected by its non-uniform mineral distribution. *Journal of Biomechanics* 34, 1573–1580.
- van der Meulen, M.C.H., Beaupré, G.S., Carter, D.R., 1993. Mechanobiologic influences in long bone crosssectional growth. *Bone* 14, 635–642.
- van Eijden, T.M.G.J., van Ruijven, L.J., Giesen, E.B.W., 2004. Bone tissue stiffness in the mandibular condyle is dependent on the direction and density of the cancellous structure. *Calcified Tissue International* 75, 502–508.
- van Rietbergen, B., Weinans, H., Huiskes, R., Odgaard, A., 1995. A new method to determine trabecular bone elastic properties and loading using micromechanical finite-element models. *Journal of Biomechanics* 28, 69–81.
- Wagner, D.W., Lindsey, D.P., Beaupre, G.S., 2011. Deriving tissue density and elastic modulus from microCT bone scans. *Bone* 49 (5), 931–938.
- Wang, X., Guyette, J., Liu, X., Roeder, R.K., Niebur, G.L., 2005. Axial-shear interaction effects on microdamage in bovine tibial trabecular bone. *European Journal of Morphology* 42(1-2), 61-70.
- Wang, C., Han, J., Li, Q., Wang, L., Fan, Y., 2012. Simulation of bone remodelling in orthodontic treatment. *Computer Methods in Biomechanics and Biomedical Engineering* 17(9), 1042-50.
- Wang, C., Zhang C., Han J., Wu H., Fan Y., 2011. Simulated evolution of the vertebral body based on basic multicellular unit activities. *Journal of Bone and Mineral Metabolism* 29(4), 466-76.
- Wang, X.L., Stronge, W.J., 2001. Micropolar theory for a periodic force on the edge of elastic honeycomb. *International Journal of Engineering Sciences* 39 (7), 821–50.
- Warren, W.E., Kraynik, A.M., 1987. Foam mechanics: the linear elastic response of two dimensional spatially periodic cellular materials. *Mechanics of Materials* 6, 27–37.
- Watzky, A., Naili, S., 2004. Orthotropic bone remodeling: case of plane stresses. *Mechanics Research Communications* 31, 617–625.
- Weinans, H., Huiskes, R., Grootenboer, H.J., 1992. The behavior of adaptive bone-remodeling simulation-models. *Journal of Biomechanics* 25, 1425–1441.
- Weiss, L., Ed., 1988. *Cell and Tissue Biology. A Textbook of Histology*, Urban and Schwarzenberg, Baltimore.
- Wolff, J., 1892. *Das Gesetz transformation der Knochen*. Berlin: Hirschwald Verlag.
- Wolframa, U., Wilke, H.-J., Zysset, P.K., 2010. Valid μ finite element models of vertebral trabecular bone can be obtained using tissue properties measured with nanoindentation under wet conditions. *Journal of Biomechanics* 43, 1731–1737.
- Xue, P., Cao, J. Chen, J., 2005. Integrated micro/macro-mechanical model of woven fabric composites under large deformation. *Composite Structures* 70, 69-80.
- Xue, P., Peng, X., Cao, J., 2003. A non-orthogonal constitutive model for characterizing woven composites. *Composites A* 34, 183–193.
- Yang, F., Chong, A.C.M., Lam, D.C.C, Tong, P., 2002. Couple stress based strain gradient theory for elasticity. *International Journal of Solids and Structures* 39(10) 2731–2743.

- Yang, J.F.C., Lakes, R.S., 1981. Transient study of couple stress effects in compact bone: Torsion. *Journal of Biomechanical Engineering* 103, 275–279.
- Yeh, O.C., Keaveny, T.M., 1999. Biomechanical effects of intra-specimen variations in trabecular architecture: a three-dimensional finite element study. *Bone* 25, 223-228.
- Yoo, A., Jasiuk, I., 2006. Couple-stress moduli of a trabecular bone idealized as a 3D periodic cellular network. *Journal of Biomechanics* 39, 2241-2252.
- Zhang, G.M., Batra, R.C., Zheng, J., 2008. Effect of frame size, frame type, and clamping pressure on the ballistic performance of soft body armor. *Composites B* 39 (3), 476–489.
- Zhu, H.X., 2010. Size-dependent elastic properties of micro- and nanohoneycombs. *Journal of the Mechanics and Physics of Solids* 58, 679–696.
- Zhu, H.X., Hobdell, J.R., Windle, A.H., 2001. Effects of cell irregularity on the elastic properties of 2D Voronoi honeycombs. *Journal of the Mechanics and Physics of Solids* 49, 857–870.

Title

Micromechanical models of network materials presenting internal length scales: applications to trabecular bone under stable and evolutive conditions.

Abstract

A methodology based on micromechanics has been developed to determine the effective behavior of network materials endowed with a discrete architecture at the microscopic level. It relies on the discrete homogenization method, which has been applied to textile monolayers and trabecular bones. The initially discrete topology of the considered network materials results after homogenization at the mesoscopic level in anisotropic micropolar effective continuum, which proves able to capture the observed internal scale effects. Such micromechanical methods are useful to remedy the difficulty to measure the effective mechanical properties at the intermediate mesoscopic level scale. The bending and torsion responses of vertebral trabecular bone beam specimens are formulated in both static and dynamic situations, based on the Cosserat theory. 3D models have been developed for describing the multiaxial yield and brittle fracture behavior of trabecular bone, including the analysis of size-dependent non-classical plastic yield. We have constructed by FE analyses a homogeneous, orthotropic couple-stress continuum model as a substitute of the 3D periodic heterogeneous cellular solid model of vertebral trabecular bone, based on the equivalent strain energy approach. Bone tissues are able to adapt their local density and load bearing capacities as well as their size and shape to mechanical stimuli. We have developed models for combined internal and external bone remodeling in the framework of the thermodynamics of irreversible processes, at both the cellular and macroscopic levels. We lastly combined anisotropic internal remodeling with fatigue continuum damage.

Key words: Bone mechanics; cellular solids; discrete homogenization; effective properties; size effects; generalized continua; bone remodeling; bone damage; brittle and plastic collapse.

Titre

Modèles micromécaniques de milieux architecturés présentant des longueurs internes: applications à l'os trabéculaire en conditions stables et évolutives.

Résumé

Des méthodes micromécaniques spécifiques ont été développées pour la détermination du comportement effectif de matériaux cellulaires dotés d'une architecture discrète à l'échelle microscopique. La méthode d'homogénéisation discrète a été appliquée à des structures tissées monocouches ainsi qu'à l'os trabéculaire. La topologie discrète initiale de ces milieux est remplacée à l'échelle mésoscopique par un milieu effectif anisotrope micropolaire, qui rend compte des effets d'échelles observés. Ces méthodes d'homogénéisation permettent d'accéder à des propriétés classiques et non classiques dont la mesure expérimentale est souvent difficile. Des modèles 3D ont été développés afin de décrire la rupture fragile et ductile de l'os trabéculaire, incorporant des effets de taille des surfaces d'écoulement plastique. Nous avons construit par des analyses éléments finis de la microstructure de l'os trabéculaire un milieu de substitution 3D homogène, orthotrope de type couple de contraintes, sur la base d'une équivalence en énergie. Les tissus osseux ont la capacité d'adapter leur densité locale et leur taille et forme aux stimuli mécaniques. Nous avons développé des modèles de remodelage interne et externe dans le cadre de la thermodynamique des processus irréversibles, aux échelles cellulaire et macroscopique. Finalement, le remodelage interne anisotrope a été couplé à l'endommagement de fatigue, dans le cadre de la théorie continue de l'endommagement.

Mots-clés: Mécanique de l'os; milieux cellulaires; homogénéisation discrète; propriétés effectives; effets de taille; milieux continus généralisés; remodelage osseux; endommagement; rupture fragile et ductile.